ice
Institution of Civil Engineers
publishing

Partial Saturation in Compacted Soils

Géotechnique Symposium in Print 2011

Edited by

Domenico Gallipoli

Chair, Géotechnique Symposium in Print 2011 sub-committee

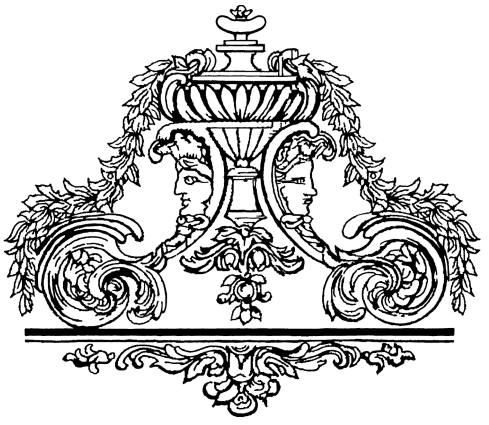

ISBN 978-0-7277-5775-3

Typeset by Keytec Typesetting Ltd, Bridport Dorset
Printed and bound in Great Britain by CPI Group (UK) Ltd, Croydon, CR0 4YY

Preface

This book contains the proceedings of the *Géotechnique* Symposium-in-Print 2011, which was held on the theme of *Partial Saturation in Compacted Soils* at the Institution of Civil Engineers on 20 June 2011. The Symposium attracted around 70 delegates, from both industry and academia, representing countries such as Australia, Czech Republic, France, Hong Kong, Italy, New Zealand, Portugal, Spain, Switzerland and UK.

The book contains the two keynote addresses delivered by Prof. Eduardo Alonso and Mr Tony O'Brien, respectively, together with the nine papers and one technical note published in the April and May 2011 issues of *Géotechnique* and presented by authors during the Symposium. These nine papers and one technical note were selected, following standard *Géotechnique* peer-review, from a total of 98 articles offered in response to a thematic call in the summer 2009. They are grouped in this book under four topics corresponding to the four Symposium sessions, namely *Material Characterization*, *Experimental Observation and Modelling*, *Benchmarking of Techniques and Models,* and *Application to Engineering Problems and Case Studies*. The book also contains a selection of questions posed by delegates after presentations during the Symposium, together with relative answers by presenters.

The idea of devoting the 16th *Géotechnique* Symposium-in-Print to the theme of *Partial Saturation in Compacted Soils* was instigated by recent advances in the study of geomaterials with multiphase or immiscible pore fluids. One application of this study relates to the design and analysis of earth structures/fills (e.g. dams and embankments, clay barriers) made of compacted soils that are unsaturated at the time of placement (i.e. pores are partly filled by water and partly filled by air). Unlike saturated soils whose pores are entirely filled by water, the presence of two immiscible pore fluids gives rise in unsaturated soils to capillary actions on the solid skeleton that affect both deformation and strength. During service life, the compacted soil will alternate between unsaturated and saturated conditions, or remain permanently unsaturated, depending on prevailing environmental actions.

Some key engineering properties of compacted soils (e.g. strength, stiffness and permeability) depend on current moisture content, which will change as a consequence of the interaction with the surrounding environment. It is therefore not surprising that, since the early 30s, civil engineers have devoted considerable effort to the study of unsaturated compacted soils. Ralph Proctor, from the Los Angeles Bureau of Waterworks and Supplies in the USA, performed a wide laboratory campaign of compaction tests on more than 200 soils, driven by the necessity of developing suitable construction protocols to maximise stability and minimize permeability of earth dams. This resulted in the definition of the 'optimum moisture content', i.e. the water content that produces the highest soil dry density for a given compaction effort.

Today, routine geotechnical design still relies on Proctor's definition of optimum water content. Nevertheless, modern experimental techniques, such as Environmental Scanning Electron Microscopy or Mercury Intrusion Porosimetry, have provided new insight into the link between stress-strain behaviour and material fabric in compacted soils. Some of the contributions in this book emphasize the 'living nature' of soil fabric, which evolves during wetting–drying cycles and induces corresponding changes of macroscopic mechanical properties over time.

Significant improvements of design practice have often originated from the formulation of general constitutive laws and principles of soil behaviour, underpinned by an understanding of material properties at the microscopic scale. During recent years, engineers and scientists have advanced fundamental knowledge of mechanical and retention behaviour of compacted soils; however, this research momentum must be sustained over time to achieve the detailed understanding of soil behaviour which is essential to produce a step change in geotechnical models and a leap in analytical capabilities.

As highlighted by some of the contributions in this book, there are still significant challenges ahead for unsaturated soil modellers. As already known from saturated soil mechanics, the accurate prediction of irreversible volumetric strains during shearing is a particularly arduous task for constitutive modellers and well-known saturated models, such as Modified Cam-Clay, significantly overestimate volumetric strains at critical state. This assumes even greater significance in unsaturated soils where water retention behaviour is intrinsically linked to volumetric straining. In this case, any error in the calculation of volumetric strains will have an impact on the computed water retention response, i.e. on the predicted variation of degree of saturation and on its effect on strength and deformation.

Moreover, the sensitivity of predictions to parameter calibration poses an additional challenge to engineers wishing to apply unsaturated models to practical problems. The adoption of different strategies in selecting parameter values, even for the same model and from the same set of experimental data, can result in different computations of soil behaviour, partly because of the large number of parameters involved. This raises doubts about the usefulness of developing ever more sophisticated constitutive laws without proposing, at the same time, robust methods for parameter calibration.

The book also includes results from two benchmark exercises undertaken by several European Universities within the "Marie Curie" Research Training Network MUSE (Mechanics of Unsaturated Soils for Engineering). A salient activity of the MUSE Network has been the comparison of experimental/modelling techniques used by researchers across the world. This activity had the twofold objective of improving current procedures and, where possible, formulating accepted standards. In this spirit, these two benchmarks make use of easily accessible data or commercially available materials so that they can be readily repeated by other researchers.

I would like to thank all members of the Symposium subcommittee, namely Eduardo Alonso, Lennart Borgesson, Federica Cotecchia, Pierre Delage, Cristina Jommi, Claudio

Mancuso, John McDougall, Andrew Ridley, Tom Schanz, Alessandro Tarantino, David Toll and Simon Wheeler, for their contribution in organizing the Symposium and reviewing manuscripts within a very tight timescale. I would also like to thank the *Géotechnique Advisory Panel*, and in particular the then Chairman, Prof. Chris Clayton, for supporting the proposal of a *Géotechnique* Symposium-in-Print on the theme of *Partial Saturation in Compacted Soils* and for their continued help throughout the organization.

This book provides a comprehensive overview of recent advances in the fast growing area of unsaturated soil mechanics, ranging from material testing to modelling and analysis of engineering boundary value problems. This knowledge will contribute to improve design of earth structures/fills by maximizing the use of locally sourced soils, with consequent gains in safety, cost and sustainability of future building practice. I wish you enjoyable reading and hope that this volume will become a valuable reference for engineers and researchers in future years.

Domenico Gallipoli
Chair, Géotechnique Symposium-in-Print 2011

Contents

Preface iii

Keynote speeches

Compacted soil behaviour: initial state, structure and constitutive modelling 3
E.E. Alonso, N.M. Pinyol and A. Gens

The assessment of old railway embankments - time for a change? 19
A.S. O'Brien

Session 1: Material Characterisation

Papers

Effects of the maximum soil aggregates size and cyclic wetting-drying on the stiffness of a lime-treated clayey soil 35
A.M. Tang, M.N. Vu and Y.-J. Cui

Technical Note

Some aspects of the behaviour of compacted soils along wetting paths 45
S. Taibi, J.M. Fleureau, N. Abou-Bekr, M.I. Zerhouni, A. Benchouk, K. Lachgueur and H. Souli

Session 2: Experimental Observation and Modelling

Papers

An insight into the water retention properties of compacted clayey soils 55
E. Romero, G. Della Vecchia and C. Jommi

Hydromechanical behaviour of compacted granular expansive mixtures: experimental and constitutive study 71
E.E. Alonso, E. Romero and C. Hoffmann

Experimental observations of the stress regime in unsaturated compacted clay when laterally confined 87
J.L. Boyd and V. Sivakumar

Session 3: Benchmarking of Techniques and Models

Papers

Benchmark of constitutive models for unsaturated soils 109
F. D'Onza, D. Gallipoli, S. Wheeler, F. Casini, J. Vaunat, N. Khalili, L. Laloui, C. Mancuso, D. Mašín, M. Nuth, J.-M. Pereira and R. Vassallo

Benchmark of experimental techniques for measuring and controlling suction 129
A. Tarantino, D. Gallipoli, C.E. Augarde, V. De Gennaro, R. Gomez, L. Laloui, C. Mancuso, G. El Mountassir, J.J. Munoz, J.-M. Pereira, H. Peron, G. Pisoni, E. Romero, A. Raveendiraraj, J.C. Rojas, D.G. Toll, S. Tombolato and S. Wheeler

Session 4: Application to Engineering Problems and Case Studies

Papers

Hydromechanical behaviour of a heterogeneous compacted soil: experimental observations and modelling 141
A. Gens, B. Valleján, M. Sánchez, C. Imbert, M.V. Villar and M. Van Geet

Modelling the response of Lechago earth and rockfill dam 161
E.E. Alonso, S. Olivella, A. Soriano, N.M. Pinyol and F. Esteban

Physical modelling of wetting-induced collapse in embankment base 183
L. Thorel, V. Ferber, B. Caicedo and I.M. Khokhar

Selected Questions and Answers 195

ice
Institution of Civil Engineers
publishing

Keynote Speeches

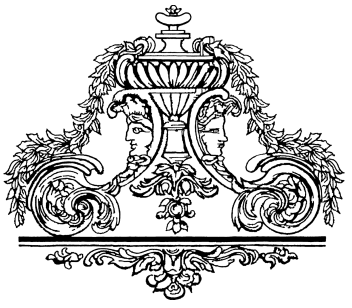

Alonso, E. E. *et al. Géotechnique* [http://dx.doi.org/10.1680/geot.11.P.134]

Compacted soil behaviour: initial state, structure and constitutive modelling

E. E. ALONSO*, N. M. PINYOL*† and A. GENS*

The paper explores the behaviour of compacted soils throughout the (dry density–water content) compaction plane by means of a conceptual framework that incorporates microstructural information. The engineering properties of compacted soils are described by an initial state in terms of a yielding stress, soil suction and a microstructural state variable. Microstructure is defined by the ratio of microvoid volume to total void volume. The pattern of variation of the microstructural parameter within the compaction plane has been determined, for some compacted soils, by analysing mercury intrusion porosimetry data. The microstructure of wet and dry compaction conditions can then be quantified. To ensure consistency, the framework is cast in the form of a constitutive model defined in terms of an effective suction and a constitutive stress that incorporate the microstructural variable. The model is shown to be consistent with a number of experimental observations and, in particular, it explains the intrinsic collapse potential of compacted soils. It predicts, for a common initial suction, a higher collapse potential for dry of optimum conditions than for wet compaction. It also predicts in a natural manner the observed evolution of soil compressibility during drained or undrained loading. Model capabilities are illustrated by application to a testing programme on statically compacted samples of low-plasticity silty clay. The compression behaviour of samples compacted wet and dry of optimum and the variation of collapse strains with confining stress have been successfully reproduced by the model.

KEYWORDS: clays; compaction; constitutive relations; fabric/structure of soils; partial saturation; plasticity; suction

INTRODUCTION

A significant proportion of the published research on unsaturated soil mechanics concerns compacted soils. It could be inferred that examining the current state of development of unsaturated soil research would provide detailed information on compacted soil behaviour. This is only partially true, however. Often, basic research is conducted in silty materials, statically compacted at a low density. These soils exhibit an open structure, sensitive to suction-induced effects. Compacted soils in practice span a much wider range of grain-size distributions. Proctor (1933) was able to show the fundamental relationship between attained density and water content for a given compaction energy. This finding defined the compaction plane (in terms of dry unit weight, γ_d, against water content, w) which is a very convenient procedure to represent the compaction states of a given soil. This plane remains the basic representation for investigating the properties of compacted soils.

This is also the starting point of the study reported in this paper. Instead of focusing on a given initial state of a compacted soil, the main objective is to explore the compaction plane. This approach will hopefully provide a wider perspective on soil compaction. The properties of compacted soils (permeability, stiffness, strength) were linked to the compaction state in some classical contributions published in the 1950s and 1960s (Leonards, 1955; Lambe, 1958; Seed & Chan, 1959; Lambe & Whitman, 1969). This idea is recovered here, but the focus now is to incorporate advances in unsaturated soil mechanics reported in the last two decades. Significant recent contributions involve the search for appropriate constitutive stress formulations, the development of elasto-plastic frameworks, and the increasing recognition of the role played by soil microstructure.

Microstructure, in particular, was very early identified as a key feature in any explanation of compacted soil behaviour associating dispersed microstructure with compaction on the wet side (wetter than optimum) and flocculated microstructure with compaction on the dry side (drier than optimum) (Lambe, 1958; Lambe & Whitman, 1969). However, direct observations of soil fabric by means of scanning electron microscopy, and the interpretation of mercury intrusion porosimetry tests reported from the 1970s (Sridharan *et al.*, 1971; McGown & Collins, 1975), led to significant changes in this initial microstructural interpretation. It was observed, for instance, that clay tended to form aggregated structures that behaved as much larger particles, especially when compacted on the dry side. It was soon accepted that water was trapped inside the clay aggregations, even if the mixture remained relatively dry. These ideas have been widely confirmed by subsequent studies (Delage *et al.*, 1996; Romero & Simms, 2008; Lee & Zhang, 2009; Monroy *et al.*, 2010).

The debate on effective stress has been a recurrent topic in unsaturated soil mechanics research since the early introduction by Bishop (1959) of an effective stress equation. This topic will be discussed further below. The unavoidable fact is, however, that modern constitutive laws for unsaturated soils that attempt to provide a comprehensive description of soil behaviour (and not just of a specific property) have been always formulated in terms of two ‘stress states’ or ‘constitutive stresses’ (Jommi, 2000; Gens, 2010). One of

Manuscript received 4 November 2011; revised manuscript accepted 3 September 2012.
Discussion on this paper is welcomed by the editor.
* Department of Geotechnical Engineering and Geosciences, Universitat Politècnica de Catalunya, Barcelona, Spain.
† International Centre for Numerical Methods in Engineering (CIMNE), Barcelona, Spain.

them is generally a function of soil suction, often the soil suction itself.

The development of elasto-plastic constitutive models provides an alternative way to characterise the initial state of compacted soils by associating model parameters and variables with the pair dry unit weight and water content (γ_d, w), which defines the 'as-compacted' condition. For instance, the dry density achieved by compaction can be related to the position of the initial yield surface after compaction. Water content, on the other hand, is controlled mainly by the current suction, s, and to a lesser extent by the void ratio. In the context of the simple elasto-plastic BBM model (Alonso *et al.*, 1990), the yield surface is essentially defined by the isotropic yield stress for saturated conditions, p_0^*. Therefore, as a starting point, the pair (p_0^*, s) may provide equivalent information to (γ_d, w), with one added advantage: they supply fundamental information for constitutive modelling.

An analysis of a limited number of soil compaction testing programmes led to the p_0^*–γ_d relationship given in Fig. 1 (Alonso & Pinyol, 2008). It can be noted that the saturated isotropic yield stress increases rapidly with dry unit weight. Also, for a given dry unit weight, the yield stress p_0^* increases significantly with soil plasticity. The plot in Fig. 1 may help to select p_0^* in the absence of specific tests. On the other hand, many $s(w, \gamma_d)$ relationships can be found in the literature (e.g. Gens *et al.*, 1995; Li, 1995; Romero *et al.*, 1999; Tarantino & Tombolato, 2005).

Thus the pair $(p_0^*, s)_{\text{as-compacted}}$ provides key information concerning the compacted state of a given soil, but it does not include any information on its microstructure. A review of microstructural effects on the compacted soil behaviour, given below, indicates that microstructure is also a significant aspect that should be introduced in a realistic modelling of compacted soils. The generalisation of techniques (particularly mercury intrusion porosimetry, MIP) to examine the evolution of soil microstructure has provided information regarding the effects of microstructure on the engineering behaviour of compacted soils. The incorporation of such effects is a key aspect of the work presented here.

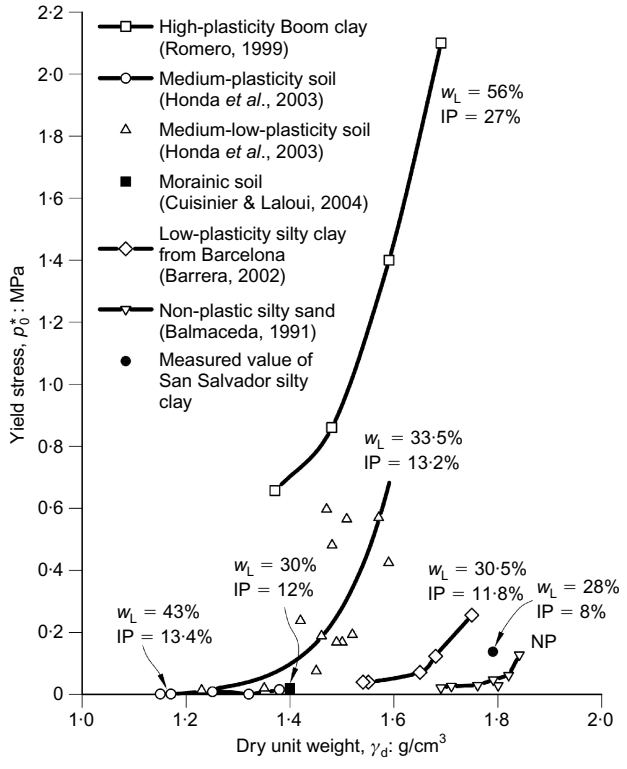

Fig. 1. Relationship between isotropic yield stress at saturated conditions and dry density of several soil types. From Alonso & Pinyol (2008). © 2008 Taylor & Francis Group, London, UK. Used with permission

In summary, the goal of this paper is to present a unified but general picture of compacted soil behaviour incorporating recent developments in unsaturated soil mechanics and microstructural considerations.

The paper is organised as follows. First, a summary of some relevant experimental work devoted to isolate the effect of microstructure on compacted soil behaviour is presented. Then a constitutive stress expression that incorporates explicitly soil microstructure is introduced. This is done through the definition of a single microstructural state variable. The interpretation of testing programmes providing data on pore size distribution has allowed this microstructural state variable to be mapped onto the compaction plane, and general trends of behaviour to be established. Compressibility and its relationship with suction and microstructure are then discussed, because this leads to a consistent description of collapse behaviour, one of the key aspects of unsaturated soil behaviour. To ensure consistency, the description of behaviour is cast in the form of a new constitutive framework that incorporates the developments and concepts described previously. Its predictive capabilities are checked against experiments.

MICROSTRUCTURE AND COMPACTED SOIL BEHAVIOUR

In this paper, information on microstructure is derived from MIP tests performed both after compaction and after the application of a given stress–suction path.

Consider, in Fig. 2, the pore size density function of a sample of low-plasticity Barcelona silty clay ($w_L = 28\%$, IP = 9·3%), statically compacted at a high void ratio ($e = 0{\cdot}82$) and then isotropically loaded in a triaxial cell to a substantially lower void ratio ($e = 0{\cdot}57$) (Buenfil *et al.*, 2004). The observation of two dominant pore sizes during compaction, especially dry of optimum, is a characteristic feature, widely observed. These two dominant pore sizes will be referred to as microporosity and macroporosity. Volumetric deformation upon isotropic loading results in a reduction of the size and volume of the macropores. In contrast, the micropores retain their partial volume and their size. Clay aggregates are readily observed in the microphotographs for $e = 0{\cdot}82$ and, to a lesser extent, for $e = 0{\cdot}57$, where it can be observed that the size of the macropores has clearly reduced.

A second example of the effect of loading and suction changes is given in Fig. 3 for Boom clay initially compacted to $e = 0{\cdot}93$ and $S_r = 0{\cdot}44$ (Romero *et al.*, 2011). The specimen was wetted at constant volume (swelling pressure path) and then dried at constant vertical stress in an oedometer cell. The stress–suction path applied is sketched in Fig. 3(a). Pore size distribution tests were performed at points 1, 2 and 3, and the results are given in Fig. 3(b). The first loading–wetting path results in a significant reduction in the size of the macropores. Further drying reduced the volume of the macropores, but the microporosity seems to remain largely unchanged throughout.

Figure 4 shows the change in pore size distribution of a sample of Barcelona silty clay, statically compacted on the dry side (sample DD), when it is wetted under a small confining stress and taken to the position DW close to saturation conditions. Some changes are observed, but in this case the 'as compacted' pore size distribution seems to be largely preserved after wetting.

This is consistent with the results of Thom *et al.* (2007) testing statically compacted kaolin, dry of optimum, which

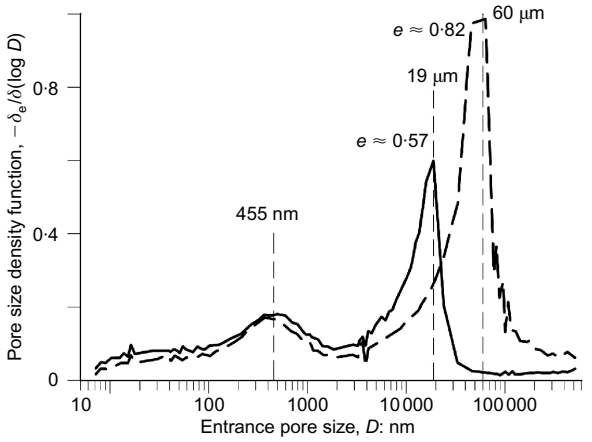

(a)

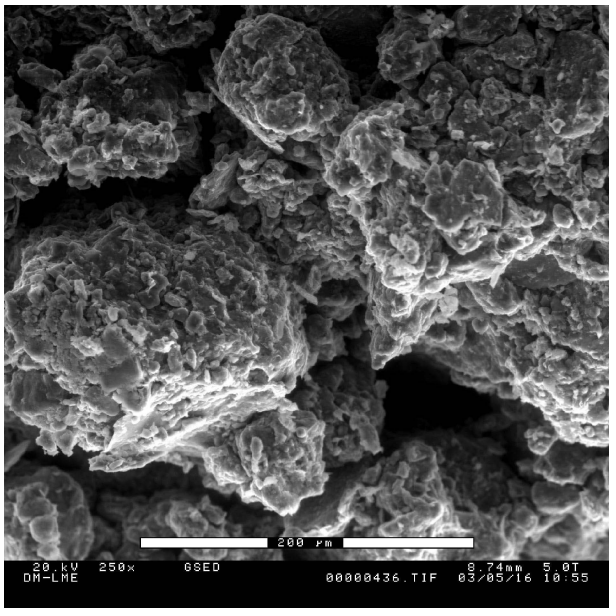

(b)

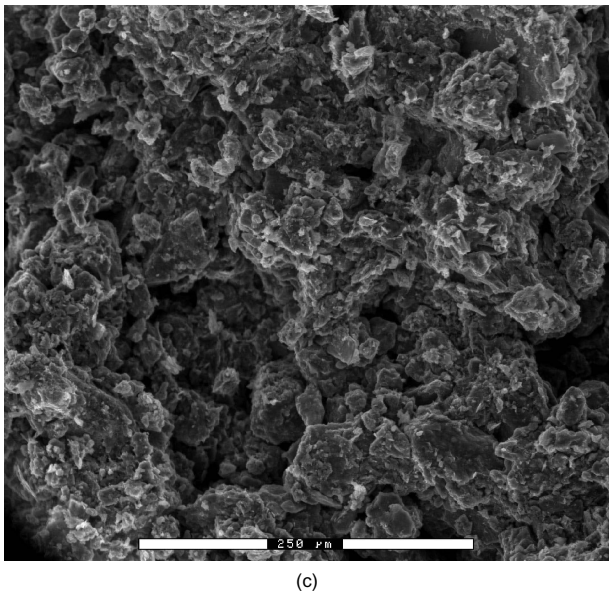

(c)

Fig. 2. Evolution of microstructure during loading. (a) Pore size distribution. (b), (c) ESEM observations, statically compacted low-plasticity Barcelona silty clay: (b) $e = 0{\cdot}82$; (c) $e = 0{\cdot}57$. After Buenfil *et al.* (2004)

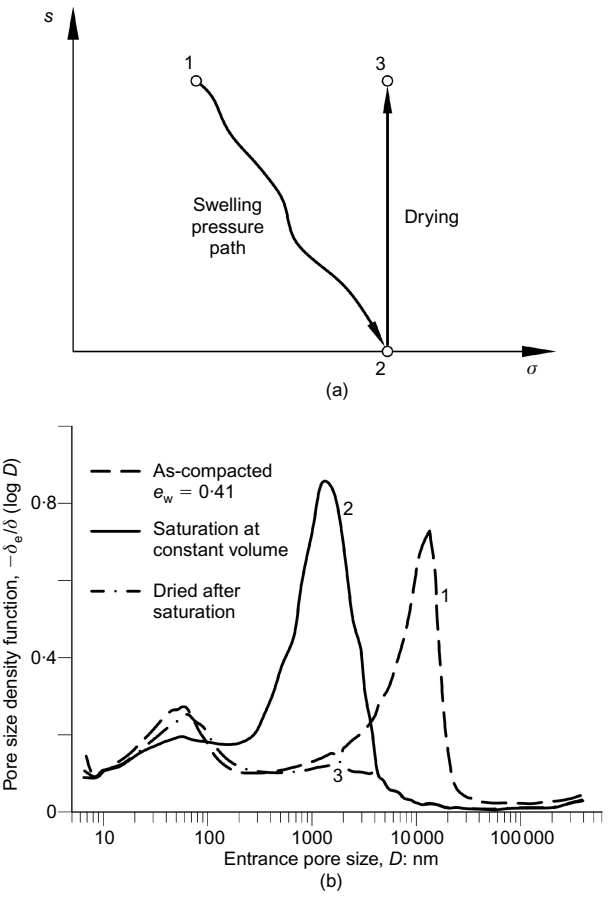

Fig. 3. Evolution of pore size distribution of compacted high-plasticity Boom clay during loading and suction changes: (a) stress path; (b) pore size distribution at three stress–suction points indicated in (a). From Romero *et al.* (2011)

indicated that the bimodal domain of voids induced by soil compaction is essentially maintained upon the application of significant stress and suction changes. However, this is not always the case. Wetting tests reported by Monroy *et al.* (2010) on statically compacted high-plasticity London Clay indicate that changes in micropores may also be significant on wetting. The higher activity of the clay probably explains the enhanced sensitivity of microporosity to suction changes.

The variation of engineering properties of a given soil when compacted at different dry densities and water contents has been often reported (Cox, 1978; Reséndiz, 1980; Lawton *et al.*, 1989, 1991; Alonso *et al.*, 1992; Benson *et al.*, 1992; Fredlund & Rahardjo, 1993; Tinjum *et al.*, 1997; Vanapalli *et al.*, 1999; Simms & Yanful, 2002; Santucci de Magistris & Tatsuoka, 2004; Jotisankasa *et al.*, 2007, 2009). However, it is not feasible to isolate microstructural effects in many of these contributions, mainly because compacting dry or wet of optimum implies not only a different microstructure, but also a different suction. In addition, compacting at different void ratios implies both a variation in macroporosity and a change in the initial yield locus. Hence conventional testing of compacted samples mixes the effects of the initial state (p_0^*, s) and of the microstructure. Therefore specifically designed testing programmes are required to isolate microstructural effects.

An interesting example of such programmes is provided by Santucci de Magistris & Tatsuoka (2004), who tested dynamically compacted specimens of low-plasticity silty sand (a residual granitic soil) in a triaxial cell. Once compacted, all samples were taken to a saturated state before testing. Because it is a low-plasticity soil, it was expected

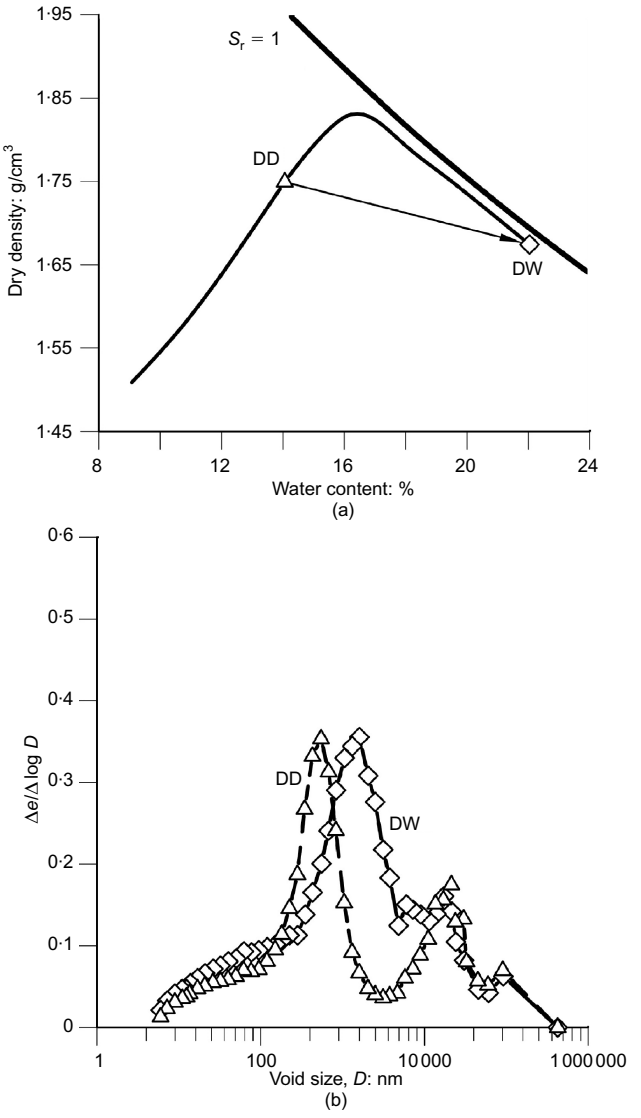

Fig. 4. Statically compacted Barcelona silty clay: (a) compaction state of samples DD and DW; (b) pore size distributions. After Suriol *et al.* (1998) and Suriol & Lloret (2007)

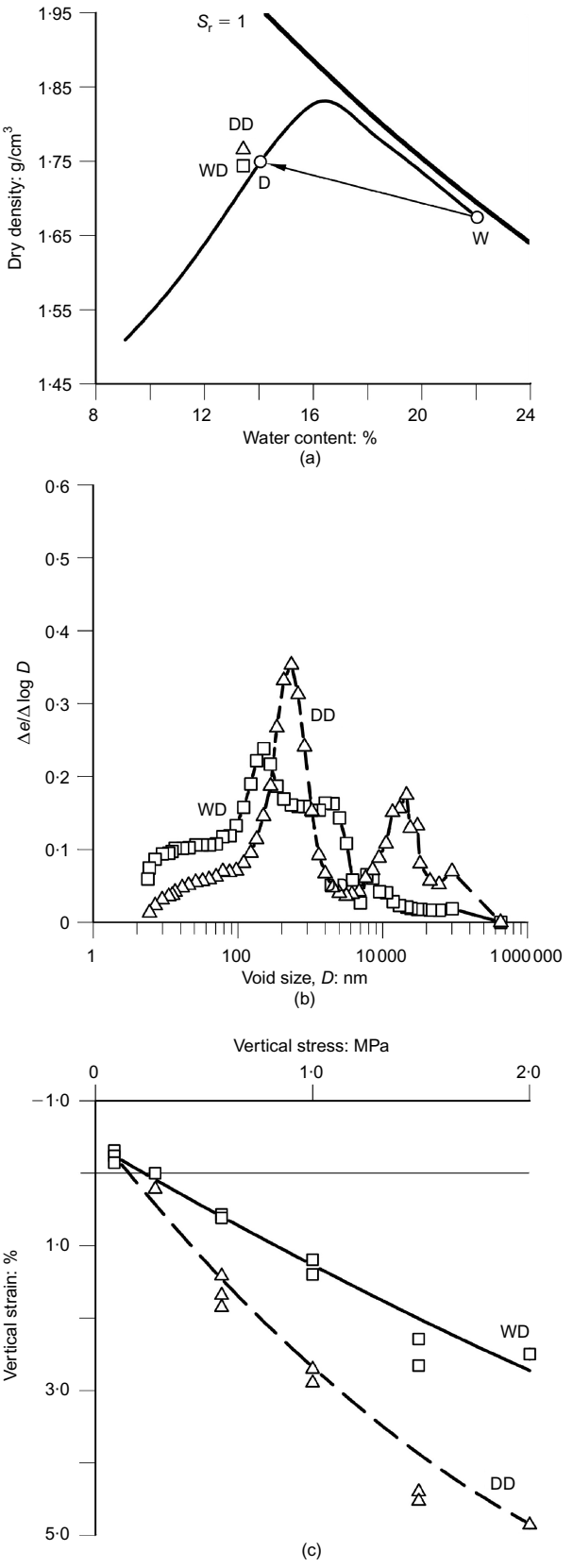

Fig. 5. Statically compacted Barcelona silty clay: (a) compaction state of samples DD and WD; (b) pore size distributions; (c) measured collapse strains in loading at constant suction and full wetting. After Suriol *et al.* (1998) and Suriol & Lloret (2007)

that the as-compacted microstructure would be essentially preserved and, naturally, suction at the testing stage was zero. They found that the slope of the virgin compression line changes moderately with moulding water content from wet to dry conditions, except for states in the vicinity of the modified Proctor optimum. Similar conclusions were reached concerning small-strain stiffness. Drained strength (the limiting q/p' ratio) was not much affected by the attained dry density, although dry compaction resulted in a moderate increase in dilatancy when compared with wet compaction.

Wheeler & Sivakumar (1995, 2000), testing statically compacted speswhite kaolin, found that the slope and intercept of normal compression lines for constant suction depend on the compaction water content and compaction stress. A similar result was found for the volumetric critical-state line.

Microstructural effects may be identified directly if specimens having a different origin (say, compacted dry and wet of optimum) are tested at a common state. Instead of selecting a saturated state, Suriol *et al.* (1998) and Suriol & Lloret (2007) tested samples of statically compacted Barcelona silty clay ($w_L = 30{\cdot}5\%$ and $IP = 11{\cdot}8\%$) in a suction-controlled oedometer cell. The approach adopted is illustrated in Fig. 5(a). Under a vertical compaction stress of 0·6 MPa and a moulding water content $w = 14\%$, the soil equilibrates at point D. A wetter sample ($w = 22\%$) under the same compaction stress lies on point W. Afterwards, samples W were dried under suction-controlled conditions

and taken to position D (they are samples WD, which should be read as 'compacted in position W and tested in position D'). In contrast, samples DD are both compacted and tested in D. The pore size distributions of samples DD and WD are given in Fig. 5(b). Samples DD exhibit a marked double porosity. Samples WD have developed a dominant intermediate pore size.

Samples DD and WD were then loaded in a suction-controlled oedometer maintaining the suction prevailing at point D (1 MPa) and then saturating the specimens under constant vertical stress. The measured vertical strains (collapse strains) are plotted in Fig. 5(c) in terms of applied vertical stress. DD specimens collapse more than WD samples, a clear indication of the effects of microstructure, since the dry density, water content and suction are the same in the two cases.

The effect of microstructure on elastic stiffness and strength will be discussed further once the constitutive stress is defined. However, a final property is discussed here: permeability. As this parameter is essentially controlled by the pore structure of the soil, it provides a good indication of microstructural changes if the permeability of samples compacted at different (γ_d, w) values is measured under saturated conditions. Again, this is especially true if microstructural changes during the saturation process are minor. Fig. 6 reproduces results published by Mitchell *et al.* (1965). The soil, a silty clay, was compacted by kneading action. Contours of equal saturated permeability are plotted in the compaction plane. Clearly, permeability is not uniquely controlled by void ratio. In fact, a strong variation is observed when, for a given void ratio, the compaction water content increases. Thus permeability reveals microstructural effects much better than mechanical tests do. The plot in Fig. 6 indicates that designs involving compacted soils in which permeability is an important issue (e.g. isolating barriers) cannot be based only on classical criteria limiting dry density and water content on the basis of mechanical tests. Adding microstructure in some manner to the constitutive behaviour of compacted soils would help to incorporate the hydraulic properties of compacted soils in a natural way.

These points can be summarised as follows.

(*a*) It is clear that the microstructure of compacted soils has a distinct effect on their geotechnical properties that is not accounted for solely by the stress pair (p_0^*, s).

(*b*) Not all the properties are equally sensitive to microstructure. One extreme case is probably the soil permeability. Conversely, the drained strength parameters do not seem to be much affected.

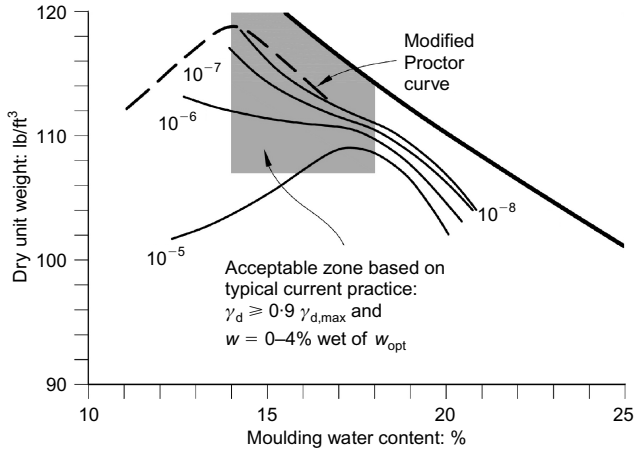

Fig. 6. Contours of permeability, under saturated conditions, for samples of silty clay compacted by kneading action (100 lb/ft³ = approx. 15·7 kg/m³). From Mitchell *et al.* (1965), with permission from ASCE

(*c*) Compressibility and, therefore, collapse and swelling potential are controlled to a significant extent by microstructure.

(*d*) Stress and suction paths applied to compacted specimens modify mainly the macroporosity, but in active soils (high-plasticity clays) changes associated with suction variations may also modify the microstructural void volume.

EFFECTIVE DEGREE OF SATURATION AND CONSTITUTIVE STRESS

A full description of the pore structure of a soil would require a large number of parameters, which would prevent the incorporation of such information into a simple constitutive formulation. Here, the pore size distribution is described by a simple state variable: the ratio of the microstructural void ratio, e_m, and the total void ratio, e. This ratio will be known here as the microstructural state variable, ξ_m.

$$\xi_m = \frac{e_m}{e} \tag{1}$$

If water has access to an initially compacted dry soil, it is expected that the microstructure will saturate first, because of the strong affinity for water of the clay platelets. Once the microvoids inside clay aggregates are saturated, any excess water will occupy the macropores. Alonso *et al.* (2010) suggested that only the water partially filling the macropores will have a significant mechanical effect on the soil. The concept behind this idea is that capillary effects will be exhibited only by the water forming menisci between aggregates and inert soil particles.

The 'effective' degree of saturation, in the sense of contributing to the constitutive stress, will then take non-zero values only for degrees of saturation in excess of ξ_m. The effective degree of saturation was assumed to vary between 0 and 1, when S_r spans the macropore space ($\xi_m \leqslant S_r \leqslant 1$). This is illustrated in Fig. 7 for the particular value $\xi_m = 0{\cdot}4$. Sketches showing the assumed distribution of water in the micro and macro volumes illustrates the

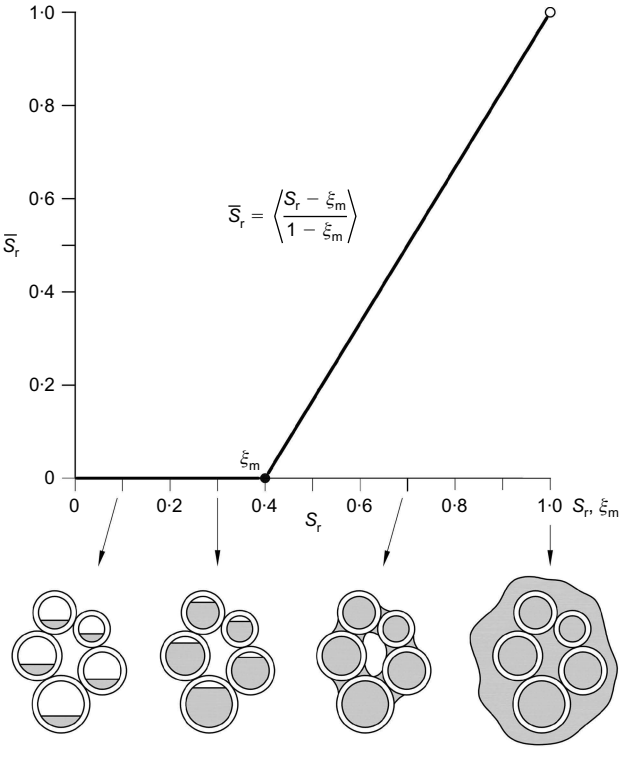

Fig. 7. Definition of effective degree of saturation

location of the water as the degree of saturation increases. The effective degree of saturation is given by the equations

$$\bar{S}_r = \frac{S_r - \xi_m}{1 - \xi_m} \text{ for } S_r > \xi_m \quad (2a)$$

$$\bar{S}_r = 0 \text{ for } S_r \leqslant \xi_m \quad (2b)$$

Equation (2a) for the effective degree of saturation was already introduced by Romero & Vaunat (2000) and Tarantino & Tombolato (2005).

It is proposed that the unsaturated soil behaviour be defined in terms of two independent stress fields.

Constitutive stress:

$$\bar{\sigma} = \sigma - p_g + \bar{S}_r s \quad (3a)$$

Effective suction:

$$\bar{s} = \bar{S}_r s \quad (3b)$$

where the effective suction and the constitutive stress have been made dependent on the void ratio, microstructural void ratio and degree of saturation by means of the effective degree of saturation. In equation (3a), σ is the total stress and p_g is the gas pressure.

Partial aspects (elastic stiffness, drained failure envelopes) of unsaturated soil behaviour were shown to be well predicted by interpreting results in terms of equation (3a) (Alonso *et al.*, 2010).

The piecewise equation (2) was smoothed in Alonso *et al.* (2010) by a continuous power law ($\bar{S}_r = (S_r)^\alpha$; $\alpha > 1$), which provides some advantages in calculation. However, the power function loses a direct reference to the microstructural state variable, ξ_m, which is a variable capable of being experimentally measured in MIP tests, as described in the next section.

Following the procedure put forward by Gesto *et al.* (2011), an alternative smoothing of $\bar{S}_r$ around the corner $S_r = \xi_m$ that maintains ξ_m as a material state variable can be achieved by the equation

$$\bar{S}_r = \frac{S_r - \xi_m}{1 - \xi_m} + \frac{1}{n} \ln \left[1 + \exp \left(-n_{smooth} \frac{S_r - \xi_m}{1 - \xi_m} \right) \right] \quad (4)$$

The number n_{smooth} defines the degree of smoothing around the corner (Fig. 8). It can be noted that equation (4) provides a small effective stress contribution for $S_r < \xi_m$ that is likely to be more realistic than the sharp transition shown in Fig. 7.

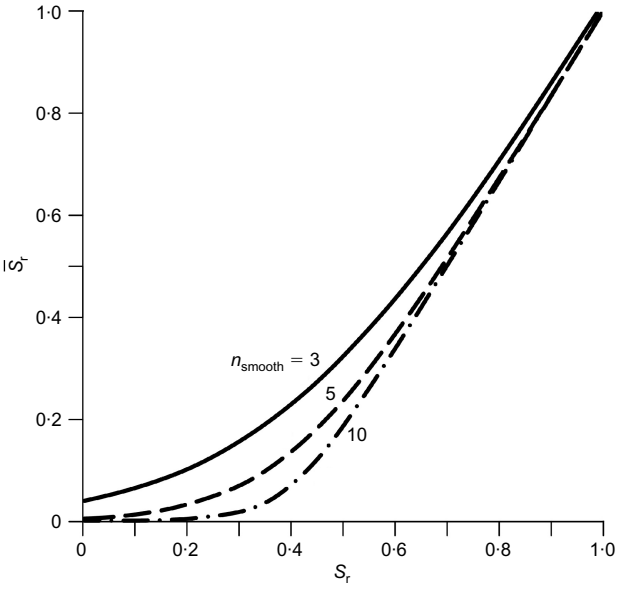

Fig. 8. Effect of parameter n_{smooth} on effective degree of saturation for $\xi_m = 0{\cdot}3$

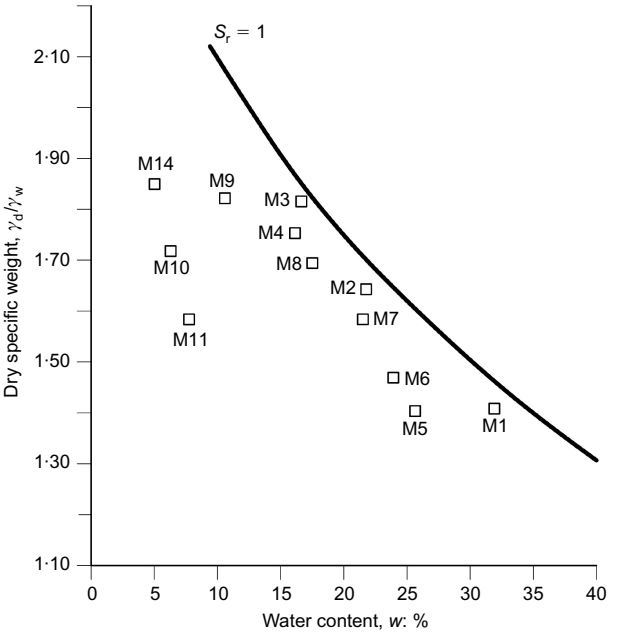

Fig. 9. Compacted samples of Boom clay tested by Merchán (2011)

MAPPING MICROSTRUCTURE ON THE COMPACTION PLANE

The microstructural state variable ξ_m was shown by Alonso *et al.* (2010) to increase with soil plasticity. However, no indication of the effect of varying compaction variables was given. A recently conducted experimental programme has explored, in a systematic manner, the microstructure of compacted Boom clay (Merchán, 2011). The attained dry densities covered a wide range (1·40–1·85 g/cm^3), spanning the values typical of practical engineering applications. Fig. 9 shows the position of samples tested in the compaction plane. MIP tests in which mercury was first intruded and then extruded after reaching a maximum pressure of 227 MPa were conducted on all samples.

There are alternative procedures available to determine the macropore and micropore volumes. If only the intrusion curve is analysed, the density distribution of pore sizes may be interpreted in a straightforward manner by calculating the areas corresponding to the two porosity levels. The density function provides the information to establish the macropore–micropore size boundary. However, this procedure becomes difficult to apply if the distinct bimodal shape is lost.

If the extrusion cumulative curve is available, Delage & Lefebvre (1984) suggested an alternative procedure to distinguish between porosity levels, as sketched in Fig. 10. Microporosity was judged to result in a reversible (elastic) volume of mercury intruded and extruded from the small voids. In contrast, mercury would be trapped in the macropores by capillary effects once the applied pressure is removed. This concept and the resulting procedure to determine the micro and macro porosities are adopted here for two reasons. First, it results in a non-ambiguous procedure to identify the two porosities. Second, the idea of a reversible behaviour of the volume change induced by pore pressures changes in the microporosity (also identified as the intra-aggregate space) is consistent with the behaviour of interacting clay platelets.

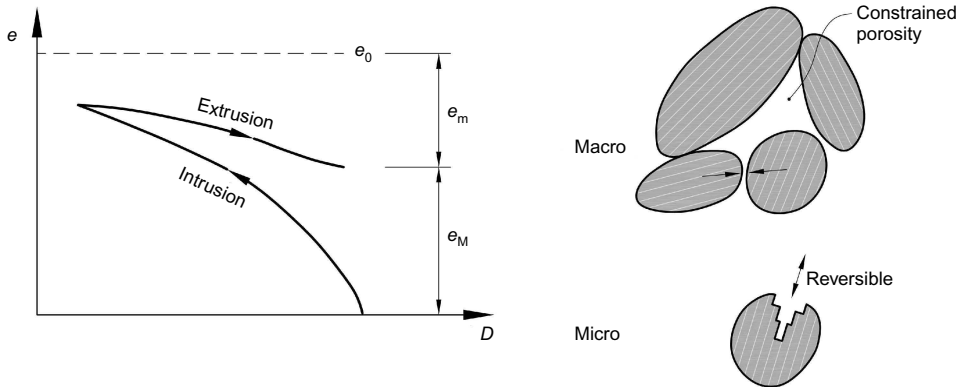

Fig. 10. Scheme of intrusion–extrusion stages of an MIP test and interpretation in terms of microvoid (e_m) and macrovoid (e_M) ratios. After a proposal by Delage & Lefebvre (1984)

This issue was further discussed by Gens & Alonso (1992). In fact, the double structure model proposed there to describe the behaviour of expansive clays highlights the reversible behaviour of the microstructure of clayey soils.

Using the Delage & Lefebvre (1984) procedure to identify macroporosity and microporosity, the microstructural state variable was determined for all the samples shown in Fig. 9. Fig. 11 shows the variation of the microstructural void ratio in the compaction plane. Interpolated contours show that e_m is essentially controlled by the compaction water content.

Derived values of the state variable ξ_m are indicated in Fig. 12 for all the compacted specimens tested. Contours of equal ξ_m are also plotted. The data show an increase of ξ_m with density that reflects the progressive reduction in void ratio. Equally relevant is the effect of compaction water content. For a given void ratio, ξ_m increases with compaction water content, reflecting the fact that samples compacted wet develop a larger quantity of micropores.

To illustrate the effect of compaction conditions, consider, for instance, two specimens essentially compacted to the same dry density and different water contents: M9 (a drier specimen) and M3 (a wetter specimen). Their microstructural states ($\xi_m = 0{\cdot}4$ for M9 and $\xi_m = 0{\cdot}6$ for M3) and the implication in terms of effective degree of saturation are shown in Fig. 13. If both samples are partially filled with water to a common degree of saturation (say $S_r = 0{\cdot}8$), their different microstructures will result in specimen M9 (drier) exhibiting a higher effective degree of saturation than M3. Therefore, under a common suction, M9 will experience a higher constitutive stress than specimen M3.

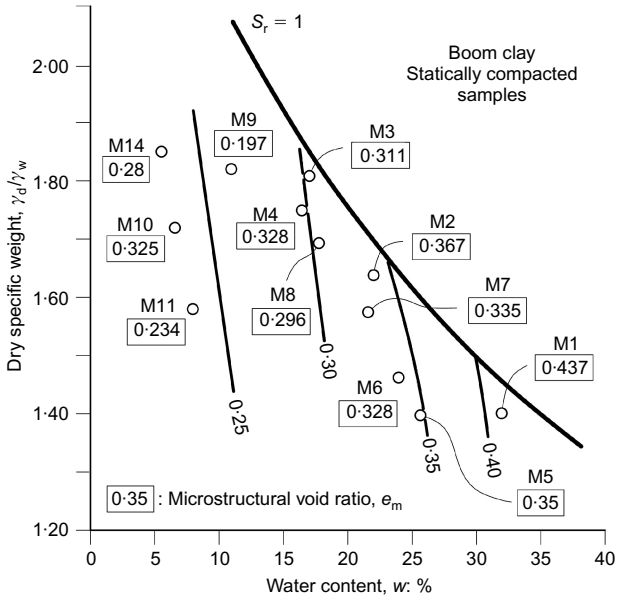

Fig. 11. Contours of equal microstructural void ratio, e_m, for compacted Boom clay. Compaction data taken from Merchán (2011)

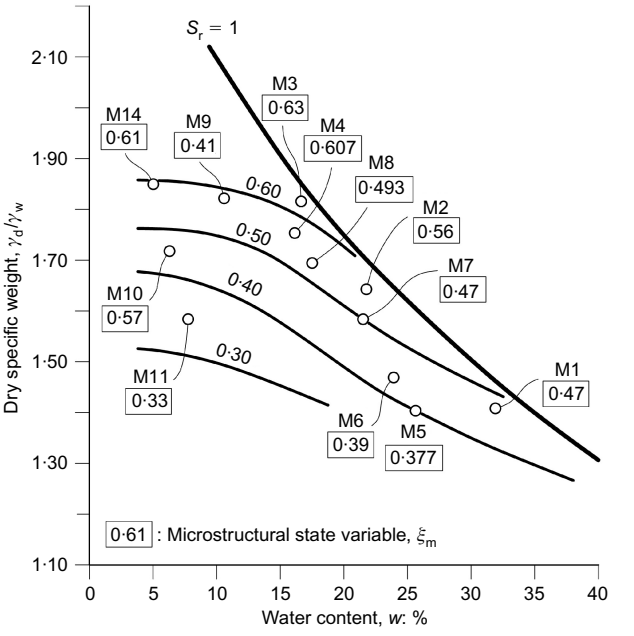

Fig. 12. Contours of equal microstructural parameter, ξ_m, for compacted Boom clay. Compaction data taken from Merchán (2011)

Other recently published data on MIP intrusion–extrusion measurements of compacted specimens support the general trend of ξ_m variation observed in Fig. 12. This is the case presented in Fig. 14, which collates data reported by Romero *et al.* (2011) on statically compacted Boom clay. Tarantino & de Col (2008) published MIP data on a few statically compacted samples of kaolin. The calculation of ξ_m has also been based on the intrusion–extrusion diagram of MIP tests (Fig. 15). The figure shows the compaction curves for increasing vertical compaction stress, the contours of equal degree of saturation, the calculated values of ξ_m for the few samples tested, and the contours for equal ξ_m. The three plots (Figs 12, 14 and 15), which correspond to two different soils and three independent testing programmes, show similar trends.

In order to demonstrate that these conceptual ideas can be integrated in a consistent manner, a constitutive model of compacted soil behaviour has been developed that includes microstructural information in terms of the state variable ξ_m.

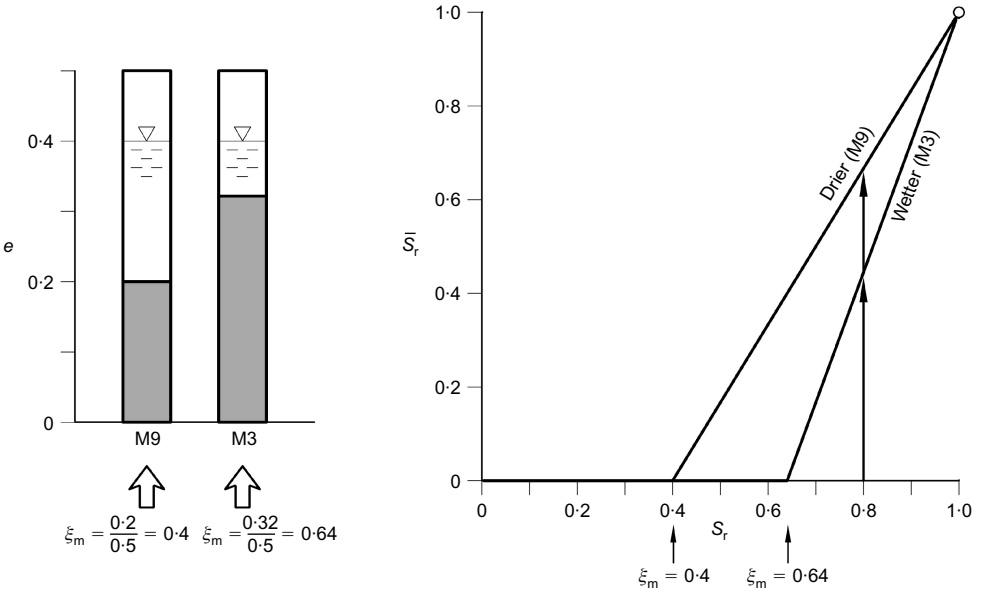

Fig. 13. Microvoid and macrovoid ratios of specimens M9 and M3 after compaction and associated effective degree of saturation for a degree of saturation of 0·8

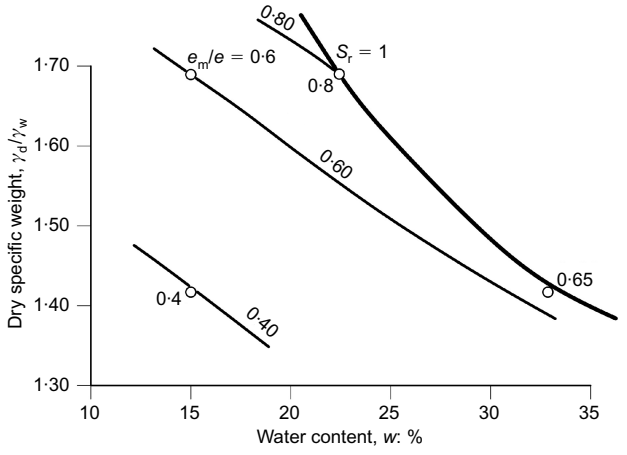

Fig. 14. Contours of equal microstructural parameter, ξ_m, for compacted Boom clay. Compaction data taken from Romero *et al.* (2011)

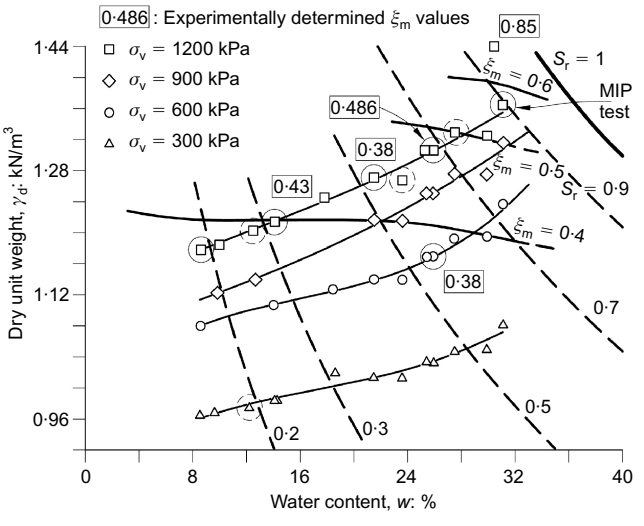

Fig. 15. Contours of equal microstructural parameter, ξ_m, for compacted kaolin. Compaction data taken from Tarantino & de Col (2008)

The first step is an analysis of compressibility, described in the next section.

A CONSTITUTIVE MODEL INCORPORATING MICROSTRUCTURAL EFFECTS

The constitutive stress defined in equation (3a) is capable of predicting strength and elastic stiffness in unsaturated states if these properties are known for a saturated state (Alonso *et al.*, 2010). This partial success is, however, far from implying that the constitutive stress thus defined can predict consistently the volumetric behaviour of wet and dry-compacted samples against stress and suction changes. Specifically, thinking in terms of different compaction conditions, the challenge is to investigate whether the volumetric behaviour of compacted samples can be predicted by considering only the initial stress state (say, p_0^* and s) and a microstructural state variable such as ξ_m. The differences in collapse behaviour shown in Fig. 5, which are basically controlled by microstructure, provide an important benchmark to check the above hypothesis.

A convenient starting point towards this goal is to review the compressibility of samples compacted dry and wet of optimum, and to interpret them in terms of effective suction. In fact, compressibility has already been shown to depend on prevailing suction (Alonso *et al.*, 1987, 1990; Wheeler & Sivakumar, 1995). If microstructure affects compressibility as well, the relationship between a compression coefficient and suction will also depend on the compaction water content (for a common initial void ratio). However, as the effective suction defined above incorporates microstructural effects, it is possible that a unique relationship between compressibility and effective suction may emerge.

Model formulation for isotropic stress states

The model is defined in terms of two variables: the constitutive stress defined in equation (3a) and the effective suction defined in equation (3b). Changes in the constitutive stress induce elastic and elasto-plastic strains respectively, according to the logarithmic relationships

$$\mathrm{d}e^{\mathrm{e}} = -\bar{\kappa}\frac{\mathrm{d}\bar{p}}{\bar{p}} \tag{6}$$

$$de^{cp} = -\bar{\lambda}\frac{d\bar{p}}{\bar{p}}_{\bar{s}=\text{constant}} \tag{7}$$

which introduce the definition of compressibility coefficients against changes in constitutive stress. The elastic index, $\bar{\kappa}$, is assumed to be constant in this paper.

It is accepted, in view of previous results, that $\bar{\lambda}$ is a function of the effective suction, given by

$$\frac{\bar{\lambda}(\bar{s})}{\lambda(0)} = f(\bar{s}) = f(\bar{S}_r s) \tag{8}$$

where $\bar{S}_r$ is defined in equation (4). Compression lines assumed by this model are plotted in Fig. 16 in terms of the constitutive stress, for different effective suctions.

The parameter $\bar{\lambda}$ is conceptually very different from the 'standard' compressibility coefficient, λ, defined in terms of net stress. In order to estimate $\bar{\lambda}$, the variation of void ratio with constitutive stress at constant effective suction is required. Suction-controlled tests do not provide such information directly, even if the microstructural void ratio is known and assumed to be constant, because the void ratio is changing during loading, and the effective suction is thereby varying continuously. During loading e reduces and $\xi_m = e_m/e$ increases. The effect of this increase is illustrated in Fig. 17. If the degree of saturation is maintained during loading (this is approximately the case of constant-suction loading), the effective degree of saturation, and therefore the effective suction will decrease (Fig. 17(a)). As a result, the coefficient $\bar{\lambda}$ will increase during loading. The effect of this continuous decrease of $\bar{S}_r s$ during loading is illustrated in Fig. 18: the actual compression curve 'travels' during loading across the compression lines plotted at constant effective suction ($\bar{S}_r s$) values. This is also the case for undrained loading (constant water content), for a double reason: the reduction in void ratio and the associated decrease in suction. The net result is that, during undrained loading, the void ratio decreases faster in terms of constitutive stress. If the degree of saturation also changes with void ratio (in a suction-controlled test, for instance), an additional change in the effective degree of saturation and the constitutive stress is introduced. Therefore, $\bar{\lambda}$ cannot be readily estimated from 'standard' laboratory compression curves relating void ratio and net stress.

Despite these difficulties, the definition of elasto-plastic compressibility in equation (7) leads to a powerful and simple model to predict the isotropic compression of unsaturated soils for a wide range of applied stresses. It reconciles existing formulations based either on a decrease (as in BBM; Alonso *et al.*, 1990) or on an increase (Wheeler & Sivakumar, 1995) of compressibility with suction, and predicts in a natural way the evolution of collapse strains with

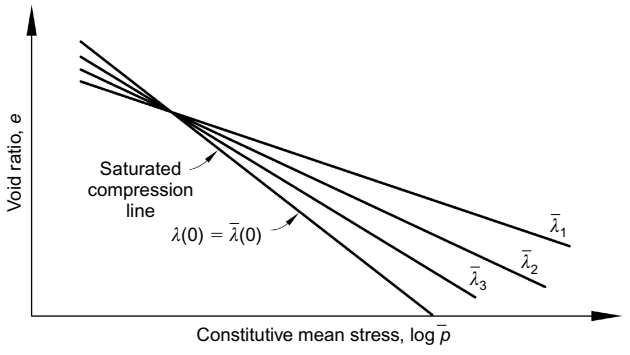

Fig. 16. Definition of compression lines in terms of constitutive stress $\log\bar{p} = \log(p_{net} + \bar{S}_r s)$.

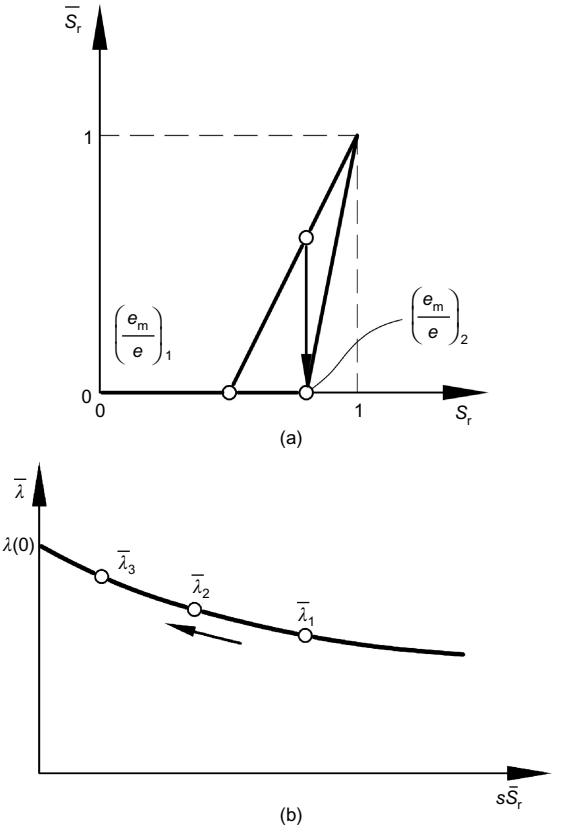

Fig. 17. (a) Effect of increasing microstructural void ratio on effective degree of saturation for constant degree of saturation; (b) effect of decreasing effective suction on compressibility coefficient, $\bar{\lambda}$

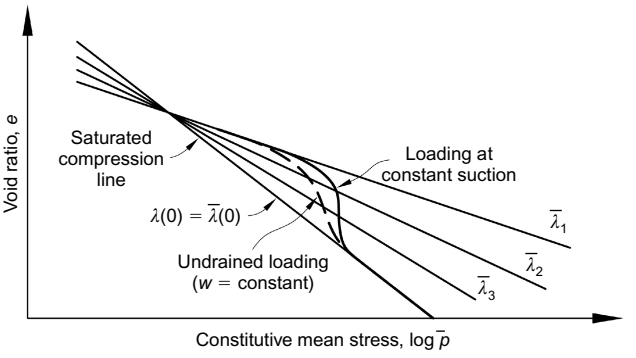

Fig. 18. Estimated compression behaviour of unsaturated soil for drained (constant suction) and undrained (constant water content) isotropic loading in terms of constitutive stress $\log\bar{p} = \log(p_{net} + \bar{S}_r s)$.

suction, which exhibits a maximum for some intermediate confining stress. This is discussed again below.

Further analysis requires the proposal of a particular relationship for the function $f(\bar{s})$ in equation (8). A difficulty in making $\bar{\lambda}$ dependent on effective suction is that the compressibility would change when the soil was saturated and subjected to suctions lower than the air-entry value. To avoid this shortcoming, the following equation is proposed for $\bar{\lambda}$ in terms of the effective suction.

$$\frac{\bar{\lambda}(\bar{s})}{\lambda(0)} = \bar{r} + (1-\bar{r})\left[1 - \left(\frac{\bar{s}}{\bar{s}_\lambda}\right)^{1/(1-\bar{\beta})}\right]^{-\bar{\beta}} \tag{9}$$

where $\bar{r}$, $\bar{\beta}$ and $\bar{s}_\lambda$ are material parameters. Equation (9) is

plotted in Fig. 19 for different values of $\bar{r}$, $\bar{\beta}$ and $\bar{s}_\lambda$. Parameter $\bar{\beta}$ controls the rate of variation of $\bar{\lambda}(\bar{s})/\lambda(0)$ with effective suction between two limits (1 and $\bar{r}$). Parameter $\bar{r}$ defines the maximum stiffness of the soil as effective suction increases ($\bar{r}\lambda(0)$). Suction $\bar{s}_\lambda$ defines the air entry value. In fact, it can be taken as being the equivalent parameter of the van Genuchten (1980) expression for the water retention relationship. Note in Fig. 19 that $\bar{\lambda}$ is essentially constant when the effective suction is smaller than $\bar{s}_\lambda$. Within this range of suctions, effective suction and suction are essentially equal.

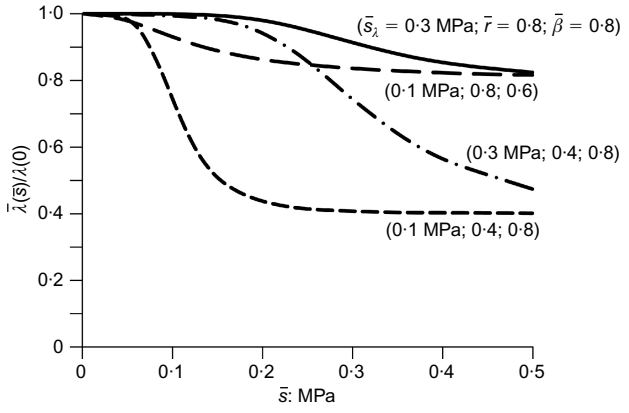

Fig. 19. Variation of isotropic compressibility with effective suction for different parameter values

The constitutive yield isotropic stress for unsaturated conditions ($\bar{p}_0$) is defined by the loading collapse (LC) yield curve

$$\frac{\bar{p}_0}{\bar{p}_c} = \left(\frac{p_0^*}{\bar{p}_c}\right)^{\frac{\lambda(0)-\kappa}{\bar{\lambda}(\bar{s})-\kappa}} \tag{10}$$

where $\bar{p}_c$ is a reference mean constitutive stress corresponding to the point where virgin compression lines for different effective suctions cross. Since the preconsolidation stress depends on the effective suction, samples compacted at the same void ratio but having different microstructural parameters will exhibit different LC loci. Equation (9) is a unique expression for the entire compaction plane. Differences in compressibility will be the result of differences in current values of suction and the microstructural state variable, ξ_m.

In order to provide an insight into the performance of the compression model defined, a synthetic example is presented. Several isotropic compression tests, run at different values of suction, which remain constant during loading, are simulated. Model parameters are listed in Table 1. The generally observed dependence of water retention on void ratio (e) has been introduced in the model in a simple way by expressing the parameter P_0 of the van Genuchten model

Table 1. Parameters and initial conditions for isotropic synthetic tests and oedometer tests on Barcelona silty clay samples

Parameter	Definition	Units	Synthetic case		Barcelona silty clay	
			Sample dry	Sample wet	Sample DD	Sample WD
Mechanical parameters						
$\bar{\kappa}$	Elastic compressibility	–	0·006		0·006	
$\bar{\lambda}(0) = \lambda(0)$	Plastic compressibility at zero effective suction	–	0·07		0·07	
ν	Poisson's ratio	–	0·3		0·3	
M	Slope of critical-state strength line	–	–		1·2	
$\bar{p}_c$	Reference stress	MPa	0·001		0·001	
$\bar{s}_\lambda$	Minimum value of effective suction affecting plastic volumetric compressibility. Equivalent to an air entry value (P_0)	MPa	0·25		0·25	
$\bar{r}$	Parameter that establishes minimum value of compressibility coefficient for high values of effective suction	–	0·8		0·8	
$\bar{\beta}$	Parameter that controls rate of increase in stiffness with effective suction	MPa^{-1}	0·75		0·8	
n_{smooth}	Parameter that defines degree of smoothing in equation (7)	–	3		3	
Water retention curve: van Genuchten model						
$S_{r\,min}$	$\frac{S_r - S_{r\,min}}{S_{r\,max} - S_{r\,min}} = \left[1 + \left(\frac{s}{P_0}\right)^{\frac{1}{1-\lambda}}\right]^{-\lambda}$	–	0		0	
$S_{r\,max}$		–	1		1	
a^{VG}		MPa	−0·25		−0·25	
b^{VG}		MPa	0·4		0·4	
λ	$P_0 = a^{VG}e + b^{VG}$	–	0·35		0·35	
Initial conditions						
e_0	Initial void ratio	–	0·538		0·538	
p_0^*	Yield stress at zero effective suction	MPa	0·45		0·45	
s_0	Initial suction	MPa	1		1	
ξ_{m0}	Initial microstructural state variable	–	0·34	0·38	0·36	0·41

as a linear function of e (Table 1). The model is explored for two 'samples' of the same soil compacted on the dry side (sample SI-D) or wet side (sample SI-W). It can be noted that the same set of parameters is used for the two specimens, the only difference being the value of the initial microstructural state variable, ξ_{m0}.

Model calculations are shown in terms of two sets of stress variables: constitutive stress and effective suction in Fig. 20, and net stress and suction in Fig. 21. The plots of volumetric strain against constitutive stress (Fig. 20) show the change in soil compressibility with applied stress, discussed above. Points corresponding to a particular value of effective suction may be identified on each compression curve, and they are indicated in the figures. Straight lines connecting these points define the compressibility coefficient $\bar{\lambda}$ of the underlying model.

The compression curves in Fig. 20 may also be represented in terms of volumetric strain against net stress and suction (Fig. 21). This plot shows the compression lines that would be recorded directly in conventional isotropic tests at constant suction. The model predicts that those 'standard' compression lines of an unsaturated soil will first respond in a stiff manner, compared with the saturated compression line;. but as deformation (and suction changes) accumulates, the compressibility index will eventually become similar to $\lambda(0)$, and then it will reach higher values in order to decrease again later when the saturated compression line is approached asymptotically. In loose soils, the first stage is often not observed, and the measured apparent compression index for a given suction exceeds the saturated value (this was the case presented by Wheeler & Sivakumar (1995)). In dense soils, the entire transition from $\lambda < \lambda(0)$ to $\lambda > \lambda(0)$ is observed, provided the applied stress is large enough. This type of result was shown, for instance, by Romero (2002), testing compacted Boom clay in a suction-controlled oedometer; by Jotisankasa *et al.* (2007), testing a compacted mixture of silt, kaolin and London Clay; and by Benatti *et al.* (2011), testing a colluvial, collapsible silty clay.

To move from Fig. 21 to Fig. 20 requires knowledge of the degree of saturation during loading, and information on the initial microstructural state variable in order to identify the variation of $\bar{\lambda}$ with effective suction through the compression lines. Two or more tests, providing the measurement of void ratio, suction and degree of saturation during compression, are required to obtain this variation, and to determine the parameters in equation (9).

The shape of the compression lines in Figs 20 and 21 indicates that the model is capable of simulating collapse strains that first increase with confining stress and then reduce, as frequently observed in collapse tests. Sometimes the final reduction in collapse is not observed, because the applied stress is not high enough; in this case, collapse seems to be an increasing function of applied stress. This is the prediction of BBM. This issue is also discussed by Sheng (2011) and Zhou *et al.* (2012a, 2012b) in the context of a model in which the plastic compressibility index

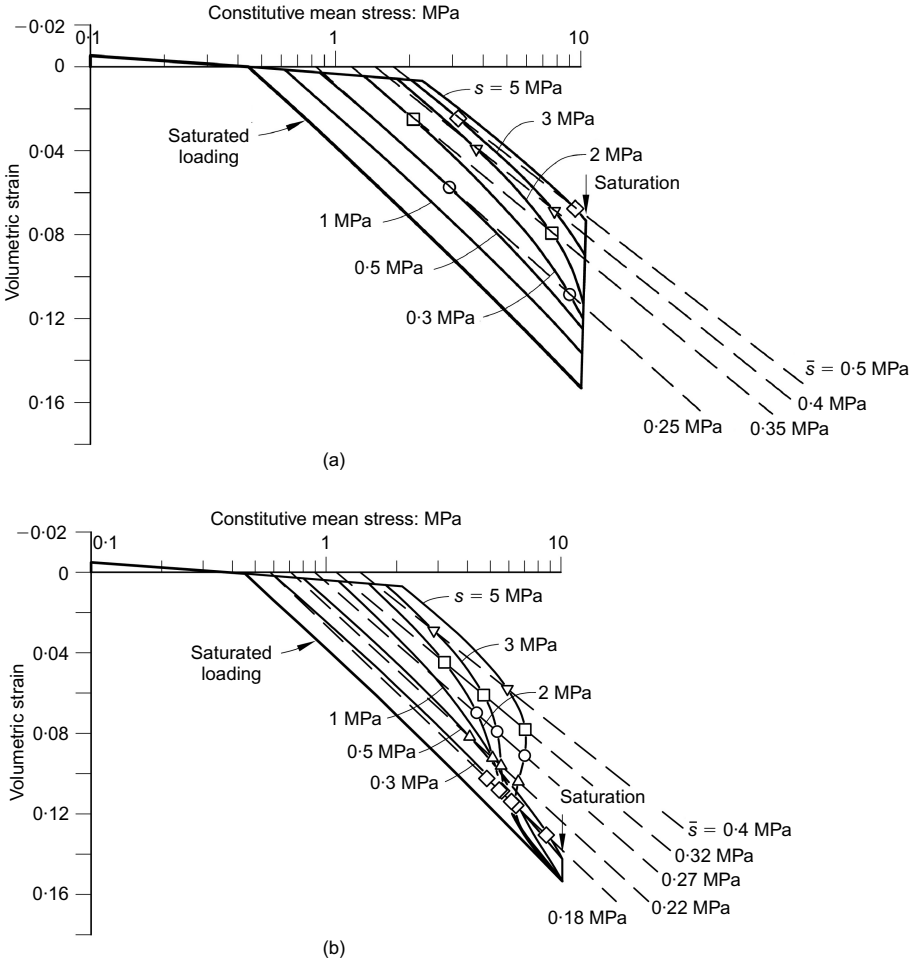

Fig. 20. Synthetic isotropic tests in terms of constitutive stress. Compression response at different constant suctions: (a) dry compaction, sample SI-D; (b) wet compaction, sample SI-W

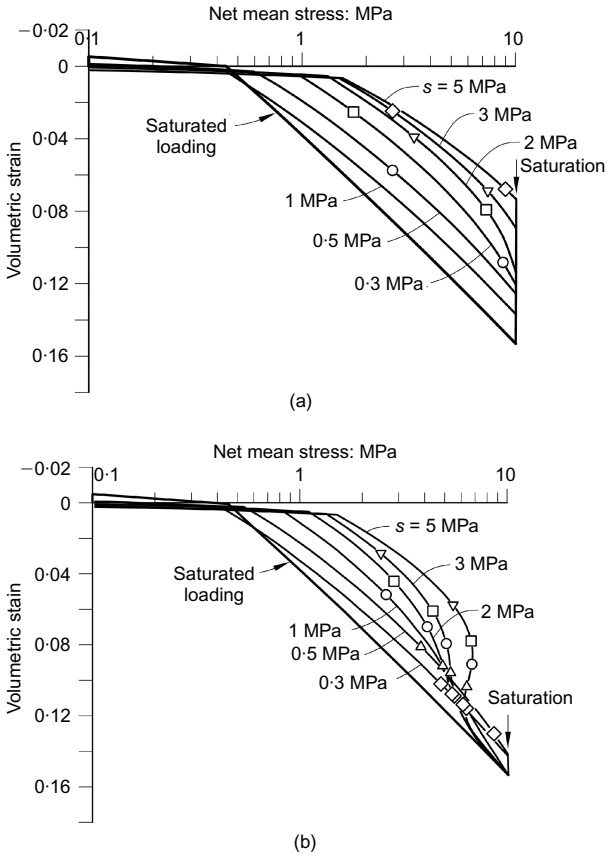

Fig. 21. Synthetic isotropic tests in terms of net stress. Compression response at different constant suctions: (a) dry compaction, sample SI-D; (b) wet compaction, sample SI-W

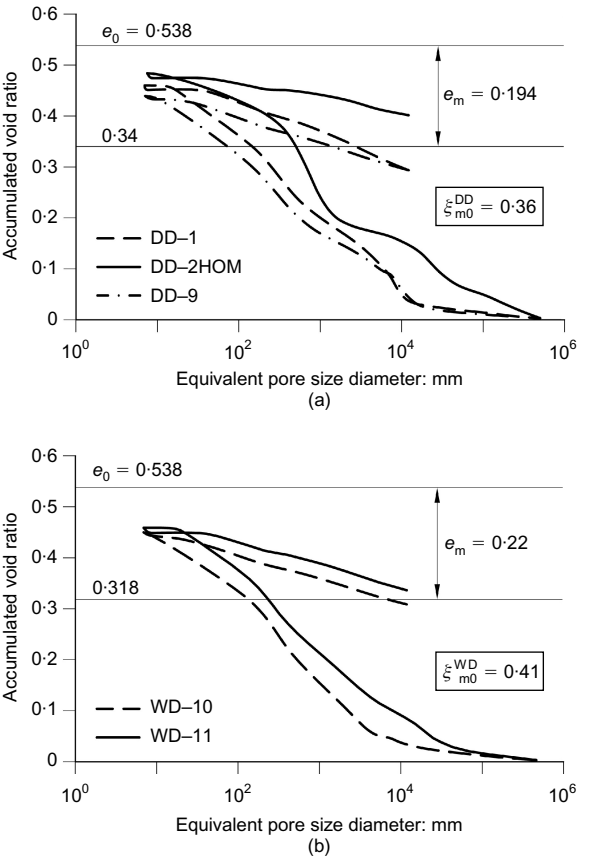

Fig. 22. MIP tests on compacted samples of Barcelona silty clay: (a) DD samples; (b) WD samples

depends on the degree of saturation. Their model also predicts collapse strains first increasing and then decreasing with applied confining stress.

Comparison of Figs 21(a) and 21(b) (or Figs 22(a) and 22(b)) finally provides the effect of soil microstructure introduced by dry and wet compaction. Dry compaction, characterised by a lower initial microstructural state variable (ξ_{m0}), results in a stiffer soil response than wet compaction. In addition, collapse strains, for any confining stress, are higher for dry compaction. This result was also measured in the real tests that are described below.

Simulation of tests on compacted Barcelona silty clay

Consider again the DD and WD tests series on compacted Barcelona clay reported by Suriol & Lloret (2007) (Figs 4 and 5). The microstructure of samples WD and DD was discussed on the basis of the intrusion curve only. The pore size density plot reproduced in Fig. 5(b) was in fact the derivative of the accumulated mercury volume during the pressure-increase phase of the test. Although it was not reported, the authors also recorded an extrusion (pressure decrease) branch. This is shown in Fig. 22 for the DD and WD samples. The available extrusion curves, performed on several samples compacted to the same initial state to check the repeatability of results, did not reach a zero rate of volume change, but they were close. The plots allow calculation of the microstructural void ratio, as suggested in Fig. 10. The following as-compacted (initial) values are derived for e_{m0} and ξ_{m0}: sample DD, $e_{m0} = 0{\cdot}19$, $\xi_{m0} = 0{\cdot}36$; sample WD, $e_{m0} = 0{\cdot}22$, $\xi_{m0} = 0{\cdot}41$. These values are consistent with the trends shown in Figs 12, 14 and 15: wet of optimum compaction results in a higher microstructural void ratio.

Collapse tests represented in Fig. 5(c) for the WD and DD samples were limited to vertical stresses not exceeding 2 MPa. However, additional oedometer tests for samples WD and DD were performed later in a high-capacity loading frame, and the vertical confining stress reached a maximum value of 8 MPa. The measured vertical strains for the full 0–8 MPa stress range are shown in Fig. 23. Collapse reaches a maximum in both types of sample for a vertical stress of about 2 MPa. At higher vertical stresses, collapse decreases gradually. The distance between the two curves also reduces as the vertical stress increases.

The model is now used to explore in more detail its ability to reproduce the observed effects of compacting dry

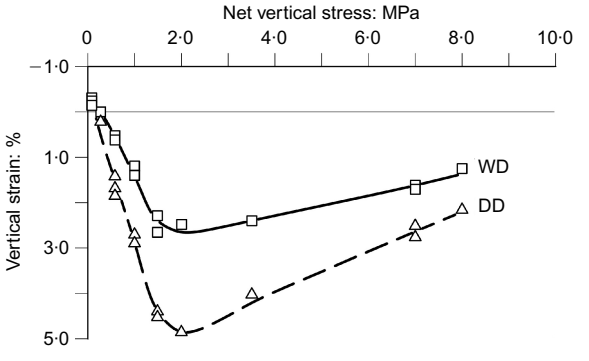

Fig. 23. Measured collapse strains of samples WD and DD of compacted Barcelona silty clay in range 0–8 MPa of confining total vertical stress

and wet of optimum (set of samples WD and DD, in Figs 5 and 23). Data are available for constant-suction oedometer loading starting on the common (dry density–water content) state (WD = DD), which corresponds to an initial suction $s = 1$ MPa.

Dry and wet of optimum compaction are distinguished exclusively by the initial microstructural state variable, ξ_{m0}. All the remaining model parameters for the two samples analysed take the same value (Table 1). The slopes of the virgin compression lines for saturated conditions ($\lambda(0)$) and the elastic coefficient ($\bar{\kappa}$) were approximated from test results. Values of $\bar{r}$ and $\bar{\beta}$, which define compressibility for unsaturated conditions, have been estimated to fit the collapse variation with stress level. The value for parameter $\bar{s}_\lambda$ corresponds to an average value of parameter P_0 of the van Genuchten water retention curves (see below). A low reference stress $\bar{p}_c$ was also selected.

The model proposed requires information on the water retention properties for the calculation of $\bar{S}_r s$. Water retention curves of Barcelona silty clay for several void ratios were reported by Barrera (2002). Fig. 24 shows the experimental data. These curves have been adopted to estimate the water retention behaviour of samples WD and DD by means of a van Genuchten (1980) model. The dependence of the water retention behaviour on void ratio has been introduced in the model in the same simple way as used for the synthetic cases presented in the previous section, that is, assuming a linear variation of the parameter P_0 (which controls the air entry value) with void ratio. The model approximation to the reported retention curves is also plotted in Fig. 24. The van Genuchten expression and the values of the parameters chosen for calculations are indicated in Table 1. The effect of the microstructure on the water retention curve has been neglected, and a unique relationship between suction, degree of saturation and void ratio has been assumed for both samples.

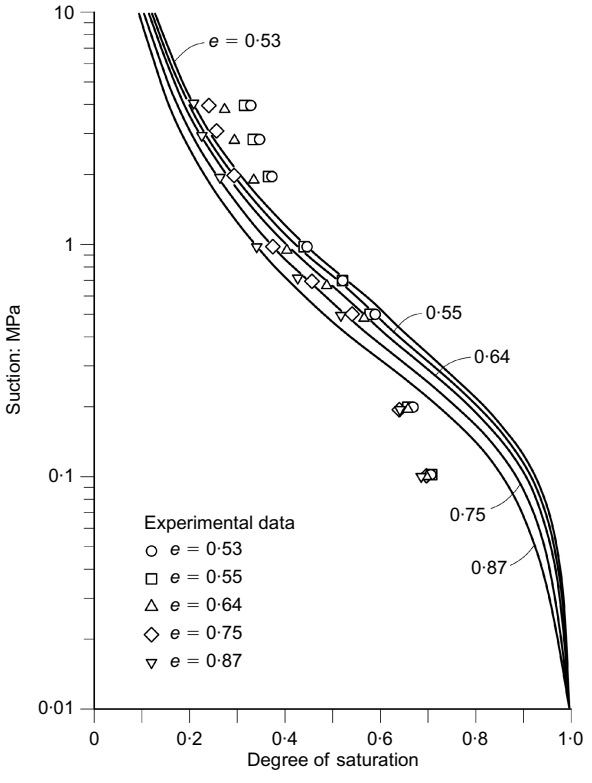

Fig. 24. Water retention data on compacted Barcelona silty clay reported by Barrera (2002) and model (van Genuchten) approximations for different values of void ratio (e)

Suriol *et al.* (1998) reported the compression curves of DD and WD samples for $s = 1$ MPa and for saturated conditions to a maximum vertical stress of 1·50 MPa only (Fig. 25). However, the reported collapse strains at different confining stresses in the range 0–8 MPa (Fig. 23) allow an estimation of the compression curves of DD and WD samples for the entire stress range. They are shown in Fig. 26.

The constitutive model was first used to reproduce the saturated compression line in the range 0–1·5 MPa (loading and unloading) (Fig. 25). The comparison between model calculations and experiments is quite satisfactory. The calculated saturated compression line was then extended to the entire loading range for the DD and WD compaction conditions (Fig. 26). The model reproduces satisfactorily the experimental results, and predicts correctly the differences in compression behaviour associated with different microstructure. It is recalled that only a single variable, namely the initial microstructural state (ξ_{m0}), distinguishes the two compaction conditions; the rest of the material parameters are identical in both samples. It is remarkable that the complexities of the microstructure can be adequately represented by a single state variable.

A further comparison of model performance and experimental data is given in Fig. 27, which shows the collapse strains of both series of tests (DD and WD) plotted in terms of net applied stress. The model correctly predicts the maximum of collapse, its progressive decay towards a zero value at high applied stresses, and the higher intrinsic collapsibility of the sample compacted dry of optimum. All these effects are linked directly with the initial microstructure of the soil

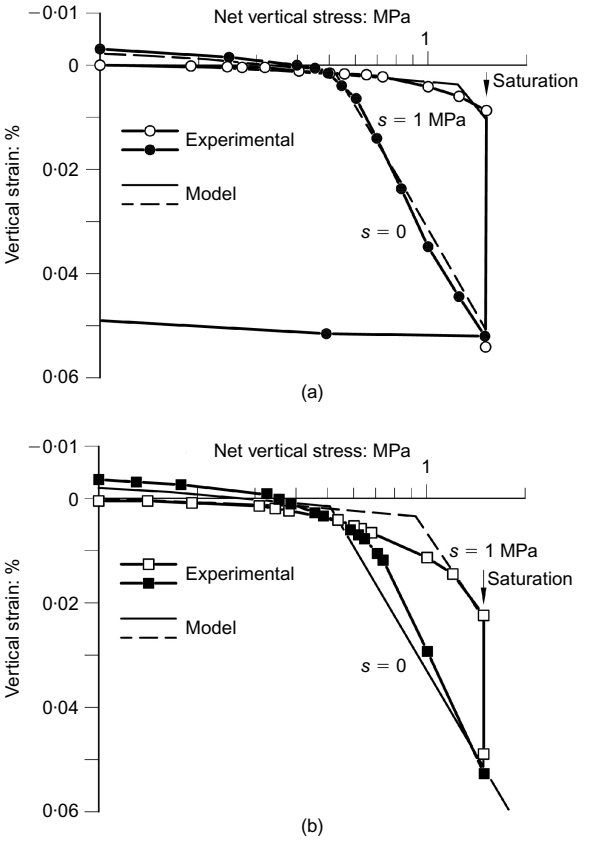

Fig. 25. Oedometric suction-controlled ($s = 1$ MPa; $s = 0$ MPa) compression curves of compacted Barcelona silty clay and model predictions: (a) DD samples; (b) WD samples. Results of a full wetting collapse test at a vertical stress of 1·5 MPa are also indicated

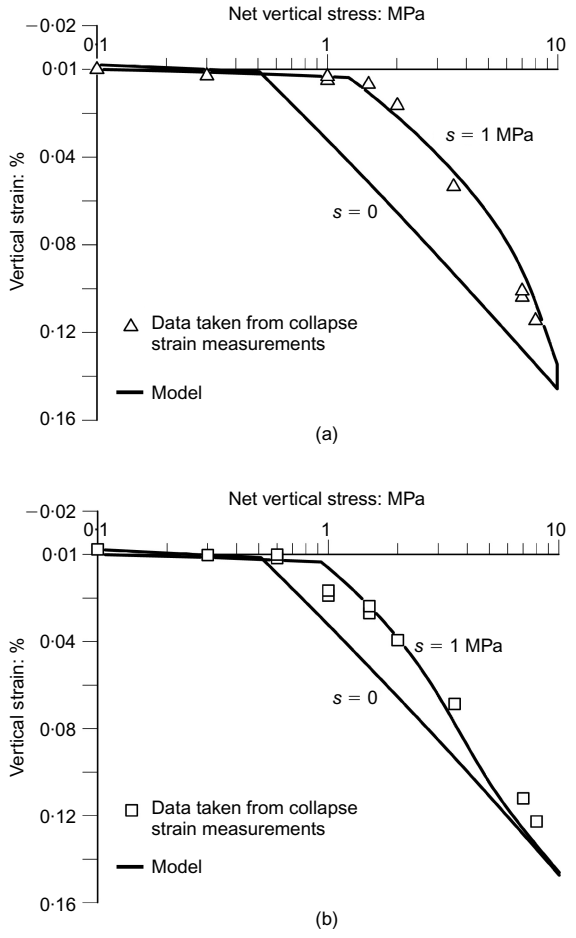

Fig. 26. Estimated experimental compression curves of compacted Barcelona silty clay in range 0–8 MPa of vertical stress and model predictions: (a) samples DD; (b) samples WD

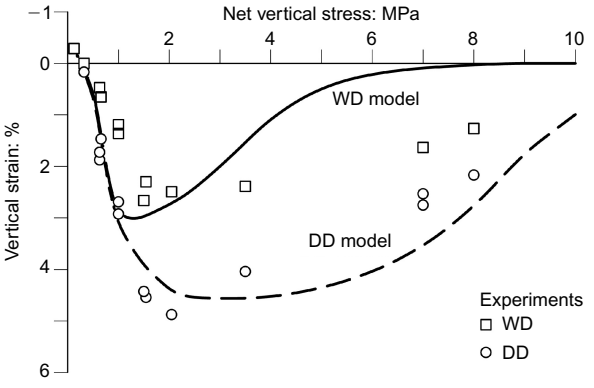

Fig. 27. Measured and calculated collapse strains of samples DD and WD

and its evolution during the application of a stress–suction path.

The initial LC yield locus of DD and WD samples is plotted in Fig. 28(a) in term of constitutive stress and effective suction, and in Fig. 28(b) in term of net stress and suction. In the first case a unique LC yield curve describes dry and wet of optimum conditions. When transformed to net stress–suction coordinates, two different initial LC curves describe dry and wet conditions. The shape of the LC yield curves in Fig. 28(b) was already advanced by Alonso *et al.* (1987) and Gens (1995) when interpreting compression and wetting tests on samples compacted wet and dry of optimum. The available model at the time (BBM)

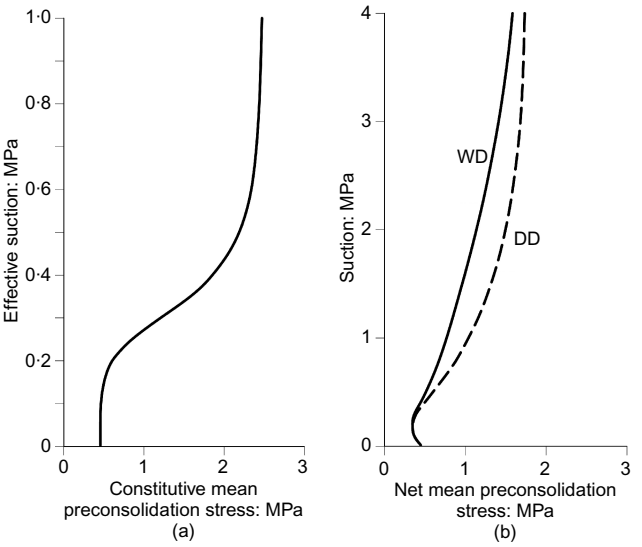

Fig. 28. Initial LC yield curves of samples DD and WD: (a) in terms of constitutive stress and effective suction; (b) in terms of net stress and suction

required a different set of parameters (namely r and β) to describe compaction-induced microstructure. The model described here confirms the assumption made in the papers mentioned, and provides a more compact and comprehensive description of compacted soil behaviour.

CONCLUDING REMARKS

Understanding the behaviour of compacted soils requires not only information on the as-compacted density and water content (or equivalent information in terms of yield stress and suction, as suggested here) but also a proper consideration of microstructure. The review of compacted soil behaviour presented in the first part of this paper has highlighted the relevance of microstructure. A conceptual framework that incorporates microstructural information and accounts for the behaviour of compacted soils throughout the compaction plane has been put forward.

Microstructure is quantified by a state variable, ξ_m, the ratio of microvoid ratio to total void ratio. The microvoid ratio tends to maintain its original 'as compacted' value during subsequent stress–suction paths in low- to medium-plasticity clayey soils. Changes in total void ratio associated with loading and suction changes, however, modify the microstructural state variable, which becomes a state parameter with direct influence on the constitutive stress and effective suction.

The interpretation of pore size distribution data of testing programmes on compacted soils, covering a reasonably complete range of dry densities and water contents, has led to the establishment of the pattern of ξ_{m0} throughout the compaction plane. This state variable opens the way for a systematic evaluation of microstructural effects on measurable 'macroscopic' engineering variables, such as elastic stiffness, strength, compressibility, yielding behaviour and permeability. All of them are influenced to a larger (permeability) or smaller (drained strength) extent by microstructure.

The framework is the basis of a constitutive model defined in terms of an effective suction and a constitutive stress that include microstructural information. The proposed constitutive stress was shown previously to be useful in predicting the elastic stiffness and strength of unsaturated soils. The present work has concentrated on the analysis of compressibility, and

on the associated concepts of collapse and yielding of unsaturated compacted soils. It has been shown that relevant engineering properties of a compacted soil can be explained by a set of common material (constitutive) parameters, the initial stress conditions defined by an initial yield stress, p_0^*, and a suction, s, and an additional state variable, ξ_m, that describes the microstructure, which varies across the compaction plane, Including ξ_m in the definition of constitutive stress and effective suction has the following significant advantages.

(*a*) It is a very simple option, because only one variable is required to quantify microstructure.
(*b*) It captures the intrinsic volumetric behaviour of compacted soils and, in particular, the observed differences when compacting dry or wet of optimum.
(*c*) It provides a realistic interpretation of experimental compression lines for a wide range of applied stresses for both constant-suction and undrained loading conditions. The collapse maximum often observed is explained in a natural way.
(*d*) Existing constitutive models can be enhanced by including ξ_m with a limited effort.

The model proposed requires information on the water retention properties. A desirable feature of the analysis in this case would be to include microstructural information, such as ξ_m, in the formulation of the water retention behaviour, a proposal already put forward by Romero *et al.* (2011). In this way, the entire coupled hydromechanical model will require only a reduced number of material parameters. It has been shown that the model is consistent with experimental observations.

Naturally, the characterisation of complex microstructure by a single variable, and the assumption that the microstructural void ratio remains unchanged, are simplifications that should be reviewed when some other aspects of compacted soil behaviour involving deviatoric loading or anisotropy effects are considered. In particular, extension of this model to expansive clays will require a relaxation of the assumption of a constant microstructural void ratio. However, the success of this approach in representing the behaviour of compacted soils suggests that it can be a very useful platform for subsequent developments and generalisations.

NOTATION

a^{VG} parameter that controls the variation of P_0 with e
b^{VG} parameter that controls the variation of P_0 with e
D pore size diameter
e total void ratio
e_M macrostructural void ratio
e_m microstructural void ratio
e_w water ratio
e^e elastic void ratio
e^{ep} elastoplastic void ratio
e_0 initial void ratio
IP plasticity index
M slope of critical-state strength line
n_{smooth} degree of smoothing
P_0 parameter of van Genuchten model
p' effective mean stress
$\bar{p}$ constitutive mean stress
p_g gas pressure
p_{net} net mean stress
p_0^* mean yield stress
$\bar{p}_c$ reference mean constitutive stress
$\bar{p}_0$ constitutive yield mean stress for unsaturated conditions
q deviatoric stress
r parameter that establishes minimum value of compressibility coefficient for high values of suction in the Barcelona basic model (Alonso *et al.*, 1990)
$\bar{r}$ parameter that establishes minimum value of compressibility coefficient for high values of effective suction
S_r degree of saturation
$\bar{S}_r$ effective degree of saturation
s suction
$\bar{s}$ effective suction
$\bar{s}_\lambda$ minimum value of effective suction affecting plastic volumetric compressibility
w water content
w_L liquid limit
w_{opt} optimum water content
α smoothing coefficient for effective degree of saturation in the paper by Alonso *et al.* (2010)
β parameter that controls rate of increase in stiffness with suction in the Barcelona basic model (Alonso *et al.*, 1990)
$\bar{\beta}$ parameter that controls rate of increase in stiffness with effective suction
γ_d dry unit weight
$\gamma_{d,max}$ maximum dry unit weight for a given compaction energy
γ_w unit weight of water
$\bar{\kappa}$ elastic compressibility index
λ plastic compressibility index in net mean stress–void ratio plane
$\bar{\lambda}$ plastic compressibility index in constitutive mean stress–void ratio plane
ν Poisson's ratio
σ total stress
$\bar{\sigma}$ constitutive stress
σ_v net vertical stress
ξ_m microstructural state variable ($= e_m/e$)
ξ_{m0} initial microstructural state variable

REFERENCES

Alonso, E. E. & Pinyol, N. M. (2008). Unsaturated soil mechanics in earth and rockfill dam engineering. In *Unsaturated soils: Advances in geo-engineering* (eds D. G. Toll, C. E. Augarde, D. Gallipoli and S. J. Wheeler), vol. 1, pp. 3–32. Boca Raton, FL, USA: CRC Press.

Alonso, E. E., Gens, A. & Hight, D. (1987). Special problem soils: general report. *Proc. 9th Eur. Conf. Soil Mech. Found. Engng, Dublin* **3**, 1087–1146.

Alonso, E. E., Gens, A. & Josa, A. (1990). A constitutive model for partially saturated soils. *Géotechnique* **40**, No. 3, 405–430, http://dx.doi.org/10.1680/geot.1990.40.3.405.

Alonso, E. E., Josa, A. & Gens, A. (1992). Modelling the behaviour of compacted soils upon wetting. In *Raul J. Marsal Volume*, pp. 207–223. Mexico City, Mexico: Sociedad Mexicana de Mecánica de Suelos (SMMS).

Alonso, E. E., Pereira, J. M., Vaunat, J. & Olivella, S. (2010). A microstructurally based effective stress for unsaturated soils. *Géotechnique* **60**, No. 12, 913–925, http://dx.doi.org/10.1680/geot.8.P.002.

Barrera, M. (2002). *Estudio experimental del comportamiento hidromecánico de suelos colapsados*. PhD thesis, Universitat Politècnica de Catalunya, Barcelona, Spain (in Spanish).

Benatti, J. C. B., Miguel, M. G., Rodrigues, R. A. & Vilar, O. M. (2011). Collapsibility study for tropical soil profile using oedometric test with controlled suction. In *Unsaturated soils* (eds E. Alonso and A. Gens), Vol. 1, pp. 193–198. Boca Raton, FL, USA: CRC Press/Balkema.

Benson, C. H., Zhai, H. & Wang, X. (1992). Estimating hydraulic conductivity of compacted clay liners. *J. Geotech. Engng ASCE* **120**, No. 2, 366–387.

Bishop, A. W. (1959). The principle of effective stress. *Tecknisk Ukeblad* **106**, No. 39, 859–863.

Buenfil, C. M., Romero, E., Lloret, A. & Gens, A. (2004). Experimental study on the hydromechanical behaviour of a silty clay. *Proc. 2nd Int. Workshop on Unsaturated Soils, Anacapri*, 15–29.

Cox, D. W. (1978). Volume change of compacted clay fill. *Proceedings of the Institution of Civil Engineers Conference on Clay Fills*, London, pp. 79–86.

Delage, P. & Lefebvre, G. (1984). Study of the structure of a sensitive Champlain clay and of its evolution during consolidation. *Can. Geotech. J.* **21**, No. 1, 21–35.

Delage, P., Audiger, M., Cui, Y. J. & Howat, M. (1996). Microstructure of a compacted silt. *Can. Geotech. J.* **33**, No. 1, 150–158.

Fredlund, D. & Rahardjo, H. (1993). *Soil mechanics for unsaturated soils*. London, UK: Wiley.

Gens, A. (1995). Constitutive modelling. Application to compacted soils. *Proc. 1st Int. Conf. on Unsaturated Soils, Paris* **3**, 1179–1200.

Gens, A. (2010). Soil–environment interaction in geotechnical engineering. *Géotechnique* **60**, No. 1, 3–74, http://dx.doi.org/10.1680/geot.9.P.109.

Gens, A. & Alonso, E. E. (1992). A framework for the behaviour of unsaturated expansive soils. *Can. Geotech. J.* **29**, No. 6, 761–773.

Gens, A., Alonso, E. E., Suriol, J. & Lloret, A. (1995). Effect of structure on the volumetric behaviour of a compacted soil. *Proc. 1st Int. Conf. on Unsaturated Soils, Paris* **1**, 83–88.

Gesto, J. M, Gens, A. & Vaunat, J. (2011). Smoothing of yield surfaces and a reformulation of multi-surface plasticity. *Proc. 11th Int. Conf. on Computational Plasticity: Fundamentals and Applications (COMPLAS XI), Barcelona, Spain*, 295–306.

Jommi, C. (2000). Remarks on constitutive modelling of unsaturated soils. In *Experimental evidence and theoretical approaches in unsaturated soils* (eds A. Tarantino and C. Mancuso), pp. 139–153. Rotterdam, the Netherlands: Balkema.

Jotisankasa, A., Ridley, A. & Coop, M. (2007). Collapse behavior of compacted silty clay in suction-monitored oedometer apparatus. *J. Geotech. Geoenviron. Engng* **133**, No. 7, 867–877.

Jotisankasa, A., Coop, M. & Ridley, A. (2009). The mechanical behaviour of an unsaturated compacted silty clay. *Géotechnique* **59**, No. 5, 415–428, http://dx.doi.org/10.1680/geot.2007.00060.

Lambe, T. W. (1958). The engineering behaviour of compacted clay. *J. Soil Mech. Found. Div. ASCE* **84**, No. SM2, 1–35.

Lambe, T. W. & Whitman, R. V. (1969). *Soil mechanics*. New York, NY, USA: Wiley.

Lawton, E. C., Fragaszy, R. J. & Hardcastle, J. H. (1989). Collapse of compacted clayey sand. *J. Geotech. Engng ASCE* **115**, No. 9, 1252–1267.

Lawton, E. C., Fragaszy, R. J. & Hardcastle, J. H. (1991). Stress ratio effects on collapse of compacted clayey sand. *J. Geotech. Engng ASCE* **117**, No. 5, 714–730.

Lee, X. & Zhang, L. M. (2009). Characteristics of dual structure pore size distribution of soil. *Can. Geotech. J.* **46**, No. 2, 129–141.

Leonards, G. A. (1955). Strength characteristics of compacted clays. *Trans. ASCE* **120**, 1420–1454.

Li, Z. M. (1995). Compressibility and collapsibility of compacted unsaturated loessial soils. *Proc. 1st Int. Conf. on Unsaturated Soils, Paris* **1**, 139–144.

McGown, A. & Collins, K. (1975). The microfabric of some expansive and collapsing soils. *Proc. 5th Panamerican Conf. Soil Mech. Found. Engng, Buenos Aires* **1**, 323–332.

Merchán, V. (2011). *Small strain stiffness and residual strength of unsaturated Boom clay: a micro-structural insight*. PhD thesis, Universitat Politècnica de Catalunya, Barcelona, Spain.

Mitchell, J. K., Hooper, D. R. & Campanella, R. G. (1965). Permeability of compacted clay. *J. Soil Mech. Found. Engng Div. ASCE* **91**, No. 4, 41–65.

Monroy, R., Zdravkovic, L. & Ridley, A. (2010). Evolution of microstructure in compacted London clay during wetting and loading. *Géotechnique* **60**, No. 2, 105–119, http://dx.doi.org/10.1680/geot.8.P.125.

Proctor, R. R. (1933). Fundamental principles of soil compaction. *Engng News Rec*. **111**, No. 9, 148–156.

Reséndiz, D. (1980). Compaction conditions, state variables and engineering properties of compacted clay. *Proceedings of the international conference on compaction*, Paris, Vol. 1, pp. 195–202.

Romero, E. (2002). *Characterization and thermo-hydro-mechanical behaviour of unsaturated Boom clay: an experimental study*. PhD thesis, Universitat Politècnica de Catalunya, Barcelona, Spain.

Romero, E. & Simms, P. (2008). Microstructure investigations in unsaturated soils. a review with special attention to mercury intrusion porosimetry and environmental scanning electron microscopy. *Geotech. Geol. Engng* **26**, No. 6, 705–772.

Romero, E. & Vaunat, J. (2000). Retention curves in deformable clays. In *Experimental evidence and theoretical approaches in unsaturated soils* (eds A. Tarantino and C. Mancuso), pp. 91–106. Rotterdam, the Netherlands: A. A. Balkema.

Romero, E., Gens, A. & Lloret, A. (1999). Water permeability, water retention and microstructure of unsaturated compacted Boom clay. *Engng Geol*. **54**, No. 1–2, 117–127.

Romero, E., Della Vecchia, G. & Jommi, C. (2011). An insight into the water retention properties of compacted clayey soils. *Géotechnique* **61**, No. 4, 313–328, http://dx.doi.org/10.1680/geot.2011.61.4.313.

Santucci de Magistris, F. & Tatsuoka, F. (2004). Effects of moulding water content on the stress–strain behaviour of a compacted silty sand. *Soils Found*. **44**, No. 2, 85–101.

Seed, H. B. & Chan, C. K. (1959). Structure and strength characteristics of compacted clays. *J. Soil Mech. Found. Div. ASCE* **85**, No. SM5, 87–128.

Sheng, D. (2011). Constitutive modelling of unsaturated soils: discussion of fundamental principles. *Proc. 5th Int. Conf. on Unsaturated Soils, Barcelona* **1**, 91–112.

Simms, P. H. & Yanful, E. K. (2002). Predicting soil-water characteristic curves of compacted plastic soils from measured pore-size distributions. *Géotechnique* **52**, No. 4, 269–278, http://dx.doi.org/10.1680/geot.2002.52.4.269.

Sridharan, A., Altschaeffl, A. G. & Diamond, S. (1971). Pore size distribution studies. *J. Soil Mech. Found. Div.* **97**, No. SM5, 771–787.

Suriol, J. & Lloret, A. (2007). Cambios en la estructura de suelos compactados frente a humedecimiento y secado. *Ingeniería Civil, Madrid* **147**, 7–76 (in Spanish).

Suriol, J., Gens, A. & Alonso, E.E. (1998). Behaviour of compacted soils in suction controlled oedometer. *Proc. 2nd Int. Conf. on Unsaturated Soils, Beijing* **1**, 463–443.

Tarantino, A. & de Col, E. (2008). Compaction behaviour of clay. *Géotechnique* **58**, No. 3, 199–214, http://dx.doi.org/10.1680/geot.2008.58.3.199.

Tarantino, A. & Tombolato, S. (2005). Coupling of hydraulic and mechanical behaviour in unsaturated compacted clay. *Géotechnique* **55**, No. 4, 307–317, http://dx.doi.org/10.1680/geot.2005.55.4.307.

Thom, R., Sivakumar, R., Sivakumar, V., Murray, E. J. & Mackinnon, P. (2007). Pore size distribution of unsaturated compacted kaolin: the initial states and final states following saturation. *Géotechnique* **57**, No. 5, 469–474, http://dx.doi.org/10.1680/geot.2007.57.5.469.

Tinjum, J. M., Benson, C. H. & Blotz, L. R. (1997). Soil-water characteristic curves for compacted clays. *J. Geotech. Geoenviron. Engng ASCE* **123**, No. 11, 1060–1069.

van Genuchten, M. T. (1980). Closed-form equation for predicting the hydraulic conductivity of unsaturated soils. *Soil Sci. Soc. Am. J.* **44**, No. 5, 892–898.

Vanapalli, S. K., Fredlund, D. G. & Rufahl, D. E. (1999). The influence of soil structure and stress history on the soil-water characteristics of a compacted fill. *Géotechnique* **49**, No. 2, 143–159, http://dx.doi.org/10.1680/geot.1999.49.2.143.

Wheeler, S. J. & Sivakumar, V. (1995). An elasto-plastic critical state framework for unsaturated soils. *Géotechnique* **45**, No. 1, 35–53, http://dx.doi.org/10.1680/geot.1995.45.1.35.

Wheeler, S. J. & Sivakumar, V. (2000). Influence of compaction procedure on the mechanical behaviour of an unsaturated compacted clay. Part 2: Shearing and constitutive modelling. *Géotechnique* **50**, No. 4, 369–376, http://dx.doi.org/10.1680/geot.2000.50.4.369.

Zhou, A.-N., Sheng, D., Sloan, S. W. & Gens, A. (2012a). Interpretation of unsaturated soil behaviour in the stress saturation space. II: Constitutive relationships and validations. *Comput. Geotech.* **43**, 111–123

Zhou, A.-N., Sheng, D., Sloan, S. W. & Gens, A. (2012b). Interpretation of unsaturated soil behaviour in the stress-saturation space, I: Volume change and water retention behaviour. *Comput. Geotech*. **43**, 178–187.

O'Brien, A. S. (2013). *Géotechnique*, 19–32 [http://dx.doi.org/10.1680/geot.sip11.ks]

The assessment of old railway embankments – time for a change?

A. S. O'BRIEN*

This paper summarises the results of several studies that have been carried out during the last 10 years on the behaviour of old railway embankments, composed of uncompacted, 'dumped' clay fill. Field observations from instrumented embankments, have shown that deformation and delayed failure are significantly affected by seasonal climate variations and by the type and spatial distribution of vegetation on the slope. Pore-water pressures (which largely control deformation and the risk of failure) vary markedly between summer and winter, due to the influence of climate and vegetation, and exhibit complex variations across an embankment. Often the pore-water pressures are negative, and the fill can be unsaturated. The dumped clay fills have a clod–matrix structure which is quite different to modern compacted fills or to natural clay. Laboratory studies indicate that this clod–matrix structure has an important effect on the shear strength, compressibility and permeability of the dumped clay fill. Numerical modelling of progressive failure and of climate–vegetation–pore-water pressure interactions provides insights into the factors which control behaviour. These studies show that the 'steady-state' assumptions typically assumed for embankment assessments are unreliable.

KEYWORDS: clays; field instrumentation; slopes; pore-water pressures; deformation; permeability

INTRODUCTION

In the UK, practising geotechnical engineers usually assume that soils are fully saturated. In particular, when assessing the stability of earthworks slopes, it is usually assumed that pore-water pressures increase hydrostatically with depth below a zero pressure line which is close to the slope surface. A significant amount (perhaps the majority) of the slope engineering currently carried out in the UK is associated with the assessment of old infrastructure earthworks, rather than the design and construction of new earthworks. Infrastructure owners in the UK have been implementing proactive asset management to improve the conditions of their earthworks. This has resulted in a growing awareness of the degradation of embankments as they get older. The task faced by Network Rail and London Underground is particularly daunting due to the old age (typically more than 100 years old) of their infrastructure embankments and to increasingly intensive use. CIRIA C592 (Perry *et al.*, 2003) outlines the requirements for cost-effective asset management, which are very different to conventional design, as the process is mainly one of comparing relative risks across the network; i.e. does embankment A need more urgent attention than embankment B. Table 1 provides a summary of some key questions for asset management engineers. In this context, conventional slope stability analyses are often of little value, as they indicate that the vast majority of old railway embankments do not comply with modern code requirements. Hence, the assumption of fully saturated soil behaviour does not provide a useful risk assessment tool. A particular challenge is to understand the reasons for apparently similar clay-fill slopes (with similar height/slope angle, and clays of similar intrinsic characteristics: clay fraction, liquid limit, etc.) behaving very differently. Many embankments, composed of high-plasticity clay fill, have been stable at slope angles of 26° to 30° (compared with a typical critical state friction angle of 20° to 25°) for over a hundred years, while others move excessively during dry summers, and others are prone to delayed failure (despite having survived many historic wet winters). The intent of this paper is to summarise several applied research studies which have been carried out during the last 10 years, and highlight the main practical implications. First, network-wide surveys of embankment deformation and failure will be described, followed by a series of field and laboratory studies at specific sites. Numerical modelling of deformation and failure, and modelling of climate–vegetation–slope pore pressure interactions will be discussed. Based on these studies, changes to current practice are suggested, and some future research needs are outlined.

NETWORK-WIDE SURVEYS

Figure 1 summarises the results of a study on train delays due to geotechnical causes, carried out by Mott MacDonald

Table 1. Rail embankment asset management – current challenges

Issue	Comment
Prioritisation	Key issue – which embankments need most urgent attention?
Stabilisation costs vs risk	How can limited funds be most effectively used?
Types of failure/deformation mechanism	Deep seated vs shallow failure, or excessive track deformation?
Consequence of failure/deformation	Train derailment, or delay, or inconvenience to neighbours?
Proactive management	When are problems likely to develop? Relevant strengths/pore pressures for assessment? Future degradation rates? Application of site observations?

* Mott MacDonald Ltd, Croydon, UK

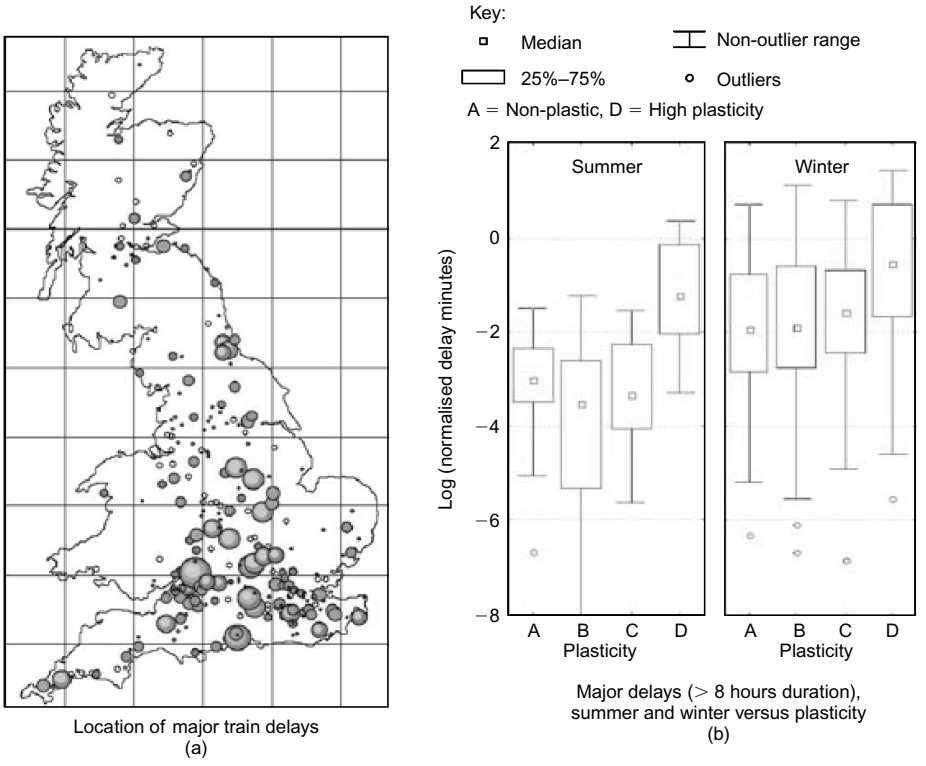

Fig. 1. Network Rail, delays due to geotechnical causes, 2000 to 2003

(2009) for Network Rail. During the period 2000–2003, it was estimated that delays due to geotechnical issues cost about £26 million. Figure 1(a) shows that the majority of these delays were located in southern England. Correlation with geological mapping indicated that these problems were mainly located in areas where high-plasticity clays are found. Statistical analysis of the data demonstrated that about 80% of the total delay time was due to a relatively small (about 20%) number of incidents. As would be expected, many of the delays occurred during the winter. Perhaps more surprisingly, for high-plasticity clays, the delays that occurred during dry summer weather were of a similar order of magnitude as those that occurred during wet winters, (Fig. 1(b)). Loveridge *et al.* (2010) discuss the results of this survey in more detail. A more recent study for the Rail Safety and Standards Board, for the period 2003–2009, has confirmed these trends (Mott MacDonald, 2011), with about 70% of the failures (excluding those due to scour or 'wash-out') located in Network Rail's Southern and Western Territories. A significant number of serviceability limit state (SLS) failures (i.e. excessive deformation) were reported during late summer/early autumn, when the effects of desiccation on high-plasticity clay fills would be anticipated to be most significant. Of the 95 ultimate limit state (ULS) failures, about half were classified as deep seated, with failure through the embankment crest. The rest of the ULS failures were classified as local crest instability, unravelling of oversteepened ash/ballast at the shoulder (typically most prevalent during the summer), or shallow, translational, failures. Delayed deep-seated failures are usually associated with slopes that have a modest cover of vegetation, such as grass or small shrubs, whereas SLS problems are usually associated with large trees being present on the slope. The embankments across the rail network are mostly between about 2 m and 8 m high, with slope angles typically between 22° and 30°. Hence, the slopes are often smaller and steeper than those which have been the focus of previous studies reported in the literature.

FIELD STUDIES

Skempton (1996) has described the construction methods which were used for these old embankments, and their resulting heterogeneity. Figure 2(a) shows a historical photograph of the construction of a railway embankment, where the clay fill was tipped onto the natural ground surface, without any systematic compaction of the clay fill. These uncompacted clay fills are often known as 'dumped' clay fills (Vaughn *et al.*, 2004). Following construction, large 'collapse-type' settlement of the unsaturated clay fills would have occurred upon rainfall infiltration. These settlements were compensated by adding readily available granular fill (such as locomotive ash or track ballast). Figure 2(b) shows a sketch of a typical rail embankment composed of clay fill. Major differences are likely to exist between a modern highway embankment of heavily compacted clay fill and an old embankment of dumped clay fill. In addition to greater heterogeneity, the old rail embankments often contain 'hidden defects', due to, *inter alia*: inclusion of old shear surfaces from historic instability (only partially removed/repaired); local high-permeability sand lenses; and remnants of topsoil/alluvium along the base of the embankment (typically there was little preparation or improvement of the underlying natural soils prior to construction). The overall shape of these embankments can be quite variable. Some embankments have retained a relatively steep uniform slope; whereas others have a 'coat-hanger' appearance with an oversteepened upper slope and a shallower lower slope.

Several field studies have been undertaken to better understand embankment deformation mechanisms. Figure 3, based on studies by Scott *et al.* (2007) of a London Underground Ltd (LUL) embankment, plots vertical deformation at an embankment crest (monitored via extensometers), track deformation and soil moisture deficit (SMD) against time. It should be noted that the SMD values which are used by Scott *et al.* are the values published by the UK's Met Office, specifically SMD for deciduous trees. Two different embankment areas were monitored, one was in an area with a dense

Embankment construction
(a)

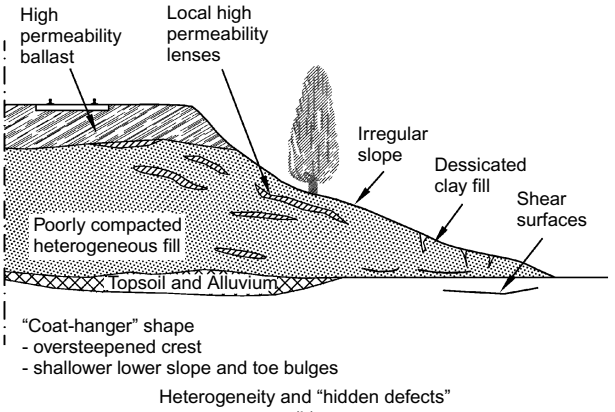

(b)

Fig. 2. Historical rail embankment, construction and typical features

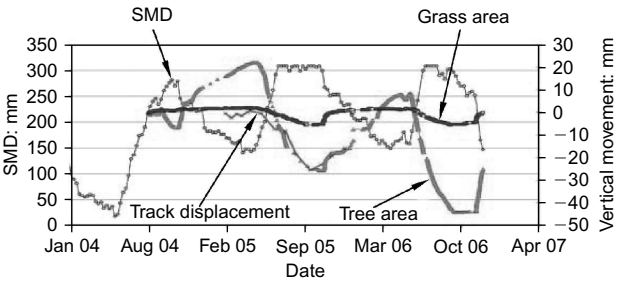

Notes:

1. SMD is Soil Moisture Deficit for deciduous trees.
2. NHBC (2003) classification system used to classify tree water demand, except that an additional class is added, Very High Water Demand (VHWD) for oaks and poplars, based on experience of the significant effects that these trees have on track deformation.

Fig. 3. Vertical deformation, influence of climate (SMD) and vegetation (after Scott *et al.*, 2007)

cover of very high water demand (VHWD) trees (oaks and poplars), while the other was predominantly a grass-covered slope. The two areas were relatively close (less than 100 m apart), and the clay fill (derived from weathered London clay, with a plasticity index of about 45–50%) was practically identical at both of the monitoring locations. Embankment deformation was more than ten times higher in the area affected by VHWD trees. Deformation in the VHWD tree area was closely correlated with changes in SMD. As SMD increased during the summer, settlement occurred, while heave occurred when SMD reduced during the winter. In the tree area, the track movement follows a similar pattern to the crest deformation.

Figures 4 and 5 summarise some recent monitoring of Network Rail embankments. One embankment is composed of Gault clay fill, and the other is composed of London clay fill. The index properties for these sites are summarised in Table 2 and can be compared with the LUL fill. Figure 4 plots horizontal displacement, via inclinometers in the mid-slope area, versus time for the Gault clay site. It can be seen that the greatest displacement is at the slope surface, and there is a seasonal trend in displacement. Displacements were less than 5 mm at depths greater than about 4 m. Outward displacement is observed between February and July, the displacement then moves inwards between August

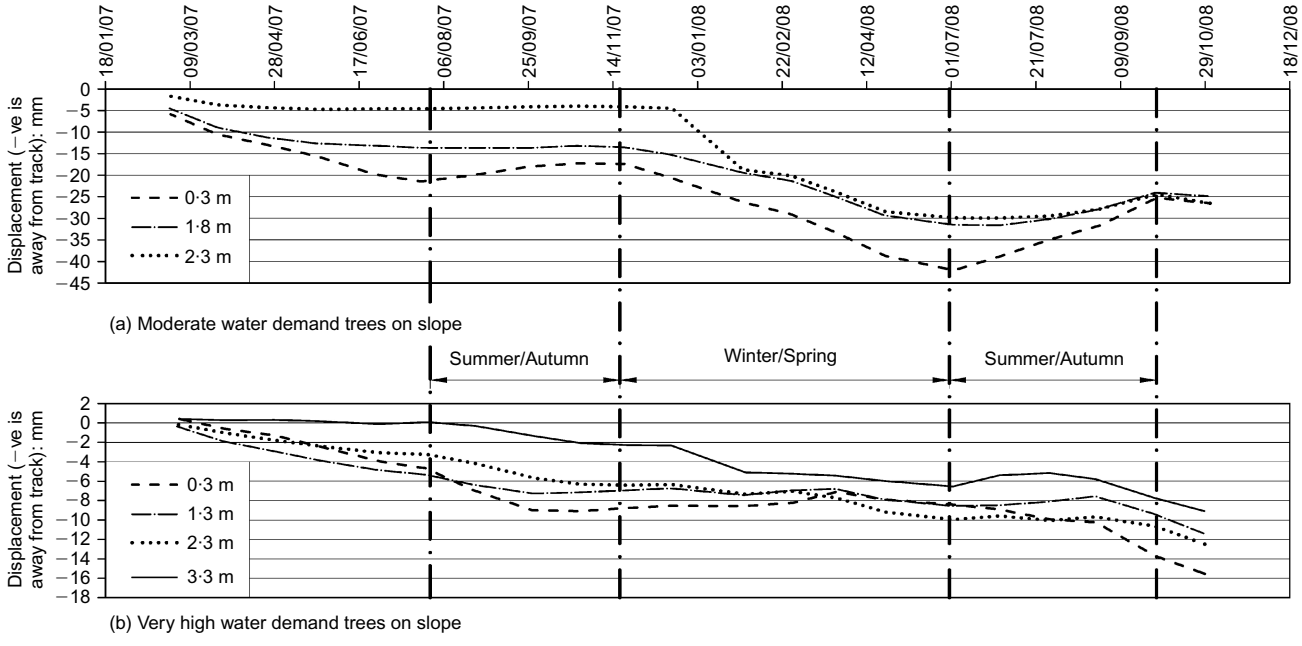

Notes:

1. Vegetation on embankment slope classified in accordance with NHBC (2003), except oak and poplar trees classified as Very High Water Demand (VHWD)

Fig. 4. Horizontal deformation versus time, Gault Clay embankment

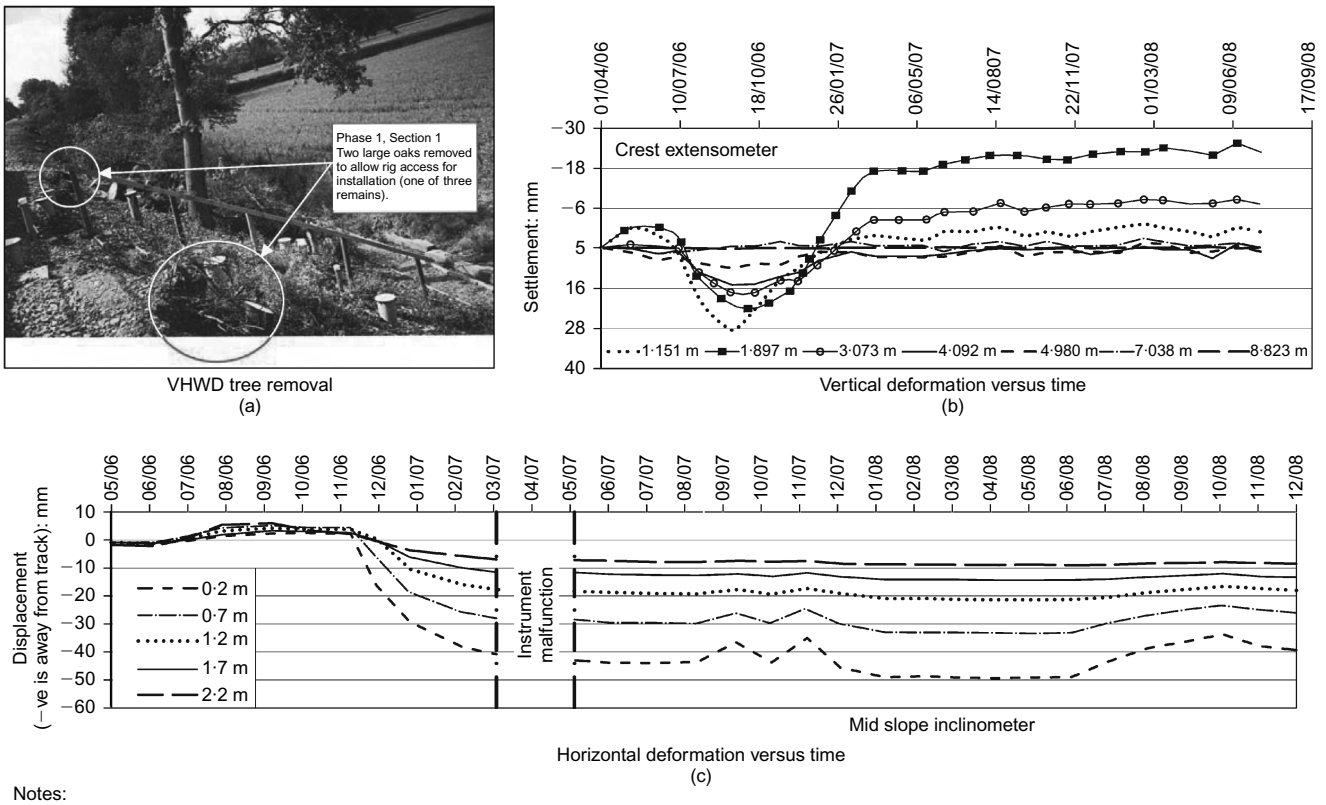

Notes:

1. Tree removal during mid-March, 2006.
2. Depths quoted are depth below slope surface.

Fig. 5. Influence of VHMD tree removal on embankment deformation, London Clay embankment

Table 2. Index properties for dumped clay fills

Site	Geology	Moisture content (%)		Liquid limit (%)		Plasticity index (%)		Clay fraction (%)	Sand/gravel fraction (%)
		Mean	SD	Mean	SD	Mean	SD		
Network Rail, Charing	Gault clay	24·9	3·3	57·4	10·9	34·1	9·1	30–60	5–40
Network Rail, Pound Green	London clay	25·1	5·0	53·8	12·5	33·0	9·7	25–50	10–40
London Underground (LUL)[(1)]	London clay	26·5–35·8	5·3–7·4	67·7–74·4	6·7–15·9	42·7–49·4	6·5–13·9	50–70	0–15

Notes:
(1) Ranges for six different LUL sites.
(2) SD = standard deviation.

and November, followed by another outward/inward cycle during the subsequent winter/summer, respectively. During the 2-year monitoring period there was a net outward movement of between 10 mm and 15 mm per annum. The inclinometer located within an area of VHWD trees showed rather smaller seasonal horizontal displacements than the inclinometers located in areas of less dense and lower water demand vegetation. Outward movement coincided with periods when SMD was less than about 10 mm. Embankment deformation correlated better with SMD than rainfall, solar radiation or evapotranspiration. Inclinometers near the crest did not show any significant deformation (i.e. greater than 5 mm). Figure 5 plots vertical and horizontal deformation against time for the London clay site. At this site, in contrast to the Gault clay site, significant vegetation was removed to allow rig access (Fig. 5(a)), and two large oak trees were removed close to the instruments. Vertical displacement (Fig. 5(b)) exhibits an initial settlement during the first summer, followed by sustained swelling which is reasonably deep seated (to a depth of about 4 m). Horizontal displacement (Fig. 5(c)) exhibits negligible movement during the first summer, followed by a relatively large outward movement during the following winter. This movement is relatively shallow, predominantly within the upper 2 m of the slope. The movements are consistent with a gradual wetting-up of the slope following the removal of VHWD trees and rainfall during the autumn/winter of 2006/2007.

Figure 6(a) plots the weather station data for rainfall at the Gault Clay site for part of the monitoring period (June 2007 to May 2008) compared against long term averages (1972 to 2000) published by the Met Office. Local SMD data published by the Met Office is plotted on Fig. 6(b).

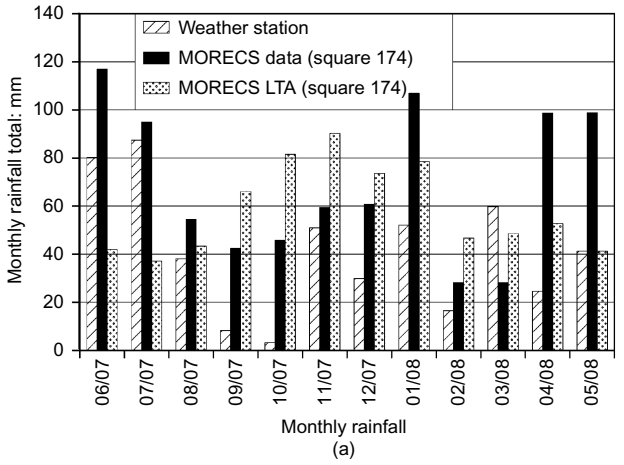

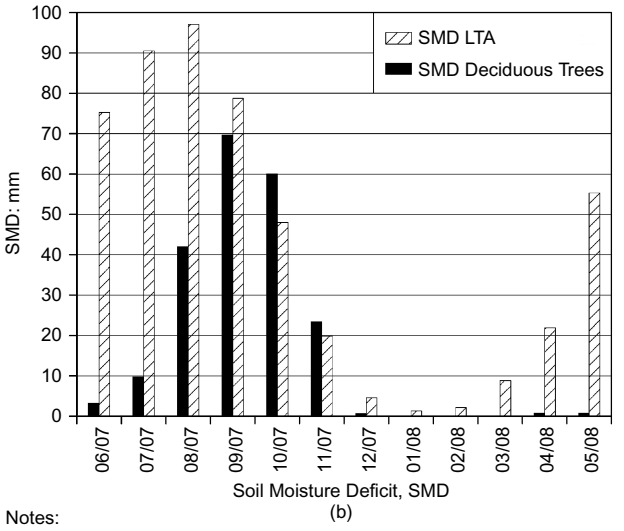

Notes:
1. MORECS = Met Office Rainfall and Evaporation Calculation System
2. LTA = Long Term Average

Fig. 6. Monthly rainfall and SMD during monitoring period, Gault clay embankment

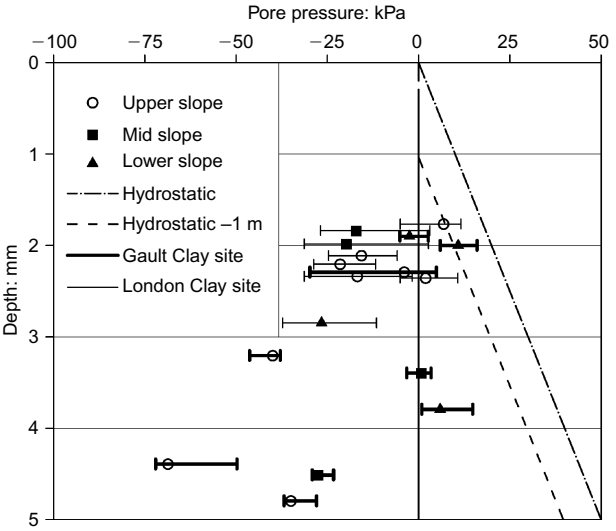

Notes:
1. Gault Clay site, monitoring between January 2007 and January 2008.
2. London Clay site, monitoring between April and December 2008.

Fig. 7. Measured porewater pressure at NR sites

Figure 7 plots pore-water pressures recorded by geopiezometers (Ridley *et al.*, 2003) against the depth below the slope surface. During the monitoring period, the rainfall pattern was unusual for south-east England, with a wetter than average summer followed by a drier than average winter. Most of the piezometers measured small suctions (up to 75 kN/m^2 negative pore pressure), especially at depths greater than 2·5 m and in the mid and upper slope areas. The piezometers used (Ridley *et al.*, 2003) are capable of measuring suctions in the field of up to about 100 kN/m^2. At shallower depths (about 2 m), higher pore-water pressures were recorded, with a few recording small positive pressures. Typically, the pore-water pressures in the lower slope area were higher than those towards the crest. These measured pore pressures need to be considered in the context of the prevailing weather conditions. During summer periods much larger suctions have been measured, especially beneath areas affected by VHWD trees; for example, O'Brien *et al.* (2004) report summer suctions between 100 kN/m^2 and 400 kN/m^2, together with seasonal changes of more than 200 kN/m^2. Maximum SMD (for deciduous trees) during the monitoring period was 70 mm, compared with a value of 279 mm during the dry summer of 2003 and a national long-term average maximum summer SMD of 124 mm. Because of the relatively wet summer followed by a dry winter, the seasonal change in pore-water pressure at the Gault clay site is relatively low, 30 kN/m^2 or less.

During the winter of 2000/2001, the UK experienced the wettest weather since records began in 1766 (Birch & Dewar, 2002). During the winter/spring period of 2001, spot measurements of pore-water pressure were recorded at several sites across the LUL network (Ridley *et al.*, 2004). These data have been re-analysed by Briggs *et al.* (2011) and are plotted on Fig. 8. At sites underlain by a low-permeability (typically weathered London clay) foundation soil (Fig. 8(a)), the piezometer data are bounded by a hydrostatic line to a depth of about 2 m below the clay-fill surface. Beneath this, the bounding profile reduces to about 60% of hydrostatic. Relatively low pressures were recorded at many locations, with about 20% of the readings close to zero pressure, and more than half the pressures being less than 20 kN/m^2. At sites underlain by a relatively high-permeability (typically chalk or river terrace deposits) foundation soil (Fig. 8(b)), virtually all the piezometers record relatively low pressures, with 85% of the data values being less than 10 kN/m^2.

SMD has often been used to assess the risk of slope instability (e.g. Ridley *et al.*, 2004). As discussed below, the comparison between SMD, site-specific pore pressure and rainfall data suggests that some care is required in using SMD data. For the Gault clay site, from December 2007 to May 2008 there were 6 months when SMD was zero (or very close to zero, less than 5 mm), which is only one month less than the historically wet winter of 2000/2001. However, winter rainfall is relatively low. This apparent inconsistency can be explained by the preceding wet summer (when SMD was less than 70 mm). Hence, the soil surface zone requires less rainfall infiltration to return to field capacity. It should be noted that SMD is a measure of moisture conditions in the near-surface soil zone, and may not be representative of pore pressure conditions at depth. Figure 6(a) indicates that the rainfall data measured at the site weather station is consistently lower than the local Met Office data (for MORECS square 174). The North Downs are located in this MORECS square and they are likely to influence weather patterns, causing differences in weather patterns across the 40 km of the MORECS square. Published Met Office data (including SMD values) remain a useful tool for considering broader patterns of behaviour, but may

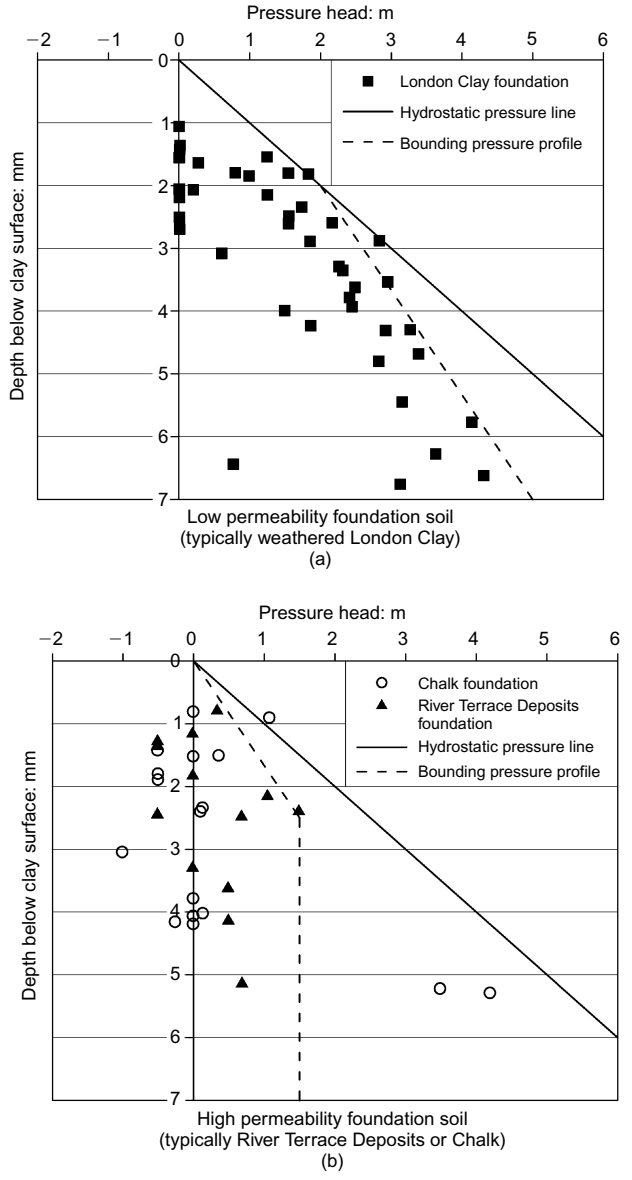

Fig. 8. Pressure heads measured across London Underground Ltd network during March/April 2001 (based on data by Ridley *et al.*, 2004)

be inadequate for assessing local earthworks risks (both for ULS and SLS conditions).

DUMPED CLAY FILL PROPERTIES

At several sites, block samples of clay fill have been obtained and suites of laboratory tests have been carried out to assess shear strength, deformation and permeability characteristics of saturated test specimens. Field tests to measure shear modulus, at very small strain (G_o) with a seismic cone, and permeability have also been carried out. Test data for LUL sites have been discussed in O'Brien *et al.* (2004) and O'Brien (2007). The LUL data are compared with the Network Rail data (for the Gault and London clay sites) in Figs 9, 10 and 11 for shear strength, compressibility and permeability, respectively. At the Gault clay site, the in situ G_o profile fluctuated between 30 MN/m^2 and 70 MN/m^2 (occasional hard bands gave higher values), and the laboratory G_o measurements were broadly similar, indicating that the block samples are of high quality. In addition to the tests on block samples, a series of tests was carried out on reconstituted specimens, which were reconsolidated to a

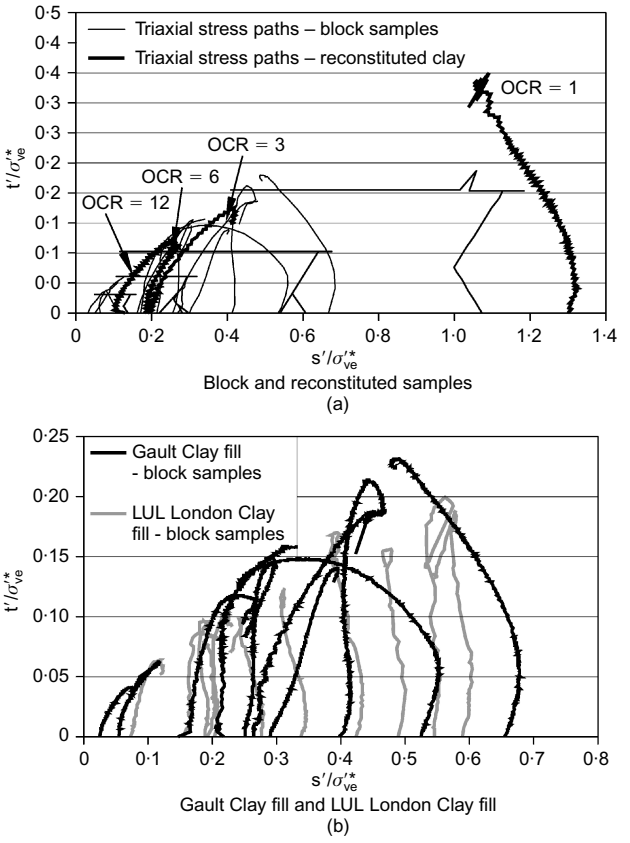

Notes:

t = $(\sigma'_v - \sigma'_h)/2$; s′ = $(\sigma'_v = \sigma'_h)/2$.
σ'^*_{ve} = equivalent pressure on ICL derived from shear zone moisture content.
ICL = intrinsic compression line.

Fig. 9. Dumped clay fills, normalised triaxial stress paths to failure

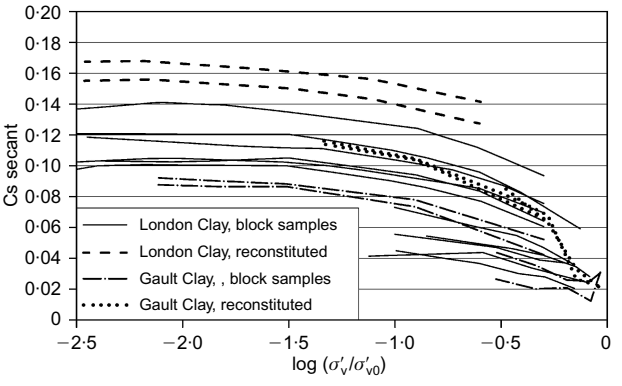

Notes:

1. σ'_v is vertical effective stress, σ'_{v0} is vertical effective stress at commencement of swelling. Cs is secant index.

Fig. 10. Dumped clay fills, swelling behaviour, Gault Clay and LUL London Clay

range of different overconsolidation ratios. For the Gault clay fill (Fig. 9(a)) shows the effective stress paths for undrained triaxial tests on block samples and reconstituted clay fill. The stresses have been normalised by the equivalent pressure on the measured oedometric intrinsic compression curve (σ'^*_{ve}) (Burland, 1990). This Hvorslev-type normalisation procedure facilitates an appraisal of the potential influence of soil structure on peak strength (Burland *et al.*,

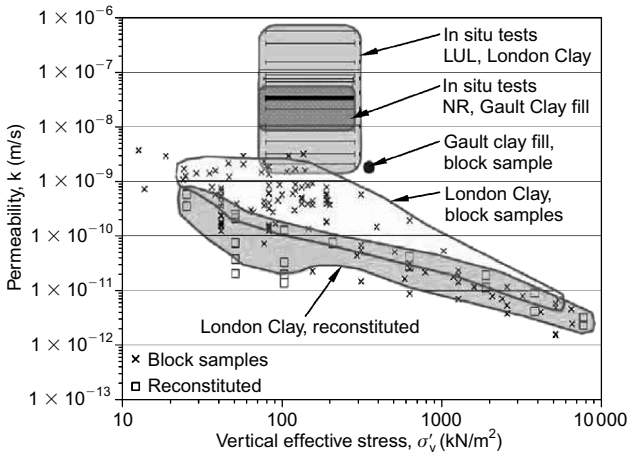

Note:

1. Slope surface measured permeability, 1×10^{-6} to 1×10^{-5} m/s (cracking??)

Fig. 11. Permeability of dumped clay fill, in situ versus laboratory test

1996). From Fig. 9(a) it can be seen that the normalised strength of the clay fill is similar to that of the overconsolidated reconstituted clay. Hence, the in situ clay-fill strength does not appear to be significantly affected by structure. The Gault clay fill tends to mobilise higher shear strength than the London clay fill from the LUL sites (Fig. 9(b)); this can probably be explained by the lower plasticity index and lower clay fraction of the Gault clay fill.

Figure 10 plots the secant swelling index (C_S, measured during oedometer tests) of reconstituted and block samples of clay fill, against the ratio of the current (σ'_v) to initial vertical effective stress (σ'_{vo}) during unloading (σ'_v/σ'_{vo}). The data fall into three bands: reconstituted clay fill, block samples of clay fill swelled from high stress (in excess of 3000 kN/m^2) and block samples of clay fill swelled from low stress (about 250 kN/m^2). The reconstituted samples exhibit the highest values of C_S, and the block samples swelled from low stress the lowest values of C_S. This is indicative of the clay fill retaining some of the 'structure' (including bonding) from the parent natural clay. The Gault clay fill is about 30–50% stiffer in swelling then the LUL London clay fill.

Laboratory and in situ permeability test data are summarised on Fig. 11. As discussed later in this paper, permeability is an important parameter. Permeability varies significantly, for a particular soil, with the degree of saturation. However, unless stated to the contrary, the permeability values quoted below are for the soil in a fully saturated state. There is a consistent trend for the laboratory values to be lower (typically by one or two orders of magnitude) than the in situ values. The in situ values (from variable-head borehole tests) cover a wide range, although tests carried out within predominantly clay fills (at depths greater than about 2 m) vary between 2×10^{-9} m/s and 5×10^{-8} m/s. Compared with published data for the in situ permeability of natural stiff overconsolidated fissured clays (e.g. Hight *et al.*, 2003), the permeability of the dumped clay fill is about an order of magnitude higher. Tests in fills affected by silt and sand lenses have measured permeabilities of between 10^{-7} m/s and 5×10^{-6} m/s. Guelph permeater tests were also carried out at the slope surface, and are representative of the permeability (most likely at conditions near 'field saturation', i.e. a degree of saturation S_r of <90%) of a small volume of soil. Derivation of the test results accounts for the unsaturated nature of the near-surface soils. Measured Guelph test permeabilities were between about $1{\cdot}0 \times 10^{-6}$ m/s and $3{\cdot}0 \times 10^{-6}$ m/s for the surface clay fills, i.e. about two to three orders of magnitude higher than the permeabilities measured at depth within the embankment.

The variable influence of structure and macrofabric on the strength, compressibility and permeability of dumped clay fills can be readily explained by a simple clod–matrix conceptual model (O'Brien, 2007). The clods represent the intact lumps of parent natural clay (which can be seen in the historical photograph shown in Fig. 2(a)). The matrix comprises both remoulded clay and foreign matter (silt, sand, etc.) introduced during handling, transportation and tipping of the fill. The test data outlined above indicate that compressibility/swelling behaviour is largely controlled by the clods, whereas the matrix mainly controls the shear strength and permeability of the clay fill. An X-ray computed tomography study at Southampton University (Watson *et al.*, 2007) has confirmed the validity of this simple conceptual model.

NUMERICAL MODELLING OF DEEP-SEATED DELAYED FAILURE

The numerical modelling of the delayed failure of old railway embankments has been described by Kovacevic *et al.* (2001) and Nyambayo *et al.* (2004), using ICFEP (Imperial College Finite Element Program), and O'Brien *et al.* (2004), using FLAC (Fast Lagrangian Analysis Code). The FLAC modelling simulates the post-peak degradation of strength towards post-rupture and then residual strength. The failure mechanism commences at the toe, and then, with an increasing number of seasonally induced pore pressure changes, the failure surface propagates along a subhorizontal surface towards the embankment core (Fig. 12). At failure, the clay-fill strength is close to residual in the vicinity of the embankment toe, whereas near the crest it is close to peak strength. This non-uniform mobilisation of strength has important practical implications for the design of potential stabilisation measures. Prior to collapse, the simulation of seasonal changes in pore pressure leads to a 'ratcheting'-type deformation mechanism being predicted by the numerical models, with outward deformation during winter being only partially recovered during summer. Field observations (Fig. 4) also suggest that a ratcheting-type deformation mechanism can develop in these embankments, and this deformation mechanism also helps to explain the 'coat-hanger' shape that is often seen (Fig. 2). This deep-seated delayed failure mechanism has also been verified by centrifuge modelling, Take & Bolton (2004). The centrifuge test showed that clay fill permeability, and rainfall duration and infiltration were likely to control the development of swelling and shear strain at the embankment toe. Numerical modelling reported by Nyambayo *et al.* (2004) has indicated that embankments with a clay-fill permeability of between 10^{-7} m/s and 10^{-8} m/s will be prone to delayed failure, whereas embankments with a clay-fill permeability of 10^{-9} m/s or less are relatively stable. The measured clay-fill permeabilities (Fig. 11) transverse across this intermediate range of permeability, which leads to embankments being prone to delayed failure. Fully coupled hydrological/mechanical modelling by Davies (2010) also showed that the bulk permeability of the clay fill is critically important, and significantly affects the risk of collapse. These numerical modelling studies were largely based on a characterisation of the LUL clay fills. Following the investigations at the Network Rail sites, additional numerical modelling has been carried out. These additional studies used the same methodology as that described by O'Brien *et al.* (2004), but the strength and compressibility characteristics were varied

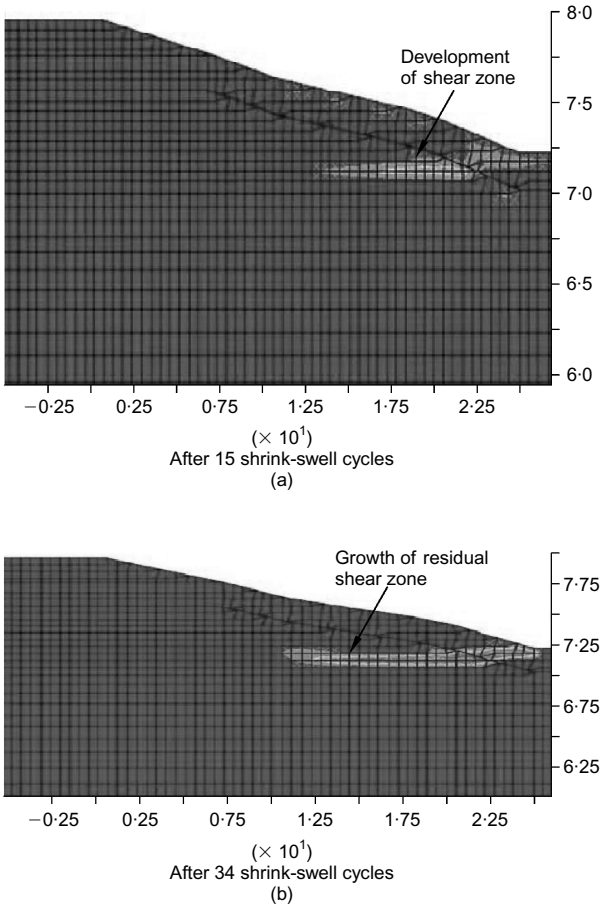

Note:

1. Embankment 7·35 m high, with 1:3·3 (V:H) slope gradient. Poorly drained, grass covered slope, intermediate plasticity clay fill.

Fig. 12. Numerical modelling of progressive failure

across a broad range in order to simulate the site-specific data described above, and the potentially more heterogeneous conditions likely to be encountered across Network Rail sites. Some of the results from this parametric study are summarised in Table 3. Appendix 1 provides a summary of the modelling and 'base case' parameters. The compressibility and strength of the clay fill (both peak and residual strength) had an influence on the number of cycles to failure, as would be expected. However, the risk of collapse (implied by the change in the number of cycles to failure) was highly sensitive to two particular factors:

(*i*) the inclusion of a thin layer of alluvium below the clay fill
(*ii*) a relatively small change in maximum winter pore pressures in the clay fill.

The presence of a more compressible layer of alluvium led to a concentration of plastic strain within this layer. Once plastic strains are initiated at the toe, the embankment with the underlying soft alluvium is less able to mobilise the required shear resistance elsewhere in the embankment. In contrast, the clay fill without an alluvial layer (because of its more uniform compressibility and shear stiffness) was able to mobilise a greater proportion of its peak shear strength. The change in winter pore pressure considered two scenarios:

(*a*) Poorly Drained: 100 kN/m^2 summer surface suction, reducing linearly with depth to zero at 2 m below the slope; zero winter surface suction.
(*b*) Well Drained: summer surface suction, same as in (a) above, but zero suction between the surface and 1 m depth during winter.

For both scenarios, the pore pressure increase below the zero suction line was about 80–90% of hydrostatic. For scenario (b), the lower winter pore pressure at the toe leads to a higher mobilised shear strength and lower plastic strains. Hence, the rate of degradation of strength, due to seasonal pore pressure changes, was far lower for scenario (b) than for scenario (a).

NUMERICAL MODELLING OF CLIMATE–PORE PRESSURE INTERACTIONS

VADOSE/w has been used to assess the influence of climate on pore pressures in embankment fill (Mott MacDonald, 2008). Further detail is given in Briggs (2011). A wide range of scenarios have been considered, including:

(*i*) changes in climate
(*ii*) changes in clay-fill permeability
(*iii*) changes in vegetation type on the embankment (VHWD trees versus grass)
(*iv*) changes in slope geometry.

The VADOSE modelling is summarised in Appendix 2. Selected output from some of the modelling is given in Figs

Table 3. Numerical modelling: influence of an alluvial layer and winter pore pressure on delayed failure

Site geometry[3]	Fill properties	Groundwater conditions	Description of parameter change	Number of cycles to failure	
$H = 4{\cdot}6$ m $G = 1{:}1{\cdot}8$[1]	Intermediate plasticity	Poorly drained	Influence of a thin layer of alluvium below embankment	33 (no alluvium)	7 (alluvium)
$H = 7{\cdot}5$ m $G = 1{:}3{\cdot}2$[2]	Intermediate plasticity	Poorly drained	Influence of a thin layer of alluvium below embankment	35 (no alluvium)	19 (alluvium)
$H = 8$ m $G = 1{:}2{\cdot}5$[2]	Intermediate plasticity	Poorly drained	Influence of a thin layer of alluvium below embankment	15 (no alluvium)	8 (alluvium)
$H = 7{\cdot}5$ m $G = 1{:}3{\cdot}2$	High plasticity	Changes simulated	Varied from 'poorly drained' to 'well drained'	14 (poorly drained)	>50 (Well drained)
$H = 4{\cdot}6$ m $G = 1{:}1{\cdot}8$	Intermediate plasticity	Changes simulated	Varied from 'poorly drained' to 'well drained'	33 (poorly drained)	>50 (well drained)

Notes:
(1) Alluvial layer assumed to be 0·5 m thick.
(2) Alluvial layer assumed to be 1·0 m thick.
(3) H = embankment height, G = slope gradient, vertical: horizontal.

13 to 16. Figure 13 shows a contour plot of pore pressures within a relatively large, shallow tree-covered embankment during a summer/winter cycle. The Newbury weather data (Smethurst *et al.*, 2006) was used for 2005/2006, which represents a dry summer/wet winter cycle (with SMD varying between zero and 150 mm), although this is not an extreme weather period. In summer, deep zones of suction are mobilised below the tree-covered slope, and during the subsequent winter the near-surface layers (upper 2 m or so) wet-up and exhibit positive pore pressures in some locations. If the trees are removed from the upper two-thirds of the slope (Fig. 14), then the depth of summer suctions is reduced, and much larger zones of positive pore pressure develop during subsequent winter periods below the grass-covered parts of the slope. Winter suctions are still maintained at depth below the lower third of the slope, which is tree covered. Because of the idealisations within this type of analysis, the outputs are not intended to be 'predictive' of the actual spatial distribution of pore pressures. However, these analyses provide useful insights into overall patterns of behaviour, and the relative importance of different variables. The clay-fill permeability has a significant effect, as would be expected, with a critical intermediate zone of permeability of between 5×10^{-8} m/s and 5×10^{-7} m/s being identified (Mott MacDonald, 2008). Pore pressures increased relatively rapidly during winter rainfall, when clay-fill permeability was 5×10^{-7} m/s, whereas negligible pore pressure change occurred if clay-fill permeability was as low as 5×10^{-9} m/s. An important consideration is the ratio of clay-fill permeability to daily rainfall. At the Gault clay site, during the monitoring period, on days when rainfall events >1 mm occurred, the average daily rainfall was about 5 mm, with a maximum of 25 mm. The rate of rainfall infiltration is limited by the saturated permeability of the clay fill, with any excess rainfall running off the slope. For a clay-fill permeability of 5×10^{-9} m/s, the maximum daily rainfall infiltration is less than 0·5 mm/day (hence most rainfall runs off the slope), whereas a clay-fill permeability of 5×10^{-8} m/s or higher allows most of the daily rainfall to infiltrate into the slope. Hence, a large number of moderately wet winter days will lead to far higher winter pore pressures than will a small number of extremely intense rainfall events.

As noted in the Introduction, many of the old railway embankments are relatively small and steep. It is interesting, therefore, to compare the influence of slope geometry on seasonal changes in pore pressure (Fig. 15). Comparing Figs 15(a) and 15(b), the smaller, steeper embankment exhibits

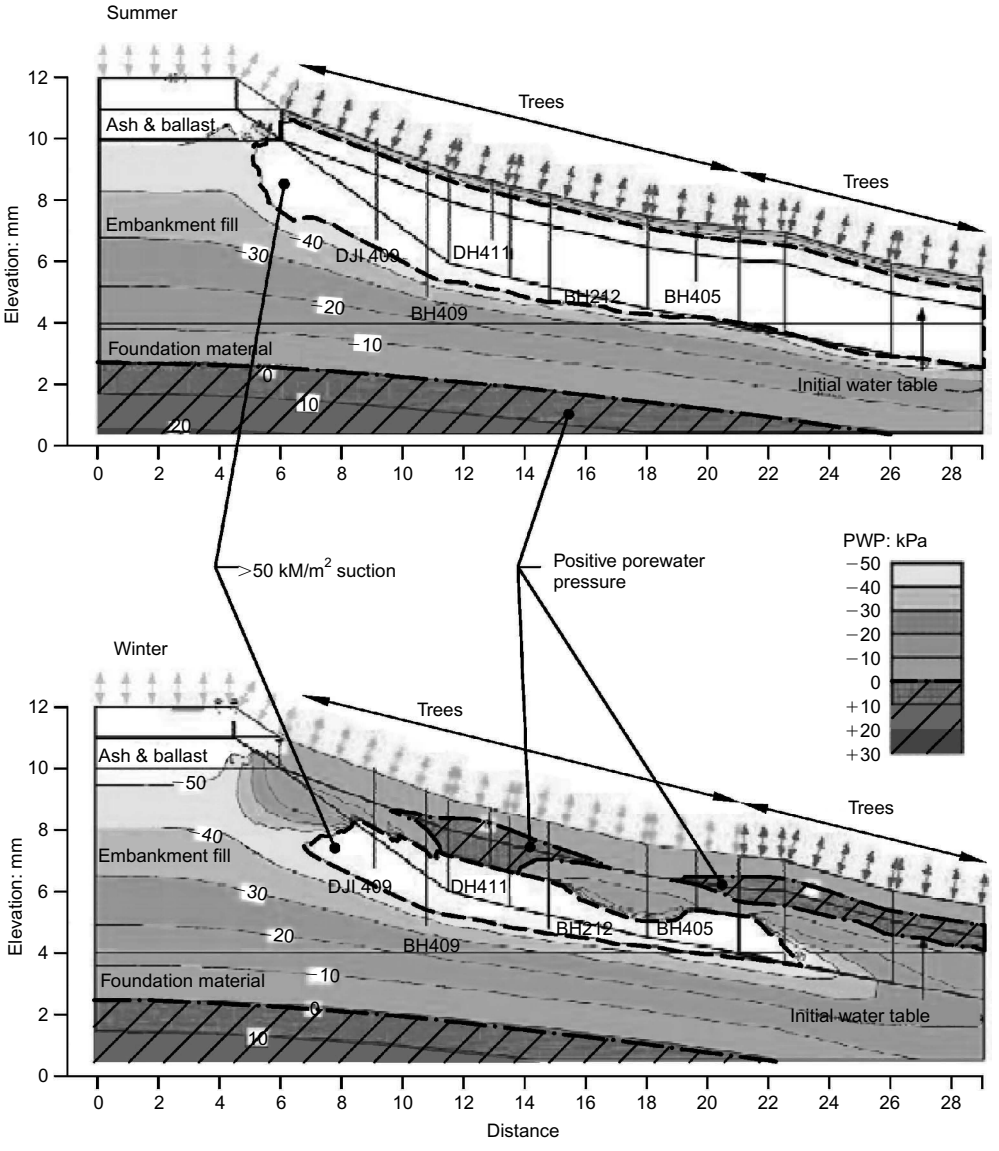

Fig. 13. Hydrogeological modelling of seasonal changes in porewater pressure (tree covered slope)

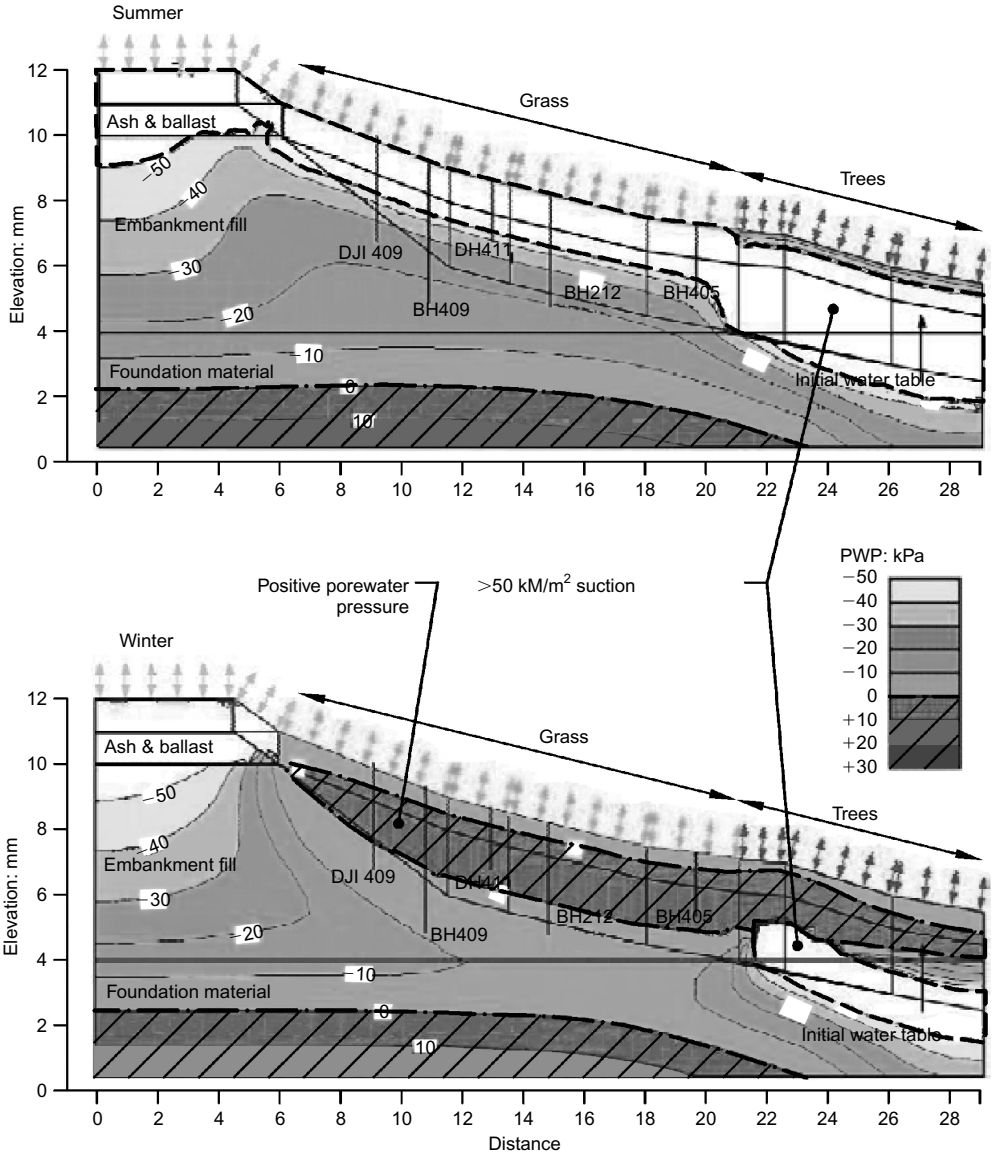

Fig. 14. Hydrogeological modelling of seasonal changes in porewater pressure (trees removed from upper slope)

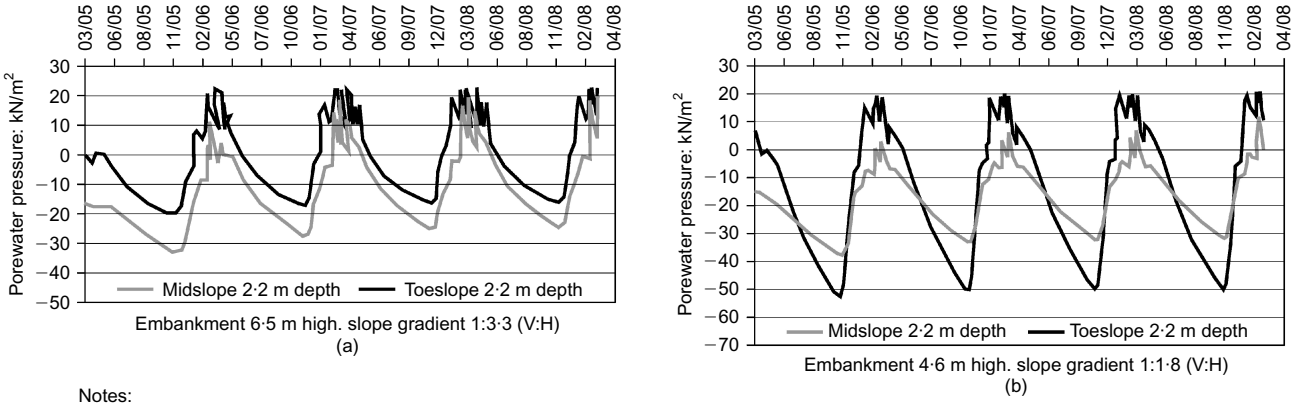

Notes:

1. Grass covered slope.
2. Newbury climate data, March 2005 to March 2008.

Fig. 15. Hydrogeological modelling, influence of embankment geometry

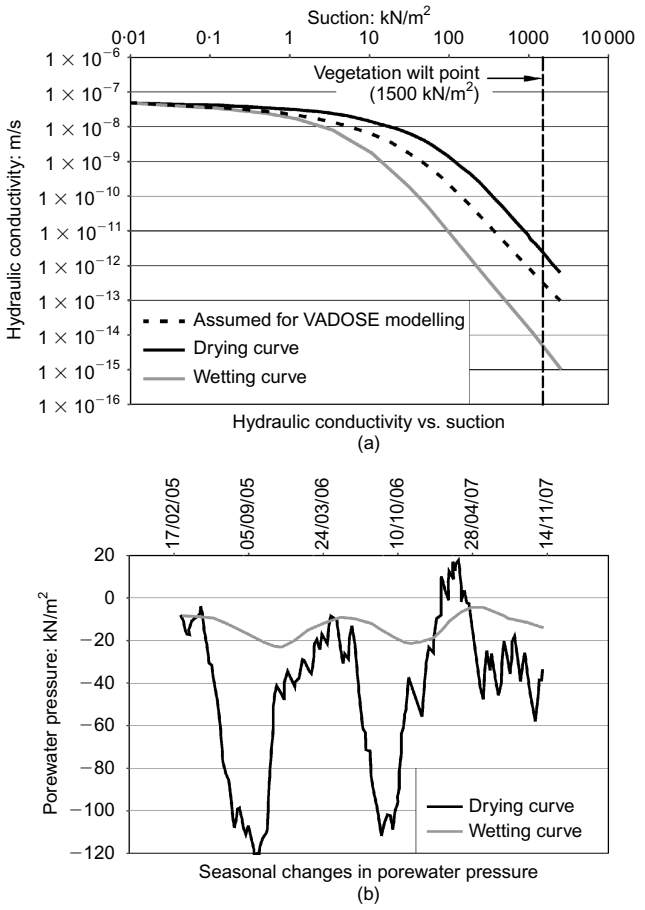

Notes:

1. "Drying" and "wetting" curves based on modified Croney (1977) curves for natural London Clay.
2. Newbury climate data. Pore water pressure at 1·9 m below surface.

Fig. 16. Influence of unsaturated hydraulic properties on seasonal changes in pore water pressure

lower pore pressures in general than does the larger, shallower embankment. In particular, for the small embankment the summer/autumn maximum suctions are relatively high in the toe slope area, and the winter maximum positive porewater pressures are relatively low in the midslope area. For both embankments the toe area has higher winter pore pressures than the midslope area. Modelling by Briggs *et al.* (2011) has shown that the permeability variations across three zones – near-surface (higher permeability) clay fill, basal clay fill, underlying foundation soil – are critical. A foundation soil permeability two orders of magnitude higher than the overlying clay fill was found to be sufficient to create underdrainage conditions, comparable to those shown in Fig. 8(b).

From Fig. 7 it can be seen that, even during a relatively wet monitoring period, the slope pore pressures fluctuate between moderate suctions and small positive pore pressures. Hence, the variation in permeability with changes in soil suction is likely to be a critical parameter. Unfortunately, measurements of unsaturated hydraulic properties, both in the laboratory and, particularly, in the field, are lacking. The significant influence of unsaturated hydraulic properties on seasonal pore pressure change are shown on Fig. 16(b). The use of the 'wetting' curve in Fig. 16(a) leads to small changes in seasonal pore pressure, in contrast to the use of the 'drying' curve, which leads to large changes in seasonal pore pressure. The modelling discussed above assumed an intermediate variation of permeability with suction, between the drying/wetting curves shown on Fig. 16(a).

The permeability characteristics of the unsaturated soil will also be significantly affected by hysteresis effects (Li *et al.*, 2005); i.e. during wetting the permeability will be lower, at a given soil suction, than during drying. Laboratory soil-column experiments (e.g. Lenhard *et al.*, 1991) highlight the importance of hysteresis effects on pore pressures developed in unsaturated soils. A major practical challenge is the lack of reliable data for the in situ hydraulic properties of unsaturated soils, in general, and for dumped clay fills (with their clod–matrix structure) in particular.

PRACTICAL IMPLICATIONS

Figure 17 schematically illustrates the degradation of mobilised clay-fill strength and pore-water pressure changes with time within old rail embankments, which have been discussed above. Figure 17 emphasises the dynamic nature of the interactions that take place between embankment clay fill, vegetation and climate; which is in stark contrast to conventional 'steady-state' assumptions. Two of the most important factors that can affect the risk of delayed failure, or excessive embankment (and rail track) deformation, are clay-fill permeability and the type of vegetation cover on the embankment slope. Both of these factors are usually ignored during conventional assessments of embankment behaviour. Hence, it is unsurprising that conventional analyses are unhelpful in the context of asset-management risk assessments. During dry summers significant train delays are caused by excessive track deformation due to VHWD trees causing desiccation of intermediate- and high-plasticity clay fills. Simple solutions for the elimination of seasonal track deformation are not available once large trees have become established across a slope. Tree removal from the crest will be most effective, but HWD and VHWD trees at the toe may still cause some seasonal track deformation. Tree removal from the lower half of the slope could lead to catastrophic collapse during wet winters, once roots have decayed and pore pressures recovered to equilibrium values, unless there is some stabilising measure to compensate. Hence, a very careful balance is required between minimis-

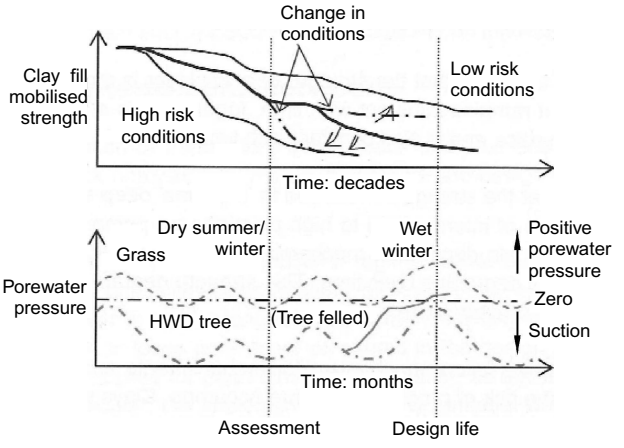

Notes:

1. High risk conditions (for slope instability) → e.g. grass covered slope. Alluvium below embankment.
2. Low risk conditions (for slope instability) → e.g. high permeability foundation soils, well drained toe, HWD/VHWD trees on slope.

Fig. 17. Rail embankments, 'dynamic' interactions with changes in conditions

ing seasonal track deformation and minimising the risk of catastrophic failures.

The field studies and hydrological modelling have illustrated the complexity of the pore pressure regime that can develop in these embankments, both in terms of spatial distribution of vegetation and climate-induced changes. The conventional approach of installing a few standpipe piezometers and monitoring for several months is unlikely to measure pore pressures that are representative of the values which may develop over several decades. Changes in weather patterns could lead to significant differences in pore pressure between a particular monitoring period and subsequent years.

CONCLUSIONS

Field observations and numerical modelling have shown that the deformation and delayed failure of old rail embankments, composed of dumped clay fills, is significantly affected by seasonal climate variations and by different types of vegetation. Intermediate- and high-plasticity clay fills are particularly vulnerable to seasonal shrink–swell deformation, which ultimately can lead to progressive failure. Climate- and vegetation-induced seasonal shrink–swell can either cause excessive track deformation or deep-seated delayed failure, depending on the type and spatial distribution of the vegetation and the prevailing weather patterns. Because of the original construction method, the fabric and structure of dumped clay fills is quite different to parent natural clay, reconstituted clay or compacted clay fill. This affects the mass permeability, strength and compressibility of the dumped clay fill, but to differing extents. The risk of failure will be mainly dependent on the maximum pore-water pressure that may develop, which is predominantly controlled by the permeability variations across three different zones (near-surface clay fill, underlying clay fill and foundation soil). The above factors that control behaviour, together with the unsaturated nature of railway embankments, needs to be considered by practising engineers. The variation of pore-water pressure with depth will seldom be hydrostatic, except perhaps within a near-surface layer, typically affected by desiccation cracking.

In terms of further research, there is a clear need for the development of more reliable methods for in situ measurement of permeability. Simple, robust equipment for downhole tests, with modern, accurate devices to measure pressure and volume change are needed. The variation in permeability between unsaturated and saturated states, including hysteresis effects, is likely to be an important factor in the seasonal changes in pore-water pressure that occur within embankments. There is an urgent need for further research into, and practical guidance on, this complex subject. Further field studies will be required to better understand the unsaturated hydraulic properties of dumped clay fills, supported by large-scale laboratory experiments (of sufficient scale to be representative of the clod–matrix fabric) under carefully controlled boundary conditions. The factors affecting desiccation cracking and associated effects on bulk permeability also need to be better understood.

ACKNOWLEDGEMENTS

The author would like to thank his many colleagues at Mott MacDonald for their contributions to the studies discussed in this paper, including: James Scott, Ashley Bown, Fleur Loveridge, Graham Taylor, Yu Sheng Hsu and Ringo Tan. Kevin Briggs carried out VADOSE modelling during his EngD research at Southampton University, and the advice of Professor William Powrie and Dr Joel Smethurst at Southampton University is also acknowledged.

The support of Brian McGinnity, for the LUL studies, and Derek Butcher and Eifion Evans for the Network Rail studies is also gratefully acknowledged.

APPENDIX 1 – FLAC

A strain-softening strength model was used, as discussed by O'Brien *et al.* (2004), with peak, post-rupture and residual strength. Peak strength can be mobilised until a defined plastic strain is developed; once this threshold is exceeded the mobilised strength reduces rapidly with increasing plastic displacement to residual strength. Table A1.1 summarises the input parameters. Displacements were converted to shear strain by dividing by the characteristic element thickness. For the Gault clay embankment 2,600 elements (or 'zones' in FLAC terminology) were used, with a characteristic dimension of 0·61 m (or about 8% of the embankment height). For the smaller, steeper London clay embankment, 1,500 elements were used, with a characteristic dimension of 0·41 m (or about 9% of the embankment height). An ash–ballast capping 1 m thick was assumed for all embankments.

Table A1.1. FLAC input parameters

Soil type	Bulk unit weight (kN/m^3)	Strength[4]			Threshold plastic strain for peak	Young's modulus (kN/m^2)	Poisson's ratio
		Peak	Post-rupture[3]	Residual[3]			
High-plasticity clay fill[1]	18·1	$c' = 5$ $\Phi' = 21$	$c' = 2$ $\Phi' = 21$	$c' = 1$ $\Phi' = 13$	6%	75 (p' + 100) Min. 5000	0·3 load 0·2 unload
Intermediate-plasticity clay fill[2]	18·8	$c' = 8$ $\Phi' = 24$	$c' = 2$ $\Phi' = 22{\cdot}5$	$c' = 1$ $\Phi' = 13$	7%	90 (p' + 100) Min. 6,000	0·3 load 0·2 unload
Alluvium	16·0	$c' = 3$ $\Phi' = 24$	$c' = 2$ $\Phi' = 22{\cdot}5$	$c' = 1$ $\Phi' = 13$	7%	45 (p' + 100) Min. 3,000	0·3 load 0·2 unload
Ash–ballast	10·5	$c' = 2$ $\Phi' = 35$	N/A	N/A	N/A	1,000	0·3 (load + unload)
Natural clay foundation	19·6	$c' = 10$ $\Phi' = 27$	$c' = 3$ $\Phi' = 24$	$c' = 1$ $\Phi' = 13$	3%	135 (p' + 100) Min. 7,500	0·2 (load + unload)

Notes:
(1) High plasticity is characterised as a plasticity index of 45–50% and a liquid limit of 70–75%.
(2) Intermediate plasticity is characterised as a plasticity index of 30–35% and a liquid limit of 55–60%.
(3) Plastic displacement of 5 mm to develop post-rupture strength, and 100 mm to develop residual strength for all strain-softening soils.
(4) The failure envelopes are curved, and can be defined either as tangent (c', Φ') values or secant ($c' = 0$, Φ') values for the particular range of mean effective stress of interest. For the purpose of this study it was convenient to use tangent fits, and for the slopes considered the mean effective stresses are less than 100 kN/m^2.

Table A2.1. VADOSE/w input parameters

Soil type	Permeability (m/s)	Van Genuchten constants					Root Depth (m)	
		AEV (kN/m^2)	θ_s	θ_r	m	n	Tree	Grass
Surface clay fill	$2{\cdot}5 \times 10^{-7}$	30	0·44	0·1	0·167	1·2	3 m	0·5
Clay fill	5×10^{-8}	30	0·44	0·1	0·167	1·2	3 m	N/A
Foundation clay	1×10^{-8}	33	0·59	0·1	0·13	1·15	N/A	N/A
Ash–ballast	4×10^{-5}	2	0·45	0·01	0·52	2·1	N/A	N/A

Notes:
(1) Surface clay fill, 1 m thick.
(2) Leaf area index = 2·7 for trees and grass during summer.
(3) AEV = air-entry value.

APPENDIX 2 – VADOSE/w

VADOSE/w calculates saturated and unsaturated water and heat flow in response to applied boundary conditions. Daily climate data (temperature, humidity, wind speed, rainfall and solar radiation) are applied to calculate water infiltration and water removal from the slope surface and from a defined rooting zone. Hence, variations in pore pressure with time, as a result of different weather patterns of different duration and intensity, can be assessed.

Assumed input parameters are summarised in Table A2.1. Unsaturated hydraulic properties were based on a modified version of the Croney (1977) soil water retention curve (SWRC) for drying measured for London clay. The dumped clay fill was assigned a lower air-entry value and a shallower gradient than the Croney curve, in order to take account of the clod–matrix structure of the fill and the wide range of pore sizes, including significant sand–gravel fraction. Van Genuchten (1980) parameters were used to develop an appropriate curve fit. The SWRCs were used to define the variation of hydraulic conductivity with suction, based on the Mualem method (Mualem, 1976). Water removal due to evaporation from an unsaturated soil is calculated using the Penman–Wilson equation (Wilson *et al.*, 1994) and transpiration is measures using a root water-uptake model (Tratch *et al.*, 1995). The leaf area index (LAI), defining the proportion of solar energy intercepted by the vegetation for transpiration (Ritchie, 1972), corresponds to full leaf cover during summer (1 April to 17 October) and zero during the winter, on the basis of typical plant leafing periods (Biddle, 1998). Reduction in root water uptake due to soil drying as the vegetation reduces transpiration was based on the Feddes *et al.* (1978) relationship.

REFERENCES

Birch, G. P. & Dewar, A. L. (2002). Earthwork failures in response to extreme weather. In: *FORDE, Proc. Of the Int. Conf. Railway Engineering, 2002, London*. Edinburgh, UK: Engineering Technics Press.

Biddle, P. G. (1998). *Tree root damage to buildings*, Vols. 1 and 2. Wantage, UK: Willowmead.

Briggs, K. M. (2011). Impacts of climate and vegetation on railway embankment hydrology. Doctor of Engineering thesis, University of Southampton, UK.

Briggs, K. M., Smethurst, J., Powrie, W. & O'Brien, A. S. (2011). Wet winter pore pressures in railway embankments. *Proc. ICE, Geotechnical Engineering* (in press).

Burland, J. B. (1990). On the compressibility and shear strength of natural clays. *Géotechnique* **40**, 329–378.

Burland, J. B., Rampello, S., Georgiannou, V. N. & Calabresi, G. I. (1996). A laboratory study of the strength of four stiff clays. *Géotechnique* **46**, 491–514.

Perry, J., Pedley, M. & Reid, M. (2003). *Infrastructure embankments – condition appraisal and remedial treatment*. CIRIA Publication C592. London, UK: CIRIA.

Croney, D. (1977). *The design and performance of road pavements*. Technical report. London, UK: Her Majesty's Stationary Office.

Davies, O. (2010). Numerical analysis of the effects of climate change on slope stability. PhD thesis, Newcastle University, UK.

Feddes, R. A., Kowaklik, P. J. & Zaradny, H. (1978). *Simulation of field water use and crop yield*. Chichester, UK: Wiley.

Hight, D. W., McMillan, F., Powell, J. J. M., Jardine, R. J. & Allenou, C. P. (2003). Some characteristics of London clay, In Proceedings, Characterisation and Engineering Properties of Natural Soils (eds T. S. Tan, K. K. Phoon, D. W. Hight & S. Leroueil), pp. 851–907. Rotterdam, Netherlands: Balkema.

Kovacevic, N., Potts, D. M. & Vaughn, P. R. (2001). Progressive failure in clay embankments due to seasonal climate change. *Proc. 15th ICSMGE*, Istanbul, **3**, 2127–2130.

Lenhard, R. J., Parker, J. C. & Kaluarachchi, J. J. (1991). Comparing simulated and experimental hysteretic two-phase transient flow phenomena. *Water Resources Research* **27**, No. 8, 2113–2124.

Li, A. G., Yue, L. G., Tham, C. & Law, K. T. (2005). Field-monitored variations of soil moisture and matric suction in a saprolite slope. *Canadian Geotechnical Journal* **42**, 13–26.

Loveridge, F. A., Spink, T. W. & O'Brien, A. S. (2010). The impact of climate and climate change on infrastructure slopes, with particular reference to southern England. *Quarterly Journal of Engineering Geology and Hydrogeology* **43**, 461–472.

Mott MacDonald (2008). *Seasonal preparedness earthworks (TSERV 567). Packages 3 & 4: Deep dive site modelling. Charing Embankment Monitoring and Modelling Report*. London, UK: Network Rail.

Mott MacDonald (2009). *Seasonal preparedness earthworks (TSERV 567). Final summary report. Recommendations for improvement to practice*. London, UK: Network Rail.

Mott MacDonald (2011). *The effects of railway traffic on embankment stability. Final Report*. RSSB 1386 (Revised). London, UK: Rail Safety and Standards Board.

Mualem, Y. (1976). A new model for predicting the hydraulic conductivity of unsaturated porous media. *Water Resource Research* **12**, 513–522.

Nyambayo, V. P., Potts, D. M. & Addenbrooke, T. I. (2004). The influence of permeability on the stability of Embankments experiencing seasonal cyclic pore water pressure changes. *Proceedings, Advances in Geotechnical Engineering. The Skempton Conference, London* **2**, 898–910. London, UK: Thomas Telford.

O'Brien, A. (2007). Rehabilitation of urban railway embankments – investigation, analysis and stabilisation. In *Proceedings of the 14th European Conference on SMGE, Madrid*. (eds V. Cuellar, E. Dapena, A. Gens, J. L. de Justo, C. Oteo, J. M. Rodrigez-Ortiz, C. Sagaseta, P. Sola & A. Sorianao E.), Vol. 1, pp. 125–143. Amsterdam, Netherlands: Millpress.

O'Brien, A., Ellis, E. A. & Russell, D. (2004). Old railway embankment fill – laboratory experiments, numerical modelling and field behaviour. *Proceedings, Advances in Geotechnical Engineering. The Skempton Conference, London* **2**, 911–921. London, UK: Thomas Telford.

Ridley, A. M., Dineen, K., Burland, J. B. & Vaughan, P. R. (2003). Soil matrix suction: some examples of its measurement and application in geotechnical engineering. *Géotechnique* **53**, 241–253.

Ridley, A., McGinnity, B. & Vaughan, P. (2004). Role of pore water pressures in embankment stability. *Proceedings of the Institution of Civil Engineers, Geotechnical Engineering* **GE4**, 193–198.

Ritchie, J. T. (1972). Model for predicting evaporation from a row crop

with incomplete cover. *Water Resources Research* **8**, 1204–1212.

Scott, J. M., Loveridge, F. & O'Brien, A. S. (2007). Influence of climate and vegetation on railway embankments, In: *Proceedings of the 14th European Conference on SMGE, Madrid* (eds V. Cuellar, E. Dapena, A. Gens, J. L. de Justo, C. Oteo, J. M. Rodrigez-Ortiz, C. Sagaseta, P. Sola & A. Sorianao), pp 659–664. Amsterdam, Netherlands: Millpress.

Skempton, A. W. (1996). Embankments and cuttings on the early railway. *Construction History* **11**, 33–49.

Smethurst, J. A., Clarke, D. & Powrie, W. (2006). Seasonal changes in pore water pressure in a grass covered cut slope in London clay. *Géotechnique* **56**, No. 8, 523–537.

Take, W. A & Bolton, M. D. (2004). Identification of seasonal slope behaviour mechanisms from centrifuge case studies. In: *Proceedings, Advances in Geotechnical Engineering. The Skempton Conference, London* **2**, 992–1004. London, UK: Thomas Telford.

Tratch, D. J., Wilson, G. W. & Fredlund, D. G. (1995). An introduction to analytical modelling of plant transpiration for geotechnical engineers. *Proceedings 48th Canadian Geotechnical Conference, Vancouver*, pp. 771–780. Richmond, Canada: Bi-Tech.

Van Genuchten, M. T. (1980). A closed form equation for predicting the hydraulic conductivity of unsaturated soils. *Soil Science Society of America Journal* **44**, 892–898.

Vaughn, P. R., Kovacevic, N. & Potts, D. M. (2004). Then and now: some comments on the design and analysis of slopes and embankments. In: *Proceedings, Advances in Geotechnical Engineering. The Skempton Conference, London*, **1**, 241–290. London, UK: Thomas Telford.

Watson, G. V. R., Dykes, T. A., Powrie, W. & Blades, A. P. (2007). The use of CT scanning in geotechnical engineering. Private communication.

Wilson, G., Fredlund, D. & Barbour, S. (1994). Coupled soil-atmosphere modeling for soil evaporation. *Canadian Geotechnical Journal* **31**, 151–161.

ice
Institution of Civil Engineers
publishing

Session 1

Material Characterisation

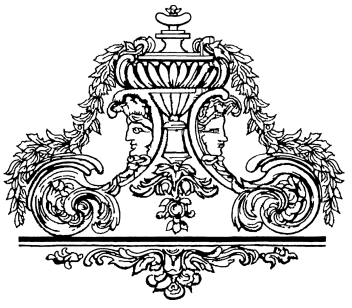

Tang, A. M. *et al.* (2011). *Géotechnique* **61**, No. 5, 421–429 [**doi:** 10.1680/geot.SIP11.005]

Effects of the maximum soil aggregates size and cyclic wetting–drying on the stiffness of a lime-treated clayey soil

A. M. TANG*, M. N. VU* and Y.-J. CUI*

Lime treatment is a well-known technique to improve the mechanical response of clayey subgrades of road pavements or clayey soils used for embankment. Several studies show that lime treatment significantly modifies the physical and hydromechanical properties of compacted soils. Nevertheless, studies on the scale effect under climatic changes are scarce. Actually, wetting–drying cycles might significantly modify the microstructure of treated soils, giving rise to changes in hydromechanical properties. This modification could be dependent on the size of soil aggregates before lime treatment. In the present work, this scale effect was studied by investigating the stiffness of a compacted lime-treated clayey soil using bender elements. The studied soil was first air-dried and ground into a target maximum soil aggregates size (D_{max}). For each aggregate size, the soil was humidified to reach the target water contents w_i, then mixed with 3% of lime powder (mass of lime divided by mass of dried soil) prior to the static compaction at a dry density of 1·60 Mg/m^3. Two initial water contents ($w_i = 14$ and 18%) and four maximum soil aggregates sizes ($D_{max} =$ 0·4, 1·0, 2·0 and 5·0 mm) were considered. After the compaction, the soil specimen (50 mm in diameter and 50 mm high) was covered by plastic film in order to prevent soil moisture changes. The soil stiffness was then monitored at variable time intervals until reaching stabilisation. Afterwards, the soil specimen was subjected to full saturation followed by air-drying to come back to its initial water content. The results show that: (a) the soil stiffness after lime-treatment is significantly dependent on the aggregate size: the finer the aggregates the higher the soil stiffness; (b) the effect of initial water content on the stiffness is negligible; and (c) the wetting–drying cycles seem to slightly increase the soil stiffness in the case of lime-treated specimens and decrease the soil stiffness in the case of untreated specimens. Furthermore, when an intensive drying was applied reducing the soil water content lower than the initial level, the soil stiffness decreased drastically after the subsequent wetting.

KEYWORDS: fabric/structure of soil; laboratory tests; soil stabilisation; stiffness; suction; time dependence

Le traitement à la chaux est une technique bien connue pour améliorer les réponses mécaniques des sols routiers ou des sols argileux utilisés pour des remblais. Plusieurs études ont montré que le traitement à la chaux modifie de façon importante les propriétés physiques and hydromécaniques des sols compactés. Néanmoins, l'étude sur l'effet d'échelle sous des sollicitations climatiques reste rare. Toutefois, les cycles d'humidification – séchage pourraient modifier significativement la microstructure des sols traités, engendrant des modifications des propriétés hydromécaniques. Ces modifications pourraient dépendre de la taille des agrégats avant le traitement à la chaux. Dans le présent travail, cet effet d'échelle a été étudié par le suivi de la raideur d'un sol argileux traité à la chaux et compacté en utilisant les éléments piézo-céramiques (bender elements). Le sol étudié a été d'abord séché à l'air et broyé à une taille maximale voulue d'agrégat (D_{max}). Pour chaque taille d'agrégat, le sol a été humidifié pour atteindre les teneurs en eau voulues, w_i, puis mélangé avec 3% de chaux en poudre (masse de la chaux divisée par masse de sol sec) avant le compactage à une densité sèche de 1,60 Mg/m^3. Deux teneurs en eau initiales (w_i = 14 et 18%) et quatre tailles maximales d'agrégats (D_{max} = 0,4 ; 1,0 ; 2,0 ; et 5,0 mm) ont été considérées. Après le compactage, l'échantillon de sol (50 mm de diamètre et 50 mm de hauteur) a été couvert d'un film plastique afin d'éviter des modifications de la teneur en eau. La raideur du sol a été ensuite suivie à des intervalles de temps variables jusqu'à ce que la stabilisation soit atteinte. Par la suite, l'échantillon de sol a été soumis à une saturation totale suivie du séchage à l'air pour revenir à la teneur en eau initiale. Les résultats montrent que : (a) la raideur du sol après le traitement à la chaux est fortement dépendante de la taille d'agrégats : plus les agrégats sont petits, plus la raideur est importante ; (b) l'effet de la teneur en eau initiale sur la raideur est négligeable ; et (c) les cycles de humidification – séchage semblent augmenter légèrement la raideur du sol dans le cas avec traitement et diminuer la raideur dans le cas sans traitement. De plus, quand un séchage intensif est appliqué, diminuant la teneur en eau à un niveau inférieur à la valeur initiale, la raideur du sol diminue radicalement après l'humidification qui suit.

INTRODUCTION

Lime stabilisation is a well-known technique in civil engineering applications such as road construction, embankments, slab foundations and piles. After Boardman *et al.* (2001), adding lime to clayey soils has been shown to lead to various reactions such as cation exchange, flocculation, carbonation and pozzolanic reaction. When quicklime (CaO) is added into a soil–water system, a highly exothermic hydration reaction occurs forming calcium hydroxide ($Ca(OH)_2$). The water consumed in the hydration reaction (and that removed from the soil system by way of evaporation) can give rise to significant change in soil hydromechanical properties. At the same time, hydration reaction results in higher concentration of Ca^{2+} and OH^- ions in the soil pore water. The immediate cation exchanges induce then an apparently dried and more friable material. Alongside the

Manuscript received 1 March 2010; revised manuscript accepted 18 November 2010. Published online ahead of print 22 March 2011. Discussion on this paper closes on 1 October 2011, for further details see p. ii.

* Ecole des Ponts ParisTech, UMR Navier/CERMES, Paris, France

cation exchange, reaction also occurs between silica and some alumina of the lattices of the clay minerals. As a result, the pozzolanic reactions create hydrated cementation and flocculation by bonding adjacent soil particles together. Such pozzolanic reactions are time dependent, the strength developing gradually over a long period (Bell, 1996), with the general effect of improving the soil hydromechanical properties. Indeed, the treatment reduces the swelling potential (Tonoz *et al.*, 2003; Al-Rawas *et al.*, 2005), increases the shear strength (Bell, 1996; Osinubi & Nwaiwu, 2006; Sivapullaiah *et al.*, 2006; Consoli *et al.*, 2009), increases the elastic modulus (Bell, 1996; Rogers *et al.*, 2006; Sakr *et al.*, 2009) and modifies the compaction properties (Bell, 1996; Osinubi & Nwaiwu, 2006; Consoli *et al.*, 2009; Le Runigo *et al.*, 2011). The water retention properties of clays can be also modified by the lime treatment (Clare & Cruchley, 1957).

Microstructural investigations on lime-treated clays show that the treatment changes the soil fabric significantly (Cai *et al.*, 2006; Russo *et al.*, 2007; Shi *et al.*, 2007; Le Runigo *et al.*, 2009; Sakr *et al.*, 2009). Moreover, the above studies have shown that the effects of lime treatment depend on lime content, soil water content, soil type, curing time, temperature, stress state and so on.

Even though numerous studies have been performed to analyse the effect of lime treatment, almost all works have involved soil specimens prepared in the laboratory, while investigations of lime-treated soil specimens taken from the field still remain rare. Bozbey & Guler (2006) investigated the feasibility of using a lime-treated silty soil as landfill liner material by conducting tests on both laboratory and field scales. They found that the hydraulic conductivity measured on the specimens prepared in the laboratory was one order of magnitude lower than that of undisturbed samples taken from the field. Kavak & Akyarh (2007) investigated the improvement of road by lime treatment based on both laboratory and field California bearing ratio (CBR) tests. They concluded that the soaked CBR values obtained in the laboratory increased significantly (16–21 times) 28 days after the treatment while that obtained from field CBR tests increased slightly (two-fold). Cuisinier & Deneele (2008) performed suction-controlled oedometer tests on soil samples taken from an embankment 3 years after the construction. They also performed the same tests on untreated soil and treated specimens prepared in the laboratory. The results show that the swelling potential of the lime-treated samples taken from the field is significantly larger than that prepared in the laboratory, but still remains lower than that of the untreated samples. They attributed the loss of stabilisation efficiency observed in field conditions to the effects of drying–wetting cycles related to climatic changes. Rao *et al.* (2001), Guney *et al.* (2007) and Khattab *et al.* (2007) also reported a reduced efficiency of lime treatment with wetting–drying cycles.

One of the main reasons explaining the difference between lime-treated soil samples prepared in the laboratory and the treated soil samples taken from the field could be the difference in soil aggregates size. Indeed, prior to compaction in the laboratory, the soil is usually ground at a few millimetres and then mixed with lime. On the contrary, in the field, the dimension of clay clods may reach several centimetres before the treatment.

The present work aims at investigating the effects of soil aggregates size on the efficiency of lime treatment under cycles of wetting and drying. For this purpose, air-dried soils were ground at four values of maximum sieve dimensions (0·4, 1·0, 2·0 and 5·0 mm) prior to lime treatment and compaction. The shear moduli of soil specimens were monitored using the bender elements method. When reaching the stabilisation of the shear moduli, wetting–drying cycles were applied in order to simulate the weathering effects.

SOIL STUDIED AND EXPERIMENTAL TECHNIQUES

The soil used in this study was taken at a site near Tours, a city in central France. Its main geotechnical properties are reported in Table 1. The grain size distribution, as obtained by dry sieving method after washing (Afnor, 1996) for elements larger than 80 μm and by hydrometer method (Afnor, 1992) for elements smaller than 80 μm, is shown in Fig. 1 (curve 'After washing'). The curve shows that washing has disaggregated the soil particles into small dimensions and almost all soil aggregates became smaller than 1 mm, with a clay fraction (< 2 μm) of 26%.

To prepare the soil samples, the air-dried soil was first ground and passed through one of the four target sieve sizes ($D_{max} = 0{\cdot}4$, 1·0, 2·0 and 5·0 mm). The soil aggregates which did not pass through the sieve were ground again. The procedure was repeated until all the soil aggregates, except some large stones, passed through the sieve. The grading curves (obtained by sieving) of the four soil subseries having different maximum soil aggregates diameter are also shown in Fig. 1. This procedure allows the soils to be prepared with the same mineral composition and various values of soil clusters D_{max}. Comparison between the curve 'After washing' and that of '$D_{max} = 0{\cdot}4$ mm' shows that washing preserved the portion of soil aggregates larger than 0·4 mm (about 20%), while the preparation of '$D_{max} = 0{\cdot}4$ mm' crushed this portion.

Table 1. Geotechnical properties of the studied soil

Soil properties	Value
Liquid limit, w_L: %	45
Plastic limit, w_p: %	21
Plasticity index, I_p: %	24
Value of blue of methylene, VBS	4·86
Carbonates content: %	0·35
Specific gravity, G_S	2·70

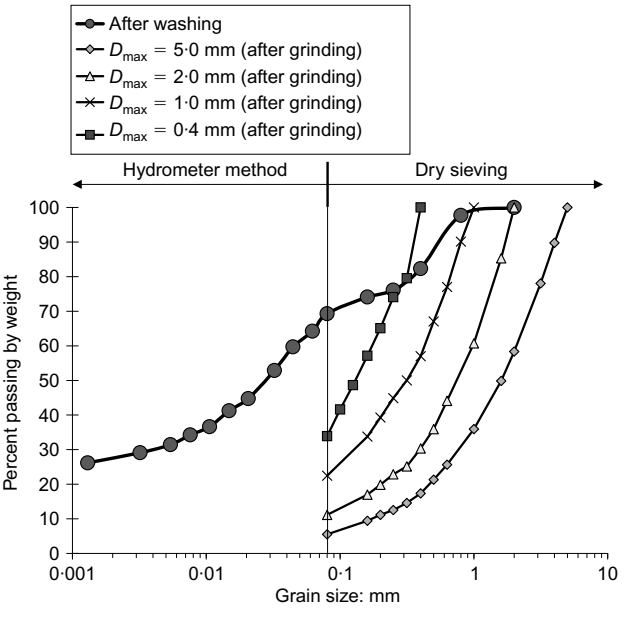

Fig. 1. Grain size distributions of the studied soil prepared by various methods

After grinding, the soil was humidified by spraying distilled water to reach prescribed initial moisture contents and sealed in a plastic box for at least 48 h for moisture content homogenisation. For each D_{max}, 14% and 18% water contents were considered. Prior to compaction, the moist soil was thoroughly mixed with lime and then poured into a mould of 50 mm diameter. The lime content studied was 3% (mass of lime divided by mass of dried soil). Static compaction was then carried out to reach a dry density of 1·60 Mg/m^3 with a final height of the soil specimen of 50 mm. After the compaction, the soil specimen was taken out of the mould and wrapped in plastic film in order to avoid any moisture exchange between soil and atmosphere. The initial dimensions and the basic properties of the compacted soil specimen are presented in Table 2.

In Fig. 2 the standard Proctor compaction curves of lime-treated and untreated soils are presented. The after-compaction conditions studied are also shown in the figure. It can be observed that the compaction curve of lime-treated soil is quite different from the untreated one. The dry density chosen for the present study (1·60 Mg/m^3) corresponds to the maximum dry density of lime-treated soil obtained by the standard Proctor compaction. The mentioned water content values (14 and 18%) both correspond to the dry side of the compaction curve and were chosen in order to preserve the soil aggregates. Indeed, Delage *et al.* (1996) showed that compaction on the dry side leads to a microstructure characterised by an assembly of aggregates, whereas compaction on the wet side leads to a more homogeneous microstructure without apparent aggregates.

Table 2. Dimensions and basic properties of soil specimens

Dimensions/basic properties	Value
Height: mm	50
Diameter: mm	50
Dry density: Mg/m^3	1·60
Initial water content: %	14 and 18
Lime content: %	3
Maximum soil aggregates size: mm	0·4; 1·0; 2·0; and 5·0

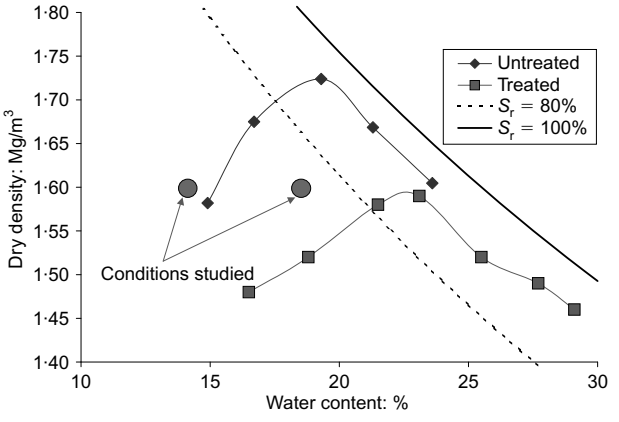

Fig. 2. Standard Proctor compaction curves and conditions studied

The bender element was used to monitor the small-strain shear modulus. The experimental set-up is shown in Fig. 3. The soil specimen was put in contact with two bender elements: the transmitter one embedded in the top base and the receiver one embedded in the bottom base. Both bender elements were connected to a control and data-logging system. A triggered sinusoidal signal was then sent to the transmitter, recording the response of the receiver at the specimen base. An example of the time-domain records collected is reported in Fig. 4, together with the indication of travel time (Δt). Considering the travel length, l, assumed equal to the specimen height (50 mm) minus the protrusions of the bender transmitter and receiver into the soil specimen (2 mm), the shear wave velocity was then calculated as $V_s = l/\Delta t$. The soil mass density (ρ) was verified after each V_s measurement by weighing the soil specimen and was used for the determination of the small-strain shear modulus: $G_{max} = \rho V_s^2$. This experimental technique is similar to that recently used by Puppala *et al.* (2006) when monitoring the shear modulus of chemically treated sulfate-bearing expansive soils and previously used by several other authors.

Once the stabilisation of G_{max} was reached, the soil specimen was first wetted, adding water with a sprayer and monitoring the change in the specimen weight until a water content of 21% (corresponding to a degree of saturation $S_r = 82\%$) was obtained. Adding more water to the soil specimen would lead to water drainage from its bottom, indicating that the water content of 21% corresponds to the maximum value that the soil specimen can retain. After reaching the target water content value and prior to the G_{max} measurements, the soil specimen was wrapped in plastic film (for at least 24 h) for moisture homogenisation. To achieve drying, the soil specimen was air-dried until the target water content was reached. Afterwards, it was wrapped in plastic film to achieve 'water content' equalisation. During wetting and drying, the water content of the soil specimen (w) was controlled by monitoring the changes in its mass (m) by the equation $w = (1 + w_i) \times m/m_i - 1$, where w_i and m_i are respectively the initial water content and the initial mass of the soil specimen. The changes in the dimensions of the specimen, as measured by a caliper after the wetting and drying stages, were found to be negligible and for this reason were ignored when calculating both V_s and the mass density. Five wetting–drying cycles were applied for each treated soil specimen. For the untreated specimens, the number of cycles was varied from two to five. The soil specimen was removed systematically from the testing device after

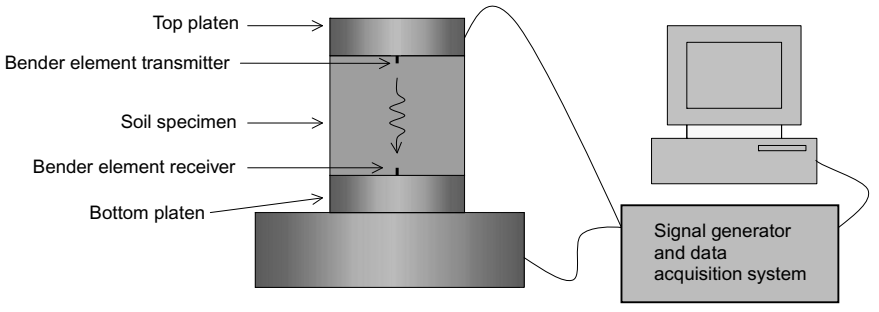

Fig. 3. Experimental set-up – bender element test

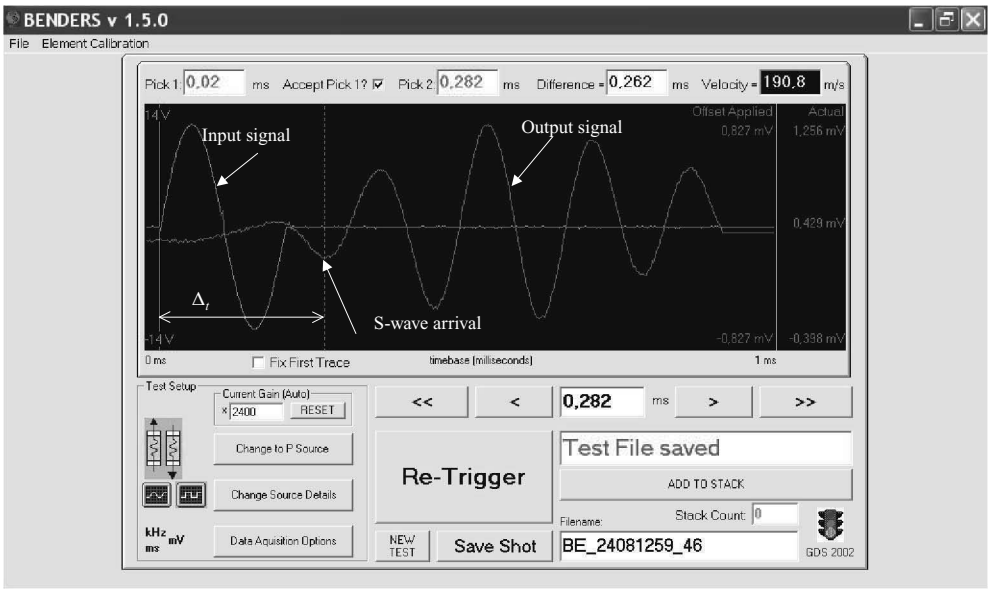

Fig. 4. Response of shear wave for the soil sample treated with 3% of lime, $D_{max} = 5$ mm, $w_i = 14\%$, 886 h after the treatment

each measurement of V_s. The bender elements were always installed in the same slots during the measurement of V_s.

Summarising, in this study two moulding water contents (14 and 18%) and four maximum soil aggregates sizes ($D_{max} = 0{\cdot}4$, 1·0, 2·0 and 5·0 mm) were considered. In each case, both treated and untreated specimens were tested. Moreover, for each test three identical specimens were investigated for replicate, corresponding to 48 soil specimens in total.

EXPERIMENTAL RESULTS

Changes of small strain shear modulus (G_{max}) after compaction

After compaction, the small strain shear modulus G_{max} was monitored in order to follow its changes with respect to time. In Fig. 5, the mean value of G_{max} (measured on three identical specimens) is plotted against time. For the untreated soil passed through a 0·4 mm sieve (Fig. 5(a)), immediately after the compaction G_{max} was equal to 65 MPa and 44 MPa for an initial water content of 14% and 18% respectively. The values increased slightly with time and stabilised after 100 h at 73 MPa and 50 MPa, respectively. In the case of treated specimens, G_{max} was equal to 108 MPa for $w_i = 14\%$ and 80 MPa for $w_i = 18\%$. Comparison with the values of untreated specimens shows that the lime treatment has a significant effect on G_{max} immediately after the compaction. With time, G_{max} increased and stabilised after 200 h at about 120 MPa for both values of w_i. The time increase of G_{max} was more significant in the case of the higher water content ($w_i = 18\%$). Interestingly, the stabilised G_{max} value has been found independent of the initial water content.

Similar observation can be made from the results of soil ground to 1·0 mm (Fig. 5(b)), 2·0 mm (Fig. 5(c)) and 5·0 mm (Fig. 5(d)) in terms of:

(*a*) immediate effect of lime treatment after compaction, characterised by a significant increase of G_{max}
(*b*) slight increase of G_{max} with time for untreated specimens
(*c*) increase of G_{max} with time for treated specimens, especially in the case of the higher water content ($w_i = 18\%$)
(*d*) stabilisation of G_{max} about 200 h after the treatment, with similar final values for both water contents.

In order to analyse the effect of maximum soil aggregates size on G_{max}, the mean final values of G_{max} and the range measured on three identical specimens are compared in Fig. 6 as a function of D_{max}. For the treated soil compacted at $w_i = 14\%$ (Fig. 6(a)), G_{max} was found to be decreasing with D_{max}, showing the highest value of 120 MPa for $D_{max} = 0{\cdot}4$ mm and the lowest of 103 MPa for $D_{max} = 5{\cdot}0$ mm. A similar observation can be made for the treated soil compacted at $w_i = 18\%$ (Fig. 6(b)), indicating that the larger the maximum soil aggregate size, the lower the value of G_{max}. For the untreated specimens, the G_{max} plotted against D_{max} data show a less clear trend for the $w_i = 14\%$ case and indicate almost constant G_{max} for the $w_i = 18\%$ case.

Changes of small strain shear modulus G_{max} under cyclic wetting–drying

Cyclic wetting–drying was carried out by controlling the water content of the soil specimen. In Fig. 7, the G_{max} plotted against time data of the soil aggregates ground to 0·4 mm are presented. The corresponding water content at each measurement is also indicated. The starting points ($t = 0$) correspond to the last points shown in Fig. 5. At the initial water content $w_i = 14\%$ (the corresponding degree of saturation is $S_{ri} = 55\%$), G_{max} was equal to 73 MPa (Fig. 7(a)) for the untreated specimen. Wetting to a water content of 21% ($S_r = 82\%$) decreased G_{max} to 28 MPa. The subsequent drying to the water content of 14% (at $t = 100$ h) increased G_{max} to 50 MPa. On subsequent wetting and drying cycles, cracks progressively developed until the bender elements signal was no longer transmitted through the soil sample. The soil may be then considered as profoundly fissured after two wetting–drying cycles. The two following parameters are proposed to characterise the changes of G_{max} under cyclic wetting–drying for untreated soils:

(*a*) the decrease of G_{max} during the first wetting path, ΔG_{max1};

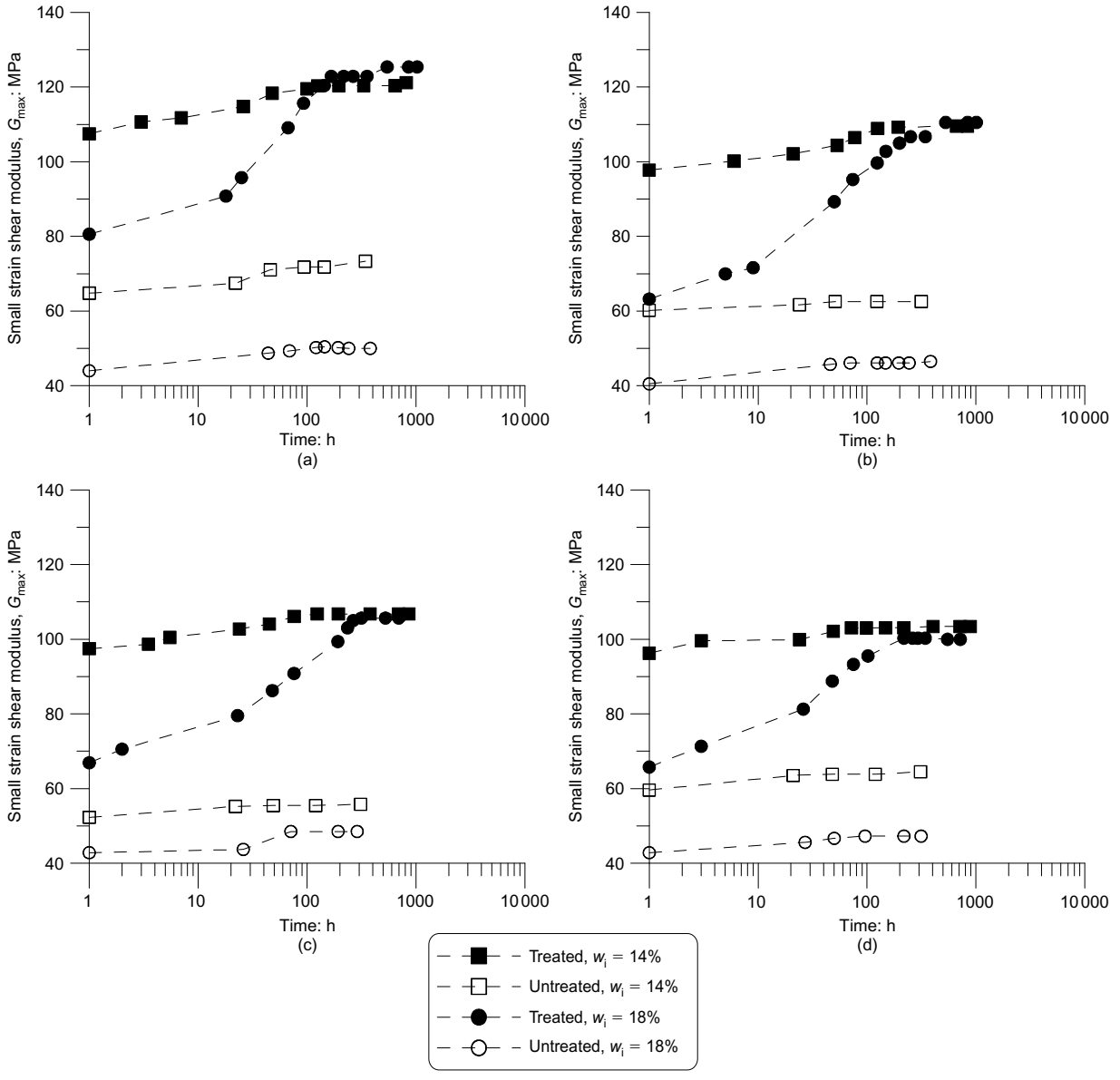

Fig. 5. Small-strain shear modulus plotted against time after compaction: (a) $D_{max} = 0{\cdot}4$ mm; (b) $D_{max} = 1{\cdot}0$ mm; $D_{max} = 2{\cdot}0$ mm; (d) $D_{max} = 5{\cdot}0$ mm

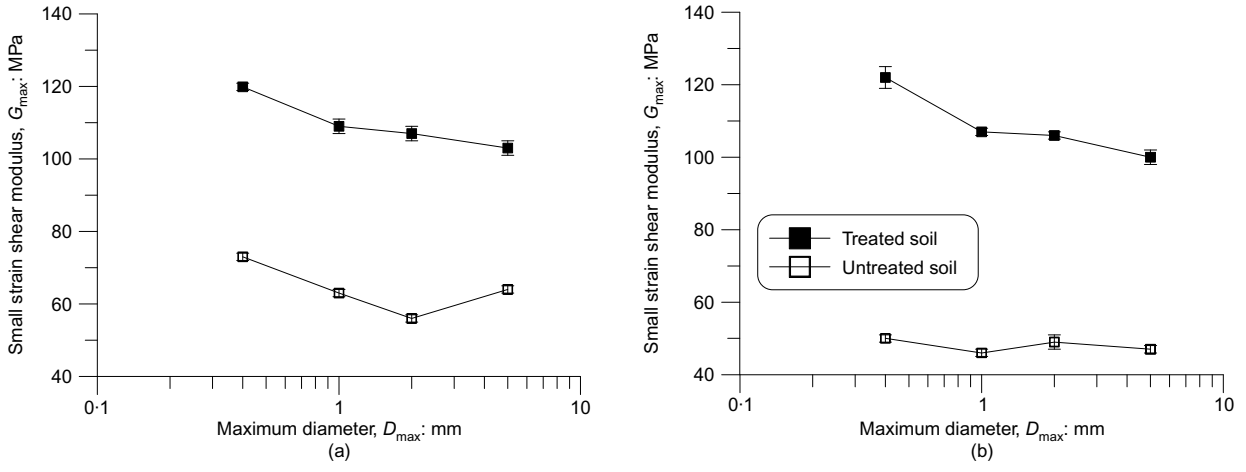

Fig. 6. Small-strain shear modulus after stabilisation plotted against maximum aggregate diameter: (a) $w_i = 14\%$; (b) $w_i = 18\%$

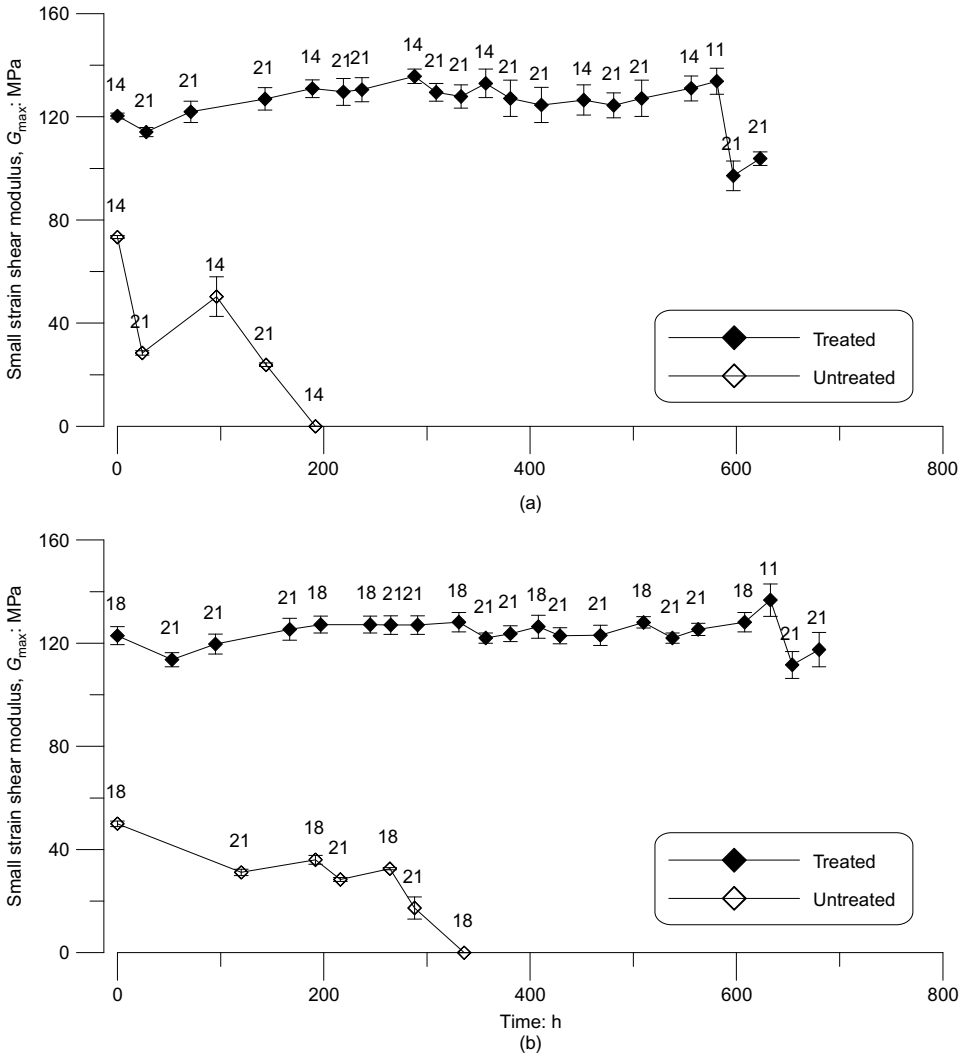

Fig. 7. Changes in small-strain shear modulus upon cyclic wetting–drying for $D_{max} = 0{\cdot}4$ mm (the corresponding water content is given above each point): (a) $w_i = 14\%$; (b) $w_i = 18\%$

(*b*) the number of wetting–drying cycles causing cracking, N_f.

Note that another parameter $\Delta G_{max1}/G_{max\,i}$ alternative to ΔG_{max1} can be used, where $G_{max\,i}$ is the initial value obtained in the wetting–drying tests. In the case of the untreated samples having $D_{max} = 0{\cdot}4$ mm, these parameters are $\Delta G_{max1} = 45$ MPa ($\Delta G_{max1}/G_{max\,i} = 62\%$), $N_f = 2$.

For the specimen treated at the initial water content of 14% (Fig. 7(a)), wetting to a water content of 21% decreased G_{max} slightly from 121 to 114 MPa. Nevertheless, when this high value of water content was maintained, G_{max} was increasing and reached 127 MPa after 100 h. The subsequent wetting and drying only induced slight changes of G_{max}. For the last drying stage (at $t = 580$ h), the water content was finally reduced to 11%. This intensive drying resulted in a significant decrease of G_{max} when the soil was wetted again to a water content of 21%; G_{max} decreased from 134 to 97 MPa. This can be explained by the development of microcracks observed on the specimen surface. Beside the parameter ΔG_{max1} described above, the decrease of G_{max} during the last wetting path ($\Delta G_{max\,f}$) can also be proposed to describe the behaviour of treated soils under a wetting–drying path. In the case of the treated samples having $D_{max} = 0{\cdot}4$ mm, these parameters are $\Delta G_{max1} = 7$ MPa ($\Delta G_{max1}/G_{max\,i} = 6\%$) and $\Delta G_{max\,f} = 37$ MPa.

For the soil specimen compacted at the initial water content of 18%, microcracks appeared on the untreated specimens after three wetting–drying cycles, leading to no bender elements vibration transmission (Fig. 7(b)). For the treated specimens, the phenomena were similar to that observed for a water content of 14%:

(*a*) slight increase after the first wetting
(*b*) small changes upon cyclic wetting–drying
(*c*) drastic decrease due to development of microcracks after an intensive drying with the water content decreased to 11%.

The changes of G_{max} upon wetting–drying for other maximum soil aggregate sizes show similar trends. The main parameters of all samples are reported in Table 3, including $\Delta G_{max1}/G_{max\,i}$. The untreated specimens compacted at a drier state (initial water content of 14%) also show diffused cracking after three wetting–drying cycles. This is not the case for the untreated specimens compacted at a wetter state (i.e. $w_i = 18\%$) except the specimens having $D_{max} = 0{\cdot}4$ mm (Fig. 7(b)). For the lime-treated specimens, wetting–drying cycles only induced small changes of G_{max}, becoming significant only on the wetting stage following an intensive drying. This effect seems to be more significant for the drier specimen (i.e. $w_i = 14\%$). The effect of D_{max} upon cyclic wetting–drying was found to be insignificant as the behav-

Table 3. Results obtained during the wetting–drying cycles (ΔG_{max1}: decrease of G_{max} during the first wetting path; $\Delta G_{max1}/G_{max\ i}$; ratio of ΔG_{max1} to the initial value of G_{max} during the wetting–drying tests; N_f: number of cycles inducing cracking; $\Delta G_{max\ f}$: decrease of G_{max} during the last wetting path)

D_{max}: mm	w_i: %	Lime treatment	ΔG_{max1}: MPa	$\Delta G_{max1}/\Delta G_{max\ i}$: %	N_f	$\Delta G_{max\ f}$: MPa
0·4	14	Yes	7	6	—	37
0·4	14	No	45	62	2	—
0·4	18	Yes	10	8	—	25
0·4	18	No	19	38	3	—
1·0	14	Yes	8	7	—	36
1·0	14	No	44	70	3	—
1·0	18	Yes	4	4	—	13
1·0	18	No	19	41	>5	
2·0	14	Yes	13	12	—	38
2·0	14	No	36	64	3	—
2·0	18	Yes	5	5	—	15
2·0	18	No	31	63	>3	—
5·0	14	Yes	9	9	—	44
5·0	14	No	47	73	3	—
5·0	18	Yes	4	4	—	22
5·0	18	No	23	49	>3	—

iour of the soil specimens having different D_{max} was quite similar. Comparison of the $\Delta G_{max1}/G_{max\ i}$ data with the ΔG_{max1} data indicates that the wetting–drying effect is more clearly evidenced by the $\Delta G_{max1}/G_{max\ i}$ parameter with $\Delta G_{max1}/G_{max\ I} \geqslant 38\%$ for untreated specimens and $\Delta G_{max1}/G_{max\ i} \leqslant 12\%$ for treated specimens.

DISCUSSION

The bender elements method is often used to monitor the changes in shear wave velocity in triaxial cells under stress confined conditions. In this case, good contact between the bender elements and the soil specimen can be ensured (Leong *et al.*, 2009; Ng *et al.*, 2009). Application of this method is much more difficult in the case of the present study where the evolution of G_{max} needs to be monitored during several days and on a large number of soil specimens. For this reason, in this work the bender elements were put in contact with the soil specimen only during the measurement and no confining pressure was applied. In order to analyse the test scattering, three specimens were tested for each D_{max} and w_i. The results showed a good repeatability of the procedure used (see Fig. 7).

The changes of G_{max} with time for the compacted soil specimens were monitored until reaching stabilisation. A slight increase of G_{max} with time was observed for the untreated specimens and is attributed to ageing effects of compacted clay soils. It is worth noting that Delage *et al.* (2006) observed significant changes in microstructure of a compacted expansive soil after compaction. These authors attributed the mentioned changes to increase in the intra-aggregate porosity caused by exchange of water between the inter-aggregate and intra-aggregate pores. Tang *et al.* (2008) also observed this phenomenon characterised by a slight increase of soil suction after compaction. The effect of suction on G_{max} was also evidenced in the present study as untreated specimens which have been compacted at lower water contents (higher suction) have higher G_{max}. Such behaviour was also observed by Sawangsuriya *et al.* (2008).

For the treated specimens, G_{max} obtained immediately after the compaction has been found to be significantly higher than that of untreated specimens prepared at the same moulding water content. The values of G_{max} of treated specimens range between 80 and 130 MPa. This result is similar to that obtained by Rogers *et al.* (2006) from cyclic triaxial tests on compacted clay treated with 2·5% of lime. The immediate increase of G_{max} with lime treatment can be partly explained by the increase of suction caused by decrease of water content after treatment due to hydration and evaporation (Boardman *et al.*, 2001), and to the cation exchanges which increase the flocculation of mineral particles.

It is worth noting that the final values of G_{max} after compaction are independent of the initial values of water content considered (14% and 18%), despite the above-mentioned effect of initial water content immediately after the treatment (Fig. 5). As described by Bell (1996), pozzolanic reactions, which take place over a long period, induce bonding between adjacent soil particles. The different evolution over time of G_{max} at different water contents (shown in Fig. 5) can then be explained as follows: the small-strain shear modulus (G_{max}) of compacted soil is mainly governed by the contacts between adjacent soil particles; immediately after the compaction, the contacts are mainly governed by the capillary suction: the higher the suction (or the lower the water content) the higher the G_{max}; over a long period, owing to pozzolanic reactions in lime-treated soil, cementation develops, gradually increasing G_{max}; when stabilisation is reached, G_{max} is governed mainly by the cementation bonds and the effect of suction (or water content) becomes less significant. The evolution of the G_{max} with time can be also explained from a microstructural point of view. Russo *et al.* (2007) studied the time-dependency of the microstructure of lime-stabilised soil samples by means of mercury intrusion porosimetry (MIP) tests. The results show significant effects of moulding water content on the pore size distribution immediately after the compaction. Nevertheless, after a curing time of 28 days the lime-stabilised samples show a very similar pore size distribution, irrespective of the moulding water content adopted. This evolution of microstructure is also similar to that observed on G_{max} in the present study.

As far as the effect of the maximum soil aggregate size (D_{max}) is concerned, the results of the treated specimens showed a lower value of G_{max} for a larger value of D_{max}. This effect was not observed for the untreated specimens. Actually, for a smaller D_{max}, the total surface of aggregates was larger and therefore more soil–lime reaction can be expected. Note that this observation is of importance from a practical point of view, since laboratory tests are usually

performed on small soil aggregates size (less than a few millimetres) while in the field they may reach several centimetres. As a consequence, particular attention should be paid when using the parameters determined in the laboratory for field application design.

As far as the effects of cyclic wetting–drying on G_{max} are concerned, data presented indicate that wetting induced a decrease and drying induced an increase of G_{max}. This can be explained by the effect of suction: wetting decreased the soil suction and thus the soil stiffness, while drying increased the soil suction and thus the soil stiffness. The same phenomenon was observed by Ng *et al.* (2009) when performing measurements of G_{max} in a suction-controlled triaxial cell. Vassallo *et al.* (2007a) used a suction-controlled resonant column torsional shear cell to study the effect of net stress and suction history on G_{max} of a compacted clayey silt. The experimental results show that G_{max} depends significantly on mean net stress and matric suction as well as stress history. Modelling criteria were proposed by Vassallo *et al.* (2007b) to describe the observed soil behaviour. In the present work, comparison between the treated specimens and untreated specimens shows that the effect of suction change on G_{max} of treated specimens is less significant than that of untreated specimens. This shows that lime treatment reinforces the soil and makes it less sensitive to 'weathering'.

The significant decrease of G_{max} during the last wetting path after an intensive drying (up to a water content of 11%) observed in this work could be explained within the framework of unsaturated soil mechanics, where the soil suction is usually considered as a stress variable. Actually, after the lime treatment, cementation bonds were progressively created under a humidity condition corresponding to the initial water content (14% or 18%). During the first wetting–drying cycle, the water content was varied in the range from w_i to the maximum value (21%). Thus, the soil suction remains lower than its maximum value (reached after the stabilisation of G_{max}). The soil state moves inside the 'elastic' zone (see Alonso *et al.* 1990; Cui & Delage, 1996) and the bonds between particles are relatively well preserved. On the contrary, on intensive drying (water content decreased to 11%), the soil suction exceeded its maximum value: large elastoplastic deformations and significant damage of bonds are thus induced as for the case of Pinyol *et al.* (2007). This damage of bonds would result in microcracking and therefore in decrease of G_{max}. On the other hand, the drying increased the soil suction, thus increasing G_{max}. The fact that a slight increase of G_{max} was observed during the drying shows that the suction effect prevailed on the bond damage. During the subsequent wetting, as the suction effect was removed, the damage effect was finally evidenced. It is also interesting to note that the decrease of G_{max} for treated samples during the last wetting path is similar to the decrease observed on untreated samples from the beginning of the wetting–drying cycles. This seems to confirm the onset of severe bond damage of the treated samples on intensive drying.

For the untreated specimens, it has been observed that wetting–drying cycles resulted in a decrease of G_{max}, especially for drier specimens (see Fig. 7 and Table 3). This can be explained by the generation of microcracks by cyclic wetting–drying under unconfined conditions (Yesiller *et al.*, 2000). In the works of Vassallo *et al.* (2007a) and Ng *et al.* (2009), the generation of microcracks was avoided as the tests were performed under confined conditions. For the treated specimens, the first wetting path equally induced a decrease of G_{max}. Nevertheless, after this decrease, the value of G_{max} increased slightly. The immediate decrease of G_{max} can be explained by the effect of suction, while the subsequent increase of G_{max} after wetting can be attributed to the onset of various reactions by water addition. This explains why Kavak & Akyarh (2007) recommended watering the lime-treated soil one week after the treatment.

CONCLUSIONS

The small strain shear modulus G_{max} of compacted lime-treated soil was investigated using bender elements. The following conclusions can be drawn.

(*a*) The lime treatment significantly increases G_{max} of the soil, giving rise to G_{max} values independent of the moulding water content about 200 h after lime treatment.

(*b*) For the four maximum soil aggregate sizes D_{max} considered, it has been observed that the larger is the value of D_{max} the lower is the value of G_{max}. This observation is interesting from a practical point of view for earthworks involving lime-treated soils. Indeed, the results obtained show that designing earthworks based on the parameters determined from laboratory tests can be misleading, because the maximum aggregate size of the soil tested in the laboratory is usually less than a few millimetres while clay aggregates in the field may reach the dimension of several centimetres.

(*c*) Owing to the appearance of microcracks, cyclic wetting–drying induced significant decrease of G_{max} of untreated specimens. For treated specimens, the changes of G_{max} during wetting–drying cycles are less significant. Only an intensive drying to water content very much lower than the initial value can induce microcracks and thus a decrease in G_{max}.

(*d*) For the treated specimens, only the first wetting induced a decrease of G_{max}. On the contrary, the subsequent cycles induced a slight increase of G_{max}. If the decrease due to wetting can be explained by the suction effect, the slight increase by further wetting–drying cycle should be attributed to the onset of various physico-chemical reactions within the soil.

ACKNOWLEDGEMENTS

The authors would like to express their great appreciation to the French National Research Agency for funding the present study, which is part of the project Terdouest 'Sustainable earthworks involving treated soils' – ANR-07 PGCU-006. The technical support of Mr Dong Jucai is also gratefully acknowledged.

REFERENCES

Afnor (1992). *Soil investigation and testing – granulometric analysis – hydrometer method*. French standard NF P 94-057 (in French).

Afnor (1996). *Soil investigation and testing – granulometric analysis – dry sieving method after washing*. French standard NF P 94-056 (in French).

Alonso, E. E., Gens, A. & Josa, A. (1990). A constitutive model for partially saturated soils. *Géotechnique* **40**, No. 3, 405–430, **doi**: 10.1680/geot.1990.40.3.405.

Al-Rawas, A. A., Hago, A. W. & Al-Sarmi, H. (2005). Effect of lime, cement and Sarooj (artificial pozzolan) on the swelling potential of an expansive soil from Oman. *Building Environ*. **40**, No 5, 681–687.

Bell, F. G. (1996). Lime stabilization of clay minerals and soils. *Engng Geol*. **42**, No. 4, 223–237.

Boardman, D. I., Glendinning, S. & Rogers, C. D. F. (2001). Development of stabilisation and solidification in lime–clay mixes. *Géotechnique* **51**, No. 6, 533–543, **doi**: 10.1680/geot.2001.51.6.533.

Bozbey, I. & Guler, E. (2006). Laboratory and field testing for utilization of an excavated soil as landfill liner material. *Waste Mgmnt* **26**, No. 11, 1277–1286.

Cai, Y., Shi, B., Ng, C. W. W. & Tang, C. S. (2006). Effect of polypropylene fibre and lime admixture on engineering properties of clayey soil. *Engng Geol*. **87**, Nos. 3–4, 230–240.

Clare, K. E. & Cruchley, A. E. (1957). Laboratory experiments in the stabilization of clays with hydrated lime. *Géotechnique* **7**, No. 2, 97–111, **doi**: 10.1680/geot.1957.7.2.97.

Consoli, N. C., Lopes, L. S. & Heineck, K. S. (2009). Key parameters for the strength control of lime stabilized soils. *J. Mater. Civ. Engng* **21**, No. 5, 210–216.

Cui, Y. J. & Delage, P. (1996). Yielding and plastic behaviour of an unsaturated compacted silt. *Géotechnique* **46**, No. 2, 291–311, **doi**: 10.1680/geot.1996.46.2.291.

Cuisinier, O. & Deneele, D. (2008). Impact of cyclic wetting and drying on the swelling properties of a lime-treated expansive clay. *Journées Nationales de Géotechnique et de Géologie de l'Ingénieur JNGG'08*, Nantes, pp. 18–20.

Delage, P., Audiguier, M., Cui,Y. J. & Howat, M. (1996). Microstructure of a compacted silty clay. *Can. Geotech. J.* **33**, No. 1, 150–158.

Delage, P., Marcial, D., Cui, J. Y. & Ruiz, X. (2006). Ageing effects in a compacted bentonite: a microstructure approach. *Géotechnique* **56**, No. 5, 291–304, **doi**: 10.1680/geot.2006.56.5.291.

Guney, Y., Sarib, D., Cetinc, M. & Tuncan, M. (2007). Impact of cyclic wetting–drying on swelling behavior of lime-stabilized soil. *Building Environ*. **42**, No. 2, 681–688.

Kavak, A. & Akyarh, A. (2007). A field application for lime stabilization. *Environ. Geol*. **51**, No. 6, 987–997.

Khattab, S. A. A., Al-Mukhtar, M. & Fleureau, J. M. (2007). Long-term stability characteristics of a lime-treated plastic soil. *J. Mater. Civ. Engng* **19**, No. 4, 358–366.

Le Runigo, B., Cuisinier, O., Cui, Y. J., Ferber, V. & Deneele, D. (2009). Impact of initial state on the fabric and permeability of a lime-treated silt under long-term leaching. *Can. Geotech. J.* **46**, No. 11, 1243–1257.

Le Runigo, B., Ferber, V., Cui, Y. J., Cuisinier, O. & Deneele, D. (2011). Performance of lime-treated silty soil under long-term hydraulic conditions. *Engng Geol*. **118**, No. 1–2, 20–28.

Leong, E. C., Cahyadi, J. & Rahardjo, H. (2009). Measuring shear and compression wave velocities of soil using bender–extender element. *Can. Geotech. J.* **46**, No. 7, 792–819.

Ng, C. W. W., Xu, J. & Yung, S. Y. (2009). Effect of wetting–drying and stress ratio on anisotropic stiffness of an unsaturated soil at very small strain. *Can. Geotech. J.* **46**, No. 9, 1062–1076.

Osinubi, K. J. & Nwaiwu, G. M. O. (2006). Compaction delay effects on properties of lime-treated soil. *J. Mater. Civ. Engng* **18**, No. 2, 250–258.

Pinyol, N., Vaunat, J. & Alonso, E. E. (2007). A constitutive model for soft clayey rocks that includes weathering effects. *Géotechnique* **57**, No. 2, 137–151, **doi**: 10.1680/geot.2007.57.2.137.

Puppala, A. J., Kadam, R., Madhyannapu, R. S. & Hoyos, L. R. (2006). Small-strain shear moduli of chemically stabilized sulfate-bearing cohesive soils. *J. Mater. Civ. Engng* **132**, No. 3, 322–336.

Rao, S. M., Reddy, B. V. V. & Muttharam, M. (2001). The impact of cyclic wetting–drying on the swelling behaviour of stabilized expansive soils. *Engng Geol*. **60**, Nos. 1–4, 223–233.

Rogers, C. D. F., Boardman, D. I. & Papadimitriou, G. (2006). Stress path testing of realistically cured lime and lime/cement stabilized clay. *J. Mater. Civ. Engng* **18**, No. 2, 259–266.

Russo, G., Vecchio, S. D. & Mascolo, G. (2007). Microstructure of a lime stabilised compacted silt. *Expl Unsaturated Soil Mech. – Springer Proc. Physics* **112**, No. 1, 49–56.

Sakr, M. A., Shahin, M. A. & Metwally, Y. M. (2009). Utilization of lime for stabilizing soft clay soil of high organic content. *Geotech. Geol. Engng* **27**, No. 1, 105–113.

Sawangsuriya, A., Edil, B. T. & Bosscher, P. J. (2008). Modulus–suction–moisture relationship for compacted soil. *Can. Geotech. J.* **45**, No. 7, 973–983.

Shi, B., Liu, Z., Cai, Y. & Zhang, X. (2007). Micropore structure of aggregates in treated soils. *J. Mater. Civ. Engng* **19**, No. 1, 99–104.

Sivapullaiah, P. V., Sridharan, A. & Ramesh, H. N. (2006). Effect of sulphate on the shear strength of limetreated kaolinitic soil. *Ground Improvement* **10**, No. 1, 23–30.

Tang, A. M., Cui, Y. J. & Barnel, N. (2008). Compression-induced suction change in a compacted expansive clay. In *Unsaturated soils: advances in geo-engineering* (eds D. G. Toll, C. E. Augarde, D. Gallipoli and S. J. Wheeler), *Proc. 1st Eur. Conf. Unsaturated Soils, Durham, UK* **1**, 369–374. Leiden: CRC Press/Balkema.

Tonoz, M. C., Gokceoglu, C. & Ulusay, R. (2003). A laboratory-scale experimental investigation on the performance of lime columns in expansive Ankara (Turkey) clay. *Bull. Engng Geol. Env.* **62**, No. 2, 91–106.

Vassallo, R., Mancuso, C. & Vinale, F. (2007a). Effect of net stress and suction history on the small strain stiffness of a compacted clayey silt. *Can. Geo. J.* **44**, No. 4, 447–462.

Vassallo, R., Mancuso, C. & Vinale, F. (2007b). Modelling the influence of stress–strain history on the initial shear stiffness of an unsaturated compacted silt. *Can. Geo. J.* **44**, No. 4, 463–472.

Yesiller, N., Miller, C. J., Inci, G. & Yaldo, K. (2000). Dessication and cracking behavior of three compacted landfill liner soils. *Engng Geol*. **57**, Nos 1–2, 105–121.

Taibi, S. *et al.* (2011). *Géotechnique* **61**, No. 5, 431–437 [**doi:** 10.1680/geot.SIP11.P.020]

TECHNICAL NOTE

Some aspects of the behaviour of compacted soils along wetting paths

S. TAIBI*, J. M. FLEUREAU†, N. ABOU-BEKR‡, M. I. ZERHOUNI§, A. BENCHOUK‡, K. LACHGUEUR‡ and H. SOULI¶

Wetting and oedometric loading tests have been performed on several clayey compacted soils. The results highlight the influence of compaction water content and compaction stress on wetting paths. Comparing the changes in degree of saturation induced by mechanical loading and hydraulic loading (wetting path under null stress), it may be noticed that the oedometric path has an opposite curve of that of the wetting path, due to the fact that the void ratio decreases under constant water content when the stress is increased in one case (compression) and increases with water content in the other (swelling).

Des essais d'humidification et oedométriques ont été réalisés sur différents sols argileux compactés. Les résultats mettent en évidence l'influence de la teneur en eau et la contrainte de compactage sur les chemins d'humidification. En comparant les variations du degré de saturation induites par le chargement mécanique et le chargement hydrique (humidification sous contrainte nulle), on note que le chemin oedométrique présente une courbe opposée à celle du chemin d'humidification, ceci est du au fait que l'indice des vides décroit à teneur en eau constante lorsque la contrainte augmente dans un cas (compression) et augmente avec la teneur en eau dans l'autre (gonflement).

KEYWORDS: clays; compaction

INTRODUCTION

Compacted soils are commonly used in the construction of soil structures such as roads, railroad embankments and earth dams. Several investigators have highlighted the influence of the hydromechanical history on the drying–wetting response of compacted soils. Also, a large number of factors, which are either not measured or difficult to control, influence the engineering behaviour of compacted soils (Guillot *et al.*, 2001; Alonso & Pinyol, 2008). Several studies have been carried out to investigate the influence of compaction stress and compaction water content on the behaviour of unsaturated clayey soils (Fleureau *et al.*, 2002; Tarantino & Tombolato, 2005; Sun *et al.*, 2006; Brown & Sivakumar, 2008; Tang *et al.*, 2008; Birle *et al.*, 2008; Tarantino & De Col, 2008). Compaction at different water contents results in different fabrics of the soil (Ahmed *et al.*, 1974; Gens *et al.*, 1995; Delage *et al.*, 1996; Vanapalli *et al.*, 1999). After observing with a scanning electron microscope (SEM) the arrangement of grains within compacted specimens, Delage *et al.* (1996) concluded that on the dry side of optimum, a well-developed granular aggregate structure with interaggregate porosity is visible. The clayey fraction forms grain joint infills (aggregate microstructure with bimodal particle size distribution (PSD), macro- and micropores). On the other hand, on the wet side of optimum, a structure of well-developed wetter clay forming a matrix that envelopes the silt grains and fills the intergranular voids is observed (matrix microstructure with monomodal PSD, mainly micropores). Vanapalli *et al.* (1999) showed that the desaturation curve of a specimen compacted dry of optimum is noticeably different from that of a specimen compacted at optimum or wet of optimum. At the same suction, the degree of saturation of the specimen compacted dry of optimum is somewhat lower than that of the two others, which is in agreement with the more open structure revealed by SEM observations. Fleureau *et al.* (2002) showed that for kaolin–sand and sand–clay mixtures, the slope of the line on the dry side of optimum in the (w, log s) coordinate system, was smaller than the slope on the wet side, as an effect of the decrease in density below the optimum. Tarantino & Tombolato (2005) showed that post-compaction suction of clayey specimens compacted at high water contents increased with increasing degree of saturation. This behaviour was explained in a qualitative fashion by invoking the coupling between mechanical and water retention behaviour occurring during compaction. Sivakumar *et al.* (2006) showed that the relationship between specific water volume and suction was unaffected by the compaction effort at suction values higher than 100 kPa, whereas Birle *et al.* (2008) showed that the soil–water retention curves in terms of gravimetric water content were independent of the initial dry density. Recently, post-compaction states of samples compacted on the dry side of optimum over a wide range of water contents and vertical stresses have been investigated by Tarantino & De Col (2008), and three water content regions were identified. As the degree of saturation is increased at constant water content by the compaction process, post-compaction suction increases at higher water contents (region I), decreases at medium water contents (region II) and remains constant at lower water contents. The authors formulated a coupled mechanical water retention model by combining features of the models presented by Wheeler *et al.* (2003) and Gallipoli *et al.* (2003b). The water retention model was formulated according to Gallipoli *et al.* (2003a).

This technical note presents some experimental results obtained on free wetting paths and from unsaturated oedometric loading tests performed on four compacted clayey soils coming from cores of earth dams, in relation to compaction water content and compaction stress.

Manuscript received 21 March 2010; revised manuscript accepted 22 December 2010. Published online ahead of print 22 March 2011. Discussion on this paper closes on 1 October 2011, for further details see p. ii.

* Laboratoire d'Ondes & Milieux Complexes, Université du Havre, France
† Laboratoire MSS-Mat, École Centrale Paris, France
‡ Laboratoire EOLE, Université de Tlemcen, Algeria
§ FONDASOL, France
¶ Laboratoire LTDS, École Nationale d'ingénieurs de Saint Etienne, France

MATERIALS AND TESTING METHODS

Materials

The materials come from the cores of four earth dams in the south of France (Vieux-pré and La Verne dams) and northwestern Algeria (Sikkak and Boughrara dams). The La Verne material is an eroded microshist containing illite, kaolinite and chlorite traces. According to USCS/LCPC classification, these materials are not very plastic (Ap). La Verne material is characterised by a small percentage of fines (10% of the material is made of particles of diameter below 80 μm), whereas the other three materials are primarily made up of fines (78% of the material is made of particles of diameter below 80 μm). Table 1 summarises the properties of the four materials.

The materials coming from the cores were passed through a sieve of 5 mm (square mesh) in order to remove the large elements, and then dried in the oven. From these material powders, various reconstitutions of samples were carried out. For compacted samples, the powder was wetted to a targeted water content. The wet powder was packed in a tight bag and carefully preserved in a moisture-controlled room during 24 h.

The soils were compacted either using the standard Proctor procedure or, in the case of Vieux-pré material, under quasi-static conditions using three different compaction stresses. Fig. 1 shows the compaction curve and changes in suction with water content for La Verne material: suction appears to be a linear function of water content in a large domain on both sides of the optimum. Fleureau *et al.* (2002) showed that in most tests, the slope of the line on the dry side is smaller than the slope on the wet side, as an effect of the decrease in density below the optimum. This is not observed for La Verne material, probably due to the scarcity of experimental data on the dry side (two experimental data only).

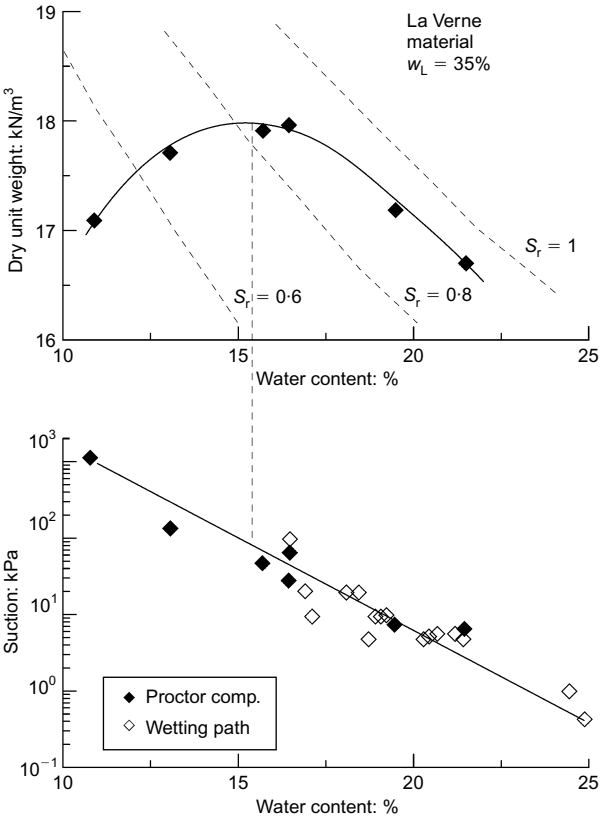

Fig. 1. Compaction curve and changes in suction with water content for La Verne material

Testing methods

Several methods were used to control or measure suction in the samples along the free drying paths (Kassif & Ben Shalom, 1971; Fleureau *et al.*, 1993; Delage *et al.*, 1992; 1998): Sintered glass tensiometric plates were used for suctions lower than 20 kPa; both air pressure and osmotic techniques were used for suctions ranging from 0·05 to 8 MPa, and salt solution desiccators for higher suctions (from 8 to 1000 MPa). Suction measurements were also made by means of the filter paper technique (ASTM D 5298-94, ASTM (1995)) and with thermocouple psychrometers (Zerhouni, 1995). Oedometer tests were carried out on unsaturated compacted samples in which the piston was equipped with a psychrometric probe in order to measure

Table 1. Main properties of the soils used in the study

Material	w_L	I_P	<80 μm: %	<2 μm: %	d_{10}: μm	d_{60}: μm	γ_s/γ_w	w_{SPO}: %	$(\gamma_d/\gamma_w)_{SPO}$
Vieux-pré	32	13	92	36	—	5	2·75	18	1·72
La Verne	35	16	10	<2	80	700	2·64	16·5	1·79
Boughrara	48	28	90	52	0·2	8·5	2·6	21	1·62
Sikkak	50	27	78	45	—	40	2·64	16	1·55
Standard	NF P94-051 (AFNOR, 1993)		NF P94-057 (AFNOR, 1992)		NF XP P94-041 (AFNOR, 1995)		NF P94-054 (AFNOR, 1991)	NF P94-093 (AFNOR, 1999)	

Table 2. Equipment used and tests done for each material

Material	Free wetting paths						Oedometer tests
	Methods used to control suction				Methods used to measure suction		
	Sintered glass tensiometric plates, $s < 20$ kPa	Air pressure technique, $0{\cdot}05 < s < 1{\cdot}5$: MPa	Osmotic technique, $0{\cdot}05 < s < 8$: MPa	Salt solution desiccators, $8 < s < 1000$: MPa	Filter paper technique	Thermocouple psychrometers	Equipped with a psychrometric probe
Boughrara	—	—	X	X	X	—	—
La Verne	X	X	X	X	X	—	—
Sikkak	—	—	X	X	X	—	—
Vieux-pré	X	X	X	X	X	X	X

the change in suction during the mechanical loading. Table 2 summarises the equipment used and the tests carried out for each material.

RESULTS AND DISCUSSION

Wetting paths

To study the influence of compaction water content, wetting tests were performed on dam materials compacted under standard Proctor conditions at different water contents on both sides of the optimum: w_{spo}, $w_{spo} + 2\%$ and $w_{spo} - 2\%$ for Sikkak and Boughrara materials, w_{spo}, $w_{spo} + 2\%$ and $w_{spo} - 3\%$ for La Verne material, with w_{spo} the standard Proctor optimum (SPO) water content.

The results are shown in Fig. 2. In the [log(s), e] plane (Figs 2(a) (right), 2(b) (right) and 2(c) (right)) there is some scatter in the data but the points generally appear close to a straight line, independently from the initial compaction water

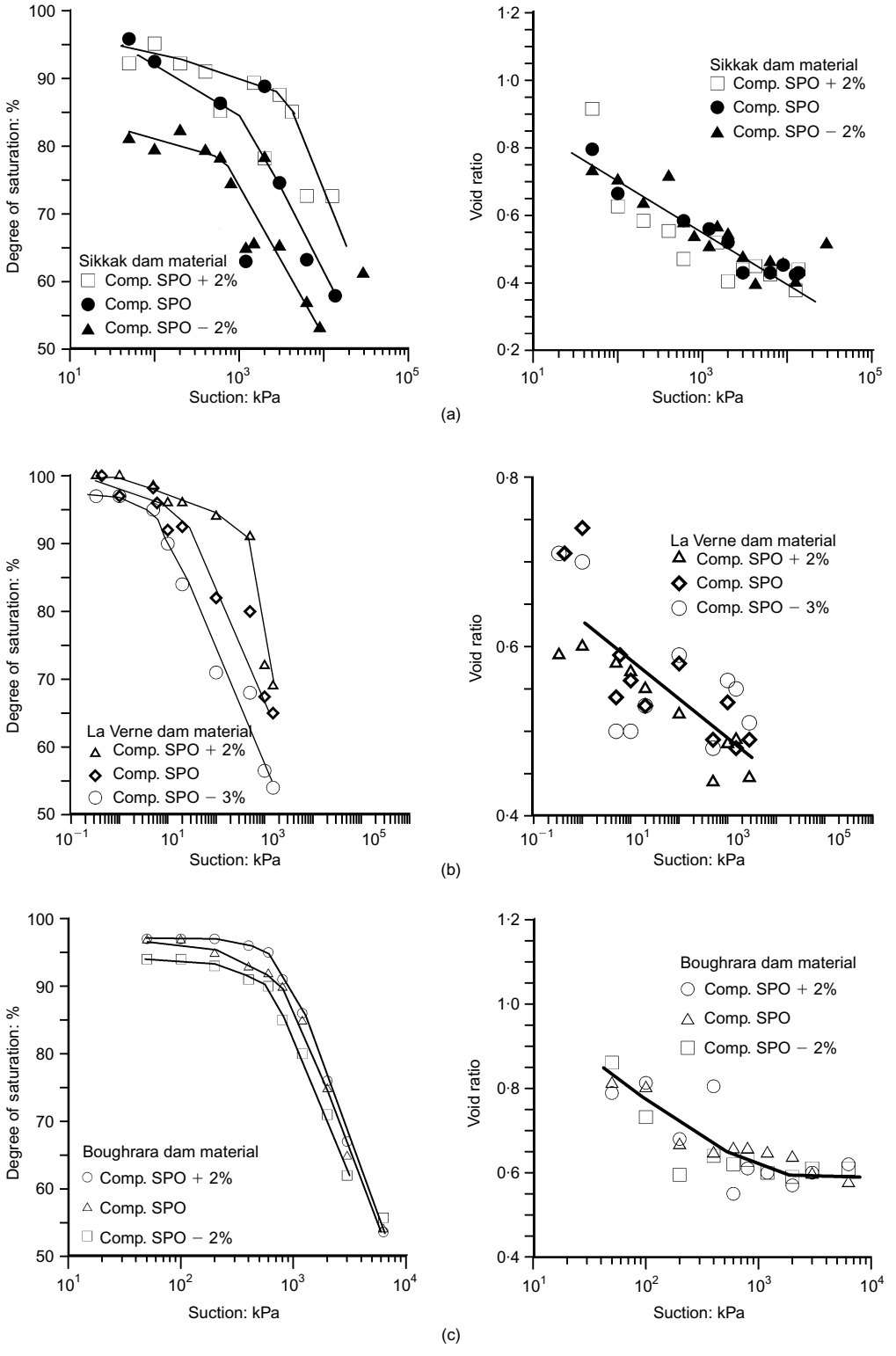

Fig. 2. Influence of compaction water content on the wetting paths of: (a) Sikkak; (b) La Verne; and (c) Boughrara materials in the [log(s), S_r] plane (left-hand side) and [log(s), e] planes (right-hand side)

content. For water contents larger than the optimum or slightly smaller, the difference between the three paths remains very small and it seems that for limited variations in initial water content, the compaction water content plays no significant role in the relationship between void ratio and suction.

In the [log(s), S_r] plane (Figs 2(a) (left), 2(b) (left) and 2(c) (left)), a difference appears between the wetting paths, the path corresponding to the specimens compacted at the optimum being located between those of the specimens at $w_{spo} - 3\%$ and $w_{spo} + 2\%$. The influence of compaction water content is well marked for degrees of saturation ranging between 70 and 90%. Indeed, for a suction of 1000 kPa for example, the difference in the degrees of saturation reaches approximately 20% between the samples compacted at $w_{spo} + 2\%$ and $w_{spo} - 2\%$. However, in the case of Boughrara dam material, this influence is less important. Furthermore, the experiments show that the influence of the compaction water content on the wetting paths is negligible when the degree of saturation falls below a certain value ($S_r \leqslant 50\%$). This result is consistent with those obtained by Vanapalli *et al.* (1999) and Thakur *et al.* (2005).

Interesting remarks can be made about the shape of the curves and, in particular about the point at which the slope of the curves changes. A typical wetting curve is presented in Fig. 3(a), which shows that a variation in slope occurs when the degree of saturation is higher than 90%. Indeed, the wetting path of unsaturated soils can be described as a two-stage process, consisting of primary and residual wetting. During primary wetting ($S_r \leqslant 80\%$), the water and air phases are continuous and the wetting path corresponds to the filling of the pores by water which replaces the air. When the degree of saturation exceeds 80% (residual wetting), the air phase becomes discontinuous. The air forms isolated bubbles within the voids and the degree of saturation varies very little. The limit between these two wetting stages corresponds to a suction which can be called 'suction of quasi-saturation'. The experiments show that this suction is influenced by the compaction water content and varies linearly in a semi-logarithmic plan (Fig. 3(b)).

To study the influence of the compaction stress on the wetting process, wetting tests were performed on Vieux-pré material compacted at the SPO water content $w_{spo} = 18\%$, to 0·5, 1 or 5 MPa. The results are shown in Fig. 4 in the [log(s), S_r] and [log(s), e] planes. In the [log(s), e] plane, it is observed that on wetting paths, the higher the compaction stress, the more significant the swelling of the specimen. In addition, it can be noticed in the [log s, S_r] plane that, on the wetting paths, the suction of resaturation increases with the compaction stress (Fig. 5).

Fleureau *et al.* (2002) proposed correlations between the standard or modified Proctor optimum water content and maximum density of clayey soils (in the range between $w_L = 25$ and $w_L = 170\%$), and their liquid limit. At SPO, the relations between the liquid limit and the optimum water content (in percent) and the maximum dry unit weight (in kN/m^3), are as follows (with the liquid limit in percent)

$$w_{spo} = 1{\cdot}99 + 0{\cdot}46w_L - 0{\cdot}0012w_L^2 \quad (1)$$

$$\gamma_{dspo} = 21 - 0{\cdot}113w_L + 0{\cdot}00024w_L^2 \quad (2)$$

Table 3 compares these parameters measured for the tested materials and calculated using these equations. There is a good agreement between the data and the predictions according to equations (1) and (2) for the optimum water content and the maximum dry unit weight. Fleureau *et al.* (2002) also showed that the wetting paths of compacted soils were generally linear in the [log(s), e] and [log(s), w] coordinate systems, under the conditions investigated. Correlations between the slopes of these lines, also called swelling indices, with respect to void ratio, C_{ms}, and water content, D_{ms}, in relation to liquid limit for specimens compacted at SPO were established by Fleureau *et al.* (2002). The equations are as follows (with the liquid limit in percent)

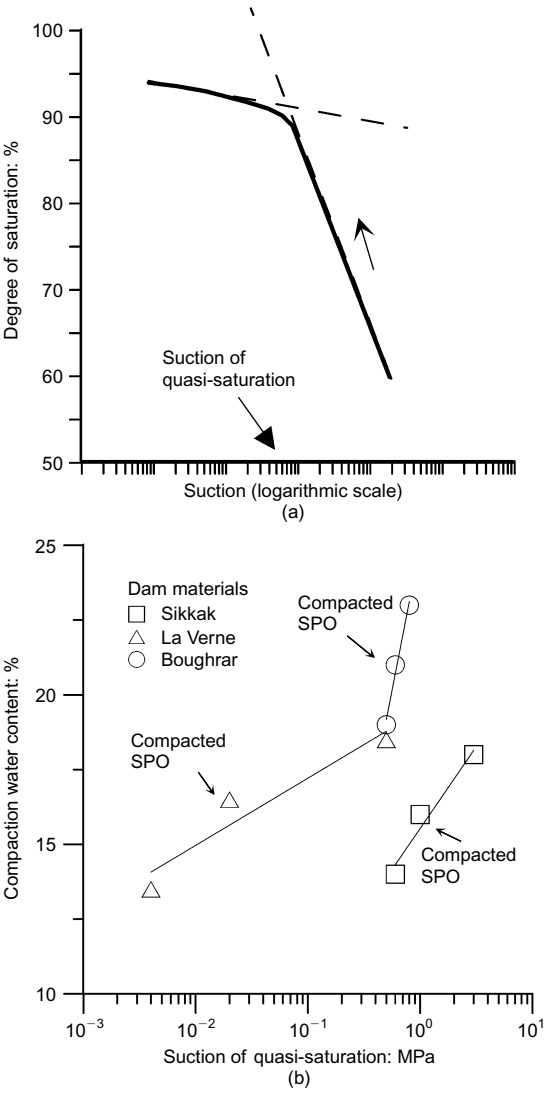

Fig. 3. Influence of compaction water content on the suction of quasi-saturation. (a) Typical wetting path of compacted soil; (b) variation of compaction water content plotted against quasi-saturation suction for the investigated materials

$$C_{ms} = \frac{-\Delta e}{\Delta[\log(s)]} = +0{\cdot}029 - 0{\cdot}0081w_L + 5{\cdot}10^{-6}w_L^2 \quad (3)$$

$$D_{ms} = \frac{-\Delta w}{\Delta[\log(s)]} = -0{\cdot}54 - 0{\cdot}030w_L + 3{\cdot}3{\cdot}10^{-6}w_L^2 \quad (4)$$

Figure 6 shows the normalised water contents w/D_{ms} (with D_{ms} calculated as a function of the liquid limit according to equation (4)) plotted against suction for the studied materials. The graph shows the validity of the liquid limit as a primary classification parameter for fine-grained clayey soils, without excluding the use of other parameters that would reduce the scatter of the data.

Mechanical undrained loading

Oedometer tests were carried out on unsaturated Vieux-pré samples, compacted to 1 MPa, corresponding to a degree of saturation of about 87% (Fig. 7). The variation of suction

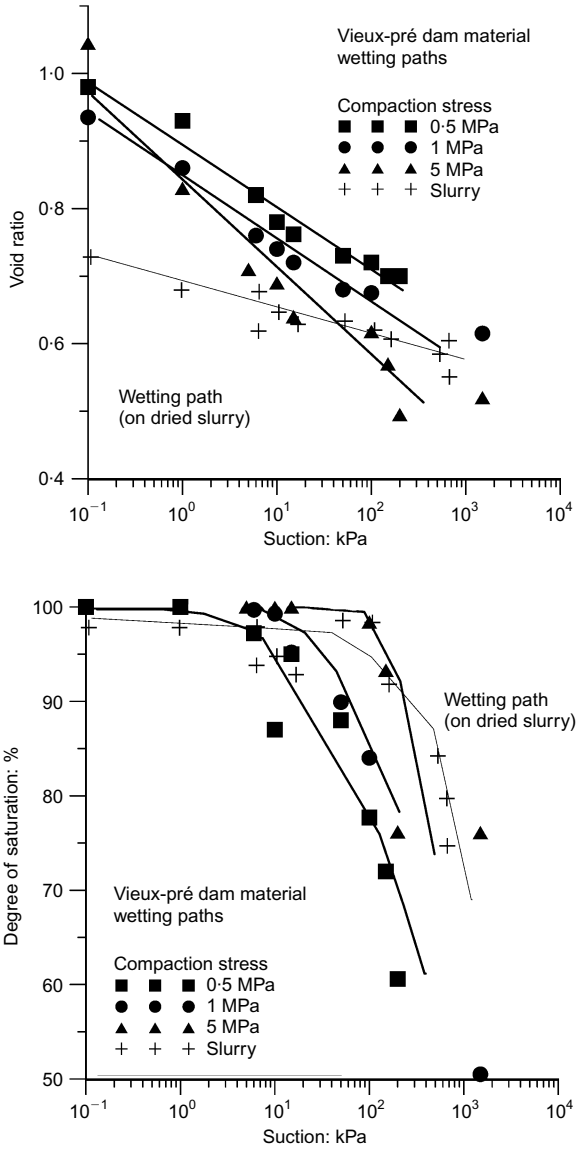

Fig. 4. Influence of compaction stress on the wetting paths of Vieux-pré dam material

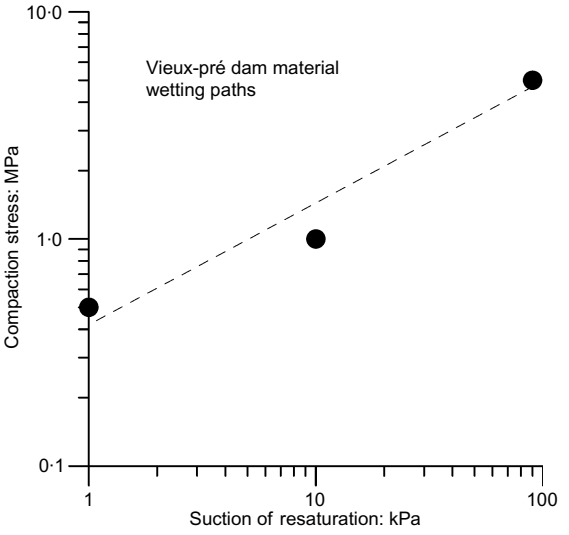

Fig. 5. Compaction stress plotted against suction of resaturation for Vieux-pré dam material

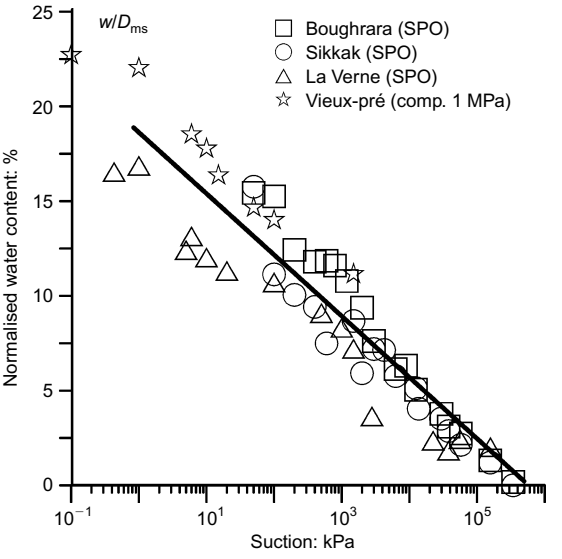

Fig. 6. Normalised water contents of soils compacted at the Proctor optimum

during the mechanical loading was measured with a psychrometric probe. In the [log(σ_v), e] plane, the normally consolidated curve derived from tests carried out on a slurry of the same material is also plotted (i.e. specimens prepared at a water content equal to 1·5 times the liquid limit). Two domains of behaviour are observed: first, the void ratio varies very slightly, until reaching the yield stress due to compaction. Indeed, if an analogy is made with the overconsolidated behaviour of saturated materials, the corresponding consolidation total stress, at the intersect between the normally consolidated (NC) consolidation line and the tangent to the loading path, is about 1300 kPa. As soon as this stress is exceeded, larger compressibility of the material is observed, with the curve tending towards that of the normally consolidated reconstituted material. At the same time, suction decreases significantly during loading (Fig. 7(b)), down to a value close to 0. It has already been

Table 3. Comparison between compaction soil properties at SPO and correlations with liquid limits

Material	w_L: %	w_{SPO}: %		$\gamma_{d\,SPO}$: kN/m^3 γ_{dSPO}	
		Experiment	Correlation	Experiment	Correlation
Boughrara dam	48	21	21·3	16·2	16·1
Sikkak dam	50	16	22	15·5	15·9
Vieux-pré dam	32	18	15·5	17·2	17·6
La Verne dam	35	16·5	16·6	17·9	17·3

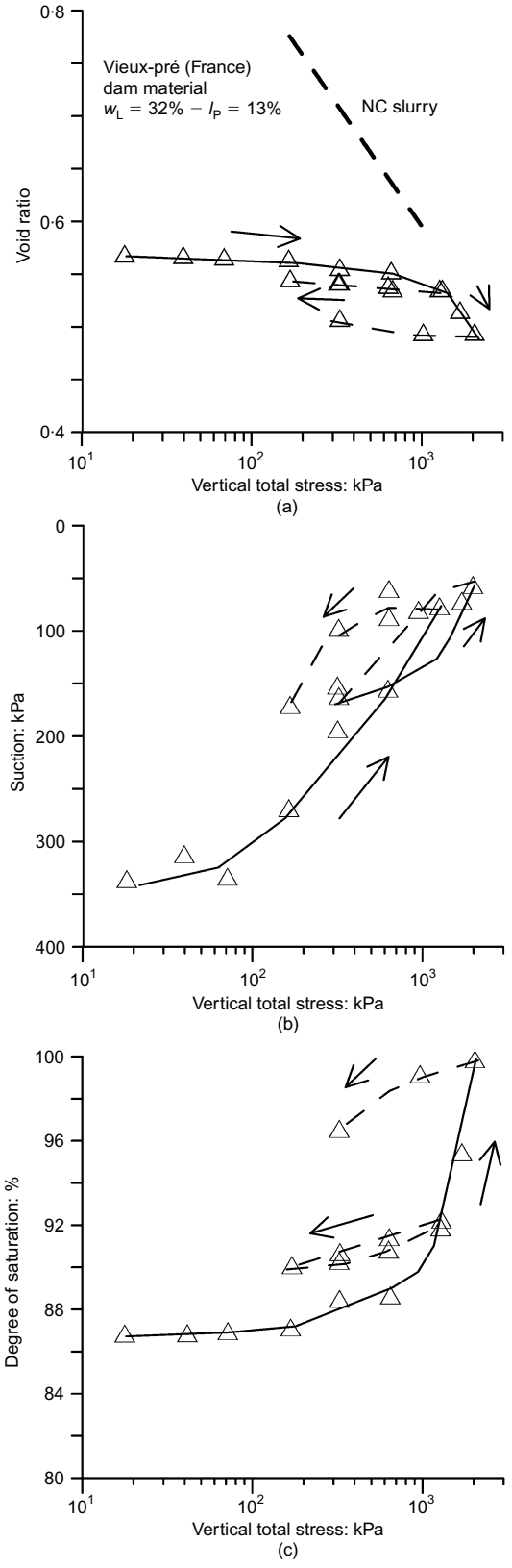

Fig. 7. Variation of: (a) void ratio; (b) suction; and (c) degree of saturation during undrained oedometer loading of Vieux-pré dam material

pointed out that the lower limit for measuring suction with a psychrometer is practically about 300 kPa (Zerhouni, 1995). However, only the suction values above 150 kPa were considered acceptable to interpret the test. Below this value, the dispersion and the discrepancy of the psychrometric measurements become too large. In addition, during the cycles, suction increases during unloading. The slopes of the unloading–reloading paths do not correspond to those of the saturated material.

In order to highlight the difference between the two wetting paths (the free wetting and the oedometric paths) performed on the soil from the same initial state, the changes in void ratio and degree of saturation were plotted in Fig. 8 against the effective vertical stress σ'_v. For simplicity, Terzaghi's effective stress definition was used, considering that the degree of saturation was larger than 85% in both cases and that the use of this definition would not result in too large an error. Fig. 8 shows how the two wetting paths lead the soil to saturation through opposite loading histories for the soil skeleton. The second conclusion that can be drawn from this comparison is the importance of carrying out undrained oedometric tests, as complements to the usually performed drained (suction-controlled) tests, as they provide additional information on the behaviour of the material, which can be useful for its modelling.

CONCLUSIONS

The aim of this note was to present some aspects of the behaviour of laboratory compacted dam materials during wetting. Some interesting features have been highlighted. Soils compacted at water contents around the optimum seem to follow the same wetting path as those compacted at the optimum in the [log(s), e] plane. However, a difference appears between the wetting paths in the [log(s), S_r] plane, the path corresponding to the specimens compacted at the optimum being located between those of the specimens compacted at w_{spo} − 3% and w_{spo} + 2%. As a confirmation of existing knowledge concerning the influence of compaction stress on wetting paths, it appears that the higher the compaction stress, the larger the swelling of the soil, and that the suction of saturation increases with the compaction stress. Correlations between the liquid limit and the main properties of the compacted soils show a good agreement for the tested materials in the normalised water contents against suction plane. Comparing the changes in void ratio induced by mechanical loading (oedometric loading at constant water content) and hydraulic loading (wetting path under null stress), the experimental evidence is provided of how the oedometric path has an opposite effect to that of

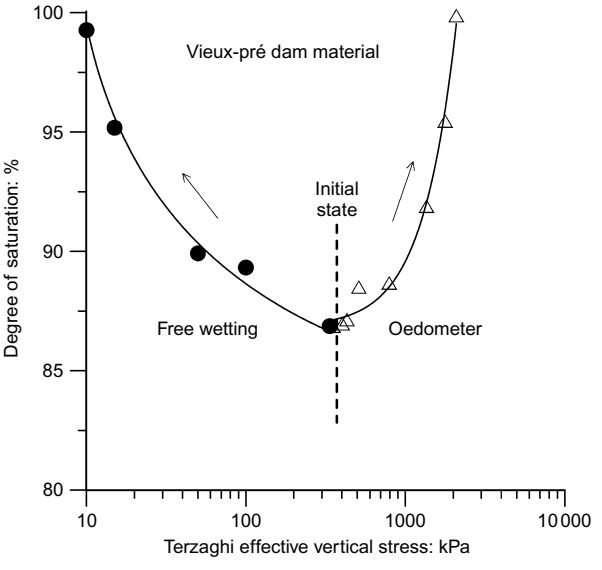

Fig. 8. Degree of saturation changes, due to oedometer loading at constant water content and free wetting, plotted against Terzaghi's effective stress

the wetting path as it leads to a decrease in void ratio, compared to an increase in the case of the free wetting test, although both tests result in an increase in degree of saturation. The results also confirm the interest of carrying out undrained tests with suction measurement (using psychrometers) complementing suction-controlled drained tests.

NOTATION

C_{ms}	swelling coefficient with respect to void ratio
D_{ms}	swelling coefficient with respect to water content
e	void ratio
I_P	plasticity index
n	porosity
Sr	degree of saturation
s	suction ($s = u_a - u_w$)
s_{spo}	suction at SPO water content and maximum density
u_a	pore-air pressure
u_w	pore-water pressure
w	water content
w_L	liquid limit
w_P	plastic limit
w_{spo}	standard Proctor optimum water content
γ_{dSPO}	specific weight at SPO water content and maximum density
γ_s	specific weight of grains
γ_w	specific weight of water
σ_v	total vertical stress

REFERENCES

Alonso, E. E. & Pinyol, N. M. (2008). Unsaturated soil mechanics in earth and rock dam engineering. In *Unsaturated soils: advances in geo-engineering* (eds D. G.Toll, C. E. Augarde, D. Gallipoli and S. J. Wheeler), pp. 3–32. London: Taylor and Francis.

AFNOR (1991). *Sols: reconnaissance et essais – Détermination de la masse volumique des particules solides des sols – Méthode du pycnomètre à eau*, AFNOR NF P94-054. France: AFNOR Groupe.

AFNOR (1992). *Sols: reconnaissance et essais – Analyse granulométrique des sols – Méthode par sédimentation*, AFNOR NF P94-057. France: AFNOR Groupe.

AFNOR (1993). *Sols: reconnaissance et essais – Détermination des limites d'Atterberg – Limite de liquidité à la coupelle – Limite de plasticité au rouleau*, AFNOR NF P94-051. France: AFNOR Groupe.

AFNOR (1995). *Sols: reconnaissance et essais – Identification granulométrique – Méthode de tamisage par voie humide*, AFNOR XP P94-041. France: AFNOR Groupe.

AFNOR (1999). *Sols : reconnaissance et essais – Détermination des références de compactage d'un matériau – Essai Proctor normal. Essai Proctor modifié*, AFNOR NF P94-093. France: AFNOR Groupe.

Ahmed, S., Lovell, C. W. & Diamond, S. (1974). Pore sizes and strength of compacted clay. *J. Geotech. Engng Div., ASCE* **100**, No. GT4, 407–425.

ASTM (American Society for Testing and Materials) (1995). Standard test method for measurement of soil potential (suction) using filter paper (D5298–94). In *1995 annual book of ASTM standards*, vol. 04–08. Philadelphia, PA: ASTM.

Birle, E., Heyer, D. & Vogt, N. (2008). Influence of the initial water content and dry density on the soil–water retention curve and the shrinkage behaviour of a compacted clay. *Acta Geotechnica* **3**, No. 3, 191–200

Brown, J. L. & Sivakumar, V. (2008). The changes in stress regime during wetting of unsaturated compacted clays when laterally confined. In *Unsaturated soils: advances in geo-engineering* (eds D. G. Toll, C. E. Augarde, D. Gallipoli and S. J. Wheeler), pp. 361–368. London: Taylor and Francis.

Delage, P., Suraj De Silva, G. P. R. & Vicol, T. (1992). Suction controlled testing of nonsaturated soils with an osmotic consolidometer. *Proc. 7th Int. Conf. on Expansives Soils, Dallas* **1**, 206–211.

Delage, P., Audiguier, M., Cui, Y. J. & Howat, M. D. (1996). Microstructure of a compacted silt. *Can. Geotech. J.* **33**, No. 1, 150–158.

Delage, P., Howat, M. D. & Cui, Y. J. (1998). The relationship between suction and swelling properties in a heavily compacted unsaturated clay. *Engng Geol*. **50**, No. 1–2, 31–48.

Fleureau, J. M., Kheirbek-Saoud, S., Soemitro, R. & Taibi, S. (1993). Behavior of clayey soils on drying–wetting paths. *Can. Geotech. J.* **30**, No. 2, 287–296.

Fleureau, J. M., Verbrugge, J. C., Huergo, P. J., Gomes Correia, A. & Kheirbek-Saoud, S. (2002). Aspects of the behaviour of compacted clayey soils on drying and wetting paths. *Can. Geotech. J.* **39**, No. 6, 1341–1357

Gallipoli, D., Wheeler, S. J. & Karstunen, M. (2003a). Modelling the variation of degree of saturation in a deformable unsaturated soil. *Géotechnique* **53**, No. 1, 105–112, **doi**: 10.1680/geot.2003.53.1.105.

Gallipoli, D., Gens, A., Sharma, R. & Vaunat, J. (2003b). An elasto-plastic model for unsaturated soil incorporating the effects of suction and degree of saturation on mechanical behaviour. *Géotechnique* **53**, No. 1, 123–136, **doi**: 10.1680/geot.2003.53.1.123.

Gens, A., Alonso, E. E., Suriol, J. & Lloret, A. (1995). Effect of structure on the volumetric behaviour of a compacted soil. *Proc. 1st Int. Conf. on Unsaturated Soils (UNSAT 95), Paris, France* (eds E. E. Alonso and P. Delage) **2**, 83–88. Rotterdam: Balkema.

Guillot, X., Al Mukhtar, M., Bergaya, F. & Fleureau, J.M. (2001). Effect of hydromechanical stresses on pore space and water retention in a clay. *Proc. 15th Int. Conf. Soil Mech. and Geotech. Engng (ICSMGE), Istanbul, Turkey* **1**, 101–105. Rotterdam: AA Balkema.

Kassif, G. & Ben Shalom, A. (1971). Experimental relationship between swell pressure and suction. *Géotechnique* **21**, No. 3, 245–255, **doi**: 10.1680/geot.1971.21.3.245.

Sivakumar, V., Tan, W. C., Murray, E. J. & McKinley, J. D. (2006). Wetting, drying and compression characteristics of compacted clay. *Géotechnique* **56**, No. 1, 57–62, **doi**: 10.1680/geot.2006.56.1.57.

Sun, D., Sheng, D. C., Cui, H. B. & Li, J. (2006). Effect of density on the soil–water-retention behaviour of compacted soil. *Proc. 4th Int. Conf. Unsaturated Soils, Arizona* **1**, 1338–1347. Reston, VA: American Society of Civil Engineers.

Tang, A. M., Cui, Y. J. & Bernel, N. (2008). Compression-induced suction in a compacted expansive clay. In *Unsaturated soils: advances in geo-engineering* (eds D. G. Toll, C. E. Augarde, D. Gallipoli and S. J. Wheeler), pp. 369–374. London: Taylor and Francis.

Tarantino, A. & Tombolato, S. (2005). Coupling of hydraulic and mechanical behaviour in unsaturated compacted clay. *Géotechnique* **55**, No. 4, 307–317, **doi**: 10.1680/geot.2005.55.4.307.

Tarantino, A. & De Col, E. (2008). Compaction behaviour of clay. *Géotechnique* **58**, No. 3, 199–213, **doi**: 10.1680/geot.2008.58.3.199.

Thakur, V. K. S., Sreedeep, S. & Singh, D. N. (2005). Parameters affecting soil-water characteristic curves of fine-grained soils. *J. Geotech. Geoenviron. Engng* **131**, No. 4, 521–524.

Vanapalli, S. K., Fredlund, D. G. & Pufahl, D. E. (1999). The influence of soil structure and stress history on the soil-water characteristics of a compacted till. *Géotechnique* **49**, No. 2, 143–159, **doi**: 10.1680/geot.1999.49.2.143.

Wheeler, S. J., Sharma, R. S. & Buisson, M. S. R. (2003). Coupling of hydraulic hysteresis and stress–strain behaviour in unsaturated soils. *Geotechnique* **53**, No. 1, 41–54, **doi**: 10.1680/geot.2003.53.1.41.

Zerhouni, M. I. (1995). Triaxial testing using psychrometers. Unsaturated soils. *Proc. 1st Int. Conf. on Unsaturated Soils (UNSAT 95), Paris, France* (eds E. E. Alonso and P. Delage) **2**, 673–678. Rotterdam: Balkema.

ice
Institution of Civil Engineers
publishing

Session 2

Experimental Observation and Modelling

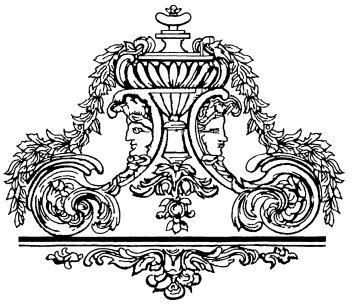

Romero, E. *et al.* (2011). *Géotechnique* **61**, No. 4, 313–328 [**doi:** 10.1680/geot.2011.61.4.313]

An insight into the water retention properties of compacted clayey soils

E. ROMERO*, G. DELLA VECCHIA† and C. JOMMI†

Experimental data from different testing methodologies on different compacted clayey soils, with dominant bimodal pore size distribution, are presented and analysed, to provide a comprehensive picture of the evolution of the aggregated fabric along hydraulic and mechanical paths. Fabric changes are analysed both from the porous network viewpoint, by means of careful mercury intrusion porosimetry investigation, and from the soil skeleton viewpoint, by quantifying swelling and shrinkage of the aggregates in an environmental scanning electron microscopy study. The consequences of the aggregated fabric evolution on the water retention properties of compacted soils are analysed and discussed. A new model for water retention domain is proposed, which introduces a dependence of the intra-aggregate pore volume on water content. The model succeeds in tracking correctly the evolution of the hydraulic state of the different soils investigated along generalised hydromechanical paths. The proposed approach brings to light coupling between intra-aggregate and inter-aggregate pores in the retention properties of compacted clayey soils. Dependence of the air entry and the air occlusion values on swelling and shrinking of aggregates, besides void ratio, is introduced and discussed.

KEYWORDS: clays; compaction; fabric/structure of soils; laboratory tests; partial saturation; suction

La présente communication expose et analyse des données expérimentales obtenues avec différentes méthodologies d'essai sur des sols argileux divers à distribution granulométrique bimodale dominante, pour tracer un tableau intégral de l'évolution de la structure d'agrégat le long de chemins hydrauliques et mécaniques. On analyse des variations de la structure du point du réseau poreux, par le biais d'un examen soigneux de la porosimétrie par intrusion de mercure, et du point de vue du squelette du sol, en quantifiant le gonflement et le retrait des agrégats dans le cadre d'une étude environnementale à microscopie à balayage électronique. On analyse les conséquences de l'évolution de la structure d'agrégats sur les propriétés de retenue de l'eau des sols compactés, et on les discute. On propose un nouveau modèle pour la retenue de l'eau, qui introduit le principe de la dépendance du volume interstitiel intra agrégats de la teneur en eau. Le modèle parvient à suivre correctement l'évolution de l'état hydraulique des différents sols examinés le long de chemins hydromécaniques généralisés. L'approche proposée dévoile le rapport entre pores intra-agrégats et inter-agrégats dans les propriétés de retenue de l'eau de sols argileux compactés. On introduit la dépendance de l'entrée d'air et les valeurs d'occlusion d'air sur le gonflement et le retrait d'agrégats, en plus de l'indice de vide, et on en discute.

INTRODUCTION AND BACKGROUND

Both suction and a measure of the amount of water content of the soil need to be considered to adequately understand, describe and predict the behaviour of unsaturated soils (e.g. Wheeler, 1996; Jommi, 2000; Vaunat *et al.*, 2000; Gallipoli *et al.*, 2003; Sheng *et al.*, 2004; Pereira *et al.*, 2005; Gens *et al.*, 2006; Romero & Jommi, 2008; Laloui & Nuth, 2009). Recently, attention has also been paid to the influence of hydraulic history on the response of unsaturated soils along generalised hydromechanical stress paths (Sun *et al.*, 2007; Romero & Jommi, 2008; Muraleetharan *et al.*, 2009).

The hydraulic state of a soil is the result of solid–fluid interaction, and it is evaluated by introducing the so-called water retention curve, which is a constitutive law that summarises the dependence on suction of the amount of water stored in a soil. Solid–fluid interactions are dominated by capillary and adsorption mechanisms. They are strongly dependent on the mineralogical composition of the soil and on its fabric, on temperature and on pore fluid chemistry. Specific surface and pore size distribution may be chosen to describe appropriately the role played by the solid phase on the retention properties of compacted soils.

Manuscript received 2 March 2010; revised manuscript accepted 14 December 2010.
Discussion on this paper closes on 1 September 2011; for further details see p. ii.
* Department of Geotechnical Engineering and Geosciences, Universitat Politècnica de Catalunya, Barcelona, Spain
† Department of Structural Engineering, Politecnico di Milano, Milano, Italy

In the formulation of conceptual water retention models, stored and adsorbed water have been traditionally quantified on a mass basis, in terms of water content, w (mass of water over solid mass), or on a volumetric basis, through degree of saturation S_r (volume of water over volume of voids), volumetric water content θ_w (volume of water over total soil volume) or water ratio e_w (volume of water over solid volume). In fact, none of these variables seems to provide definite advantages in the description of the water retention behaviour, as the example presented in Fig. 1 demonstrates. Bentonite-enriched sand, which was used as an engineered barrier in the gas migration test at the Grimsel underground laboratory (Olivella & Alonso, 2008), was compacted on the dry side of optimum. Relevant properties of the material are summarised in Table 1. The stress paths followed in the laboratory in terms of vertical net stress, $(\sigma_v - u_a)$, and matric suction, s (difference between pore air pressure u_a and pore water pressure u_w), which replicated the in situ test, are shown in Fig. 1(a). Starting from the as-compacted state (point A in the figure), the sample was subjected to wetting at constant volume (path AB). Afterwards, the sample underwent a series of unloading (BC, EF), drying (CD), loading (DE) and wetting (FG) paths. Changes in void ratio e along the stress paths are reported in Fig. 1(b). The evolution of the hydraulic state of the material along the hydromechanical paths is reported in Figs 1(c)–1(e) adopting different water content measures. As it can be appreciated from the three figures, which plot the evolution of the hydraulic state of the material, retention properties are far from being intrinsic, or *characteristic*. Swelling, shrinkage, loading and unloading all affect the water storage capacity

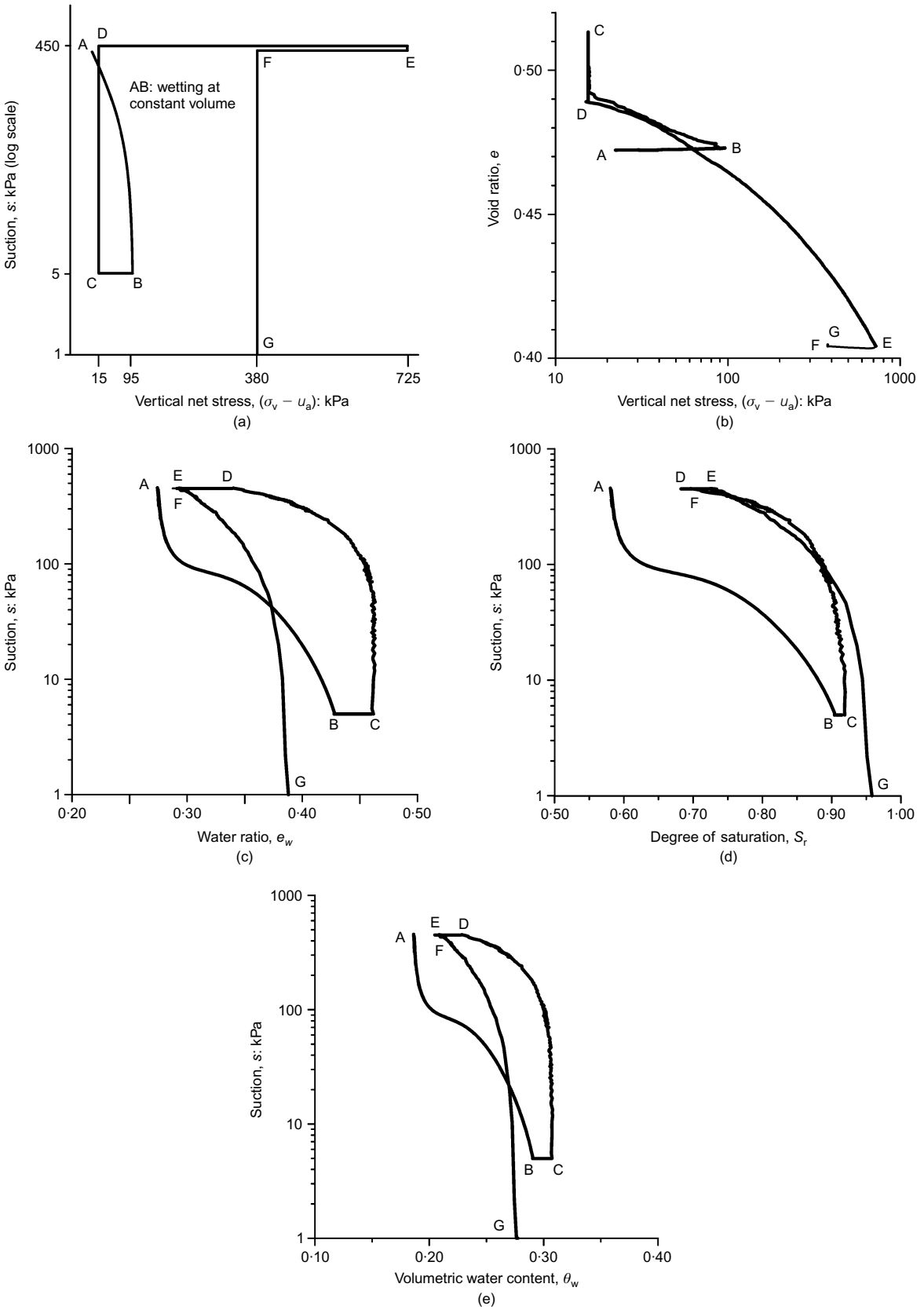

Fig. 1. Hydromechanical paths on sand–bentonite mixture compacted at the dry side of optimum. (a) Stress path followed; (b) volume change response; (c) water retention behaviour in terms of water ratio; (d) water retention behaviour in terms of degree of saturation; (e) water retention behaviour in terms of volumetric water content

of the material, but none of the adopted variables allows full normalisation of the water retention paths.

Even the concepts of 'drying' and 'wetting' may be ambiguous if they are not referred to a specific water measure. For example, the compression path DE at constant suction causes a decrease of water ratio (Fig. 1(c)), e_w, which suggests a drying process, whereas the same path develops in Fig. 1(d) with increasing S_r, which entails a

Table 1. Properties of soils used in the present study

Soil	Mineralogy	Liquid limit, w_L: %	Plastic limit, w_P: %	Density of solids ρ_s: Mg/m^3	% Particles < 2 μm	Total specific surface: m^2/g
Barcelona clayey silt*	Illitic clay fraction	32	16	2·66	15	12
Boom Clay†	Illitic-kaolinitic clay fraction	56	29	2·70	50	53
Febex bentonite‡	Montmorillonite > 90% Ca^{2+} (38%) Na^{+} (23%)	102	53	2·70	64–70	725
MX-80 bentonite§	Montmorillonite 82–85% Na^{+} (82%) Ca^{2+} (13%)	520	46; 62	2·65	80–90	522; 700
Bentonite-enriched sand¶	80/20 proportion on dry mass basis of quartz sand/Kunigel V1 sodium bentonite	36	—	2·65	20	137

* Barrera (2002).
† Romero *et al.* (1999); Romero & Vaunat (2000).
‡ Lloret *et al.* (2003); Villar *et al.* (2005).
§ Delage (2002); Villar *et al.* (2005); Delage *et al.* (2006).
¶ Romero *et al.* (2002).

wetting process. In fact, the hydraulic state can be affected by adding or removing water, hence filling or emptying a given pore volume, or by changing the volume of the pores. As a way to tackle this conflict, Tarantino (2009) introduced the concept of *hydraulic* wetting related to a process which increases water volume, in contrast to the term *mechanical* wetting, associated with an increase in the degree of saturation due to a decrease of void ratio.

In the past few years, much research has been devoted to analyse the evolution of retention curves with void ratio, both from the experimental and the theoretical viewpoints. Dependence of water retention curves on volumetric state variables and strain history was underlined by Romero *et al.* (1999), Vanapalli *et al.* (1999), Kawai *et al.* (2000), and more recently by Tarantino (2009). The hysteretic nature of water retention curves was recently addressed by Kohgo (2008), Miller *et al.* (2008) and Nuth & Laloui (2008), not only in the light of the well-known pore constriction effect, but also as a consequence of soil deformability.

To provide a reminder of the effects of porosity on water retention properties, data from wetting paths, performed at different void ratios e, on three different soils, namely Barcelona clayey silt, Boom Clay and Febex bentonite, are shown in Fig. 2. Relevant properties of the soils are summarised in Table 1, which shows that these three materials cover a wide range of clayey soils with different plasticity index values. All the soils were compacted on the dry side of optimum, and the as-compacted samples display clear bimodal pore size distributions, due to the formation of aggregates during compaction. Psychrometric measurements (WP4 dew-point mirror psychrometer), vapour equilibrium, and constant volume wetting and drying paths performed by axis translation, were adopted to explore a wide range of suction, and to provide consistent pictures of the water retention curves. Here, and in the following, water ratio $e_w = w\,Gs = S_r\,e$ (where Gs is the specific gravity of the soil particles) is chosen to describe the amount of water in compacted soils (Toll, 1995), basically because it is strongly indicated to handle adsorption mechanisms. The role played by void ratio on capillary mechanisms can be naturally accounted for.

The data presented in the figure show that two regions can be distinguished in the water retention curves, as suggested by Romero *et al.* (1999) and Romero and Vaunat (2000). At low suction values, the amount of water stored in the soil is high enough to saturate the pores inside the

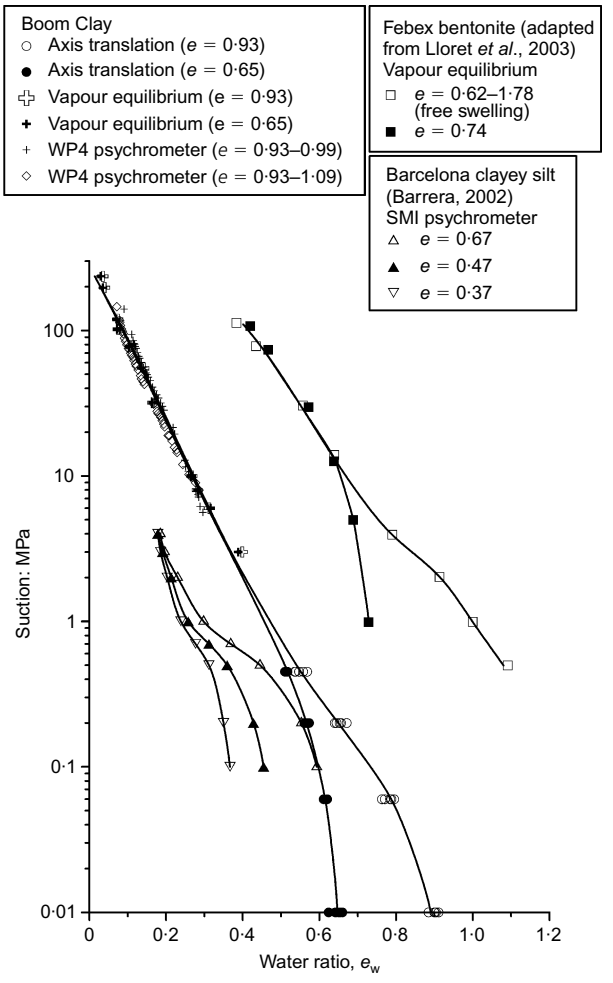

Fig. 2. Wetting paths performed on three materials compacted on the dry side of optimum (Boom Clay, Febex bentonite and Barcelona clayey silt) at different void ratios

aggregates – which will be termed 'intra-aggregate pores' or 'micropores' – and to partly fill the pores between the aggregates – 'inter-aggregate pores' or 'macropores'. In the latter region, capillary storage mechanisms dominate, which clearly depend on the characteristic dimensions of interconnected macropores, hence on porosity. On the other hand, at

e_w lower than 0·2 for Barcelona clayey silt, 0·4 for Boom Clay and 0·6 for Febex clay, the influence of void ratio is found to be negligible, which indicates a region dominated by adsorptive storage mechanisms, where water with lower mobility is held inside the intra-aggregate porosity. In a main wetting path, intra-aggregate pores will be saturated before water begins to be stored in the macropores.

The relative contributions of capillarity and adsorptive surfaces forces had already been highlighted by Or & Tuller (1999), derived from physically based models. The authors concluded that capillary forces dominate at low suction values, whereas adsorptive forces rule the hydraulic behaviour at suctions higher than 1 MPa. The amount of adsorbed water is strongly linked to the specific surface (Tuller & Or, 2005), and it is influenced by the soil intra-aggregate structure and by the chemical interactions of the solid surface with the pore fluid. The link between water affinity, specific surface and liquid limit was discussed by De Bruyn *et al.* (1957), Black (1962), and more recently by Aubertin *et al.* (2003) and Frydman & Baker (2009).

Identical conclusions may be drawn if the retention behaviour is analysed on drying paths. As an example, data on Boom Clay samples at different void ratios subjected to main drying are reported in Fig. 3. The experimental data show that dependence on void ratio may be again appreciated only for water ratios above $e_w = 0{\cdot}4$.

Dependence of water retention properties on void ratio has been analysed and modelled in previous years mainly focusing on the evolution of the air-entry or the air-occlusion suction values in drying or wetting processes, respectively (see, for instance, Huang *et al.*, 1998; Vanapalli *et al.*, 1999; Kawai *et al.*, 2000; Gallipoli *et al.*, 2003; Nuth and Laloui, 2008; Maŝín, 2009). Experimental data presented in Fig. 4 suggest supporting this approach. The data come from different wetting paths, performed on samples of Boom Clay compacted at initial void ratio $e_0 = 0{\cdot}93$. Wetting was performed under oedometer conditions, at the different vertical net stresses indicated in the figure. The water retention data are enclosed by the wetting retention curves at constant void ratio $e = 0{\cdot}93$ and $e = 0{\cdot}65$. The degree of saturation S_r of the samples corresponding to the different suctions is reported within brackets. The air occlusion suction range, which is bounded by the curves $S_r = 0{\cdot}85$ and $S_r = 0{\cdot}90$, obtained by interpolation of relevant experimental data, is shown in the figure. This zone clearly progresses towards larger matric suction values at decreasing void ratio.

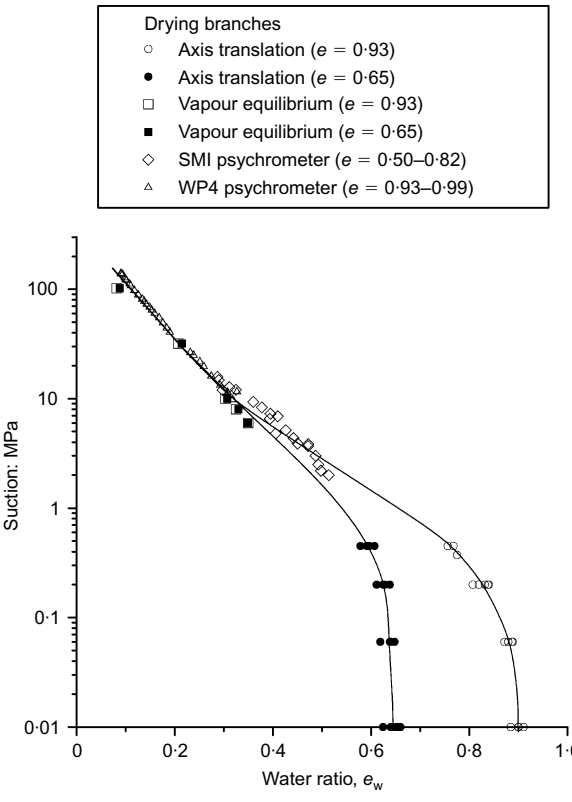

Fig. 3. Main drying paths for compacted Boom Clay at different void ratios

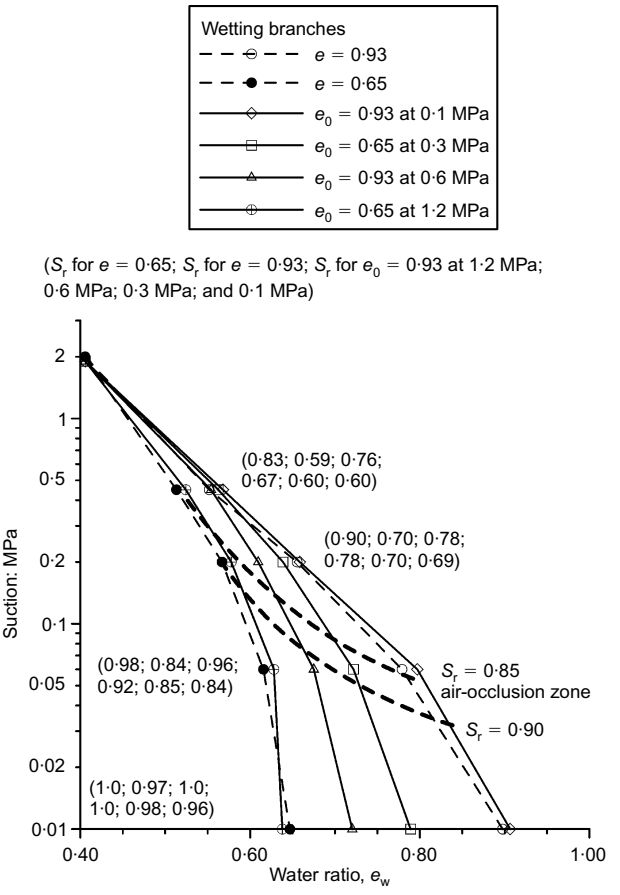

Fig. 4. Air-occlusion zone evolution along wetting paths for compacted Boom Clay ($e_0 = 0{\cdot}93$) in oedometer at different vertical net stresses

Given this picture, an experimental programme was planned to analyse in greater detail the evolution of water retention properties of compacted clayey soils. Besides the role played by void ratio, activity of the clay fraction and solid–fluid interaction were investigated, with special attention to the inter-playing role of the different structure levels. As will be shown, aggregates will continue exchanging water even after reaching saturation. The potential for shrinkage and swelling of the aggregates will affect the inter-aggregate porosity and will influence the current retention properties of the soil. A new model for the water retention domain, in which the clay activity is taken into account by means of a physically based interpretation, is proposed, to show the important effects of the evolution of the compacted soil microstructure promoted by hydraulic paths, besides mechanical paths.

A MICROSTRUCTURAL INSIGHT INTO WATER RETENTION PROCESSES

To analyse the evolution of microstructure along different hydraulic and mechanical paths, a microstructural study

using mercury intrusion porosimetry (MIP) and environmental scanning electron microscopy (ESEM) was undertaken. Details of the techniques adopted can be found in Romero & Simms (2008).

Experimental investigation

Mercury intrusion porosimeter data are commonly used to analyse compacted soil fabric (see Delage *et al.*, 1996; Romero *et al.*, 1999; Monroy *et al.*, 2010; among others). The evolution of the pore size density function, PSD, of compacted soils along drying or wetting paths was analysed by Cui *et al.* (2002), Simms & Yanful (2001, 2005), Koliji *et al.* (2006) and Delage *et al.* (2006). Models of the water retention curve directly based on PSD were also proposed (refer, for example, to Simms & Yanful, 2002, 2004; Romero & Simms, 2008). Here, the experimental investigation was aimed at analysing in detail the evolution of intra-aggregate porosity and at quantifying this evolution along generalised coupled hydromechanical paths.

Samples of Boom Clay were prepared by static compaction on the dry side of optimum, at void ratio $e = 0{\cdot}93$ and water ratio $e_w = 0{\cdot}41$ ($S_r = e_w/e = 0{\cdot}44$). The samples were then subjected to different mechanical and hydraulic paths. The PSD of all the samples was evaluated afterwards, by means of MIP tests performed on freeze-dried specimens.

Sensitivity of the intra-aggregate pores to hydraulic and mechanical paths is exemplified by the data presented in Fig. 5, where the PSD of the as-compacted sample is compared to those of samples subjected to loading at constant water content, wetting at constant volume or wetting in oedometer at null vertical stress (free saturation). The as-compacted sample is characterised by a clear bimodal distribution with dominant pore modes around 13 μm (macropores) and 60 nm (micropores). Loading the sample at vertical stress of 0·6 MPa shifts the size of dominant macropores towards a slightly lower value, while the micropore volume and its dominant pore size are not affected. On the contrary, the two saturation paths affect both inter-aggregate and intra-aggregate pores. After saturation, the two samples display a similar fabric dominated by the single peak at around 1·2 μm, which is originated by both expansion of the micropores and reduction of macropores. The PSD function of a sample, which was further subjected to a drying path up to a total suction of 100 MPa (relative humidity around 50%) after wetting at constant volume, is shown in Fig. 6. It may be observed that the inter-aggregate porosity underwent an important reduction on shrinkage, which is evidenced by the small dominant peak around 2 μm. On the contrary, the intra-aggregate porosity is almost completely recovered, as similarity of the PSDs of the dried and the as-compacted samples, at entrance pore sizes below 1 μm, demonstrates. Therefore, it appears that the aggregates created by compaction on the dry side of optimum tend to swell and shrink almost reversibly, and that they may be considered a permanent feature of the compacted soil fabric.

A complementary view on the latter observations is qualitatively provided by the ESEM photomicrographs, taken at different hydraulic states, shown in Fig. 7. The aggregates and the inter-aggregate pore space are clearly visible in the ESEM image corresponding to the initial as-compacted state (Fig. 7(a)), whereas intra-aggregate pores are indistinguishable. Macropores correspond to the dark areas in the figure. Their typical size, 7 μm and 11 μm in Fig. 7(a), is similar to that estimated from MIP data (Fig. 5). The ESEM photomicrograph in Fig. 7(b) shows the relatively uniform fabric of the compacted soil sample after wetting at constant volume. Expansion of the aggregates and occlusion of the macropores, already evidenced by MIP results (Fig. 5), can be appreciated. Nonetheless, typical aggregated fabric is still visible, although the aggregates fused together during hydration. Upon subsequent drying (Fig. 7(c)), a network of shrinkage cracks appears in the looser zones between densely packed aggregates, which recovers the permanent aggregated fabric. Similar ESEM photomicrographs, displaying fused aggregates for fully hydrated compacted samples, were recently shown by Monroy *et al.* (2010).

Data interpretation

To provide a quantitative measure of intra-aggregate porosity for any hydraulic state of the soil, a criterion to distinguish the latter from inter-aggregate porosity must be chosen. Three possible ways, which can be adopted to

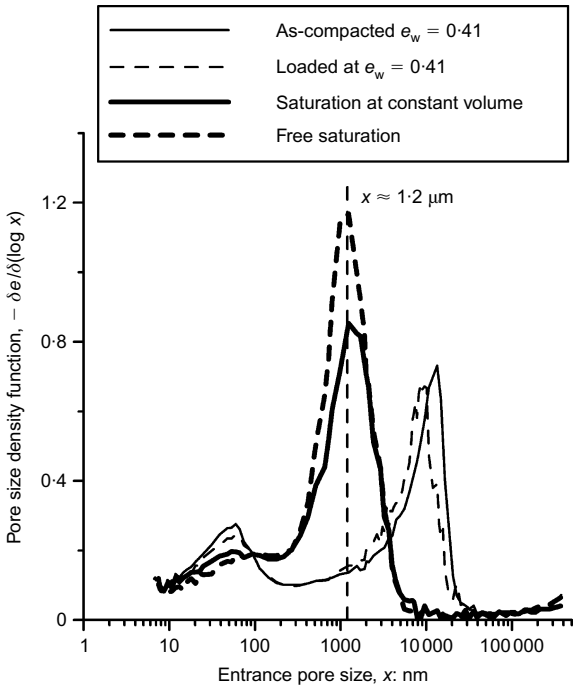

Fig. 5. PSD functions of compacted Boom Clay subjected to different hydromechanical paths

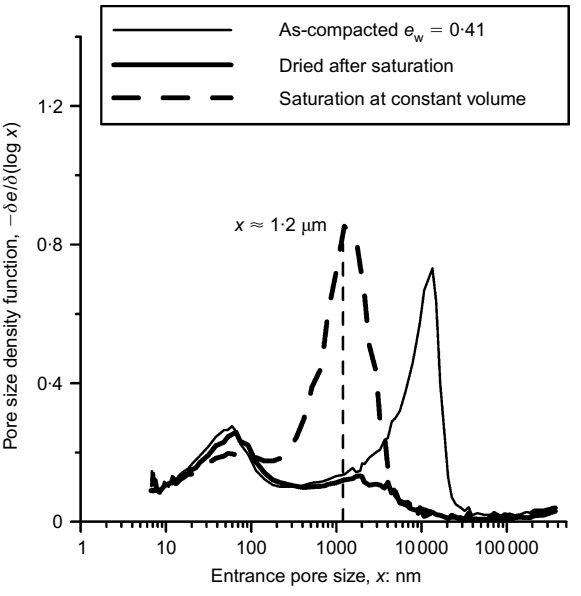

Fig. 6. PSD functions of compacted Boom Clay subjected to different hydraulic paths

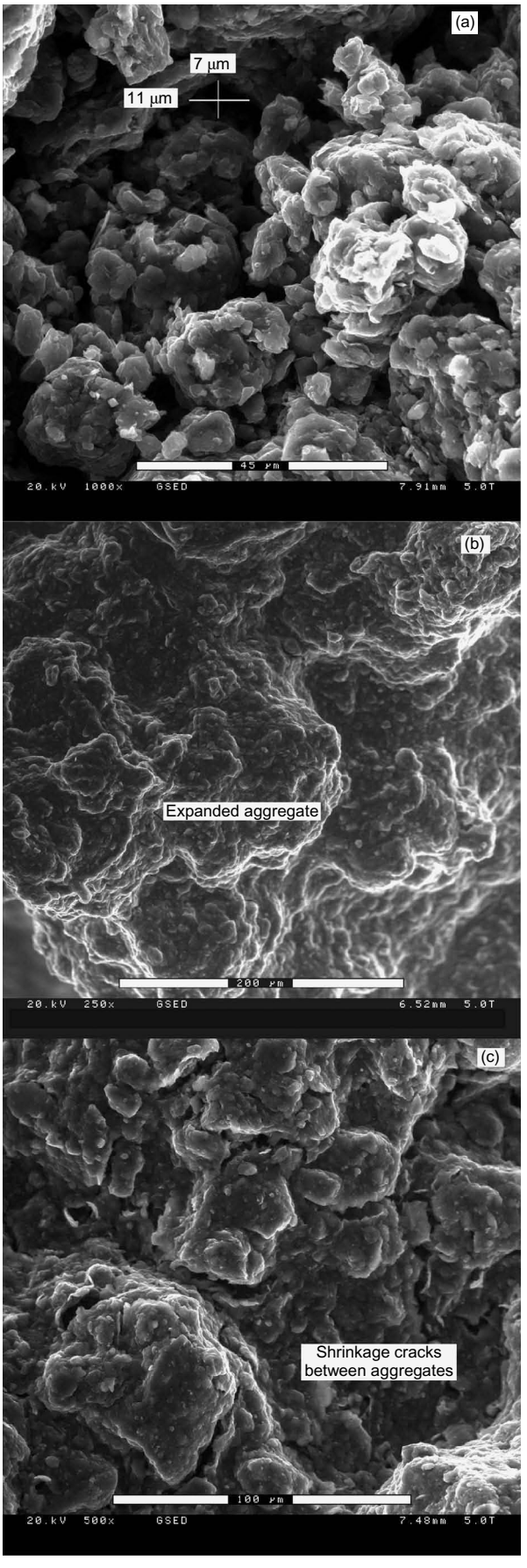

Fig. 7. ESEM photomicrographs on compacted Boom Clay at different hydraulic states: (a) as-compacted state; (b) after isochoric saturation; (c) after isochoric saturation and drying

estimate the intra-aggregate porosity are described in Fig. 8, with reference to Boom Clay data. If the intra-aggregate porosity region is defined as the domain in which the retention curve is not sensitive to void ratio, the pores having size smaller than 300−400 nm can be identified from Fig. 8(a), according to the Laplace equation. A second possibility is to use the as-compacted PSD function, and to separate intra-aggregate porosity from inter-aggregate porosity by an entrance pore size bounded by the as-compacted dominant modes. Data for Boom Clay obtained by MIP for $e = 0{\cdot}93$, shown in Fig. 8(b), would suggest a discriminating pore size ranging from 200 to 400 nm. Although useful, the two criteria are fundamentally based on the characteristic PSD of the as-compacted soil, and they may give somewhat ambiguous results if swelling and shrinking of the aggregates become appreciable as the total water content changes.

Following the proposal of Delage & Lefebvre (1984) and Delage *et al.* (1996), a third criterion may be adopted, based on data from a mercury intrusion/extrusion cycle. The first intrusion fills all the accessible and interconnected pore space, whereas on complete releasing of pressure, mercury is extruded only from the non-constricted pores, which are identified with the intra-aggregate pores. The difference between the intrusion and extrusion branches describes the entrapped (constricted) porosity, which is related to the inter-aggregate pore space. According to this criterion, the same MIP data on compacted Boom Clay would suggest that a slightly larger entrance pore size of approximately 800 nm distinguished micropores from macropores for this sample. The latter criterion would be appropriate to account for active microporosity, provided freeze-dried samples were subjected to careful intrusion/extrusion cycles after any loading-hydraulic path.

A possible alternative criterion is suggested here, which was used to elaborate most of the data discussed in the following. The new criterion stems from the assumption, confirmed by the data presented previously, that the size of the inter-aggregate pores is always larger or equal to that of the intra-aggregate pores. Therefore, for any compacted soil, a delimiting pore size must exist, which is an upper bound for the intra-aggregate porosity and a lower bound for the inter-aggregate porosity at the same time. This delimiting pore size can be determined, once and for all, from MIP data on samples after compaction and saturation at constant volume, which promotes swelling of the aggregates and reduction of the inter-aggregate porosity. The data presented in Fig. 6 show that the two mechanisms result in a single pore mode, from which intra-aggregate and inter-aggregate pores are not distinguishable. As a consequence, in fully hydrated states the single pore mode can be partially assigned to the intra-aggregate pore space and partially to the inter-aggregate one. The same conclusion holds independently of the mechanical constraints imposed during saturation, as the data for free-swelling in Fig. 5 demonstrate. Following these observations, the delimiting pore size may be assumed to coincide with the dominant peak of the PSD function determined by MIP after wetting. For Boom Clay, the data in Fig. 5 give a consistent value of $1{\cdot}2$ μm.

Definition of the delimiting pore size allows for separating the micropores volume from that of the macropores in a straightforward manner, for any sample. Intra-aggregate (or microstructural) void ratio, e_m (micropores volume over solid volume), and inter-aggregate (or macrostructural) void ratio, e_M (macropore volume over solid volume), are adopted with this aim, as they provide additive decomposition of void ratio $e = e_m + e_M$. Integration on PSD data of the pore volume between the minimum detectable pore size and the delimiting pore size, normalised by solid volume, gives the microstructural void ratio of the sample under consideration. For

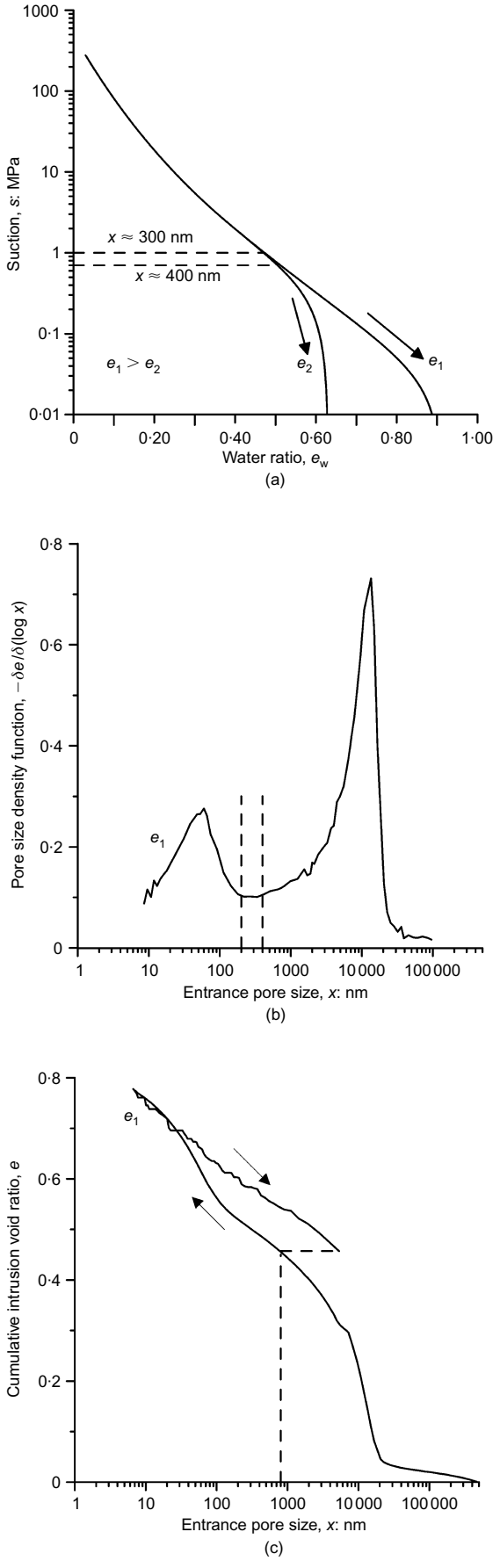

Fig. 8. Different criteria to discriminate the intra-aggregate void ratio on compacted Boom Clay: (a) from water retention curves at different void ratios; (b) from PSD function of the as-compacted material; (c) from separation between constricted and non-constricted porosity

example, based on the PSD functions presented in Fig. 5, $e_m = 0{\cdot}38$ could be calculated for the as-compacted sample and $e_m = 0{\cdot}69$ for the sample saturated at constant volume.

Hydromechanical evolution of water retention capacity

To evaluate the influence of compaction water content and of subsequent hydraulic paths on the evolution of micropores, samples of Boom Clay were subjected to different hydraulic and mechanical paths, namely wetting, drying and loading paths at constant e_w, starting from two different initial states, A and B in Fig. 9, with $e_{wA} = 0{\cdot}41$ and $e_{wB} = 0{\cdot}51$. At the end of each path, e_m was evaluated from MIP data adopting the same delimiting pore size (1·2 μm). The data collected and plotted in Fig. 9 suggest a non-linear evolution of the microstructural void ratio, showing a change in the slope around the shrinkage limit of the soil, which replicates the trend of a typical shrinkage curve.

For low water ratios, e_m increases slowly with e_w. The microstructural degree of saturation, S_r^m, defined as the volume of water inside the intra-aggregate pores over micropore volume, is lower than one ($S_r^m < 1$), while the macrostructural degree of saturation, S_r^M, defined as the volume of water inside the inter-aggregate pores over the macropore volume, is null ($S_r^M = 0$). The data cross the bisecting line ($e_w = e_m$) at a value of e_m, which will be denoted by e_m^*, which corresponds to a water ratio that is sufficient to saturate the aggregates ($S_r^m = 1$) but which leaves the inter-aggregate pores empty ($S_r^M = 0$). Starting from this point, an increase in the soil water content will partially continue to fill the saturated and still expanding aggregates, and partially be stored in the inter-aggregate pores. Therefore, for water ratios above e_m^*, part of the allowable water will be exchanged by the swelling (or shrinking, in the drying processes) aggregates, at $S_r^m = 1$. The remaining part will affect the macroscopic degree of saturation ($0 \leqslant S_r^M \leqslant 1$). As a first approximation, evolution of the microstructural void ratio for $e_w > e_m^*$ can be described by a linear interpolation with slope equal to β (Fig. 9).

A complementary investigation based on ESEM was undertaken to analyse the evolution of the microstructure from the aggregate deformation standpoint, by tracking swelling and shrinkage of a single aggregate during wetting and drying. The ESEM technique jointly with digital image analysis has already been adopted by Montes-H *et al.* (2003a, 2003b), Romero & Simms (2008) and Airò Farulla *et al.* (2010), to estimate the swelling–shrinkage behaviour of clayey materials at different water potentials at the aggregate scale.

The wetting and drying paths imposed on the soil samples, as shown in Fig. 10(a), were controlled by means of relative humidity. The absolute vapour pressure of the environmental chamber and the temperature of the sample holder were controlled. Microscopic observations were performed on isolated aggregates of Boom Clay and Febex bentonite powder, compacted on the dry side of optimum, at relative humidity around 50%. Images of the same aggregate were recorded at the different equalisation stages (maintained at least for 15 min), starting from point A at relative humidity of 33%, which represents the initial reference state. The volumetric strain ε_v of the aggregate at the different wetting and drying equalisation stages, presented in Fig. 10(b), was quantified by means of the expression (Romero & Simms, 2008)

$$\varepsilon_v = \gamma \varepsilon_{2D} = 1{\cdot}5\left(\frac{A - A_o}{A_o}\right) \quad (1)$$

where A and A_o are the areas of the aggregate at equalisation and at the initial reference states, respectively. A value

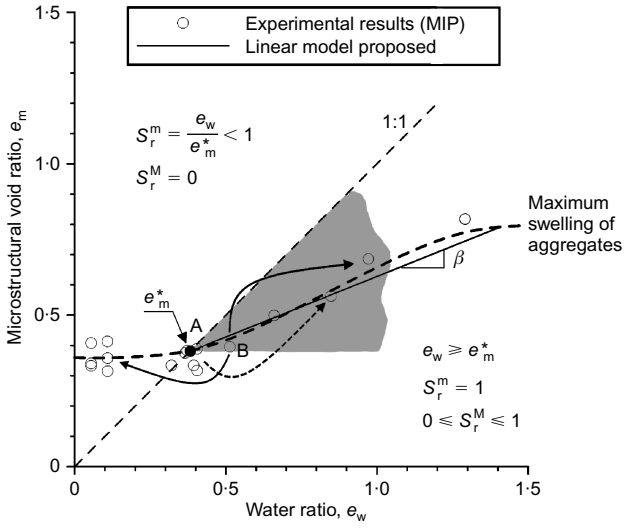

Fig. 9. Evolution of microstructural void ratio with water ratio from MIP tests on compacted Boom Clay: experimental data and conceptual interpretation

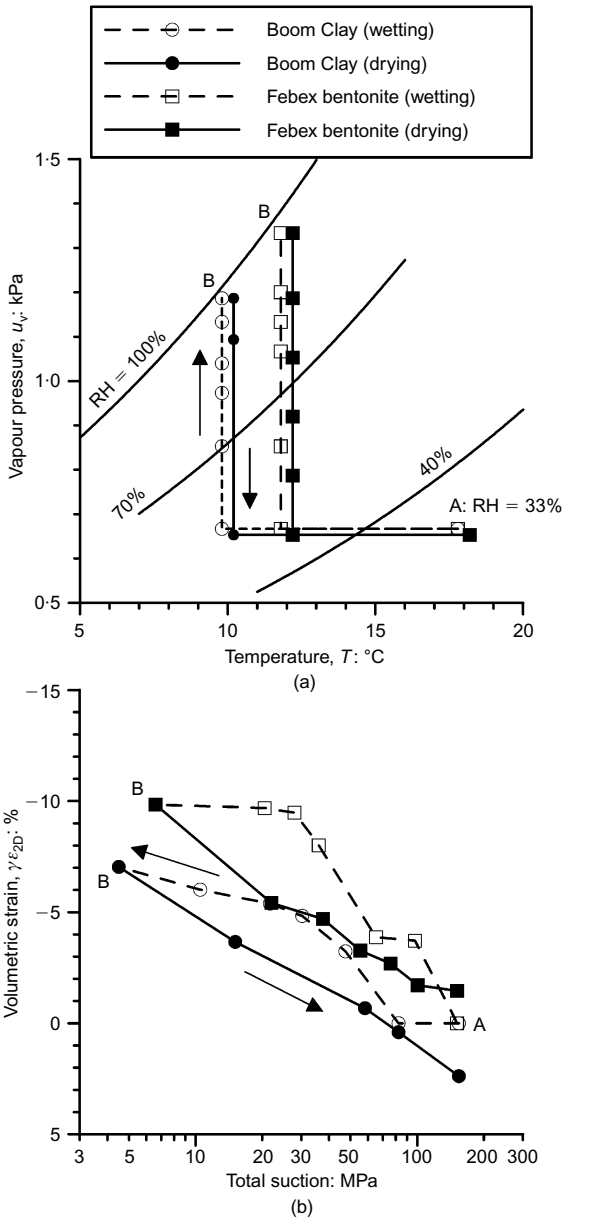

Fig. 10. Wetting–drying paths followed at microstructural scale: (a) paths performed under controlled relative humidity in ESEM; (b) evolution of volumetric strain along the different wetting–drying stages

of $\gamma = 1{\cdot}5$ was adopted to account for isotropic straining in the direction perpendicular to the image plane, in which ε_{2D} was determined.

The data obtained in the ESEM investigation on Boom Clay are superposed over the data obtained by MIP in Fig. 11, which provides an overall picture of the evolution of the microstructural void ratio for different water ratios. The ESEM data were plotted after converting suction into water ratio by means of the retention data presented in Fig. 2. The current void ratio was calculated, based on volumetric strain, assuming that void ratio for the lowest attainable value of suction after the wetting path AB matched the value detected by MIP (an initial/reference microstructural void ratio for Boom Clay of 0·31 was used). Taken all together, the data suggest a value of $e_m^* = 0{\cdot}38$, and an interpolating slope $\beta = 0{\cdot}40$ to track the evolution of the intra-aggregate pore volume at increasing water ratio for $e_w > e_m^*$.

An equivalent plot is depicted in Fig. 12 for compacted bentonites. Relevant properties of the different materials are summarised in Table 1. Different data sets are plotted, namely the ESEM data on Febex bentonite already presented (Fig. 10(b)), MIP data on Febex bentonite from Lloret *et al.* (2003) and Romero *et al.* (2005), and data on MX-80 bentonite from Delage *et al.* (2006). The separation between micro- and macroporosity for Febex bentonite was defined with the proposed criterion, applied to MIP results from wetting at constant volume presented in Romero *et al.* (2005). For MX-80 bentonite, the criterion illustrated in Fig. 8(a) was adopted, based on data of the water retention curve of MX-80 powder and of compacted samples wetted at constant volume presented by Delage *et al.* (2006). Few data were found in the literature to complement the microstructural void ratio information for high values of e_w. Data of saturated Na-bentonite and Ca-bentonite from Pusch & Karnland (1986; 1996), who gave the amount of microstructural void ratio at given total void ratios, are also presented. As a first approximation, the data suggest a value of $e_m^* = 0{\cdot}56$. A tentative average value of $\beta = 0{\cdot}43$ can be suggested for the compacted bentonites.

It is worth noting that, owing to the aggregate potential for swelling, the intra-aggregate void ratio becomes more and more relevant to the total porosity as the total void ratio decreases. The ratio between microstructural void ratio and total void ratio is plotted in Fig. 13 for saturated bentonite and saturated Boom Clay, as a function of void ratio. Microstructural void ratio, inferred from the previous values of e_m^* and β, is compared in the figure with previous literature data. For compacted Boom Clay the comparison is made with data from Romero *et al.* (1999), who reported the void volume fraction in which water shows low mobility (water permeability lower than 0·01 of the saturated one, as indicated in the figure). The saturated Na- and Ca-bentonite literature data provided by Pusch & Karnland (1986, 1996) were compared with the corresponding microstructural void ratios obtained with $e_m^* = 0{\cdot}56$ and $\beta = 0{\cdot}43$ and assuming full saturation, for given e. Consistent trends between reported data and results of the present study can be observed.

As already suggested by Romero & Vaunat (2000), e_m^* should depend on the plasticity of the clay. Good correlation between e_m^* and the total specific surface S_s (reported in Table 1) is shown in Fig. 14, based on the data presented in this paper and on further data on different soils. Data from

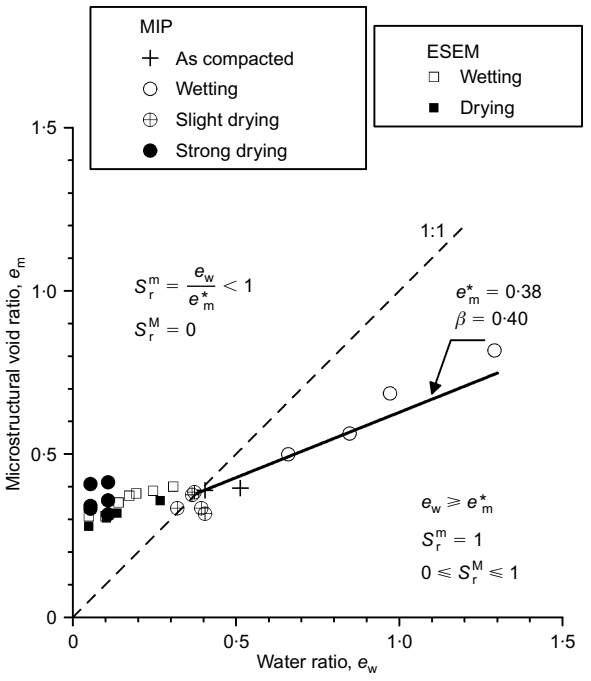

Fig. 11. Evolution of microstructural void ratio with water ratio from MIP and ESEM results on compacted Boom Clay

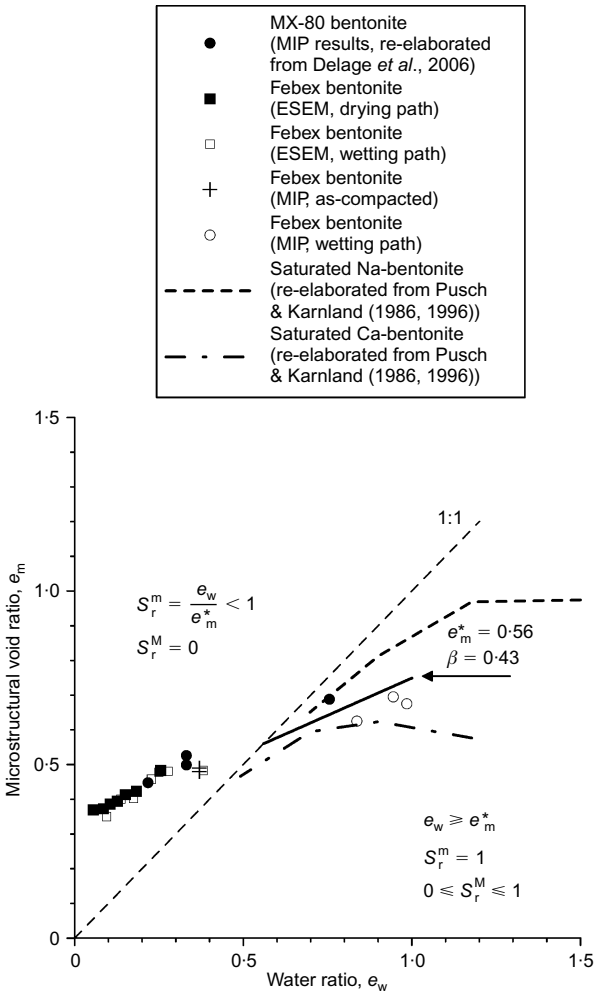

Fig. 12. Evolution of microstructural void ratio with water ratio from MIP and ESEM results on compacted bentonite (Febex and MX-80). Estimated evolution using Pusch & Karnland (1986, 1996) data. Average linear fit proposed for compacted bentonites

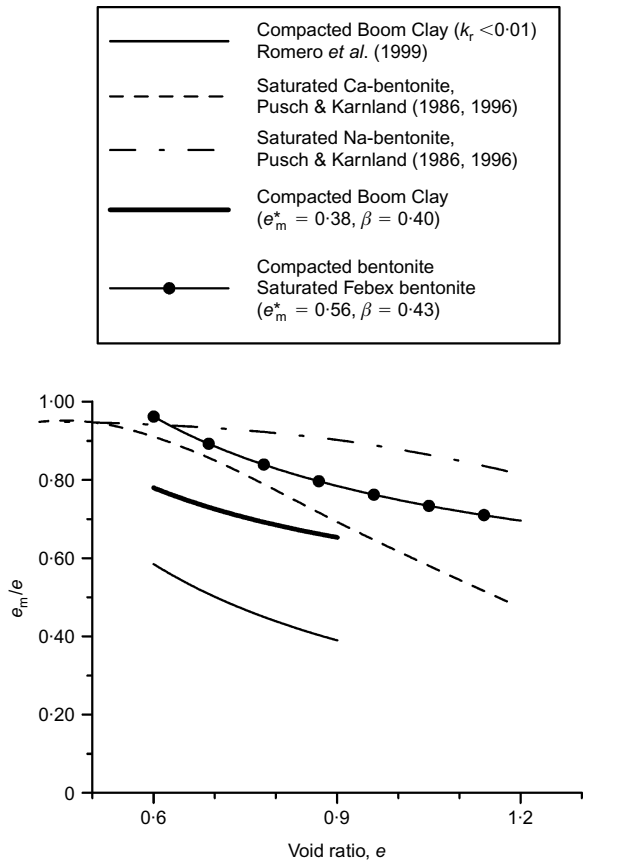

Fig. 13. Evolution of the ratio (e_m/e) with void ratio e for different clayey soils. Results reported in the literature and obtained in the present study

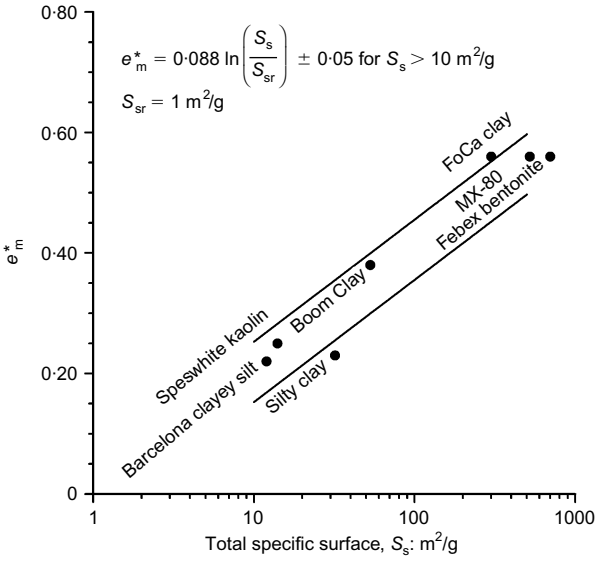

Fig. 14. Correlation between total specific surface and e_m^*

the literature were estimated from PSD and water retention data (see, for example, Tarantino (2009) for Speswhite kaolin with $S_s = 14$ m²/g, and Delage (2002) for FoCa7 clay with $S_s = 300$ m²/g). Also the slopes β in e_m: e_w, describing the tendency of the aggregates to swell, appear to be linked to the plasticity of the clayey soils (see Table 1 and Table 2), but further research is needed to propose reliable correlations of the two microstructural parameters with traditional geotechnical classification properties.

Table 2. Micro- and macrostructural parameters for the different soils used in the simulations shown in Figs 15, 16 and 22

Soil	e_m^*	β	Wetting		Drying		s_{max}: MPa	n
			s_m^*: MPa	b	s_m^*: MPa	b		
Barcelona clayey silt	0·22	0·22	2·0	7·0	—	—	1000†	3·50
Boom Clay	0·38	0·40	2·4	12	6·7	6·5	500	1·34
Bentonite Febex, MX-80	0·56	0·43	25*	12*	—	—	>1000*	1·50*
Bentonite-enriched sand	0·25	0·85	0·32	14	0·70	1·5	1000†	1·34

* Febex bentonite.
† Oven drying conditions (limited information in the high suction range).

A WATER RETENTION MODEL ACCOUNTING FOR FABRIC CHANGES

The hydraulic model: microstructural and macrostructural domains

Exploiting the previous experimental observations, a new water retention model is proposed for clays with intrinsic and permanent aggregated structure, accounting for swelling and shrinkage of the aggregates induced by total water content changes. To model the hydraulic behaviour, the amount of water adsorbed in the micropore volume is distinguished from that stored in the inter-aggregate void space. Micro- and macropore retention mechanisms may be described separately, yet ensuring continuity of the whole retention model and of its first derivatives, as suggested by Della Vecchia (2009). The choice for continuity comes from the observation of MIP data, showing PSD functions which are usually continuous with their first derivatives, and allows for taking into account the influence of swelling aggregates on water exchange mechanisms in a straightforward way. The model proposed to describe the water retention domain is written in terms of the work-conjugate variables water ratio, e_w, and suction, s (Houlsby, 1997).

For high suction values, water is adsorbed only in the micropores. A simple analytical expression for the main wetting and drying branches describing the water stored in the micropores, which does not depend on the void ratio e, may be assumed for e_w

$$e_w = \frac{b e_m^*}{\ln\left(s_{max}/s_m^*\right)}\left[\frac{b + \ln\left(s_{max}/s_m^*\right)}{b + \ln\left(s/s_m^*\right)} - 1\right] \tag{2}$$

where e_m^* is the water ratio corresponding to fully saturated micropores and empty macropores, s_m^* is the suction corresponding to e_m^*, s_{max} is the maximum suction attainable for $e_w = 0$ and b is a parameter describing the average slope of the curve for high values of suction. In the absence of specific data, a value of $s_{max} = 1$ GPa, corresponding to oven drying, may be assumed.

For $s < s_m^*$, corresponding to $e_w > e_m^*$, water ratio is the sum of the water stored inside the microstructural porosity and the water which partially fills the macropores. Micropores and macropores are assumed to be in local equilibrium, hence subjected to the same suction, s. The key issue in the formulation is that the microstructural water ratio is not constant for $e_w > e_m^*$, owing to continuous swelling and shrinkage of the aggregates at changing water content. Its evolution with water ratio is based on the conceptual framework presented previously. For the sake of simplicity, e_m can be described by a linear reversible envelope, as a function of the two independent parameters, e_m^* and β

$$e_m = e_m^* + \beta\left(e_w - e_m^*\right) \text{ for } e_w > e_m^*, \text{ with } 0 \leqslant \beta < 1 \tag{3}$$

where β quantifies the swelling tendency of the aggregates.

The dependence on e of the part of the curve which describes the predominant capillary mechanisms in the inter-aggregate pores may be achieved by adopting the linear scaling criterion proposed by Romero & Vaunat (2000). For e_w ranging between $e_m^* \leqslant e_w \leqslant e$, the water ratio reads

$$e_w = e_m + (e - e_m) \times \left\{1 - \frac{\ln\left[1 + (s/s_m)\right]}{\ln 2}\right\}\left(\frac{1}{1 + (\alpha s)^n}\right)^m \tag{4}$$

where m and n are independent parameters (van Genuchten, 1980), e and e_m are the current total and microstructural void ratios, respectively. The reference suction s_m is calculated, also for $e_w > e_m^*$, based on the microscopic branch of the water retention curve (equation (2))

$$s_m = s_m^* \exp\left\{\frac{b e_m^*[b + \ln\left(s_{max}/s_m^*\right)]}{b e_m^* + e_m \ln\left(s_{max}/s_m^*\right)} - b\right\} \tag{5}$$

The two parameters m and n are assumed not to depend on e as suggested by Romero & Vaunat (2000), Gallipoli *et al.* (2003) and Tarantino (2009). A suitable dependence of the air entry value on void ratio e is recovered by simply imposing the two analytical expressions (2) and (4) to be continuous, together with their first derivatives, at $s = s_m$. This choice links the value of α, which is inversely related to the air-entry or air-occlusion values respectively, to the set of independent parameters (m, n and microstructural parameters)

$$\alpha = \frac{\left(H^{-1/m} - 1\right)^{1/n}}{s_m} \tag{6a}$$

where

$$H = \frac{2(\ln 2)[b + \ln\left(s_{max}/s_m^*\right)]}{b + (e - e_m)\ln\left(s_{max}/s_m^*\right)} - b \tag{6b}$$

The choice to link the air-entry (or air-occlusion) value to both the parameters describing the microstructure and those describing the macrostructure is strongly justified by the observation that both a reduction in the total void ratio and an increase in the aggregate volume will reduce the mean dimension of macropores, and therefore they will correspondingly increase the air-entry (or air-occlusion) value.

The behaviour inside the current main retention domain, which is bounded by main wetting and main drying curves, is assumed to be described by a linear relationship linking the suction and the degree of saturation increments

$$\mathrm{d}S_r = -k_s \,\mathrm{d}s \tag{7a}$$

where k_s describes the slope of reversible hydraulic paths. The previous expression can be rewritten as

$$de_w = \frac{e_w}{e} de - e\, k_s\, ds \tag{7b}$$

which describes both reversible hydraulic and mechanical changes in water ratio in a suitable way.

Model capabilities

The capabilities of the proposed model are first illustrated with reference to the experimental data presented in Fig. 2 and Fig. 3. In the simulations, the values for the microstructural parameters e_m^* and β were taken from the available MIP and ESEM studies (Fig. 11 and Fig. 12). In the case of Barcelona clayey silt, water retention data were used to assign the value of e_m^*, following the criterion described in Fig. 8(a), while β was considered part of the model calibration. The suctions $s_{m\,D,W}^*$ (D for drying, W for wetting) were assigned based on the available retention data in all cases. The remaining parameters, $b_{D,W}$ and n were calibrated by best fit with experimental data. It is worth noting that, in all cases, the same value of n was adopted for the drying and the wetting branches. In addition, although the choice would not be necessary, the relationship between the two parameters n and m

$$m = 1 - \frac{1}{n} \tag{8}$$

was exploited, to reduce the number of the independent parameters of the macroscopic part of the model to just one. The whole set of parameters adopted in the simulations is summarised in Table 2.

Experimental data for Boom Clay at constant void ratio along main drying and wetting paths are compared to model simulations in Fig. 15. The macrostructural parameter, $n = 1{\cdot}34$, was calibrated on the drying branch corresponding to $e = 0{\cdot}92$, in Fig. 3. The remaining branches of the water retention domain were blind predicted. The four branches are remarkably well caught, in spite of the adoption of a single independent macroscopic parameter.

The comparison between experimental data and numerical simulations of main wetting curves of compacted Febex bentonite ($n = 1{\cdot}5$) and Barcelona clayey silt ($n = 3{\cdot}50$) at different constant void ratios are shown in Fig. 16. Again, the simulations performed after calibration of a single macroscopic parameter allow for tracking correctly the dependency of the retention domain on void ratio.

Microstructural effects on air-entry value

To appreciate the influence of active swelling/shrinking aggregates on the macroscopic branches of the water retention domain, experimental data from a previous work by Romero *et al.* (2002, 2003) are analysed.

Mixtures of bentonite-enriched sand, S/B 80/20 (sand/bentonite with 20% bentonite on dry mass basis), were prepared from Kunigel V1 sodium bentonite, which acts as filling material, and uniform silica sand (with dominant particle size around 1 mm), which forms the shielding skeleton. Two different mixtures were prepared on the dry side of optimum at $e_w = 0{\cdot}29$ and $e = 0{\cdot}42$ ($S_r = 0{\cdot}69$). The first mixture was prepared with distilled water, preserving the swelling characteristics of bentonite. Lead nitrate powder in a concentration of 1% of dry sand/bentonite mass was added to the mixing water in the second mixture. The nitrate ions can precipitate and cement the stacks of smectite, acting as inhibitor of the swelling potential of the natural bentonite (Auboiroux *et al.*, 1996; Alawaji, 1999; Romero *et al.*, 2003). The comparison between the behaviour of the two compacted materials allows the study of the structural

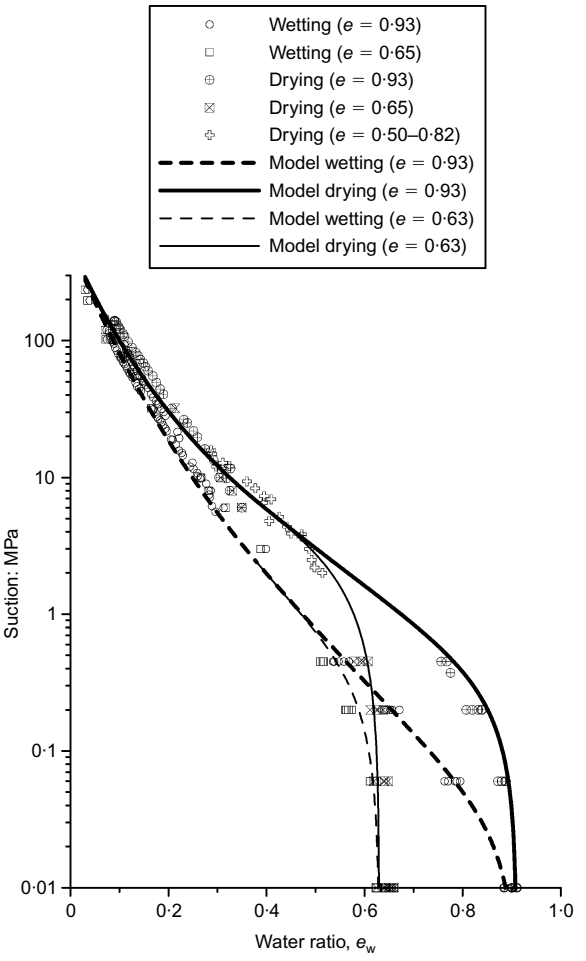

Fig. 15. Comparison between water retention experimental data and model predictions at different void ratios for dry-side compacted Boom Clay (wetting and drying paths)

changes induced by an active microstructure compared to an inhibited, or inert, one.

The PSD functions of the as-compacted samples, and those of the two mixtures after saturation, are compared in Fig. 17 (all the samples were freeze-dried before mercury intrusion). The as-compacted mixture displays multi-modal porosity, characterised by one pore mode at inter-grain scale (macroporosity, with pore sizes between sand grains around 150–250 μm, corresponding to around 20% of the dominant particle size) and two pore modes at the clay-aggregation scale (microporosity, with pore sizes smaller than 30 μm). The criterion illustrated in Fig. 8(b) was adopted in this case, owing to the presence of the shielding sand skeleton, which constrains the macropore dimensions to a minimum value of 30 μm (Romero *et al.*, 2003).

On wetting, the saturated mixture with inert bentonite approximately preserved the PSD function of the as-compacted state. On the contrary, the mixture with active bentonite preserved the two modes of the microporosity, which were shifted towards larger pore sizes as a consequence of microstructure swelling. The inter-grain pore mode was lost owing to the expansion of bentonite, which completely invaded the macroporosity of the shielding skeleton.

The observation is qualitatively confirmed by the ESEM images collected in Fig. 18. The photomicrograph of the as-compacted state, which is displayed in Fig. 18(a), shows clearly detectable sand grains, nearly covered by clay aggregations. Interconnecting clay bridges, crossing and hindering inter-grain pores, can also be distinguished. An average

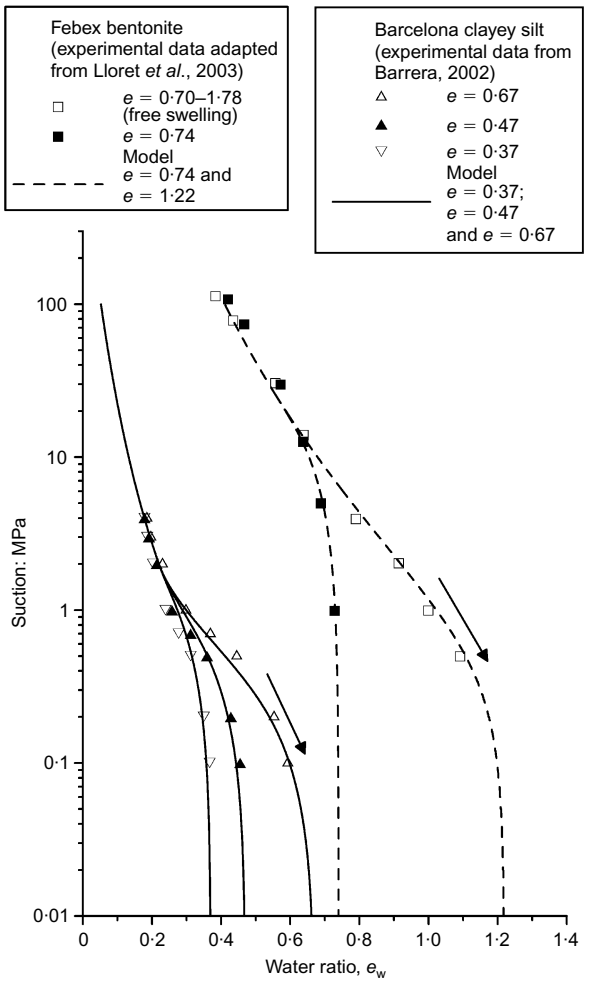

Fig. 16. Comparison between water retention experimental data and model predictions at different void ratios for compacted Febex bentonite and Barcelona clayey silt (wetting paths)

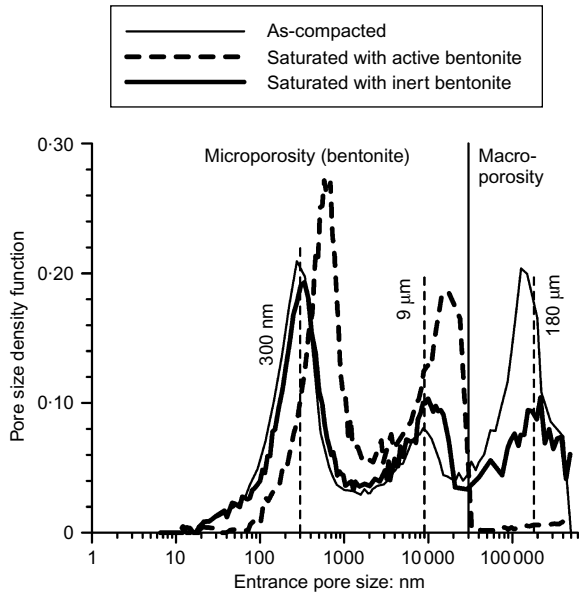

Fig. 17. PSD function of the as-compacted and saturated states for two different bentonite-enriched sand mixtures, with active and inert bentonite

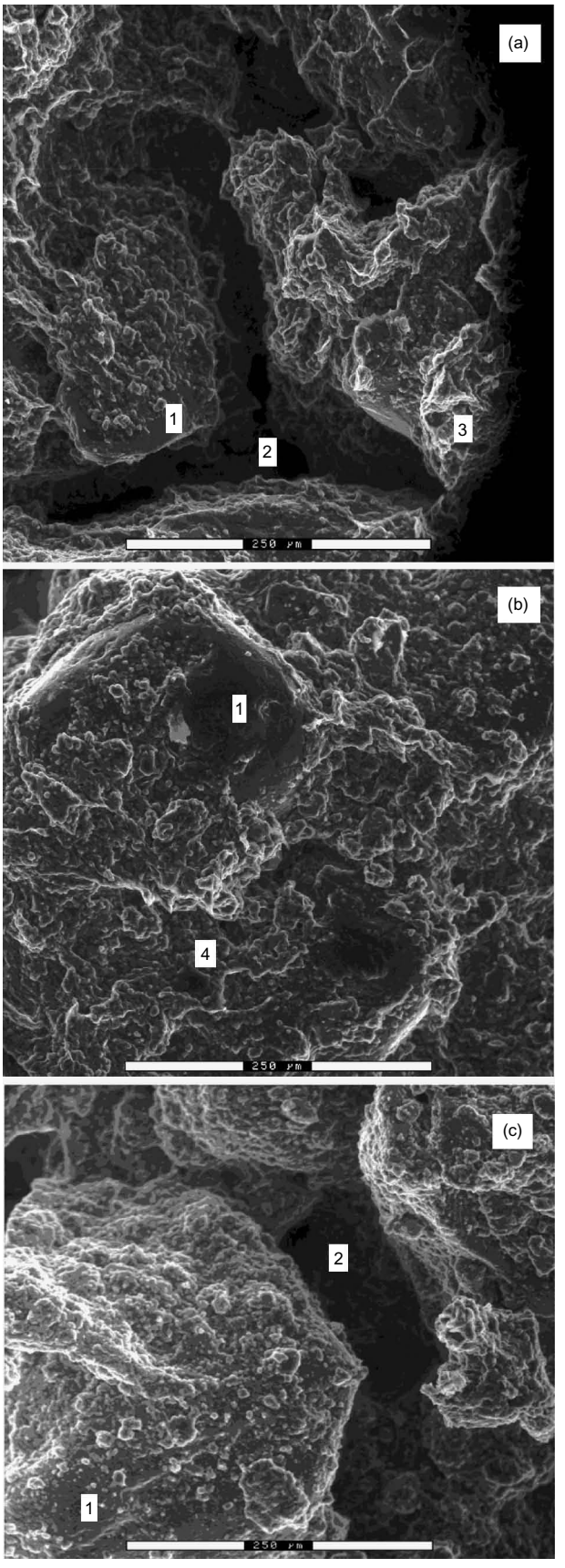

Fig. 18. ESEM photomicrographs of bentonite-enriched sand mixtures: (a) as-compacted mixture; (b) saturated mixture with active bentonite; (c) saturated mixture with inert bentonite. (1: sand grain; 2: inter-grain macroporosity (100–200 µm); 3: clay aggregations; 4: occluded macroporosity)

inter-grain pore size between 100 and 200 μm is detected, which is in agreement with PSD measurements (Fig. 17). On wetting, invasion of the inter-grain macroporosity by active bentonite is clearly observed in Fig. 18(b), whereas in the mixture with inert bentonite the macroporosity is preserved (Fig. 18(c)). Microstructural void ratio e_m, associated with pore sizes lower than 30 μm, and degree of bentonite filling F, which is the volume of bentonite divided by total pore volume, of the different mixtures at different states are reported in Table 3. The latter was calculated with the expression reported in the table and quantifies the inter-grain porosity occlusion undergone on active bentonite swelling. The different e_m values at known water ratios were used to estimate the microstructural water retention parameters (e_m^* and β), which are plotted in Fig. 19. Owing to the low constraint imposed by the macroporosity, bentonite is almost completely free to develop its swelling potential and fill the inter-grain porosity, which is reflected in a high value of parameter β.

As a consequence of the microstructural changes undergone on wetting, the mixtures will display different water retention properties. Assimilating mercury injection to air intrusion during a desorption path at constant porosity (Romero & Simms, 2008), PSD data were exploited to estimate the branches of the water retention curves that the two samples would follow upon drying, if their microstructure were *frozen* at the end of the first wetting path. Results for the mixtures with active and inert bentonite after undergoing saturation are compared to those for the as-compacted material in Fig. 20. The comparison clearly shows that the estimated drying branch of the water retention curve of the mixture with inert bentonite previously saturated does not differ substantially from the drying branch of the as-compacted mixture that did not undergo a saturation path. On the contrary, the estimated drying branch of the mixture with active bentonite, which had previously undergone saturation, displays a higher water retention capacity with a much higher air-entry value, due to disappearance of macropores. It is worth noting that the curve drawn for active bentonite is an upper bound for the actual drying branch of the water retention domain, which in the latter case is affected by the progressive shrinkage of the aggregates upon suction increase.

To highlight the capabilities of the proposed model to follow the evolution of the water retention properties when they are affected by microstructure activity, data from compacted bentonite-enriched sand with active bentonite are compared to numerical simulations along a relevant part of the stress path already presented in Fig. 1 (ABCDE in Fig. 1(a)), describing a path comprising wetting at constant volume, unloading, drying at constant net stress, and loading.

The path was simulated assuming active bentonite, with $\beta = 0{\cdot}85$, and the simulations were compared to the results of numerical simulations in which the swelling potential of the bentonite was reduced, by assuming $\beta = 0{\cdot}11$, based on

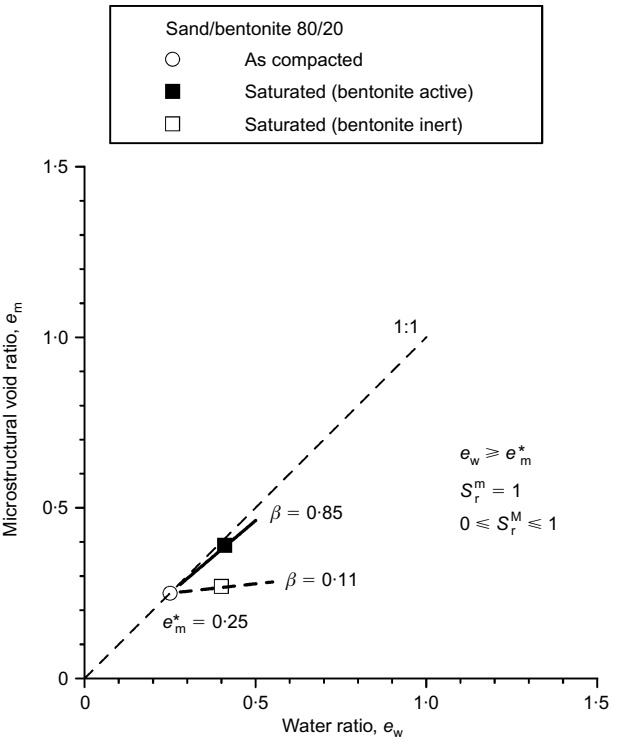

Fig. 19. Evolution of microstructural void ratio with water ratio for compacted bentonite-enriched sand with active bentonite ($\beta = 0{\cdot}85$) and inert bentonite ($\beta = 0{\cdot}11$)

the previous experimental data in Fig. 19. All the other model parameters were kept equal in the two simulations (see Table 2). Again a single macroscopic parameter, $n = 1{\cdot}34$, was adopted for the macroscopic part of the retention domain.

Fairly good agreement can be observed between the results of the simulation with active bentonite and the experimental data in Fig. 21. The wetting path AB induces swelling of the aggregates, increasing the air-occlusion value progressively as the total water ratio increases. On the contrary, the curve predicted for inert bentonite describes a much lower water retention capacity along the first wetting path A′B′, as expected for a less active mixture, in which the sand fraction dominates the retention properties at low values of suction. When drying starts, along path C′D′, an air-entry value lower than the experimental one for active bentonite is predicted, owing to the still available macroporosity, which was not occluded on first wetting.

The previous simulations are exploited to provide a picture of the capability of the model to describe the dependence of the air-entry value on the void ratio and on the swelling potential of the aggregates. The values of suction corresponding to two degrees of saturation, $S_r = 0{\cdot}90$ and $S_r = 0{\cdot}95$, which may reasonably correspond to the onset of

Table 3. Microstructural characterisation of bentonite-enriched sand at different states

State and mixture	e_m	$e_M = e - e_m$	F: %
As-compacted, sand–bentonite mixture $e = 0{\cdot}42$	0·28	0·14	77
Saturated, active bentonite $e = 0{\cdot}41$	0·39	0·02	97
Saturated, inert bentonite $e = 0{\cdot}40$	0·29	0·11	81

Note: $F = [e_m + (f\rho_s/\rho_{sB})]/[e + (f\rho_s/\rho_{sB})]$, where ρ_s is average density of solid particles, ρ_{sB} is particle density of bentonite (a constant value was assumed $\rho_{sB} = \rho_s$) and f is the mass fraction of bentonite in the mixture.

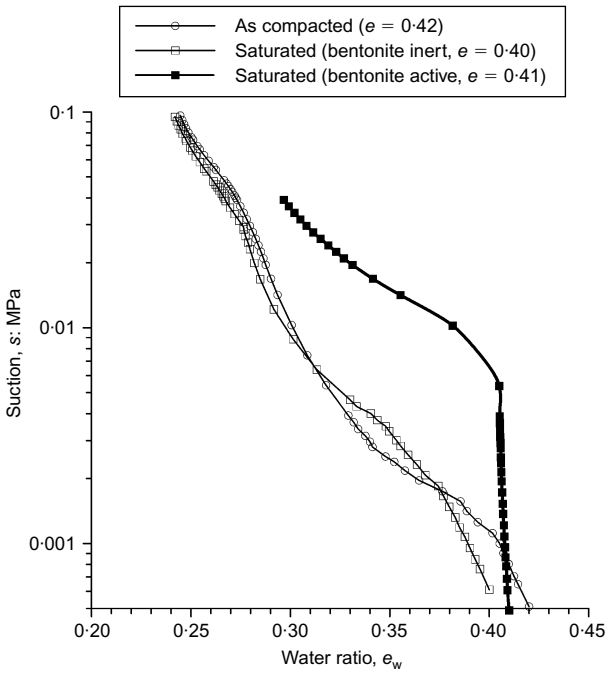

Fig. 20. Drying branches of water retention curves derived from MIP data for saturated bentonite-enriched sand mixtures, with active and inert bentonite, compared to the as-compacted state

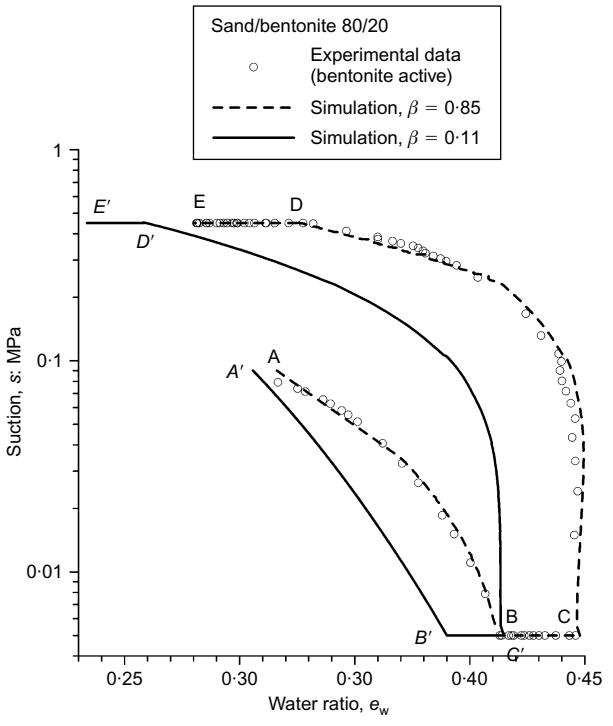

Fig. 21. Water retention data for compacted bentonite-enriched sand with active bentonite compared to numerical simulations along the stress path ABCDE in Figs 1(a) and 1(b), and expected water retention features for the same mixture with inert bentonite

air entry, are depicted in Fig. 22, as a function of void ratio. Two sets of curves are plotted for the two values $\beta = 0{\cdot}11$ and $\beta = 0{\cdot}85$, corresponding to low and high activity, respectively. The figure demonstrates how the model is able to predict an increase in the air-entry value at decreasing e. Increasing β shifts the curves towards higher values of suction, and models correctly the contribution of the swelling potential of the clay aggregates.

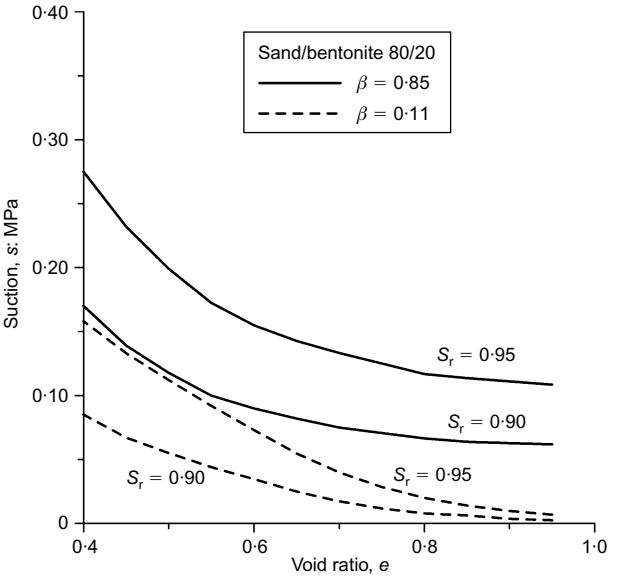

Fig. 22. Evolution with e and β of the air-entry suction zone ($S_r = 0{\cdot}90$ and 0·95) along drying branches (parameters from sand–bentonite mixtures)

SUMMARY AND CONCLUSIONS

Experimental data from different testing methodologies on different compacted clayey soils, characterised by an aggregated bimodal pore size distribution, allowed the analysis of the effects of coupled hydromechanical paths on fabric evolution and on water retention properties. Fabric evolution was tracked from both the porous network and the soil skeleton viewpoint by means of a combined MIP and ESEM experimental programme.

The main outcomes of the study may be summarised as follows. Compaction on the dry side of optimum gives the soil an aggregated fabric, characterised by bimodal pore size distribution. Starting from the as-compacted state, any saturation path leads to a fabric dominated by a single pore mode. Nonetheless, in a new drying path compacted soils tend to recover a double porosity network. Similarity of the PDSs at intra-aggregate entrance pore size of the dried sample and the as-compacted state suggests that the aggregations created by compaction on the dry side of optimum are a permanent feature of the compacted soil fabric.

The fabric of the soil continuously evolves as the void ratio and the water content change. To track this evolution, the inter-aggregate pore volume, e_M, was distinguished from the intra-aggregate one, e_m. The physical interpretation of the collected data is based on the assumption that a reference intra-aggregate pore volume e_m^*, corresponding to saturated micropores and completely empty macropores, can be defined. For $e_w > e_m^*$, increasing water content is partitioned between the swelling aggregates, which remain saturated, and macropores, in which the degree of saturation increases. As a first approximation, the amount of swelling of the aggregates for $e_w > e_m^*$ can be described by a reversible linear interpolation with slope β. Collected data on different clayey soils show consistent trends and validate the proposed approach.

Similarly to the intra-aggregate pore volume, the instantaneous retention capacity of compacted soils evolves continuously with water content. A description of the evolution of the intra-aggregate water ratio and of the corresponding suction is introduced in the model previously proposed by Romero & Vaunat (2000), enhancing the capability of describing the evolving water retention domain. A relatively simple model for soil retention behaviour is proposed, able

to account for the dependence of the air-entry value on both the current void ratio and the intra-aggregate pore space. Remarkably, the microstructural parameters introduced in the model, e_m^* describing intra-aggregate pore space, and β, which takes into account the swelling tendency of the aggregates, have a clear physical meaning. A dependence of these two parameters on common soil properties, like specific surface and consistency limits, is expected.

Experimental data of main drying and main wetting branches of compacted Boom Clay and other clayey soils are compared to model simulations. The model seems to capture the main features of wetting and drying branches for different water contents, not only in terms of water storage capacity but also in terms of evolution of air-entry or air-occlusion values. The model capabilities are illustrated by comparison between numerical simulations and experimental data on two compacted bentonite-enriched sand mixtures, prepared with active or inert bentonite. The effects of microstructural changes on retention properties, especially those linked to air-entry value changes detected by experimental data, are well tracked.

The collected experimental data and their consistent interpretation highlight that the storage capacity of soil is not at all a *characteristic* of the soil itself. In fact, it is the result of the continuous evolution of both void ratio and the pore size distribution, which is affected by both hydraulic and mechanical loading history. The interaction between the solid and the liquid phases, resulting in swelling and shrinking of the aggregates, plays a definite role in this evolution.

ACKNOWLEDGEMENT

The experimental work related to the characterisation of the sand/bentonite was supported by NAGRA (Nationale Genossenschaft für die Lagerung radioaktiver Abfälle) through GMT Emplacement Project.

REFERENCES

Airò Farulla, C., Ferrari, A. & Romero, E. (2010). Volume change behaviour of a compacted scaly clay during cyclic suction changes. *Can. Geotech. J.* **47**, No. 6, 688–703, **doi:** 10.1139/T09-138.

Alawaji, H. (1999). Swell and compressibility characteristics of sand–bentonite mixtures inundated with liquids. *Appl. Clay Sci.* **15**, No. 3–4, 411–430.

Aubertin, M., Mbonimpa, M., Bussière, B. & Chapuis, R. P. (2003). A model to predict the water retention curve from basic geotechnical properties. *Can. Geotech. J.* **40**, No. 6, 1104–1122.

Auboiroux, M., Baillif, P., Touray, J. C. & Bergaya, F. (1996). Fixation of Zn^{+2} and Pb^{+2} by a Ca-montmorillonite in brines and dilute solutions: Preliminary results. *Appl. Clay Sci*. **11**, No. 2–4, 117–126.

Baldi, G., Hueckel, T. & Pellegrini, R. (1991). *Developments in modelling of thermo-hydro-geomechanical behaviour of Boom clay and clay based buffer materials*, Report EUR 13365. Brussels: Nuclear Science and Technology, Commission of European Communities.

Barrera, M. (2002). *Estudio experimental del comportamiento hidro-mecánico de suelos colapsables*. PhD thesis, Universitat Politècnica de Catlunya, Barcelona, Spain. See http://www.tdx.cat/TDX-0604102-095524 for further details.

Black, W. P. M. (1962). A method of estimating the California bearing ratio of cohesive soils from plasticity data. *Géotechnique* **12**, No. 4, 271–282, **doi**: 10.1680/geot.1962.12.4.271.

Cui, Y. J., Loiseau, C. & Delage, P. (2002). Microstructure changes of a confined swelling soil due to suction controlled hydration. In *Unsaturated Soils* (eds J. F. T. Jucá , T. M. P. de Campos and F. A. M. Marinho), *Proc. 3rd Int. Conf. on Unsaturated Soils, Recife, Brazil* **2**, 593–598. Lisse: AA Balkema.

De Bruyn, C. M. A., Collins, L. E. & Williams, A. A. B. (1957). The specific surface, water affinity, and potential expansiveness of clays. *Clay Mineralogy Bull*. **3**, 120–128.

Delage, P. (2002). On the behaviour of engineered clay barriers for nuclear waste disposal. In *Environmental geomechanics* (eds L. Vulliet, L. Laloui and B. A. Schrefler), *Proceedings of the international workshop on environmental geomechanics*, Monte Verita, Ascona, Switzerland, pp. 161–172. Lausanne: EPFL Press.

Delage, P. & Lefebvre, G. (1984). Study of the structure of a sensitive Champlain clay and its evolution during consolidation. *Can. Geotech. J.* **21**, No. 1, 21–35.

Delage, P., Audiguier, M., Cui, Y. & Howat, M. (1996). Microstructure of a compacted silt. *Can. Geotech. J.* **33**, No. 1, 150–158.

Delage, P., Marcial, D., Cui, Y. J. & Ruiz, X. (2006). Ageing effects in a compacted bentonite: a microstructure approach. *Géotechnique* **56**, No. 5, 291–304, **doi**: 10.1680/geot.2006.56.5.291.

Della Vecchia, G. (2009). *Coupled hydro-mechanical behaviour of compacted clayey soils*. PhD thesis, Politecnico di Milano, Milan, Italy.

Frydman, S. & Baker, R. (2009). Theoretical soil-water characteristic curves based on adsorption, cavitation, and a double porosity model. *Int. J. Geomech*. **9**, No. 6, 250–257.

Gallipoli, D., Wheeler, S. J. & Karstunen, M. (2003). Modelling the variation of degree of saturation in a deformable unsaturated soil. *Géotechnique* **53**, No. 1, 105–112, **doi**: 10.1680/geot.2003.53.1.105.

Gens, A., Sanchez, M. & Sheng, D. (2006). On constitutive modelling of unsaturated soils. *Acta Geotechnica* **1**, No. 3, 31–147.

Houlsby, G. T. (1997). The work input to an unsaturated granular material. *Géotechnique* **47**, No. 1, 193–196, **doi**: 10.1680/geot.1997.47.1.193.

Huang, S., Barbour, S. L. & Fredlund, D. G. (1998). Development and verification of a coefficient of permeability function for a deformable unsaturated soil. *Can. Geotech. J.* **35**, No. 3, 411–424.

Jommi, C. (2000). Remarks on the constitutive modelling of unsaturated soils. In *Experimental evidence and theoretical approaches in unsaturated soils* (eds A. Tarantino and C. Mancuso), *Proceedings of an international workshop on unsaturated soils*, Trento, Italy, pp. 139–153. Rotterdam: AA Balkema.

Kawai, K., Kato, S. & Karube, D. (2000). The model of water retention curve considering effects of void ratio. In *Unsaturated soils for Asia* (eds H. Rahardjo, D. G. Toll and E. G. Leong), *Proceedings of the Asian conference on unsaturated soils, UNSAT-ASIA 2000*, Singapore, pp. 329–334. Rotterdam: AA Balkema.

Kohgo, Y. (2008). A hysteresis model of soil water retention curves based on bounding surface concept. *Soils Found*. **48**, No. 5, 633–640.

Koliji, A., Laloui, L., Cuisinier, O. & Vulliet, L. (2006). Suction induced effects on the fabric of a structured soil. *Transp. in Porous Media* **64**, No. 2, 261–278.

Laloui, L. & Nuth, M. (2009). On the use of the generalised effective stress in the constitutive modelling of unsaturated soils. *Comput. Geotechnics* **36**, No. 1–2, 20–23.

Lloret, A., Villar, M.V., Sánchez, M., Gens, A., Pintado, X. & Alonso, E. E. (2003). Mechanical behaviour of heavily compacted bentonite under high suction changes. *Géotechnique* **53**, No. 1, 27–40, **doi**: 10.1680/geot.2003.53.1.27.

Maŝín, D. (2009). Predicting the dependency of a degree of saturation on void ratio and suction using effective stress principle for unsaturated soils. *Int. J. Numer. Analyt. Methods Geomech*. **34**, No. 1, 73–90, **doi**: 10.1002/nag.808.

Miller, G. A., Khoury, C. N., Muraleetharan, K. K., Liu, C. & Kibbey, T. C. G. (2008). Effects of soil skeleton deformations on hysteretic soil water characteristic curves: Experiments and simulations. *Water Resources Res*. **44**, No. W00C06, 1–10, **doi**: 10.1029/2007WR006492.

Monroy, R., Zdravkovic, L. & Ridley, A. (2010). Evolution of microstructure in compacted London Clay during wetting and loading. *Géotechnique* **60**, No. 2, 105–119, **doi**: 10.1680/geot.8.P.125.

Montes-H, G., Duplay, J., Martinez, L. & Mendoza, C. (2003a). Swelling–shrinkage kinetics of MX80 bentonite. *Appl. Clay Sci*. **22**, No. 6, 279–293.

Montes-H, G., Duplay, J., Martinez, L., Geraud, Y. & Rousset-

Tournier, B. (2003b). Influence of interlayer cations on the water sorption and swelling–shrinkage of MX80 bentonite. *Appl. Clay Sci*. **23**, No. 5–6, 309–321.

Muraleetharan, K. K., Liu, C., Wei, C., Kibbey, T. C. G. & Chen, L. (2009). An elastoplatic framework for coupling hydraulic and mechanical behavior of unsaturated soils. *Int. J. Plasticity* **25**, No. 3, 473–490, **doi**: 10.1016/j.ijplas.2008.04.001.

Nuth, M. & Laloui, L. (2008). Advances in modelling hysteretic water retention curve in deformable soils. *Comput. Geotechnics* **35**, No. 6, 835–844.

Olivella, S. & Alonso, E. E. (2008). Gas flow through clay barriers. *Géotechnique* **58**, No. 3, 157–176, **doi**: 10.1680/geot.2008.58.3.157.

Or, D. & Tuller, M. (1999). Liquid retention and interfacial area in variably saturated porous media: upscaling from single pore to sample scale model. *Water Resources Res*. **35**, No. 12, 3591–3606.

Pereira, J.-M.., Wong, H., Dubujet, P. & Dangla, P. (2005). Adaptation of existing behaviour models to unsaturated states: Application to CJS model. *Int. J. Numer. Analyt. Methods Geomech*. **29**, No. 11, 1127–1155.

Pusch, R. & Karnland, O. (1986). *Aspects of the physical state of smectite-adsorbed water*. Stockholm, Sweden: SKB Swedish Nuclear Fuel and Waste Management Co., Technical Report TR 86-25.

Pusch, R. & Karnland, O. (1996). Physico/chemical stability of smectite clays. *Engng Geol*. **41**, No. 1–4, 73–85.

Romero, E. & Jommi, C. (2008). An insight into the role of hydraulic history on the volume changes of anisotropic clayey soils. *Water Resources Res*. **44**, No. W00C06, 1–16. **doi**: 10.1029/2007WR006558.

Romero, E. & Simms, P. (2008). Microstructure investigation in unsaturated soils: A review with special attention to contribution of mercury intrusion porosimetry and environmental scanning electron microscopy. *Geotech. Geol. Engng* **26**, No. 6, 705–722.

Romero, E. & Vaunat, J. (2000). Retention curves of deformable clays. In *Experimental evidence and theoretical approaches in unsaturated soils* (eds A. Tarantino A. and C. Mancuso), *Proceedings of an international workshop on unsaturated soils*, Trento, Italy, pp. 91–106. Rotterdam: AA Balkema.

Romero, E., Gens, A. & Lloret, A. (1999). Water permeability, water retention and microstructure of unsaturated Boom clay. *Engng Geol*. **54**, No. 1–2, 117–127.

Romero, E., Knobelsdorf, J., Alonso, E. E. & Vaunat, J. (2002). Hydro-mechanical behaviour of 80/20 sand–bentonite mixture. In *Environmental geomechanics* (eds L. Vulliet, L. Laloui and B. A. Schrefler), *Proceedings of an international workshop on environmental geomechanics*, Monte Verita, Ascona, Switzerland, pp. 347–352. Lausanne: EPFL Press.

Romero, E., Castellanos, E. & Alonso, E. E. (2003). *Laboratory tests on compacted sand/bentonite/lead nitrate buffer material for the GMT emplacement project*, Project Report GMT/IR 02–01. Switzerland: NAGRA.

Romero, E., Hoffmann, C., Castellanos, E., Suriol, J. & Lloret, A. (2005). Microstructural changes of compacted bentonite induced by hydro-mechanical actions. In *Advances in understanding engineered clay barriers* (eds E. E. Alonso and A. Ledesma), *Proceedings of an international symposium on large scale field tests in granite*, Sitges, Spain, pp. 193–202. Leiden: AA Balkema.

Sheng, D., Sloan, S. W. & Gens, A. (2004). A constitutive model for unsaturated soils: thermomechanical and computational aspects. *Comput. Mech*. **33**, No. 6, 453–465, **doi**: 10.1007/s00466-003-0545-x.

Simms, P. H. & Yanful, E. K. (2001). Measurement and estimation of pore shrinkage and pore distribution in a clayey till during soil-water characteristic curve tests. *Can. Geotech. J.* **38**, No. 4, 741–754.

Simms, P. H. & Yanful, E. K. (2002). Predicting soil-water characteristic curves of compacted plastic soils from measured pore-size distributions. *Géotechnique* **52**, No. 4, 269–278, **doi**: 10.1680/geot.2002.52.4.269.

Simms, P. H. & Yanful, E. K. (2004). Estimation of soil-water characteristic curve of clayey till using measured pore-size distribution. *J. Environ. Engng* **130**, No. 8, 847–854.

Simms, P. H. & Yanful, E. K. (2005). A pore-network model for hydromechanical coupling in unsaturated compacted clayey soils. *Can. Geotech. J.* **42**, No. 2, 499–514.

Sun, D. A., Sheng, D. & Sloan, S. W. (2007). Elastoplastic modelling of hydraulic and stress–strain behaviour of unsaturated soils. *Mech. Mater.* **39**, No. 3, 212–221.

Tarantino, A. (2009). A water retention model for deformable soils. *Géotechnique* **59**, No. 9, 751–762, **doi**: 10.1680/geot.7.00118.

Toll, D. G. (1995). A conceptual model for the drying and wetting of soil. *Proc. 1st Int. Conf. Unsaturated Soils* (eds E. E. Alonso and P. Delage), *Paris, France* **2**, 805–810. Rotterdam: AA Balkema.

Tuller, M. & Or, D. (2005). Water films and scaling of soil characteristic curves at low water contents. *Water Resources Res*. **41**, No. W09403, 1–6, **doi**: 10.1029/2005WR004142.

Vanapalli, S. K., Fredlund, D. G. & Pufahl, D. E. (1999). The influence of soil structure and stress history on the soil-water characteristics of a compacted till. *Géotechnique* **49**, No. 2, 143–159, **doi:** 10.1680/geot.1999.49.2.143.

van Genuchten, M. T. (1980). A closed-form equation for predicting the hydraulic conductivity of unsaturated soils. *Soil Sci. Soc. Am. J.* **44**, 892–898.

Vaunat, J., Romero, E. & Jommi, C. (2000). An elastoplastic hydromechanical model for unsaturated soils. In *Experimental evidence and theoretical approaches in unsaturated soils* (eds A. Tarantino and C. Mancuso), *Proceedings of an international workshop on unsaturated soils*, Trento, Italy, pp. 121–138. Rotterdam: AA Balkema.

Villar, M. V., Romero, E. & Lloret, A. (2005). Thermo-mechanical and geochemical effects on the permeability of high-density clays. In *Advances in understanding engineered clay barriers* (eds E. E. Alonso and A. Ledesma), *Proceedings of an international symposium on large scale field tests in granite*, Sitges, Spain, pp. 177–191. Leiden: AA Balkema.

Wheeler, S. J. (1996). Inclusion of specific water volume within an elasto-plastic model for unsaturated soil. *Can. Geotech. J.* **33**, No. 1, 42–57.

Alonso, E. E. *et al.* (2011). *Géotechnique* **61**, No. 4, 329–344 [**doi:** 10.1680/geot.2011.61.4.329]

Hydromechanical behaviour of compacted granular expansive mixtures: experimental and constitutive study

E. E. ALONSO*, E. ROMERO* and C. HOFFMANN*

Compacted granular mixtures of high-density bentonite pellets have been evaluated as an alternative buffer material to fill the empty space around nuclear waste disposal canisters in horizontal drifts. Despite the obvious benefits of these compacted mixtures (the backfilling operation becomes easier and the gaps between the host rock and the buffer are minimised), there are several aspects of concern such as the effective blockage of the large inter-pellet pores due to granule swelling – this blockage improves the water permeability properties – and the tendency to develop initial collapses before reaching an adequate swelling pressure. Selected test results of a comprehensive laboratory experimental programme are presented to gain insight into the hydromechanical response of this multi-porosity compacted material. To improve the information on local transient behaviour, simulation-assisted techniques using a double-structure constitutive model are used. The paper presents a physically based one-dimensional model to simulate experimental results of different transient processes, such as the progressive loss of permeability during wetting and the occurrence of concurrent phenomena during fast flooding at constant stress (initial collapse of the granular arrangement and parallel expansion of granules).

KEYWORDS: compaction; clays; fabric/structure of soils; laboratory tests; partial saturation; suction

On a évalué des mélanges granulaires compactés de pastilles de bentonite à densité élevée, en alternative à la matière tampon, pour le remplissage d'un espace vide autour de récipients d'élimination de déchets nucléaires, dans des galeries horizontales. En dépit des avantages évidentes de ces mélanges compactés (simplification de l'opération de remblayage, et minimisation des écarts entre la roche hôte et le rampon), plusieurs aspects suscitent une certaine inquiétude, notamment l'obturation effective de pores inter pastilles de grande taille sous l'effet du gonflement des pastilles – cette obturation renforçant les propriétés de perméabilité de l'eau – et la tendance à la production d'effondrements initiaux avant la réalisation d'une pression de gonflement adéquate. Des résultats d'essai sélectionnés d'un programme expérimental intégral en laboratoire sont présentés, afin de mieux comprendre la réaction hydromécanique de cette matière compactée à multiporosité. Pour renforcer les informations sur un comportement transitoire local, on fait usage de techniques à simulation faisant usage d'un modèle constitutif à double structure. La communication présente un modèle unidimensionnel à base physique pour simuler les résultats expérimentaux de différents processus transitoires, par exemple la perte progressive de la perméabilité au cours du mouillage, et la présence de phénomènes simultanés au cours d'inondations rapides à contrainte constante (effondrement initial de la configuration granulaire et expansion parallèle de granules).

INTRODUCTION

Compaction in difficult emplacement conditions and filling the empty space around nuclear canisters in horizontal drifts is a major challenge to demonstrate the feasibility of engineering barriers. Specifically, the 'engineered barrier (EB) experiment' (Mont Terri, Switzerland; Alonso & Hoffmann, 2007; García-Siñeriz *et al.*, 2008) was designed to demonstrate the suitability of compacted granular expansive mixtures. Since these mixtures can be emplaced using automated techniques, the backfilling operation becomes much easier and the remaining gaps, usually found when working with block barriers, can be minimised. In this way, a better contact between canister and backfill, as well as between buffer and host geological medium, is ensured and it makes the backfilling operation more accurate.

In spite of the obvious benefits of compacted granular expansive mixtures there are several aspects of concern in these types of mixtures. One important aspect is that significant uncertainties exist on the capabilities of state-of-the-art hydromechanical models to simulate material behavioural features, which is an obvious consequence of the complex nature of the material. One of the outstanding characteristics of this material, which influences most of its properties, is the multi-modal nature of its porous networks. This multimodal porosity and the highly expansive nature of the pellets control all the hydraulic and mechanical properties of the mixture. Important aspects of the complex nature of hydration under constant volume are the progressive blockage of the large pores due to granule swelling – this blockage greatly reduces the permeability – and the tendency to develop initial collapse strains before generating the final swelling pressure.

The paper starts with the description of the geotechnical properties and microstructural features of the mixture, together with a presentation of selected test results that will show the complex nature of the material. However, macroscopic experiments are insufficient to provide an overall behavioural picture of the material. Simulation-assisted techniques using a physically based double-structure model are required to obtain further insight into specific features and local phenomena that are beyond the measurable scale. The numerical model developed is described in some detail in the paper, and will be used later to capture the occurrence of concurrent phenomena during fast flooding (expansion of granules and a parallel collapse of the granular arrangement) and the progressive decrease of the water permeability due to the occlusion of the larger pores. Finally, computed results and the observed behaviour are compared, and some conclusions are derived.

Manuscript received 4 March 2010; revised manuscript accepted 22 November 2010.
Discussion on this paper closes on 1 September 2011, for further details see p. ii.
* Department of Geotechnical Engineering and Geosciences, Universitat Politècnica de Catalunya, Barcelona, Spain

BEHAVIOUR OF PELLETS AND PELLET MIXTURES

Bentonite granules (pellets) were obtained from Febex bentonite powder (Lloret *et al.*, 2003). Powder was preheated to 120°C and then compacted using a roller. As a result of this process, very high dry density granules (up to a dry density of 1·95 Mg/m^3) with very low water content were obtained. Basic properties of Febex bentonite (Lloret *et al.*, 2003; Hoffmann, 2005) and the as-compacted state of the pellets, as reported by Hoffmann *et al.* (2007), are shown in Table 1. The tested material was based on the mixture actually used under emplacement conditions. The grain size distribution was adjusted to a maximum size between 4 and 15 mm compatible with the dimensions of the testing cells and to a minimum size of 0·4 mm to avoid segregation during preparation. Fig. 1 shows the pellet material for a maximum particle size of 4 mm. Specimens were prepared by dry-side static compaction (at water contents ranging between 3 and 4%) to dry densities varying between 1·30 and 1·50 Mg/m^3. Applied vertical stresses to reach given dry densities are presented in Fig. 2 (this information will be later used to define the initial position of the loading–collapse (LC) yield locus, as proposed by Alonso *et al.*, 1990). Table 1 summarises the main properties of the compacted mixture. Total suction values for both high-density pellets and compacted mixtures were obtained from water retention data presented below.

Fig. 1. Photograph of the granular expansive material with a maximum pellet size of 4 mm

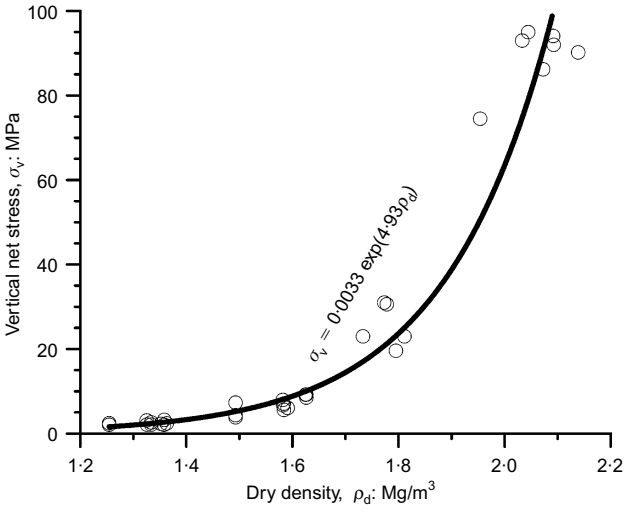

Fig. 2. Vertical stress applied on dry-side static compaction at water contents between 3 and 4% and for different target dry densities

Table 1. Material properties: Febex bentonite powder, high-density pellets and compacted granular expansive mixtures

FEBEX bentonite

Mineralogy	Liquid limit*†, w_L: %	Plastic limit*†, w_p: %	Density of solids*, ρ_s : Mg/m^3	% particles* < 75 μm	% particles < 2 μm
Montmorillonite > 90% Ca^{2+} (38%) Na^{+} (23%)	93–102	47–53	2·70	85	64–70

Pellet

Dry density*, ρ_d : Mg/m^3	Void ratio*, e_0	Water content*: %	Degree of saturation: %	Total suction*: MPa	Max. fabrication stress: MPa
1·95	0·38	3–4	21–28	250–300	50–60

Compacted granular mixtures

Dry density, ρ_d : Mg/m^3	Void ratio, e_0	Water content: %	Degree of saturation: %	Total suction: MPa	Max. fabrication stress: MPa
1·30	1·08	3–4	8–10	250–300	2
1·50	0·80	3–4	10–14	250–300	5–6

* Hoffmann (2005); Hoffmann *et al.* (2007)
† Lloret *et al.* (2003)

Mercury intrusion porosimetry (MIP) tests were performed to characterise the multiple-porosity network of a high-density freeze-dried pellet and a pluviated mixture at a dry density of 1·15 Mg/m^3. Fig. 3(a) shows the pore size density function of the high-density pellet, in which two types of intra-pellet (microporosity) pore modes are identified: a larger inter-aggregate mode at around 3 μm between aggregations and an intra-aggregate mode at 13 nm. The porosity size density function (PSD) of the pluviated mixture shown in Fig. 3(b) displays an additional pore mode associated with the inter-pellet voids (macropores) at around 250 μm. Fig. 1 shows pore sizes even larger than this inter-pellet value, which have not been detected by MIP (maximum pore sizes detected by this technique are around 500 μm). This remarkable multi-modal pore structure is a relevant characteristic of the material.

Consider now the macroporosity. It regulates the water retention and water permeability properties of the medium, which are affected by any hydromechanical change modifying this void space. Moreover, the existence of macroporosity also allows for the arrangement of the skeleton (collapse) during wetting. Fig. 4 shows the changes undergone by the PSD functions along different stress paths. The largest macropores not only decrease on loading (Fig. 4(a)), but also when the mixture is wetted (occlusion of part of the macroporosity on pellet swelling as indicated in Figs 4(b), 4(c)). On pellet swelling a new mode emerges at a pore size around 400 to 750 nm.

Another relevant property of the pellet mixture is that the hydraulic response of the material on first water injection is characterised by the high connectivity of the inter-pellet void network. Therefore, high inflow rates are expected. However, as the dense pellets hydrate – at the expense of the free circulating water – they swell and fill the macropores and the permeability decreases several orders of magnitude. This behaviour is illustrated in Fig. 5(a), which shows the time evolution of the water permeability during a constant volume infiltration test of a mixture at a dry density 1·30 Mg/m^3 and subjected to a water backpressure of 20 kPa. In this infiltration test, the inflow and outflow water volumes are monitored. The outflow volume rate is interpreted as a flow through the interconnected inter-pellet voids (macropores) and it is used to derive the evolution of the Darcy permeability of the mixture. The difference between inflow and outflow defines the water stored in the sample, which is used to estimate the evolution of the degree of saturation. After a short initial phase where very high permeability values are computed, the permeability decays rapidly and reaches asymptotically the saturated value at the end of the test. The change in permeability has also been plotted against the current degree of saturation in Fig. 5(b). The plot shows the fast obstruction of the open pore network when the degree of saturation changes from 0·6 to 0·7.

From a mechanical viewpoint, the evolution of the PSD function has also important consequences. Fig. 6(a) shows the time evolution of swelling pressure that was monitored by means of total pressure cells PE3 and PE7 located in the central section – in which the compacted pellet buffer is placed – of the 'engineered barrier experiment' tunnel (García-Siñeriz *et al.*, 2008). The injection of water through an artificial hydration system is also indicated as complementary information of the progression of the hydraulic state. The swelling pressure evolution shows clear transient drops, which can be associated with local collapse phenomena of the granular fill. Relative humidity values obtained by sensors emplaced near these total pressure cells allow the estimation of the corresponding total suctions by the psychrometric law. Fig. 6(b) shows the in situ stress paths followed by these points PE3 and PE7 in a suction–cell pressure plane. Local swelling pressure drops occur at total suctions around 100 MPa. An equivalent result was obtained from constant-volume oedometer tests performed at two dry densities (1·30 and 1·50 Mg/m^3). Figs 7(a) and 8(a) present the development of vertical, horizontal and mean net stress on hydration of both samples. Again, transient stress reductions are detected in both samples at relatively early hydration stages. Changes in degree of saturation were converted into time evolution of suction – assuming local equilibrium – using water retention data. In this way, stress paths followed on constant volume hydration could be plotted in Figs 7(b) and 8(b). Note that the peak in swelling pressure at an intermediate suction is only observed in the lighter sample. The stress paths presented in Fig. 7(b) recall the same pattern of behaviour observed under in situ conditions with local collapse phenomena developing at a slightly lower suction in the laboratory specimens (around 10 MPa). Water retention curves on wetting at constant volume for two dry densities of the mixture and the pellet are given in Fig. 9, which shows the important dependence on void ratio.

Another aspect having important mechanical consequences, in which the multi-porosity network plays a crucial role, refers to the application of different wetting rates to saturate the mixture. Two techniques were used to perform wetting under load tests (at a constant vertical net stress of 0·3 MPa) following the same stress paths under oedometer conditions of a specimen with an initial dry density of 1·30 Mg/m^3. The first technique involves saturation with liquid water (fast wetting) under small pressure (20 kPa), whereas in a second procedure, a vapour equilibrium technique was used (slow wetting). In the test involving wetting with liquid water, the injected water volume was controlled and suction values were derived from water retention data assuming local equilibrium of moisture. In the second test,

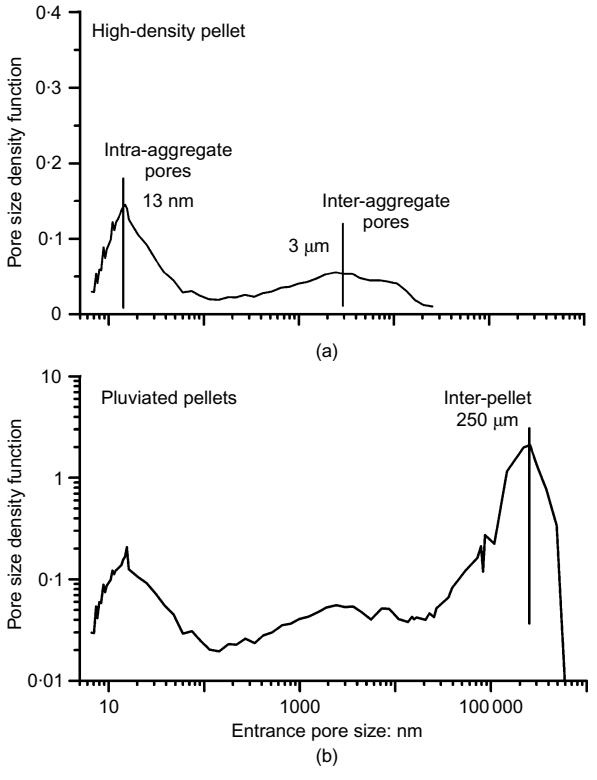

Fig. 3. Pore size density functions of the pellet-based material (Hoffmann *et al.*, 2007): (a) high-density pellet; (b) pluviated mixture at a dry density 1·15 Mg/m^3

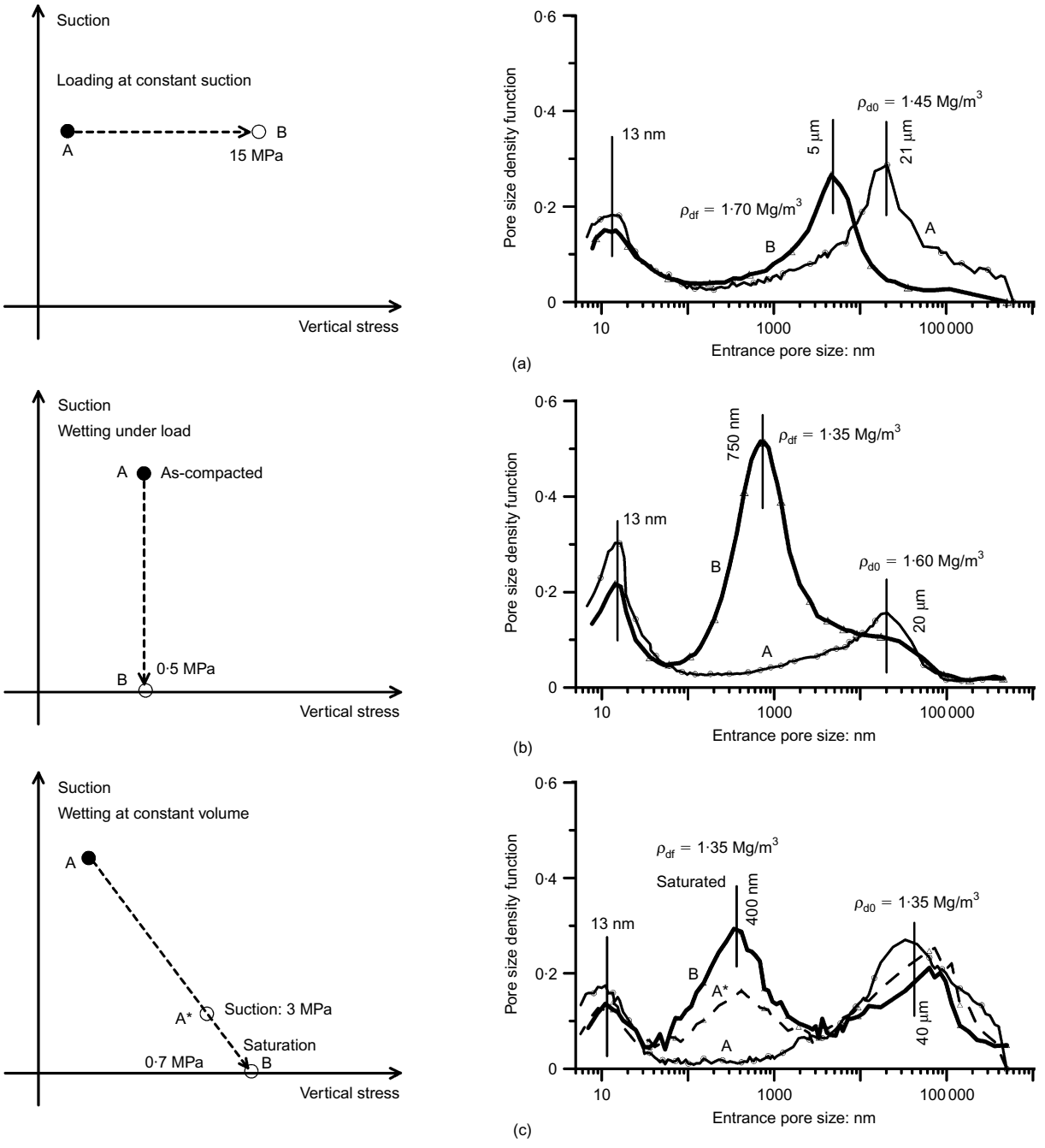

Fig. 4. Effects of stress paths on pore size density functions for the granular expansive material: (a) loading at constant suction; (b) wetting under constant load; (c) wetting at constant volume

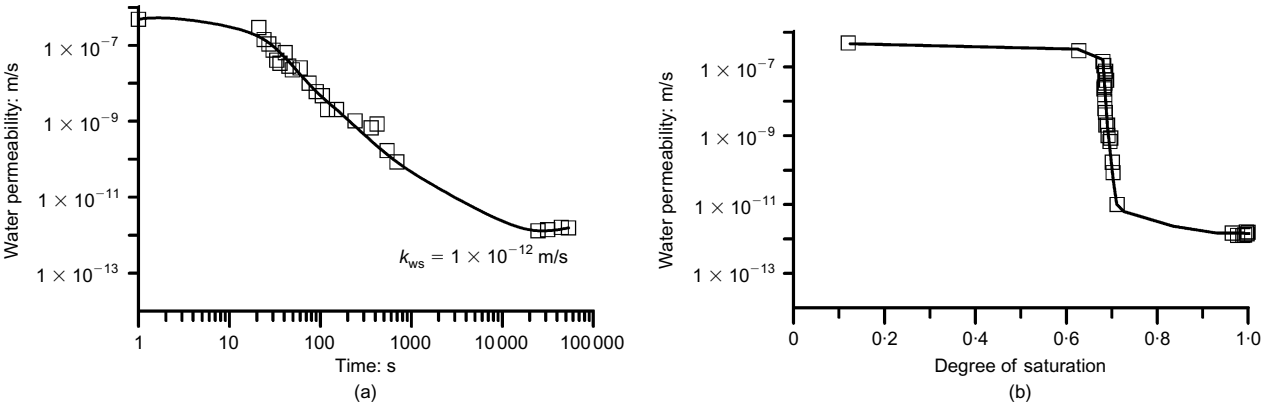

Fig. 5. Evolution of water permeability during a fast infiltration test at constant volume (Hoffmann *et al.*, 2007): (a) time evolution; (b) evolution in terms of degree of saturation

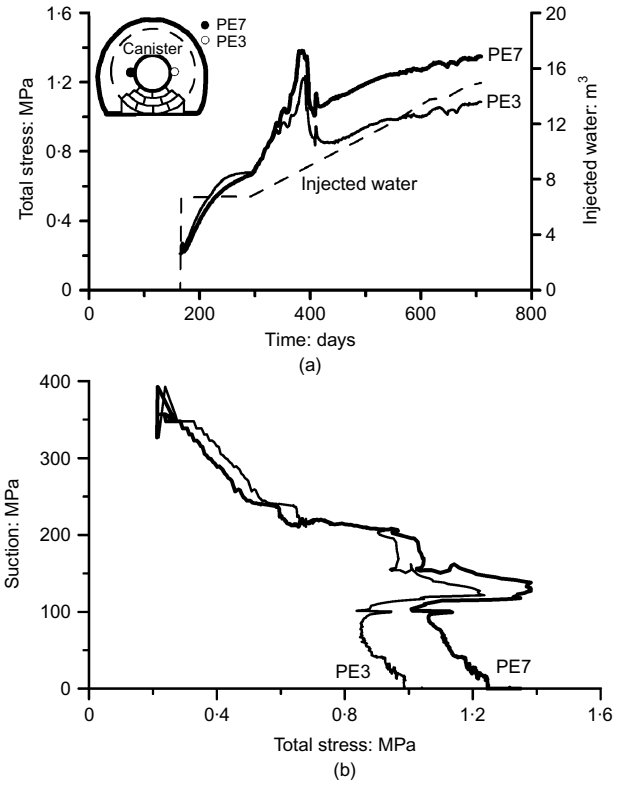

Fig. 6. (a) Measured total stresses (swelling pressures) and injected water during the hydration phase of the engineered barrier (EB) experiment for sensors PE3 and PE7. (b) In situ stress paths followed during water injection

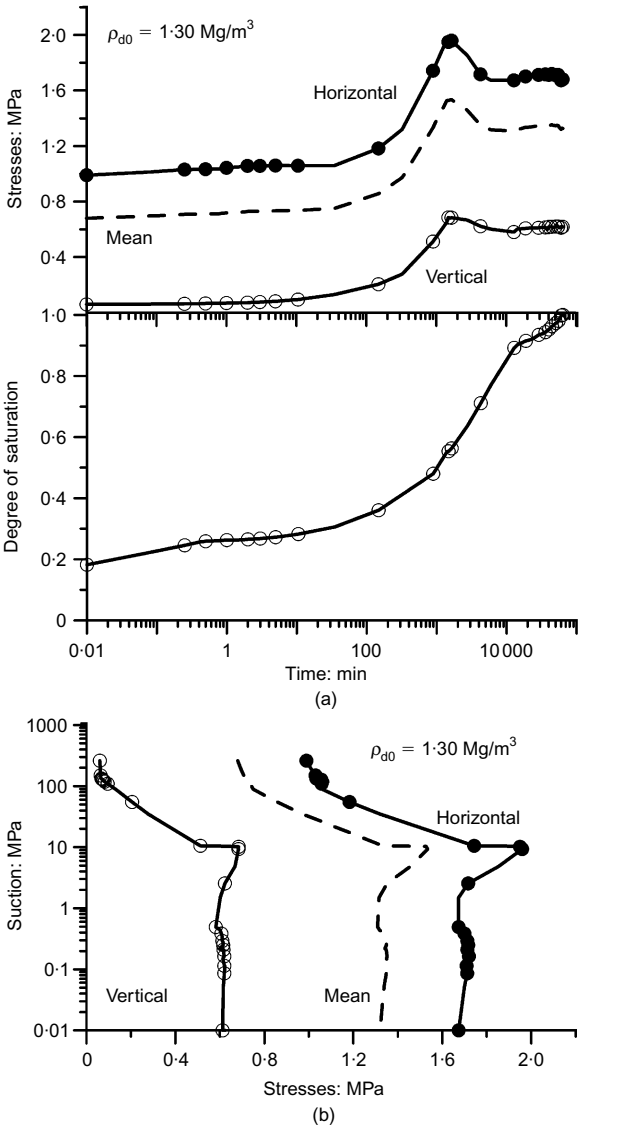

Fig. 7. (a) Time evolution of stresses and degree of saturation during wetting at constant volume (dry density 1·30 Mg/m^3). (b) Stress paths followed during the hydration phase

the wetting path was initially performed in a stepwise manner by varying total suction using relative humidity control (down to a total suction 3 MPa). The test ends in a soaking stage. The stress paths followed are indicated in Fig. 10. A different behaviour was observed in both tests during the saturation process. When liquid water was injected (Fig. 11(a)), an initial collapse 'AB' was observed immediately after inundation. Then, the expanding granules started to swell and a net swelling deformation was measured 'BC'. At a final stage, however, when the specimen was close to saturation, additional compression deformations were registered, 'CD'. In the vapour transfer case (Fig. 11(b)), a net swelling deformation was measured from the beginning of the test and for all the subsequent vapour equilibrium stages 'AB' until reaching a suction value of around 3 MPa (point 3 in Fig. 10(b)). Then, at the final stage, when liquid water was injected to bring suction to zero, a sudden collapse 'BC' was initially observed followed by some final swelling deformations 'CD'. Despite the different techniques used, both samples ended at practically the same volumetric strain (point 'D' in Figs 11(a) and 11(b)).

Differences in the observed behaviour can be interpreted as follows. Regarding the fast liquid test, the high initial permeability of the specimen macrostructure explains its rapid saturation, when water under some pressure is applied at the specimen boundaries. Water infiltrates fast into the sample, the inter-pellet voids become saturated and the intergranular forces – which maintain the stable arrangement of pellets – are reduced. Then, a global collapse of the granular structure takes place ('AB' in Fig. 11(a)), the magnitude of which depends on the applied stress level. Later, as the expansive pellets progressively hydrate, a delayed swelling response is measured ('BC' in Fig. 11(a)). Water is driven from the open connected macroporosity to the intra-pellet voids until equilibrium is reached. The macroscopically observed behaviour is the result of both mechanisms and their interaction. This explanation includes implicitly the assumption that two different water potentials co-exist inside the specimen, which is one of the criteria that will guide the development of the physical model described in the next section. The water filling the macropores is considered to have a macro potential not necessarily in equilibrium with the water potential inside the aggregates. Equilibrium will be reached when both water potentials become equal.

However, when the vapour equilibrium technique is used, the large pores remain essentially unsaturated, while water is slowly transferred to the pellets. Under these conditions, macro and micro water potentials remain similar or close together along the wetting process. Capillary forces holding the macrostructural arrangement slowly change and collapse progressively evolves. In parallel, the pellets gradually swell, which leads to an overall (net) expansion evolution throughout the initial wetting process ('AB' in Fig. 11(b)). A residual collapse ('BC' in Fig. 11(b)) is developed on further macrostructural arrangement induced by liquid water transfer before attaining a similar volumetric deformation at the final stage in both tests.

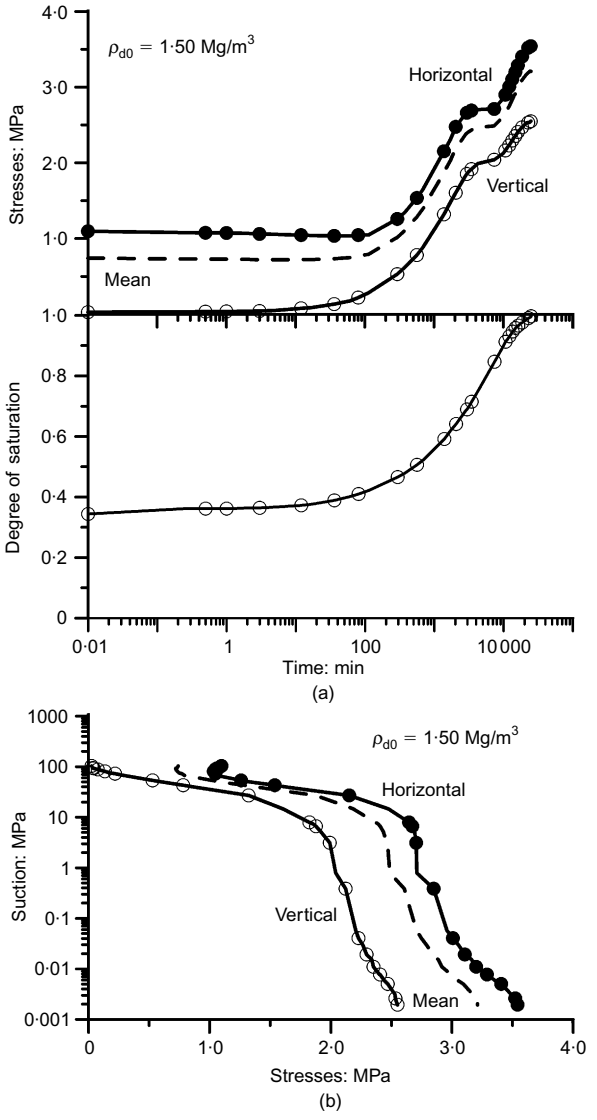

Fig. 8. (a) Time evolution of stresses and degree of saturation during wetting at constant volume (dry density 1·50 Mg/m^3). (b) Stress paths followed during the hydration phase

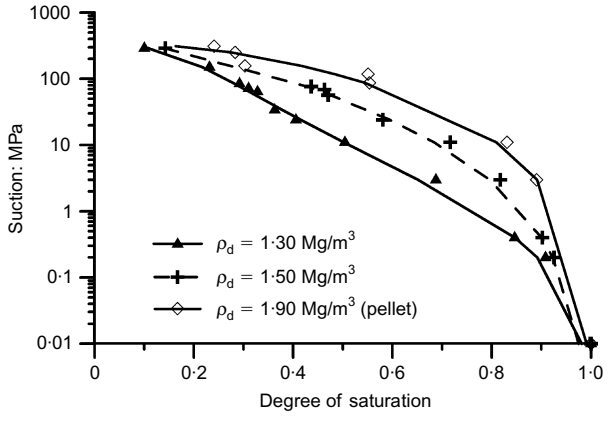

Fig. 9. Water retention curves along a wetting path at constant volume of the pellet and the granular mixtures at different dry densities

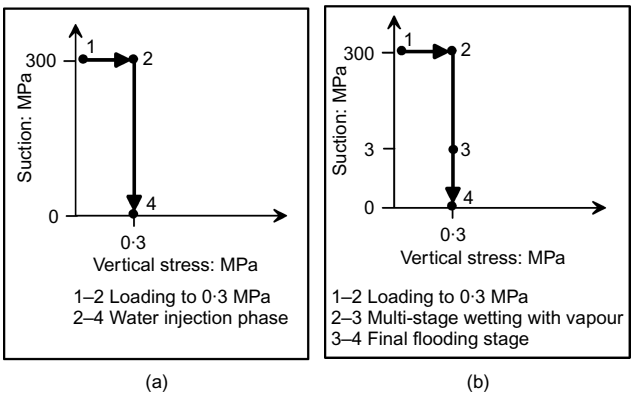

Fig. 10. Stress paths followed during infiltration tests at constant vertical stress (mixture at an initial dry density of 1·30 Mg/m^3): (a) fast flooding test with liquid injection; (b) slow wetting test with vapour transfer technique

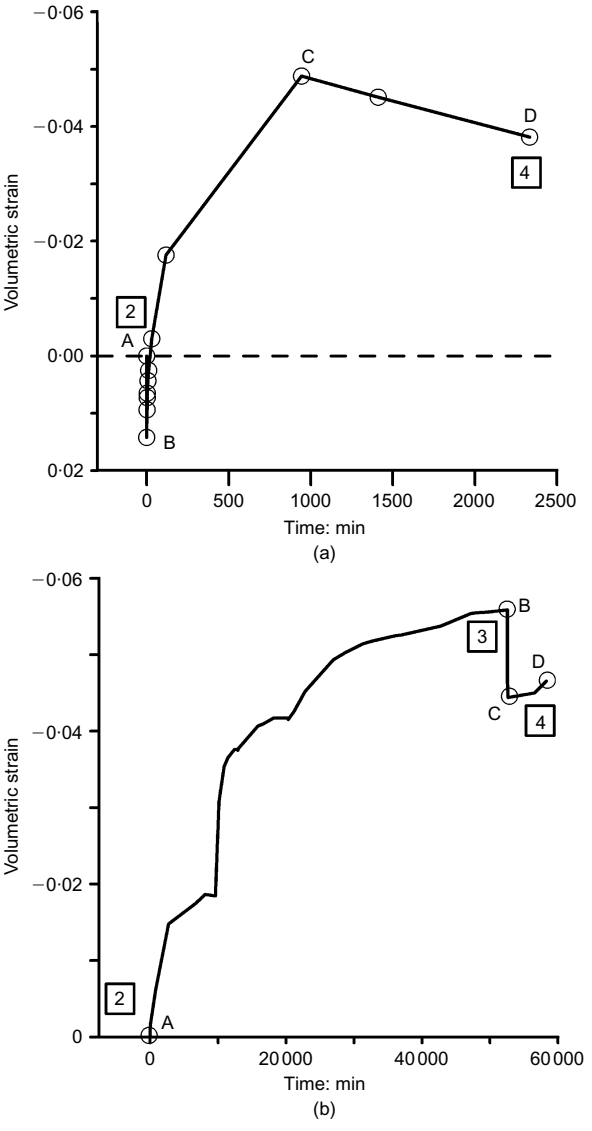

Fig. 11. Time evolution of volumetric strains during infiltration tests at constant vertical stress (mixture at an initial dry density of 1·30 Mg/m^3): (a) fast flooding test with liquid injection; (b) slow wetting test with vapour transfer technique

A WORKING MODEL

The objective of this section is to briefly describe a one-dimensional (1D) working model implemented in a finite-difference computer code, which will be used to gain insight into the different wetting-induced phenomena previously outlined. The detailed description of its implementation is described in Hoffmann (2005). A key aspect in the formulation is to adopt a physical representation of the real medium, which allows the capture of those transient and local phenomena that are far from the measurement scale used in conventional laboratory tests. The granular arrangement of pellets is substituted by an equivalent porous medium consisting of a collection of 1D elements assembled together to emulate the granular packing. In line with the ideas outlined above, each element has two structural components representing the macro- and the microstructural level. Structural parts of each element are connected in a hierarchical way specifying that the microstructure is enclosed by the macrostructure. An important consequence of this assumption is that all the assembled elements are connected through their macrostructures and no connection is admitted between microstructural parts of two adjacent elements. When a specimen is subjected to liquid water wetting, water flows through the open interconnected macroporosity and pellets (microstructure) become hydrated by exchanging water with the macrostructure. Fig. 12 shows the real media (Fig. 12(a)) and the equivalent 1D one (Fig. 12(b)), in which the macrostructural void ratio e_M (interconnected and outside the pellets) is separated from the microstructural one e_m (inside pellets). In Fig. 12(d), the hydration process is also schematically represented by means of a macrostructural flow and water exchanges between macro- and microstructural levels.

The guiding criteria behind the working model are described below, giving five main points.

Two different structural levels are considered. A microstructural level associated with the pore volume inside the pellets and a macrostructural one related to the granular arrangement of pellets. The microstructural void ratio (associated with the pore volume inside pellets) can be estimated from the dry density of the pellets $e_m = \rho_s/\rho_{dp} - 1$, where ρ_s and ρ_{dp} are the solid and pellet dry density, respectively. Figs 12(b) and 12(c) show the macrostructural elements and

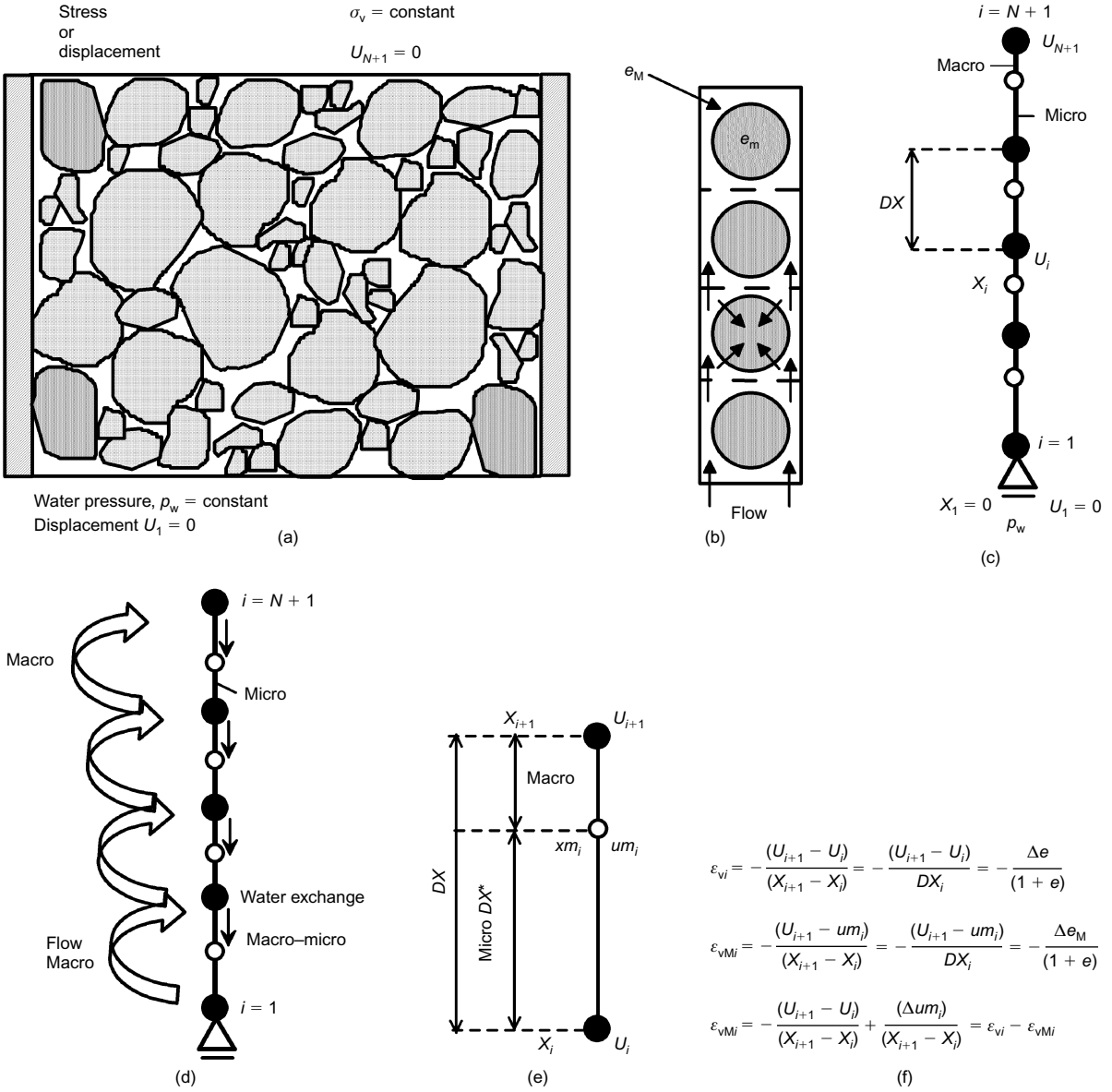

Fig. 12. Equivalent 1D double-porosity media used in the working model: (a) real medium; (b) equivalent 1D medium; (c) space discretisation; (d) scheme of the hydration process; (e) nodal displacements; and (f) strain and nodal displacement relationships

the embedded microstructural ones. Nodal displacements U_i and microstructural ones um_i are indicated in Fig. 12(e). Strain and nodal displacement relationships for both levels are also summarised in Fig. 12(f).

Two complementary water potential fields. The discussion in a previous section suggested that a single water potential field was not enough to interpret the transient behaviour of expansive materials with a marked multi-modal porosity distribution. Therefore, in addition to the net stress, two complementary water potential fields are assumed to coexist in the working model. One is associated with the water adsorbed inside pellets –microstructural suction s_m – while

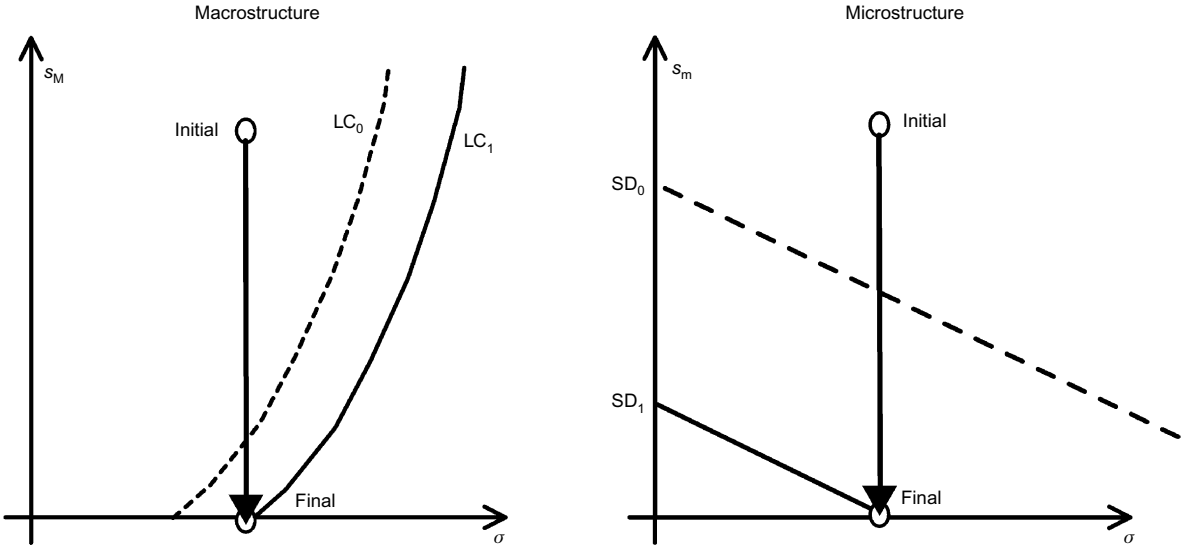

Fig. 13. Wetting paths at constant stress plotted in the macrostructural suction (s_M) and microstructural suction (s_m) planes. Activation of macrostructural yield locus LC and microstructural yield locus SD during wetting

Table 2. Micro- and macrostructural hydromechanical parameters used in the simulation (refer to the Appendix)

Mechanical microstructural parameters

κ_m	λ_m	χ	SD_o (initial): MPa
0·015	0·035	0·9	70–100

Hydraulic microstructural parameters

k_{im}: m^2	λ_p	S_{resm}	p_{wm}: MPa	λ_{wm}	p_{sm}: MPa	λ_{sm}
1×10^{-22}	1·5	0·01	16·6	0·130	3000	0·1

Macrostructural reversible compressibility parameters

Dry density, ρ_d : Mg/m^3	κ_{po}	α_p	κ_{so}	α_{sp}	α_{ss}: MPa^{-1}	p_{ref}: MPa
1·30	0·07–0·09	−0·003	0·001	0·185	0·010	0·008
1·50	0·05–0·06	−0·003	0·025	0·120	0·003	0·008

Macrostructural LC yield locus parameters

Dry density, ρ_d : Mg/m^3	σ^*_{vo}: MPa	σ^c: MPa	$\lambda(0)$	r	β: MPa^{-1}
1·30	0·022–0·065	0·08	0·18–0·20	0·45–0·65	0·007
1·50	1·5–1·9	0·08	0·16–0·17	0·65–0·85	0·004

Hydraulic macrostructural parameters

Dry density, ρ_d : Mg/m^3	k_{iM}: m^2	λ_p	S_{resM}	p_{wM}: MPa	λ_{wM}	p_{sM}: MPa	λ_{sM}
1·30	1×10^{-16}	1·5	0·01	0·95	0·217	1000	0·02
1·50	1×10^{-16}	1·5	0·01	4·15	0·237	2500	0·001

the other is related to the water stored between granules – macrostructural suction s_M – which has a dominant capillary retention component. Lack of local equilibrium between both suctions may occur depending on the wetting rate and boundary conditions. Different laboratory protocols lead to different histories of macro- and microstructural changes and therefore to different transient specimen responses. For the purpose of discussing the experimental behaviour observed under oedometer conditions, it is convenient to work with two stress spaces: the space (σ, s_M) associated with the macrostructure and the space (σ, s_m) associated with the microstructural level (Fig. 13).

Different volume change mechanisms are defined for each structural level. The ideas put forward by Alonso *et al.* (1990) in the Barcelona basic model (BBM) are used to describe the volume change mechanisms acting at macrostructural level. On the other hand, the volume change response of the microstructure is described with the elastoplastic model proposed by Gens & Alonso (1992) and Alonso *et al.* (1999), which extends the BBM framework to expansive materials. The positions of the yield loci in Fig. 13 mark the initiation of activation of irreversible strains: the LC curve in the case of the macrostructural irreversible compression and the suction-decrease (SD) curve in the case of microstructural changes (irreversible expansion). A summary of the model formulation for volume change under isotropic stress state is given in the Appendix. More details can be found in Alonso *et al.* (1999).

Double-structure approach. In order to reproduce the hydraulic response of the bentonite pellet mixture, a double-structure approach was adopted. Advective fluxes of water in each level are computed using a generalised Darcy's law (equation (1) below), which incorporates a relative permeability k_r as a function of the micro- and macrostructural degrees of saturation (S_{rm} and S_{rM}) and intrinsic permeability values k_i depending on the respective micro- and macrostructural void ratio (e_m and e_M respectively). S_{rm} and S_{rM} are related to their corresponding suctions, s_m and s_M, through two independent modified van Genuchten's (1980) retention curves (equation (2) below), in which p_{wm} and p_{wM} are the air-entry values corresponding to the micro- and macrostructure, respectively; S_{resm} and S_{resM} are the residual degrees of saturation for micro- and macrostructure; and p_{sm}, p_{sM}, λ_{sm} and λ_{sM} are experimental parameters. Relative permeability is defined as a potential function of degree of saturation (micro or macro) with a common power parameter λ_p

$$\begin{aligned} k_{wm} &= k_{rm}(S_{rm})\ k_{im}(e_m); \\ k_{wM} &= k_{rM}(S_{rM})\ k_{iM}(e_M) \\ \text{with} \quad k_{rm} &= (S_{rm})^{\lambda_p} \\ \text{and} \quad k_{rM} &= (S_{rM})^{\lambda_p} \end{aligned} \tag{1}$$

$$\begin{aligned} S_{rm} &= S_{resm} + (1 - S_{resm})\left[1 + \left(\frac{s_m}{p_{wm}}\right)^{\lambda_{wm}/(1-\lambda_{wm})}\right] \\ &\quad \times \left(1 - \frac{s_m}{p_{sm}}\right)^{\lambda_{sm}} \\ S_{rM} &= S_{resM} + (1 - S_{resM})\left[1 + \left(\frac{s_M}{p_{wM}}\right)^{\lambda_{wM}/(1-\lambda_{wM})}\right] \\ &\quad \times \left(1 - \frac{s_M}{p_{sM}}\right)^{\lambda_{sM}} \end{aligned} \tag{2}$$

The granular media is conceived as a continuum having the properties of the assembly of pellets. Water flows in the Darcy sense through the (macro) pores of the granular media. The mass balance equation of water in the macrocontinuum reads

$$\frac{\partial}{\partial t}(\phi_M S_{rM}) - \nabla \cdot (k_M \nabla \varphi_M) = f^w_{M \to m} \tag{3}$$

where M refers to the macro component. The rate of change of porosity ϕ_M with time requires the calculation of volumetric strains, which is made through the BBM. They depend on stress and macro suction changes. The macro retention curve (equation (2)) allows also the calculation of the rate of changes of degree of saturation. Macro permeability has already been defined in terms of void ratio and degree of saturation. It may be calculated for changes in suction and stress.

The connection of the macro analysis with individual pellets is included in the source/sink term $f^w_{M \to m}$ which describes the water flow rate, wetting or drying the pellets. Equation (3) may eventually be written in terms of macro suction (the gravitational component of potential φ_M is negligible in the tests performed).

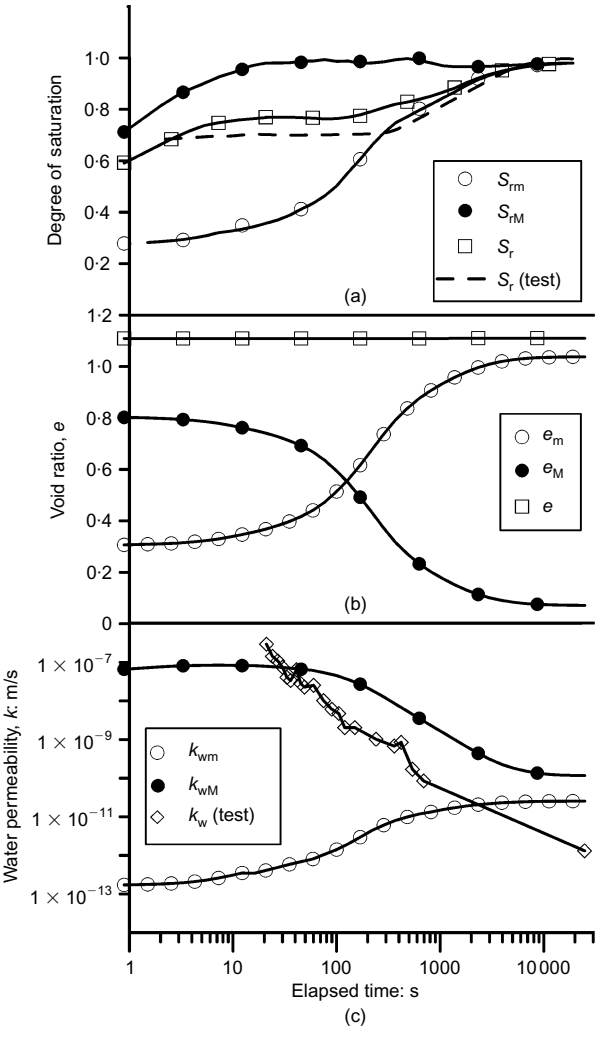

Fig. 14. Fast infiltration test at constant volume (dry density 1·30 Mg/m³): (a) simulated evolutions of the different components of degree of saturation and comparison with overall degree of saturation results; (b) simulated evolutions of the different components of void ratio; (c) simulated evolutions of the water permeability (micro- and macrostructural). Comparison with test results

Flow of water hydrating and wetting every pellet in the model is also described as a boundary value problem (BVP). Suction s_M provides the boundary condition for the water flow in pellets. Water mass balance equation inside a pellet is given by

$$\frac{\partial}{\partial t}(\phi_m S_{rm}) - \nabla \cdot (k_m \nabla \varphi_m) = 0 \quad (4)$$

similar to equation (3) but now in terms of microstructural variables. Note that no sink or source term is included in equation (4) because the water interchange with the macroporosity is made at the pellet's boundaries. Deformations inside the pellets are calculated through the expansive model. Equation (4) may eventually be written in terms of micro suction s_m by neglecting the gravitational component of potential φ_m.

The oedometric tests performed were simulated by the 1D model sketched in Fig. 12. Stress equilibrium is trivial in this case. Fig. 12(d) provides the definition of micro and macro deformations in terms of the calculated nodal displacements for the two BVPs described.

The calculation process is described as follows:

(*a*) The macro BVP is first solved for the first time increment. Water sinks or sources from pellets are assumed to be zero. Likewise pellet deformations are set to zero. The solution provides a first spatial distribution of macro-suction, $s_M(x)$.
(*b*) A local BVP is solved for each one of the pellets included in the sample (N pellets in Fig. 12). The boundary suction for each pellet is given by $s_M(x)$ from the first step (*a*). The calculation provides, for each pellet, the flow in or out ($f^w_{M\to m}$) and the pellet global deformation (Δum).
(*c*) Pellet's boundary flow and deformations are compared with the initial calculation (or the previous calculation in the iterative process). Global pellet expansion is also

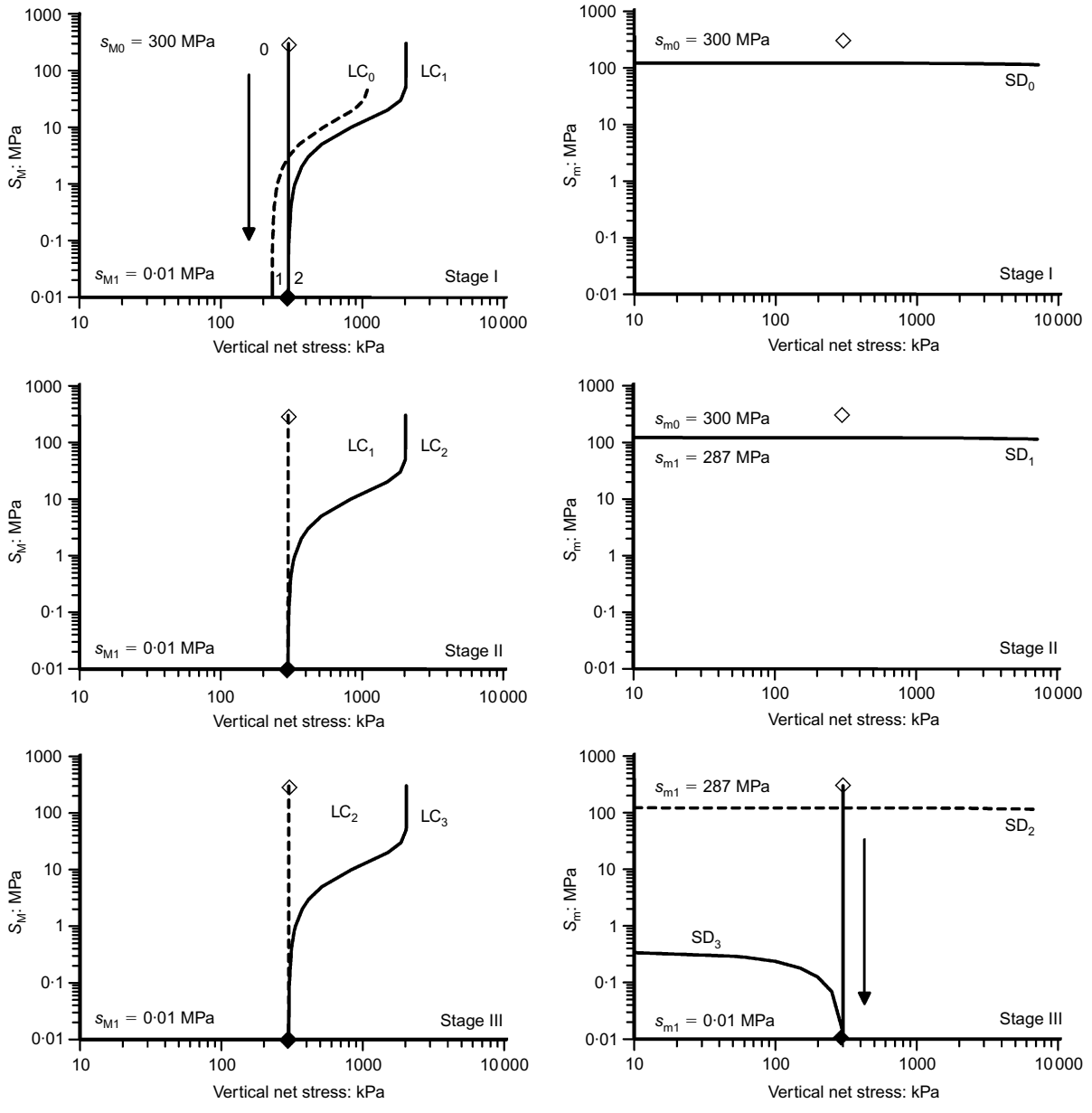

Fig. 15. Simulated stress paths in the vertical net stress–suction planes: (σ_v, s_M) and (σ_v, s_m) for the fast flooding test (liquid injection) at constant vertical stress (mixture at an initial dry density of 1·30 Mg/m^3). Evolutions of LC and SD yield loci

compared with the initial calculation (or the previous calculation in the iterative process). If differences are small, variables are updated, a new time step is added and the calculation resumes in step (*a*). Otherwise an internal calculation loop through steps (*a*), (*b*) and (*c*) is followed until convergence.

The following additional data and remarks define the calculations made.

(*a*) Water retention curves for the pellets and the mixture are given in Fig. 9.
(*b*) The dependence of permeability on void ratio was derived from saturated permeability data on samples compacted at different dry densities. The effect of degree of saturation was directly determined by means of some percolation tests (Fig. 5).
(*c*) The size of the pellet is given by DX^* in Fig. 12(e). DX^* describes the pellet radius. Its value is defined by a characteristic size (D_{50} of grain size distribution curve was selected). Once DX^* is defined the macro volume of the element is derived from the total density of the specimen.
(*d*) The number of elements (pellets) in the model of an oedometer test derives from the condition that the maximum pellet size (D_{max}) in the pellet grain size distribution is no bigger that one-fifth of the specimen thickness. Then, the number of elements is given by $N = 5D_{max}/D_{50}$.

SIMULATION-AIDED INTERPRETATION OF TESTING RESULTS

This section shows the capability of the physical model to simulate the tests described in the section headed 'Behaviour of pellets and pellet mixtures'. The simulations will allow the capture of transient and local processes not detected at conventional laboratory scale. For example, by providing the evolutions of micro- and macrostructural suctions (or alternatively the progressive changes of micro- and macrostructural degrees of saturation), the model will assist in the physical interpretation of such complex phenomena that are beyond measurable scale. A systematic procedure was used to obtain the set of parameters required from a comprehensive and independent experimental programme described elsewhere (Hoffmann, 2005; Hoffmann *et al.*, 2007). Material parameters associated with the microstructure were obtained from tests performed on compacted samples at the dry density and initial water content of the bentonite pellets (Table 1). Table 2 summarises the set of parameters used in the computations.

Infiltration test at constant volume. Water permeability decrease due to macropore occlusion

In order to interpret the hydraulic phenomena involved – specifically to account for water permeability variations associated with macroporosity changes induced by pellet swelling – the infiltration test under constant volume (Fig. 5), performed on a mixture with dry density of 1·30 Mg/m^3, was simulated. Water was injected at a constant backpressure of 20 kPa. Calculated evolutions of volumetric variables (void ratio and degree of saturation both at micro- and macroscale) are plotted against time in Figs 14(a) and 14(b). These tests help to elucidate the expected evolution of soil structure, which is information not readily available from conventional laboratory techniques.

The model shows the fast increase of S_{rM} as liquid water floods the macropores (only simulated results beyond a time $t = 1$ s are plotted, S_{rM} is already close to 0·70). The extremely open macroporosity helps injected water to flow through the macropores, causing this structural level to become rapidly saturated (Fig. 14(a)). On the contrary, the dense microstructural level, which undergoes swelling as shown in Fig. 14(b), is hydrated at a much slower rate. The evolution of the overall degree of saturation S_r, which follows closely the experimental results, is calculated from both micro- and macrostructural contributions as

$$S_r = \frac{e_m}{e} S_{rm} + \frac{e_M}{e} S_{rM} \tag{5}$$

As shown in Fig. 14(c), the model is able to reproduce in a satisfactory way the evolution on wetting of the macroscopic water permeability k_{wM}. This water permeability is initially expected to increase due to the fast increase of S_{rM} (this condition is not detected in the figure since S_{rM} already starts at a relatively high value). After macropore saturation, the k_{wM} evolution consistently follows the important water permeability drop obtained in the experimental data presented in Fig. 14(c). It is seen how k_{wM} is gradually declining due to pellet swelling, which causes the progressive occlusion of the macroporosity (Fig. 14(b)).

Influence of the wetting rate. Liquid against vapour imbibition

Oedometer results obtained during wetting under constant vertical net stress of 0·3 MPa, performed on low-density mixtures (dry density 1·30 Mg/m^3) are now interpreted using the model. A striking characteristic of these two tests with different water absorption rates was the different volumetric features observed on identical samples, despite being subjected to the same overall stress–suction path (Fig. 10). The

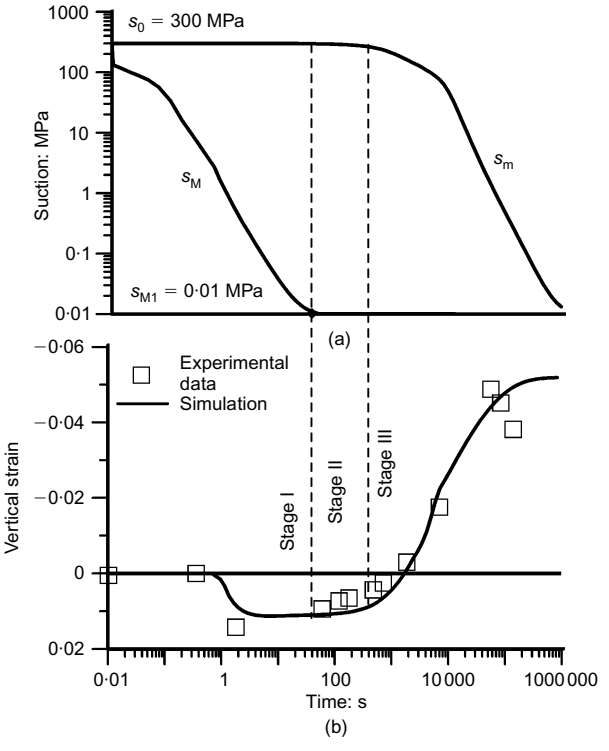

Fig. 16. Fast flooding test (liquid injection) at constant vertical stress (mixture at an initial dry density of 1·30 Mg/m^3): (a) simulated time evolutions of micro- and macrostructural suctions; (b) simulated time evolution of vertical strain and comparison with experimental results

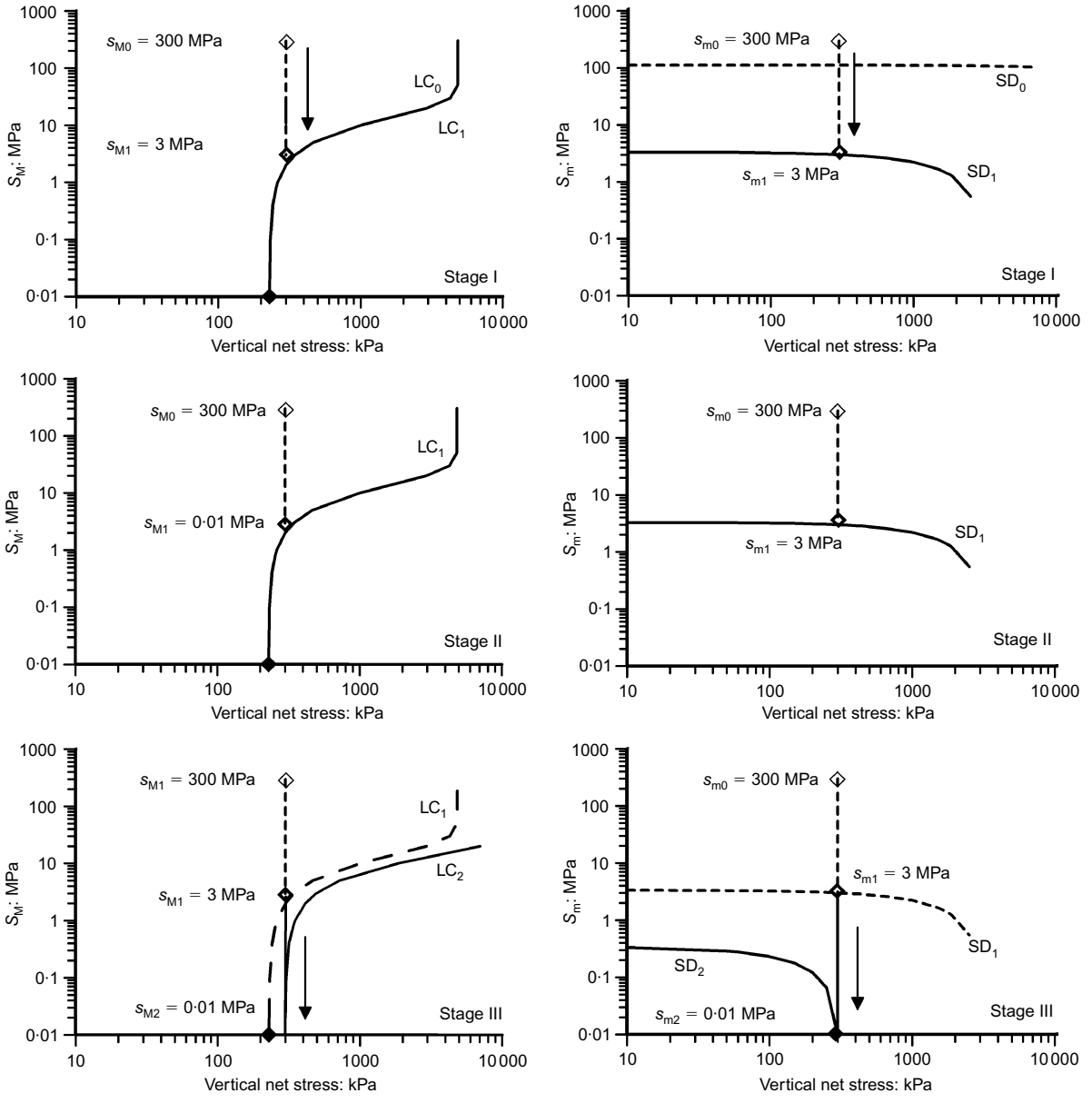

Fig. 17. Simulated stress paths in the vertical net stress–suction planes: (σ_v, s_M) and (σ_v, s_m) for the slow wetting test (vapour transfer technique) at constant vertical stress (mixture at an initial dry density of 1·30 Mg/m^3). Evolutions of LC and SD yield loci

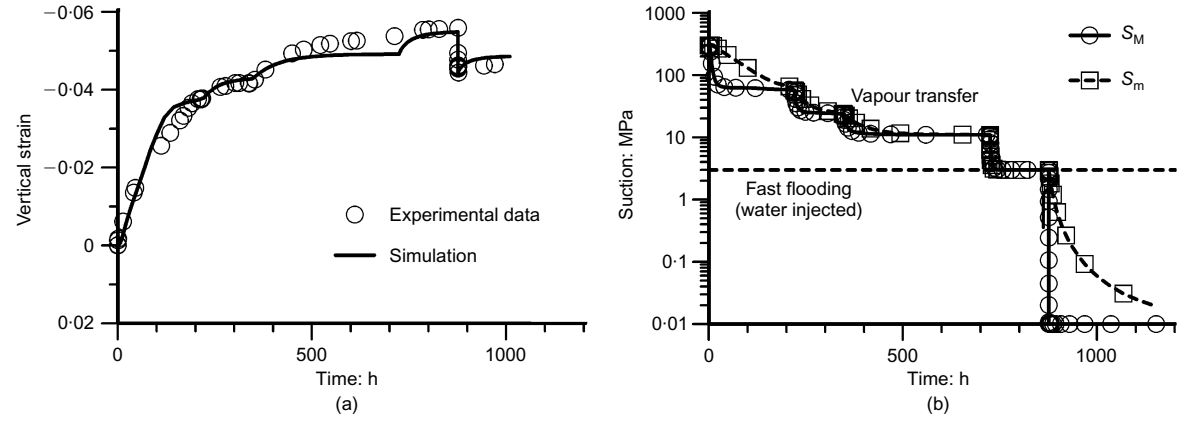

Fig. 18. Slow wetting test (vapour transfer technique) at constant vertical stress (mixture at an initial dry density of 1·30 Mg/m^3): (a) simulated time evolution of vertical strain and comparison with experimental results; (b) simulated time evolutions of micro- and macrostructural suctions

application of the model will provide the evolution of s_M and s_m and will help to explain the overall volume change response observed.

Regarding the liquid water test or fast flooding experiment (Figs 10(a) and 11(a)), the extremely open macroporosity contributes to the flow of water along the macropores, causing this structural level to become saturated in a relatively short period. A consequence of this phenomenon implies that the two defined suctions inside the mixture evolve at different rates. Suction evolutions are characterised by an important and fast reduction of s_M (associated with the development of collapse) and a delayed decrease of s_m inside the dense pellets inducing swelling. This is indicated in Fig. 15, in which the evolutions of the two defined suctions inside the specimen are represented in two vertical net stress–suction planes: (σ_v, s_M) and (σ_v, s_m). Stage I in Figs 15 and 16(a) represents the initial part of the test, where the macrostructural level becomes essentially saturated ($s_M = 0$), and the expanding pellets remain at the initial suction (s_{mo}) and, accordingly, do not swell. On macrostructural suction reduction, conditions for a potential collapse of the sample develop. In the constitutive model this collapse is controlled by the location of the yield surface (LC_0) in Fig. 15 (left) associated with the granular packing. The initial position of LC_0 is defined by the as-compacted condition in terms of the initial suction of the mixture (Table 1) and the vertical stress applied on compaction (Fig. 2). As the LC_1 yield surface moves to position LC_2, dragged by the decreasing macro suction, a collapse is predicted as shown in Fig. 16(b). After this initial first stage, a water exchange between both levels starts and the dense bentonite granules begin to swell as the microstructural suction decreases (stage III in Fig. 16(b)). The microstructural suction reduces in search of the 'boundary condition' imposed by s_M. During this s_m reduction, both elastic and plastic strains are computed. Plastic strains – associated with s_m decrease – are activated

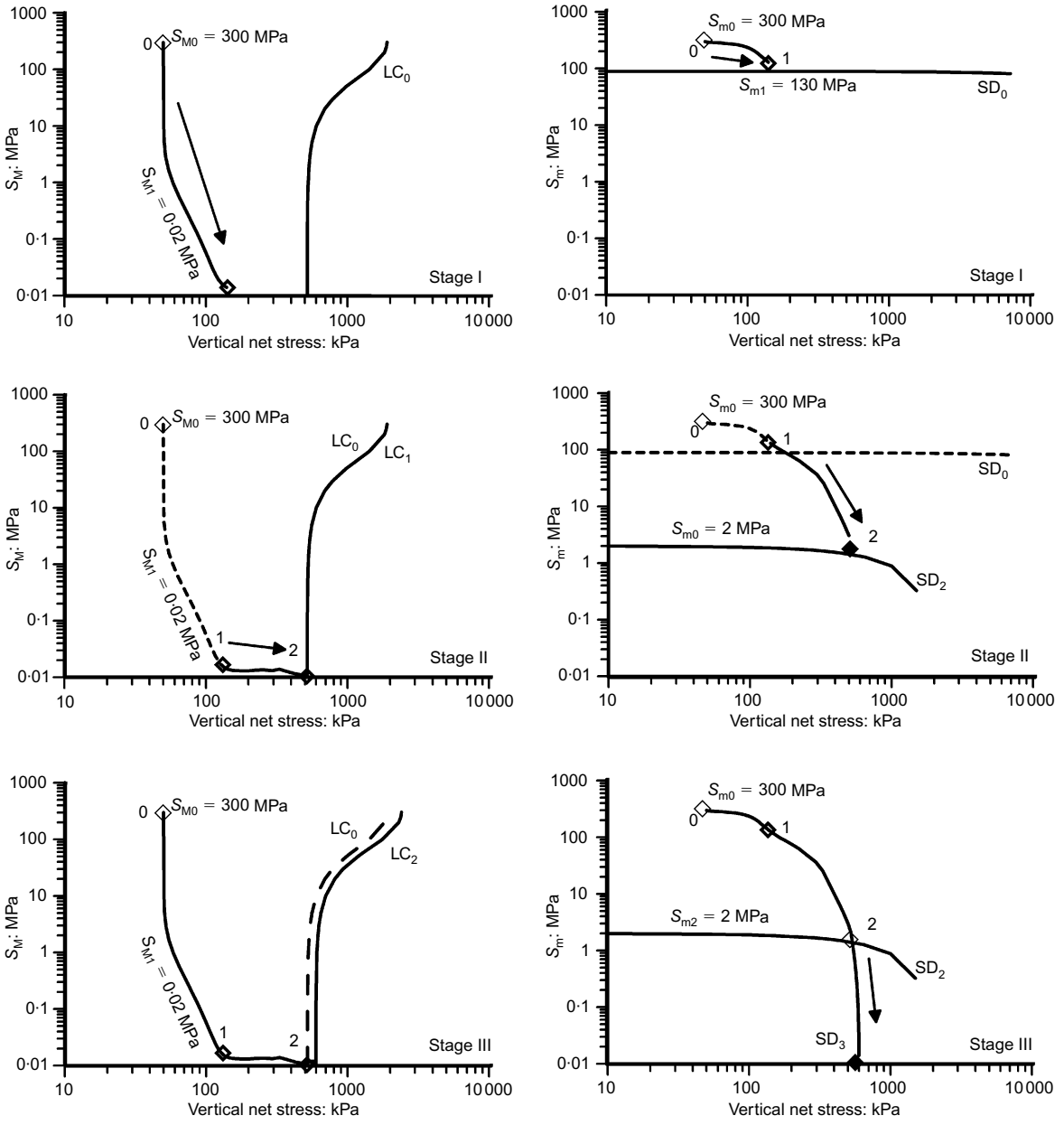

Fig. 19. Simulated stress paths followed by the mixture at dry density 1·30 Mg/m^3 during wetting at constant volume, using the two vertical net stress–suction planes ((σ_v, s_M) and (σ_v, s_m)). Evolutions of LC and SD yield loci

on dragging the SD yield locus (Fig. 15 (right)). Relevant equations are given in the Appendix.

In the vapour transfer wetting test (slow water absorption test) only net swelling deformations were recorded from the very beginning of the hydration process (Fig. 11(b)). In this case, no substantial differences between the two suction components are expected during the wetting process. This is shown in the simulation reported in Figs 17 and 18(b). Virtually, nearly local equilibrium conditions are prevailing throughout the process. The stress paths followed in the two vertical net stress–suction planes ((σ_v, s_M) and (σ_v, s_m)) have been represented in Fig. 17. During the vapour transfer stages (stages I and II in Fig. 17) some collapse deformations (associated with s_M changes and the activation of LC yield locus) and important swelling deformations (associated with s_m changes and the dragging of SD yield locus) take place simultaneously. A net volumetric expansion is computed, which corresponds to the observed behaviour (Fig. 18(a)). The simulation also captures the final volumetric compression, associated with the activation of the LC curve during the final flooding stage, as well as the delayed microstructural swelling ('BC' and 'CD' in Fig. 11(b)).

Swelling pressure tests

Tests results were given in Figs 7 and 8 for mixtures at dry densities of 1·30 and 1·50 Mg/m^3 respectively. The simulated response, plotted in the two vertical net stress–suction planes ((σ_v, s_M) and (σ_v, s_m)), is given in Fig. 19 and later in Fig. 21. In the case of the sample at a dry density of 1·30 Mg/m^3, the macrostructural suction decayed rapidly and the macropore level became saturated in a relatively short period, because of the extremely open macroporosity (Fig. 19 (left) and Fig. 20(a)). On the contrary, the microstructural suction decreased at a much slower rate, as shown in Figs 19 (right) and 20(a). The macrostructural stress path in Fig. 19 (left) indicates that on suction reduction no LC yield curve is activated, and the stable granular packing undergoes an elastic vertical net stress increase necessary to maintain the constant volume condition. The microstructural stress path shows increasing swelling pressures on suction reduction. It induced some small final dragging of the LC yield curve in order to maintain the null volume change condition. Despite this final LC yield curve activation, no decrease of the swelling pressure was detected, against the observed measurements (Fig. 20(b)). The swelling pressure increased monotonically to an ultimate value around 0·6 MPa, which reproduces well the final experimental value.

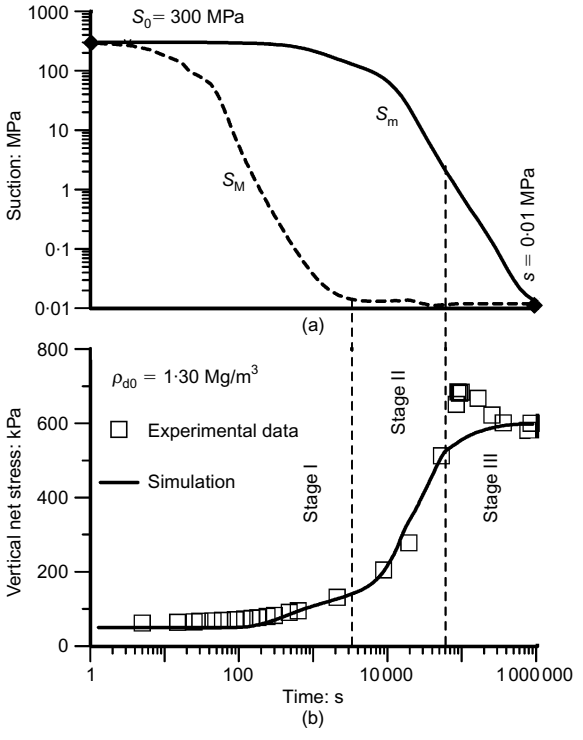

Fig. 20. Swelling pressure test (mixture at dry density 1·30 Mg/m^3): (a) simulated time evolutions of micro- and macrostructural suctions; (b) simulated time evolution of vertical stress and comparison with experimental results

In the high-density mixture (1·50 Mg/m^3), the macrostructural suction decreased at a lower rate compared to the low-density mixture, because of its lower macrostructural water permeability (Fig. 21 (left) and Fig. 22(a)). Fig. 21 (left) shows how the saturation path brings the macrostructural stress state towards the yield locus LC as a consequence of the important swelling pressure developed. The collapse tendency experienced by the macrostructure, when the LC yield locus is activated, is compensated for by the swelling trend at microscopic scale (Fig. 21 (right)) to maintain the null volume change condition. Some volumetric strain hardening occurred (activation of the LC in Fig. 21 (left)) due to some reduction in the macrostructural pore space at the expense of the microstructural swelling. An interesting aspect to remark, which is detected in Fig. 22, is the calculated suction change during wetting. The macrostructural suction decreases monotonically down to a low value (around $s_M = 0{\cdot}05$ MPa), but afterwards the decaying trend is reverted. At this point, the still high value of s_m demands water, which is supplied by liquid stored in the macrostructure. This condition originates a slight increase of the macrostructural suction along stage II in Fig. 22, which is finally reverted towards a monotonic decrease during stage III. This unusual condition is not easy to detect with conventional measuring techniques. But if it is correct it helps to understand why the swelling pressure tends to level off and then re-activate its increasing tendency (stage II in Fig. 22(b)).

SUMMARY AND CONCLUSIONS

Dry-side compacted granular expansive mixtures have been investigated by different macroscopic tests (fast and slow infiltration tests, swelling under load and swelling pressure tests) to study their complex behaviour on wetting. This response arises from its multi-modal pore network exhibiting distinct pore sizes, which are controlled by the hydromechanical paths followed during testing.

A most important feature of behaviour is the progressive loss of water permeability induced by the blockage of the large inter-pellet pores due to granule swelling and the development in time of swelling strains and swelling pressures during wetting.

Experimental results and some microstructural observations seem to be consistent with the idea that two different water potentials (suctions), not necessarily in equilibrium, may coexist at a given time. Nevertheless, this sub-division into two suction components is far from being measured by conventional laboratory procedures, and alternative techniques for the interpretation of the observed phenomena are required. Within this context, simulation-assisted techniques are essential.

The paper presented the rationale behind a physically based and double-porosity 1D model, which was further used successfully to simulate selected experimental results.

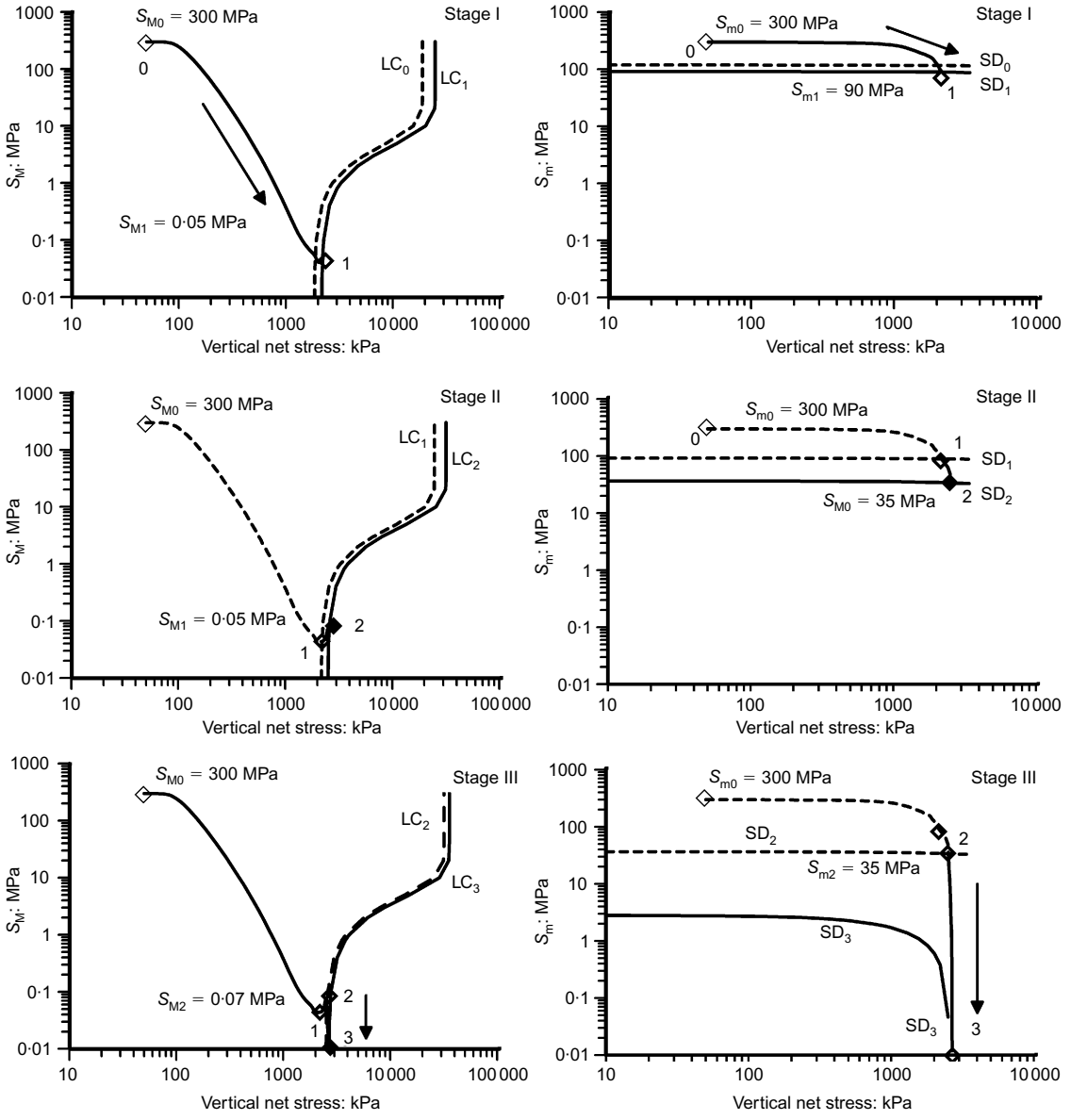

Fig. 21. Simulated stress paths followed by the mixture at dry density 1·50 Mg/m^3 during wetting at constant volume, using the two vertical net stress–suction planes ((σ_v, s_M) and (σ_v, s_m)). Evolutions of LC and SD yield loci

However, the most appropriate use of the working model came up when assisting in the interpretation of competing and coupled processes and by providing further insight into the phenomena, which were beyond the measurable scale used in conventional laboratory techniques.

ACKNOWLEDGEMENTS

The work described has been supported by ENRESA through the 'Engineered barrier emplacement experiment in opalinus clay (EB experiment)' (2000–2003). The authors also acknowledge the financial support provided by the EC under the contract FIKW-CT-2000-00017.

APPENDIX. SUMMARY OF MODEL FORMULATION FOR ISOTROPIC STRESS STATES

The proposed model integrates two different behavioural features for both structural levels. At macrostructural level (rearrangement of the granular structure), the elastoplastic BBM model (Alonso *et al.*, 1990) is adopted. It assumes that volume change for isotropic states is controlled by two independent stress variables: mean net stress p and macrostructural suction s_M. On the other hand, soil fabric at microstructural level is assumed to react in a pure volumetric and elastoplastic manner against changes in generalised microstructural effective stress $\hat{p}$ (Gens & Alonso, 1992; Alonso *et al.*, 1999). In the model developed, the net mean stress, p, was replaced by vertical net stress σ when using the 1D working model for the interpretation of oedometer results.

Elastic deformations

A non-linear law provides microstructural volumetric changes

$$d\varepsilon_{vm}^{e} = -\frac{de_m}{1+e_m} = \frac{\kappa_m}{1+e_m}\frac{d\hat{p}}{\hat{p}} = \frac{d\hat{p}}{K_m} \tag{6}$$

where κ_m is a constant compressibility index of the microstructure and $\hat{p}$ is the generalised microstructural effective stress defined as

$$\hat{p} = p + \chi s_m \tag{7}$$

The elastic behaviour at macrostructural level is expressed by

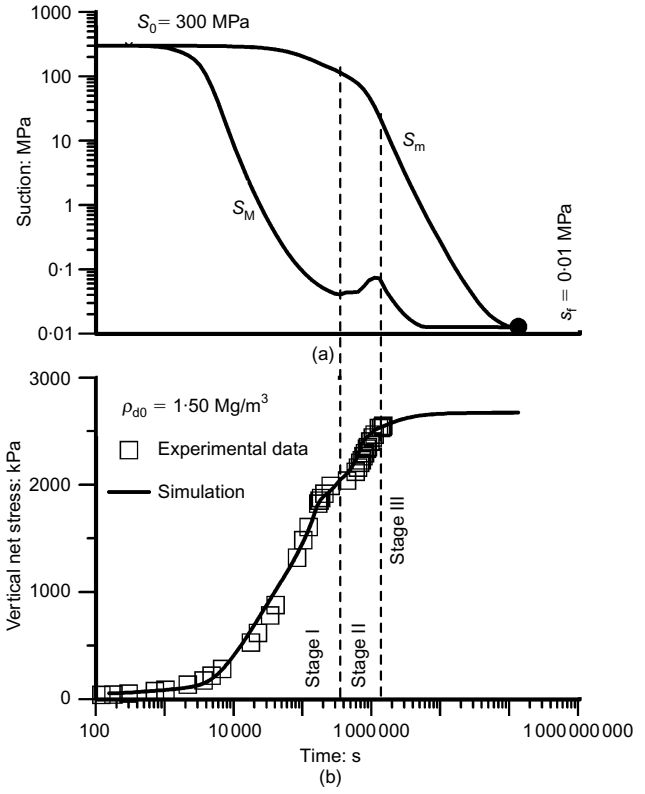

Fig. 22. Swelling pressure test (mixture at dry density 1·50 Mg/m^3): (a) simulated time evolutions of micro- and macrostructural suctions; (b) simulated time evolution of vertical stress and comparison with experimental results

$$\mathrm{d}\varepsilon^e_{vM} = -\frac{\mathrm{d}e_M}{1+e} = \frac{\mathrm{d}p}{K_{pM}} + \frac{\mathrm{d}s_M}{K_{sM}} \tag{8}$$

where $K_{pM} = (1+e)p/\kappa_p$ and $K_{sM} = (1+e)(s_M + p_{atm})/\kappa_s$ are the elastic bulk moduli with respect to p and s_M changes (p_{atm} is the atmospheric pressure). Compressibility moduli against p and s_m changes are $\kappa_p(s_M) = \kappa_{po}(1 + \alpha_p s_M)$ and

$$\kappa_s(s_M,\ p) = \kappa_{so}\left[1 + \alpha_{sp}\ln s_M\left(\frac{p}{p_{ref}}\right)\right]e^{\alpha_{ss}s_M}$$

Plastic deformations and hardening laws

Irrecoverable compressive deformations at macrostructural level induced on activation of the LC yield curve on loading and wetting (Fig. 13), are given by

$$\mathrm{d}\varepsilon^p_{vM} = \frac{[\lambda(0) - \kappa_p(s_M)]}{1+e}\frac{\mathrm{d}p_o}{p_o} \tag{9}$$

$$p_o = p^c\left(\frac{p^*_o}{p^c}\right)^{\frac{\lambda(0)-\kappa(s_M)}{\lambda(s_M)-\kappa(s_M)}} \tag{10}$$

$$\lambda(s_M) = \lambda(0)\left[r + (1-r)e^{-\beta s_M}\right] \tag{11}$$

where $\lambda(s_M)$ is the slope of the virgin compression line at suction s_M.

The hardening law for LC is

$$\frac{\mathrm{d}p^*_o}{p^*_o} = \frac{(1+e_M)}{\lambda(0) - \kappa_p(s_M)}\mathrm{d}\varepsilon^p_{vM} \tag{12}$$

The SD (suction-decrease) yield locus, corresponding to the microstructural level, is considered to be parallel to the neutral line at constant $\hat{p}$ (Fig. 13). Irrecoverable expansive deformations at microstructural level associated with the activation of the SD yield locus on wetting are given by

$$SD_0 - \hat{p} = 0 \tag{13}$$

$$\mathrm{d}\varepsilon^p_{vm} = \frac{(\lambda_m - \kappa_m)}{1+e_m}\frac{\mathrm{d}\hat{p}}{\hat{p}} \tag{14}$$

Hardening of SD yield surface is governed by the plastic microstructural strain

$$\frac{\mathrm{d}SD_o}{SD_o} = \frac{(1+e_m)}{\lambda_m - \kappa_m}\mathrm{d}\varepsilon^p_{vm} \tag{15}$$

Parameters of the model (κ_m, χ, λ_m, κ_{po}, α_p, α_{sp}, α_{ss}, p_{ref}, $\lambda(0)$, r, β, p^c) are summarised in Table 2.

REFERENCES

Alonso, E. E. & Hoffmann, C. (2007). Modelling the field behaviour of a granular expansive barrier. *Physics Chem. Earth* **32**, Nos 8–14, 850–865.

Alonso, E. E., Gens, A. & Josa, A. (1990). A constitutive model for partially saturated soils. *Géotechnique* **40**, No. 3, 405–430, **doi**: 10.1680/geot.1990.40.3.405.

Alonso, E. E., Vaunat, J. & Gens, A. (1999). Modelling the mechanical behaviour of expansive clays. *Engng Geol.* **54**, No. 1–2, 173–183.

García-Siñeriz, J. L., Rey, M. & Mayor, J. C. (2008). The engineered barrier experiment at Mont Terri Rock Laboratory. *Andra, Sci. Technol. Ser.* **334**, 65–75.

Gens, A. & Alonso, E. E. (1992). A framework for the behaviour of unsaturated expansive clays. *Can. Geotech. J.* **29**, No. 6, 1013–1032.

Hoffmann, C. (2005). *Caracterización hidromecánica de mezclas de pellets de bentonita. Estudio experimental y constitutivo* (in Spanish). PhD thesis, Universitat Politècnica de Catalunya, Barcelona. See http://www.tdx.cat/TDX-0518105-163209 for further details (accessed 03/09/2010).

Hoffmann, C., Alonso, E. E. & Romero, E. (2007). Hydro-mechanical behaviour of bentonite pellet mixtures. *Physics Chem. Earth* **32**, Nos 8–14, 832–849.

Lloret, A., Villar, M. V., Sánchez, M., Gens, A., Pintado, X. & Alonso, E. E. (2003). Mechanical behaviour of heavily compacted bentonite under high suction changes. *Géotechnique* **53**, No. 1, 27–40, **doi**: 10.1680/geot.2003.53.1.27.

van Genuchten, M. T. (1980). A closed-form equation for predicting the hydraulic conductivity of unsaturated soils. *Soil Sci. Soc. Am. J.* **44**, No. 5, 892–898.

Boyd, J. L. & Sivakumar, V. (2011). *Géotechnique* **61**, No. 4, 345–363 [**doi:** 10.1680/geot.2011.61.4.345]

Experimental observations of the stress regime in unsaturated compacted clay when laterally confined

J. L. BOYD* and V. SIVAKUMAR†

Construction processes often involve reformation of the landscape, which will inevitably encompass compaction of artificially placed soils. A common application of fill materials is their use as backfill in many engineering applications, for example behind a retaining wall. The post-construction behaviour of clay fills is complex with respect to stresses and deformation when the fills become saturated over time. Heavily compacted fills swells significantly more than the lightly compacted fills. This will produce enhanced lateral stresses if the fill is laterally restrained. The work presented in this paper examines how the stress regime in unsaturated clay fills changes with wetting under laterally restrained conditions. Specimens of compacted kaolin, with different initial conditions, were wetted to various values of suction under zero lateral strain at constant net overburden pressure which allowed the concept of K_0 (the ratio between the net horizontal stress and the net vertical stress) to be examined. Tests were also carried out to examine the traditional concept of the earth pressure coefficient 'at rest' under loading and unloading and its likely effects on the stress–strain properties. The results have shown that the stress regime (i.e. the lateral stress) changes significantly during wetting under laterally restrained conditions. The magnitude of the change is affected by the initial condition of the soil. The results have also indicated that the earth pressure coefficient 'at rest' during loading (under the normally consolidated condition) is unaffected by suction and such loading conditions inevitably lead to the development of anisotropic stress–strain properties

Les procédés de construction comportent souvent une altération du paysage, comprenant inévitablement le tassement de sols placés artificiellement. Une application commune des matériaux de remblayage est leur utilisation comme remblai dans de nombreuses applications d'ingénierie, par exemple derrière un mur de soutènement. Le comportement post-construction des remblais d'argile est complexe, en ce qui concerne les contraintes et la déformation, lorsque les remblais finissent par être saturés. Les remblais fortement tassés gonflent beaucoup plus que des remblais légèrement compactés, ce qui engendre un renforcement des contraintes latérales si le remblai est encastré latéralement. Les travaux décrits dans la présente communication examinent la façon dont le régime de contrainte dans des remblais d'argile non saturés évolue en fonction de leur mouillage, lorsqu'ils sont encastrés latéralement. Pour ceci, on procède au mouillage de spécimens de kaolin compacté, présentant différentes conditions initiales, avec différentes valeurs d'aspiration sous une déformation latérale nulle avec une pression de recouvrement net constante, qui permettait l'examen du concept de K_0 (ratio entre la contrainte horizontale nette et contrainte verticale nette). On a également effectué des essais pour examiner le concept traditionnel du coefficient de pression de la terre « au repos », en condition de sollicitation et de décharge, et ses effets probables sur les propriétés de contrainte-déformation. Les résultats indiquent que le régime de contraintes (autrement dit les contraintes latérales) varie de façon significative sous l'effet du mouillage, dans des conditions d'encastrement latéral. L'état initial du sol affecte l'envergure de ces variations. Les résultats indiquent également que le coefficient de pression de la terre « au repos », au cours de la sollicitation (en condition de consolidation normale), n'est pas affecté par l'aspiration, et que ces sollicitations donnent lieu inévitablement au développement de propriétés de contrainte-déformation anisotropes.

KEYWORDS: retaining walls; stress path; suction

INTRODUCTION

Construction processes often involve reformation of the landscape, which will inevitably encompass compaction of artificially placed soils. During compaction, soils are generally placed in an unsaturated state for ease of placement. The increasing economic and environmental costs of granular fill materials are causing the construction industry to look for alternative construction materials, such as site-won clayey soils (i.e. the material excavated from the site or nearby location). A common application of fill materials is their use as backfill in many engineering applications, for example behind a retaining wall. The post-construction behaviour of clay fills is complex with respect to stresses and deformation when the fills become saturated over time.

The behaviour of unsaturated soils is not covered by engineering standards with respect to geotechnical design. Guidelines do, however, exist for the performance of on-site compaction (*Design Manual for Roads and Bridges*, Highways Agency, 1995; *Specification for Highway Works*, Highways Agency, 2004). Difficulties encountered when unsaturated soils become saturated include loss of shear strength and volumetric responses ranging from collapse compression to swelling (Alonso *et al.*, 1990; Charles, 1993; Lu & Likos, 2004; Sivakumar *et al.*, 2010a). Volume change behaviour is the biggest problem when working with unsaturated soils, where collapse compression can lead to excessive

Manuscript received 8 December 2009; revised manuscript accepted 7 December 2010.
Discussion of this paper closes on 1 September 2011; for further details see p. ii.
* University of Ulster, Newtonabbey (formerly postgraduate student at Queen's University Belfast).
† School of Planning, Architecture and Civil Engineering, Queen's University Belfast, Belfast.

settlements while swelling can produce ground heave (Sitharam *et al.*, 1995; Skinner, 2001); both of these can lead to differential settlements (Charles *et al.*, 1993; Skinner *et al.*, 1999; Blanchfield & Anderson, 2000).

Since the early 1990s, research in the topic of unsaturated soils has focused on the development of constitutive models (Alonso *et al.*, 1990; Toll, 1990; Wheeler, 1991; Delage & Graham, 1995; Wheeler & Sivakumar, 1995; Cui & Delage, 1996; Tang & Graham, 2002; Blatz & Graham, 2003; Gallipoli *et al.*, 2003; Wheeler *et al.*, 2003; Tarantino, 2007; Sivakumar *et al.*, 2010a, 2010b). The basic Barcelona model uses the classical assumption of elastic behaviour prior to yielding and elasto-plastic behaviour after yielding. Suction is also considered as one of the stress parameters that affects yielding.

Saturation of heavily compacted clays produces a greater volumetric swelling response than lightly compacted clays (Alonso *et al.*, 1990; Wheeler & Sivakumar, 1995; Thom *et al.*, 2007). Fig. 1 shows the results where the heavily compacted specimens swelled significantly more than the lightly compacted specimens during wetting from initial suction of 960 kPa (Sivakumar *et al.*, 2010a). This suggests that in situ heavily compacted fill is more likely to produce swelling during wetting than lightly compacted fill. An important question remains, what effects would the wetting have on the stress regime within heavily compacted fills and therefore on the buried or rigid retaining structures?

Consider an element of soil behind the face of the retaining structure, back-filled with compacted clay as shown in Fig. 2. In temperate climates the water table will rise over time and the fill becomes saturated. This wetting process could produce volumetric responses of either swelling or collapse. If swelling takes place under laterally confined conditions the likely consequence will be the development of high lateral stresses acting on the rigid retaining structure. The increase in lateral stresses may cause stability issues with the wall (Chen, 1987; Carder, 1988). In a limited study, Maswoswe (1985) examined the stress path of unsaturated compacted specimens of glacial till during wetting (under K_0 conditions) in which the suction was reduced to zero (soaking tests). The stress path for the specimens wetted under K_0 conditions ended on the saturated, normally consolidated K_0 line.

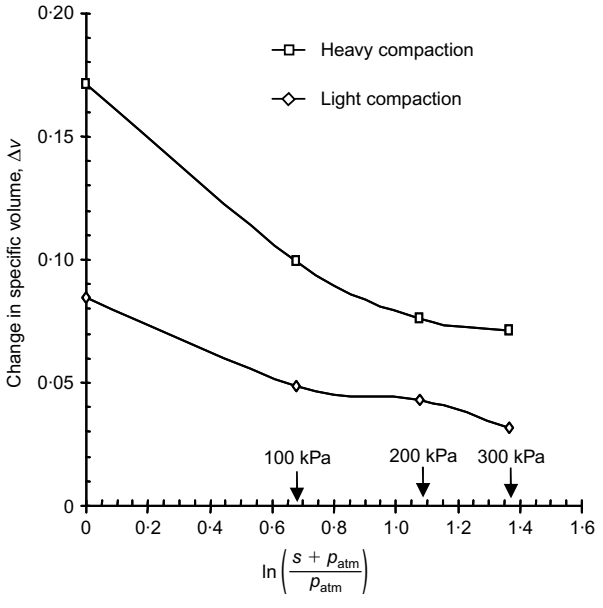

Fig. 1. Change in specific volume plotted against ln $(s + p_{atm})/p_{atm}$ during wetting for kaolin soil, both lightly and heavily compacted (after Sivakumar *et al.*, 2010a)

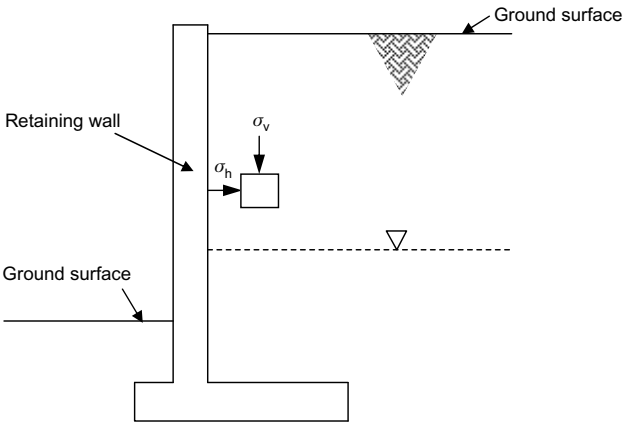

Fig. 2. Compacted fill placed behind a retaining structure

The work presented in this paper examines how the stress regime in unsaturated clay fills changes with wetting under laterally restrained conditions. Specimens of compacted kaolin with different initial conditions were wetted to various values of suction under laterally restrained conditions at constant net overburden pressure. This allowed the concept of K_0 (the ratio between the net horizontal stress and the net vertical stress) given by the following equation to be examined.

$$K_0 = \frac{\sigma_h - u_a}{\sigma_v - u_a} \tag{1}$$

where σ_v, σ_h and u_a are the total vertical, total horizontal and pore air pressures respectively.

Alonso *et al.* (1990) presented the Barcelona basic model (BBM), which is defined in terms of four stress state variables: mean net stress $\bar{p}$, deviator stress q, suction s and specific volume v. The model is intended for use with slightly or moderately expansive soils. Isotropic loading conditions are modelled using two yield curves, the loading collapse (LC) yield locus and the suction increase (SI) yield locus, which are shown in Fig. 3. When the state of the soil is inside the yield curve a reduction in suction (path AB) will lead to swelling until the LC yield locus is reached. Further reduction in the suction (path BC) will lead to plastic collapse. An increase in compactive effort will lead

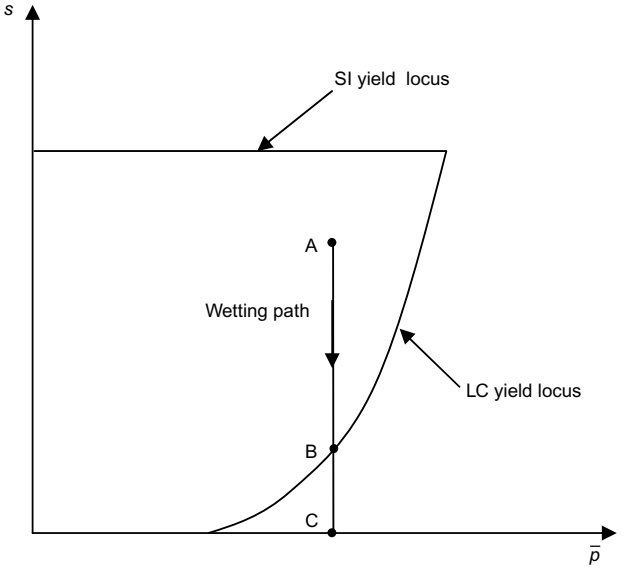

Fig. 3. Loading collapse and SI yield loci in the $\bar{p}$–s plane for isotropic conditions

to an enlargement of the yield locus, including a change in shape (Maãtouk *et al.*, 1995; Wheeler & Sivakumar, 2000). The size of the yield locus is also affected by the compaction water content and the type of compaction (Maãtouk *et al.*, 1995; Wheeler & Sivakumar, 2000; Estabragh *et al.*, 2004; Sivakumar *et al.*, 2010a). The work presented in this paper assesses the effects of compaction effort and compaction water content on the development of lateral stresses and therefore on the earth pressure coefficient K_0.

In saturated soil the magnitude of K_0 is given by the ratio between the horizontal effective stress and the vertical effective stress. The value of K_0 is constant for normally consolidated clays and increases with over-consolidation ratio (OCR). As part of the research presented here an attempt is also made to assess the concept of K_0 resulting from loading and unloading. The following section describes the experimental programme undertaken to meet these tasks.

EXPERIMENTAL PROGRAMME

The subject of this research is the response of compacted fill, retained behind a rigid structure when subjected to wetting. Obviously research of this calibre requires a sophisticated testing system and suitable testing programme. The following sections give details on the

(*a*) sampling technique
(*b*) experimental set-up
(*c*) control program
(*d*) testing programme.

Sampling

The material chosen for the present research was commercially available speswhite kaolin clay supplied by WhitChem Ltd. The original intention of the authors was to complement the current research with work previously reported by the research team at Queen's University Belfast (QUB) (Wheeler & Sivakumar, 1995; Sivakumar & Wheeler, 2000; Wheeler & Sivakumar, 2000; Sivakumar *et al.*, 2006; Thom, 2007; Sivakumar *et al.*, 2010a; 2010b). Initial characterisation performed on kaolin purchased for the present research deviated considerably from the characteristics reported in the above literature studies. This was caused by significant differences between the material used in the present research and that used in the previous research, which was identified to be the percentage of the clay fraction, with a 40% clay-sized fraction in the material used in the present research as opposed to an 80% clay-sized fraction in the material used previously. Table 1 lists the characteristics of the material used in the current research.

The method chosen for preparing 50 mm diameter, 100 mm high specimens was that proposed by Sivakumar *et al.* (2010a). Dry kaolin powder was mixed with water at targeted moisture contents in a domestic food mixer before being passed through a 1·18 mm aperture sieve. Large aggregates not passing through the sieve were broken up using a pestle and mortar and sieved again. The material was stored in an air-tight container in a temperature-controlled environment for 48 h. A 100 mm diameter rubber membrane was placed around a 100 mm diameter pedestal of a standard triaxial cell and sealed to the base using two O-rings. A membrane stretcher was placed around the membrane and the top of the membrane was folded at the top of the stretcher. A 100 mm diameter dry porous disc was placed on the pedestal and the sieved material was filled slowly into the membrane. With the membrane full, a top cap of dry porous stone was placed on the moistened kaolin, the membrane stretcher was removed and the top cap was sealed with two O-rings. The height of the uncompressed sample was just over 225 mm and the diameter was about 100 mm. The cell was assembled and pressurised to the required value, based on the target initial specific volume. Any excess air pressure, developed as a result of the application of the external pressure, was allowed to drain from the top and bottom of the sample. There was no evidence of water drainage during this process. Although consolidation usually took place quickly, the sample was left in the compression system for 3 days as a standard procedure. At the end of this time the confining pressure was reduced to zero. The size of the sample after compression was approximately 70 mm in diameter and 140 mm high. A thin-walled sample tube was used to extract a specimen of 50 mm diameter and 100 mm high (Fig. 4). Specimens for the present research were produced at two different initial water contents: 23% and 25% (representing dry fill and wet fill) and at two different compression pressures: 375 kPa and 750 kPa (representing unengineered fill and engineered fill). The relevant initial specific volumes of these specimens are listed in Table 2.

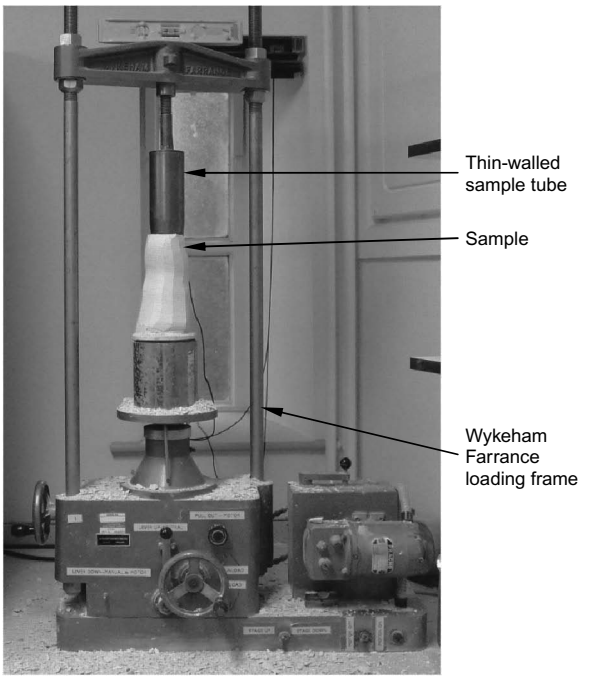

Fig. 4. Set-up for specimen cutting

Table 1. Characteristics of current research material

Percentage clay-sized fraction	Liquid limit	Plastic limit	Plasticity index	Activity	Clay mineral identified by XRD*
40%	70%	34%	36%	90%	Kaolinite, mica and quartz

* XRD: X-ray diffraction

Table 2. Initial characteristics of compressed fill for K_0 testing programme

w: %	ρ_b: kg/m^3	Relative to standard Proctor, $\rho_b/\rho_{b(St\ Proc)}$	Fill name	v	v_w	S_r: %	s: kPa	Applied suction: kPa				
								Zero	100	150	200	300
23	1557	0·95	Dry unengineered	2·088	1·600	55·2	811	—	√	—	—	—
	1701	1·05	Dry engineered	1·925	1·607	65·8	1035	√	√	√	√	√
25	1640	0·96	Wet unengineered	2·022	1·666	65·2	704	—	√	—	—	—

Experimental set-up

The experimental system was designed and fabricated in such a way that it can be used for model wetting, loading and unloading of unsaturated compacted specimens, when laterally confined. A 'twin cell' recently developed at QUB was used in the research (Sivakumar *et al.*, 2006), although some modifications were made in order to meet the requirements of the present research. Fig. 5(a) shows the cross-sectional view of the modified twin-cell system. The system was instrumented with internal strain gauges, inclinometers (Jardine *et al.*, 1984) to measure axial strain and a strain belt to measure diametric strain (manufactured by Imperial College Consultants). In addition, the inner cell was assembled under water for accurate measurements of specimen volume change (Sivakumar *et al.*, 2006).

The testing programme aimed to replicate the in situ behaviour of compacted fill when laterally restrained, for example behind a retaining wall. Under these conditions the overburden pressure will not change (assuming no further loading is applied post-construction). Therefore, in the present research, throughout the wetting stage the control program was used to maintain a constant net vertical pressure. The cell pressure was used to maintain the zero lateral strain condition. In the event of an increase in cell pressure (i.e. in order to contain lateral expansion) a constant vertical pressure was maintained by altering the lower chamber pressure, thus applying a negative deviator stress. This required a special tension loading arrangement on the top cap. The supporting base of the inner cell was threaded and it was screwed on to the threaded pedestal of the Bishop and Wesley stress path apparatus (Fig. 5(b)).

The tension loading mechanism was based on the design of a manhole key. A photograph of the key is shown in Fig. 5(g). The key had one end threaded on to the load cell and the other end was formed to a bucket shape. Fig. 5(f) shows the special arrangement made on the top cap to apply tension loading. This consisted of a metal bracket which had a small slot in the middle, slightly wider than the key thickness. Fig. 5(e) shows the arrangement during testing when the key was engaged in position with the top cap. After slotting in place, the key was turned through 90°. The other end of the load cell was attached to the top plate of the outer cell. The load cell end was threaded on to an end cap, which had three threaded bars protruding from it. A stainless steel plate was located on the other end of the threaded rods as shown in Fig. 5(d). Nuts and washers were placed either side of the plate, which allowed manual adjustment to be made on the location of the plate if required. The load cell was fastened to the top plate of the outer cell using a custom-made bolt (50 mm diameter head and 120 mm long) threaded through the stainless steel plate located on the threaded rods (Fig. 5(c)). The bolt could be gently turned until its flat face interfaced with the top plate of the outer cell. This bolt was held in position by locating another cap which was fastened to the top plate of the outer cell. When fastened fully, the underside of this cap flushed with the top face of the bolt so that any movement of the load cell was restricted.

Control program

The control program Triax version 5·1 (Toll, 1999) was utilised to control the required testing conditions automatically. Suction was controlled using the axis translation technique (Hilf, 1956). Stepper motor-driven regulators were used for controlling pore air pressure, pore water pressure, cell pressure and deviator stress. K_0 control was automatically achieved by controlling confining pressure during wetting, loading and unloading.

Testing programme

Table 2 lists the tests conducted in the research. Additional tests were also conducted in order to establish the LC yield locus traced by the initial compression process. The majority of the tests involved four stages, which are described as follows.

(*a*) Initial application of relevant confining, pore water and pore air pressures: the initial state of the specimen, after extraction using a sampling tube is represented by O in Fig. 6(a). At this stage the initial mean net stress and deviator stress in the specimen are zero. The suction in the specimen refers to the values independently measured using a Wescor PST-55 thermocouple psychrometer, which are listed in Table 2. The cell, pore water and pore air pressures were ramped at a rate of 25 kPa/min in order to achieve target suction values of 300, 200, 150, 100 kPa or zero at the drainage boundaries and a mean net stress of 50 kPa.. The state of the specimen immediately after the application of these pressures is represented by point A in Fig. 6(a). During this initial application of pressures the condition of K_0 was not activated and the process resulted in a small influx of water into the specimen (0·60 cm^3).

(*b*) Wetting of the specimen to a pre-selected suction: in this stage the externally applied suction at the drainage boundaries was allowed to equalise within the specimen, which usually lasted about 7 days. During this period the condition of K_0 was activated with a lateral strain tolerance of 0·005% (representing 0·0025 mm on a 50 mm diameter specimen). The state of the specimen after equalisation is represented by points B, C, D, E and F when the specimen has reached the target suction values of 300, 200, 150, 100 kPa and zero respectively. However, mean net stress at this point is determined by the response of the soil to meet the condition of zero lateral strain. The authors are aware that the control is based on the strain performance of the specimen at the centre, while the wetting begins at the base of the specimen, where the pore water pressure is controlled. The original intention of the research was to wet the specimen slowly by reducing the suction from its initial

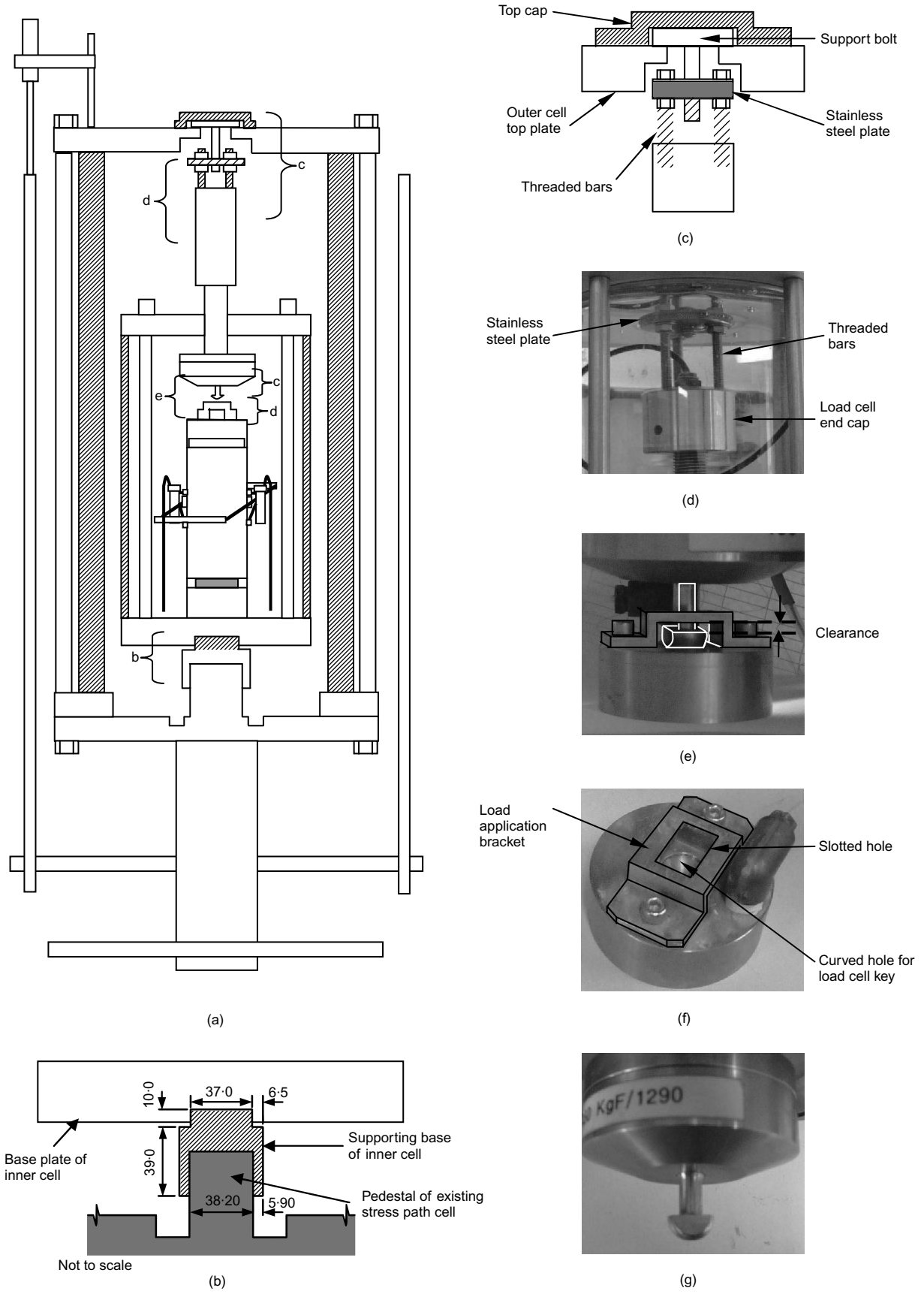

Fig. 5. Testing equipment: (a) modified twin-cell system; (b) threaded pedestal of outer cell; (c) arrangement for supporting load cell end; (d) load cell end arrangement; (e) key and bracket engaged during loading; (f) top cap loading bracket; and (g) load cell key

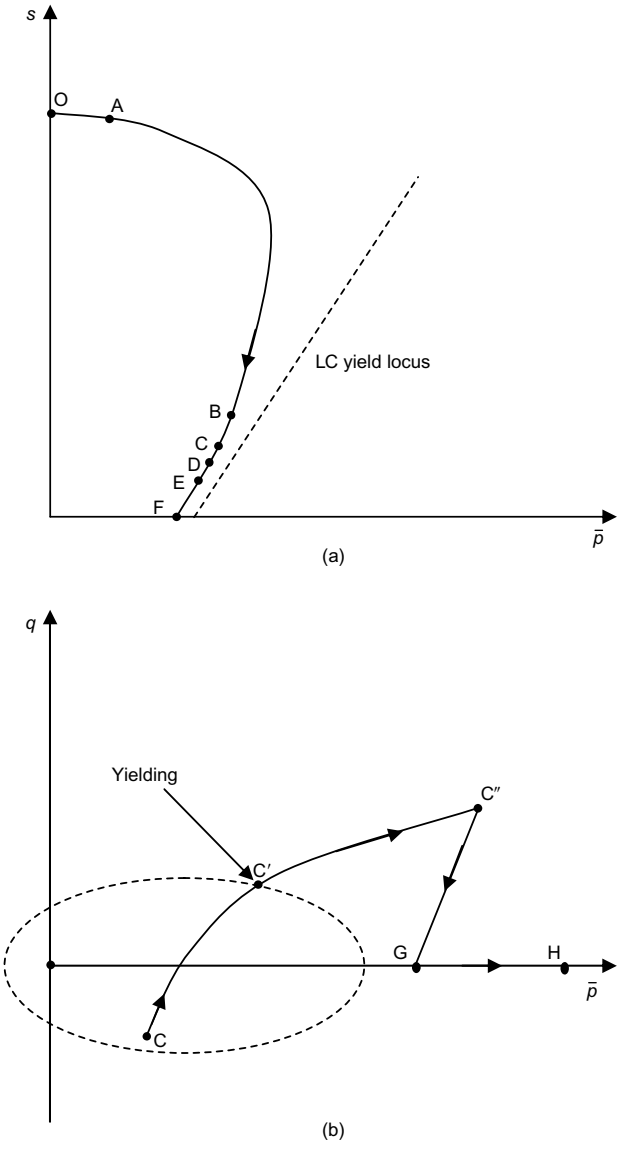

Fig. 6. Stress paths during experiments: (a) K_0 wetting and (b) K_0 loading, K_0 unloading and isotropic loading

value to zero over a long period. However, the plan was abandoned owing to problems encountered in the control program (i.e. with the older version of Triax, which operated on DOS mode).

(*c*) Loading of the specimen under constant suction: the deviator stress was increased at pre-selected rates. The K_0 loading begins from the point where the stress path terminated during K_0 wetting. A typical case for a suction value of 200 kPa is schematically illustrated in Fig. 6(b) (i.e. point C). Three different rates were adopted: 0·6 kPa/h for the first 3 days; 0·4 kPa/h until a sign of yielding was noted and 0·2 kPa/h for the remainder of the loading stage. The reason for adopting the lower rates at the later stages of the loading was to avoid a rapid increase in confining pressure in order to meet K_0 conditions, particularly when the specimen has yielded. During the entire loading the suction was maintained at a constant value.

(*d*) Unloading under constant suction: during this stage the deviator stress was reduced to zero, under constant suction, at a rate of 0·6 kPa/h (path C″G in Fig. 6(b)) while the horizontal strain was maintained at zero. In one of the tests the specimen, subsequent to K_0 unloading, was taken through isotropic loading until a clear sign of yielding under constant suction was achieved (path GH in Fig. 6(b)).

RESULTS AND DISCUSSION

Owing to the complex nature of the experimental programme the results are discussed under specific headings to simplify the presentation:

(*a*) initial characterisation of the specimen with reference to the initial position of the yield locus
(*b*) conceptual modelling
(*c*) K_0 in unsaturated soils during wetting and the effects of initial conditions on its magnitude
(*d*) effects of bi-modal pore size distribution on the deformation under K_0 conditions
(*e*) K_0 during loading and unloading and the effects of initial conditions on its magnitude
(*f*) K_0 loading-induced anisotropy.

Initial characterisation of the specimen with reference to the initial position of the yield locus

As part of characterisation the specimens were tested under isotropic stress conditions (i.e. without K_0 control) and subsequently sheared under drained conditions. During equalisation water flowed into the specimen. The intake of water was 37·3, 20·2, 12·5 and 9·9 cm^3 for suctions of zero, 100, 200 and 300 kPa respectively. Fig. 7 shows the changes in specific volume of dry engineered specimens (23H) plotted against suction. A significant amount of swelling was observed in the case of the dry-engineered specimen wetted to zero suction, although as expected the swelling was limited under other values of suction.

Subsequent to the initial equalisation, the specimens were taken through isotropic compression at constant suction. Fig. 8(a) shows the compression lines plotted against natural logarithm of mean net stress for dry engineered specimens (23H). A simple graphical construction was used to determine the approximate yield stress. Although there are other methods available to determine yield stresses (Crooks & Graham, 1976) the Casagrande (1936) technique was chosen for the present purpose. The relevant yield stresses measured at suction values of zero, 100, 200 and 300 kPa were plotted

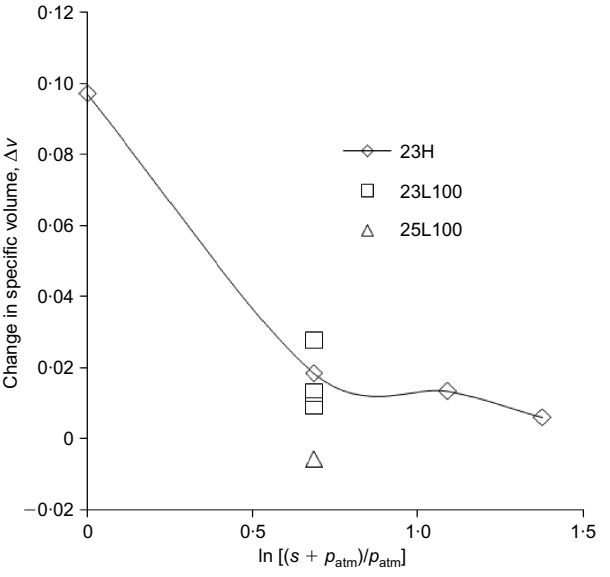

Fig. 7. Change in specific volume plotted against suction during wetting (dry engineered specimens – 23H)

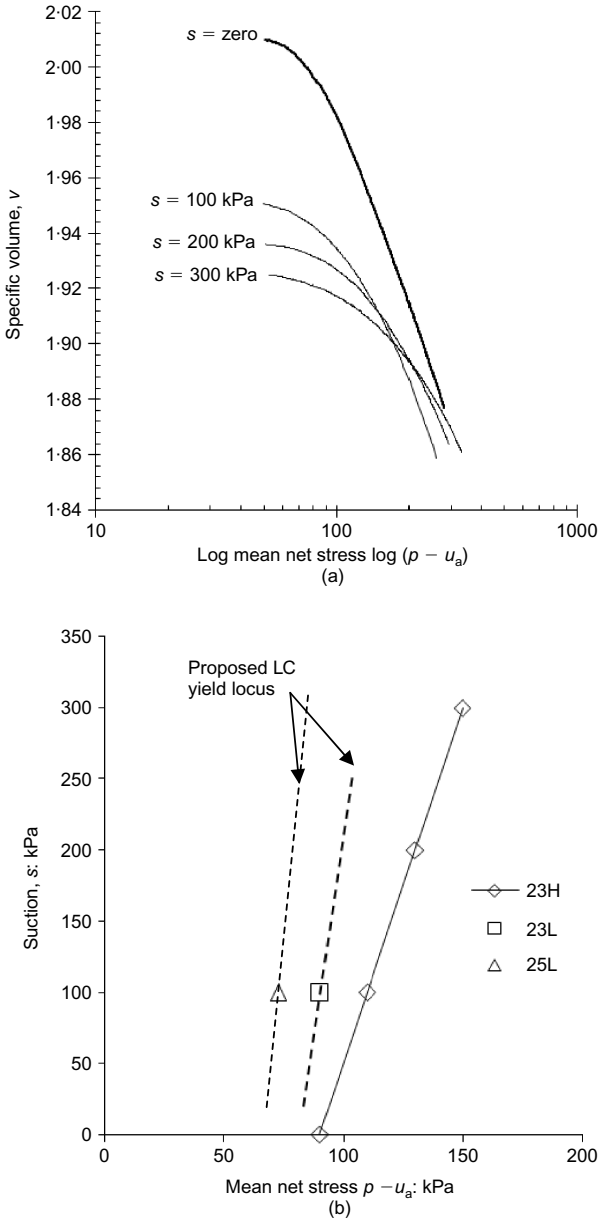

Fig. 8. Sample response to isotropic loading of dry engineered specimens: (a) specific volume plotted against logarithm of mean net stress and (b) loading collapse yield loci (LCYL) for dry engineered specimens (23H), including proposed LCYL for dry unengineered (23L) and wet unengineered specimens (25L)

to form the LC yield locus as shown in Fig. 8(b). The form of the LC yield locus is a straight line in s–$\bar{p}$ space and the shape of it is in close agreement with the previously reported data on kaolin by Sivakumar *et al.* (2010a), although distinctly different from the proposals of Alonso *et al.* (1990), Wheeler & Sivakumar (1995) and Sivakumar & Wheeler (2000). The form of the yield locus that was reported by Alonso *et al.* (1990) and Wheeler & Sivakumar (1995) was a curve, which was obtained on specimens that were one-dimensionally compressed before testing. The one-dimensional loading history, inherited by the specimen during its initial formation, may have led to a degree of anisotropy. Sivakumar *et al.* (2010a) reported LC yield locus, which was a straight line in s–$\bar{p}$ space and it was obtained using specimens prepared by isotropic compression before testing. This should have led to specimens inheriting isotropic stress–strain properties. Further details on this aspect can be found in Sivakumar *et al.* (2010a).

The estimated yield stresses at a suction value of 100 kPa on the dry unengineered specimen (23L) and wet unengineered specimen (25L), denoted by square and triangular data points respectively, are also included in Fig. 8(b). The positions of the LC yield loci shown using broken lines in Fig. 8(b) for these two specimens are only an approximation. The wetting under K_0 conditions originated from point A (Fig. 6(a)). If the wetting path remains inside the yield locus the specimen would swell axially as well as laterally. The lateral expansion is restricted by an increase in confining pressure and therefore the position of the LC yield locus shown in Fig. 8(b) is the prelude to most of the discussion presented in this paper. In order to simplify the presentation of the data, a conceptual view of the anticipated behaviour is presented first and subsequently validated with the observed response of the soil.

Conceptual modelling

Figure 9(a) shows a three-dimensional schematic view of the yield surface in q–$\bar{p}$–s space. The intersection of the yield surface on a constant q plane is shown in Fig. 9(b). The cross-section of the yield surface parallel to the constant suction plane is an ellipse and its major principal axis coincides with the mean net stress plane as shown in Fig. 9(c). The cross-section of the yield surface parallel to the constant $\bar{p}$ plane is also shown in Fig. 9(d). The initial position of the specimen is represented by point O, where the mean net stress is zero, the deviator stress is zero and the initial suction in the specimen is listed in Table 2. Upon the application of initial pressures, the state of the specimen moves to point A, where $q = 0$ and $\bar{p} = 50$ kPa, the zero lateral strain condition is invoked at this point. The initial position of each specimen is well within the LC yield locus, thus any reduction in suction will result in radial and axial expansion, provided the wetting paths do not cross the yield surface. Upon lateral swelling the control program is activated to increase the lateral pressure to restrain the lateral expansion. ABCDEF represents the wetting path during which the lateral strain was maintained at zero. Points B, C, D, E and F represent target suction values of 300, 200, 150, 100 kPa and zero respectively. The vertical stress is maintained at 50 kPa during the wetting and therefore the stress path will be contained on a plane with a slope of 2/3, as shown in Fig. 9(a). The relevant projections of the stress paths on s–$\bar{p}$, q–$\bar{p}$ and q– s are also shown in Figs 9(b)–9(d).

Continued swelling, caused by the wetting, instigates a further increase in lateral pressure. Such an increase in the lateral pressure, together with the continued reduction in deviator stress (an increase in negative deviator stress, Fig. 9(d)) also triggers inter-aggregate slippage, creating a tendency for collapse settlement. This in theory implies that the stress path approaches the yield surface, initially inherited by the specimen during its formation, as shown in Fig. 9(a). This particular situation is represented by point X. The point at which the wetting path approaches the yield surface depends on the initial conditions of the specimen. At the point when the specimen approaches close to the yield surface, the collapse settlement will become imminent and the control system activates to decrease the lateral stress in order to maintain the zero lateral stress condition. Therefore the direction of the stress path will change and the stress state of the specimen moves slightly back inside the yield surface. This process will continue until the suction in the specimen has fully equalised at the pre-selected suction value. Since the suction applied to the specimen was reduced in one single step from its initial value to the relevant target suction, the lateral stress will increase and decrease often

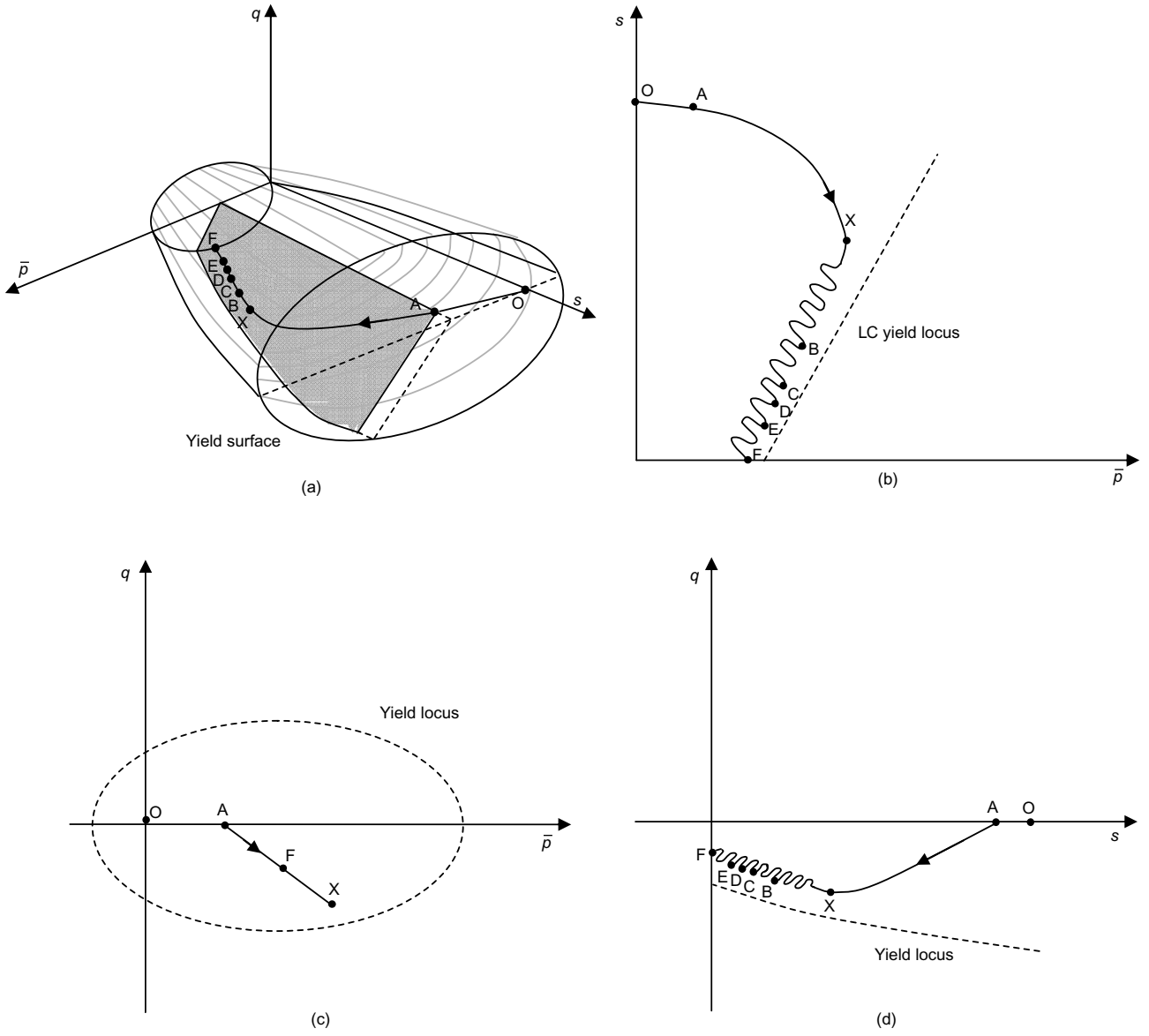

Fig. 9. Conceptual modelling in: (a) $q–\bar{p}–s$ space; (b) $s–\bar{p}$ plane; (c) $q–\bar{p}$ plane; and (d) $q–s$ plane

until equilibrium is achieved. This can result in fluctuations of deviator stress and mean net stress. The fluctuation could be avoided if the suction was reduced slowly from its initial value. The stress path traversing close to the yield surface is therefore represented by a wavy curve to reflect the nature in which the control program attempts to maintain zero lateral strain conditions. The data presented in the next section quantify this conceptual view.

K_0 in unsaturated soils during wetting and the effects of initial conditions on its magnitude

Five tests were conducted on dry engineered specimens having an initial specific volume of 1·925. The specimens were brought to suction values of zero, 100, 150, 200 and 300 kPa from the initial suction of 1035 kPa generated at the time of specimen preparation. The results obtained from these tests are analysed in various forms, culminating with the assessment of K_0 in unsaturated soils subjected to wetting. Table 3 lists the phase values after the K_0 wetting stage was completed.

Figure 10 shows the change in specific water volume plotted against time. A specific point on each curve is marked with a circular point. The relevance of these points will be discussed later in this paper. The relevant changes in specific water volume caused by wetting the specimens to suctions of zero, 100, 150, 200 and 300 kPa under laterally constrained conditions were 0·359, 0·213, 0·175, 0·149 and 0·080, respectively. The equalisation phase was terminated when the water flow into the specimen was less than 0·1%/day with respect to the dry mass of the specimen. The influx of water resulted in an increase (or decrease) in the specimen volume and therefore a change in the lateral strain. A tolerance level of ±0·0025 mm (±0·005% in terms of lateral strain) was set as a trigger level and Fig. 11 shows how well this condition was achieved.

Figure 12 shows the lateral and vertical net stresses plotted against time for the tests equalised under suction values of zero, 100 and 300 kPa. The lateral net stress increased rapidly at the beginning of the equalisation process implying that the specimen attempted to expand laterally. There were some fluctuations in the net lateral stress as the equalisation stage progressed. The reason for this fluctuation is the fact that the stress path upon wetting under K_0 conditions was operating close to the yield surface (Fig. 9). This was also instigated by a steep decrease in suction from

Table 3. Phase values after K_0 wetting

Test	v	v_w	S_r: %	$\bar{p}$: kPa	q: kPa
23H0	1·987	1·984	96·9	66	−24
23H100	1·973	1·844	86·8	69	−29
23H150	1·988	1·782	79·2	77	−40
23H200	1·997	1·751	75·3	83	−49
23H300	1·947	1·686	72·4	84	−50
23L100	2·125	1·839	74·6	54	−8
25L100	2·034	1·802	77·5	69	−34

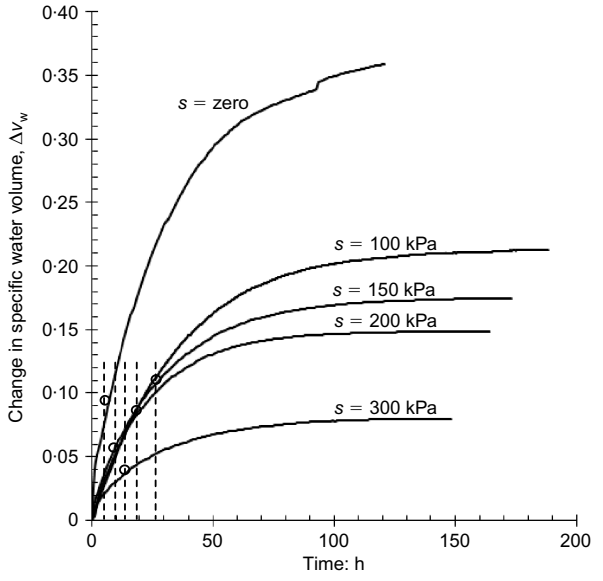

Fig. 10. Change in specific water volume during K_0 wetting of dry engineered specimens

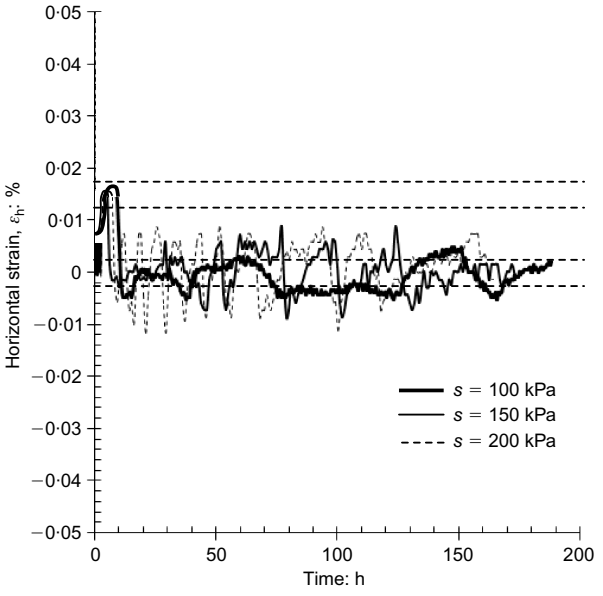

Fig. 11. Horizontal strain plotted against time for dry engineered specimens equalised under suction values of 100, 150 and 200 kPa

its initial value of 1035 kPa to a much lower value as discussed in the conceptual view of the anticipated behaviour. As shown in Fig. 12 the vertical net stress remained constant at 50 kPa in every test during the course of wetting.

It was obviously a concern that the K_0 condition was activated based on the lateral strain measured at the mid-height of the specimen, whereas the wetting front moves upwards from the base. It could be argued that the specimen at the bottom may have swelled laterally before the K_0 control became activated, based on the specimen response at mid-height. The height of the specimen used in the present study was 100 mm. The radial strain gauge was located at mid-height of the specimen. The pads attached on the arms of the axial strain gauges were located 23 mm above the base of the specimen and 37 mm below the top of the specimen, as shown in Fig. 13. During the equalisation stage, the wetting front moved from the bottom of the specimen (where the high air entry filter stone was located) to the top where the low air entry filter was located. Therefore, the lower arms of the inclinometers would be the first to respond to the effects of wetting and soon after that the lateral strain gauge attached at the mid-height. Fig. 14 shows some interesting behaviour where the raw readings from the axial strain gauge and the lateral pressures are plotted against time (during the first 100 min of K_0 wetting). It appears that the time lag between the start of the K_0 wetting and the lateral strain response (represented by an increase in lateral pressure) is around 5 min, thus confirming that the wetting front is not merely a line separating two zones with different suctions, but rather it is a moving zone where change occurs gradually.

Figure 15 shows the K_0 plotted against time for specimens equalised at target suction values of zero, 100, 150, 200 and 300 kPa respectively. By default, the response of K_0 was similar to the behaviour observed in the case of horizontal net stress as shown in Fig. 12. At the beginning of the wetting, the specimens were subjected to an imposed K_0 condition of 1 and this K_0 value increased to maximum values of 2·3, 3·0, 2·1, 2·3 and 2·0 for suction values of 300, 200, 150, 100 kPa and zero respectively. The values of K_0 when the suction in the specimen stabilised at the pre-selected values were: 1·5, 1·6, 1·8, 2·0 and 2·0 respectively for suction values of zero, 100, 150, 200 and 300 kPa. In the case of low suction values, K_0 reduced significantly after reaching a peak. The reason for this response lies in the fact that the wetting path was traversing inside, but close to the yield surface initially inherited by the specimen (see Fig. 9).

At the beginning of wetting the horizontal net stress was 50 kPa and it increased to a maximum value of 111, 141, 104, 116 and 116 kPa in the case of specimens wetted to target suction values of zero, 100, 150, 200 and 300 kPa respectively. This particular state can be represented by point X in Fig. 16(a) where suction is plotted against mean net stress. The lateral stresses when the equalisation process was terminated (i.e. when the externally applied suction equalised within the specimen) were 74, 79, 90, 99 and 101 kPa respectively and the stress states referring to these values are represented by points F, E, D, C and B in Fig. 16 respectively for suctions of zero, 100, 150, 200 and 300 kPa. Note here that the actual value of suction when the lateral stress reached a peak (point X in Figs 16(a) and 16(c)) was not

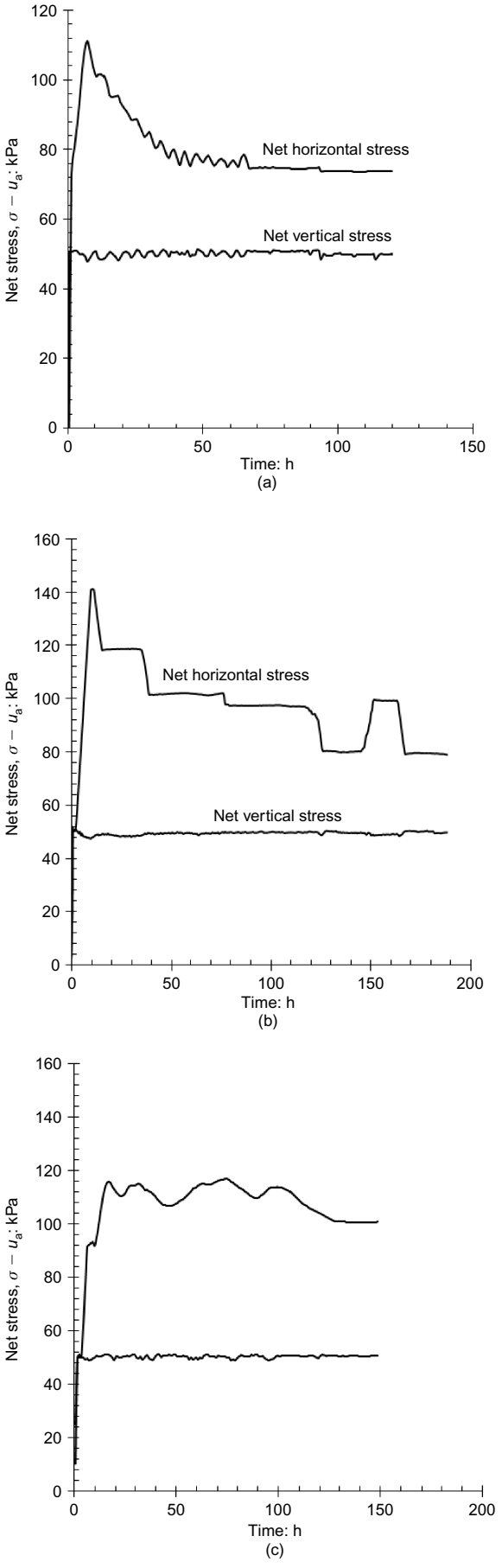

Fig. 12. Horizontal and vertical net stress plotted against time for specimens equalised under suction value of (a) zero, (b) 100 and (c) 300 kPa

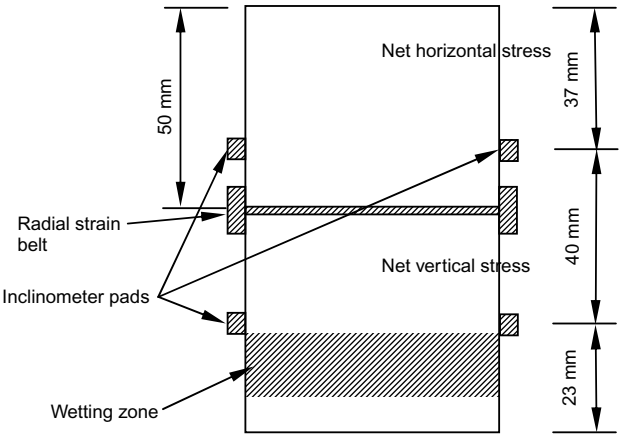

Fig. 13. Strain gauge positioning

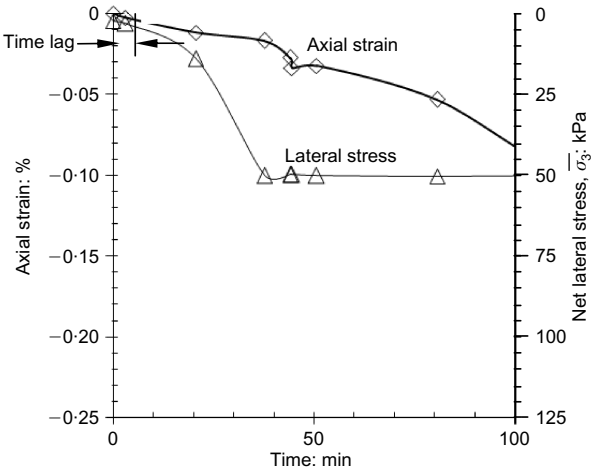

Fig. 14. Initial strain gauge and net lateral pressure response during wetting

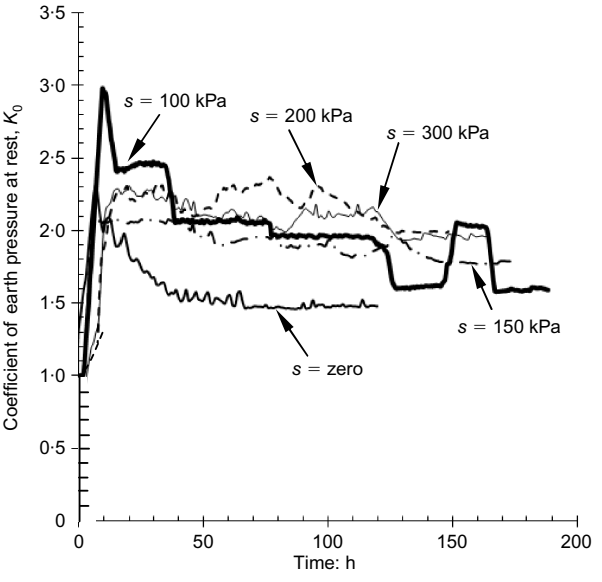

Fig. 15. K_0 plotted against time for specimens of dry engineered specimens during equalisation

known. The changes in the specific water volume leading up to these maximum lateral stress state conditions were 0·090, 0·055, 0·110, 0·085 and 0·04 respectively for tests carried out to reach target suction values of zero, 100, 150, 200 and

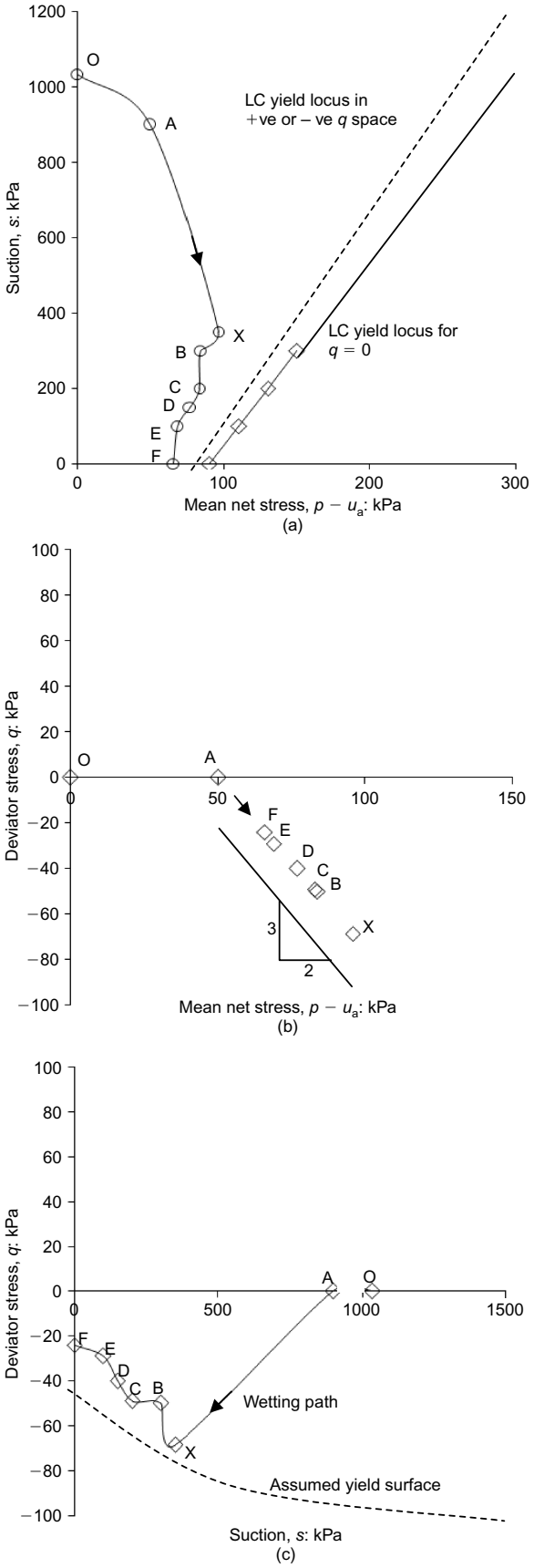

Fig. 16. Stress paths during K_0 equalisation in: (a) s–$\bar{p}$ space; (b) q–$\bar{p}$ space; and (c) q–s space

300 kPa (denoted by circular data points in Fig. 10) respectively with an average of 0·076. This change in average specific water volume corresponds to an approximate suction value of 350 kPa, estimated based on the end condition of the samples, shown in Fig. 10 when the suctions have fully equalised within the specimens.

The initial position of the LC yield locus referring to the initial compaction is also included in Fig. 16(a). Point X refers to the average maximum lateral stress condition for each test. It appeared that the positions of the stress states at the end of the K_0 wetting were well inside the yield locus, thus implying that any tendency for possible collapse settlement upon wetting was minimal. It should be noted that the LC yield locus shown in Fig. 16(a) was plotted on the $q = 0$ plane. A possible position of this LC yield curve for the conditions in positive and negative q space is also illustrated in Fig. 16(a) using a broken line. Under these conditions it can be argued that the maximum lateral stress condition, together with a deviator stress component, could result in the stress state of the specimen being much closer to the original yield surface than it appeared on the two-dimensional plot.

The net overburden pressure was kept constant at 50 kPa during wetting. This implied that the slope of the stress path $\mathrm{d}q/\mathrm{d}\bar{p}$ in the q–$\bar{p}$ plane was constant and equal to 3/2. For information, the stress paths that the specimens followed during wetting are shown in Figs 16(b) and 16(c) in q–$\bar{p}$ and q–s planes. The extreme point on the stress path refers to the maximum lateral stress conditions and the end conditions are marked with the points B, C, D, E and F for suction values of 300, 200, 150, 100 kPa and zero. Path AX was inside the yield surface and the paths X to B, C, D, E and F traversed close to the yield surface.

Figures 17(a) and 17(b) show the coefficient of earth pressure 'at rest' (K_0) for unsaturated soil plotted against suction for all five tests. Fig. 17(a) refers to the maximum K_0 condition and Fig. 17(b) refers to K_0 values achieved at the end of the equalisation stage. Fig. 17(a) is not an accurate representation of the soil behaviour, as the actual suction values corresponding to the K_0 maximum values were unknown. However, previous discussion on the lateral stresses stated the fact that the amounts of water that flowed into the specimen when the lateral stress was at a maximum were generally similar and suggested therefore that the maximum lateral stress conditions occurred at a similar value of suction, approximately 350 kPa in all five tests, regardless of the targeted suction. Fig. 17(b) shows a more realistic view of the K_0 variation with suction. The values of K_0 reduced slowly as the suction reduced to zero.

A limited study was carried out to investigate the effects of the initial specimen conditions on the lateral stresses required to maintain zero lateral stress conditions. A single test was performed on an unengineered wet specimen and an unengineered dry specimen equalised under a suction value of 100 kPa. Fig. 18 shows the lateral stress plotted against time during the course of wetting for all three specimens, in which the suction was reduced from its initial value to 100 kPa. The maximum lateral stress observed in the case of the engineered dry specimen was 140 kPa, and those for the unengineered dry specimen and wet unengineered specimen were 93 and 85 kPa respectively. The reduced maximum lateral stress in the case of the unengineered specimens confirmed the fact that the yield surfaces inherited by the unengineered specimens were well inside the yield surface for the engineered specimen (Fig. 8). Fig. 19 shows the position of the LC yield locus and the stress path during wetting of dry engineered, wet unengineered and dry unengineered specimens. The position of the LC yield locus and the stress path during K_0 wetting has been well established for a dry engineered specimen (as discussed earlier), although this was not the case for dry unengineered and wet unengineered specimens. In these two cases the research focused on a suction value of 100 kPa and the LC yield loci are assumed to pass through the yield stresses identified at

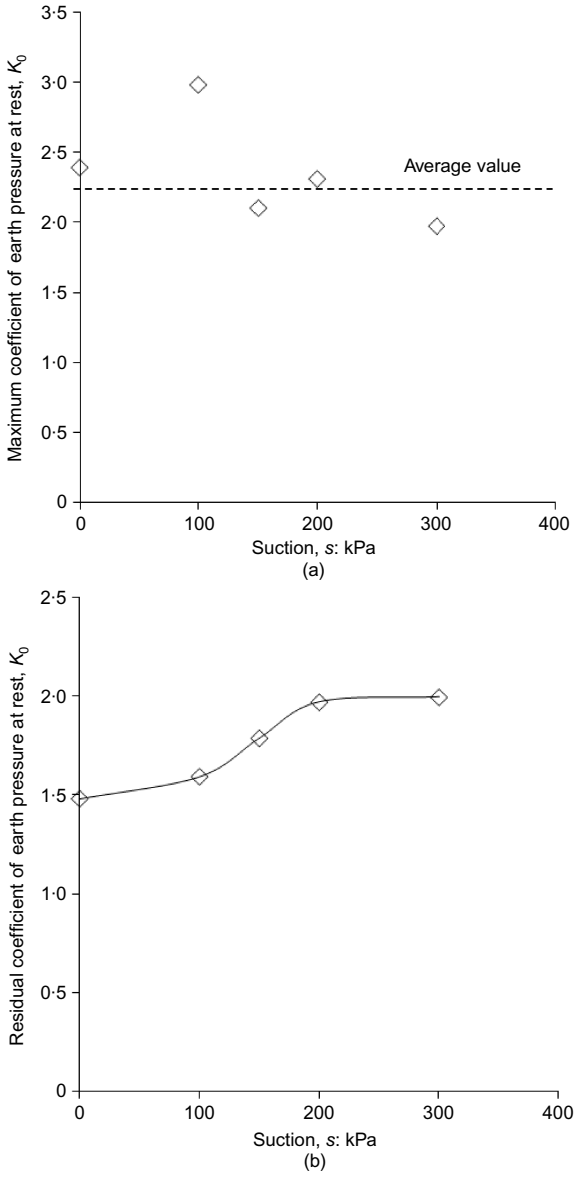

Fig. 17. Coefficient of earth pressure at rest plotted against suction: (a) maximum values and (b) residual values

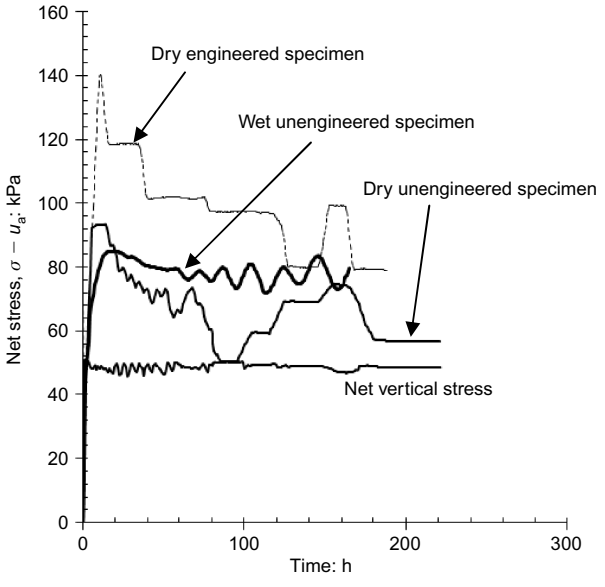

Fig. 18. Horizontal and vertical net stress plotted against time for a dry engineered specimen, a dry unengineered specimen and a wet unengineered specimen

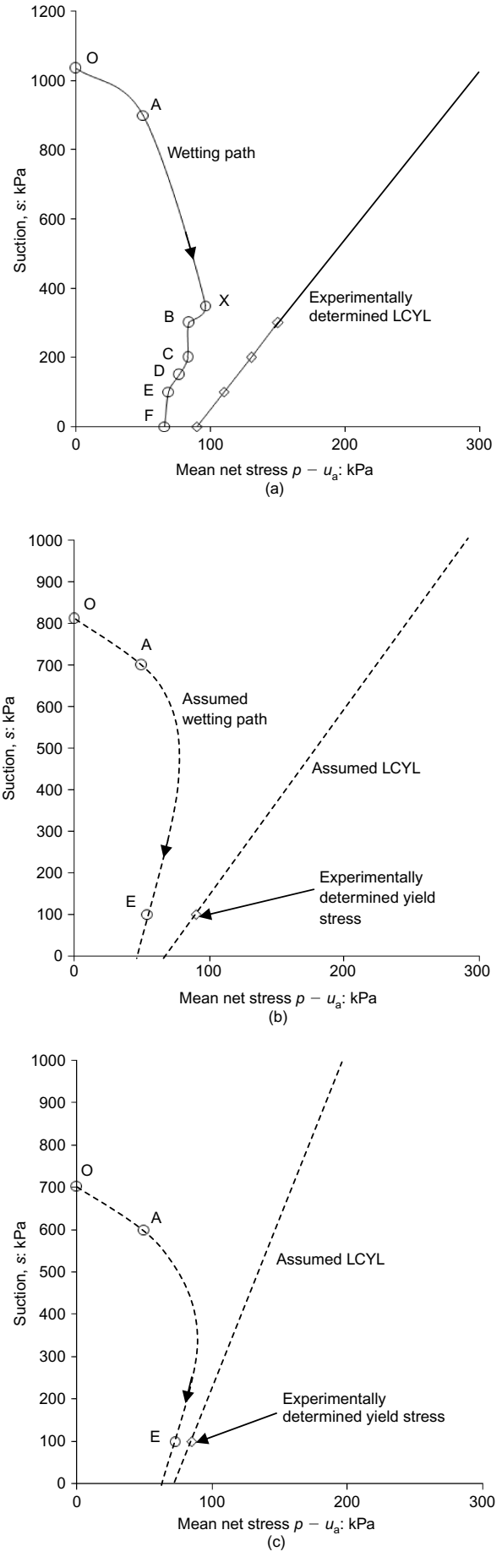

Fig. 19. Yielding behaviour of compacted samples in the s–$\bar{p}$ plane for: (a) dry engineered specimens; (b) dry unengineered specimen; and (c) wet unengineered specimen

this suction value. While substantial evidence was gathered to confirm the position of the K_0 stress path during wetting to be slightly inside the LC yield surface in the $\bar{p}-s-q$ space, it can be argued that the K_0 stress path will never cross the LC yield surface inherited by the specimen during its initial formation, regardless of the initial conditions (i.e. compaction water content and compaction effort) since any contraction initiated by approaching the yield surface will trigger the zero lateral strain conditions, thus reducing the lateral pressure, and the stress path will be reversed back slightly inside the yield surface.

Figures 20(a) and 20(b) show the K_0 values at the time of peak lateral stress and equalised lateral stress plotted against suction obtained on the dry engineered and wet unengineered specimens. Also included on the figures are the relevant values obtained from the dry engineered specimen. Peak and ultimate K_0 values for both dry and wet unengineered specimens were below (or very close to) the values obtained for the dry engineered specimen, confirming the fact that the yield surfaces for dry and wet unengineered specimens were inside that of the dry engineered specimen.

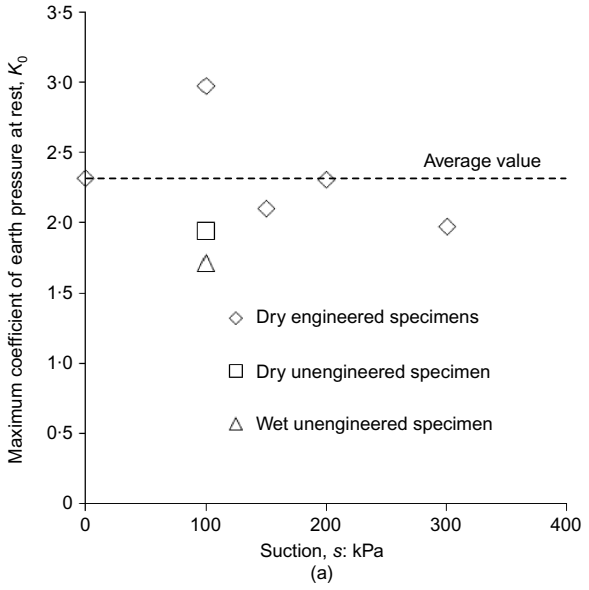

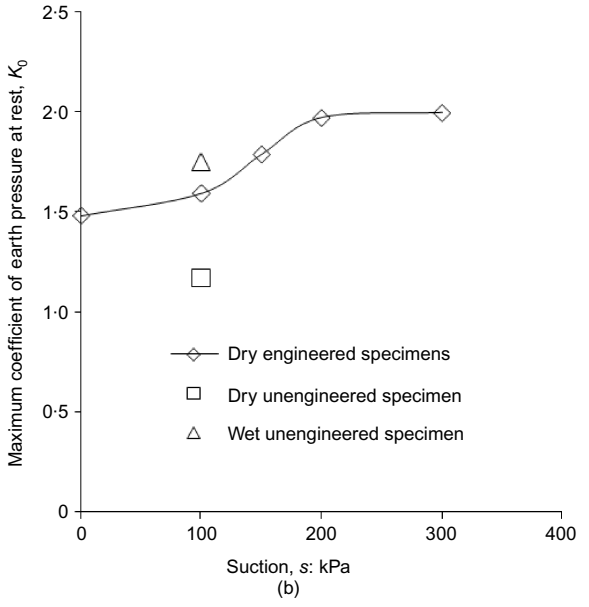

Fig. 20. Coefficient of earth pressure at rest plotted against suction: (a) maximum value and (b) equalisation value

Effects of bi-modal pore size distribution on the deformation under K_0 conditions

Unsaturated soils are constituted of an aggregated structure, with a clear bi-modal pore size distribution (Fig. 21). Ahmed *et al.* (1974), Gens & Alonso (1992), Delage *et al.* (1996), Qi *et al.* (1996), Sivakumar & Wheeler (2000), Lloret *et al.* (2003) and Cuisinier & Laloui (2004) have demonstrated the effects of an aggregated structure on the hydromechanical behaviour of unsaturated soils. Thom *et al.* (2007) and Sivakumar *et al.* (2010a) have reported experimental evidence, using MIP analysis to support the view that aggregates expand into the larger macro-voids during wetting. Figs 22(a) and 22(b) show the evolution of bi-modal distribution before and after wetting of unengineered and engineered specimens, prepared at identical water content (Sivakumar *et al.*, 2010a). The initial macro pore size distribution of a lightly compressed specimen was significantly higher than that of a heavily compressed specimen. However, the wetting resulted in very similar macro pore size distributions. If the aggregates are idealised as spherical for simplicity, upon wetting they become distorted as they expand into the macro voids where the restriction for expansion is less (Fig. 23). This implies that the effective size of the pore space will reduce and the evidence for this is explicitly shown in Fig. 22, particularly in a heavily compressed sample. The effect of aggregated structure during wetting under laterally confined conditions (i.e. under anisotropic loading conditions) is remarkable.

Figure 24 shows the axial and lateral strain plotted against time for suction values of zero, 100, 150, 200 and 300 kPa. A condition of zero lateral strain was imposed; hence no significant change in the lateral strain occurred. However, the vertical strains of the specimens increased significantly depending on the targeted suction values. The axial strain in the case of 300 kPa of suction was 0·64%, and this increased to 3·36% when the suction dropped to zero. However, the real challenge was to justify the observed response of the specimen in relation to the axial strain. Fig. 12 clearly shows that the lateral stresses reached a peak value and then began to reduce as the wetting progressed. The reductions in the lateral stresses after reaching the peak were significant when the targeted suctions were 200 kPa or lower. The net vertical

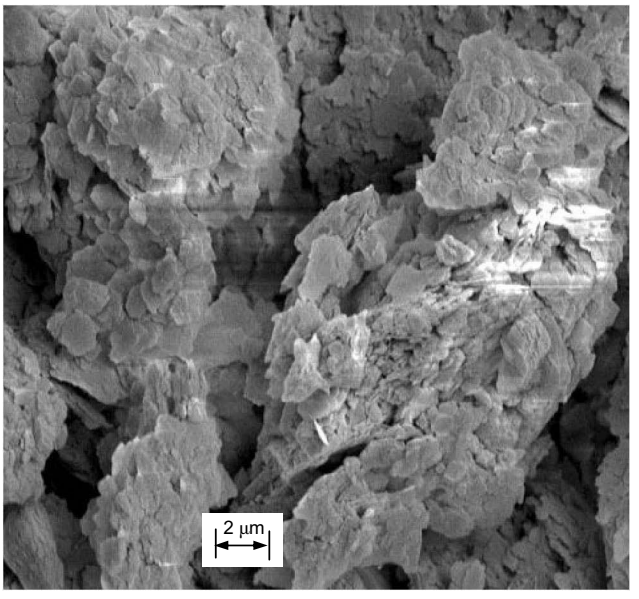

Fig. 21. The bi-modal pore size distribution of unsaturated compacted clay shown by scanning electron microscopy (after Sivakumar *et al.*, 2010a)

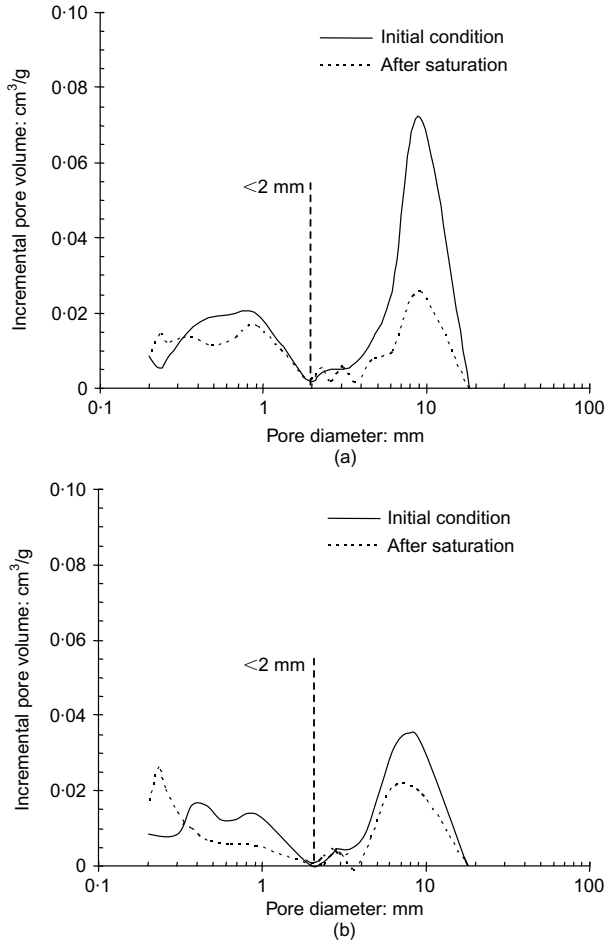

Fig. 22. Pore size distributions of specimens before and after wetting (Sivakumar *et al.*, 2010a): (a) lightly compressed sample; (b) heavily compressed sample

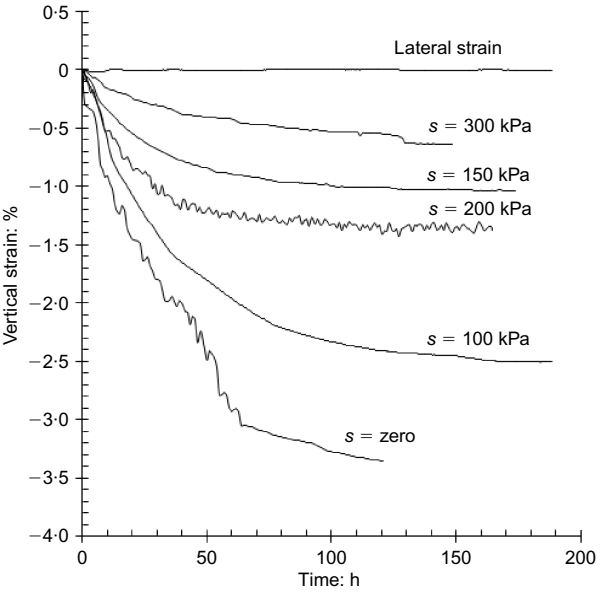

Fig. 24. Axial and lateral strain plotted against time for specimens equalised undersuction values of zero, 100, 150, 200 and 300 kPa

stress was kept constant at 50 kPa. Under these conditions, the specimens continued to swell axially under constant vertical stress. The reason for this lies in the structure of unsaturated soils.

The suction in the aggregates is very high and this was reduced to a lower value during the wetting process. The aggregates absorbed water and tried to expand both axially and laterally. The expansion of the aggregate can result in two different phenomena:

(*a*) the inter-aggregate contacts are pushed apart causing overall increase in volume
(*b*) expansion of the aggregates into the larger voids between the aggregates, causing reduced inter-aggregate voids but marginal changes in the overall volume.

Consider, for example, the case of an engineered specimen, where the tendency for inter-aggregate slippage is marginal (Sivakumar *et al.*, 2010a) and the inter-aggregate pore space is limited, therefore the most likely consequence of wetting would be an increase in overall volume of the specimen. The question remains, what will be the level of swelling in the vertical and lateral directions when the specimen is subjected to anisotropic loading?

At the beginning of the K_0 wetting, the loading conditions were isotropic, whereby the specimens were subjected to 50 kPa of net vertical and lateral stress. As the equalisation progressed the lateral stresses increased substantially in order to contain the lateral expansion. Therefore, the aggregates, which were expanding or trying to expand in three directions, would now prefer to expand in the vertical direction,

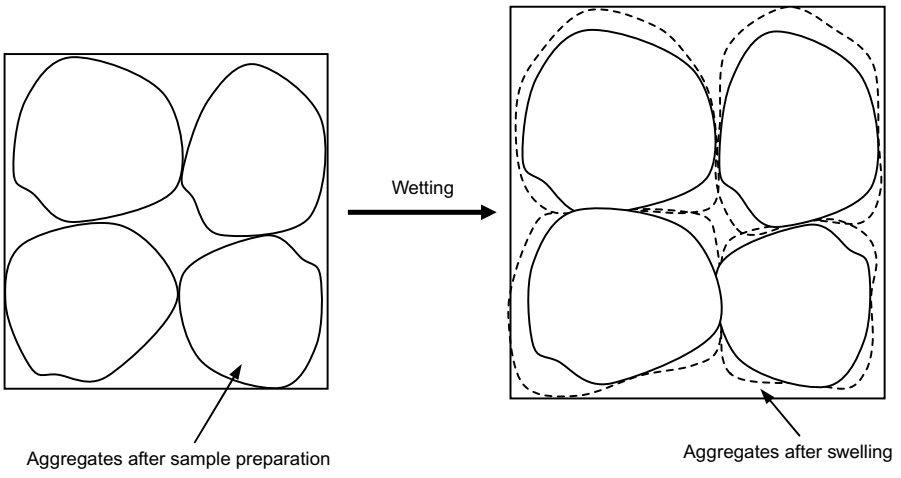

Fig. 23. Aggregated structure subjected to wetting

as opposed to the lateral direction, since the resistance to the expansion in the vertical direction is less than in the lateral direction; however this does not exclude the aggregates expanding into macro voids. Further investigation is necessary in order to ascertain the validity of this statement.

K_0 during loading and unloading and the effects of initial conditions on its magnitude

As part of the research, the specimens were subjected to increasing deviator stress starting from the stress state corresponding to the end of K_0 wetting (marked by points B, C, D, E and F in Fig. 16(b)). Table 4 lists the phase values after K_0 loading and unloading.

Figure 25 shows axial strain plotted against deviator stress (in logarithmic scale) for tests conducted at suction values of zero, 200 and 300 kPa. Estimated yield pressures in terms of mean net stress and deviator stress were (80, 0), (158, 38), (172, 51), (224, 42) and (266, 93) for suction values of zero, 100, 150 200 and 300 kPa respectively. Fig. 26 shows the stress path followed by the specimen equalised at 200 kPa during K_0 loading. The solid line shows the experimental results and the dash-dotted line shows the average specimen response.

The previous discussion suggested that the K_0 wetting path traversed near the boundary of the yield surface. It was also suggested that the stabilised stress state of the specimen at the end of wetting under K_0 conditions was close to the yield surface as indicated by points B, C, D, E and F in Figs 16(a), 16(b) and 16(d). The subsequent increase in deviator stress therefore takes the specimen inside the yield surface initially and on the yield surface upon continued loading (indicated by average paths BB′B′′, CC′C′′, DD′D′′, EE′E′′ and FF′F′′ in Fig. 27 for suction values of 300, 200, 150, 100 kPa and zero respectively). The pattern observed in the relationship between deviator stress and mean net stress during the K_0 loading was similar to that of saturated soils. The gradient of the K_0 path prior to yielding was high and it gradually reduced to a constant value as the loading progressed. The most interesting observation is that the slope of the K_0 line after yielding μ was reasonably constant and unaffected by the suction value. The following equation was used to calculate the K_0 value:

$$K_0 = \frac{3-\mu}{3+2\mu} \tag{2}$$

The K_0 value after yielding is plotted against suction in Fig. 28. The K_0 values appear to be unaffected by the suction value, but more importantly, they are very similar to the K_0 values reported for reconstituted saturated kaolin. Equation (3) relates the gradient of the critical state line $M(s)$ to the effective angle of internal friction ϕ' for a soil. The relationship is unaffected by the apparent cohesion given by the suction value. The gradient of the critical state line $M(s)$ is 0·8 (critical state line is not shown here due to the space limitation). Therefore, the effective angle of internal friction for the soil is 22°. Assuming $K_0 = 1 - \sin(\phi')$ (Jaky, 1948), this yields a K_0 value of 0·65 under saturated conditions.

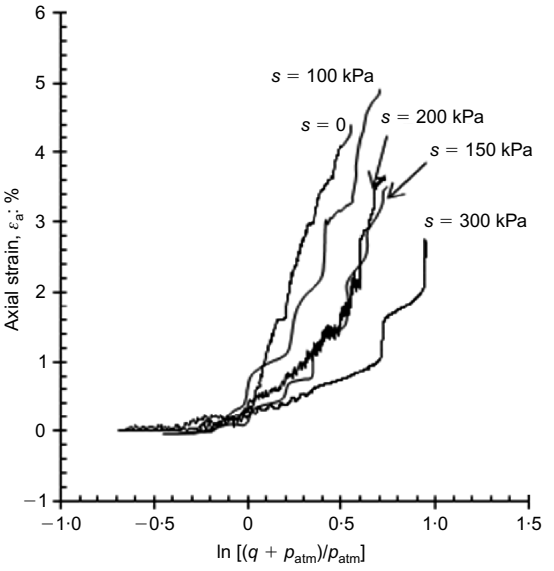

Fig. 25. Axial strain plotted against logarithm of deviator stress for suction values of zero, 100, 150, 200 and 300 kPa

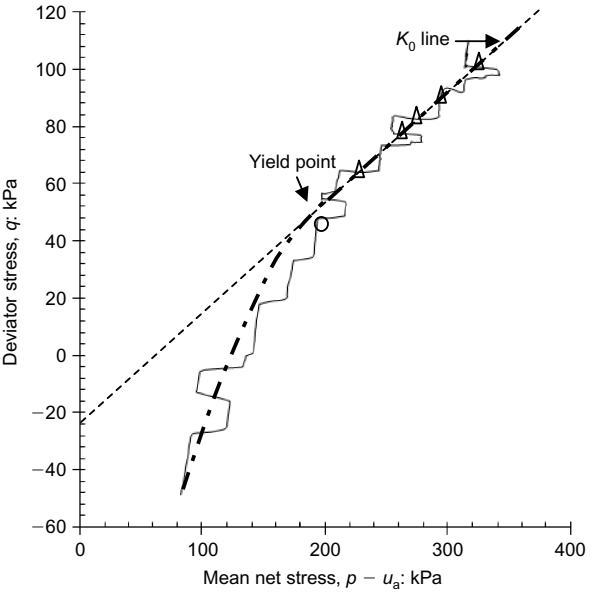

Fig. 26. Stress path during K_0 loading of specimen equalised to 200 kPa of suction

Table 4. Phase values after K_0 loading and K_0 unloading

Test	After K_0 loading						After K_0 unloading				
	$\bar{p}$: kPa	q: kPa	s: kPa	v	v_w	S_r: %	$\bar{p}$: kPa	q: kPa	v	v_w	S_r: %
23H0	237	74	0	1·826	1·895	100·0	206	0	1·881	1·893	100·0
23H100	352	130	100	1·840	1·803	92·6	—	—	—	—	—
23H150	326	108	150	1·889	1·755	84·9	—	—	—	—	—
23H200	314	105	200	1·907	1·730	80·3	—	—	—	—	—
23H300	465	159	300	1·855	1·653	76·3	276	0	1·855	1·651	76·1
23L100	161	37	100	1·963	1·820	85·2	115	0	1·963	1·824	85·5
25L100	299	53	100	1·854	1·777	90·9	—	—	—	—	—

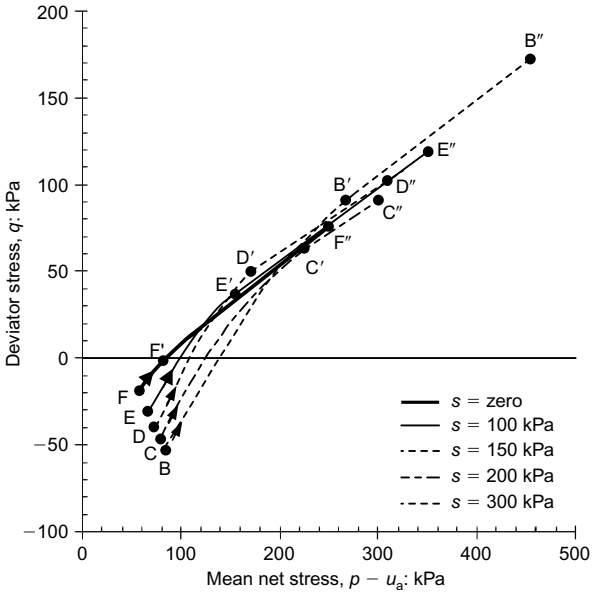

Fig. 27. Stress paths during K_0 loading of specimens equalised to zero, 100, 150, 200 and 300 kPa of suction

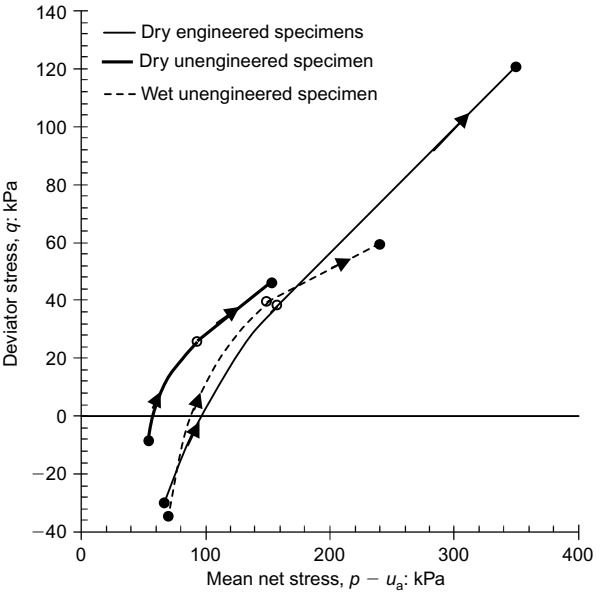

Fig. 29. Stress paths during K_0 loading for dry engineered, dry unengineered and wet unengineered specimens

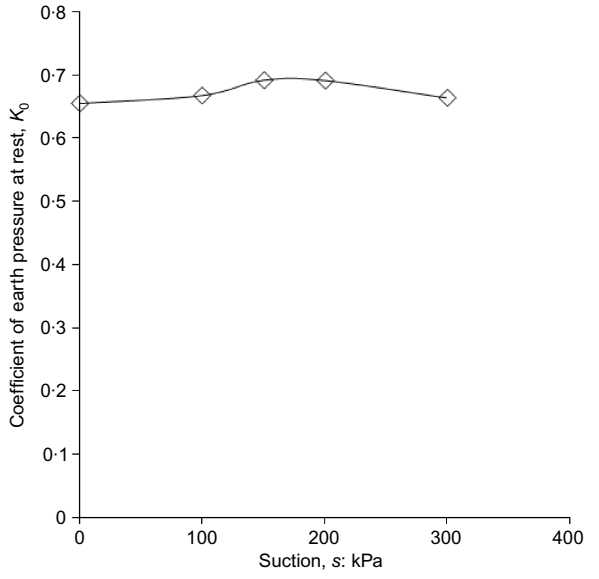

Fig. 28. Variation of the coefficient of earth pressure at rest with suction during K_0 loading

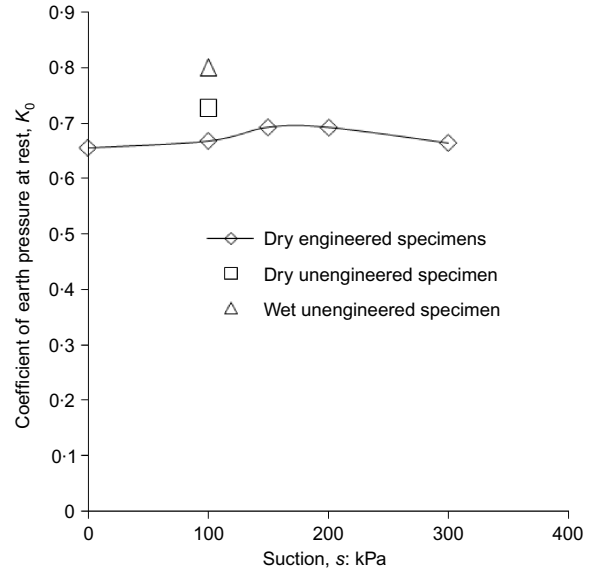

Fig. 30. The effect of initial conditions on the variation of the coefficient of earth pressure at rest against suction

$$M(s) = \frac{6 \sin \phi'}{3 - \sin \phi'} \tag{3}$$

A limited number of tests were performed in order to examine the effects of initial conditions of the specimen on the position of the K_0 path. Fig. 29 shows the average stress paths obtained for dry engineered, dry unengineered and wet unengineered specimens. Each specimen was subjected to an increasing deviator stress from the end point of the K_0 wetting stage. The open circular data points on the stress paths indicate the estimated yield stress from the stress–strain curves. The yield stresses identified in terms of mean net stress, deviator stress were (158, 38), (94, 26) and (150, 40) for dry engineered, dry unengineered and wet unengineered specimens respectively. As expected the yield stresses in the case of the dry unengineered and wet unengineered specimens were smaller than that of the dry engineered specimen. Fig. 30 shows the K_0 value plotted against suction. The slope of the K_0 line μ was affected by the initial conditions and therefore the K_0 value was also affected; however, further data are needed to confirm this remark.

The specimens were unloaded under K_0 conditions. Three unloading tests were performed, with suction values of zero and 300 kPa for specimens of dry engineered specimens and with a suction value of 100 kPa on a specimen of dry unengineered fill. The unloading paths are shown in Fig. 31. The specimens were stiff and overconsolidated, therefore the lateral strain was rarely affected by the reduction in vertical stress. The lateral pressure reduced slightly only at the end of the unloading path. For presentation purposes an approximate path was sketched connecting the start of the unloading and the end state of the soil based on the average lateral stresses. The behaviour observed was comparable with the behaviour traditionally observed in saturated soils.

K_0 loading-induced anisotropy

Soil structure inherited either during deposition, or post-deposition influences stress–strain behaviour and conse-

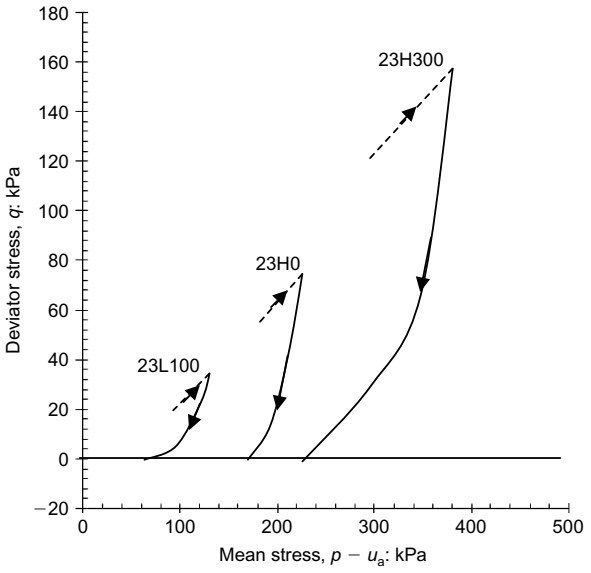

Fig. 31. Stress paths during K_0 unloading

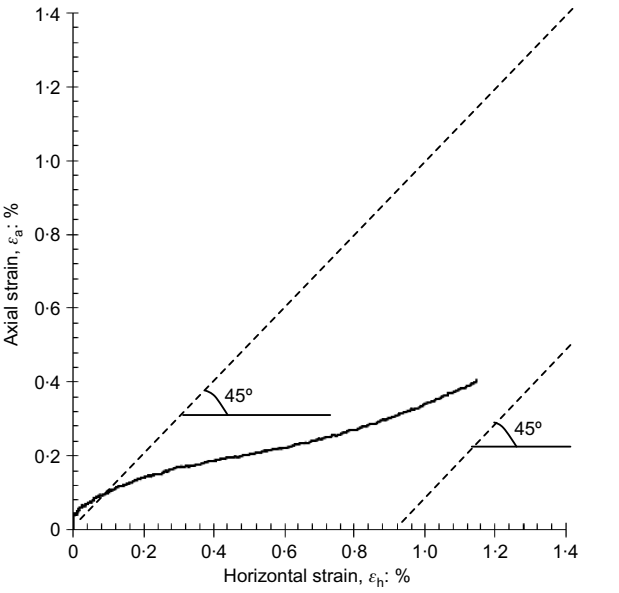

Fig. 32. Vertical strain plotted against horizontal strain during isotropic loading

quently the yielding characteristics. It is widely accepted that the yield locus separating elastic behaviour from elasto-plastic behaviour is elliptical and symmetrical about the mean effective stress axis, for soils with an isotropic stress history (Graham *et al.*, 1988; Sivakumar *et al.*, 2001). The rotation of the yield locus for unsaturated soils also appears to be true, despite the distinctly more complex structure, which is largely attributed to the bi-modal pore size distribution (Zakaria *et al.*, 1995; Cui & Delage, 1996; Sivakumar *et al.*, 2010b). The data reported here focuses on whether the anisotropic loading history was responsible for making the specimen behave anisotropically.

As part of this research one specimen that was taken through K_0 unloading was subsequently isotropically loaded (the dry unengineered fill equalised under a suction value of 100 kPa). Note that the specimens for the present research were extracted from samples initially compressed under isotropic stress conditions. Therefore, specimens should have inherited isotropic stress–strain properties. During the subsequent isotropic compression the lateral strain experienced by the specimen was considerably greater than the vertical strain. This indicates that K_0 loading has generated anisotropic stress–strain properties as shown in Fig. 32. In the early stages of loading, the stress–strain behaviour was marked by anisotropy. However, the continued isotropic loading caused the stress–strain properties to tend toward isotropic behaviour, indicated by the ratio between the lateral and axial strain approaching the 45° line as shown in Fig. 32. This observation provides some evidence to support the view that a previous K_0 stress history indeed inflicted a degree of anisotropy in terms of the specimen stress–strain properties.

CONCLUSIONS

Carefully controlled tests were conducted using the twin-cell stress path apparatus in order to examine the effects of wetting of unsaturated soils in relation to the stress regime under lateral confinement. Investigations were also carried out in order to examine the traditional concept of K_0 upon loading and unloading. The following concluding remarks can be made.

(*a*) The wetting of compacted clay specimens results in an increase in lateral stresses and therefore an increase in K_0. The magnitude of increase in the lateral stress is affected by the initial condition of the soil such as the initial specific volume and compaction water content.

(*b*) The position of the LC yield locus is an important factor that determines the likely response of the soil. During wetting under laterally restrained conditions the stress path traverses inside, but close to the LC yield locus. The stress path will never cross the yield locus under the above testing conditions even for unengineered specimens.

(*c*) The bi-modal pore size distribution has a particular influence on the volumetric response during wetting under anisotropic loading conditions. The work has shown that the aggregates attempt to expand in a vertical direction rather than a lateral direction as the resistance to expansion in the lateral direction is high, due to high lateral pressures.

(*d*) The maximum lateral stress condition (or K_0) is generally affected by the initial condition but unaffected by the target suction value under wetting. The final K_0 value reduced gradually with applied suction.

(*e*) The K_0 during loading (under normally consolidated conditions) is unaffected by suction and its value is approximately equivalent to that of reconstituted kaolin.

(*f*) K_0 loading induced a degree of anisotropy in the specimen that resulted in a significant difference in the stress–strain characteristics of the soil, which inherited isotropic properties before being subjected to anisotropic (K_0) loading.

The above conclusions have implications for geotechnical structures constructed on or using compacted clay fills. An example is the use of heavily compacted fills for backfilling retaining walls. The fill may become saturated owing to environmental changes (i.e. rainfall) The saturation of the fill will be associated with a rapid increase in lateral stresses, as identified from the present research. This can lead to instability of the retaining structures.

ACKNOWLEDGEMENTS

Funding for the research was provided by DEL (NI). The authors would like to thank Dr G. Gallagher (GSI, NI) and K. V. Senthilkumaran (P. J. Carey Ltd) for their support to research at Queen's University Belfast.

NOTATION

K_0 coefficient of earth pressure at rest
$M(s)$ slope of the critical state line in the $q-\bar{p}$ plane for unsaturated soils
$\bar{p}$ mean net stress
q deviator stress
s suction
u_a pore air pressure
v specific volume
μ slope of the K_0 line in the $q-\bar{p}$ plane
$\mu(s)$ intercept of the critical state line in the $q-\bar{p}$ plane
σ_h total horizontal stress
σ_v total vertical stress
ϕ' effective angle of internal friction

REFERENCES

Ahmed, S., Lovell, C. W. & Diamond, S. (1974). Pore sizes and strength of compacted clay. *J. Geotech. Engng Div. ASCE* **100**, No. 4, 407–425.

Alonso, E. E., Gens, A. & Josa, A. (1990). A constitutive model for partially saturated soils. *Géotechnique* **40**, No. 3, 405–430, **doi**: 10.1680/geot.1990.40.3.405.

Blanchfield, R. & Anderson, W. F. (2000). Wetting collapse in opencast coalmine backfill. *Proc. Inst. Civil Engrs – Geotech. Engng* **143**, No. 3, 139–149.

Blatz, J. A. & Graham, J. (2003). Elastic–plastic modelling of unsaturated soil using results from a new triaxial test with controlled suction. *Géotechnique* **53**, No. 1, 113–122, **doi**: 10.1680/geot.2003.53.1.113.

Carder, D. R. (1988). Earth pressures on retaining walls and abutments. *Ground Engng* **21**, No. 5, 7–10.

Casagrande, A. (1936). The determination of the pre-consolidation load and its practical significance. *Proc. 1st Int. Conf. Soil Mech., Cambridge, Massachusetts* **3**, 60–64.

Charles, J. A. (1993). *Building on fill: geotechnical aspects*. Watford, UK: The Building Research Establishment.

Charles, J. A., Burford, D. & Hughes, D. B. (1993). Settlement of opencast coal mining backfill at Horsley 1973–1992. In *Engineering fills* (ed. Clarke). London: Thomas Telford, pp. 429–440.

Chen, F. H. (1987). Lateral expansion pressure on basement walls. *Proc. 6th Int. Conf. Expansive Soils, New Delhi, India* **1**, 55–59.

Crooks, J. H. A. & Graham, J. (1976). Geotechnical properties of the Belfast estuarine deposit. *Géotechnique* **26**, No. 2, 293–315, **doi**: 10.1680/geot.1976.26.2.293.

Cui, Y. J. & Delage, P. (1996). Yielding and plastic behaviour of an unsaturated compacted silt. *Géotechnique* **46**, No. 2, 291–311, **doi**: 10.1680/geot.1996.46.2.291.

Cuisinier, O. & Laloui, L. (2004). Fabric evolution during hydromechanical loading of a compacted silt. *Int. J. Numer. Analyt. Methods Geomech*. **28**, No. 6, 483–499.

Delage, P. & Graham, J. (1995). Mechanical behaviour of unsaturated soils: Understanding the behaviour of unsaturated soils requires reliable conceptual models. *Proc. 1st Int. Conf. Unsaturated Soils, Paris, France* **3**, 1223–1256.

Delage, P., Audigiuer, M., Cui, Y. J. & Howat, M. D. (1996). Microstructure of a compacted silt. *Can. Geotech. J.* **33**, No. 1, 150–158.

Estabragh, A. R., Javadi, A. A. & Boot, J. C. (2004). Effect of compaction pressure on consolidation behaviour of unsaturated silty soil. *Can. Geotech. J.* **41**, No. 3, 540–550.

Gallipoli, D., Gens, A., Sharma, R. & Vaunat, J. (2003). An elasto-plastic model for unsaturated soil including the effect of saturation degree on mechanical behaviour. *Géotechnique* **53**, No. 1, 123–135, **doi**: 10.1680/geot.2003.53.1.123.

Gens, A. & Alonso, E. E. (1992). A framework for the behaviour of unsaturated expansive clays. *Can. Geotech. J.* **29**, No. 6, 1013–1032.

Graham, J., Crooks, J. H. A. & Lau, S. L. K. (1988). Technical Note: Yield envelopes: identification and geometric properties. *Géotechnique* **38**, No. 1, 125–134, **doi**: 10.1680/geot.1988.38.1.125.

Highways Agency (1995). In association with the Scottish Development Department, the Welsh Office & the Department for the Environment for Northern Ireland. Earthworks design and preparation of contract documents, HA 44/91. In *Design manual for roads and bridges, 4, Geotechnical drainage*. London: Highways Agency.

Highways Agency (2004). In association with the Scottish Development Department, the Welsh Office & the Department for the Environment for Northern Ireland. *Manual of contract documents for highways works MCHW1; Specification for highways works*, Series 600, Earthworks. London: Highways Agency.

Hilf, J. N. (1956). *An investigation of pore water pressure in compacted cohesive soils*, Technical Memorandum 654. Denver, Colorado: US Department of Interior Bureau of Reclamation.

Jaky, J. (1948). Pressure in soils. *Proc. 2nd Int. Conf. Soil Mechanics and Foundation Engineering, Rotterdam, the Netherlands* **1**, 130–107.

Jardine, R. J., Symes, M. J. & Burland, J. B. (1984). The measurement of soil stiffness in the triaxial apparatus. *Géotechnique* **34**, No. 3, 323–340, **doi**: 10.1680/geot.1984.34.3.323.

Lloret, A., Villar, M. V., Sanchez, M., Gens, A., Pintado, X. & Alonso, E. E. (2003). Mechanical behaviour of heavily compacted bentonite under high suction changes. *Géotechnique* **53**, No. 1, 27–40, **doi**: 10.1680/geot.2003.53.1.27.

Lu, N. & Likos, W. J. (2004). *Unsaturated soil mechanics*. Chichester: John Wiley.

Maãtouk, A., Leroueil, S. & La Rochelle, P. (1995). Yielding and critical state of a collapsible unsaturated silty soil. *Géotechnique* **45**, No. 3, 465–477, **doi**: 10.1680/geot.1995.45.3.465.

Maswoswe, J. (1985). *Stress path for a compacted soil during collapse due to wetting*. PhD thesis, Imperial College London, UK.

Qi, Y., Al-Mukhtar, M., Alcover, J. F. & Bergaya, F. (1996). Coupling analysis of macroscopic and microscopic behaviour in highly consolidated Na-laponite clays. *Appl. Clay Sci*. **11**, No. 2, 185–197.

Sitharam, T. G., Sivapullaiah, P. V. & Subba Rao, K. S. (1995). Shrinkage behaviour of compacted unsaturated soils. *Proc. 1st Int. Conf. Unsaturated Soils, Paris, France* **1**, 195–200.

Sivakumar, V. & Wheeler, S. J. (2000). Influence of compaction procedure on the mechanical behaviour of an unsaturated compacted clay, Part 1: Wetting and isotropic compression. *Géotechnique* **50**, No. 4, 359–368, **doi**: 10.1680/geot.2000.50.4.359.

Sivakumar, V., Doran, I. G., Graham, J. & Johnson, A. (2001). The effect of anisotropic elasticity on the yielding characteristics of overconsolidated natural clay. *Can. Geotech. J.* **38**, No. 1, 125–137.

Sivakumar, R., Sivakumar, V., Blatz, J. & Vimalan, J. (2006). Twin-cell stress path apparatus for testing unsaturated soils. *Geotech. Testing J., ASTM* **29**, No. 2, 1–5.

Sivakumar, V., Sivakumar, R., Brown, J., Murray, E. J. & Mackinnnon, P. (2010a). Constitutive modelling of unsaturated kaolin (with isotropic and anisotropic stress history). Part 1: Wetting and compression behaviour. *Géotechnique* **60**, No. 8, 581–594, **doi**: 10.1680/geot.8.P.007.

Sivakumar, V., Sivakumar, R., Murray, E. J., Brown, J. & MacKinnon, P. (2010b). Constitutive modelling of unsaturated kaolin (with isotropic and anisotropic stress history). Part 2: Performance under shear loading. *Géotechnique* **60**, No. 8, 595–609, **doi**: 10.1680/geot.8.P.008.

Skinner, H. D. (2001). Construction on fill. *Proceedings of the problematic soils symposium*, Nottingham, pp. 127–143.

Skinner, H. D., Charles, J. A. & Watts, K. S. (1999). Ground deformations and stress redistribution due to a reduction in volumes of zones of soil at depth. *Géotechnique* **49**, No. 1, 111–126, **doi**: 10.1680/geot.1999.49.1.111.

Tang, G. X. & Graham, J. (2002). A possible elastic-plastic framework for unsaturated soils with high-plasticity. *Can. Geotech. J.* **39**, No. 4, 894–907.

Tarantino, A. (2007). Technical Note: A possible critical state framework for unsaturated compacted soils. *Géotechnique* **57**, No. 4, 385–389, **doi**: 10.1680/geot.2007.57.4.385.

Thom, R. (2007). *Performance of unsaturated soil under monotonic and repeated loading*. PhD thesis, Queen's University of Belfast, UK.

Thom, R., Sivakumar, V., Sivakumar, R., Murray, E. J. & Mackinnon, P. (2007). Technical Note: Pore size distribution of

unsaturated compacted kaolin: the initial states and final states following saturation. *Géotechnique* **57**, No. 7, 469–474, **doi**: 10.1680/geot.2007.57.7.469.

Toll, D. G. (1990). A framework for unsaturated soil behaviour. *Géotechnique* **40**, No. 1, 31–44, **doi**: 10.1680/geot.1990.40.1.31.

Toll, D. G. (1999). A data acquisition and control system for geotechnical testing. In *Computing developments in civil and structural engineering* (eds B. Kumar and B. H. V. Topping). Edinburgh: Civil-Comp Press, pp. 237–242.

Wheeler, S. J. (1991). Technical note: An alternative framework for unsaturated behaviour. *Géotechnique* **41**, No. 2, 257–261, **doi**: 10.1680/geot.1991.41.2.257.

Wheeler, S. J. & Sivakumar, V. (1995). An elasto-plastic critical state framework for unsaturated soil. *Géotechnique* **45**, No. 1, 35–53, **doi**: 10.1680/geot.1995.45.1.35.

Wheeler, S. J. & Sivakumar, V. (2000). Influence of compaction procedure on the mechanical behaviour of an unsaturated compacted clay. Part 2: shearing and constitutive modelling. *Géotechnique* **50**, No. 4, 369–376, **doi**: 10.1680/geot.2000.50.4.369.

Wheeler, S. J., Sharma, R. S. & Buisson, M. S. R. (2003). Coupling of hydraulic hysteresis and stress–strain behaviour in unsaturated soils. *Géotechnique* **53**, No. 1, 41–54, **doi**: 10.1680/geot.2003.53.1.41.

Zakaria, I., Wheeler, S. J. & Anderson, W. F. (1995). Yielding of unsaturated compacted kaolin. *Proc. 1st Int. Conf. Unsaturated Soils, Paris, France* **1**, 223–228.

ice
Institution of Civil Engineers
publishing

Session 3

Benchmarking of Techniques and Models

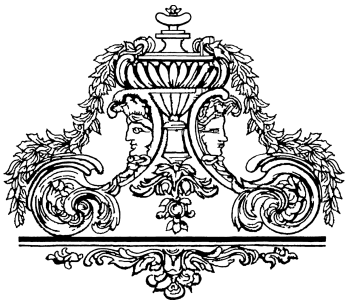

D'Onza, F. *et al.* (2011). *Géotechnique* **61**, No. 4, 283–302 [**doi:** 10.1680/geot.2011.61.4.283]

Benchmark of constitutive models for unsaturated soils

F. D'ONZA[1], D. GALLIPOLI[1], S. WHEELER[1], F. CASINI[2], J. VAUNAT[3], N. KHALILI[4], L. LALOUI[5], C. MANCUSO[6], D. MAŠÍN[7], M. NUTH[8], J. M. PEREIRA[9] and R. VASSALLO[10]

The paper presents a collaborative piece of research undertaken by seven research teams from different universities within the 'Mechanics of Unsaturated Soils for Engineering' (MUSE) network. The objective is to benchmark different approaches to constitutive modelling of mechanical and water retention behaviour of unsaturated soils by comparing simulations of suction-controlled and constant water content laboratory tests. A set of 13 triaxial and oedometer laboratory tests, covering the mechanical and water retention behaviour of an unsaturated compacted silty soil under a variety of stress paths, has been provided by one of the seven participating teams. This data set has been used by the other six teams for calibrating a constitutive model of their choice, which has been subsequently employed for predicting strains and degree of saturation in three of the 13 tests used for calibration, as well as in one 'blind' test for which experimental results had not been previously disclosed. By comparing predictions from all teams among themselves and against experimental data, the work highlights the capability of some of the current modelling approaches to reproduce specific features of the mechanical and water retention behaviour of unsaturated soils helping to identify potential areas of weakness where future research should focus. It also demonstrates the dispersion of results to be expected when different constitutive models, independently calibrated by different teams of researchers, are used to predict soil behaviour along the same stress path.

KEYWORDS: constitutive relations; laboratory tests; partial saturation; plasticity; suction

La présente communication présente des travaux de recherche réalisés par sept équipes de recherche de différentes universités, au sein du réseau MUSE. L'objectif de cette recherche est de comparer différentes méthodes pour la modélisation constitutive de comportements mécaniques et de retenue de l'eau de sols non saturés, en comparant des simulations d'essais en laboratoire avec aspiration contrôlée et teneur en eau constante. Une des sept équipes participant à cette recherche a fourni un ensemble de 13 essais triaxiaux et sur oedomètre en laboratoire, portant sur le comportement mécanique et de retenue de l'eau d'un sol silteux compacté, soumis à une série de chemins de contrainte. Cet ensemble de données a été utilisé par les six autres équipes pour le calibrage d'un modèle constitutif de leur choix, qui a été utilisé par la suite pour prédire les déformations et le degré de saturation dans trois des 13 tests utilisés pour le calibrage, ainsi que dans un test anonyme, pour lequel les résultats expérimentaux n'avaient pas été divulgués précédemment. En comparant les prédictions de toutes les équipes entre elles et en fonction de données expérimentales, cette recherche met en lumière la capacité que présentent certaines méthodes de modélisation actuelles pour la reproduction des caractéristiques spécifiques du comportement mécanique et de retenue de l'eau de sols non saturés, afin de contribuer à l'identification de zones de faiblesse potentielles sur lesquelles on devrait concentrer les travaux de recherche dans l'avenir. Elle démontre également la dispersion de résultats à prévoir lorsque l'on utilise différents modèles constitutifs, calibrés indépendamment par différentes équipes de chercheurs, pour prédire le comportement du sol le long du même chemin de contraintes.

INTRODUCTION

This paper presents a collaborative piece of research undertaken by seven universities to benchmark different mechanical and water retention soil models. The objective is to demonstrate the variability of predictions typically obtained when the soil response along a given hydromechanical stress path is independently simulated by different researchers using different constitutive models, albeit calibrated from a single set of experimental data. From an engineering perspective, this provides an indication of the discrepancies of predicted behaviour that can potentially occur in geotechnical design as a result of both the choice of constitutive model and the subsequent calibration on the basis of suction-controlled laboratory data.

The benchmarking exercise took place in the framework of a wider scientific programme carried out between 2004 and 2008 by the 'Mechanics of Unsaturated Soils for Engineering' (MUSE) 'Marie Curie' Research Training Network with the financial support of the European Commission. It involved seven teams of researchers at different universities, namely the Universitat Politècnica de Catalunya (UPC) in Spain, the University of Glasgow (UGLAS) in the UK, the Università di Napoli Federico II (UNINA) in Italy, the École Nationale des Ponts et Chaussées (ENPC) in France, the École Polytechnique Fédérale de Lausanne (EPFL) in Switzerland, the University of New South Wales (UNSW) in Australia and Charles University (CU) in the Czech Republic.

Manuscript received 7 March 2010; revised manuscript accepted 11 January 2011.
Discussion on this paper closes on 1 September 2011, for further details see p. ii.

[1] School of Engineering, University of Glasgow, Glasgow, UK
[2] Institute for Geotechnical Engineering, ETHZ, Zurich, Switzerland
[3] Departamento de Ingeniería del Terreno, Cartográfica y Geofísica, Universitat Politècnica de Catalunya, Barcelona, Spain
[4] School of Civil and Environmental Engineering, University of New South Wales, Sydney, Australia
[5] Soil Mechanics Laboratory, École Polytechnique Fédérale de Lausanne, Lausanne, Switzerland
[6] Dipartimento di Ingegneria Idraulica, Geotecnica ed Ambientale, Università di Napoli Federico II, Napoli, Italy
[7] Faculty of Science, Charles University, Prague, Czech Republic
[8] Soil Mechanics Laboratory, École Polytechnique Fédérale de Lausanne, Lausanne, Switzerland
[9] Université Paris-Est, Navier – Cermes, Ecole des Ponts ParisTech, Marne-la-Vallée, France
[10] Dipartimento di Strutture, Geotecnica, Geologia Applicata, Università della Basilicata, Italy

At the start of the exercise, UPC provided the other six teams with results from a set of 13 laboratory tests on compacted silt published in the PhD thesis of Casini (2008). The six teams then chose a constitutive model, calibrated the relevant parameter values on the basis of the laboratory data provided and predicted the deformation as well as the water retention behaviour during three of the 13 calibration tests plus one blind test for which experimental results had not been published.

The exercise was coordinated by UGLAS, which circulated spreadsheets with laboratory test results together with an accompanying document containing soil data and a description of the sample preparation procedure. The six teams of constitutive modellers were asked to refrain from looking at additional information contained in the PhD thesis of Casini (2008) or related publications. Standard return forms were also circulated for completion by each team with their predictions. Teams also had to provide the list of parameter values used in their simulations, together with a brief description of the procedure followed during calibration of their chosen model.

Readers interested in replicating this benchmarking exercise by using a constitutive model of their choice can download electronic copies of the specification document, return forms and experimental data spreadsheets from the MUSE website (http://muse.dur.ac.uk/) or, alternatively, contact one of the authors to obtain copies of the relevant documentation.

CONSTITUTIVE MODELS

Seven constitutive models have been considered, one for each team with the exception of UGLAS that returned predictions from two models (see Table 1). Hereafter, the theoretical bases of the different constitutive frameworks are compared with reference to the water retention behaviour, stress tensor definition, effect of suction on mechanical behaviour and nature of irreversible deformation. For the detailed formulation of each model, the reader is invited to refer to the original articles listed in Table 1.

Water retention models

All water retention models assume a relationship between degree of saturation S_r and suction $s = u_a - u_w$ (where u_a and u_w are the pore-air and pore-water pressures respectively) that depends on volumetric strain, by predicting a shift of the S_r–s curve towards the higher suction range as porosity decreases.

Models are divided into two primary groups depending on whether hydraulic hysteresis is neglected (CU, ENPC, UGLAS-1, UGLAS-2 and UNINA) or accounted for (EPFL and UNSW). In the former group, irreversible changes of degree of saturation during wetting–drying cycles are caused by irreversible volumetric strains alone whereas, in the latter group, they are attributable to both plastic volumetric strains and water retention hysteresis.

The five models of the first primary group are further sub-divided into two categories depending on the form of the relationship linking degree of saturation, suction and changes in pore volume. In the first category, UGLAS-1, UGLAS-2 and UNINA adopt the Van Genuchten water retention curve (Van Genuchten, 1980)

$$S_r = (1 + (\alpha s)^n)^{-m} \tag{1}$$

where m and n are model parameters. The effect of soil deformability is introduced by expressing parameter α (related to the air entry suction) as a power function of void ratio following the Gallipoli, Wheeler and Karstunen water retention model (Gallipoli *et al.*, 2003).

In the second category, the ENPC and CU models adopt the Brooks and Corey water retention curve (Brooks & Corey, 1964)

$$S_r = \left(\frac{s}{s_e}\right)^{-\lambda} \Rightarrow \log S_r = -\lambda \log \frac{s}{s_e} \tag{2}$$

described by a line in the $\log S_r$–$\log s$ plane with slope λ and intercept s_e (the latter coinciding with the air entry suction). The effect of soil deformability is introduced by expressing the slope λ and air entry suction s_e as functions of porosity according to different mathematical formulations in the two models.

In the second primary group, the EPFL and UNSW models assume a 'main' hysteretic loop, described by a main drying and a main wetting curve, which bounds the region of attainable values for degree of saturation and suction. The major difference between these two models lies in the definition of the main curves, which are parallel straight lines in the $\log S_r$–$\log s$ plane for UNSW (i.e. lines described by equation (2) with s_e equal to either the air entry or air expulsion suction depending on whether a main drying or wetting line is considered) and parallel straight lines in the S_r–$\log s$ plane for EPFL. A family of scanning lines of fixed slope spans the distance between the two main curves to simulate suction reversals starting from main wetting or main drying conditions. In both models, volumetric strains produce a rigid translation of the main hysteretic loop along the suction axis, that is a translation that keeps the slope and the relative distance of the main lines constant. A residual value of degree of saturation is also introduced as a lower limit when suction grows large.

Definition of constitutive stress tensor

Depending on the model considered, the constitutive stress tensor $\boldsymbol{\sigma}'$ is differently defined as a function of net stress $\boldsymbol{\sigma} = \boldsymbol{\sigma}_{tot} - u_a \cdot \mathbf{1}$ (where $\boldsymbol{\sigma}_{tot}$ is the total stress tensor and $u_a \cdot \mathbf{1}$ is the isotropic tensor of pore air pressure), suction s and degree of saturation S_r.

The following general definition of the constitutive stress tensor is introduced to help in distinguishing between different formulations

$$\boldsymbol{\sigma}' = \boldsymbol{\sigma} + \chi_1 \cdot s \cdot \mathbf{1} + \chi_2 \cdot \mathbf{1} \tag{3}$$

where χ_1 is a factor between zero and one weighing the effect of suction on the solid skeleton and χ_2 is an additive term measuring energy changes in the phase interfaces (Coussy & Dangla, 2002).

Gens (1996) defined three classes of constitutive stresses depending on whether (a) $\chi_1 = 0$, (b) $\chi_1 = \chi_1(s)$ depends on suction but not degree of saturation for $s > s_e$ (with $\chi_1 = 1$ for $s \leqslant s_e$) or (c) $\chi_1 = \chi_1(S_r)$ depends on degree of saturation and possibly suction (with $\chi_1 = 1$ for $S_r = 1$). However, Gens (1996) did not consider the additive term χ_2 measuring energy changes in the phase interfaces in equation (3), and his classification is here expanded to introduce a fourth class of constitutive stresses to contemplate this extra case.

Both second and third classes define the constitutive stress as the sum of the net stress tensor plus the product of the isotropic suction tensor multiplied by a scalar coefficient varying between zero and one. A constitutive stress of the third class can therefore be recast into a constitutive stress of the second class (and vice versa a constitutive stress of the second class can be recast into a constitutive stress of the third class) by using the chosen water retention model to relate degree of saturation to suction. Of course, this water

Table 1. Constitutive models used by participating teams

Team	Water retention model	Mechanical model	Difference with published versions	Reference saturated mechanical model
CU	Mašín (2010)	Mašín & Khalili (2008)	The definition of the constitutive stress variable takes into account the dependency of air entry value on void ratio, as predicted by the adopted water retention model proposed by Mašín (2010).	Mašín (2005)
EPFL	Nuth & Laloui (2008)	Nuth & Laloui (2007)	The published mechanical model uses the Van Genuchten (1980) equation to calculate degree of saturation as a function of suction. However, an improved water retention model has been used here, which incorporates the effects of both hydraulic hysteresis and soil density as described by Nuth & Laloui (2008).	Hujeux (1985)
ENPC	Brooks & Corey (1964)	Pereira *et al.* (2005)	The influence of soil density on water retention behaviour is modelled by extending the Brooks and Corey water retention curve (Brooks & Corey (1964)) to incorporate the following dependency of slope, λ and air-entry suction, s_e on porosity, ϕ $\lambda(\phi) = \lambda_0 \exp(-A \cdot (\phi - \phi_{ref}))$ $s_e(\phi) = s_{e0} \exp(-A \cdot (\phi - \phi_{ref}))$ where λ_0, s_{e0}, A and ϕ_{ref} are model parameters.	Cambou & Jafari (1988)
UGLAS 1	Gallipoli *et al.* (2003)	Alonso *et al.* (1990)	None	Roscoe & Burland (1968)
UGLAS 2	Gallipoli *et al.* (2003)	D'Onza *et al.* (2010)	None	Wheeler *et al.* (2003)
UNINA	Gallipoli *et al.* (2003)	Wheeler & Sivakumar (1995)	The published version of the mechanical model has been extended by adding: (*a*) a Hvorslev surface of slope h in the constant suction q–p' plane to model peak strength on the dry side of the yield locus (*b*) a non-associated flow rule following the approach proposed by Cui & Delage (1996) relating increments of plastic shear strain $d\varepsilon_s^p$ and plastic volumetric strains $d\varepsilon_v^p$ as $\frac{d\varepsilon_s^p}{d\varepsilon_v^p} = c_1 + \frac{c_2(q/p_0)}{1 - [q/(Mp + \mu)]}$ where p_0, M and μ have the same meaning as in the work by Wheeler & Sivakumar (1995) while c_1 and c_2 are additional model parameters (c_2 takes different values depending on whether the stress state is on the dry or wet side of the yield locus) (*c*) an additional yield limit for suction increase similar to the existence of the SI yield curve in the BBM (Alonso *et al.*, 1990).	Unlike others, this model does not assume any particular saturated parent formulation.
UNSW	Khalili *et al.* (2008)		None	Khalili *et al.* (2005)

retention model can also incorporate a dependency of the relationship between degree of saturation and suction on volumetric strains and/or hydraulic hysteresis as relevant. In spite of such similarities, the distinction between the second and third class of constitutive stresses is retained in this work, consistent with the proposal by Gens (1996), because this makes it possible to distinguish between formulations depending on the 'parent' definition of constitutive stress from which multiple 'child' definitions of constitutive stress of another class can be obtained by combination with different water retention relationships.

The UGLAS-1, UGLAS-2 and UNINA models are formulated in terms of the net stress tensor, hence they fall in the first class for which $\chi_1 = 0$ and $\chi_2 = 0$.

The CU and UNSW models adopt a constitutive stress of the second class for which χ_1 depends on suction for $s > s_e$ while $\chi_2 = 0$. In the CU model the factor χ_1 is expressed as

$$\chi_1 = \left(\frac{s}{s_e}\right)^{-\gamma} \tag{4}$$

where γ is a model parameter (Khalili & Khabbaz, 1998) whereas, in the UNSW model, χ_1 varies according to a hysteretic law, similar to the water retention model, defined by a pair of main drying and main wetting lines of constant slope in the $\log\chi_1$–$\log s$ plane having the form of equation (4). Scanning lines of fixed slope describe the variation of χ_1 during suction reversals starting from main wetting or main drying conditions.

Owing to the particular choice of water retention relationship in the CU model, the primary constitutive stress can be recast in an alternative form consistent with the third class by combining equation (2) with equation (4) to yield

$$\chi_1 = S_r^{\gamma/\lambda} \tag{5}$$

The same is true for the constitutive stress adopted by UNSW if the soil state belongs to a main drying or main wetting curve.

The EPFL model is formulated in terms of a constitutive stress of the third class and assumes $\chi_1 = S_r$ while $\chi_2 = 0$.

Finally, the ENPC model is formulated in terms of a constitutive stress of the fourth class with $\chi_1 = S_r$ while χ_2 provides a measure of the energy change in the phase interfaces through the following integral

$$\chi_2 = \frac{2}{3}\int_{S_r}^{1} s(S_r)\mathrm{d}S_r \tag{6}$$

where $s(S_r)$ is the inverse of the assumed water retention curve (Coussy & Dangla, 2002; Dangla, 2002).

Models adopting a constitutive stress tensor of the first class incorporate a suction-induced cohesive term into their critical strength equation while models adopting a constitutive stress tensor of second, third and fourth classes predict critical strength by means of a purely frictional law with no suction-induced cohesive term. In addition, if a constitutive stress of the second, third or fourth class is employed, there is no need for an independent relationship linking elastic strains to suction.

Effect of suction on mechanical behaviour

All models incorporate suction as a scalar constitutive variable in addition to the constitutive stress tensor. The ENPC, EPFL, UGLAS-1, UGLAS-2, UNINA and UNSW models adopt an elasto-plastic formulation where suction defines the expansion of the yield or bounding surface together with the spacing and slope of the constant-suction normal compression lines. The CU model adopts a hypoplastic formulation, where no distinction is made between elastic and plastic strains, but suction is still included in a similar manner by controlling the size of the bounding surface through the Hvorslev equivalent stress. For the sake of simplicity, the term 'yield' is used in the following to indicate stress states corresponding to the onset of irreversible deformations in classical plasticity models as well as stress states corresponding to bounding conditions in bounding surface plasticity or hypoplastic models.

An increase of suction has a similar effect in all models producing an increase of the mean yield constitutive stress in the absence of irreversible strains. This increase of mean yield constitutive stress corresponds to an expansion of the yield surface in the stress space. In the CU, ENPC, EPFL and UNSW models, this expansion is homologous in the q–p' plane (p' is the mean constitutive stress and q is the deviator stress) at constant Lode angle with the centre of homology coinciding with the origin.

Note that, in the elasto-plastic formulations by EPFL and UNSW, suction is introduced as a hardening parameter rather than a stress variable. Nevertheless, in order to simplify terminology, and given that the practical effects of suction are similar in all models, the expression 'yield curve' is generally used in the following to denote the variation of yield stress in the s–p' plane, regardless of whether suction is introduced as a stress variable or a hardening parameter.

Models are here distinguished according to the form of the yield curve in the s–p' plane for $s > s_e$. A classification applicable to all models, regardless of the type of constitutive stress adopted, is introduced based on the following general expression of yield curve in the s–p' plane

$$p'_0(s) = \omega_1 \cdot p'_0(s_e)^{\omega_2} + \omega_3 \tag{7}$$

In equation (7), $p'_0(s)$ is the mean yield constitutive stress for $s > s_e$ and $p'_0(s_e)$ is the mean yield constitutive stress at $s = s_e$, which coincides with the volumetric hardening parameter in the elasto-plastic models. For $s \leqslant s_e$, the mean yield constitutive stress $p'_0(s)$ is calculated from the principle of effective stresses for saturated soils taking into account the definition of constitutive stress. The three symbols ω_1, ω_2 and ω_3 denote three functions of suction governing the increase of mean yield constitutive stress with increasing suction.

Three classes of models are thus defined according to the following three cases:

(*a*) $\omega_1 = \omega_1(s)$ is a function of suction (with $\omega_1 = 1$ when $s = s_e$) while $\omega_2 = 1$ and $\omega_3 = 0$ are both constant
(*b*) $\omega_1 = \omega_1(s)$ and $\omega_2 = \omega_2(s)$ are both functions of suction (with $\omega_1 = 1$ and $\omega_2 = 1$ when $s = s_e$) while $\omega_3 = 0$ is constant
(*c*) $\omega_1 = \omega_1(s)$ and $\omega_3 = \omega_3(s)$ are both functions of suction (with $\omega_1 = 1$ and $\omega_3 = 0$ when $s = s_e$) while $\omega_2 = 1$ is constant.

If the saturated normal compression line and the volumetric elastic law are given, the choice of one of the above three classes of yield curve implicitly fixes the form of the constant-suction normal compression lines. If the saturated normal compression line and the elastic compression law are both represented by straight lines in the v–$\ln p'$ plane (where v is the specific volume and p' is the mean constitutive stress), a yield curve of the first class corresponds to a family of parallel straight constant-suction normal compression lines, a yield curve of the second class corresponds to a family of straight constant-suction normal compression lines of variable slopes and a yield curve of the third class corresponds to a family of curved constant-suction normal

compression lines (see Appendix for a proof). In the Appendix it is shown that the slope and spacing of constant-suction normal compression lines are governed by the functions $\omega_1 = \omega_1(s)$ and $\omega_2 = \omega_2(s)$, respectively.

The EPFL and UNSW models adopt yield curves of the first class. The CU, UGLAS-1, UGLAS-2 and UNINA models adopt yield curves of the second class (with $s_e = 0$ for UGLAS-1, UGLAS-2 and UNINA). Note, however, that the particular model calibration by UNINA produces parallel constant-suction normal compression lines in the v–$\ln p'$ plane and thus $\omega_2 = 1$ (see equation (17)), which changes the class of yield curve from second to first. Finally, the ENPC model assumes a yield curve of the third class, although, again, the particular model calibration by ENPC implies $\omega_3 = 0$ (see equation (18)), which changes the class of yield curve from third to first.

In the second class, the CU, UGLAS-1 and UGLAS-2 models assume that the functions $\omega_1 = \omega_1(s)$ and $\omega_2 = \omega_2(s)$ are related through an exponential law as

$$\omega_1(s) = p_{\text{ref}}^{(1-\omega_2(s))} \tag{8}$$

where p_{ref} is a reference pressure such that the yield curve reduces to a straight vertical line in the s–p' plane when $p'_0(s_e) = p_{\text{ref}}$, as shown by combining equations (7) and (8).

A classification matrix of the different models, according to the type of constitutive stress tensor and yield curve, is given in Table 2.

Irreversible mechanical behaviour

A first distinction can be made depending on the way irreversible mechanical behaviour is incorporated in the different formulations. In the ENPC, EPFL, UGLAS-1, UGLAS-2, UNINA and UNSW models, irreversibility of strains is introduced by making use of standard elasto-plastic principles. The CU model is instead formulated in the context of the hypoplasticity theory, which does not distinguish between elastic and plastic strains but describes irreversible behaviour by means of an incrementally non-linear stress–strain relationship, where material stiffness depends on both stress state and direction of strain vector. Although being algebraically different, the CU model is based on critical state soil mechanics, similarly to the other models (Gudehus & Mašín, 2009) and incorporates the so-called swept-out-memory surface (Mašín & Herle, 2005) as an alternative to the yield surface of elasto-plastic models.

A second distinction can be made between models that account for anisotropy of irreversible strains (ENPC, EPFL, UGLAS-2, UNINA and UNSW) and models that do not (CU and UGLAS-1).

Among anisotropic models, two groups are distinguished depending on whether anisotropy of plastic strains but not anisotropy of yielding and plastic hardening is taken into account or, alternatively, anisotropy of plastic strains, yielding and plastic hardening are all considered.

The former group, which includes EPFL, UNINA and UNSW, assume constant-suction yield surfaces aligned with the hydrostatic axis in the principal stress space, whose evolution is governed by volumetric but not rotational hardening. Yielding and plastic hardening therefore depend only on the magnitude of the three principal stresses but not on their orientation with respect to the external reference system. Anisotropy of plastic strains is accounted for by introducing a non-associative flow rule that predicts irreversible shear strain during mechanical loading or wetting on the hydrostatic axis.

The latter group of models, including ENPC and UGLAS-2, adopt constant-suction yield surfaces which are aligned at an angle with the hydrostatic axis in the principal stress space and whose evolution is governed by both volumetric and rotational hardening. In this case, yielding and plastic hardening depend on the value of the three principal stresses as well as on their orientation with respect to the external reference system. Given the inclination of the yield surface, both associative (as in the UGLAS-2 model) and non-associative flow rules (as in the ENPC model) can predict anisotropic plastic strains during loading or wetting on the hydrostatic axis.

Among the isotropic models, CU and UGLAS-1 assume constant-suction yield surfaces aligned along the hydrostatic axis, with isotropic irreversible strains predicted during plastic loading or wetting on the hydrostatic axis. In particular, the UGLAS-1 model adopts a non-associative flow rule with no shear component for stress states on the hydrostatic axis.

Models can also be classified depending on whether a smooth or sharp transition between elastic and plastic behaviour is predicted. CU and UNSW adopt models of the first type, based on a hypoplastic formulation in the case of CU and bounding surface plasticity in the case of UNSW. Both these models predict a gradual build up of irreversible strains and show continuous derivatives of the stress–strain curve during monotonic loading. On the other hand, ENPC, EPFL, UGLAS-1, UGLAS2 and UNINA adopt models of the second type, which result in a discontinuity of the derivative of the stress–strain curve at the onset of yielding (although, in the case of EPFL, a different choice of model parameters can also produce a smooth response consistent with the behaviour of the first group of models).

EXPERIMENTAL DATA SET

Experimental data were obtained from suction-controlled triaxial and oedometer tests on compacted samples of Jossigny silt (Casini, 2008). Fig. 1 shows the grading curve of this soil, which includes 5% sand, 70% silt and 25% clay. The specific gravity is equal to 2·69 with a liquid limit of 32% and a plastic limit of 17%, which classifies the soil as

Table 2. Mechanical models classification matrix (parentheses indicate change of class due to calibration)

Yield/bounding curve	Constitutive stress			
	(a) $\chi_1 = 0, \chi_2 = 0$	(b) $\chi_1 = \chi_1(s), \chi_2 = 0$	(c) $\chi_1 = \chi_1(S_r), \chi_2 = 0$	(d) $\chi_1 = \chi_1(S_r), \chi_2 = \chi_1(S_r)$
(a) $\omega_1 = \omega_1(s)$	(UNINA)	UNSW	EPFL	(ENPC)
(b) $\omega_1 = \omega_1(s)$ and $\omega_2 = \omega_2(s)$	UGLAS-1 UGLAS-2 UNINA	CU	—	—
(c) $\omega_1 = \omega_1(s)$ and $\omega_3 = \omega_3(s)$	—	—	—	ENPC

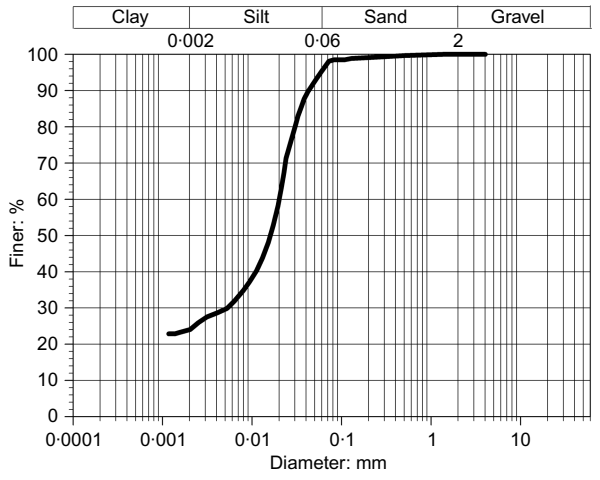

Fig. 1. Grading curve of Jossigny silt

silty clay of low plasticity according to the USCS classification.

Loose soil was initially mixed to a target water content of 13%. By assuming that the water content of the wet mixture was equal to the target value, an appropriate mass of soil was compacted in layers by one-dimensional static compression to achieve a target dry unit weight of 14·5 kN/m^3. Triaxial samples of 7 cm diameter were compacted in four layers to a height of 14 cm, while oedometer samples of 5 cm diameter were compacted in a single layer to a height of 2 cm. This required the application of pressures ranging from 150 kPa to 200 kPa for each layer. No measurement of suction was performed after compaction.

It was subsequently noticed that water content during compaction was in some cases slightly different from the target value, which caused a variation of the post-compaction values of void ratio and degree of saturation among samples.

Calibration tests

The data set circulated for calibration of the different models included the following 13 tests (here identified by using the same codes as in the PhD thesis of Casini (2008)).

(*a*) Four compression tests performed in triaxial cells at constant suction of 200 kPa. Of these, one test involved isotropic loading (TX03) and three tests involved anisotropic loading (TX04, TX08 and TX09).
(*b*) Four compression tests followed by shearing performed in triaxial cells at constant suction of 200 kPa. Of these, one test involved isotropic loading prior to shearing (TX02), two tests involved anisotropic loading prior to shearing (TX06 and TX07) and one test involved no loading prior to shearing (TX01).
(*c*) Five Ko-compression tests (EDO-sat, EDO-10, EDO-50, EDO-100 and EDO-200) performed in an oedometer under saturated conditions and at constant suctions of 10 kPa, 50 kPa, 100 kPa and 200 kPa, respectively. All tests followed loading–unloading–reloading paths at constant suction. In addition, the test at a suction of 200 kPa included two wetting–drying cycles, before loading and after reloading, under a constant vertical net stress.

All tests are summarised in Table 3, which also lists the post-compaction values of void ratio and degree of saturation, together with the net stress and suction imposed during initial equalisation prior to the start of the test. Note that, in Table 3, p denotes the mean net stress (which is in general different from the mean constitutive stress p'), σ_v denotes the vertical net stress (which is in general different from the vertical constitutive stress σ'_v), u_a denotes the pore air pressure and η denotes the ratio between the increments of deviator and mean net stress during loading.

The stress paths for the tests carried out in the triaxial cells (TX01, TX02, TX03, TX04, TX06, TX07, TX08 and TX09) are shown in Fig. 2 (tests with loading only) and Fig. 3 (tests with loading followed by shearing). All loading stages were performed by ramping radial net stress at a constant rate of 5 kPa/h while the shearing stages were performed by imposing a constant axial compression rate of 0·2 mm/h. The stress paths for the tests carried out in the oedometer cells (EDO-sat, EDO-10, EDO-50, EDO-100 and EDO-200) are shown in Fig. 4. All loading and unloading stages were performed by imposing discrete increments of vertical net stress, with each increment maintained for a period between 8 and 16 h to ensure dissipation of excess pore-water pressures. In test EDO-200, the two wetting–drying cycles were performed by changing suction in intervals of 50 kPa.

During all tests, water exchange from/to the sample was measured by means of two double-walled burettes and a differential pressure transducer. One burette was connected to the pore-water drainage line while the second burette was isolated to provide a reference constant water level. The differential pressure transducer measured the water level change in the first burette with respect to the reference one and this was translated into a corresponding change of pore-water volume.

Blind test

The stress path for the blind test is shown in Fig. 5. After equalisation at $q = 0$ kPa, $p = 20$ kPa and $s = 100$ kPa, the sample was isotropically loaded at a constant suction of 100 kPa and subsequently sheared at constant water content. It was not known a priori whether suction would increase or decrease during constant water content shearing, hence the initial loading stage was performed at a lower constant suction of 100 kPa compared to the suction of 200 kPa imposed during the triaxial tests used for calibration of model parameters. This ensured that the measured suction variation during constant water content shearing would fall between a suction of zero and 200 kPa, which is the range covered by the calibration data. A constant water content shearing stage was deliberately chosen for the blind test so as to assess the ability of the different models to predict strongly coupled hydromechanical soil behaviour.

During shearing at constant water content, suction was measured by means of the axis translation technique. The pore-water drainage line was isolated so that no pore-water changes were allowed while the pressure transducer was kept in communication with the sample. Suction was then measured as the difference between the applied constant pore-air pressure and the pore-water pressure measured by the transducer.

COMPARISON OF PREDICTED AND EXPERIMENTAL BEHAVIOUR

All six teams returned predictions for tests TX02, TX07 and EDO-200 as well as for the blind test. The initial values of void ratio and degree of saturation (i.e. the values of void ratio and degree of saturation corresponding to the equalisation stress state) were also predicted for each test. 'Incremental' models predicting changes of void ratio, such as those by CU, EPFL, ENPC and UNSW, calculated the initial

Table 3. Summary of tests used during calibration of constitutive models

Test code	Stress path	Post-compaction void ratio	Post-compaction degree of saturation	Initial equalisation
Triaxial loading				
TX03	Isotropic load ($\eta = \Delta q/\Delta p = 0$) @ $s = 200$ kPa	0·86	0·43	$q = 0$ kPa, $p = 20$ kPa, $s = 200$ kPa
TX04	Anisotropic load ($\eta = \Delta q/\Delta p = 0{\cdot}375$) @ $s = 200$ kPa	0·82	0·42	$q = 8$ kPa, $p = 20$ kPa, $s = 200$ kPa
TX08	Anisotropic load ($\eta = \Delta q/\Delta p = 0{\cdot}750$) @ $s = 200$ kPa	0·87	0·44	$q = 20$ kPa, $p = 27$ kPa, $s = 200$ kPa
TX09	Anisotropic load ($\eta = \Delta q/\Delta p = 0{\cdot}875$) @ $s = 200$ kPa	0·81	0·42	$q = 19$ kPa, $p = 22$ kPa, $s = 200$ kPa
Triaxial loading followed by shearing at constant radial net stress				
TX01	No load @ $s = 200$ kPa	0·85	0·44	$q = 0$ kPa, $p = 10$ kPa, $s = 200$ kPa
TX02	Isotropic load ($\eta = \Delta q/\Delta p = 0$) @ $s = 200$ kPa	0·83	0·43	$q = 0$ kPa, $p = 10$ kPa, $s = 200$ kPa
TX06	Anisotropic load ($\eta = \Delta q/\Delta p = 0{\cdot}750$) @ $s = 200$ kPa	0·83	0·40	$q = 15$ kPa, $p = 20$ kPa, $s = 200$ kPa
TX07	Anisotropic load ($\eta = \Delta q/\Delta p = 0{\cdot}750$) @ $s = 200$ kPa	0·83	0·40	$q = 15$ kPa, $p = 20$ kPa, $s = 200$ kPa
Ko loading				
EDO-sat	Load–unload–reload @ saturation	0·82	0·42	$\sigma_v = 1$ kPa, $s = 0$ kPa
EDO-10	Load–unload–reload @ $s = 10$ kPa	0·82	0·38	$\sigma_v = 20$ kPa, $s = 10$ kPa
EDO-50	Load–unload–reload @ $s = 50$ kPa	0·82	0·41	$\sigma_v = 20$ kPa, $s = 50$ kPa
EDO-100	Load–unload–reload @ $s = 100$ kPa	0·82	0·41	$\sigma_v = 20$ kPa, $s = 100$ kPa
EDO-200	Wet–dry @ $\sigma_v = 20$ kPa Load–unload–reload @ $s = 200$ kPa Wet–dry @ $\sigma_v = 800$ kPa	0·81	0·38	$\sigma_v = 20$ kPa, $s = 200$ kPa

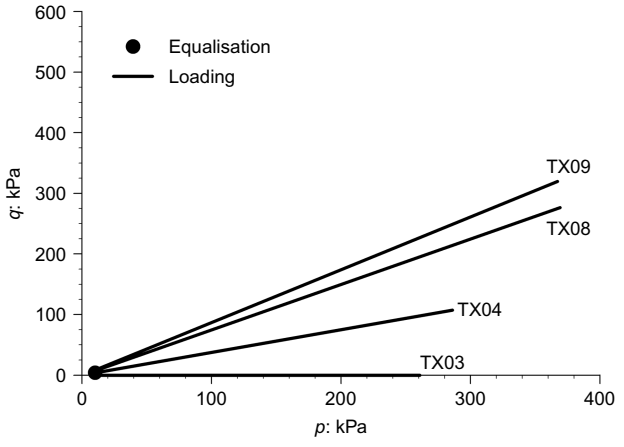

Fig. 2. Stress paths for tests involving triaxial compression: TX03 – isotropic compression until a mean net stress of 260 kPa; TX04 – anisotropic compression ($\eta = 0{\cdot}375$) until a mean net stress of 285 kPa; TX08 – anisotropic compression ($\eta = 0{\cdot}750$) until a mean net stress of 370 kPa; and TX09 – anisotropic compression ($\eta = 0{\cdot}875$) until a mean net stress of 370 kPa

void ratio in each test by following a stress path originating from a single reference value of void ratio corresponding to the equalisation stress state in the blind test, which was estimated on the basis of available data. On the other hand, 'integrated' models that incorporate void ratio as a state variable, such as those by UNINA, UGLAS-1 and UGLAS-2, calculated the initial void ratio directly from the equalisation stress state in each test.

Models were calibrated by the different teams using all 13 tests provided and trying to give the best interpretation possible of the full set of experimental data. The chosen parameter values for all constitutive models are listed in Table 4.

Two general observations can be made here about the calibration approaches followed by the different teams. First, ENPC and UNSW calibrated their respective water retention models considering the entire set of available data, including constant-suction oedometric and triaxial loading stages as well as the wetting–drying cycles of test EDO-200. On the other hand, CU, UGLAS-1, UGLAS-2 and UNINA used the constant-suction oedometric and triaxial loading stages but not the wetting–drying cycles of EDO-200, while EPFL only used the loading and wetting–drying stages of test EDO-200.

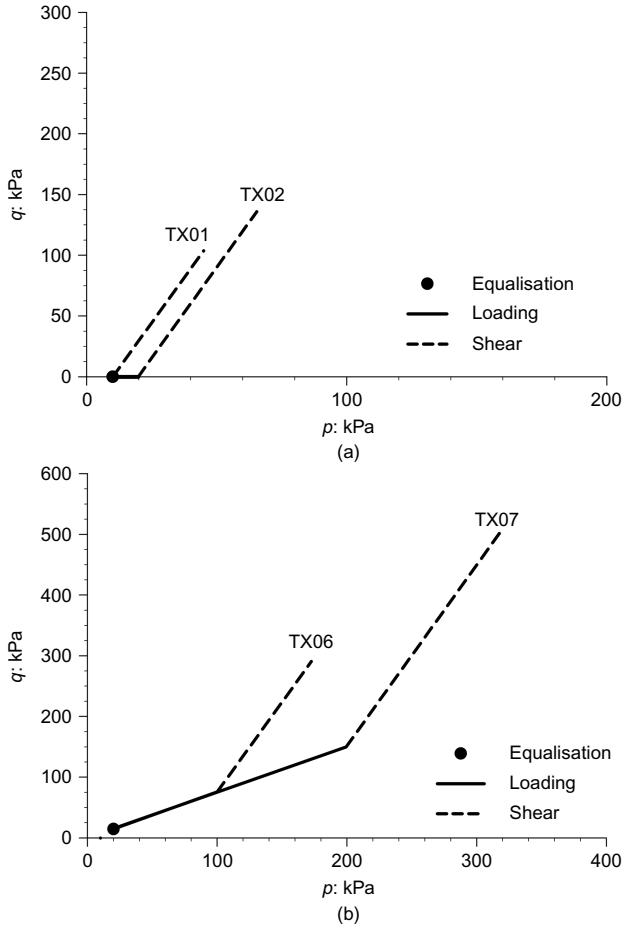

Fig. 3. Stress paths for tests involving triaxial compression followed by shearing: (a) TX01 – shearing to critical state (no compression) and TX02 – isotropic compression until a mean net stress of 20 kPa followed by shearing to critical state; (b) TX06 – anisotropic compression ($\eta = 0{\cdot}750$) until a mean net stress of 100 kPa followed by shearing to critical state and TX07 – anisotropic compression ($\eta = 0{\cdot}750$) until a mean net stress of 200 kPa followed by shearing to critical state

Second, because only one experimental isotropic compression at $s = 200$ kPa was available from test TX03, all teams made use of additional data from constant-suction oedometric compression to calibrate the isotropic part of their mechanical models.

Teams ENPC, EPFL and UNSW, whose models adopt yield curves of the first class in the s–p' plane, started by defining the shape of the yield curve based on measured yield stresses with the spacing between constant-suction normal compression lines becoming then fixed as a consequence (see Appendix for the relationship between the shape of the yield curve and spacing of constant-suction normal compression lines). In the ENPC model, the shape of the yield curve was defined to match the yield stresses from the five oedometric tests whereas, in the case of EPFL and UNSW, test EDO-200 was replaced by the isotropic loading of test TX03 at $s = 200$ kPa. This resulted in a steeper predicted yield curve between $s = 50$ kPa and $s = 200$ kPa for these two models.

Teams CU, UGLAS-1, UGLAS-2 and UNINA, whose models adopt yield curves of the second class, started instead by defining the spacing between constant-suction normal compression lines on the basis of the five oedometric tests, which in turn fixed the shape of the yield curve in the s–p' plane. A detailed explanation of the calibration procedure followed by UGLAS can be found in the work by Gallipoli *et al.* (2010).

In all seven models, the slopes of constant-suction normal compression lines were mainly determined from oedometric tests, although ENPC, UGLAS-1, UGLAS-2 and UNINA took some account of data from the loading stages of the triaxial tests at $s = 200$ kPa.

In the following, predictions for tests TX02, TX07 and EDO-200, as well as for the blind test, are compared among themselves and with experiments.

Triaxial test TX02

Figure 6 compares predicted and experimental data during the shearing stage of test TX02. Results from the loading stage are not presented given that the maximum mean net stress applied during this stage was only 20 kPa, with all models predicting small and mainly reversible changes of void ratio and degree of saturation over this limited stress range.

With reference to Fig. 6, three types of results can be distinguished:

(*a*) mechanical uncoupled results depending only on the mechanical model but not on the water retention model
(*b*) hydraulic uncoupled results depending only on the water retention model but not on the mechanical model
(*c*) coupled results depending on both mechanical and water retention models.

CU, UGLAS-1, UGLAS-2, UNINA and UNSW all adopt stress tensors not depending on degree of saturation. Thus, for constant-suction tests, predictions in the q–ε_a and ε_v–ε_a planes (see Figs 6(a) and 6(b)) by these five teams (ε_a and ε_v are the axial and volumetric strains, respectively) represent mechanical uncoupled results. The corresponding predictions by ENPC and EPFL represent instead coupled results as, in this case, the constitutive stress path is influenced by the chosen water retention model through the dependency of the constitutive stress tensor on degree of saturation.

Predictions in the S_r–ε_v plane (see Fig. 6(c)) represent instead hydraulic uncoupled results for all teams. This is because all water retention models postulate a link between degree of saturation, suction and porosity, which can be recast as a link between degree of saturation, suction and volumetric strain, once the initial value of porosity at the start of shearing is taken into account. As a consequence, the shape of the predicted curve in the S_r–ε_v plane depends on the water retention relationship alone, although the range of volumetric strains over which degree of saturation varies does depend also on the predicted mechanical response.

Finally, the predicted S_r–ε_a relationships in Fig. 6(d) represent coupled results, as the shape of these curves comes from the combination of the previous S_r–ε_v and ε_v–ε_a curves in Figs 6(b) and 6(c) respectively.

In Fig. 6(a), the q–ε_a relationships predicted by CU, UGLAS-1, UGLAS-2, UNINA and UNSW show an initial stiff response, that is in good agreement with experiments, as well as a relatively accurate prediction of critical strength. On the other hand, ENPC and EPFL predict lower values of initial stiffness and overestimate critical strength. Small changes of degree of saturation are calculated in Fig. 6(c) for both these models, which suggests that their different predictions in the q–ε_a plane are not attributable to the influence of the water retention relationship on the constitutive stress path (caused by the dependency of the constitutive stress tensor on degree of saturation). Instead the low shear stiffness predicted by the ENPC model is due to the narrow elastic range in the deviatoric plane and the particular kinematic hardening law inherited by the parent saturated

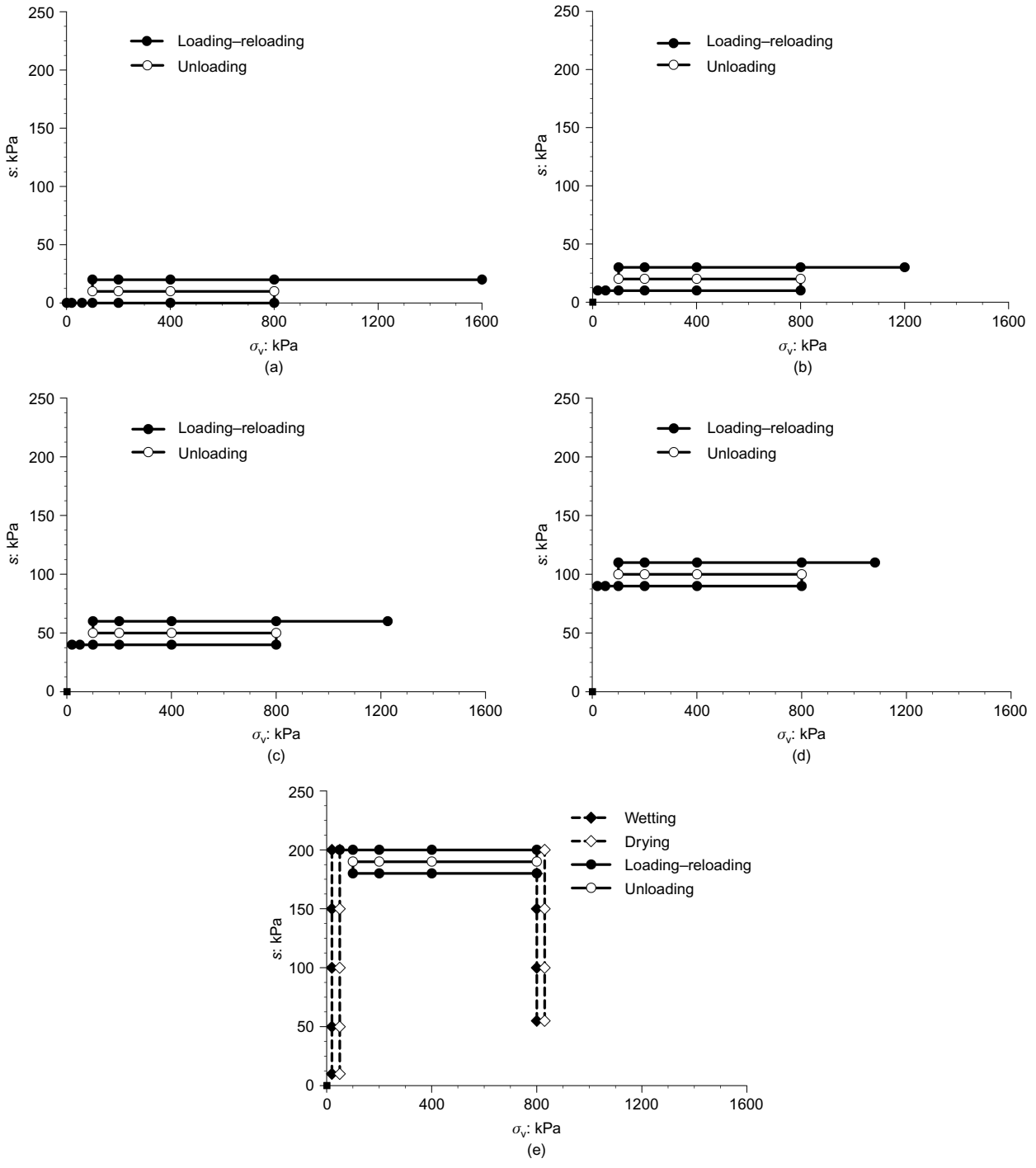

Fig. 4. Stress paths for tests involving Ko loading: (a) EDO-sat – loading to a vertical effective stress of 800 kPa, unloading to 100 kPa and reloading to 1600 kPa; (b) EDO-10 – loading to a vertical net stress of 800 kPa, unloading to 100 kPa and reloading to 1200 kPa; (c) EDO-50 – loading to a vertical net stress of 800 kPa, unloading to 100 kPa and reloading to 1226 kPa; (d) EDO-100 – loading to a vertical net stress of 800 kPa, unloading to 100 kPa and reloading to 1080 kPa; (e) EDO-200 – wetting to a suction of 10, drying to 200 kPa, loading to a vertical net stress of 800 kPa, unloading to 100 kPa, reloading to 800 kPa, wetting to a suction of 55 and drying to 200 kPa

model (see Table 1). The kinematic hardening law of the parent saturated model is also responsible for the significant overestimation of critical strength in the ENPC case. On the other hand, the low initial stiffness predicted by the EPFL model is mainly the consequence of the underestimation of the elastic stiffness at low stresses.

In Fig. 6(b) all models except ENPC correctly predict dilatant behaviour, although the magnitude of dilation is underestimated in all cases. For the models predicting dilatant behaviour, the magnitude of the volumetric strain at the end of shearing depends on the relative positions of the constant-suction normal compression and critical state lines. It is therefore not surprising that the most accurate predictions are produced by the UNINA model, which offers complete flexibility in defining position and slope of constant-suction critical state lines in the v–$\ln p'$ plane. On the other hand, in the EPFL and UNSW models, the position of constant-suction critical state lines can be varied to fit experimental data but their slope is constant and equal to the slope of normal compression lines. The least flexibility is

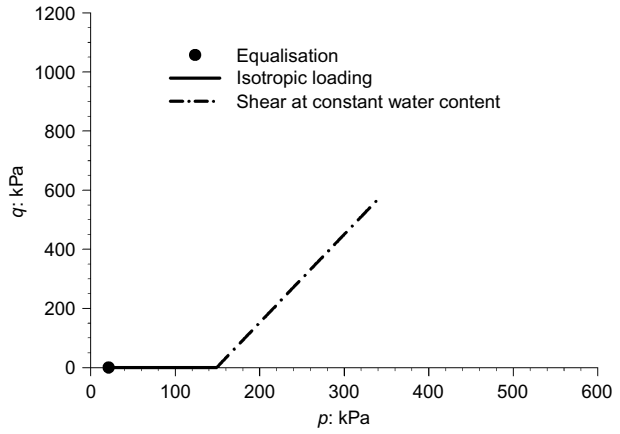

Fig. 5. Stress paths for the blind test involving isotropic compression until a mean net stress of 150 kPa followed by shearing to critical state at constant water content

offered by the CU, UGLAS-1 and UGLAS-2 models, for which the distance between constant-suction normal compression and critical state lines is fixed in their respective constitutive formulations. Hence, the underestimation of dilatant behaviour by the CU and UGLAS-1 models in Fig. 6(b) is a consequence of the excessive spacing between constant-suction critical state and normal compression lines in the $v-\ln p'$ plane (similar to excessive spacing between saturated critical state and normal compression lines in the modified Cam-clay model). Rather surprisingly, however, the volumetric strain predicted at the end of shearing by the UGLAS-2 model provides one of the best matches to the experimental data. This accurate prediction is caused by rotational hardening of the anisotropic yield locus, which results in a smaller distance between constant-suction normal compression and critical state lines for the UGLAS-2 model compared to the CU and UGLAS-1 models.

Figure 6(c) shows hydraulic uncoupled predictions running

Table 4. Model parameter values used by participating teams (values below double line represent initial values of state variables)

Team	Mechanical model parameters		Water retention model parameters	
	Symbol (units)	Value	Symbol (units)	Value
CU	ϕ_c(°)	36·0	s_{e0} (kPa)	10
	λ^* (–)	0·09	λ_{p0} (–)	0·25
	κ^* (–)	0·0025	e_0 (–)	0·7
	N (–)	0·925	—	—
	r (–)	0·03	—	—
	n (–)	0·055	—	—
	l (–)	0	—	—
	m (–)	2	—	—
	Saturated Hvorslev stress (kPa)	33·3	—	—
ENPC	K_0^e (kPa)	15 000	s_{e0}(kPa)	5·0
	n (–)	0·6	λ_0 (–)	3·78
	ν (kPa)	0·35	A (–)	16·0
	K_0^p (kPa)	600	ϕ_{ref} (–)	0·465
	γ (–)	0·8	—	—
	a (kPa^{-1})	0·021	—	—
	ϕ_0 (–)	7·05	—	—
	β_0 (–)	−0·08	—	—
	R_e (–)	0·1	—	—
	R_c (–)	0·6	—	—
	k_1 (–)	0·3	—	—
	k_2 (–)	0	—	—
	k_3 (–)	0	—	—
	k_4 (–)	0	—	—
	Q_0 (kPa)	47	—	—
	X (–)	Null tensor	—	—
EPFL	K_i (kPa)	150 000	K_h (–)	18
	G_i (kPa)	120 000	β_h (–)	10
	n^e (–)	1	s_e (kPa)	3
	ϕ' (°)	31·0	π_H (kPa)	350
	β_0 (–)	17	s_{DI} (kPa)	15
	α (–)	0·75	S_{res} (–)	0·01
	a (–)	0·02	—	—
	b (–)	0·01	—	—
	c (–)	0·0001	—	—
	d (–)	2	—	—
	r^e_{dev} (–)	0·01	—	—
	r^e_{iso} (–)	0·1	—	—
	γ_s (–)	1·8	—	—
	Ω (–)	2×10^{-5}	—	—
	p'_{CR} (kPa)	27	—	—

(*continued*)

Table 4. (*continued*)

Team	Mechanical model parameters		Water retention model parameters	
	Symbol (units)	Value	Symbol (units)	Value
UGLAS-1	κ (–)	0·004	ϕ (kPa^{-1})	1·318
	κ_s (–)	0·006	ψ (–)	6·036
	G (kPa)	36 000	m (–)	0·146
	$N(0)$ at $p' = p_c$ (–)	−0·4928	n (–)	1·341
	$\lambda(0)$ (–)	0·1358	—	—
	r (–)	1·19597	—	—
	β (kPa^{-1})	0·00397	—	—
	p_c (kPa)	826 699 057	—	—
	k (–)	0·138	—	—
	M (–)	1·45	—	—
	p_0^* (kPa)	30	—	—
UGLAS-2	κ (–)	0·004	ϕ (kPa^{-1})	1·318
	κ_s (–)	0·006	ψ (–)	6·036
	G (kPa)	36 000	m (–)	0·146
	$N(0)$ at $p' = p_c$ (–)	−0·42641	n (–)	1·341
	$\lambda(0)$ (–)	0·1358	—	—
	r (–)	1·19597	—	—
	β (kPa^{-1})	0·00397	—	—
	p_c (kPa)	508 841 924	—	—
	k (–)	0·138	—	—
	M (–)	1·45	—	—
	μ (–)	92·047	—	—
	b (–)	1	—	—
	$p_m(0)$ (kPa)	30	—	—
	α	0·144	—	—
UNINA	κ (–)	0·003	ϕ (kPa^{-1})	0·51
	κ_s (–)	0·003	ψ (–)	4·81
	λ_s (–)	0·09	m (–)	0·22
	G (kPa)	5000	n (–)	1·04
	h (–)	1·2	—	—
	c_1 (–)	−0·2	—	—
	c_2 wet side (–)	0·5	—	—
	c_2 dry side (–)	0·1	—	—
	λ (–)	0·130/0·130*	—	—
	N (–)	1·753/1·880*	—	—
	M (–)	1·455/1·455*	—	—
	μ (kPa)	0/40*	—	—
	Ψ (–)	0·130/0·100*	—	—
	Γ (–)	1·665/1·820*	—	—
	$p_0(0)$ (kPa)	52	—	—
UNSW	κ (–)	0·0004	s_{ex} (kPa)	5·0
	ν (–)	0·30	s_{ae} (kPa)	15·0
	ϕ'_c (°)	35·9	λp (–)	0·24
	λ (–)	0·16 for $s \geqslant s_{ex}$ or s_{ae}	ξ (–)	0·08
	N(–)	2·67 for $s \geqslant 100$ kPa 2·62 for $s = 50$ kPa 2·56 for $s \leqslant s_{ex}$ or s_{ae}	ζ (–)	0·2
	N (–)	2·25	—	—
	R (–)	1·40	—	—
	A (–)	1·0	—	—
	k_m (–)	20·0	—	—
	Isotropic saturated yield stress (kPa)	98·7	—	—

* The two values refer to $s = 0$ and 200 kPa respectively (linear interpolation was used for intermediate suctions)

approximately parallel to the experiments in the S_r–ε_v plane, which confirms that all water retention models capture reasonably well the variation of degree of saturation with volumetric strain (with the only exception of EPFL).

The vertical shift between curves in Fig. 6(c) is caused by the different initial values of void ratio predicted at the start of the loading stage (i.e. after equalisation), which has an impact on the corresponding calculation of degree of saturation. As previously mentioned, initial values of void ratio at equalisation are computed by incremental models following

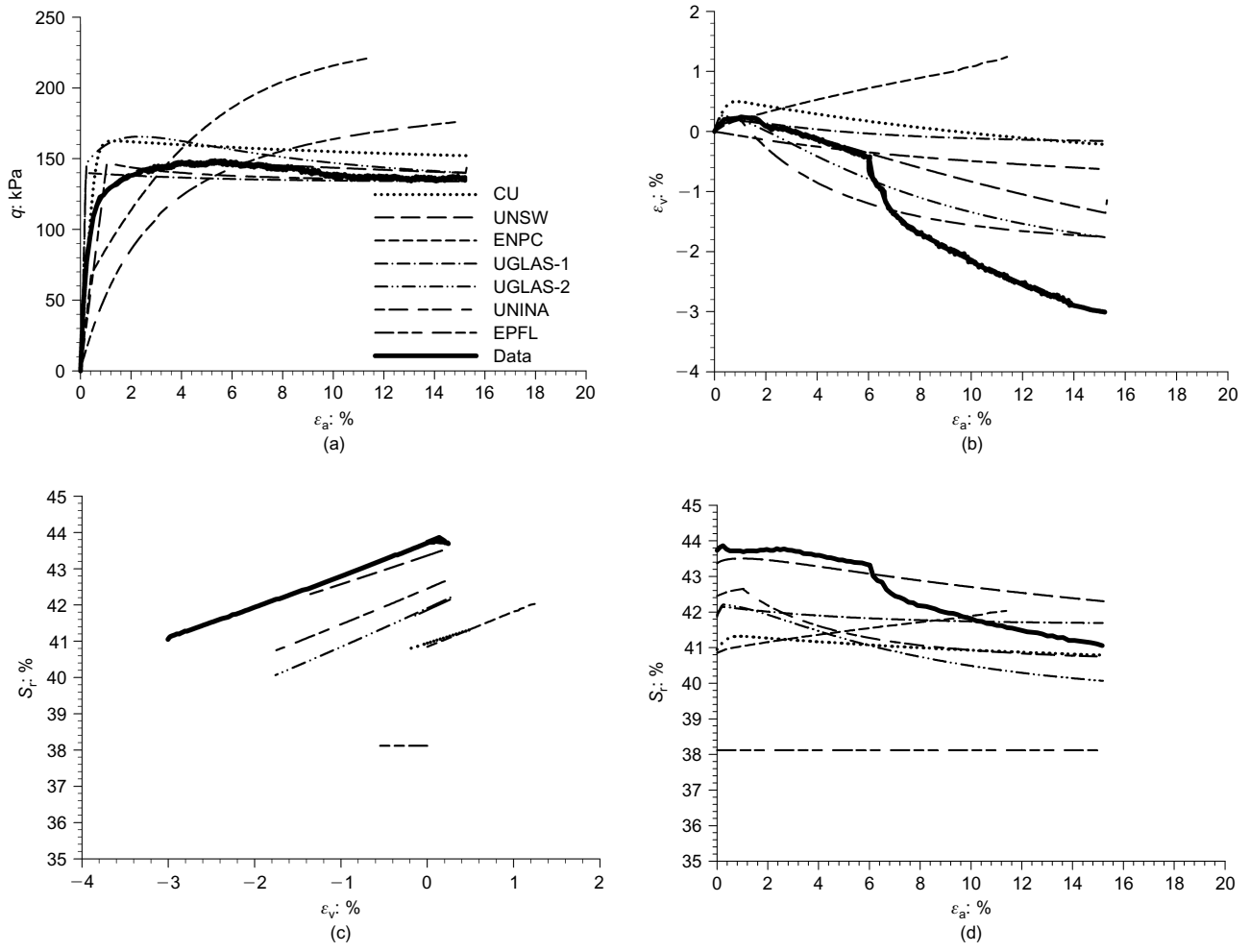

Fig. 6. Predicted and experimental behaviour during shearing stage of test TX02: (a) deviator stress (q) plotted against axial strain (ε_a); (b) volumetric strain (ε_v) plotted against axial strain (ε_a); (c) degree of saturation (S_r) plotted against volumetric strain (ε_v); (d) degree of saturation (S_r) plotted against axial strain (ε_a)

a stress path originating from a reference soil state where void ratio had been previously estimated. There also appears to be a systematic error between predicted and experimental values of void ratio at the start of each test; that is all predictions appear to make an error of consistent sign, which can be either positive or negative. This is due to the large experimental scatter of the post-compaction values of void ratio among the tested samples (see Table 3). These differences are not entirely erased during equalisation and produce a discrepancy of consistent sign between experimental and predicted values at the start of each test.

Unlike the uncoupled hydraulic predictions of Fig. 6(c), different models provide distinct mechanical uncoupled predictions (or nearly mechanical uncoupled predictions in the case of ENPC and EPFL) in Fig. 6(b), with markedly different forms of variation of volumetric strain with axial strain. The differences between predictions in Fig. 6(b) are also reflected in the variability of coupled predictions in Fig. 6(d).

Triaxial test TX07

Predicted and experimental results are compared for test TX07 in Fig. 7 (loading stage) and Fig. 8 (shearing stage). Figs 7(a), 8(a) and 8(b) show mechanical uncoupled predictions for CU, UGLAS-1, UGLAS-2, UNINA and UNSW, whereas they show coupled predictions for ENPC and EPFL (because of the different definition of constitutive stress in these two groups of models). Figs 7(b) and 8(c) present hydraulic uncoupled predictions for all models. Finally, Figs 7(c) and 8(d) show coupled predictions resulting from the combination of the previous two sets of results.

As expected, ENPC, EPFL, UNINA, UGLAS-1 and UGLAS-2 predict a sharp change of stiffness at yielding in Fig. 7(a) while CU and UNSW show a gradual transition from elastic to plastic behaviour that better reproduces the experimental trend. Consistent predictions of yield stresses are obtained by the different models, which are also in reasonably good agreement with experiments. The smaller preconsolidation stress predicted by ENPC is again the consequence of the narrow elastic range assumed in the deviatoric plane by this model.

The prediction by ENPC also shows a stiffer post-yield response compared to other curves, a behaviour that is similarly observed during constant-suction loading in the blind test and test EDO-200, as will be shown later. It is interesting to note that the ENPC model predicts the stiffest post-yield response in the e–$\ln p$ plane (where e is the void ratio) despite assuming the smallest plastic stiffness in the e–$\ln p'$ plane, as indicated by the relatively small value of parameter K_0^p in Table 4. This apparently surprising result is the consequence of the incorporation of the additive term χ_2 in the constitutive stress definition of equation (3), which results in a comparatively stiffer response when void ratio is plotted against mean constitutive stress rather than mean net stress. It also suggests that the particular choice of constitutive stress tensor has an influence on calibration of plastic stiffness.

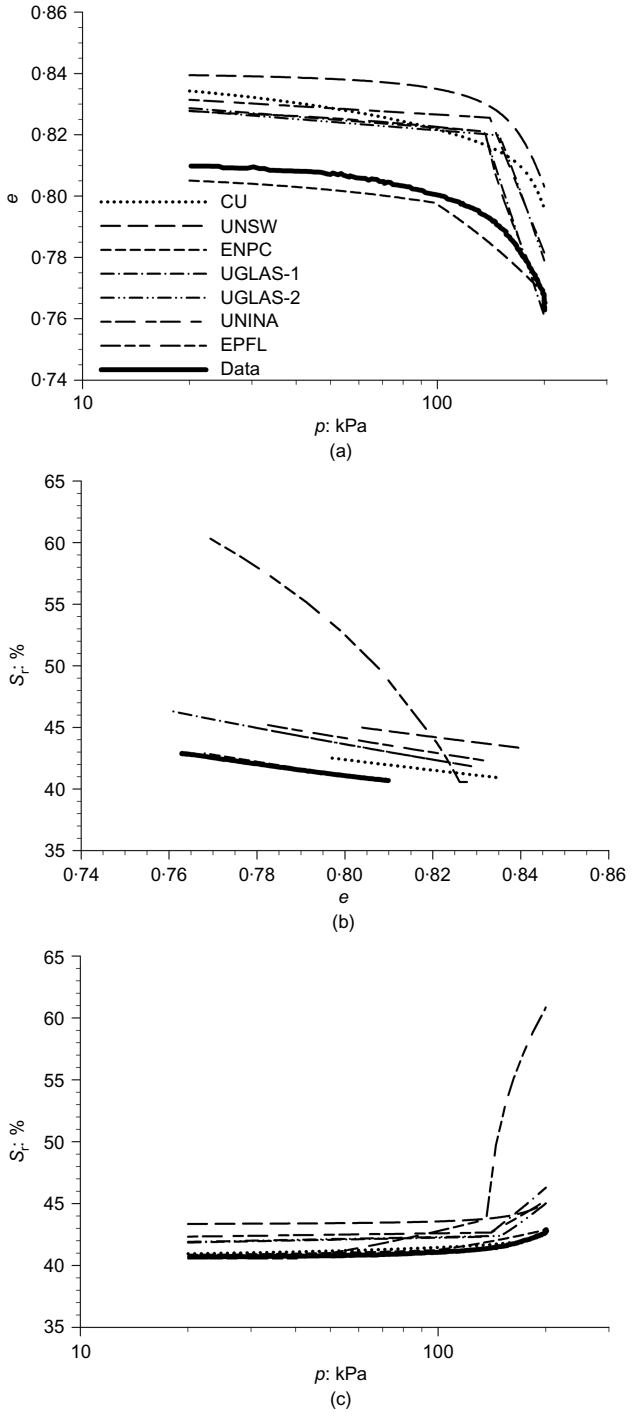

Fig. 7. Predicted and experimental behaviour during loading stage of test TX07: (a) void ratio (e) plotted against mean net stress (p); (b) degree of saturation (S_r) plotted against void ratio (e); (c) degree of saturation (S_r) plotted against mean net stress (p)

Hydraulic uncoupled predictions in Figs 7(b) and 8(c) confirm that all water retention models capture relatively well the dependency of degree of saturation on volumetric strain, with the only exception of EPFL which significantly overestimates the increase of degree of saturation during the compression stage. This is due to the particular water retention calibration performed by this team and, more specifically, to the choice of an excessively large value of parameter π_h (see Table 4), which relates degree of saturation to volumetric strain and had been selected on the basis of test EDO-200 alone.

With regard to the shape of predicted curves, the relationship between degree of saturation and void ratio in Fig. 7(b), or between degree of saturation and volumetric strain in Fig. 8(c), shows smaller differences between models than the relationship between volumetric strain and axial strain in Fig. 8(b) (with the exception of EPFL). This confirms the greater uniformity of hydraulic uncoupled predictions compared to mechanical uncoupled predictions and, hence, indicates that greater consistency exists between water retention models compared to mechanical models at least for paths that do not involve suction or stress reversals. Similarly to test TX02, Fig. 8(b) shows that the prediction of the final volumetric strain is least accurate for CU and UGLAS-1, which is again due to the overestimation of the distance between constant-suction normal compression and critical state lines as previously explained. On the other hand, the most accurate prediction is this time provided by ENPC followed by UNINA.

Coupled predictions mirror features of mechanical uncoupled predictions because of their dependency on both mechanical and water retention models. For example, the sharp mechanical yielding predicted by classic elasto-plastic models is also evident in the coupled predictions of Fig. 7(c) but not in the hydraulic uncoupled predictions of Fig. 7(b). Owing to the greater accuracy of hydraulic uncoupled predictions compared to mechanical uncoupled predictions, potential errors in the predicted shape of coupled relationships are mainly the consequence of inadequacies of the mechanical model rather than the water retention model (with the exception of EPFL where the calibration of the water retention model is responsible for the large deviation from experimental results).

Blind triaxial test

Predicted and experimental results are compared for the blind test in Fig. 9 (loading stage at $s = 100$ kPa) and Fig. 10 (shearing stage at constant water content). As previously discussed, Fig. 9(a) shows relatively large errors of consistent sign for the predicted initial values of void ratio, although, unlike test TX07, experimental values are now underestimated by all teams.

Compared to test TX07, greater inconsistencies exist between predicted yield stresses in Fig. 9(a). In particular, ENPC, UGLAS-1, UGLAS-2 and UNINA underestimate yield stress while EPFL and UNSW overestimate it.

Calibration of the former group of four models took into account all five constant-suction oedometric compressions when defining the shape of the yield curve in the s–p' plane. This was done either directly, by fitting yield stresses at different suctions, as in the case of ENPC, or indirectly, by fixing the spacing and slopes of constant-suction normal compression lines in the v–$\ln p'$ plane, as in the case of UGLAS-1, UGLAS-2 and UNINA. In all four cases, once the shape of the yield curve had been defined, its position was adjusted to optimise prediction of yield stresses during both triaxial and oedometric tests. Fig. 9(a) shows that the above procedure predicts a decrease of yield stress with decreasing suction that slightly underestimates the measured value at $s = 100$ kPa.

In the UNSW and EPFL models, the shape of the yield curve in the s–p' plane was instead defined after replacing the yield stress of test EDO-200 with that of the isotropic loading of test TX03 (also at $s = 200$ kPa), which resulted in a steep variation of yield stress with suction. For $s \geqslant 50$ kPa, the yield stress remained approximately constant and equal to the value measured at $s = 200$ kPa in test TX03 so that the experimental yield stress at $s = 100$ kPa is overestimated (see Fig. 9(a)).

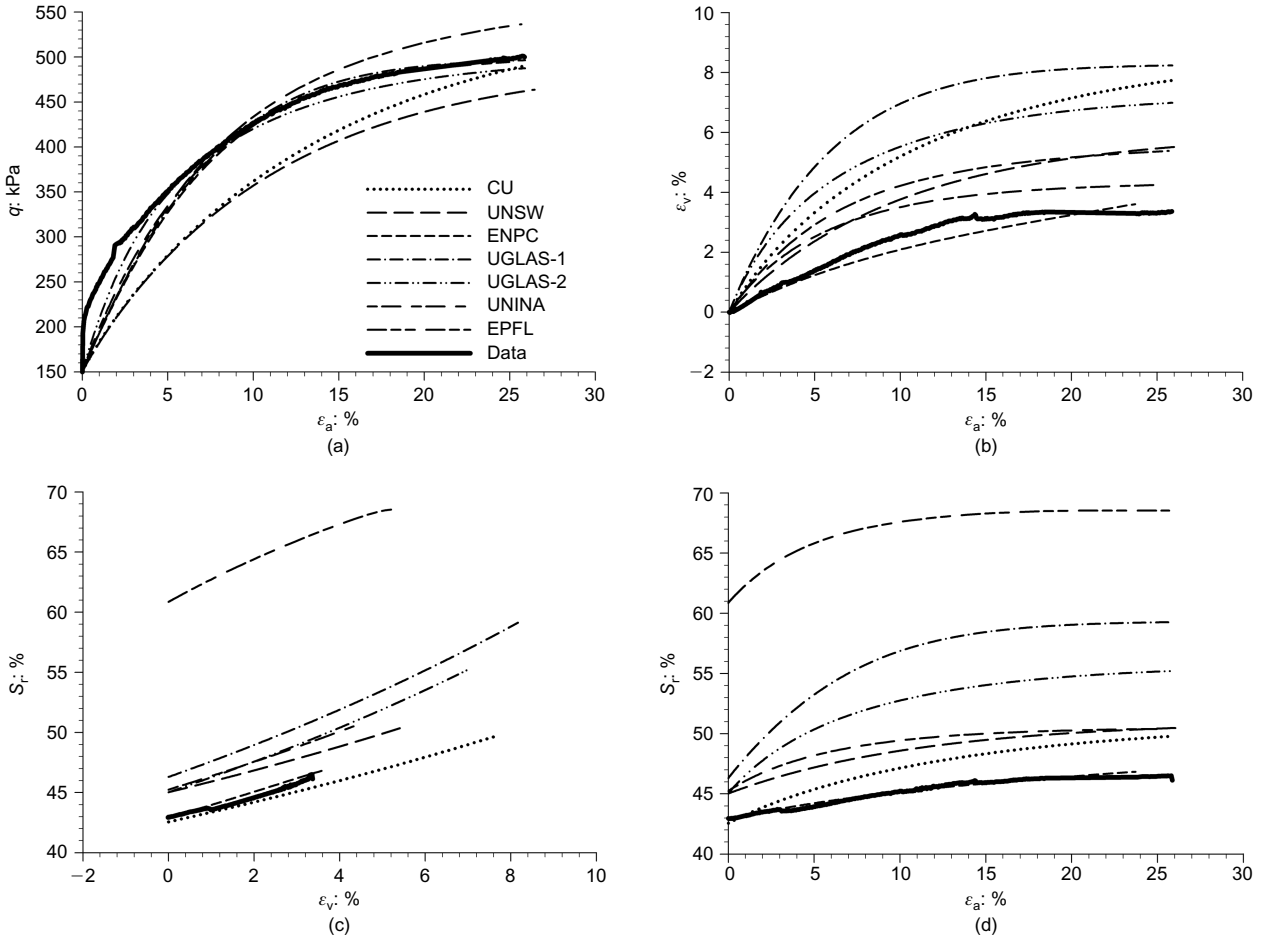

Fig. 8. Predicted and experimental behaviour during shearing stage of test TX07: (a) deviator stress (q) plotted against axial strain (ε_a); (b) volumetric strain (ε_v) plotted against axial strain (ε_a); (c) degree of saturation (S_r) plotted against volumetric strain (ε_v); (d) degree of saturation (S_r) plotted against axial strain (ε_a)

Similarly to test TX07, remarkably consistent shapes are obtained for the hydraulic uncoupled predictions in the S_r–e plane for six of the seven models (Fig. 9(b)), with the different simulation from EPFL caused by an inappropriate choice of value for parameter π_h as previously explained. Coupled predictions in Fig. 9(c) are obtained by combining the two sets of curves in Figs 9(a) and 9(b) respectively. Coupled predictions therefore show features from both the above sets of results, such as the occurrence of a sharp yielding point similar to Fig. 9(a), and the large increase of degree of saturation predicted by EPFL similar to Fig. 9(b). The initial value of degree of saturation is consistently overestimated by all models in Figs 9(b) and 9(c), which corresponds to the systematic underestimation of initial void ratio in Fig. 9(a).

During the subsequent shearing stage at constant water content, six out of seven models calculate similar values of critical strength within a range of about 50 kPa (Fig. 10(a)). All predictions, however, fall short of the experimental critical strength by a margin greater than 100 kPa owing to the unexpectedly high critical strength measured during constant water shearing. This is considerably higher than the strength recorded in tests TX01, TX02, TX06 and TX07 at a suction of 200 kPa, despite a value of suction lower than 200 kPa being measured at critical state during constant water shearing.

Prediction of volumetric strains in Fig. 10(b) show that, unlike tests TX02 and TX07, the CU and UGLAS-1 models provide the closest match to the experimental data, followed by UNINA and UGLAS-2. The accurate prediction of volumetric strain at critical state by the CU and UGLAS-1 models is rather unexpected and inconsistent with the previous simulations of tests TX02 and TX07. This rather surprising result is possibly the consequence of the disagreement between measured and predicted values of suction during constant water content shearing, as it will be shown later.

Considering all shearing stages in test TX02, test TX07 and the blind test, UNINA provides the most accurate prediction of volumetric strains overall, which is an expected result given the flexibility of this model in fitting the experimental volumetric behaviour at critical state. Rather unexpected is perhaps the good accuracy of UGLAS-2, which confirms that the adoption of an anisotropic yield locus (i.e. a yield locus inclined at an angle with respect to the hydrostatic axis in the principal stress space) improves prediction of volumetric strains at critical state.

Similarly to tests TX02 and TX07, the shape of the predicted curves in the S_r–ε_v plane (Fig. 10(c)) is closer to the experimental data compared to predicted curves in the ε_v–ε_a plane (Fig. 10(b)). Note, however, that – unlike the constant suction tests TX02 and TX07 – in this case the predicted curves in the S_r–ε_v plane do not depend on the water retention model but only on the initial values of degree of saturation, S_{r0} and void ratio, e_0 at the start of shearing. The curves in Fig. 10(c) can in fact be calculated by imposing the condition of zero water content change during shearing while taking into account the relation between void ratio and volumetric strain, that is $e = e_0 - \varepsilon_v(1 + e_0)$

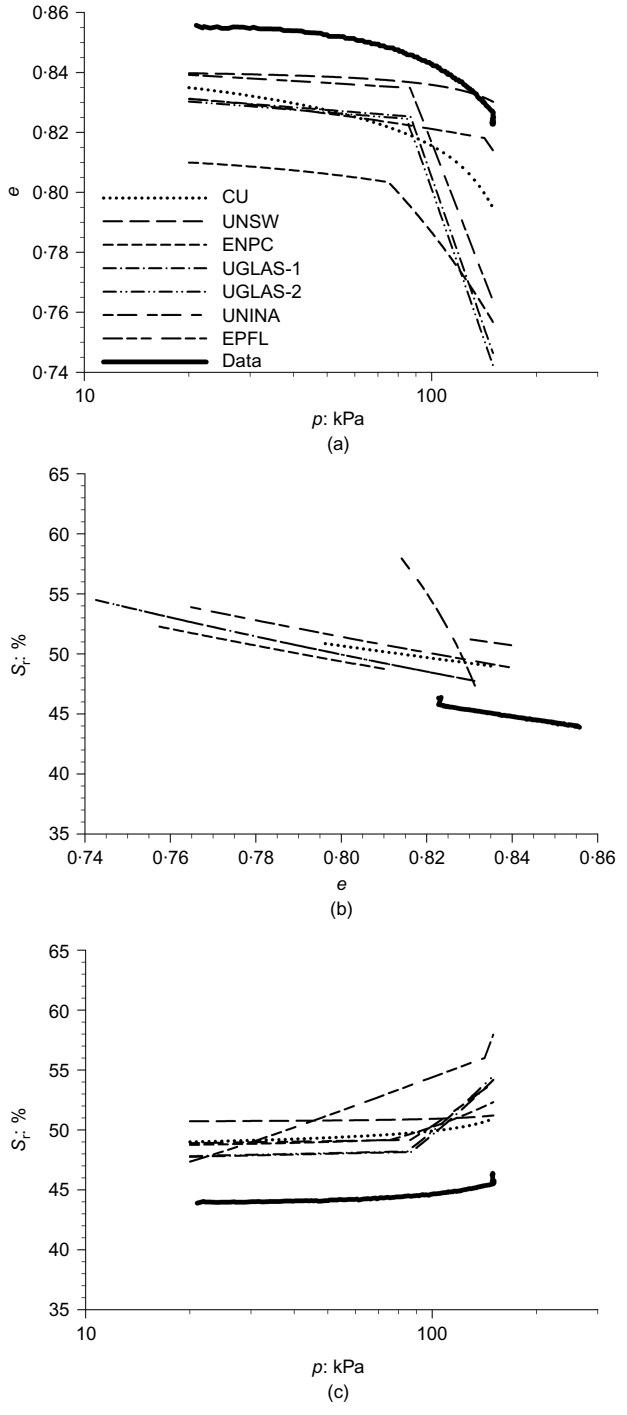

Fig. 9. Predicted and experimental behaviour during loading stage of blind test: (a) void ratio (e) plotted against mean net stress (p); (b) degree of saturation (S_r) plotted against void ratio (e); (c) degree of saturation (S_r) plotted against mean net stress (p)

$$S_r e = S_{r0} e_0 \Rightarrow S_r = \frac{S_{r0} e_0}{e_0 - \varepsilon_v(1 + e_0)} \Rightarrow S_r = \frac{S_{r0} n_0}{n_0 - \varepsilon_v} \qquad (9)$$

where n_0 is the value of porosity at the start of shearing. Consistent with equation (9), teams predicting large volumetric strains in Fig. 10(b), such as CU and UGLAS-1, also predict large increases of degree of saturation in Fig. 10(c).

Because the shape of predictions in the S_r–ε_v plane (Fig. 10(c)) does not depend on the water retention model, the shape of predictions in the S_r–ε_a plane (Fig. 10(d)) is also independent of the water retention model and is governed by the mechanical model alone. Therefore, unlike tests TX02 and TX07, the variability of shapes of predicted curves in the S_r–ε_a plane is largely attributable to the variability of shapes of predicted curves in the ε_v–ε_a plane (Fig. 10(b)) (the smaller difference between the shapes of predicted curves in the S_r–ε_v plane, which is caused by the different initial values of degree of saturation and void ratio, has a much smaller effect on the variability of shapes of predicted curves in the S_r–ε_a plane compared to tests TX02 and TX07). In fact, if the S_r–ε_a predictions are shifted along the vertical axis to start from the same point, a similar distribution of curves as for the ε_v–ε_a predictions is obtained (the two distributions would look even more similar if the shape of the predicted S_r–ε_v relationships in Fig. 10(c) were exactly the same for all models which, according to equation (9), would only happen if the initial values of degree of saturation, S_{r0} and void ratio, e_0 coincided in all predictions).

During constant water shearing, the occurrence of volumetric strain and the consequent variation of degree of saturation induce a change of suction according to the chosen water retention model. The variation of suction calculated by the different models during shearing is presented in Fig. 10(e), together with the corresponding experimental data.

Figure 10(e) shows significant discrepancies between predictions and even opposite trends. This contradictory range of responses during constant water shearing is explained by the incidence of two contrasting factors, trying to control the variation of suction in opposite directions. For all water retention models, an increase of degree of saturation at constant volumetric strain induces a drop in suction as $\partial s/\partial S_r < 0$ while, on the other hand, a compressive volumetric strain at constant degree of saturation produces an increase of suction as $\partial s/\partial \varepsilon_v > 0$. Whether a drop or an increase of suction is predicted therefore depends on which of the above two factors is dominant.

Given that all predicted S_r–ε_v curves in Fig. 10(c) are approximately parallel, the corresponding increments of degree of saturation and volumetric strain are approximately the same for all models at any point during shearing. The prediction of opposite suction gradients in Fig. 10(e) cannot therefore be attributed to differences in the ratio between increments of degree of saturation and volumetric strain predicted by the distinct models. On the other hand, it depends on whether the chosen water retention model implies greater sensitivity of suction to changes of degree of saturation rather than volumetric strain or vice versa; that is it depends on the relative magnitude of the two partial derivatives $\partial s/\partial S_r$ and $\partial s/\partial \varepsilon_v$.

In summary, at any point during shearing, the direction of suction variation depends on the water retention model alone while the magnitude of such variation depends also on the mechanical model, which controls the magnitude of volumetric strain and, hence, change of degree of saturation during constant water content shearing. This is consistent with the fact that the absolute values of the final suction changes in Fig. 10(e) are largest for CU and UGLAS-1, which are also the two models predicting the largest increases of volumetric strain and degree of saturation over the entire shearing stage (see Fig. 10(c)).

UGLAS-1, UGLAS-2 and UNINA all use the same water retention model (see Table 1), although UGLAS-1 and UGLAS-2 adopt different parameter values compared to UNINA (see Table 4), but the predicted suction variation follows opposite directions, with UGLAS-1 and UGLAS-2 predicting an increase of suction but UNINA showing a slight drop. This demonstrates that the sign of the suction gradient in Fig. 10(e) does not necessarily depend on the

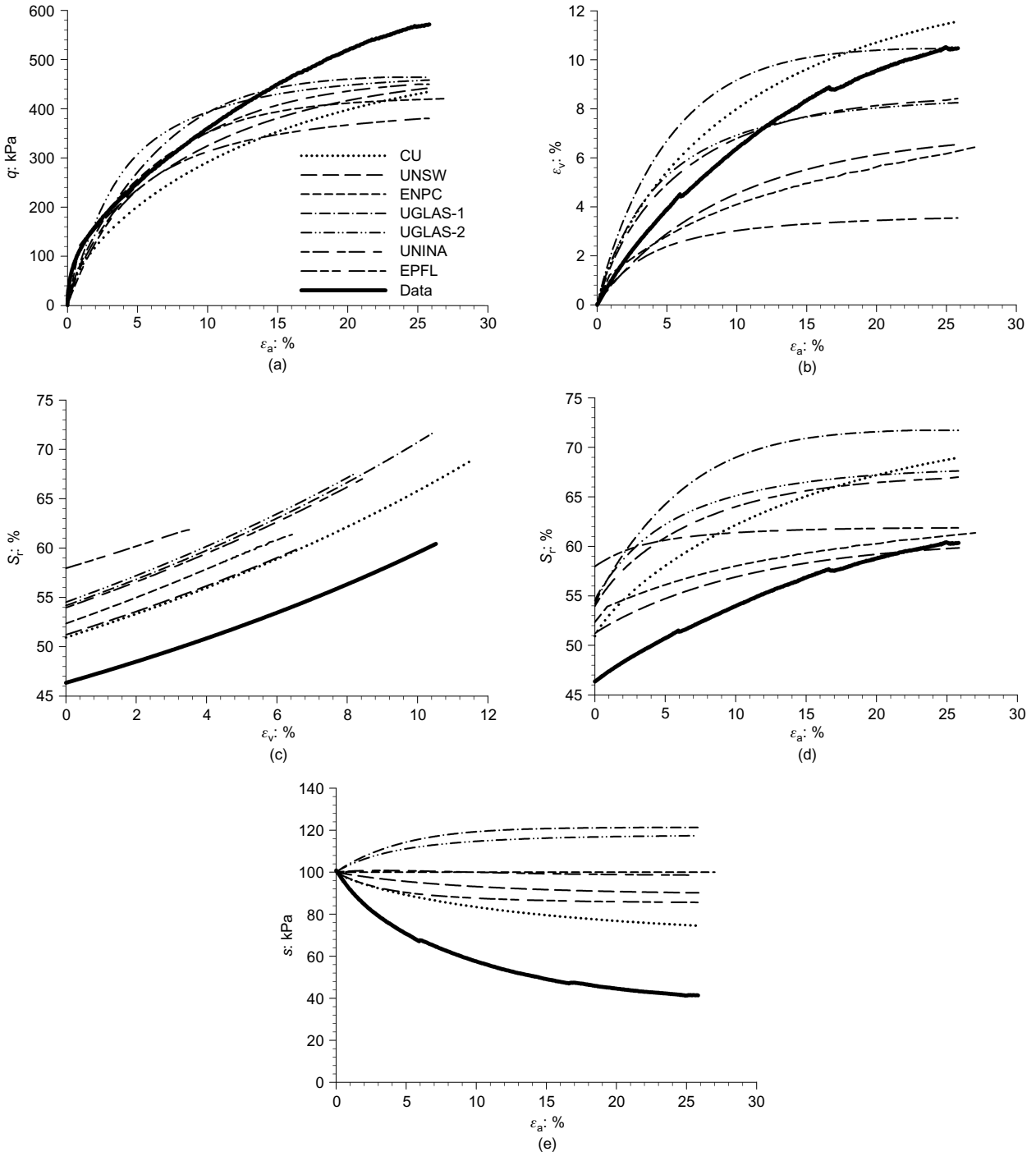

Fig. 10. Predicted and experimental behaviour during shearing stage of blind test: (a) deviator stress (q) plotted against axial strain (ε_a); (b) volumetric strain (ε_v) plotted against axial strain (ε_a); (c) degree of saturation (S_r) plotted against volumetric strain (ε_v); (d) degree of saturation (S_r) plotted against axial strain (ε_a); (e) suction (s) plotted against axial strain (ε_a)

chosen type of water retention model but can also be a consequence of the particular calibration of one given model. This example also shows that constant water content tests can prove useful in refining calibration of water retention models owing to the high sensitivity of the predicted response to the relevant parameter values.

It is also important to highlight here that any error in the prediction of suction during constant water, or partly drained, shearing will impact on the prediction of other important variables such as, for example, the strength at critical state.

Oedometric test EDO-200

Predicted and experimental results are compared for the oedometric test EDO-200 in Fig. 11 (first wetting–drying cycle stage at $\sigma_v = 20$ kPa), Fig. 12 (loading–unloading–reloading stage at $s = 200$ kPa) and Fig. 13 (second wetting–drying cycle stage at $\sigma_v = 800$ kPa).

Figure 11 compares predicted and experimental data during the first wetting–drying cycle for the two hysteretic models of EPFL and UNSW (Fig. 11(a)) and for the five non-hysteretic models of CU, ENPC, UGLAS-1, UGLAS-2 and UNINA (Fig. 11(b)). Predicted variations of void ratio

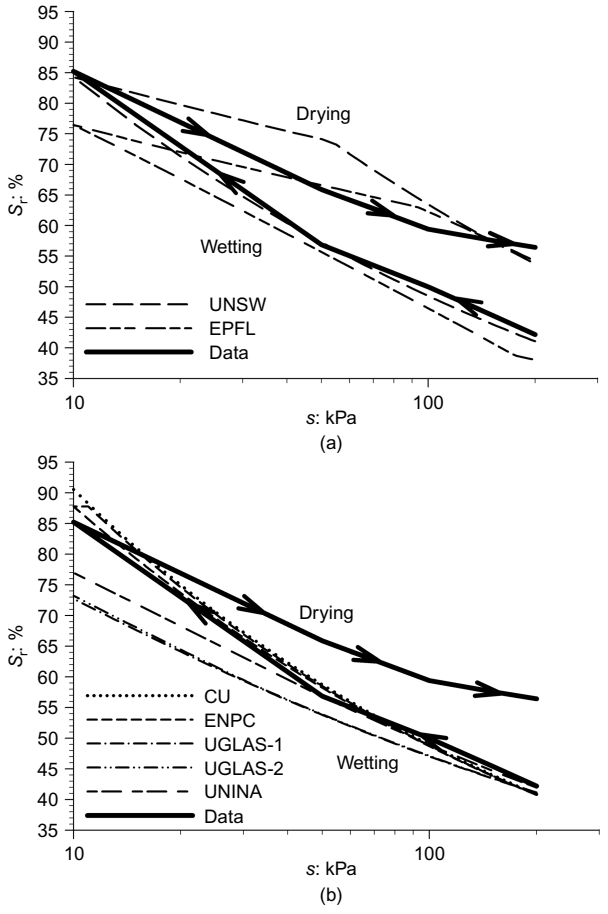

Fig. 11. Predicted and experimental behaviour during first wetting–drying cycle of test EDO-200: (a) variation of degree of saturation (S_r) plotted against suction (s) for hysteretic water retention models (EPFL and UNSW) and (b) variation of degree of saturation (S_r) plotted against suction (s) for non-hysteretic water retention models (CU, ENPC, UGLAS-1, UGLAS-2 and UNINA)

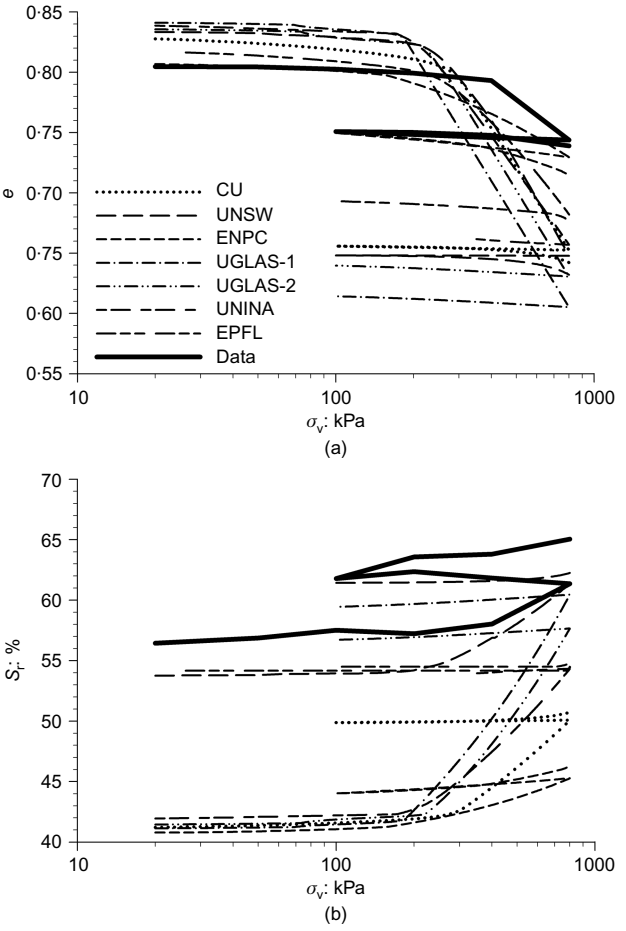

Fig. 12. Predicted and experimental behaviour during loading–unloading–reloading cycle of test EDO-200: (a) variation of void ratio (e) plotted against vertical net stress (σ_v) and (b) variation of degree of saturation (S_r) plotted against vertical net stress (σ_v)

are not presented here owing to their limited interest (they are very small and largely reversible).

Inspection of Figs 11(a) and 11(b) confirms that incorporation of hydraulic hysteresis improves considerably the prediction of degree of saturation during the wetting–drying cycle with both EPFL and UNSW accurately capturing the irreversible change of degree of saturation at the end of the cycle. As expected, CU, ENPC, UGLAS-1, UGLAS-2 and UNINA generally predict reversible changes of degree of saturation. Only the ENPC model shows a slight irreversibility in the predicted variation of degree of saturation around the inversion point because of the occurrence of a small amount of plastic volumetric strains. Predictions by CU and ENPC match relatively well the wetting branch of the cycle while predictions by UGLAS-1, UGLAS-2 and UNINA lie close to the experiments at the start of wetting but then tend to fall below the measured data as suction is reduced.

Predicted and experimental results during the loading–unloading–reloading cycle are compared in Figs 12(a) and 12(b). Fig. 12(a) shows larger differences between predicted yield stresses compared to the anisotropic loading stage at the same level of suction in test TX07 (see Fig. 7(a)). This is caused by the variability of the stress paths computed by the different models under radially constrained conditions, which leads to yielding over different regions of the stress space. Plastic deformation after yielding is overestimated by all models (with the only exception of ENPC) owing to underestimation of the yield stress rather than underestimation of plastic stiffness. In the case of ENPC, the prediction of a stiffer post-yield response (as already observed during the loading stages of test TX07 and the blind test) compensates for the underestimation of the yield stress, resulting in a better match to the experimental data compared to other models.

In Fig. 12(b), the degree of saturation predicted at the start of loading by the five non-hysteretic models (i.e. CU, ENPC, UGLAS-1, UGLAS-2 and UNINA) is considerably smaller than the experimental value because of the significant underestimation at the end of the previous drying stage. On the other hand, the overestimation of volumetric compression during loading in Fig. 12(a) tends to produce a corresponding overestimation of the increase of degree of saturation in Fig. 12(b).

Figure 13 compares predicted and experimental data during the second wetting–drying cycle both in terms of deformation (Fig. 13(a)) and water retention (Figs 13(b) and 13(c)). At the start of wetting, the predicted values of void ratio and degree of saturation are in all cases lower than the experiments due to accumulated errors during the previous test stages.

During wetting, the amount of collapse depends on the spacing between constant-suction normal compression lines. The CU, ENPC, UGLAS-1, UGLAS-2 and UNINA models predict a noticeable amount of collapse in Fig. 13(a). In these models, the spacing between constant-suction normal

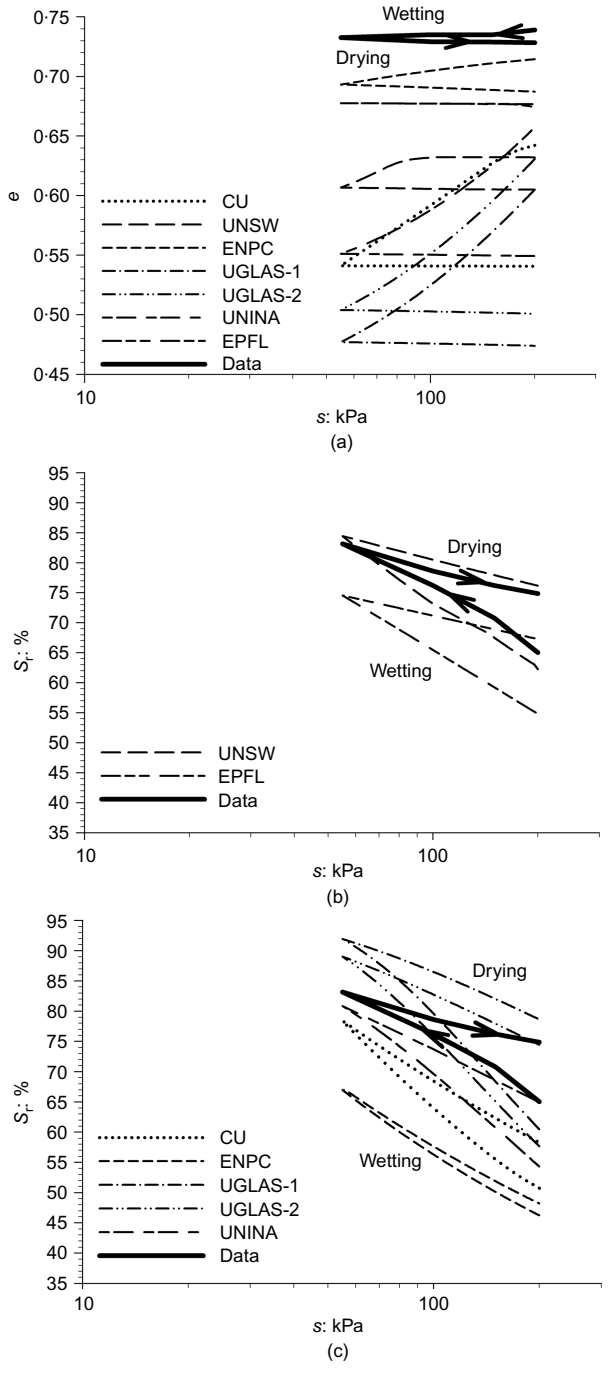

Fig. 13. Predicted and experimental behaviour during second wetting–drying cycle of test EDO-200: (a) variation of void ratio (e) plotted against suction (s); (b) variation of degree of saturation (S_r) plotted against suction (s) for hysteretic water retention models (EPFL and UNSW); (c) variation of degree of saturation (S_r) plotted against suction (s) for non-hysteretic water retention models (CU, ENPC, UGLAS-1, UGLAS-2 and UNINA)

compression lines had been calibrated by taking into account data from all five constant-suction oedometric compression curves. However, one difference between the CU, UGLAS-1, UGLAS-2 and UNINA models (which largely overestimate collapse during wetting) and the ENPC model (which predicts instead a smaller and more accurate value of collapse) is that, in the former case, spacing had been directly fixed to match the distance between constant-suction oedometric compression curves whereas, in the latter case, it had been indirectly fixed by defining the shape of the yield curve in the s–p' plane.

As for the other two models, EPFL predicts a negligible amount of collapse while, in the case of UNSW, collapse is concentrated during the later stages of wetting when suction changes from about 80 kPa to 55 kPa. This is due to the fact that, as mentioned previously, both these models assume a yield curve in the s–p' plane that becomes very steep when suction becomes greater than 50 kPa in the case of EPFL and 80 kPa in the case of UNSW. This implies the existence of very small distances between constant-suction normal compression lines in the v–$\ln p'$ plane for suctions greater than the above values.

The variation of degree of saturation is presented in Fig. 13(b) for the two hysteretic models and in Fig. 13(c) for the five non-hysteretic models. In this case, unlike the first wetting–drying cycle, all seven models predict some irreversible increase in degree of saturation at the end of the cycle, albeit for different reasons. The relatively accurate prediction of the change of degree of saturation by some of the non-hysteretic models is the consequence of the overestimation of volumetric collapse during wetting. On the other hand, the irreversible changes of degree of saturation predicted by the two hysteretic models are predominantly caused by water retention hysteresis, given the small or negligible changes of void ratio predicted by these models during the wetting–drying cycle.

CONCLUSIONS

The paper presents the results from a collaborative piece of research undertaken by seven universities to benchmark different approaches to modelling mechanical and water retention behaviour of unsaturated soils. Seven different constitutive models have been independently calibrated by different teams of researchers based on the same set of 13 suction-controlled triaxial and oedometer tests performed on compacted silty soil samples. The calibrated constitutive models have then been used to predict soil behaviour during three of the 13 calibration tests, as well as during one 'blind' test whose results had not been previously published.

The main features of the seven models are first compared with particular reference to water retention behaviour, stress tensor definition, effect of suction on the mechanical response and nature of irreversible deformation. Through this comparison, a model classification matrix has been proposed based on the adopted type of constitutive stress and yield curve in the s–p' plane (see Table 2). The intrinsic link between the definition of the yield curve in the s–p' plane and constant-suction normal compression lines in the v–$\ln p'$ plane has also been highlighted. The proposed classification is not necessarily restricted to the models considered in this work and could be generally extended to other formulations in the literature.

Predictions from different models are interpreted in the context of the respective analytical formulations and calibration choices made by participating teams. Models with similar features appear to produce qualitatively coherent predictions although quantitative discrepancies are often observed. In several cases, these discrepancies are the consequence of the chosen calibration approach rather than the specific features of the model. For example, UGLAS-1, UGLAS-2 and UNINA all used the same water retention model; nevertheless the suction variation predicted by UGLAS-1 and UGLAS-2 during constant water content shearing in the blind test follows an opposite direction compared to UNINA. This is due to the selection of different parameter values by UGLAS-1 and UGLAS-2 compared to UNINA, which emphasises the difficulties associated with model calibration and, especially, the importance of identifying the most sensitive aspects of soil behaviour for the

selection of particular model parameters. In general, these results highlight the danger of formulating ever more sophisticated constitutive models without dedicating the necessary attention to the development of robust procedures for selecting parameter values.

Based on the analysis of all results, it is concluded that hydraulic uncoupled predictions (i.e. predictions governed only by the water retention model) show smaller differences among teams and are generally closer to the experimental data than mechanical uncoupled predictions (i.e. predictions governed only or predominantly by the mechanical model). This also confirms that a greater degree of uniformity exists across water retention models in comparison to mechanical models.

The variation of volumetric strain during shearing appears particularly difficult to predict and this is intrinsically related to the ability of each model of matching the distance between constant-suction normal compression and critical state lines in the v–$\ln p'$ plane. Potential inaccuracies in the prediction of volumetric strain during shearing have also consequences on the corresponding prediction of degree of saturation because of the assumed dependency of degree of saturation on soil porosity. Errors in the calculated relationship between degree of saturation and axial strain during shearing are therefore more likely to be the consequence of an inaccurate prediction of volumetric strain by the mechanical model rather than a deficiency of the water retention model itself.

During shearing at constant water content, the relationships between suction and axial strain predicted by the different teams show significant discrepancies and even opposite trends. This is caused by the strong sensitivity of this type of prediction to the chosen water retention model and its calibration. The direction of suction variation depends on the chosen water retention model alone and, more specifically, on the relative sensitivity of suction variation to changes in degree of saturation and volumetric strain. The magnitude of suction variation depends instead on the size of the changes of degree of saturation and volumetric strain, which is governed by both mechanical and water retention models.

Any error in the prediction of suction during constant water content (or partly drained) shearing will impact on the prediction of strength at critical state. Therefore the choice of an accurate and well-calibrated water retention model becomes particularly important during analyses that involve strong hydromechanical coupling.

ACKNOWLEDGEMENTS

The financial support of the European Commission through funding of the 'Marie Curie' research training network MUSE ('Mechanics of Unsaturated Soils for Engineering' – contract: MRTN-CT-2004-506861) is acknowledged. Contributions by Dr Claudia Zingariello of the UNINA team and Drs Michael Habte and Adrian Russell of the UNSW team are also gratefully acknowledged.

APPENDIX

A linear relationship in the v–$\ln p'$ plane is assumed for the saturated normal compression line corresponding to $s = s_e$

$$v = N - \lambda \ln p'_0(s_e) \tag{10}$$

where λ is the slope and N is the intercept at $p'_0(s_e) = 1$.

By following an elastic path inside the yield locus in the s–p' plane, the specific volume at a yield stress $p'_0(s)$ is obtained as

$$v = N - \lambda \ln p'_0(s_e) + \Delta v^e|_{s_e}^{s} - \kappa \ln \frac{p'_0(s)}{p'_0(s_e)} \tag{11}$$

where $\Delta v^e|_0^s$ is the elastic change of specific volume when suction varies from s_e to s while κ is the slope of the elastic compression line in the v–$\ln p'$ plane.

By substituting for $p'_0(s_e)$ from equation (7) into equation (11) and rearranging, one obtains the following expression for the constant-suction normal compression line at suction s

$$\begin{aligned} v = N &+ \frac{\lambda - \kappa}{\omega_2} \ln \omega_1 + \Delta v^e|_{s_e}^{s} \\ &- \frac{\lambda - \kappa}{\omega_2} \ln (p'_0(s) - \omega_3) - \kappa \ln p'_0(s) \end{aligned} \tag{12}$$

which can be rewritten in the following simpler form

$$v = N(s) - \lambda(s) \ln p'_0(s) \tag{13}$$

The slope $\lambda(s)$ and spacing $N(s)$ of constant-suction normal compression lines are therefore given by

$$\lambda(s) = \frac{\lambda - \kappa}{\omega_2} \frac{\ln (p'_0(s) - \omega_3)}{\ln p'_0(s)} + \kappa \tag{14}$$

$$N(s) = N + \frac{\lambda - \kappa}{\omega_2} \ln \omega_1 + \Delta v^e|_{s_e}^{s} \tag{15}$$

For each of the three classes of yield curve, the slope $\lambda(s)$ and spacing $N(s)$ of constant-suction normal compression lines are therefore given as follows.

Class (a)

$$\left.\begin{matrix} \omega_2 = 1 \\ \omega_3 = 0 \end{matrix}\right\} \Rightarrow \begin{matrix} \lambda(s) = \lambda \\ N(s) = N + (\lambda + \kappa) \ln \omega_1 + \Delta v^e|_{s_e}^{s} \end{matrix} \tag{16}$$

Constant-suction normal compression lines have constant slope, while spacing depends on function ω_1.

Class (b)

$$\omega_3 = 0 \Rightarrow \begin{matrix} \lambda(s) = \dfrac{\lambda - \kappa}{\omega_2} + \kappa \\ N(s) = N + \dfrac{\lambda - \kappa}{\omega_2} \ln \omega_1 + \Delta v^e|_{s_e}^{s} \end{matrix} \tag{17}$$

Constant-suction normal compression lines have variable slope depending on function ω_2 and spacing depending on function ω_1.

Class (c)

$$\omega_2 = 1 \Rightarrow \begin{matrix} \lambda(s) = (\lambda - \kappa) \dfrac{\ln (p'_0(s) - \omega_3)}{\ln p'_0(s)} + \kappa \\ N(s) = N + (\lambda - \kappa) \ln \omega_1 + \Delta v^e|_{s_e}^{s} \end{matrix} \tag{18}$$

Constant-suction normal compression lines are not straight lines in the v–$\ln p'$ plane (i.e. the secant slope depends on stress state) and spacing depends on function ω_1.

REFERENCES

Alonso, E. E., Gens, A. & Josa, A. (1990). A constitutive model for partially saturated soils. *Géotechnique* **40**, No. 3, 405–430, **doi**: 10.1680/geot.1990.40.3.405.

Brooks, R. N. & Corey, A. T. (1964). Hydraulic properties of porous media. *Colorado State Univ. Hydrol. Pap.* **3**, 1–27.

Cambou, B. & Jafari, K. (1988). Modèle de comportement des sols non cohérents. *Revue Française de Géotechnique* **44**, 43–55.

Casini, F. (2008). *Effetti del grado di saturazione sul comportamento meccanico di un limo*. PhD thesis. Universitá degli Studi di Roma 'La Sapienza', Rome.

Coussy, O. & Dangla, P. (2002). Approche énergétique du comportement des sols non saturés. In *Mécanique des sols non saturés* (eds O. Coussy and J.-M. Fleureau). Paris, France: Lavoisier.

Cui, Y. J. & Delage, P. (1996). Yielding and plastic behaviour of an unsaturated compacted silt. *Géotechnique* **46**, No. 2, 291–311, **doi**: 10.1680/geot.1996.46.2.291.

Dangla, P. (2002). Plasticité et hysteresis. In *Mécanique des sols non saturés* (eds O. Coussy and J.-M. Fleureau). Paris, France: Lavoisier.

D'Onza, F., Gallipoli, D. & Wheeler, S. (2010). Effect of anisotropy on the prediction of unsaturated soil response under triaxial and oedometric conditions. *Proc. 5th Int. Conf. Unsaturated Soils, Barcelona* (eds E. E. Alonso and A. Gens), pp. 787–794. Rotterdam: Balkema.

Gallipoli, D., Wheeler, S. & Karstunen, M. (2003). Modelling the variation of degree of saturation in a deformable unsaturated soil. *Géotechnique* **53**, No. 1, 105–112, **doi**: 10.1680/geot.2003.53.1.105.

Gallipoli, D., D'Onza, F. & Wheeler, S. (2010). A sequential method for selecting parameter values in the Barcelona basic model. *Can. Geotech. J.* **47**, No. 11, 1175–1186.

Gens, A. (1996). Constitutive modelling: application to compacted soils. *Proc. 1st Int. Conf. Unsaturated Soils, Paris* (eds E. E. Alonso and P. Delage), **3**, 1179–1200. Rotterdam: Balkema.

Gudehus, G. & Mašín, D. (2009). Graphical representation of constitutive equations. *Géotechnique* **59**, No. 2, 147–151, **doi**: 10.1680/geot.2009.59.2.147.

Hujeux, J. (1985). Une loi de comportement pour le chargement cyclique des sols. *Génie Parasismique*, pp. 287–353. Paris: Les éditions de l'ENPC.

Khalili, N., Habte, M. A. & Valliappan, S. (2005). A bounding surface plasticity model for cyclic loading of granular soils. *Int. J. Numer. Methods Engng* **63**, No. 14, 1939–1960.

Khalili, N., Habte, M. A. & Zargarbashi, S. (2008). A fully coupled flow deformation model for cyclic analysis of unsaturated soils including hydraulic and mechanical hysteresis. *Comput. Geotechnics* **35**, No. 6, 872–889.

Khalili, N. & Khabbaz, M.H. (1998). A unique relationship for χ for the determination of the shear strength of unsaturated soils. *Géotechnique* **48**, No. 5, 681–687, **doi**: 10.1680/geot.1998.48.5.681.

Mašín, D. (2005). A hypoplastic constitutive model for clays. *Int. J. Numer. Analyt. Methods Geomech*. **29**, No. 4, 311–336.

Mašín, D. (2010). Predicting the dependency of a degree of saturation on void ratio and suction using effective stress principle for unsaturated soils. *Int. J. Numer. Analyt. Methods Geomech*. **34**, No. 1, 73–90.

Mašín, D. & Herle, I. (2005). State boundary surface of a hypoplastic model for clays. *Comput. Geotechnics* **32**, No. 6, 400–410.

Mašín, D. & Khalili, N. (2008). A hypoplastic model for mechanical response of unsaturated soils. *Int. J. Numer. Analyt. Methods Geomech*. **32**, No. 15, 1903–1926.

Nuth, M. & Laloui, L. (2007). New insight into the unified hydro-mechanical constitutive modelling of unsaturated soils. *Proc. 3rd Asian Conf. Unsaturated Soils, Nanjing, China* (eds Z. Z. Yin, Y. P. Yuan, and A. C. F. Chiu), pp. 109–126. Beijing: Science Press.

Nuth, M. & Laloui, L. (2008). Advances in modelling hysteretic water retention curve in deformable soils. *Comput. Geotechnics* **35**, No. 6, 835–844.

Pereira, J. M., Wong, H., Dubujet, P. & Dangla, P. (2005). Adaptation of existing behaviour models to unsaturated states: application to CJS model. *Int. J. Numer. Analyt. Methods Geomech*. **29**, No. 11, 1127–1155.

Roscoe, K. H. & Burland, J. B. (1968). On the generalised stress–strain behaviour of wet clay. In *Engineering plasticity* (eds J. Heyman and F. A. Leckie), pp. 535–609.Cambridge: Cambridge University Press.

Van Genuchten, M. T. (1980). A closed-form equation for predicting the hydraulic conductivity of unsaturated soil. *Soil Sci. Soc. Am. J.* **44**, No. 5, 892–898.

Wheeler, S. & Sivakumar, V. (1995). An elasto-plastic critical state framework for unsaturated soil. *Géotechnique* **45**, No. 1, 35–53, **doi**: 10.1680/geot.1995.45.1.35.

Wheeler, S., Näätänen, A., Karstunen, M. & Lojander, M. (2003). An anisotropic elastoplastic model for soft clays. *Can. Geotech. J.* **40**, No. 2, 403–418.

Tarantino, A. *et al.* (2011). *Géotechnique* **61**, No. 4, 303–312 [**doi:** 10.1680/geot.2011.61.4.303]

Benchmark of experimental techniques for measuring and controlling suction

A. TARANTINO[1], D. GALLIPOLI[2], C. E. AUGARDE[3], V. DE GENNARO[4], R. GOMEZ[5], L. LALOUI[6], C. MANCUSO[7], G. EL MOUNTASSIR[1], J. J. MUNOZ[8], J.-M. PEREIRA[9], H. PERON[6], G. PISONI[10], E. ROMERO[11], A. RAVEENDIRARAJ[12], J. C. ROJAS[2], D. G. TOLL[3], S. TOMBOLATO[10] and S. WHEELER[2]

The paper presents a benchmarking study carried out within the 'Mechanics of Unsaturated Soils for Engineering' (MUSE) network aimed at comparing different techniques for measurement and control of suction. Techniques tested by the eight 'Mechanics of Unsaturated Soils for Engineering' research teams include axis-translation (pressure plate and suction-controlled oedometer), high-capacity tensiometer and osmotic technique. The soil used in the exercise was a mixture of uniform sand, sodium bentonite (active clay) and kaolinite (non-active clay), which were all commercially available. Samples were prepared by one team and distributed to all other teams. They were normally consolidated from slurry under one-dimensional conditions (consolidometer) to a given vertical stress. The water retention characteristics of the initially saturated specimens were investigated along the main drying path. Specimens were de-saturated by applying suction through the liquid phase when using an axis-translation technique or osmotic method and de-saturated by air-drying, when suction was measured using high-capacity tensiometers. In general, the same technique was tested by at least two teams. The water retention curves obtained using the different techniques are compared and discrepancies are discussed in the paper.

Cette communication présente une étude comparative réalisée dans le cadre du réseau MUSE, dans le but de comparer différentes techniques de mesure et de régulation de l'aspiration. Parmi les techniques testées par les huit équipes de chercheurs de MUSE, indiquons la translation d'axes (plaque de pression et oedomètre à succion contrôlée), un tensiomètre à capacité élevée, et une technique osmotique. Le sol utilisé pour cette tâche était un mélange de sable uniforme, de bentonite de sodium (argile active), et de kaolinite (argile non active), tous disponibles dans le commerce. Une équipe préparait les échantillons, qu'elle distribuait ensuite à toutes les autres équipes. Ces échantillons étaient généralement consolidés à partir de boues dans des conditions unidimensionnelles (consolidomètre), jusqu'à une contrainte verticale donnée. On recherchait ensuite les caractéristiques de retenue de l'eau de spécimens initialement saturés, le long du chemin de séchage principal, et on procédait à la désaturation de spécimens par l'application d'une aspiration par séchage à l'air, succion étant mesurée avec des tensiomètres à capacité élevée. En général, la même technique était testée par un minimum de deux équipes. On procéda ensuite à une comparaison des courbes de retenue d'eau obtenue avec les différentes techniques : les divergences sont discutées dans la communication.

KEYWORDS: laboratory tests; partial saturation; suction

INTRODUCTION

Suction plays a key role in the mechanical and hydraulic behaviour of unsaturated soils and its measurement is therefore an essential requirement for predictive purposes. Different techniques are available for suction measurement and control, which are based on equilibrium through either the liquid or vapour phase. Consistency among different techniques and reproducibility of suction measurements among different laboratories are crucial in the implementation of unsaturated soil mechanics into routine engineering practice. The paper tackles this problem by comparing four techniques for suction measurement and control, namely the pressure plate, the axis-translation oedometer, the high-capacity tensiometer and the osmotic method, which fall into the category of liquid equilibrium. Eight different laboratories across Europe were involved in this 'round robin' benchmark study with the aim of estimating confidence level of suction measurement. To cross-check experimental results, tests using the pressure plate, the axis-translation oedometer and the high-capacity tensiometer were replicated by two different laboratories. Only the osmotic method was tested by a single laboratory.

The eight laboratories participating in this benchmark study were participants in the 'Mechanics of Unsaturated Soils for Engineering' (MUSE) project. This is a major research and training network funded by the European Union involving six European universities as full partners, three European universities as associated partners and five industrial partners. Details about the project can be obtained by visiting the MUSE website (2005). The academic institutions involved in this benchmarking study were: University of

Manuscript received 1 March 2010; revised manuscript accepted 29 November 2010.
Discussion on this paper closes on 1 September 2011, for further details see p. ii.
[1] Department of Civil Engineering, University of Strathclyde, UK
[2] Department of Civil Engineering, University of Glasgow, UK
[3] School of Engineering and Computing Sciences, Durham University, UK
[4] Schlumberger, Pau, France
[5] Departament d'Enginyeria del Terreny, Cartogràfica i Geofísica, Universitat Politècnica de Catalunya, Barcelona, Spain
[6] École Polytechnique Fédérale de Lausanne, EPFL, Switzerland
[7] Dipartimento di Ingegneria Idraulica, Geotecnica ed Ambientale, Università di Napoli Federico II, Napoli, Italy
[8] Universidad Nacional de San Juan Instituto de Investigaciones Antisísmicas 'Ing. Aldo Bruschi', San Juan, Argentina
[9] Université Paris-Est, Laboratoire Navier – CERMES, Ecole des Ponts ParisTech, Marne-la-Vallée, France
[10] Dipartimento di Ingegneria Meccanica e Strutturale, Università degli Studi di Trento, Italy
[11] Geotechnical Laboratory, Departament d'Enginyeria del Terreny, Cartogràfica i Geofísica, Universitat Politècnica de Catalunya, Barcelona, Spain
[12] Atkins, London, UK

Glasgow in the UK (MUSE coordinator), Durham University in the UK, Università di Trento in Italy, École Nationale des Ponts et Chaussées in France, Universitat Politècnica de Catalunya in Spain, Università di Napoli 'Federico II' in Italy, École Polytechnique Fédérale de Lausanne in Switzerland (associated partner) and University of Strathclyde in the UK (associated partner). The acronyms used to identify the different academic institutions are given later in Table 2.

The soil used in this experimental programme was prepared by mixing sand, kaolinite and bentonite. To ensure that 'identical' specimens were tested, samples were prepared at UNITN and shipped to the MUSE teams, with the exception of one team that only produced samples in its own laboratory. Each laboratory was then requested to determine the water retention curve (WRC) starting from the saturated condition (main drying WRC).

MATERIAL AND SAMPLE PREPARATION

The soil used in the exercise was obtained by mixing three different geomaterials, a uniform sand (Hostun sand), an active clay (MX-80 sodium bentonite) and a non-active clay (Speswhite kaolin), which are all commercially available (Table 1). The mixture made it possible to prepare a soil with a 'suitable' WRC by modifying the mass fraction of each component of the mixture. The mixture was required to generate a WRC having an air-entry suction not exceeding 100–200 kPa, as the suction range of several axis-translation apparatuses used in the benchmarking exercise was limited to 500–600 kPa. It was also desirable that the slope of the WRC beyond the air-entry suction was not steep, as small errors in the values of suction controlled or measured would have produced very scattered data in the WRC. Finally, the mixture was expected to generate a WRC developing over a large range of suction so that the same mixture could be used for matric suction measurement/control (equilibrium by way of liquid transfer) and total suction measurement/control (equilibrium by way of vapour transfer), even if this benchmark study essentially focuses on matric suction. Preliminary tests were carried out at UNITN by testing different mixtures and it was found that the following composition produced the mixture with the aforementioned features: 70% Hostun sand, 20% MX80 bentonite and 10% Speswhite kaolin.

The majority of samples were prepared at UNITN and shipped to seven of the eight teams involved in this study. One team only produced the samples in its own laboratory (UPC), whereas UNINA tested samples produced both by UNITN and in its own laboratory. Samples used by the different partners are summarised in Table 2. In the following, the term 'sample' will be used only for the soil prepared within the oedometer/consolidometer and the term 'specimen' will refer to the material used to determine the WRC.

The procedure for sample preparation at UNITN is briefly illustrated below. The detailed procedure is described in a MUSE document (Tarantino, 2007) and can be made available on request. The three soils were first dry mixed using a spatula. A small amount of dry mixture was placed in a plastic bowl (60 g) and about 50 g of demineralised water was added. The soil and the water were mixed together using the spatula to squeeze lumps. This procedure was repeated six times until all the dry soil was mixed with water. At this stage, the soil–water mixture was quite dense and additional water was added to reach a water content of 128%. The slurry was poured into a one-dimensional consolidometer about 110 mm in diameter and 150 mm high. Vertical pressure was increased at the rate of 3·3 kPa/h and, when the final vertical stress of 101 kPa was reached (after 31 h), the vertical pressure was maintained constant for 41 h. At the end of consolidation the sample was unloaded as fast as possible to limit swelling and a water content of 0·53 was recorded. The sample was finally put in a plastic bag, in turn put in an airtight plastic container and stored in a high-humidity room until shipping.

UPC consolidated the sample from slurry directly in the axis-translation oedometer subsequently used to determine the WRC. The slurry was consolidated by applying a ramp from 0 to 100 kPa over 1·5 days and by keeping the 100 kPa vertical pressure constant for the subsequent 4 days. UNINA, in addition to the sample prepared by the UNITN, tested a sample prepared in its own laboratory using the same procedure as adopted by UNITN.

APPARATUS AND EXPERIMENTAL PROCEDURES

Teams using the same type of equipment (pressure plate, axis-translation oedometer and high-capacity tensiometer) were invited to use their own experimental procedure. There

Table 1. Index properties of soils used to prepare the mixture

	Clay: %	Silt: %	Sand: %	w_p	w_l	Gs	d_{50}: mm
Hostun sand (De Gennaro *et al.*, 2004)	—	—	100	—	—	2·65	0·38
MX-80 bentonite (Tang & Cui, 2005)	60	40	—	35	519	2·76	—
Speswhite kaolin (Tarantino & Tombolato, 2005)	80	20	—	32	64	2·61	—

Table 2. Samples used by different teams

Participant	Acronym	Sample prepared by Università di Trento	Sample prepared in its own laboratory
University of Glasgow, UK	UGLAS	•	—
Durham University, UK	UDUR	•	—
Università di Trento, Italy	UNITN	•	—
École des Ponts ParisTech, France	ENPC	•	—
École Polytechnique Fédérale de Lausanne, Switzerland	EPFL	•	—
University of Strathclyde, UK	USTRAT	•	—
Università di Napoli 'Federico II', Italy	UNINA	•	•
Universitat Politècnica de Catalunya, Spain	UPC	—	•

is high variability between procedures adopted across geotechnical laboratories and this variability was therefore part of the benchmark study. All tests were carried out in temperature-controlled rooms.

Pressure plate (EPFL, UGLAS, USTRAT)

Pressure plate tests were performed by EPFL and UGLAS to determine the main drying WRC. USTRAT only applied a single level of suction to three 'identical' specimens to investigate the influence of contact pressure on the water retained at a given suction.

Commercial equipment was used by all teams, as summarised in Table 3. The porous ceramic plate was saturated by filling the cell with de-aired water and then applying a positive pressure to force water to flow through the ceramic, while maintaining the pressure underneath the ceramic plate at atmospheric pressure. This procedure was repeated several times until the permeability of the ceramic attained a constant value. The applied pressures and the numbers of saturation cycles adopted by different teams are reported in Table 3.

Sizes of specimens, cut and trimmed from the samples provided by UNITN, are given in Table 3. EPFL placed eight specimens on the plate and no vertical pressure was applied. UGLAS and USTRAT placed three specimens on the ceramic plate, and a small vertical pressure was applied to improve contact (0·6 kPa for UGLAS and 0·3, 4·7 and 8·2 kPa respectively for USTRAT). In all pressure plate tests, a tray filled with water remained within the pressure chamber to increase the relative humidity and minimise moisture content losses due to evaporation.

Each level of suction was maintained for a sufficient time to allow for moisture equilibration, which was assessed using different approaches. EPFL regularly weighed specimens (twice a week for low suction steps, once a week for high suction steps) and equilibrium was considered to be reached once the rate of water content decrease was $\Delta w < 0{\cdot}2\%$/day. UGLAS monitored the burette connected to the water reservoir underneath the ceramic plate. An acceptable rate of burette water volume change was determined by weighing specimens on successive days during the first three suction steps and equilibrium was assumed to be reached when the rate of water content decrease was $\Delta w < 0{\cdot}04\%$/day. It should be noted that specimens tested at EPFL and UGLAS have different heights, 12 and 20 mm respectively, and this results in different flow rates at a given 'degree of suction equalisation'. For example, Terzaghi's theory of consolidation for saturated elastic geomaterials (Atkinson, 1993) predicts that the flow rate per unit solid mass at the same degree of consolidation is inversely proportional to the square of specimen height. When specimen height is increased from 12 to 20 mm, the flow rate decreases by 2·8 and this figure is not significantly different from the ratio between rates of water content decrease adopted by EPFL and UGLAS.

USTRAT did not monitor water content changes as the only purpose of this test was to investigate the effect of contact pressure. Suction was simultaneously applied to the three specimens uninterruptedly for 12 days.

At equilibrium at a given suction level, EPFL removed a single specimen from the pressure plate apparatus (with the exception of three specimens for the last suction steps) to determine water content and also air and total volume by immersion in Kerdane (Péron *et al.*, 2007). EPFL therefore adopted the approach of one-specimen–one-point. UGLAS used a single specimen to determine the entire WRC and water content at each suction level was back-calculated from the final water content. Measurement of the WRC at UGLAS was made in triplicate.

Axis-translation oedometer (UNINA and UPC)

The equipment used at UNINA is a Wissa oedometer (Wissa & Heiberg, 1969) modified to control matric suction (Rampino *et al.*, 1999) and to measure water content changes (Rojas *et al.*, 2007) whereas UPC used an oedometer designed and constructed in their own geotechnical laboratory (Hoffmann *et al.*, 2005) (Table 4).

UNINA applied suction using the water-subpressure technique (water pressure is maintained constant and air pressure is progressively increased to increase suction), whereas UPC applied suction using the air-overpressure technique (air and water pressure are initially increased simultaneously, then air pressure is maintained constant and water pressure is decreased to increase suction) (Romero, 2001). To minimise air diffusion underneath the high-air-entry ceramic, the water pressure was raised to values greater than atmospheric (50 kPa for UNINA and in the range 100–490 kPa for UPC) according to Romero (2001).

Table 3. Summary of procedures adopted in pressure plate testing

	EPFL (École Polytechnique Fédérale de Lausanne)	UGLAS (University of Glasgow)	USTRAT (University of Strathclyde)
Apparatus	1500F1 (Soil Moisture Corporation)	1500F1 (Soil Moisture Corporation)	532-132 (ELE)
AEV of ceramic plate	1·5 MPa ($s > 0{\cdot}3$ MPa) 0·5 MPa ($s \leqslant 0{\cdot}3$ MPa)	1·5 MPa	1·5 MPa
Saturation pressure	0·8 MPa (AEV = 1·5 MPa) 0·4 MPa (AEV = 0·5 MPa)	0·8 MPa (AEV =1·5 MPa)	1·6 MPa (AEV = 1·5 MPa)
Saturation cycles	6	3	1
Ceramic plate measured permeability	$6{\cdot}5 \times 10^{-11}$ m/s (AEV = 1·5 MPa) $2{\cdot}2 \times 10^{-10}$ m/s (AEV = 0·5 MPa)	N/A	$2{\cdot}5 \times 10^{-11}$ m/s (AEV = 1·5 MPa)
Specimen size	$\phi = 45$ mm, $h = 12$ mm	$\phi = 75$ mm, $h = 20$ mm	$\phi = 38$ mm, $h = 20$ mm
Initial suction applied	10 kPa	20 kPa	N/A
Water content measurement	One specimen per measurement	Multiple measurement on same specimen	One specimen per measurement
Total volume measurement	Immersion in Kerdane	None	None
Equilibrium (water loss)	$\Delta w < 0{\cdot}2\%$/day (by weight)	$\Delta w < 0{\cdot}04$ %/day (burette connected to drainage line)	N/A
Balance resolution	0·01 g (to monitor equalisation) 0·001 g (final water content)	0·01 g	0·001 g
Vertical pressure	0 kPa	0·6 kPa	0·3, 4·7 and 8·2 kPa

Table 4. Summary of procedures adopted in axis-translation oedometer testing

	UNINA (Università di Napoli)	UPC (Universitat Politècnica de Catalunya)
Apparatus	Rampino *et al.* (1999), Rojas *et al.* (2007)	Hoffmann *et al.* (2005)
AEV of ceramic plate	0·5 MPa (Soil Moisture Corporation)	1·5 MPa (Soil Moisture Corporation)
Saturation pressure	0·65 MPa	2 MPa (AEV =1·5 MPa)
Saturation cycles	6	1
Specimen size	$\phi = 79$ mm, $h = 25$ mm (UNINA) $\phi = 79$ mm, $h = 15$ mm (UNITN)	$\phi = 50$ mm, $h = 12$ mm
Ceramic plate measured permeability	$2{\cdot}6 \times 10^{-10}$ m/s	1 to 7×10^{-11} m/s

The high-air-entry ceramic was saturated using two different approaches. At UNINA, water was forced to flow through the ceramic by increasing air pressure in the chamber while continuously flushing the water reservoir underneath for 1 h. The water reservoir was then closed for another 1 h and this cycle was repeated until the measured permeability attained a constant value (Table 4). At UPC, de-aired water was forced to flow through the ceramic disc using a GDS Instruments pressure/volume controller (with no air–water interface) until permeability attained a value in the range between 1·0 and $7{\cdot}0 \times 10^{-11}$ m/s; that is the range of permeability of 1·5 MPa air-entry value (AEV) ceramics measured over 15 years at UPC. In addition, diffusion of air through the saturated ceramic disc was measured and it was checked that the coefficient of diffusion for air was lower than 5×10^{-10} m^2/s (Romero, 1999; Airò Farulla & Ferrari, 2005; Delage *et al.*, 2008).

The pore-water volume change was measured by UNINA using a system of two double-walled burettes (Rojas *et al.*, 2007), whereas a GDS pressure–volume controller was used by UPC to monitor the pore-water volume change. The saturation of the water drainage line was ensured by periodically flushing the drainage line and the reservoir underneath the high-air-entry ceramic disc (every 1 h at UNINA and at 3-day intervals or when relatively high diffused air volumetric rates were measured at UPC).

The specimen in the oedometer was initially loaded to 100 kPa net axial stress to avoid lateral shrinkage during drying. The procedure of air pressurisation at high degrees of saturation is discussed by Di Mariano *et al.* (2000), Romero (2001) and Delage *et al.* (2008).

Equilibrium was considered to be attained when no changes in volume were recorded and water content changed linearly with time. This is due to either air diffusion towards the water reservoir underneath the ceramic plate or water evaporation into the air pressure line (Airò Farulla & Ferrari, 2005). In tests carried out at UNINA, the differential pressure transducer recorded a negative water-volume rate, suggesting that evaporation was the dominant mechanism, and a correction was made to account for evaporation effects according to Airò Farulla & Ferrari (2005). In tests carried out at UPC, evaporation effects were negligible and no correction was made.

Osmotic method – ENPC

The WRC at ENPC was determined using the osmotic method (Cui & Delage, 1996; Delage *et al.*, 1998). A partially saturated specimen was sealed in a tube-shaped cellulosic semi-permeable membrane having molecular weight cut-off (MWCO) of 3500 (regenerated cellulose (RC) dialysis membrane, Spectra/Por 3, MWCO 3500) and immersed in an aqueous solution of PEG with molecular weight of 20 000. A magnetic stirrer was used in order to improve the kinetic exchange of water and ensure the homogeneity of the PEG solution.

The value of PEG concentration was obtained by measuring the refractive Brix index (Br) of the PEG solution

$$c_{\mathrm{PEG}} = \frac{Br}{90 - Br} \tag{1}$$

where c_{PEG} is the PEG concentration in kg PEG/kg water. To relate the PEG concentration to suctions, two relationships can be adopted. The first was proposed by Delage *et al.* (1998) based on data from Williams & Shaykewich (1969)

$$s = 11\, c_{\mathrm{PEG}}^2 \tag{2}$$

where s is the suction in MPa. The second relationship is based on calibration data by Dineen & Burland (1995) and was recently confirmed by Tang *et al.* (2010) using the same PEG and semi-permeable membrane used to desaturate the MUSE soil. The two calibration curves are shown in Fig. 1.

A total of eight cylindrical specimens 19·5 mm in diameter and 26 ± 1 mm high were cut from a sample prepared at UNITN. Each specimen was immersed into a PEG solution for 4 days, removed from the tubular membrane to determine its mass and volume, and re-immersed in the PEG

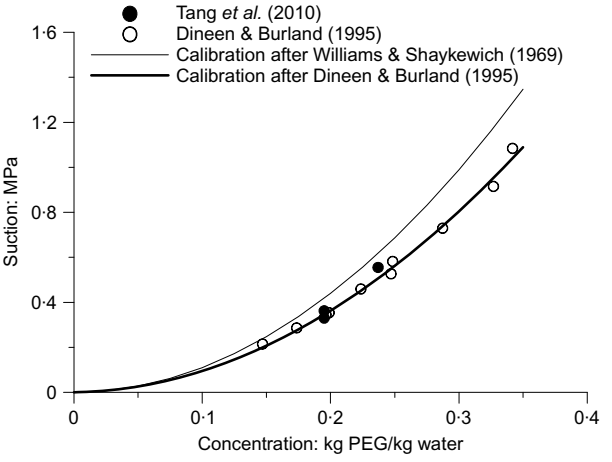

Fig. 1. Calibration curve relating PEG concentration to the osmotically generated suction

solution using a new membrane. Once the weight of specimen attained a stable value, typically after 9 to 12 days, final water content was determined by oven-drying and the total volume was determined by immersion in Kerdane.

High-capacity tensiometer (UNITN and UDUR))

Trento high-capacity tensiometers (Tarantino & Mongiovì, 2002; 2003) were used to measure matric suction at UNITN, whereas a tensiometer developed by Durham University and Wykeham Farrance Ltd (Lourenço *et al.*, 2006, 2008, 2011) were used for measurement at UDUR.

The tensiometers were first calibrated using the procedures outlined by Tarantino & Mongiovì (2003) and Lourenço *et al.* (2008) for the UNITN and UDUR tensiometer respectively. The saturation of the UNITN tensiometer porous ceramic was checked according to the procedure illustrated by Tarantino (2004).

The experimental procedure adopted at UNITN involved air-drying samples to a given water content and storage for at least 1 week to ensure moisture equilibration. Specimens 80 mm in diameter and 20 mm high were then cut from the air-dried samples and suction measurements were carried out in a suction measurement box (Tarantino & Mongiovì, 2002). To improve contact with the specimen a paste made of Speswhite kaolin was applied on the porous stone of the tensiometer. Water content and degree of saturation were determined for each specimen at the end of the suction measurement.

At UDUR, a single specimen was cut and placed in an air-tight box (Lourenço *et al.*, 2011). The tensiometer was placed in a hole drilled in the top plate of the box over the centre of the specimen and was held in place by the ring sealing the hole. When measurement stabilised, the tensiometer was removed, the specimen was set on its side to allow air drying and the measurement was repeated. The water content at each drying stage was back-calculated from the final water content. As shrinkage was not uniform, that is the specimen ceased to be cylindrical, volume measurements required for the degree of saturation were unreliable and water retention data were processed only in terms of water content.

EVALUATION OF TECHNIQUES FOR SUCTION CONTROL AND MONITORING

To better discuss the experimental results, it may be convenient to examine the path followed by the specimens during one-dimensional loading and unloading and subsequent drying. Upon loading in the consolidometer, the specimen moves along the normal consolidation line. As the vertical stress is increased to its final value σ'_{vc}, the mean effective stress increases to the value p'_c (point A in Fig. 2) given by

$$p'_c = \frac{1 + 2k_0}{3}\sigma'_{vc} \tag{3}$$

where k_0 is the coefficient of earth pressure at rest. At this stage the specimen is saturated and the void ratio e equals the water ratio e_w (e_w being the volume of water per volume of solids). Even though the total vertical stress is reduced to zero very rapidly, some water enters the specimen and the mean effective stress reduces to p'_0 (point B in Fig. 2). After removal from the consolidometer, the saturated specimen therefore has suction s_0 equal to p'_0.

When using the pressure plate and the osmotic method, an initial small suction s_i was applied to the specimen, which brought the specimen to point C in Fig. 2(a) along the 'saturated' unloading–reloading line. Subsequent drying at zero net stress ($p = 0$) first brought the saturated specimen again to point A along the 'saturated' unloading–reloading line (path C–B–A) and then along the 'saturated' normal consolidation line. At a given suction, s^0_{AEV}, the soil desaturated (point D in Fig. 2(a)) and the water ratio e_w decreased more rapidly than void ratio e. In Fig. 2, it is assumed that the AEV s^0_{AEV} is higher than the preconsolidation pressure p'_c, which is the case of the MUSE soil. Accordingly, all specimens are expected to desaturate at the same suction, s^0_{AEV}, irrespective of the initial suction applied s_i.

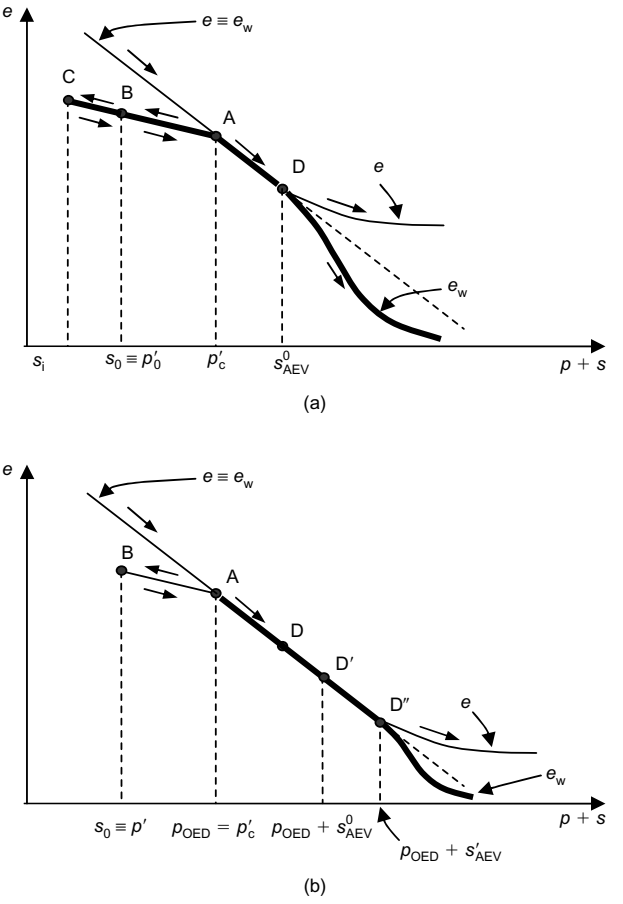

Fig. 2. Hydraulic and mechanical path associated with consolidation and drying: (a) pressure plate and osmotic method; (b) axis-translation oedometer

When measuring suction using the tensiometer, the specimens were directly desaturated from point B (the specimens are not resaturated) and therefore followed the path B–A–D. Again, since the AEV s^0_{AEV} is higher than the preconsolidation pressure p'_c for the MUSE soil, the soil tested using the tensiometer would be expected to desaturate at the same suction as the pressure plate and osmotic method (point D).

The case of the axis-translation oedometer is examined in Fig. 2(b). After removal from the consolidometer, net stress was increased at zero suction to match the preconsolidation pressure ($p_{OED} = p'_c$, point A in Fig. 2(b)). Starting from this point, suction was progressively increased from zero to the AEV s^0_{AEV} recorded under zero net stress (point D′ in Fig. 2(b)). At this suction level, the soil was still saturated but the void ratio was lower than the void ratio recorded at the same suction under zero net stress (compare points D and D′ in Fig. 2(b)). As a lower void ratio increases the air-entry suction (Gallipoli *et al.*, 2003; Tarantino, 2009), the soil is therefore expected to desaturate at a higher suction, s'_{AEV} (point D′′ in Fig. 2(b)).

Bearing in mind these paths, the results from the pressure plate tests (Fig. 3) are now examined. The WRC at UGLAS

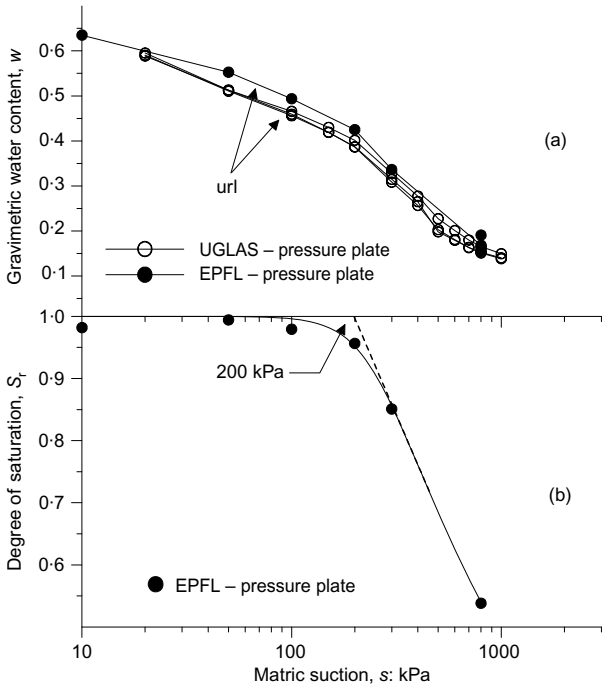

Fig. 3. Results from pressure plate tests (UGLAS and EPFL) in terms of (a) water content and (b) degree of saturation

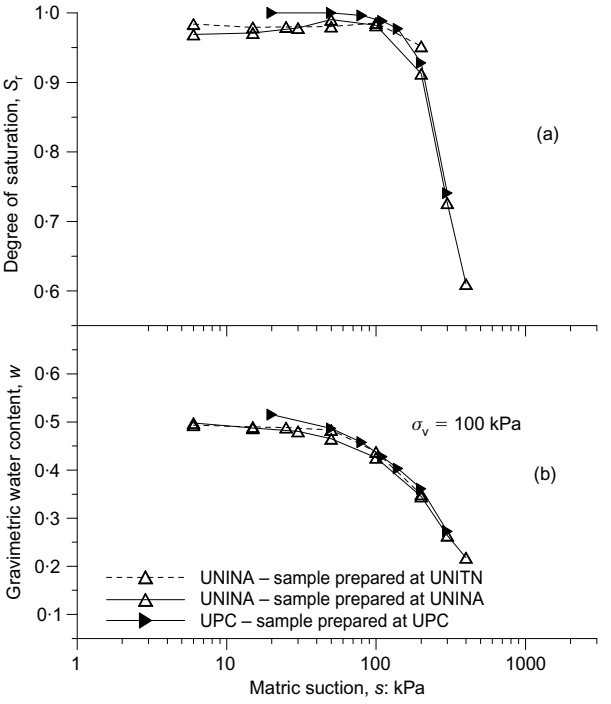

Fig. 4. Results from axis-translation oedometer (UNINA and UPC) in terms of (a) degree of saturation and (b) water content

was determined on three specimens simultaneously placed on the pressure plate. These three curves are nearly identical, suggesting that the three specimens had similar suction at the beginning of the pressure plate test. This point is very important as the success of the benchmark exercise depends on the reproducibility of the initial state of the specimens.

The results from EPFL are also shown in Fig. 3(a) in terms of water content and in Fig. 3(b) in terms of degree of saturation. The soil remains quasi-saturated up to suctions of about 200 kPa. In the range 100–200 kPa, the specimen moves from the saturated unloading–reloading line (url) to the normal consolidation line, as discussed in Fig. 2(a). In the saturated and quasi-saturated range ($s < 200$ kPa), EPFL data slightly overestimate water content with respect to UGLAS data. This may be associated with the different vertical pressure applied to improve contact, no pressure for EPFL and 0·6 kPa for UGLAS, as discussed later in the paper. The different water content may also arise from the water sucked out of the ceramic plate when releasing the air pressure. In contrast to UGLAS, EPFL did not close the water reservoir drainage valve before releasing the air pressure. However, the amount of water that could move into the specimen in the few minutes between reducing the air pressure and weighing the specimen is not expected to be significant because of the low permeability of the high-air-entry value (HAEV) ceramic (Noguchi, 2009). Beyond 200 kPa suction, EPFL and UGLAS data appear to be consistent.

The results from the axis-translation oedometers are shown in Fig. 4. Concerning the tests carried out at UNINA, one curve refers to a sample prepared at the UNITN, and the other one refers to a sample prepared at the UNINA, following the same procedure adopted at the UNITN. The data obtained at UPC also refer to a sample prepared at UPC. It is interesting to observe that these three curves are very similar, demonstrating that samples tested in this exercise can be reproduced if the procedure for sample preparation is carefully followed. Tests carried out within this benchmark exercise could therefore be potentially duplicated by other laboratories as the 'ingredients' of the MUSE mixture are all commercially available.

Water retention data from axis-translation oedometer cannot be directly compared to those obtained in the pressure plate because of the different total stress applied. However, as the specimens remain saturated at suctions lower than 100 kPa (Fig. 4), data in this range can be analysed in terms of mean effective stress $p' = p + s$, p being the mean total stress and s the suction.

By using equation (3) and assuming $k_0 = 1 - \sin\phi'$ (ϕ' being the effective angle of friction), the axis-translation oedometer curves in the range 0–100 kPa in Fig. 4(b) can be re-plotted in terms of mean effective stress p' in the plane ($p + s$, w) by tentatively assuming $\phi' = 20°$ or $\phi' = 30°$ (Fig. 5). Clearly the assumption $k_0 = 1 - \sin\phi'$ is only valid in the normally consolidated states, which are assumed to be reached as p' exceeds 70–80 kPa . Data are consistent with those obtained using the pressure plate and this essentially confirms the hydraulic and mechanical paths figured out in Fig. 2, taking into account that the transition from overconsolidated to normal consolidated states was assumed to be sharp in Fig. 2 and is indeed smooth.

The water retention data obtained by using the osmotic

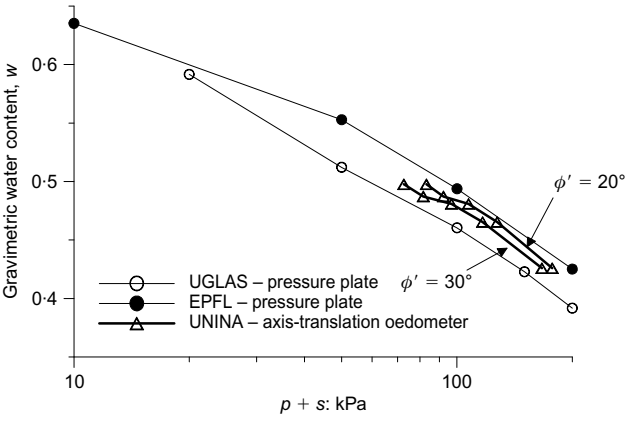

Fig. 5. Comparison of axis-translation data (pressure plate and oedometer) in the saturated range

method (ENPC) are shown in Fig. 6. Two curves are plotted based on the calibrations by Williams & Shaykewich and Dineen & Burland respectively. At a given water content, differences in the suctions predicted by the two calibration curves range from $\Delta s = 30$ kPa at $s = 200$ kPa to $\Delta s = 150$ kPa at $s = 800$ kPa. These differences are relevant and, in the following, only the curve based on the Dineen & Burland calibration will be discussed. Again, the soil starts desaturating in the range 100–200 kPa.

Figure 7 shows the results obtained using the high-capacity tensiometers (UNITN and UDUR). Apart from a UDUR data point at $s = 35$ kPa and a significant difference in suction measured at a water content of about 0·2, the two data sets appear to be consistent. Once again, the soil appears to start desaturating in the range 100–200 kPa.

To compare the water retention data using the pressure plate, the osmotic method and the high-capacity tensiometer, experimental results obtained by EPFL, ENPC and UNITN were analysed respectively. These data allow the comparison to be made both in terms of water content and degree of saturation (water retention data from UGLAS and UDUR were only provided in terms of water content and were shown to be similar to those obtained by EPFL and UNITN respectively). The three WRCs are shown in Fig. 8 and are augmented by total suction measurements using the WP4 dewpoint potentiometer performed at UPC. Data are consistent at low suctions (in the range where the soil is saturated) and also at high suction ($s > 700$ kPa). At high suctions, there appears to be continuity with the dewpoint potentiometer data. Discrepancies are observed in the medium range of suction (shaded area in Fig. 8). This range corresponds to the range where the soil starts desaturating as shown in Fig. 9 and in particular in the range where the air phase is present in occluded form in the pore space.

Inspection of Fig. 9 shows that data in terms of degree of saturation are not consistent with data in terms of water content (the ENPC water retention data lie between the UNITN and EPFL data in Fig. 8(a) and appear to bound the UNITN and EPFL data in Fig. 9). This is associated with errors in the estimate of total volume, as shown in Fig. 10, where the degree of saturation and void ratio are plotted against water content. There is an inevitable data scattering which causes the apparent discrepancy between water retention data in terms of water content and degree of saturation shown in Fig. 8(a) and Fig. 9 respectively. If a unique function is used to relate the degree of saturation to water content, as shown by the thick curve in Fig. 10(a), data clearly regain consistency as illustrated in Fig. 9(b).

The discrepancy observed in the medium range of suction (shaded area in Fig. 8) is perhaps the most remarkable result of this exercise. It appears that suction in the pressure plate is overestimated with respect to suction measured by the high-capacity tensiometer and the osmotic technique (based on tensiometer calibration) in the range of degree of saturation above 0·7–0·8. The suction difference in this range of degrees of saturation appears to be significant. For example, suction measured by the tensiometer at $w \sim 0{\cdot}3$ is around 200 kPa, whereas the suction applied in the pressure plate is 400 kPa at the same water content.

Similar effects were previously observed by Chahal & Yong (1965) for both initially saturated and initially unsaturated specimens. These authors also observed greater discrepancies

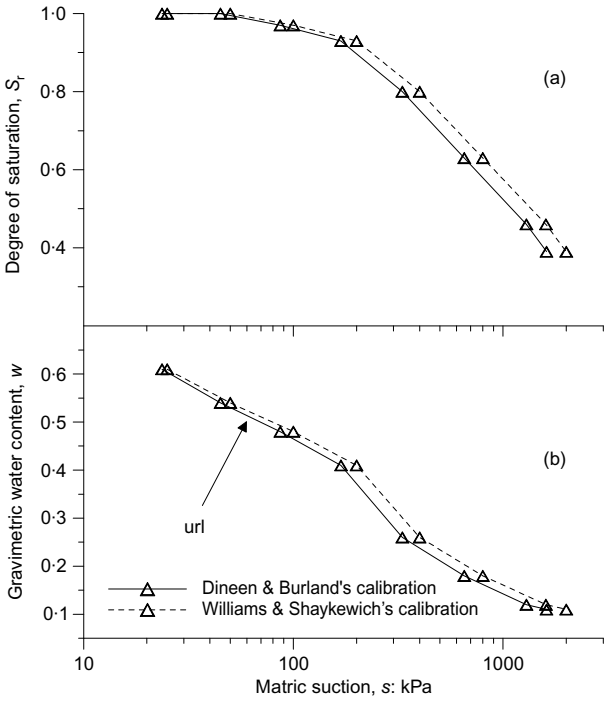

Fig. 6. Results from the osmotic technique (ENPC) in terms of (a) degree of saturation and (b) water content

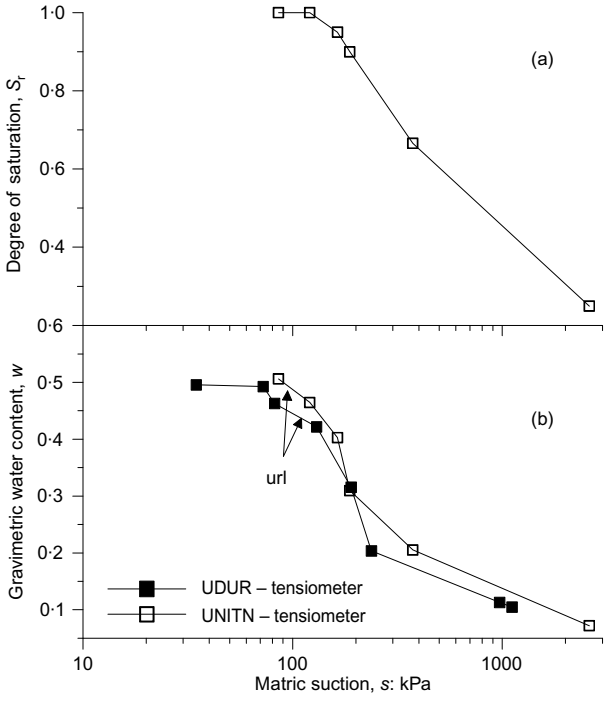

Fig. 7. Results from the high-capacity tensiometer (UNITN and UDUR) in terms of (a) degree of saturation and (b) water content

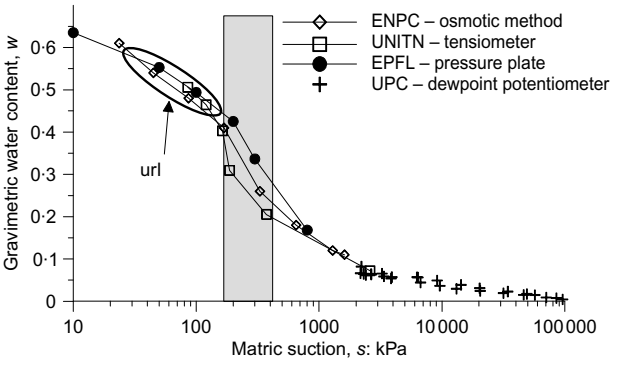

Fig. 8. Comparison between pressure plate (EPFL), osmotic method (ENPC), tensiometer (UNITN) and WP4 dewpoint potentiometer (UPC) in terms of water content

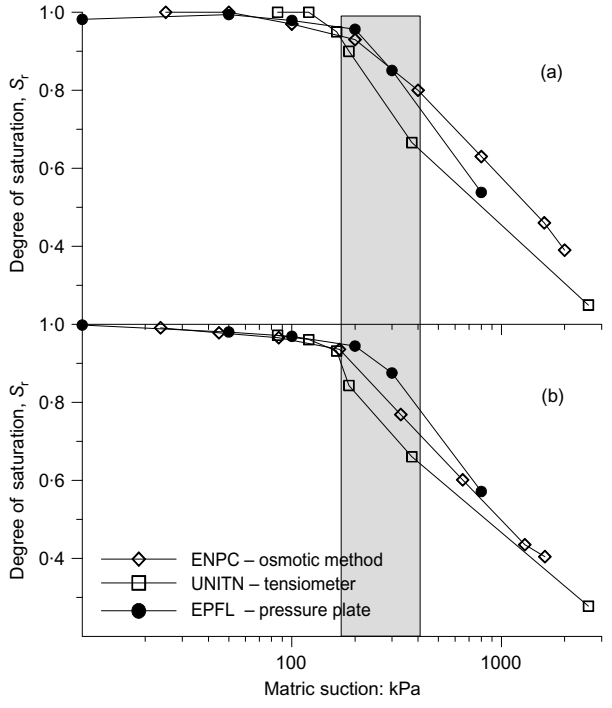

Fig. 9. Comparison between pressure plate (EPFL), osmotic method (ENPC) and tensiometer (UNITN) in terms of degree of saturation: (a) raw data; (b) corrected using a single function w–S_r

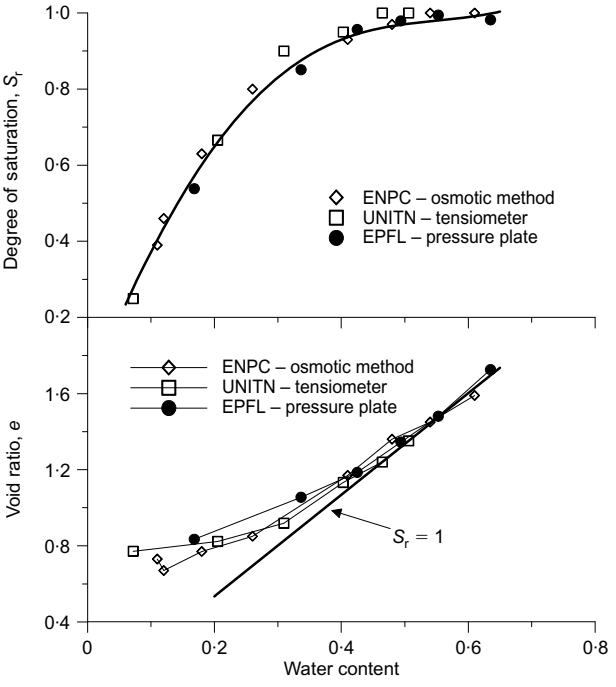

Fig. 10. Relationship between phase variables in pressure plate (EPFL), osmotic method (ENPC) and tensiometer (UNITN) tests

as suction exceeded the air-entry suction, that is in the range where the soil starts desaturating and air is discontinuous. Lourenço *et al.* (2006) also observed that suction in the pressure plate is overestimated with respect to the tensiometer.

A possible explanation of this effect was provided by Marinho *et al.* (2008) considering the capillary tube conceptual model. A capillary tube representing a quasi-saturated state contains an entrapped air cavity at some elevation below the atmospheric air–water interface (Fig. 11(a)). If, in the laboratory environment, this same capillary tube is sealed and subjected to an elevated air pressure, the relatively high compressibility of the air cavity will lead to a significant reduction in the cavity's volume. As the gas–liquid–solid junction of the outer meniscus initially remains fixed, the curvature of the air–water interface will increase because of the compression of the entrapped air cavity as shown in Fig. 11(b). As a result, the pressure differential between air and water, which is controlled by the meniscus curvature, will increase.

Another point to be addressed is the apparent discrepancy between the osmotic method and the high-capacity tensiometer, as shown in Fig. 8. Inspection of this figure shows that the difference essentially concerns the ENPC data point at $w \sim 0{\cdot}27$. However, the difference between suction applied by the osmotic method and suction measured by the tensiometer is $\Delta s = \sim 40$ kPa and it is not significantly greater than the standard deviation of the error associated with the Dineen & Burland's calibration curve ($\Delta s_\sigma = \sim 25$ kPa). As a result, no conclusions can be drawn about possible differences between the tensiometer and osmotic method and further investigation is required.

Another interesting comparison concerns the two techniques based on axis-translation, the pressure plate (EPFL) and the oedometer (UNINA). As shown in Fig. 12(c), the air-entry suction for the UNINA specimens (axis-translation oedometer) is lower than the air-entry suction of the EPFL specimens (pressure plate). This is surprising as the air-entry suction of the axis-translation oedometer would have been expected to be equal to or greater than that recorded in the pressure plate according to the hydraulic path sketched in Figs 2(b) and 2(c). It then appears that the pressure plate overestimated suction also with respect to the axis-translation oedometer. As a result, the mechanism illustrated in Fig. 11 is not sufficient to explain the higher water content measured in the pressure plate at a given suction.

The main difference between the oedometer and pressure plate is the vertical stress applied to the specimen. This affects the hydromechanical response of the specimens but it is also expected to control the nature of the contact with the high-air-entry ceramic plate. To investigate this effect, a specific test was devised and carried out at USTRAT. Three specimens cut from the same sample were simultaneously placed in the pressure plate, each specimen loaded with a different weight to apply vertical stresses of 0·3, 4·7 and

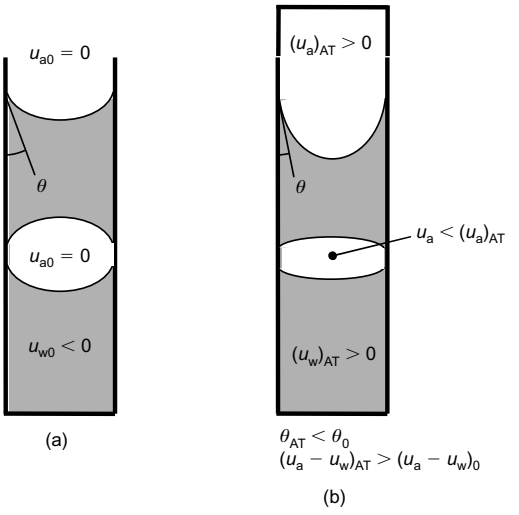

Fig. 11. Axis-translation technique in presence of occluded air: (a) negative water pressure; (b) positive water pressure

8·2 kPa respectively. A suction of 200 kPa was applied and the specimens were left to equilibrate for 12 days.

It was found that water content recorded upon the application of 200 kPa decreases significantly as the vertical stress increases (Fig. 12(a)). It is worth noting that the vertical stress applied has very little mechanical effect. The degree of saturation of the three specimens was equal to unity before placing them in the pressure plate and a degree of saturation equal to unity was measured after the application of the 200 kPa suction. Accordingly, their mechanical responses were controlled by the effective stress. The mean effective stress is given by the sum of the suction applied (200 kPa) plus one-third of the vertical stress applied, 0·1, 1·6 and 2·7 kPa respectively. The increase in mean stress associated with the weight is therefore very small and cannot justify a change in water content of about 3%. The result shown in Fig. 12(a) then seems to demonstrate that the contact pressure has a significant effect on water content. This can tentatively be explained by assuming that air tends to fill the gaps between the specimen and the plate, thus reducing the average hydraulic gradient between soil water and water in the high-air-entry ceramic. At the extreme, if a continuous gap were to form between the specimen and the plate (as if the specimen were suspended over the plate), no water exchange would occur. These air cavities tend to collapse as the vertical stress is increased and thus the water pressure in the porous ceramic tends to be transmitted more uniformly to the specimen.

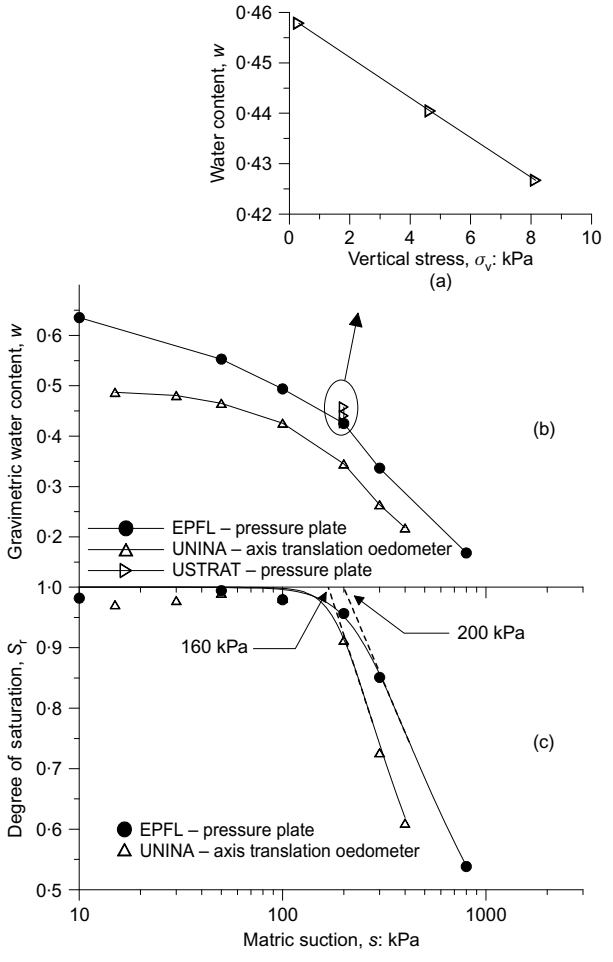

Fig. 12. Comparison between axis-translation oedometer (UNINA) and pressure plate (EPFL) and effect of contact pressure on water content (USTRAT)

CONCLUSIONS

The paper has presented a 'round robin' benchmark test aimed at comparing different techniques for the measurement and control of suction. The soil tested consisted of a mixture of kaolinite, bentonite and sand, all of which are commercially available. Samples were prepared by one laboratory (Università di Trento) to ensure that 'identical' samples were tested by all other teams. However, samples prepared by normal consolidation from slurry at two different laboratories (Università di Napoli Federico II and Universitat Politècnica de Catalunya) showed similar responses to those samples prepared at the Università di Trento. It would therefore be possible for other laboratories to prepare their own samples to duplicate the tests presented in this paper and check their own equipment and procedures.

Techniques tested by the eight MUSE research teams included axis-translation (pressure plate and axis-translation oedometer), high-capacity tensiometer, osmotic technique and dewpoint potentiometer. The water retention characteristics of the initially saturated samples were investigated along the main drying path. Samples were de-saturated by applying suction through the liquid phase when using axis-translation technique or osmotic method and de-saturated by air-drying when suction was measured using high-capacity tensiometers or dewpoint potentiometer.

When the same technique was tested by two different laboratories (pressure plate, axis-translation oedometer and high-capacity tensiometer), very similar WRCs were obtained, which is a remarkable result in a round robin test. It therefore appears that techniques for suction measurement or control are sufficiently reliable to be successfully used in routine engineering practice.

Differences were observed between the pressure plate and the tensiometer. In particular, the pressure plate seems to overestimate suction at given water content in the range of high degrees of saturation, that is where air is in occluded form. This finding is in agreement with experimental evidence from the literature.

The pressure plate appears to overestimate suction also with respect to the axis-translation oedometer where non-zero total stress is applied to the specimen. It is suggested that this difference is associated with the different contact pressure between the specimen and the high-air-entry ceramic plate. A specifically designed test has demonstrated that contact pressure can significantly change the equilibrium water content at a given applied suction.

ACKNOWLEDGEMENTS

The authors wish to acknowledge the support of the European Commission by way of the 'Marie Curie' Research Training Network contract number MRTN-CT-2004-506861. The helpful discussions with Anh-Minh Tang from the École des Ponts – ParisTech, UR Navier/CERMES are also gratefully acknowledged.

REFERENCES

Airò Farulla, C. & Ferrari, A. (2005). Controlled suction oedometric tests: analysis of some experimental aspects. *Proceedings of an international symposium on advanced experimental unsaturated soil mechanics (EXPERUS)*, Trento, Italy, pp. 43–48. Rotterdam: Balkema.

Atkinson, J. H. (1993). *An introduction to the mechanics of soils and foundations: through critical state soil mechanics*. London: McGraw-Hill.

Chahal, R. S. & Yong, R. N. (1965). Validity of the soil water characteristic determined with the pressurized apparatus. *Soil Sci*. **99**, No. 2, 98–103.

Cui, Y. J. & Delage, P. (1996). Yielding and plastic behaviour of an

unsaturated compacted silt. *Géotechnique* **46**, No. 2, 291–311, **doi**: 10.1680/geot.1996.46.2.291.

De Gennaro, V., Canou, J, Dupla, J. C. & Benahmed, N. (2004). Influence of loading path on the undrained behaviour of a medium loose sand. *Can. Geotech. J.* **41**, No. 1, 166–180.

Delage, P., Howat, M. D. & Cui, Y.-J. (1998). The relationship between suction and swelling properties in a heavily compacted unsaturated clay. *Engng Geol*. **50**, No. 1–2, 31–48

Delage, P., Romero, E. & Tarantino, A. (2008). Keynote lecture: Recent developments in the techniques of controlling and measuring suction. *Proc. 1st Eur. Conf. Unsaturated Soils, Durham, UK* **1**, 33–52.

Di Mariano, A., Airò Farulla, C. & Valore, C. (2000). Retention curves and 1-D behaviour of a compacted tectonised unsaturated clay. In *Experimental evidence and theoretical approaches in unsaturated soils* (eds A. Tarantina and C. Mancuso), *Proceedings of an international workshop on unsaturated soils*, Trento, Italy, pp. 47–64. Rotterdam: Balkema.

Dineen, K. & Burland, J. B. (1995). A new approach to osmotically controlled oedometer testing. *Proc. 1st Conf. Unsaturated Soils (UNSAT'95), Paris* (eds E. E. Alonso and P. Delage) **2**, 459–465. Rotterdam: AA Balkema.

Gallipoli, D., Wheeler, S. J. & Karstunen, M. (2003). Modelling the variation of degree of saturation in a deformable unsaturated soil. *Géotechnique* **53**, No. 1, 105–112, **doi**: 10.1680/geot.2003.53.1.105.

Hoffmann, C., Romero, E. & Alonso, E. E. (2005). Combining different controlled-suction techniques to study expansive clays. *Proceedings of an international symposium on advanced experimental unsaturated soil mechanics* (eds A. Tarantino, E. Romero and Y. J. Cui), Trento, Italy, pp. 61–67. Leiden: AA Balkema.

Lourenço, S. D. N. (2008). *Suction measurements and water retention in unsaturated soils*. PhD thesis, Durham University, Durham, UK.

Lourenço, S. D. N., Gallipoli, D., Toll, D. G. & Evans, F. D. (2006). Development of a commercial tensiometer for triaxial testing of unsaturated soils. *Proc. 4th Int. Conf. Unsaturated Soils, Phoenix* (eds G. A. Miller, C. E. Zapata, S. L. Houston and D. G. Fredlund) **2**, 1875–1886. Reston: ASCE, Geotechnical Special Publication 147.

Lourenço, S. D. N., Gallipoli, D., Toll, D. G., Augarde, C., Evans, F. & Medero, G. (2008). Calibrations of a high-suction tensiometer. *Géotechnique* **58**, No. 8, 659–668, **doi**: 10.1680/geot.2008.58.8.659.

Lourenço, S. D. N., Gallipoli, D., Toll, D. G., Augarde, C. E. & Evans, F. D. (2011). A new procedure for the determination of the soil water retention curve by continuous drying using high suction tensiometers. *Can. Geotech. J.* **48**, No. 2, 327–335.

Marinho, F. A. M., Take, A. & Tarantino, A. (2008). Tensiometeric and axis translation techniques for suction measurement. *Geotech. Geol. Engng* **26**, No. 6, 615–631.

MUSE website (2005). MUSE 'Marie Curie' Research Training Network. See http://muse.dur.ac.uk for further details (accessed 31 August 2005).

Noguchi, T. (2009). *Comparison of major suction measurement techniques used to determine the soil water retention curves*. MEng dissertation, Durham University, Durham, UK.

Péron, H., Hueckel, T. & Laloui, L. (2007). An improved volume measurement for determining soil water retention curves. *Geotech. Testing J.* **30**, No. 1, 1–8.

Rampino, C., Mancuso, C. & Vinale, F. (1999). Laboratory testing on an unsaturated soil : equipement, procedures, and first experimental results. *Can. Geotech. J.* **36**, No. 1, 1–12.

Rojas, J. C., Mancuso, C. & Vinale, F. (2007). Stress state and hysteresis influence upon the SWRC of a silty sand using the modified oedometer apparatus. *International congress on development, environment and natural resources: multi-level and multi-scale sustainability*, Cochabamba, Bolivia, 11–13 July 2007, vol. 1, pp. 145–153.

Romero, E. (1999). *Characterisation and thermo-hydro-mechanical behaviour of unsaturated boom clay: an experimental study.* PhD thesis, Universitat Politècnica de Catalunya, Barcelona, Spain.

Romero, E. (2001). Controlled-suction techniques. *Proc. 4° Simpósio Brasileiro de Solos Nâo Saturados Ñ SAT'2001* (eds W. Y. Y. Gehling and F. Schnaid), *PortoAlegre, Brazil* **1**, 535–542.

Tang, A.-M. & Cui, Y.-J. (2005). Controlling suction by the vapour equilibrium technique at different temperatures and its application in determining the water retention properties of MX80 clay. *Can. Geotech. J.* **42**, No. 1, 287–296.

Tang, A.-M., Cui, Y.-J., Qian, L.-X., Delage, P. & Ye, P. W.-M. (2010). Calibration of the osmotic technique of controlling suction with respect to temperature using a miniature tensiometer. *Can. Geotech. J.* **47**, No. 3, 359–365.

Tarantino, A. (2004). Panel report: Direct measurement of soil water tension. *Proc. 3rd Int. Conf. Unsaturated Soils* (eds J. F. T. Jucá, T. M. P. de Campos and F. A. M. Marinho) **3**, 1005–1017.

Tarantino, A. (2007). *Task A3: Benchmarking methods of suction control – Preparation of soil samples*. MUSE internal report.

Tarantino, A. (2009). A water retention model for deformable soils. *Géotechnique* **59**, No. 9, 751–762, **doi**: 10.1680/geot.7.00118.

Tarantino, A. & Mongiovì, L. (2002). Design and construction of a tensiometer for direct measurement of matric suction. *Proc. 3rd Int. Conf. Unsaturated Soils* (eds J. F. T. Jucá, T. M. P. de Campos and F. A. M. Marinho) **1**, 319–324.

Tarantino, A. & Mongiovì, L. (2003). Calibration of tensiometer for direct measurement of matric suction. *Géotechnique* **53**, No. 1, 137–141, **doi**: 10.1680/geot.2003.53.1.137.

Tarantino, A. & Tombolato, S. (2005). Coupling of hydraulic and mechanical behaviour in unsaturated compacted clay. *Géotechnique* **55**, No. 4, 307–317, **doi**: 10.1680/geot.2005.55.4.307.

Williams, J. & Shaykewich, C. F. (1969). An evaluation of polyethylene glycol PEG 6000 and PEG 20000 in the osmotic control of soil water matrix potential. *Can. J. Soil Sci.* **102**, No. 6, 394–398.

Wissa, A. E. Z. & Heiberg, S. (1969). *A new one-dimentional consolidation test*. Cambridge, MA: Massachusetts Institute of Technology, Research Report 69–9.

ice
Institution of Civil Engineers
publishing

Session 4

Application to Engineering Problems and Case Studies

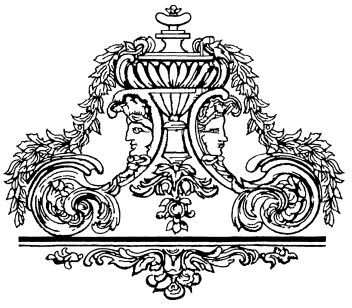

Gens, A. *et al.* (2011). *Géotechnique* **61**, No. 5, 367–386 [**doi:** 10.1680/geot.SIP11.P.015]

Hydromechanical behaviour of a heterogeneous compacted soil: experimental observations and modelling

A. GENS*, B. VALLEJÁN*, M. SÁNCHEZ†, C. IMBERT‡, M. V. VILLAR§ and M. VAN GEET¶

The paper describes a theoretical and experimental study of the coupled hydromechanical behaviour of a compacted mixture of bentonite powder and bentonite pellets intended as sealing material in underground repositories for nuclear waste. One of the main advantages of the use of powder/pellets mixtures is the reduction of the compaction effort required to achieve the value of average dry density necessary to attain the required swelling potential. However, the heterogeneous fabric of the material requires special approaches in order to describe adequately its behaviour during hydration. A double porosity formulation is presented to account for the presence of two distinct structural levels in the material. Hydraulic equilibrium between the two porosities is not assumed; instead a water exchange term between them is postulated. The formulation is applied to the modelling of a number of one-dimensional swelling pressure tests performed in the CEA (Commisariat à l'Énergie Atomique, France) and CIEMAT (Spain) laboratories. A very satisfactory quantitative description of the experimental observations is obtained that includes a number of complex behaviour features such as size effects and non-monotonic development of swelling pressures. Some microfabric observations using X-ray tomography and mercury intrusion porosimetry lend support to the conceptual approach adopted. The formulation is then applied to the analysis of a long-term large-scale sealing test performed at the Hades underground facility in Belgium, using the same set of hydraulic and mechanical parameters employed in the modelling of the laboratory tests. Although the field observations exhibit a much higher degree of scatter, the basic behaviour of the field sealing test is satisfactorily simulated. A formulation that incorporates basic features of the microfabric of the mixture is thus able to span successfully over a large range of space and time scales.

KEYWORDS: compaction; expansive soils; fabric/structure of soils; full-scale tests; laboratory tests; partial saturation

La présente communication décrit une étude théorique et expérimentale du comportement hydromécanique mixte d'un mélange compacté de poudre et de granulés de bentonite utilisé comme matériau d'étanchéité dans des dépôts souterrains de déchets nucléaires. Un des principaux avantages de l'utilisation de mélanges poudre/granulés est la réduction du travail de compactage nécessaire pour réaliser la densité sèche moyenne requise pour obtenir le potentiel de gonflement spécifié. Toutefois, la structure hétérogène du matériau nécessite l'emploi de méthodes particulières pour la description adéquate de son comportement au cours de l'hydratation. On présente une formulation à double porosité pour prendre en considération la présence de deux niveaux structurels distincts dans le matériau. On ne suppose pas l'existence d'un équilibre hydraulique entre les deux porosités, mais on postule une condition d'échange d'eau entre elles. On applique la formulation pour la modélisation d'un certain nombre d'essais de pression de gonflement unidimensionnels effectués dans les laboratoires de la CEA (en France) et de CIEMAT (en Espagne). On obtient ainsi une description extrêmement satisfaisante des observations expérimentales , y compris un certain nombre de caractéristiques complexes du comportement, par exemple les effets de la taille et le développement non monotones des pressions de gonflement. Certaines observations des micro-tissus effectuées en tomographie aux rayons X et en porosimétrie par intrusion de mercure (MIP) soutiennent le principe conceptuel adopté. On applique ensuite la formulation à l'analyse d'un essai d'étanchéité à grande échelle et à long terme, effectuée dans l'installation souterraine Hades en Belgique, en utilisant le même ensemble de paramètres hydrauliques et mécaniques utilisé pour la modélisation des essais en laboratoire. Bien que les relevés sur le terrain présentent une diffusion bien plus élevée, on réalise une simulation satisfaisante du comportement de base de l'essai d'étanchéité sur le terrain. On dispose ainsi d'une formulation comprenant les caractéristiques de base du micro-tissu du mélange couvrant avec succès une vaste plage d'échelles spatiales et des temps.

INTRODUCTION

The construction of deep underground repositories for high-level nuclear waste requires the excavation of shafts, or ramps, as well as horizontal drifts that give access to the waste emplacement area. Much attention has been given to engineered barriers placed around the waste (Gens *et al.*, 1998; 2009b) but the sealing of access shafts and drifts to block potential preferential pathways for radionuclide migration is of comparable importance (IAEA, 1990; Gens, 2003). Compacted bentonite is often considered as a suitable backfill material, not only because of its low permeability and favourable retardation properties, but also for its capability, on hydration, to fill gaps and voids that may arise from excavation irregularities or other causes. Therefore, in order to ensure the long-term safety of the repository, the backfill material must have enough swelling potential upon hydration to perform the sealing function satisfactorily. As swelling potential depends essentially on the dry density of the sealing material (Imbert & Villar, 2006), it may be necessary

Manuscript received 3 March 2010; revised manuscript accepted 20 October 2010. Published online ahead of print 22 March 2011. Discussion on this paper closes on 1 October 2011, for further details see p. ii.

* Department of Geotechnical Engineering and Geosciences, Universitat Politècnica de Catalunya, Barcelona, Spain.
† Texas A & M University, College Station, USA.
‡ CEA (Commisariat à l'Énergie Atomique), Gif sur Yvette, France.
§ CIEMAT, Madrid, Spain.
¶ ONDRAF/NIRAS, Brussels, Belgium.

to apply a significant compaction effort in order to achieve an adequate density value. Often, this causes operational difficulties as it is difficult to ensure a uniform and intense compaction in enclosed, irregularly shaped spaces. Precompacted bentonite blocks are sometimes used but they leave gaps between them and they are also difficult to accommodate when shafts and drifts have uneven excavation surfaces, a feature that is almost unavoidable in many cases. An interesting alternative is to use, as sealing material, a mixture of bentonite powder and highly compacted bentonite pellets (Volckaert *et al.*, 1996). In this way, the average dry density is already quite high on placement due to the contribution of the high-density pellets. Consequently, only modest compaction efforts may be required after putting the material in place and, in any case, a minimum density is always ensured. As an example, Fig. 1 shows the sealing of an experimental shaft backfilled with a compacted mixture of bentonite powder and pellets.

The resulting material is obviously highly heterogeneous, consisting of a mixture of relatively low-density bentonite powder with high-density bentonite pellets. The behaviour of such material upon hydration is likely to be complex and must be properly understood if a sufficient degree of confidence in the design and performance of the seal is to be achieved. A conceptual framework leading to a good understanding of this behaviour should also be of benefit for other heterogeneous compacted materials, such as, for instance, the often-encountered case of compacted clayey soils containing large lumps of intact material.

In this paper, some basic features of the hydration behaviour of this heterogeneous compacted soil are presented first. Afterwards, the theoretical formulation required for the analysis of this type of material is briefly described. The formulation is then applied to the modelling of a series of one-dimensional swelling pressure tests performed in the laboratory. Finally, the analysis is upscaled to the description of a full-scale sealing test performed in an underground laboratory.

BASIC FEATURES OF THE BEHAVIOUR OF POWDER–PELLETS MIXTURES DURING HYDRATION

The behaviour of the powder–pellets mixture during hydration has been examined by means of laboratory swelling pressure tests (Imbert & Villar, 2006). Note that the hydration of a shaft or tunnel seal due to the inflow of host rock water is akin to a swelling pressure test due to the confinement provided by the excavation walls. Swelling pressure tests are, therefore, very appropriate to examine the behaviour relevant to seal hydration.

Mixtures of 50% bentonite powder and 50% bentonite pellets by dry weight have been tested. FoCa clay, a calcium bentonite from the Paris Basin, has been selected for the study. The major component of the clay fraction is an interstratified clay mineral of 50% calcium beidellite and 50% kaolinite. It has also a number of accessory minerals and the major exchangeable cation is Ca^{2+}. It also contains, in decreasing amounts, Mg^{2+}, Na^{+} and K^{+} (Volckaert *et al.*, 2000). Pellets are manufactured by dynamic compaction of the powder between two rotating wheels. The dimensions of the pellets (Fig. 2) are $25 \times 25 \times 15$ mm and their average dry density is $1{\cdot}89$ g/cm^3. Compaction water content lies in the range 4–5%.

The swelling pressure tests were performed in the laboratories of CEA (Commisariat à l'Énergie Atomique, France) and CIEMAT (Spain). Samples were statically compacted to the desired density and were subsequently tested in oedometers equipped with load cells. The specimens were hydrated from the bottom, sample deformation was prevented and the evolution of swelling pressure recorded. Water intake during the test was also measured. Because of the low permeability of the bentonite, tests had to be run over extended periods generally lasting several months. Deionised water was used for hydration as the water from the site where the in situ test has been performed has a very low salinity, thus minimising potential chemical effects on results. In fact, the influence of the salinity of the solution on swelling pressure has been considered negligible or small for highly compacted bentonites, especially when divalent cations predominate because diffuse double layers are poorly developed (Pusch, 1994; Castellanos *et al.*, 2008). The issue of chemical effects on the hydromechanical behaviour of bentonite has been discussed in detail in Guimarães *et al.* (2007).

Typical results of the oedometer swelling pressure tests are shown in Fig. 3. They correspond to specimens of different lengths (5, 10 and 12 cm) compacted to a common dry density of $1{\cdot}60$ g/cm^3. The diameter of the samples is 12 cm in order to accommodate a representative number of pellets. Several remarks can be made.

(*a*) The evolution of the swelling pressure is very characteristic suggesting a rather complex pattern of behaviour. Swelling pressure increases rapidly at the beginning of the test, until reaching a peak value. Afterwards, the measured pressure drops to a minimum

Fig. 1. Mixture of bentonite pellets and bentonite powder used as sealing material in an experimental shaft

Fig. 2. Pellets of FoCa clay used in the investigation. The dimensions of the pellets are 25 × 25 × 15 mm

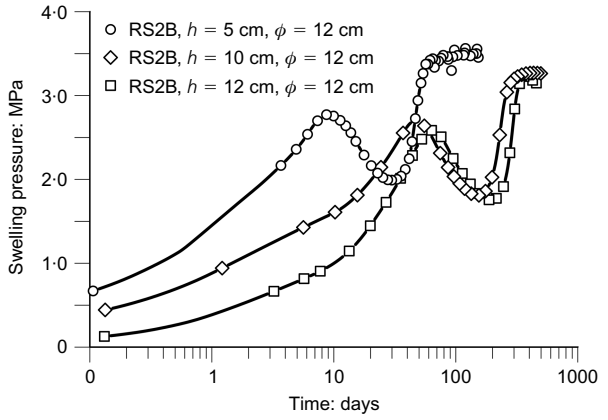

Fig. 3. Evolution of observed swelling pressures of a 50/50 powder/bentonite mixture. Tests performed at CEA laboratory at dry density of 1·60 g/cm^3

value to start later a new increase until reaching a stationary swelling pressure value at the end of the test. The same pattern of behaviour has been observed in the tests performed at other dry densities.

(*b*) There is a clear influence of the sample length on the rate of development of the swelling pressure. The longer the specimen, the slower the hydration kinetics is. This fact should be taken into account when transferring laboratory test results to field conditions where scale and hydration paths are bound to be quite different.

(*c*) The final swelling pressure at the end of the test is similar for the three samples, irrespective of length. Indeed, as Fig. 4 indicates, it has been found that final swelling pressure depends basically on dry density. It can be noted that the relationship between dry density and final swelling pressure for mixtures is very similar to that obtained in the same type of tests performed on samples of compacted bentonite powder (Imbert & Villar, 2006).

Interactions in the microfabric of the material during hydration must underlie the observed macroscopic behaviour. Direct observations of the hydration process were obtained by Van Geet *et al.* (2005) using microfocus X-ray computed tomography. A 50/50 powder–pellet mixture of FoCa clay at

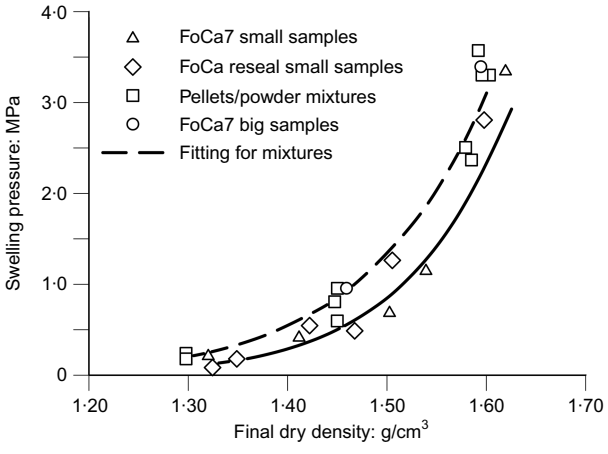

Fig. 4. Variation of swelling pressures of FoCa bentonite with dry density from tests performed in the CEA and CIEMAT laboratories. The dashed line corresponds to the relationship for 50/50 pellets/powder mixtures and the continuous line corresponds to compacted powder

a dry density of 1·36 g/cm^3 and an average water content of 5·67% was placed in a methacrylate cylindrical cell. The sample was 7 cm high and 3·8 cm in diameter. Hydration was performed from the bottom of the sample under constant volume conditions. During the first 1·5 months, water was supplied at a very low pressure; afterwards water was injected at a pressure of 0·5 MPa during four additional months. A permeability determination was performed at the end of the test using a 0·6 MPa water pressure. X-ray tomography observations could be performed at specified time intervals. From the computation of the linear X-ray attenuation coefficient, the density distribution throughout the sample could be determined. Fig. 5 shows the density distribution on a vertical slice through the centre of the sample at different times of the experiment. It can be noted:

(*a*) at the initial state there is a clear difference in density between pellets and powder

(*b*) during hydration, the density of the pellets reduces (swelling) whereas the density of the powder rises because of both soil compression and water content increase; the changes move gradually from bottom to top following the progress of hydration

(*c*) an apparently homogeneous specimen is obtained at the end of the test.

Further information is provided in Fig. 6 that shows the incremental density changes between the stages depicted in Fig. 5. It can be observed how hydration rises from the bottom of the specimen towards the top, causing density changes due to the swelling of the pellets and to the increase in saturation. Very little density change occurs after 2·5 months where the specimen has become much more homogeneous. It is also interesting to note that, in the initial stages of the test, the surfaces of the pellets away from the hydration front show some swelling due to the local exchange of water between powder and pellets.

THEORETICAL FORMULATION

Balance equations

The adoption of a double porosity model appears to be eminently suited to describe the heterogeneous nature of the material. Probably this concept was first introduced by Barrenblatt *et al.* (1960) (as quoted in Ghafouri & Lewis, 1996) to simulate flow through rigid, fissured porous media and it was later enlarged to consider the coupling between fluid flow and soil deformation (e.g. Aifantis, 1980; Wilson & Aifantis, 1982; Gens *et al.*, 1993; Khalili *et al.*, 1999; Callari & Federico, 2000). Here, the formulation developed in Sánchez (2004) is adopted.

The overall medium is assumed to consist of two overlapping but distinct continua. The macrostructure refers to the large-scale arrangement of soil particle aggregates and the relatively large pores between them. It is expected that, initially, most of the macrostructural pores belong to the bentonite powder. The microstructure refers to the clay particles and the micropores and interparticle spaces associated with them. A large proportion of the micropores lie initially in the high-density pellets but there will also be micropores in the clay particle aggregates present in the powder. Ideally, the microporosity of the powder aggregates should be distinguished from that in the pellets but, in that case, the number of interactions and parameters multiply leading to a cumbersome formulation that is difficult to apply in practice. As shown later, a double porosity model appears to be sufficient to describe the hydromechanical behaviour of the material. In the following, subscript M will stand for the macrostructure and subscript m for the microstructure. Accordingly, macroporosity and microporosity are

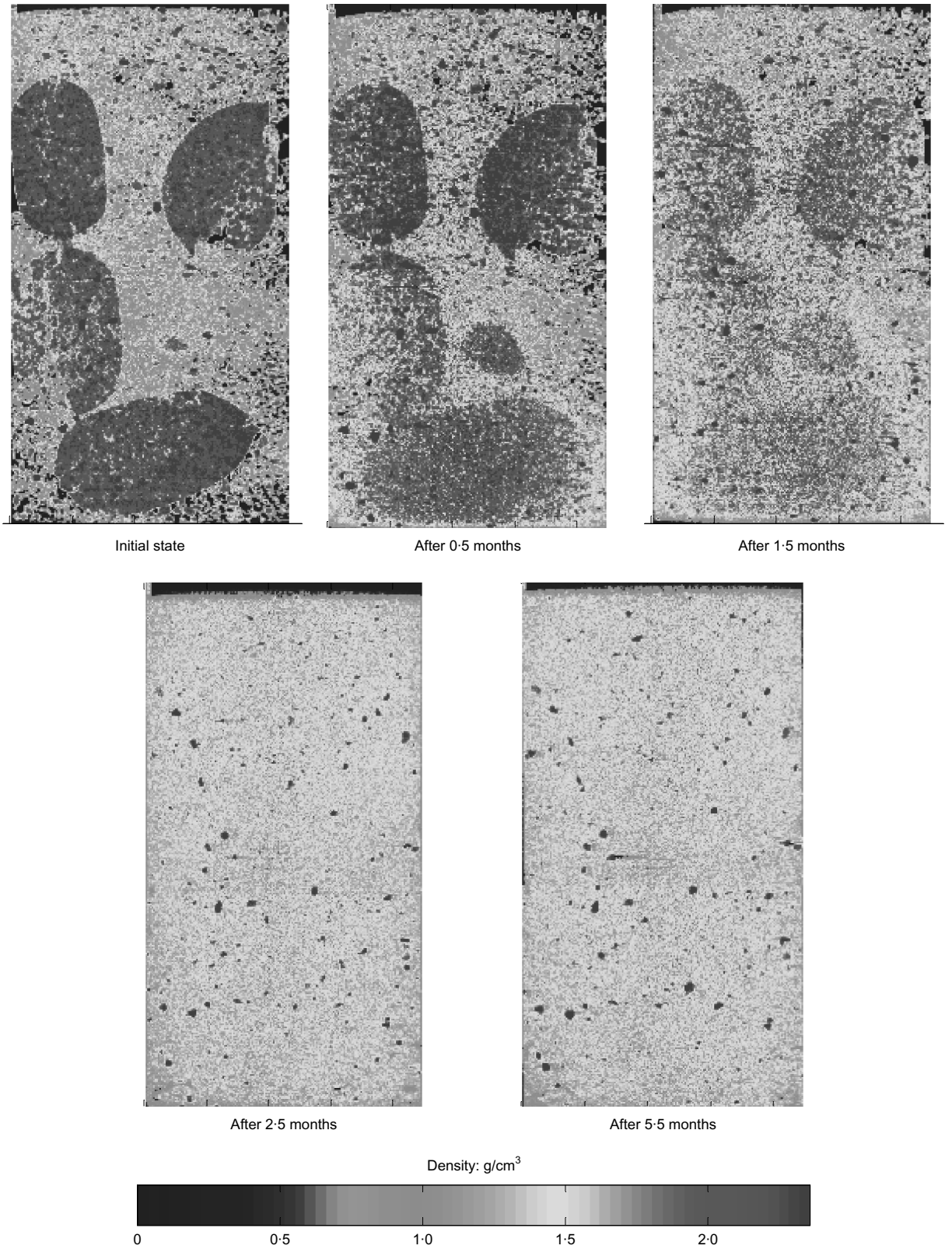

Fig. 5. Distribution of densities on a vertical slice through the centre of the sample observed at different stages of hydration (after Van Geet *et al.*, 2005). The specimen is 7 cm high and 3·8 cm in diameter

denoted as φ_M and φ_m respectively. Macroporosity and microporosity are defined as the volume of macropores and micropores, respectively, divided by the total volume of the soil. Thus, total porosity φ equals $\varphi_M + \varphi_m$. The degree of saturation of the macroporosity, S_{wM}, is the volume of macropores occupied by water over the volume of the macropores; an equivalent definition holds for the microporosity degree of saturation, S_{wm}.

An important feature is that hydraulic equilibrium between the two continua is not assumed; that is, at each point of the domain the water potentials in the two continua may be different, leading to an exchange of water between them (Fig.

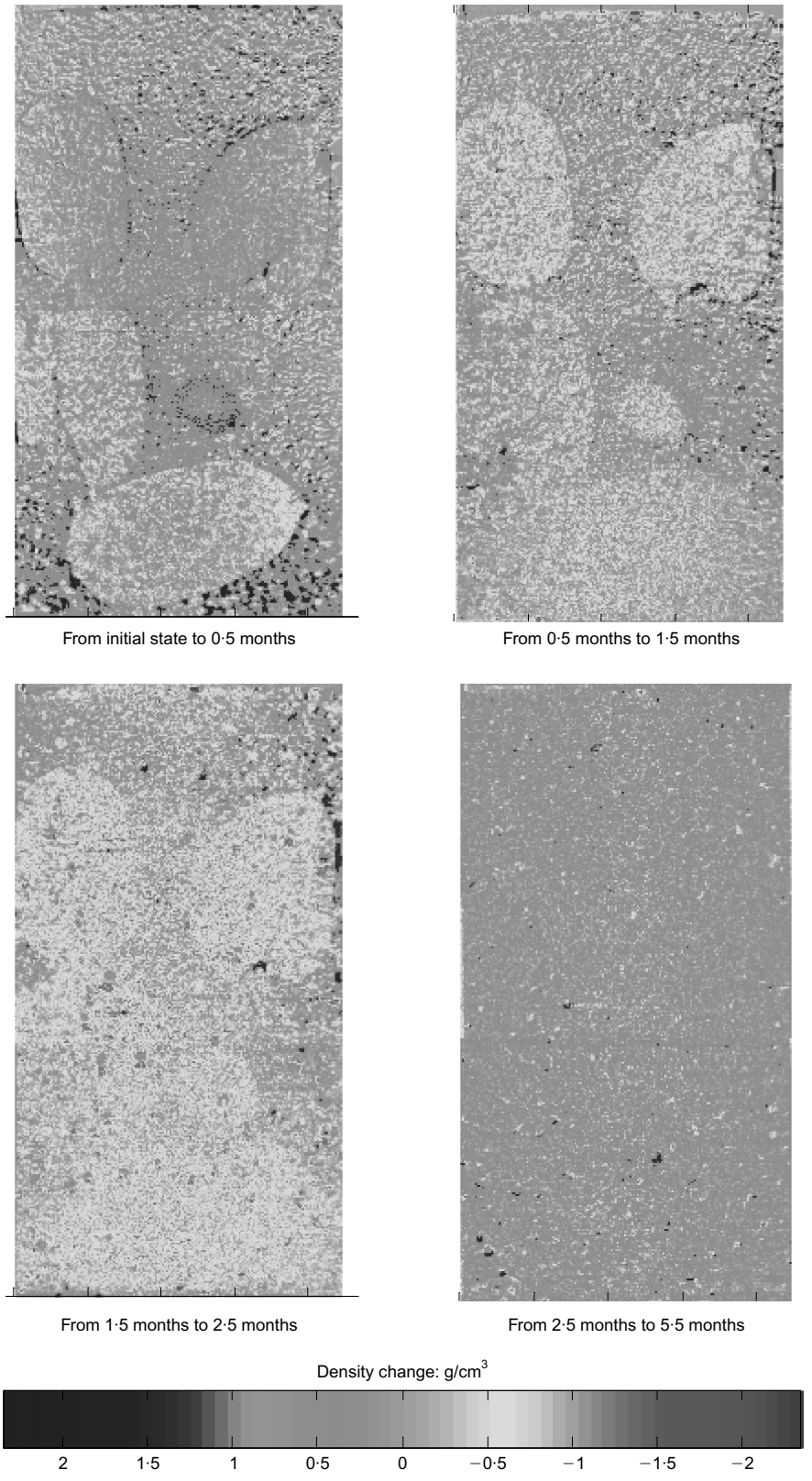

Fig. 6. Distribution of incremental density changes on a vertical slice through the centre of the sample observed at different stages of hydration (after Van Geet *et al.*, 2005). The specimen is 7 cm high and 3·8 cm in diameter

7). For simplicity, a linear relationship is assumed (e.g. Wilson & Aifantis, 1982) where water exchange is described by

$$\Gamma^{w} = \gamma(\psi_M - \psi_m) \tag{1}$$

where Γ^{w} is the water exchange term, γ is a parameter (often called the leakage parameter) and ψ is the total water potential. It is assumed that only matric and gravitational potential contribute to the total potential of the macrostructure but an additional osmotic component may also contribute to the microstructural potential (Gens, 2010). Here, potential is defined in pressure units. As the water exchange is local in space, the gravitational potential will be the same

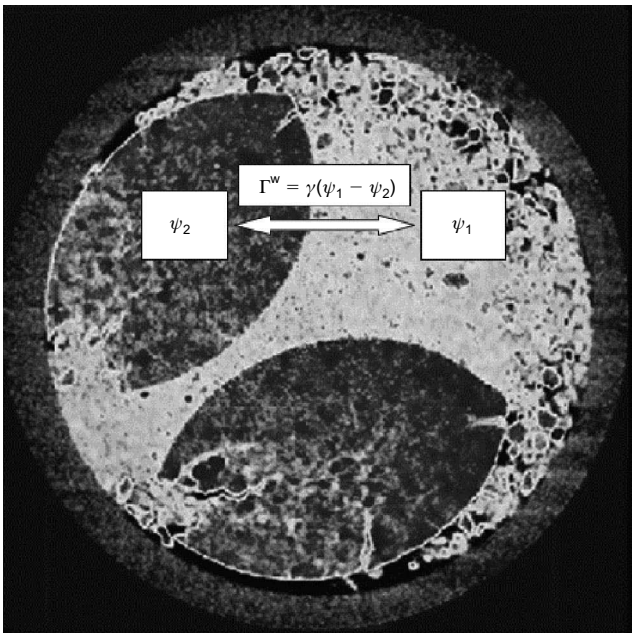

Fig. 7. Scheme of a double porosity material with a water exchange term

for the two media. Water exchange will therefore be driven by suction differences alone.

Using the concept of material derivative, the balance equation for the solid phase can be written, for the case of a single porosity medium, as:

$$\frac{\mathrm{D}\varphi}{\mathrm{D}t} = \frac{(1-\varphi)}{\rho_\mathrm{s}}\frac{\mathrm{D}\rho_\mathrm{s}}{\mathrm{D}t} + (1-\varphi)\,\dot{\varepsilon}_\mathrm{v} \tag{2}$$

where D(.)/Dt denotes material derivative, ρ_s is the solid density, $\dot{\varepsilon}_\mathrm{v}$ is the volumetric strain increment and t is time. For the case of double porosity equation (2) becomes (Sánchez, 2004)

$$\begin{aligned}\frac{\mathrm{D}\varphi}{\mathrm{D}t} = \frac{\mathrm{D}\varphi_M}{\mathrm{D}t} + \frac{\mathrm{D}\varphi_m}{\mathrm{D}t} = \frac{(1-\varphi)}{\rho_\mathrm{s}}\frac{\mathrm{D}\rho_\mathrm{s}}{\mathrm{D}t} \\ + (1-\varphi_M-\varphi_m)\,(\dot{\varepsilon}_{\mathrm{v}M} + \dot{\varepsilon}_{\mathrm{v}m})\end{aligned} \tag{3}$$

where it has been assumed that the total volumetric deformation is the sum of the volumetric deformations of each medium.

The water mass balance equation for the case of two overlapping flow media is

$$\frac{\partial}{\partial t}\left(\rho_\mathrm{w} S_{\mathrm{w}j}\phi_j\right) + \nabla\cdot\left(\boldsymbol{j}_{\mathrm{w}j}\right) \pm \Gamma^\mathrm{w} = f_j^\mathrm{w}; \quad j = M,\, m \tag{4}$$

where $S_{\mathrm{w}j}$ is the liquid saturation of medium j, $\boldsymbol{j}_{\mathrm{w}j}$ is the total mass fluxes of water in the liquid phase and f_j^w is the external mass supply of water per unit volume in medium j. The possible presence of dissolved air in the liquid phase is neglected for simplicity.

Finally, it is assumed that total stresses for the overall medium affect equally the macro- and the microstructure. The equilibrium equation is

$$\nabla\cdot\boldsymbol{\sigma} + \boldsymbol{b} = \boldsymbol{0} \tag{5}$$

where $\boldsymbol{\sigma}$ is the total stress tensor and $\boldsymbol{b}$ is the vector of body forces. In contrast, the total deformation of the medium is obtained from the sum of the deformations of each domain.

To perform numerical analyses, this set of balance equations is incorporated into a computer code by way of a suitable discretisation procedure. The analyses reported in the paper have been performed with a modified version of Code_Bright (Olivella *et al.*, 1996) that incorporates the double porosity formulation.

Hydraulic constitutive equations

Liquid flow is governed by Darcy's law

$$\boldsymbol{q}_{\mathrm{w}j} = -\boldsymbol{K}_{\mathrm{w}j}\left(\nabla\psi_j\right) = -\boldsymbol{K}_{\mathrm{w}j}\left(\nabla p_{\mathrm{w}j} - \nabla\rho_{\mathrm{w}j}\boldsymbol{g}\right); \quad j = M,\, m \tag{6}$$

where $\boldsymbol{q}$ is the mass liquid flow (with respect to the solid phase), $\boldsymbol{K}_\mathrm{l}$ is the liquid permeability tensor, p_l is the liquid pressure, ρ_l is the liquid density and $\boldsymbol{g}$ is the gravity vector. The permeability tensor is expressed as

$$\boldsymbol{K}_{\mathrm{w}j} = \boldsymbol{k}_j\frac{k_{\mathrm{r}j}}{\mu_j}; \quad j = M,\, m \tag{7}$$

where $\boldsymbol{k}$ is the intrinsic permeability, k_r is the relative permeability that expresses the effect of degree of saturation (or suction) on global permeability and μ_j is the liquid viscosity. Intrinsic permeability depends on many factors such as pore size distribution, pore shape, tortuosity and porosity. Here a dependence of intrinsic permeability on porosity is adopted

$$\boldsymbol{k}_j = k_\mathrm{o}\exp\left(b(\phi_j - \phi_\mathrm{o})\right); \quad j = M,\, m \tag{8}$$

where ϕ_o is a reference permeability for which the intrinsic permeability is k_o. Relative permeability is given by the empirical relationship

$$k_{\mathrm{r}j} = S_{\mathrm{e}j}^{\lambda}; \quad j = M,\, m \qquad S_\mathrm{e} = \frac{S_\mathrm{l} - S_\mathrm{lr}}{S_\mathrm{ls} - S_\mathrm{lr}} \tag{9}$$

where S_e is the effective degree of saturation, S_lr is the residual degree of saturation and S_ls is the degree of saturation in saturated conditions, normally taken as 1.

Finally the retention curve relates suction (or matric potential) with degree of saturation. There are a number of different expressions designed to fit experimentally determined retention curves. A modified form of the Van Genuchten (1980) law has been used here

$$S_{\mathrm{e}j} = \left[1 + \left(\frac{s}{P_\mathrm{o}}\right)^{1/(1-\lambda_\mathrm{o})}\right]^{-\lambda_\mathrm{o}}\left(1 - \frac{s}{P_\mathrm{d}}\right)^{\lambda_\mathrm{d}}; \quad j = M,\, m \tag{10}$$

where s is the matric suction and P_o, P_d, λ_o and λ_d are model parameters.

Mechanical constitutive law

It has been postulated that the behaviour of highly expansive clays is better described assuming two levels of structure, a macrostructural level and a microstructural level, akin to the two porosities considered in the formulation just described (Gens & Alonso, 1992). In this work, the mathematical model formulated in terms of generalised plasticity (Sánchez *et al.*, 2005) is used.

The model assumes that the physicochemical phenomena occurring at the microstructural level are basically reversible and largely volumetric. Then the deformations arising from microstructural phenomena can be obtained from a non-linear elastic model dependent on a microstructural mean stress ($\hat{p}$) defined as

$$\hat{p} = p + s_m \tag{11}$$

where p is the net mean stress and s_m is the microstructural suction.

In the p–s plane, the line corresponding to constant microstructural mean stresses ($\hat{p}$) is referred to as the neutral loading line (F_{NL}) since no microstructural deformation occurs when the stress path moves on it (Fig. 8(a)). The neutral loading line (NL) divides the p–s plane into two parts, defining two main microstructural stress paths: a microstructural contraction path (MC, $\dot{\hat{p}} > 0$) and a microstructural swelling path (MS, $\dot{\hat{p}} < 0$).

The increment of the microstructural elastic deformation is expressed as a function of the increment of the microstructural mean stress

$$\dot{\varepsilon}_{vm} = \frac{\dot{\hat{p}}}{K_m}; \quad K_m = \frac{1 + e_m}{\kappa_m}\hat{p} \tag{12}$$

where $\dot{\varepsilon}_{vm}$ is the microstructural volumetric strain increment, K_m is the microstructural bulk modulus, e_m is the microstructural void ratio and κ_m is a model parameter. The behaviour of the macrostructural level is defined by the Barcelona basic model (BBM) (Alonso *et al.*, 1990). For completeness, the main BBM equations are presented in the Appendix.

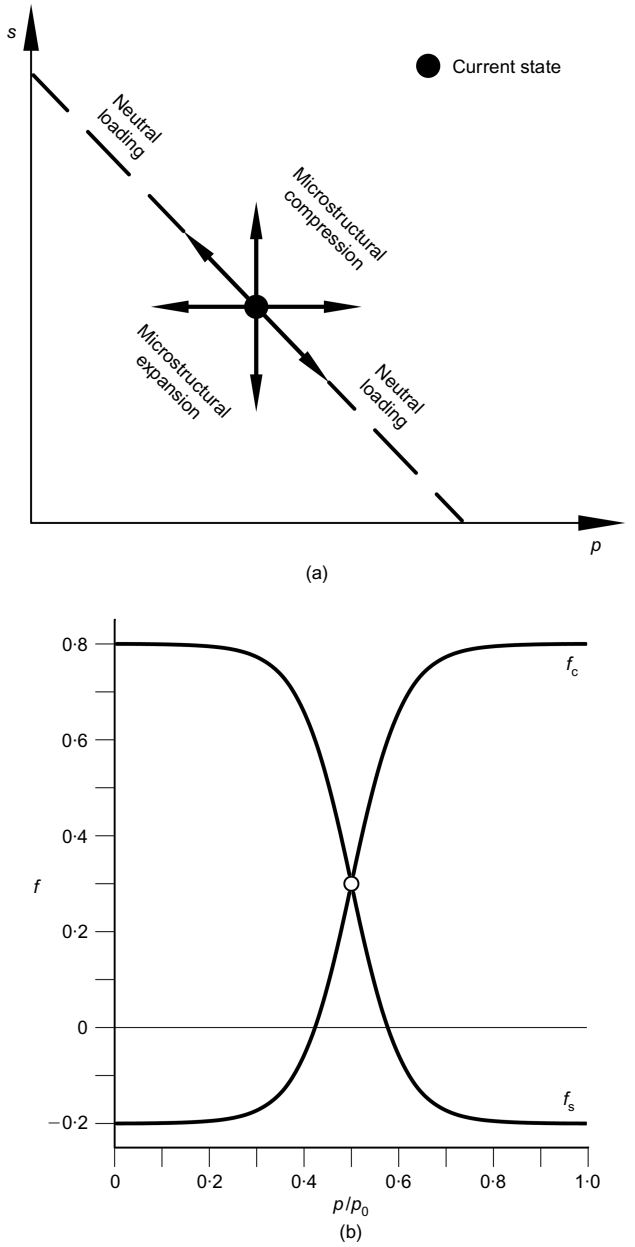

Fig. 8. Double structure mechanical constitutive law for expansive clays: (a) microstructural model; (b) interaction functions

A fundamental assumption of the framework is that microstructural behaviour is not affected by the macrostructure state but it only responds to changes in the driving variables (i.e. stresses and suction) at local microstructural level. In contrast, plastic macrostructural strains may result from deformations of the microstructure. It is postulated that plastic macrostructural strains can be expressed as

$$\dot{\varepsilon}^{p}_{vM} = f\,\dot{\varepsilon}_{vm} \tag{13}$$

where $\dot{\varepsilon}^{p}_{vM}$ is the macrostructural plastic strain arising from the deformation of the microstructure. Two interaction functions f are defined: f_c for MC paths and f_s for MS paths (Fig. 8(b)). In the case of isotropic loading, the interaction functions depend on the ratio p/p_o where p_o is the yield mean net stress at the current macrostructural suction value. The ratio p/p_o is a measure of the degree of openness of the macrostructure relative to the applied stress state. When this ratio is low it implies a dense packing of the material, it is then expected that the microstructural swelling (MS path) will affect strongly the global arrangements of clay aggregates, inducing large macrostructural plastic strains. If the p/p_o ratio comes close to 1, the state of the material approaches the BBM loading–collapse (LC) yield surface and it becomes collapsible. In that case, the multiplying effect of microstructural strains may be small or even negative. In this work, the following form of interaction function has been used

$$f_\alpha = f_{\alpha 0} + f_{\alpha i}\left(1 - \frac{p}{p_o}\right)^{n_\alpha}; \quad \alpha = s \text{ (swelling)},\ c \text{ (contraction)} \tag{14}$$

Although this form of formulating the interplay between microstructure and macrostructure is conceptually quite simple, it has proved able to accommodate a wide range of different interaction phenomena (Gens & Alonso, 1992).

MODELLING SWELLING PRESSURE TESTS

Features of the tests and model parameters

The formulation outlined above has been applied to the modelling of a number of swelling pressure tests performed on specimens of 50/50 powder/pellets mixtures compacted to two different densities (1·45 g/cm^3 and 1·60 g/cm^3) and with a range of different lengths. The main characteristics of the tests are given in Table 1. The pellets always have the same density; the variation in the density of the samples arises from the different initial powder densities.

According to the formulation, it is necessary to estimate the initial microstructural and macrostructural porosity both in the pellets and in the powder. Mercury intrusion porosimetries (MIPs) were performed on the pellets, a typical result is shown in Fig. 9. There is always some degree of arbitrariness in the distinction between the two types of pores, pore size distribution being a continuum. Here, a pore size of 100 nm has been selected for this purpose based on the fact that there is a clear change of slope in the pore size density functions determined experimentally. This value is also consistent with other previous estimations in similar materials (Touret *et al.*, 1990; Romero, 1999; Lloret *et al.*, 2003). For the powder, the distinction between porosities was made on the bases of experimental pore size determinations reported previously (Romero, 1999; Marcial, 2003)

Table 1. Main characteristics of the swelling pressure tests

Test label	Sample height: mm	Diameter: mm	Void ratio of sample	Dry density of sample: g/cm^3	Initial water content of sample: %	Dry density of pellets: g/cm^3	Initial water content of pellets: %	Dry density of powder: g/cm^3	Initial water content of powder: %	Laboratory
MGR7	50	100	0·84	1·45	8·30	1·89	4·60	1·175	12·00	CIEMAT
MGR9	100	100	0·84	1·45	5·25	1·89	5·00	1·182	5·80	CIEMAT
RS2J	50	120	0·84	1·45	4·78	1·89	4·00	1·175	5·00	CEA
RS2B	50	120	0·67	1·60	8·07	1·89	4·31	1·385	11·83	CEA
RS2E	100	120	0·67	1·60	4·78	1·89	4·49	1·390	5·07	CEA
RS2F	120	120	0·67	1·60	4·78	1·89	4·49	1·390	5·07	CEA

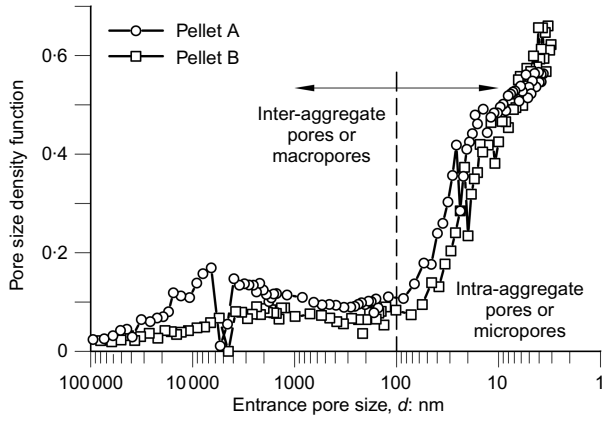

Fig. 9. Pore size density functions for two pellets

using the same threshold value. From this ensemble of results, it was found that the proportion of microporosity with respect to total porosity of compacted samples could be closely approximated by

$$v_m/v_T = 0{\cdot}0632\,\gamma_d^{3{\cdot}89} \tag{15}$$

where γ_d is the dry density in g/cm^3, v_m is the microstructural pore volume and v_T is the total pore volume. Fig. 10 shows the assumed variation of the different porosities (and void ratios) with as-compacted dry density. It is apparent that microporosity increases significantly in the highly compacted samples both in absolute and relative terms. Lacking more specific information, the initial proportions of water in the microstructure and in the macrostructure are assumed to be similar to those of the porosity components.

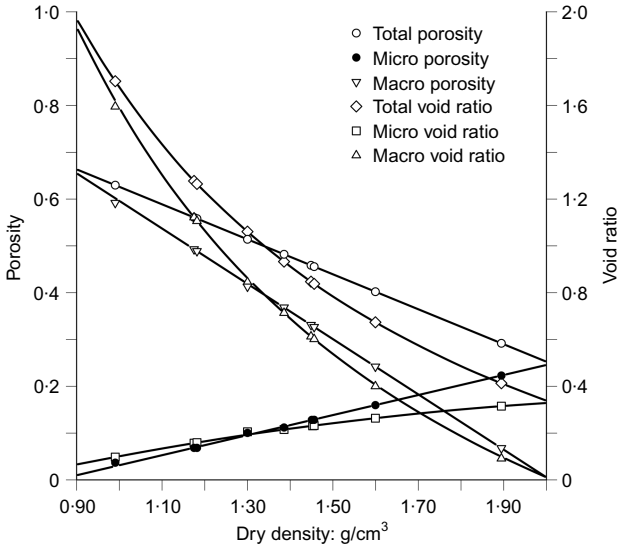

Fig. 10. Relationship between micro, macro and total porosities and dry density after compaction

The hydraulic parameters are presented in Table 2. There have been quite a number of determinations of the retention curve of compacted FoCa clay at different densities. They are shown in Fig. 11 together with the retention curves adopted in this work. The retention curves' parameters for the micro- and macroporosity have been estimated from the results of the higher and the lower density samples, respectively, as micropores are dominant in the high-density specimens and macropores predominate in the low-density specimens. Intrinsic permeability values and their variation have been derived from laboratory permeability tests on compacted FoCa clay at different dry densities, the results of which are summarised in Gens *et al.* (2009a). For relative permeability, an exponent value of 3 is adopted for the macrostructure, a value that has been obtained in several infiltration tests on homogeneous compacted bentonite (Gens *et al.*, 2009a). A lower exponent is assumed for the microstructure as it is conjectured that unsaturation has a lower impact on water mobility in the vicinity of clay particle surfaces. The leakage parameter is sometimes associated with some geometric characteristics of the medium, such as the specific surface of the matrix block (Barrenblatt *et al.*, 1960), the number of fractures and fracture intervals (Warren & Root, 1963) or the average size of clay blocks (Callari & Federico, 2000). Because of lack of relevant geometric information in this case, the leakage parameter was obtained from back-analysis and the same value was used in all the analyses. It should be recalled that, although most of the microporosity is initially present in the pellets, there is also some microporosity in the powder. Therefore, water exchanges between porosity levels will take place both in the powder and the pellets with, probably, some differences in the kinetics. However, a single leakage parameter has been used in the analyses for simplicity.

The parameters of the mechanical constitutive model are collected in Table 3. They were determined from back-calculation of laboratory oedometer tests on compacted FoCa clay (Volckaert *et al.*, 2000; Yahia-Aïssa *et al.*, 2000; Cui *et al.*, 2002). It should be noted that only one interaction function is required as only the microstructural swelling mechanism is engaged in the swelling pressure test. It should be stressed that although some BBM parameters of the macrostructure depend on the initial density of the powder, the parameters characterising the behaviour of the microstructure remain unchanged throughout all the analyses performed.

Swelling pressure tests at dry density 1·45 g/cm^3

Tests MGR7, RS2J and MGR 9 were performed on samples with a dry density of 1·45 g/cm^3. The estimated initial porosities and suctions are listed in Table 4. Figs

Table 2. Hydraulic parameters

Constitutive law	Expression	Parameter	Micro	Macro
Retention curve	$S_e = \frac{S_l - S_{lr}}{S_{ls} - S_{lr}} = \left[1 + \left(\frac{s}{P_o}\right)^{1/(1-\lambda_o)}\right]^{-\lambda_o} \left(1 - \frac{s}{P_d}\right)^{\lambda_d}$	P_o: MPa λ_o P_d: MPa λ_d S_{ls} S_{lr}	378·95 0·899 800 2·243 1·0 0·0	15 0·064 750 3·899 1·0 0·0
Intrinsic permeability High-density samples, $\gamma_d > 1{\cdot}60$ g/cm^3 $\boldsymbol{k}_j = k_o \exp(b(\phi_j - \phi_o))$		k_o: m^2 ϕ_o b	$2{\cdot}9 \times 10^{-20}$ 0·40 8·00	
Low-density samples, $\gamma_d < 1{\cdot}60$ g/cm^3 $\boldsymbol{k}_j = k_o \exp(b(\boldsymbol{\phi}_j - \boldsymbol{\phi}_o))$		k_o: m^2 ϕ_o b	$2{\cdot}9 \times 10^{-20}$ 0·40 11·00	
Relative permeability $k_r = S_e^{\lambda}$		λ S_{ls} S_{lr}	1·15 1·00 0·00	3·00 1·00 0·00
Leakage parameter $\Gamma^w = \gamma(\psi_1 - \psi_2)$		γ: kg s^{-1} m^{-3} MPa^{-1}	$5{\cdot}00 \times 10^{-5}$	

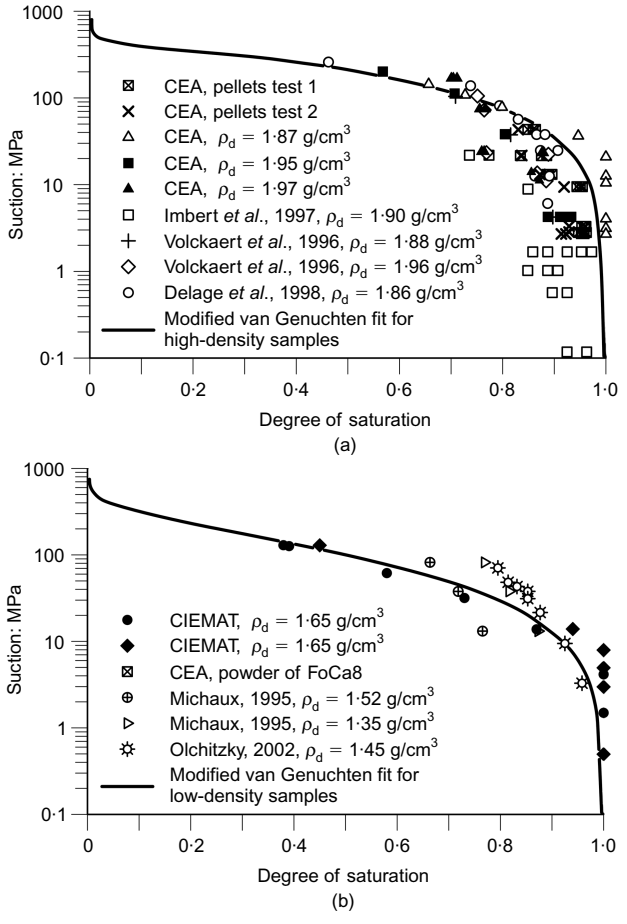

Fig. 11. Retention curves for FoCa clay: (a) samples with dry densities in the range 1·65–2·0 g/cm^3; (b) samples with dry densities in the range 1·35–1·65 g/cm^3

12(a)–12(c) show the computed evolution of swelling pressures compared with the measured values. Tests were run until macroscopic observations indicated that stationary conditions were achieved; test durations were over 200 days for the 5 cm long samples and 570 days for the 10 cm long sample.

In general, the rate of swelling pressure development at the start of the tests is underestimated by the analyses but the magnitude of the first peak and the time required to reach it are adequately reproduced by the calculations. Subsequent behaviour is also well modelled, including the observed reduction of swelling pressure and the final rise to the final steady-state value. In spite of having two different lengths, the pattern of behaviour is very similar in all three tests although, of course, the times required to reach the first peak and the stationary condition are longer for the taller specimen (MGR9). The swelling pressure rise in test MGR7 at day 120 is due to an increase of the injected water pressure. This pressure increase stage was not applied in the other tests. Figs 12(d)–12(f) indicate that the water intake of the tests is also well reproduced although, again, it can be noted that the observed rate of water inflow is larger than the computed value at the initial stages of the tests.

As the modelling appears to represent satisfactorily the real system, interesting information might be obtained by analysing in more detail some of the results of the analyses. For space reasons, attention is focused on test MGR9, but results from other tests are used when required. Fig. 13(a) shows the time evolution of macrostructural and microstructural suctions at three different points of sample MGR9: near the bottom hydration boundary (vertical coordinate $y = 0{\cdot}0$ m), at the centre of the sample ($y = 0{\cdot}05$ m) and near the top of the sample ($y = 0{\cdot}0975$ m). It can be observed that, at the bottom boundary, the macrostructural and microstructural suctions reduce rapidly, but they differ at the beginning of the test because of the delay in water transfer

Table 3. Parameters of the mechanical constitutive model

Constitutive law	Expression	Parameter	Low-density samples	High-density samples
BBM				
Elastic part	$\dot{\varepsilon}_v^e = -\frac{\kappa}{1+e_M}\frac{dp}{p} - \frac{\kappa_s}{1+e_M}\frac{ds_M}{s_M + p_{atm}}$	κ κ_s	0·010 0·022	0·010 0·041
Yield locus	$p_0 = p_c\left(\frac{p_0^*}{p_c}\right)^{(\lambda_{(0)}-\kappa)/(\lambda_{(s)}-\kappa)}$ $\lambda(s) = \lambda(0)[r + (1-r)e^{-\beta s}]$	p_o^*: MPa p_c: MPa r $\lambda(0)$ β: MPa^{-1}	0·14 0·005 0·65 0·23 0·025	0·38 0·005 0·72 0·20 0·035
BExM				
Microstructural behaviour	$K_m = \frac{1+e_m}{\kappa_m}\hat{p}$	κ_m	0·045	
Interaction function (microstructural swelling)	$f_s = f_{s0} + f_{si}\left(1 - \frac{p}{p_0}\right)^{n_s}$	f_{s0} f_{si} n_s	−2·0 1 2	

Table 4. Initial conditions of the swelling pressure tests

Test label	Sample height: mm	Dry density of sample: g/cm^3	Total porosity, n_T	Macro-porosity, n_M	Micro-porosity, n_m	Macrop. suction, s_M: MPa	Microp. suction, s_m: MPa
MGR7	50	1·45	0·46	0·33	0·13	212	285
MGR9	100	1·45	0·46	0·33	0·13	284	321
RS2J	50	1·45	0·46	0·33	0·13	298	343
RS2B	50	1·60	0·40	0·16	0·24	207	237
RS2E	100	1·60	0·40	0·16	0·24	284	314
RS2F	120	1·60	0·40	0·16	0·24	284	314

between the two porosities. Eventually, however, they come together and remain in equilibrium for the remainder of the test. Interestingly, at the other two points the two porosities come into equilibrium before they are reached by the hydration front, that is before they exhibit any suction reduction. They also maintain this equilibrium condition throughout the rest of the test. The analysis suggests, therefore, that non-equilibrium between the two porosity levels is only likely to affect the early stages of the test. Fig. 13(b) shows the same information for one of the shorter (5 cm) samples: MGR7. The results obtained are qualitatively very similar, although hydration occurs earlier as the flow path is now shorter. The time required to reach steady-state condition is, as expected, also shorter.

The cause underlying the characteristic temporary drop in swelling pressure is the collapse of the macrostructure that, in the constitutive model, corresponds to reaching the LC yield surface in the BBM. This is illustrated in Fig. 14, where the stress paths (in macrostructural suction – vertical net stress space) followed by the same three points of test MGR9 are plotted. The initial position of the LC yield surface is also shown. In the section of the stress path that moves towards the LC surface, stress increase appears to be more significant than suction reduction. Once the LC yield surface is reached, the vertical stress drops to compensate the tendency of the macrostructure to collapse so that the sample length is kept constant. It can also be noted that the point of start of the collapse does not coincide exactly with the plotted LC; this is because, by then, the yield surface has moved slightly due to the interaction with the microstructural strains (MS, microstructure swelling) that develop from the very start of the test.

The interplay between the various aspects of the problem may be more readily seen by referring to Fig. 15, which contains details of the evolution of test MGR9 for the same three points considered above. Fig. 15(a) shows the evolution of vertical swelling pressures that are, naturally, the same for all three points because of equilibrium requirements. Fig. 15(b) shows the variations in time of the macrostructural and microstructural specific volume. There is a monotonic increase of microstructural porosity (or specific volume), the start of which is staggered in time as the various points respond to the different arrivals of the hydration front. The changes in macrostructural porosity are more complex. At the bottom of the specimen, the macrostructural porosity increases slightly at the beginning of the test because of suction reduction. However, on reaching the LC yield surface (indicated in the figure), there is a sharp reduction of macrostructural porosity due to structural collapse. This results in a translation of the LC yield surface towards the right, indicated by the increase in value of the saturated preconsolidation pressure, p_o^* (Fig. 15(c)). At the other two points, there is initially a reduction of the macrostructural porosity due to the compression applied by the swelling of

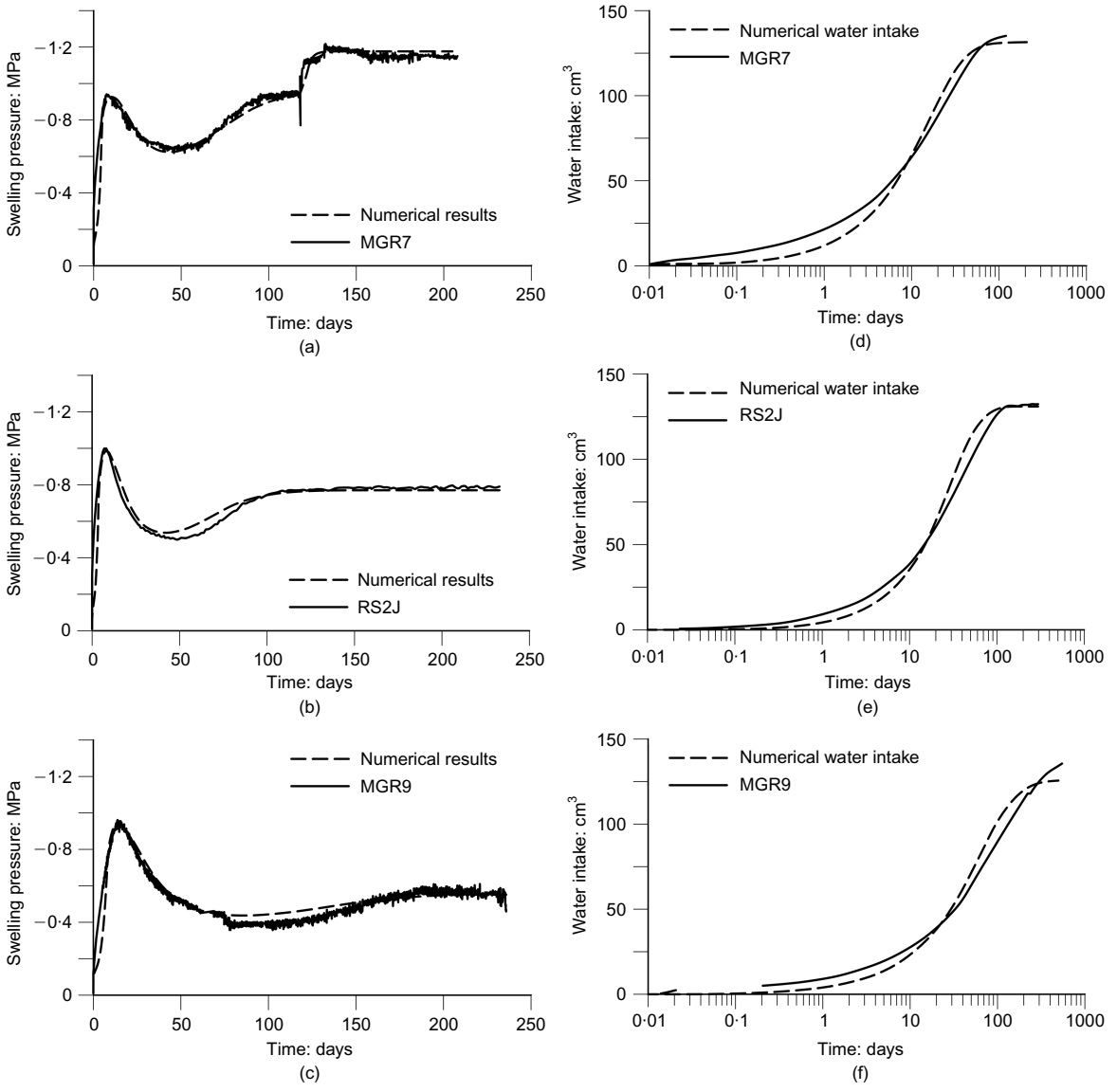

Fig. 12. Observations compared with computed results for tests on samples of 1·45 g/cm^3 dry density: (a)–(c) swelling pressure evolution for tests MGR7, RS2J and MGR9; (d)–(f) evolution of accumulated water intake for tests MGR7, RS2J and MGR9

the bottom part of the sample. Eventually, however, the points also reach the LC yield surface and collapse ensues. The final stage of reduction of macrostructural porosity is also partially associated with the increase of vertical stress caused by the swelling of the microstructure. In this final stage, the evolution of porosities is the same in all three points, consistent with the homogeneity of the samples observed at the end of the tests.

Microstructural observations

Determination of the pore size distribution could provide a valuable independent confirmation of the capability of the formulation to represent fabric changes of the material during hydration. Unfortunately, the pore size distribution of the samples after hydration was determined, using the MIP technique, only in the case of specimen MGR9. Four samples from different locations of the specimens were freeze-dried prior to pore size determination. The relationships between the cumulative intrusion porosity and entrance pore size for the four samples are shown in Fig. 16(a). It can be observed that there is a large amount of non-intruded porosity. Using these data, it is possible to derive the pore size density functions depicted in Fig. 16(b). By analogy with other materials (Wan *et al.*, 1995; Monroy, 2005; Romero *et al.*, 2005), it is likely that the large family of pores in the range of 200–500 nm was not present in the initial material but it is a consequence of the hydration process. Those pores would be the product of a reduction in size of larger macropores to accommodate the increase of micropore volume due to hydration. A direct check is not possible, however, as there were no MIP tests performed on the mixture before the test.

The proportions of porosity belonging to different ranges of pore sizes are listed in Table 5. The non-intruded volume has been ascribed to the ultra-microporosity smaller than 6 nm. Maintaining the boundary between microporosity and macroporosity at 100 nm, the final microstructural porosity falls in the range of 49–62%. Alternatively, Delage & Lefebvre (1984) suggested that microporosity could be estimated from the trapped volumes after mercury extrusion. In the present case, this criterion yields microporosity percentages ranging from 45% to 61%, quite consistent with the pore size density determination.

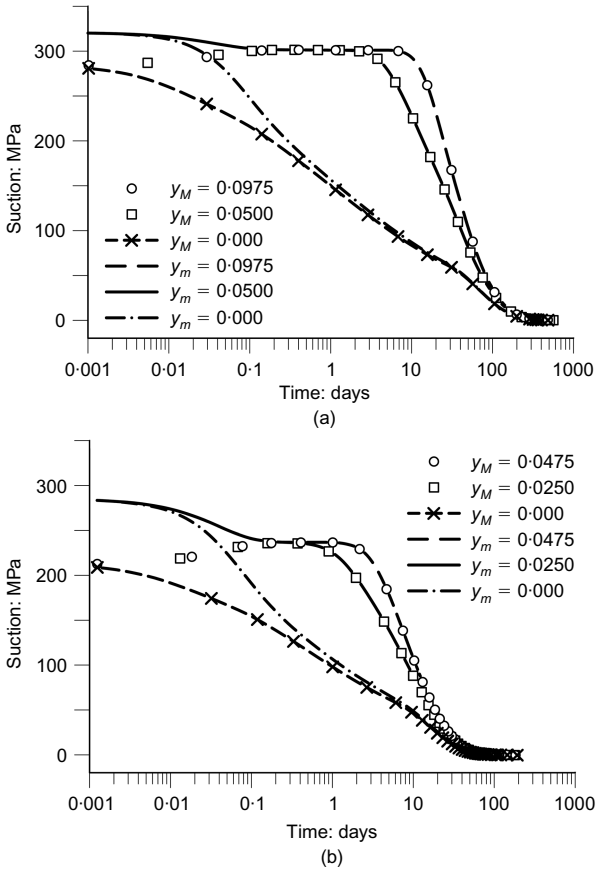

Fig. 13. Computed evolution of macrostructural and microstructural suctions at three different points of the sample: (a) test MGR9; (b) test MGR7

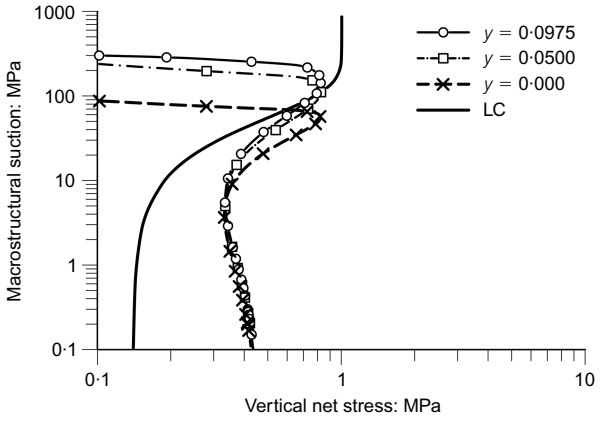

Fig. 14. Computed stress path (macrostructural suction–vertical stress) for three different points of sample MGR9. Only the initial LC yield surface is shown for clarity

In turn, the analyses predict that, in this test, microporosity increases from the initial value of 0·127 to 0·283 at the end of the test, whereas macroporosity decreases from 0·329 to 0·173. Therefore, the final microporosity represents 62% of the total pore volume, a rather satisfactory agreement with observations. The fact that the proportion of microporosity varies monotonically from the bottom to the top of the sample might suggest that, in spite of the long test duration and the constant values of macroscopic observations, the material was not completely saturated at the end of the test in the regions further away from the hydration boundary. This would imply the existence of a porosity level with a much lower leakage coefficient. This possibility, however, does not seem to prevent the model from achieving a good description of the macroscopic test results.

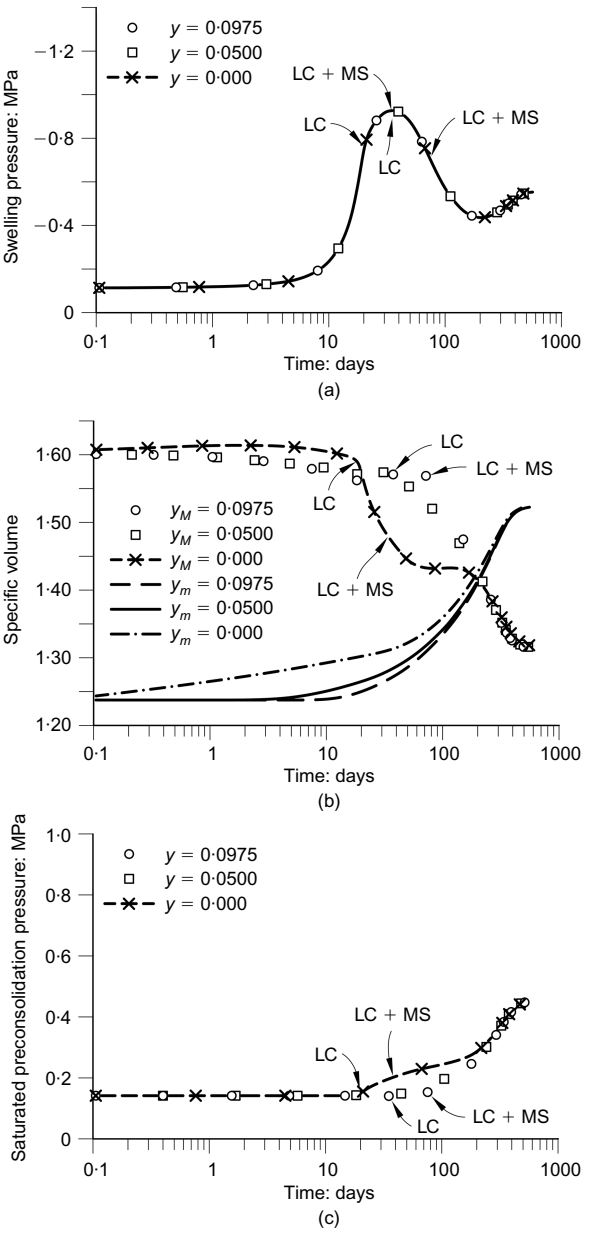

Fig. 15. Computed evolution of: (a) swelling pressure; (b) macrostructural and microstructural specific volumes; (c) saturated preconsolidation pressure for three points of test MGR9. Arrows indicate the point at which the various yield mechanisms are activated

Swelling tests at dry density 1·60 g/cm^3

Three tests performed on samples with a dry density of 1·60 g/cm^3 (RS2B, RS2E and RS2F) are considered. Their lengths are 5, 10 and 12 cm respectively. The estimated initial porosities and suctions are listed in Table 4. Computed evolutions of swelling pressures compared with the measured values are shown in Figs 17(a)–17(c). Testing times ranged from 150 to 500 days depending on specimen length. The overall behaviour of these tests is similar to that of the looser samples but, in this case, the final swelling pressures are much higher and the swelling pressure drop after the first peak is comparatively smaller. At any rate, the model reproduces very satisfactorily the observed behaviour. The evolution of water intake is also well matched (Figs

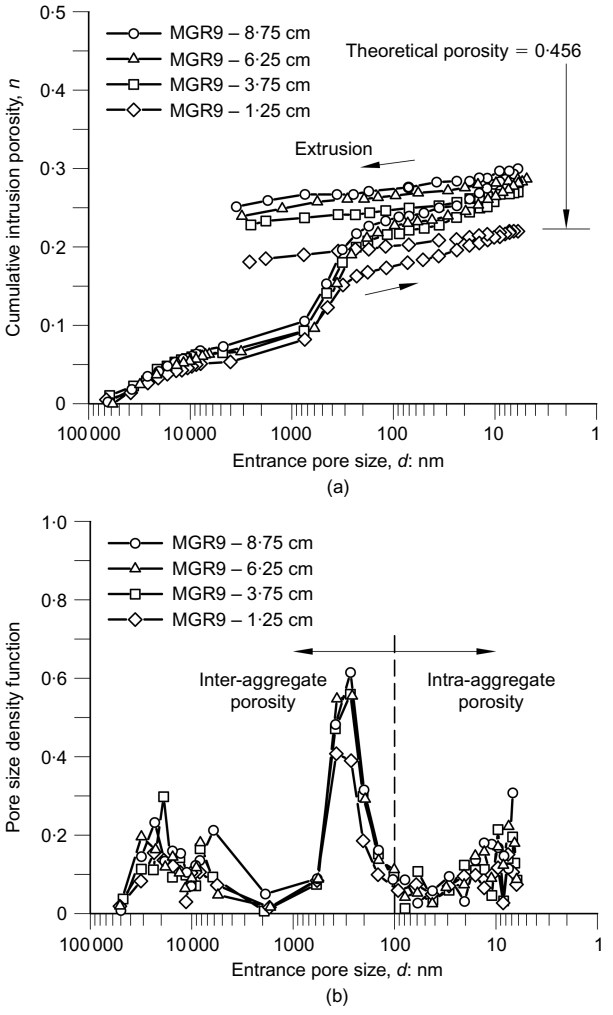

Fig. 16. Porosimetry results for four samples taken at the end of test MGR9: (a) cumulative intrusion porosities; (b) pore size density functions

17(d)–17(f)); some discrepancies at the end of the test have been attributed to small leakages in some of the very long-term tests.

Some results of the 10 cm sample (RS2E) are now presented so that they can be directly compared with the results of test MGR9. The evolutions of macrostructural and microstructural suctions at three different points (bottom, middle and top of the specimen) of test RS2F obtained in the analysis are plotted in Fig. 18. They are similar to those of the looser samples (Fig. 13). In this case, establishing equilibrium between the suctions at the two porosities takes a little longer and the onset of collapse is also delayed somewhat. The stress paths for the same three points are presented in Fig. 19. The initial LC is now further to the right to account for a denser macrostructure. It is also apparent that the drop in vertical stress after reaching the LC is now smaller if compared with the looser specimens (Fig. 14). Finally, Fig. 20 shows the computed evolution of swelling pressure, macrostructural and microstructural specific volumes, and saturated preconsolidation pressure for the same three points. Again the same overall behaviour as in test MGR9 is observed but now the relative variation of the macro and micro specific volumes is more limited than in the case of the tests on looser specimens. Also, in the final stages of the test, the evolution of porosities is the same in all three points, corresponding to a homogenised condition of the sample. The pattern of saturated preconsolidation pressure variation in time is again similar to that of the looser specimens, but a much higher final value is reached by the denser samples.

A LARGE-SCALE SEALING TEST

Description of the test

A large-scale sealing test (named the shaft sealing test) has been performed in the Hades underground research facility (URF) shown in Fig. 21. The URF is located in Mol (Belgium) and it has been excavated at a depth of 220 m in Boom Clay, an overconsolidated plastic clay of Rupelian age (28–34 million years). The sealing test has been performed in an experimental shaft located at the end of the main test drift (Fig. 22(a)). To this end, the bottom part of the shaft was filled with grout and the concrete lining was removed at the location of the seal. The sealed section is about 2·2 m in diameter and 2·25 m high. The sealing material is a mixture of 50% powder and 50% highly compacted pellets of FoCa clay, the same mixture as in the laboratory swelling pressure tests. The seal is kept in place with a top concrete lid about 1 m thick (Fig. 22(b)). A large number of sensors measuring pore water pressure, total stress, displacement and relative humidity were installed to follow the hydromechanical evolution of the seal and the surrounding host rock. In the seal, most instruments are located on six rods of stainless steel connected to a central tube. Those rods are located in two groups of three rods, each at two levels: the instrumented level top (ILT) and the instrumented level bottom (ILB). The ILT is located at 180 cm and the ILB at 65 cm from the bottom of the plug. Some instrumentation is also located at the hydration level top (HLT) and at the hydration level bottom (HLB). The instrumented sections are indicated in Fig. 22(b). Several filters inside the sealed section enabled artificial hydration to reduce the time required to attain saturation.

After coating the concrete plug with a resin, the clay mixture was installed using approximately 12 tons of powder/pellets mixture. The first 60 cm were compacted with a vibro-compactor specially designed for the project. After compaction the mixture had a dry density of 1·54 g/cm^3. The rest of the mixture of powder and pellets was not compacted in order to avoid damage of the sensors, resulting in a dry density of 1·39 g/cm^3. A top view of the shaft during backfill installation has been provided in Fig. 1. Some details of the installation are shown in Fig. 23.

Table 5. Pore size distribution measured in four samples obtained from test MGR9 after hydration

	Entrance pore size	Percentage of total porosity			
		$y = 8{\cdot}75$ cm	$y = 6{\cdot}50$ cm	$y = 3{\cdot}25$ cm	$y = 1{\cdot}25$ cm
Macroporosity	>1000 nm	~21	~20	~19	~17
Mesoporosity	100–1000 nm	~30	~30	~28	~21
Microporosity	20–100 nm	~ 5	~5	~ 6	~5
Ultra-microporosity	<20 nm	~44	~45	~47	~57

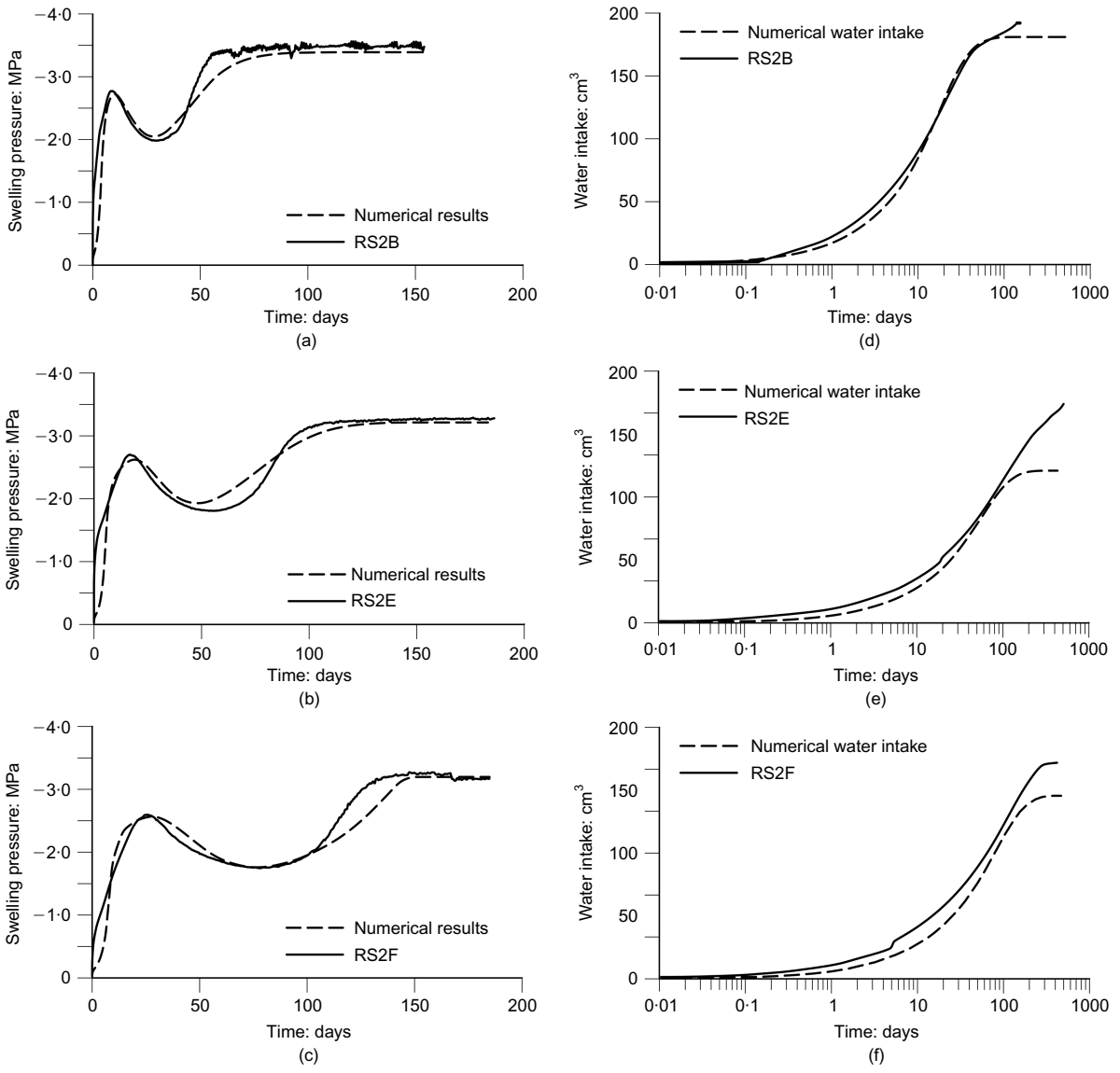

Fig. 17. Observations compared with computed results for tests on samples of 1·60 g/cm^3 dry density: (a)–(c) swelling pressure evolution for tests RS2B, RS2E and RS2F; (d)–(f) evolution of accumulated water intake for tests RS2B, RS2E and RS2F

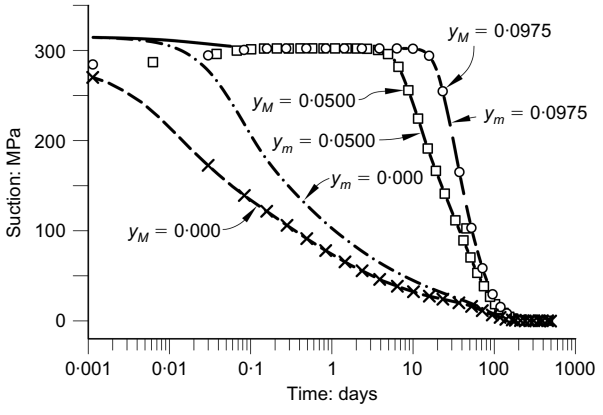

Fig. 18. Computed evolution of macrostructural and microstructural suctions at three different points of test RS2F

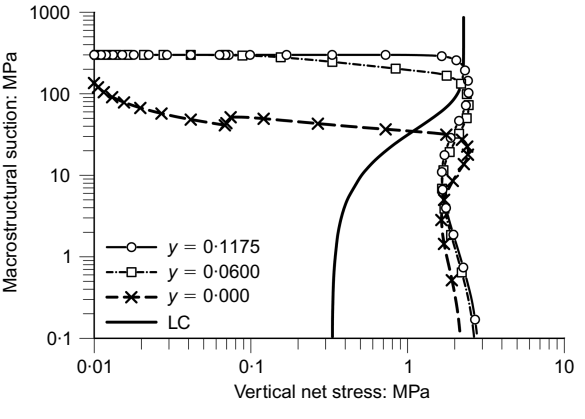

Fig. 19. Computed stress path (macrostructural suction–vertical stress) for three different points of sample RS2E. Only the initial LC yield surface is shown for clarity

After backfilling the shaft and closing the seal, a 7-month period was allowed to elapse to achieve steady-state conditions in the zone around the test. Afterwards, artificial hydration was applied during 6 years. Some leakage problems occurred in the early stages of the test and hydration had to be stopped and re-started on some occasions. The water injection pressure was increased gradually up to a value of 300 kPa, approximately, measured at the elevation

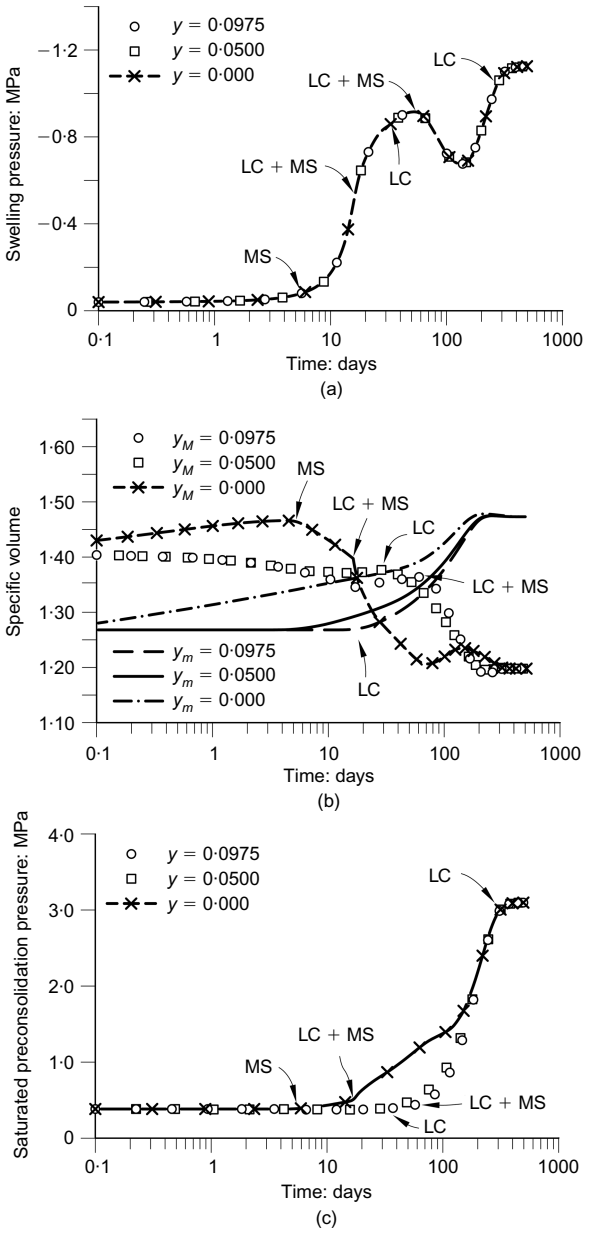

Fig. 20. Computed evolution of: (a) swelling pressure; (b) macrostructural and microstructural specific volumes; (c) saturated preconsolidation pressure for three points of test RS2E. Arrows indicate the point at which the various yield mechanisms are activated

of the main drift. After seal saturation, various gas and liquid permeability tests have been performed but only the hydration stage is considered in this paper.

Seal hydration and modelling

The hydration of the seal has been simulated using the theoretical formulation outlined above. The finite-element mesh used in the coupled hydromechanical analysis is depicted in Fig. 24 together with the main boundary conditions. Advantage has been taken of the basically axisymmetric nature of the test. The initial characteristics of the pellets–powder mixture installed in the shaft are listed in Table 6. The hydraulic and mechanical parameters of the backfill material are the same as those used in the analyses of the swelling pressure tests (Tables 2 and 3). The challenge is to be able to cover a large-scale span (from laboratory to field conditions) using the same formulation, conceptual model and parameters. The estimated partition of porosities and the initial suction values are given in Table 7. As the natural Boom Clay parameters have only a limited impact on results, they are not given here. Boom Clay parameters and the procedures used for their determination are reported in Gens *et al.* (2009a). Some selected results concerning suctions and stresses in the sealing material are now presented.

Figure 25(a) shows the variation in time of the suction measured in the relative humidity sensors located on the rods of the ILT, an instrumentation level located in the uncompacted part of the backfill. There are only two sensors because the one oriented towards the west failed from the start. The sensor closer to the rock (RH-S-ILT-E) appeared to hydrate only a little faster than the one placed near the centre (RH-S-ILT-N), suggesting that the natural hydration from the host Boom Clay is not dominant. The computed suction evolutions are quite close to observations in this case and the analysis also shows a somewhat faster hydration in the sensor closer to the rock boundary. The readings of the relative humidity sensors located at the ILB are plotted in Fig. 25(b). In this case, the instrumented level is situated in the compacted backfill but very close to the boundary between the two zones. Now, there are large differences between the readings of the different sensors, significantly larger than those obtained in the modelling. The analysis also suggests that hydration should be slower at this level because of the lower permeability of the compacted material. This is borne out by the observations except for the sensor placed quite close to the central injection tube (RH-S-ILB-W). It is strongly suspected that a direct connection between hydration tube and the zone of the sensor was established during one of the injection pressure increase episodes.

The evolutions of vertical stresses at 16 points located at different heights of the seal are shown in Fig. 26 and compared with the results of the analysis. From top to bottom they are located in (a) hydration level top, (b) instrumentation level top, (c) instrumentation level bottom and (d) hydration level bottom. The usual difficulties associated with trying to measure stresses precisely are apparent in the plots. It can also be noted that stress development is not axisymmetric; departures from that condition vary depending on the instrumentation level considered. The response of the sensors does not appear to be simultaneous with hydration; this may be perhaps attributed in part to a lack of close contact with the backfill after installation. In spite of those difficulties, the analysis appears to give correctly the rough magnitude of the hydration swelling pressure as well as the rate of stress increase in the later stages of the test. Naturally, the axisymmetric analysis does not discriminate between different directions. It should be stressed that the same set of parameters used in the modelling of the laboratory tests has been adopted for the analysis of the shaft sealing test.

It is interesting to observe that the model only predicts a rather muted drop in the value of the vertical stress in the second year of the test. Although the density of the backfill is low, the effect of macrostructural collapse is minor because it is averaged out among different zones. This is a consequence of the very different scale of this test as compared with the laboratory ones. At small scales, different stages of macrostructural collapse may be occurring at the same time in practically the entire sample, leading to a large drop in swelling stress. At the scale of a field case, this simultaneity is more unlikely and the collapse in some zones is at least partially compensated by the non-collapsing behaviour of other zones. It should be noted that the test observations do not record any instance of sharp vertical

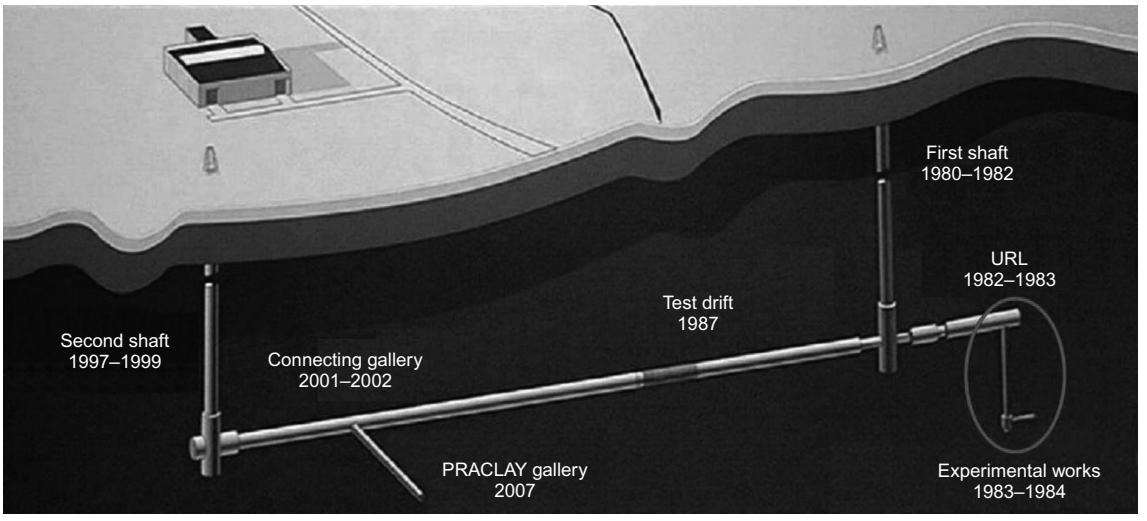

Fig. 21. The Hades underground research facility: the experimental shaft where the sealing test was installed is indicated

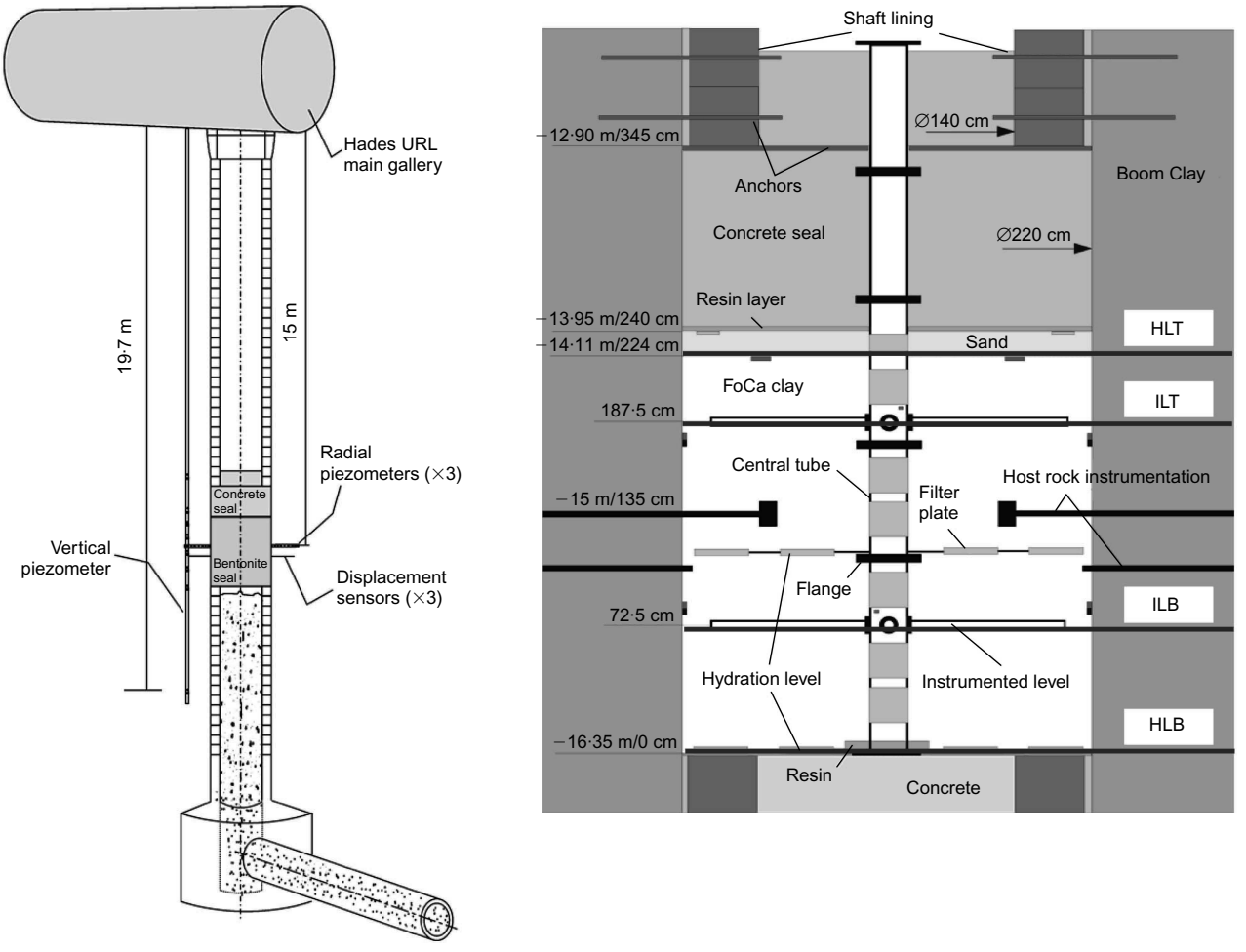

Fig. 22. (a) Schematic overview of the location of the seal inside the experimental shaft. (b) Layout of the test including instrumentation levels. HLT: hydration level top; ILT: instrumentation level top; ILB: instrumentation level bottom; HLB: hydration level bottom

stress reduction, although some slowing down in the rate of increase (or even some local stress reductions) can be noted in some sensors during the second year of testing. In addition, analysis results and observations largely agree in the steady increase of vertical stress at the end of the test.

CONCLUDING REMARKS

The use of compacted mixtures of bentonite powder and bentonite pellets as backfill material in underground repositories for nuclear waste is an attractive proposition because it reduces significantly the compaction effort that is required

Fig. 23. (a) Rod instrumented with total stress, water pressure, displacement and suction sensors. (b) Installation of a piezometer in the host medium

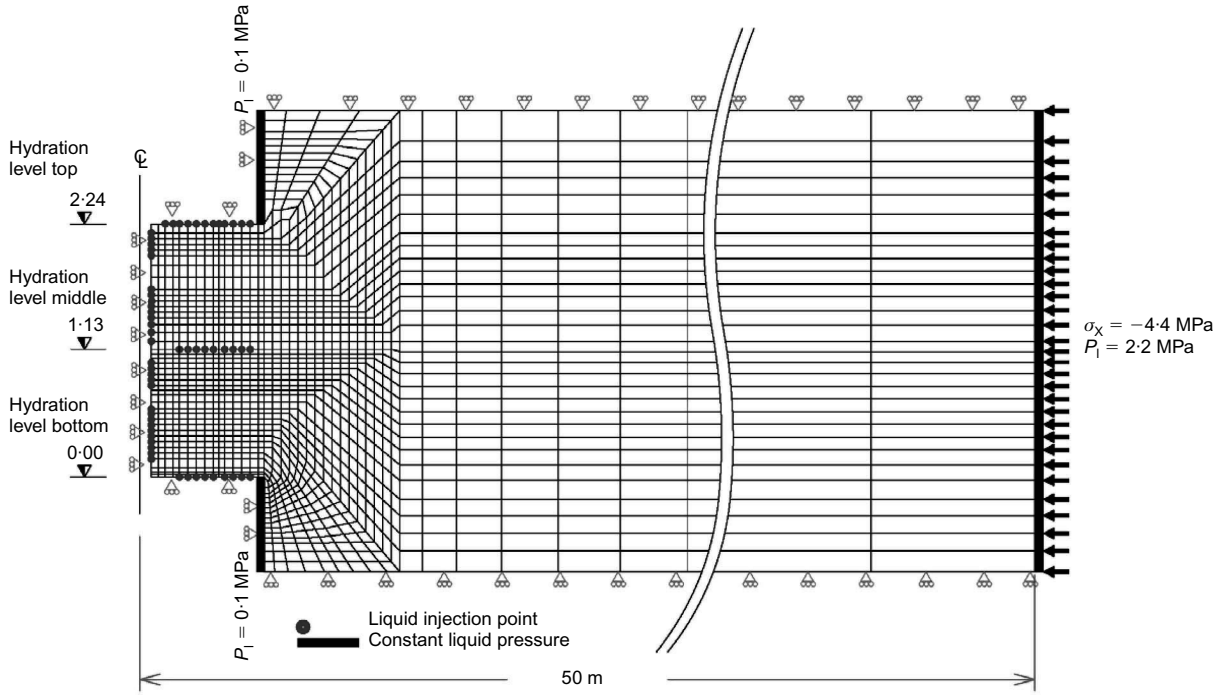

Fig. 24. Axisymmetric finite-element mesh and boundary conditions used in the analysis of the shaft sealing test

Table 6. Main characteristic of the pellets/powder mixture installed in the experimental shaft

Height: cm	Void ratio of mixture	Dry density of mixture: g/cm^3	Initial water content of mixture: %	Dry density of pellets: g/cm^3	Initial water content of pellets: %	Dry density of powder: g/cm^3	Initial water content of powder: %
Compacted zone							
60	0·734	1·543	6·00	1·894	4·49	1·302	7·51
Uncompacted zone							
164	0·929	1·387	6·00	1·894	4·49	1·093	7·51

to achieve the value of dry density needed to provide an adequate swelling potential on hydration. However, the heterogeneous fabric of the material results in a quite complex behaviour during hydration.

In the paper, it has been demonstrated that a double porosity approach, involving both hydraulic and mechanical aspects, is able to provide the necessary theoretical framework to undertake satisfactorily the hydromechanical model-

Table 7. Initial conditions of the pellets–powder mixture used in the shaft sealing test

	Dry density of mixture: g/cm^3	Total porosity, n_T	Macrostructural porosity, n_M	Microstructural porosity, n_m	Macrostructural suction, s_M: MPa	Microstructural suction, s_m: MPa
Compacted seal	1·543	0·423	0·278	0·145	272	279
Uncompacted seal	1·387	0·482	0·366	0·116	280	308

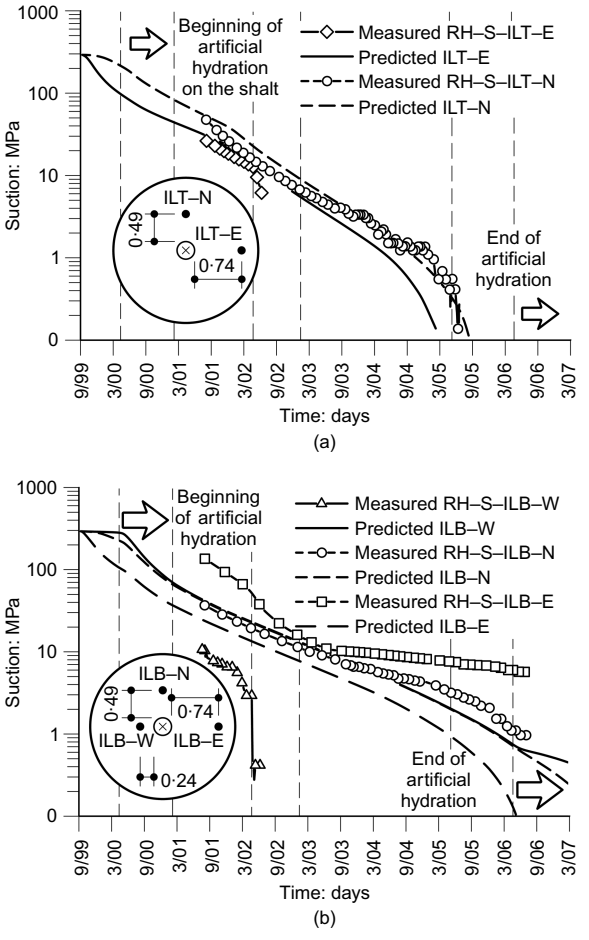

Fig. 25. Variation of suction with time: computed results and observations: (a) instrumented level top; (b) instrumented level bottom

ling of this material. The formulation (and associated computer code) results in close quantitative reproduction of a number of swelling pressure tests performed on samples of different densities and lengths. In addition, a detailed examination of the computational results provides valuable insights and understanding of the basic processes that underlie the observed macroscopic behaviour. Moreover, microfabric information using X-ray tomography and MIP provide additional support for the conceptual approach adopted.

Using the same parameters as in the modelling of laboratory tests, the application of the formulation to a field-scale long-term sealing test performed in the Hades URF has resulted in a quite adequate description of the main behaviour features of the backfill during hydration. The capability of the formulation to span over quite large ranges of space and time scales is thus established. In addition, because the formulation is based, albeit roughly, on the actual composition of the material, it is capable of providing important insights that are key in the building up of confidence in the eventual repository design. In fact, the conceptual approach developed in the context of the research reported in this paper is quite general and it can be readily applied to other types of heterogeneous compacted soils. A better understanding of their hydromechanical behaviour should thereby ensue.

ACKNOWLEDGEMENTS

The work reported has been co-funded by ANDRA, CIEMAT, ONDRAF-NIRAS and the European Commission (EC contract FIKW-CT-2000-00010). The support of the Spanish Ministry of Science and Innovation through grant BIA 2008-06537 is also gratefully acknowledged.

APPENDIX

A detailed description of the BBM model can be found in Alonso *et al.* (1990). Here, the more relevant equations of the particular version of the BBM used are presented. The model is defined in terms of the following stress invariants

$$p = \frac{1}{3}(\sigma_x + \sigma_y + \sigma_z) \tag{16}$$

$$J^2 = 0{\cdot}5 \text{ trace } (\boldsymbol{s}^2) \tag{17}$$

$$\theta = -\frac{1}{3}\sin^{-1}\left(1{\cdot}5\sqrt{3} \text{ det } \boldsymbol{s}/J^3\right) \tag{18}$$

$$\boldsymbol{s} = \boldsymbol{\sigma} - p\boldsymbol{I} \tag{19}$$

$$\boldsymbol{\sigma} = \boldsymbol{\sigma}_t - \boldsymbol{I}p_f \tag{20}$$

where $p_f = p_g$ if $p_g > p_l$, otherwise $p_f = p_l$. p_g is the gas pressure and p_l is the liquid pressure. $\boldsymbol{I}$ is the identity tensor.

The LC yield surface (F_{LC}) can be expressed as

$$F_{LC} = 3J^2 - \left[\frac{g(\theta)}{g(-30)}\right]^2 M^2(p + p_s)(p_o - p) = 0 \tag{21}$$

where M is the slope of the critical state, p_o is the apparent unsaturated isotropic preconsolidation pressure, g is a function of Lode's angle and p_s considers the dependence of shear strength on suction. The following relationships complete the definition of the yield surface

$$p_s = ks_M \tag{22}$$

$$p_0 = p_c\left(\frac{p_0^*}{p_c}\right)^{(\lambda_{(0)}-\kappa)/(\lambda_{(s)}-\kappa)} \tag{23}$$

where k is a parameter that accounts for the increase of shear strength with suction, p_c is a reference stress, κ is the elastic stiffness parameter for changes in net mean stress, p_0^* is the preconsolidation net mean stress for saturated conditions. $\lambda_{(s)}$ is the compressibility parameter for changes in net mean stress for virgin states of the soil that depends on macrostructural suction, s_M, according to

$$\lambda_{(s)} = \lambda_{(0)}\left[r + (1-r)e^{-\beta s_M}\right] \tag{24}$$

where r is a parameter which defines the minimum soil compressibility (at infinity suction) and β is a parameter which controls the rate of decrease of soil compressibility with macrostructural suction.

The hardening law is expressed as a rate relation between

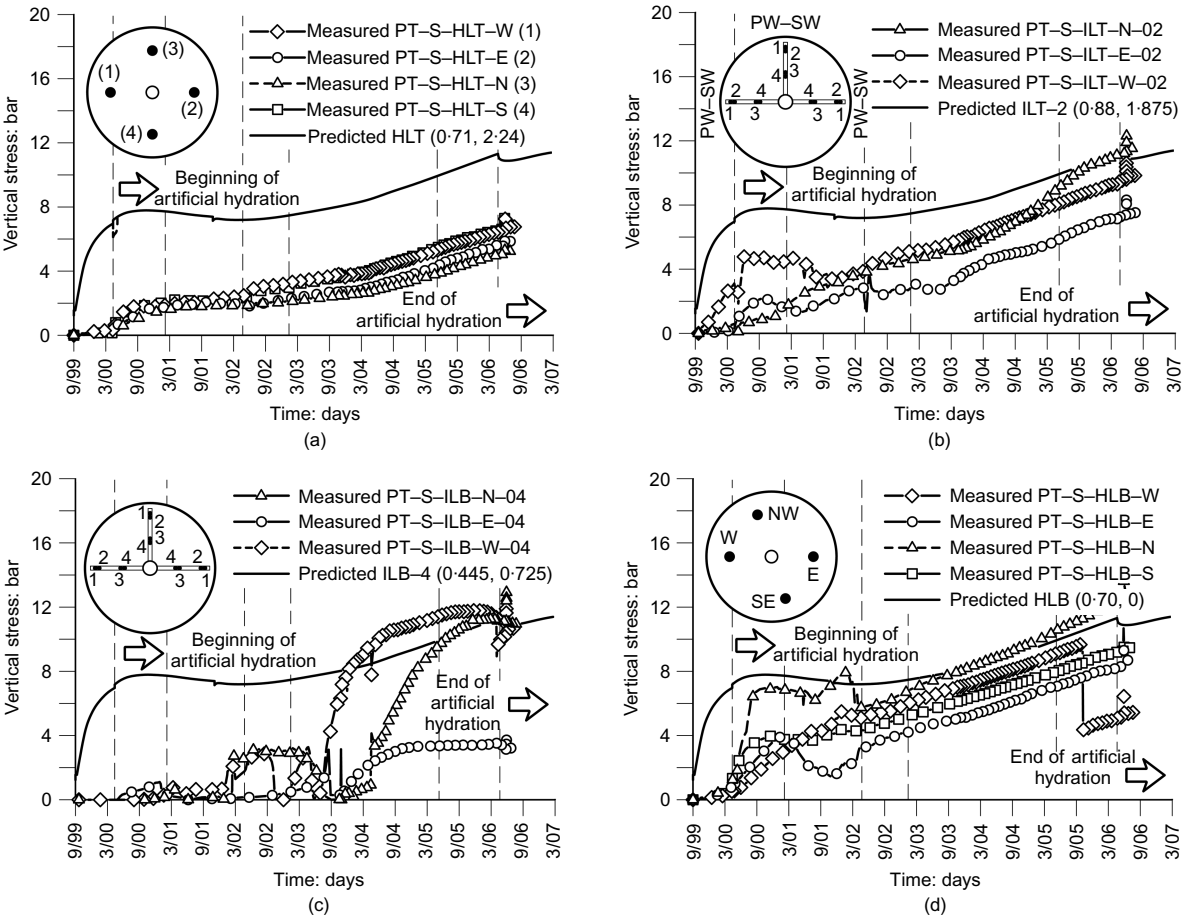

Fig. 26. Variation of vertical stresses with time: computed results and observations: (a) hydration level top, $r = 0{\cdot}71$ m; (b) instrumented level top, $r = 0{\cdot}88$ m; (c) instrumented level bottom, $r = 0{\cdot}445$ m; (d) hydration level bottom, $r = 0{\cdot}70$ m (r is the radial coordinate)

volumetric plastic strain and the saturated isotropic preconsolidation stress, p_0^*, as

$$\frac{\dot{p}_0^*}{p_0^*} = \frac{(1 + e_M)}{(\lambda_{(0)} - \kappa)} \dot{\varepsilon}_{vM}^p \tag{25}$$

where e_M is the macrostructural void ratio, κ is the elastic compression index for changes in net mean stress and $\lambda_{(0)}$ is the compression index for changes in net mean stress for virgin states of the soil in saturated conditions.

Regarding the direction of the plastic strain increment, a non-associated flow rule in the plane $s_M = \text{constant}$

$$G = \alpha 3J^2 - \left[\frac{g(\theta)}{g(-30)}\right]^2 M^2(p + p_s)(p_0 - p) = 0 \tag{26}$$

where α is determined from the condition that the flow rule predicts zero lateral strains in a K_0 stress path.

Finally, the macrostructural elastic volumetric strains are computed as

$$\dot{\varepsilon}_{vM}^e = -\frac{\kappa}{1 + e_M}\frac{\mathrm{d}p}{p} - \frac{\kappa_s}{1 + e_M}\frac{\mathrm{d}s_M}{s_M + p_{atm}} \tag{27}$$

where κ and κ_s are model parameters and p_{atm} is the atmospheric pressure (100 kPa).

REFERENCES

Aifantis, E. (1980). On the problem of diffusion in solids. *Actha Mechanica* **37**, No. 3–4, 65–296.

Alonso, E. E., Gens, A & Josa, A. (1990). A constitutive model for partially saturated soils, *Géotechnique* **40**, No. 3, 405–430, **doi**: 1680/geot.1990.40.3.405.

Barrenblatt, G., Zeltov, I. & Kochina, N. (1960). Basic concepts in the theory of seepage of homogeneous liquids in fissured rocks. *Pirkl. Mater. Mekh*. **24**, 852–864.

Callari, C. & Federico, F. (2000). FEM validation of a double-porosity elastic model for consolidation of structurally complex clayey soils. *Int. J. Numer. Analyt. Methods Geomech*. **24**, No. 4, 367–402.

Castellanos, E., Villar, M. V., Romero, E., Lloret, A. & Gens, A. (2008). Chemical impact on the hydro-mechanical behaviour of high density FEBEX bentonite. *Phys. Chem. Earth* **33**, Suppl. 1, S516–S526.

Cui, Y., Yahia-Aissa, M. & Delage, P. (2002). A model for the volume change behaviour of heavily compacted swelling clays. *Engng Geol*. **64**, No. 2–3, 233–250.

Delage, P. & Lefebvre, G. (1984). Study of the structure of a sensitive Champlain clay and its evolution. *Can. Geotech. J.* **21**, No. 1, 21–35.

Delage, P., Howat, M. D. & Cui, Y. (1998). The relationship between suction and swelling properties in a heavily compacted unsaturated clay. *Engng Geol*. **50**, No. 1–2, 31–48.

Gens, A. (2003). The role of geotechnical engineering for nuclear energy utilisation. *Proc. 13th Eur. Conf. Soil Mech. Geotech. Engng, Prague* **3**, 25–67.

Gens, A. (2010). Soil–environment interactions in geotechnical engineering. 47th Rankine Lecture. *Géotechnique* **60**, No. 1, 3–74, **doi**: 10.1680/geot.9.P.109.

Gens, A. & Alonso, E. E. (1992). A framework for the behaviour of unsaturated expansive clays. *Can. Geotech. J.* **29**, No. 6, 1013–1032.

Gens, A., Alonso, E. E., Lloret, A. & Batlle, F. (1993). Prediction of long term swelling of expansive soft rock: a double-structure approach. In *Geotechnical engineering of hard soils–soft rocks* (eds A. Anagnostopoulos, F. Schlosser, N. Kalteziotis and R. Frank), Vol. 1, pp. 495–500. Rotterdam: Balkema.

Gens, A., García-Molina, A. J., Olivella, S., Alonso, E. E. &

Huertas, F. (1998). Analysis of a full scale in situ test simulating repository conditions. *Int. J. Numer. Analyt. Methods Geomech*. **22**, No. 7, 515–548.

Gens, A., Filippi, M., Vallejan, B. *et al.* (2009a). *RESEAL II project – Final report on modelling (WP4)*, SCK–CEN report ER-80. Brussels: SCK–CEN (Studiecentrum voor Kernenergie–Centre d'Etude de l'énergie Nucléaire (Belgian Nuclear Research Centre)).

Gens, A., Sánchez, M., Guimarães, L. do N. *et al.* (2009b). A full-scale in situ heating test for high-level nuclear waste disposal: observations, analysis and interpretation. *Géotechnique* **59**, No. 4, 377–399, **doi**: 10.1680/geot.2009.59.4.377.

Ghafouri, H. & Lewis, R. (1996). A finite element double porosity model for heterogeneous deformable porous media. *Int. J. Numer. Analyt. Methods Geomech* **20**, No. 11, 831–844.

Guimarães, L. do N., Gens, A. & Olivella, S. (2007). Coupled thermo-hydro-mechanical and chemical analysis of expansive clay subject to heating and hydration. *Transp. Porous Media* **66**, No. 3, 341–372.

IAEA (International Atomic Energy Agency) (1990). *Sealing of underground repositories for radioactive wastes*, IAEA Technical Report Series No. 319. Vienna: IAEA.

Imbert, V. & Villar, M. V. (2006). Hydro-mechanical response of a bentonite pellets/powder mixture upon infiltration. *Appl. Clay Sci*. **32**, No. 3–4, 197–209.

Imbert, C., Fleureau, J.-M., Kheirbek-Saoud, S. & Deprez, L. (1997). *Caracterisation hydrique des materiaux de l'experience PRACLAY.* Fontenay-aux-roses, France: Commissariat à l'energie atomique (CEA), Technical Report (in French).

Khalili, N., Valliappan, S. & Wan, C. (1999). Consolidation of fissured clay. *Géotechnique* **49**, No. 1, 75–89, **doi**: 10.1680/geot.1999.49.1.75.

Lloret, A., Villar, M. V., Sánchez, M. *et al.* (2003). Mechanical behaviour of heavily compacted bentonite under high suction changes. *Géotechnique* **53**, No. 1, 27–40, **doi**: 10.1680/geot.2003.53.1.27.

Marcial, D. (2003). *Comportement hydromécanique et microstructural des matériaux de barrière ouvragée*. PhD thesis, École Nationale des Ponts et Chaussées, France.

Michaux, L. & Loubignac, J. M. (1995). *Evolution de la microstructure de l'argile Fo-Ca-7 compactée lors d'un cycle d'hydration/deshydration à 25°C*. Fontenay-aux-roses, France: Commissariat à l'energie atomique, Technical Report (in French).

Monroy, R. (2005). *The influence of load and suction changes on the volumetric behaviour of compacted London Clay.* PhD thesis, Imperial College, London.

Olchitzky, E. (2002). *Couplage hydromécanique et perméabilité d'une argile gonflante non saturée sous sollicitations hydriques et thermiques: courte de sorption et perméabilité à l'eau*. PhD thesis, Ecole Nationale des Ponts et Chaussées, Marne La Vallée, Paris, France (in French).

Olivella, S., Gens, A., Carrera, J. & Alonso, E. E. (1996). Numerical formulation for a simulator (CODE_BRIGHT) for the coupled analysis of saline media. *Engng Comput*. **13**, No. 7, 87–112.

Pusch, R. (1994). *Waste disposal in rock*, Developments in Geotechnical Engineering, Vol. 76. Amsterdam: Elsevier.

Romero, E. (1999). *Characterization and thermo-hydro-mechanical behaviour of unsaturated Boom clay: an experimental study.* PhD thesis, Universitat Politecnica de Catalunya, Spain.

Romero, E., Hoffmann, C., Castellanos, E., Suriol, J. & Lloret, A. (2005). Microstructural changes of compacted bentonite induced by hydro-mechanical actions. In *Advances in understanding engineered clay barriers* (eds E. E. Alonso and A. Ledesma), pp. 193–202. Rotterdam: Balkema.

Sánchez, M. (2004). *Thermo-hydro-mechanical coupled analysis in low permeability media*. PhD thesis, Universitat Politecnica de Catalunya, Spain.

Sánchez, M., Gens, A., Guimarães, L. do N. & Olivella, S. (2005). A double structure generalized plasticity model for expansive materials. *Int. J. Numer. Analyt. Methods Geomech*. **29**, No. 8, 751–787.

Touret, O., Pons, C., Tessier, D. & Tardy, Y. (1990). Etude de la répartition de l'eau dans des argiles saturées Mg^{2+} aux fortes teneurs en eau. *Clay Minerals* **25**, No. 2, 217–223.

Van Geet, M., Volckaert, G. & Roels, S. (2005). The use of microfocus X-ray computed tomography in characterising the hydration of a clay pellet/powder mixture. *Appl. Clay Sci*. **29**, No. 2, 73–87.

Van Genuchten, M. T. (1980). A closed-form equation for predicting the hydraulic conductivity of unsaturated soils. *Soil Sci. Soc. Am. J.* **44**, 892–898.

Volckaert, G., Bernier, F., Alonso, E. *et al.* (1996). *Thermal-hydraulic-mechanical and geochemical behaviour of the clay barrier in radioactive waste repositories (model development and validation)*, Nuclear Science and Technology, EUR 16744. Luxembourg: Commission of the European Communities.

Volckaert, G., Dereeper, B., Put, M. *et al.* (2000). *A large-scale* in situ *demonstration test for repository sealing in an argillaceous host rock RESEAL project – phase I*, EUR 19612, 273 pp. Luxembourg: European Commission.

Wan, A. W. L., Gray, M. N. & Graham, J. (1995). On the relations of suction, moisture content and soil structure in compacted clays. *Proc. 1st Int. Conf. Unsaturated Soils, Paris* **1**, 215–222. Rotterdam: Balkema.

Warren, J. & Root, P. (1963). The behaviour of naturally fracturated reservoirs. *Soc. Petrol. Engrs J.* **228**, No. 8, 244–255.

Wilson, R. & Aifantis, E. (1982). On the theory of consolidation with double porosity. *Int. J. Engng Sci*. **20**, No. 9, 1019–1035.

Yahia-Aïssa, M., Delage, P. & Cui, Y. J. (2000). Volume change behaviour of a dense compacted swelling clay under stress and suction changes. In *Experimental evidence and theoretical approaches in unsaturated soils* (eds A. Tarantino and C. Mancuso), pp. 65–74. Rotterdam: Balkema.

Alonso, E. E. *et al.* (2011). *Géotechnique* **61**, No. 5, 387–407 [**doi:** 10.1680/geot.SIP11.P.013]

Modelling the response of Lechago earth and rockfill dam

E. E. ALONSO*, S. OLIVELLA*, A. SORIANO†, N. M. PINYOL* and F. ESTEBAN‡

Lechago dam (Teruel, Spain) is a 40 m high zoned earth and rockfill dam sitting on soft continental deltaic deposits. A relatively narrow central clay core is stabilised by wide rockfill shoulders. The dam was well instrumented and continuous records of stress development, pore-water pressures and vertical displacements are available for the construction period. Compaction conditions were followed by means of laboratory and in situ control tests. Core clay material was investigated by means of tests performed on compacted specimens of tertiary clays. Rockfill samples were excavated in outcrops of highly fractured Cambrian quartzitic shale. A testing programme on compacted rockfill gravels was conducted under relative humidity control in a large-diameter oedometer and triaxial cells. A coupled finite-element model has been developed to analyse the tests performed and dam behaviour during construction. Model predictions, essentially based on laboratory tests, are compared with measurements during construction. The predicted response of the dam under an assumed programme of impounding is also given. In the future, once impounding occurs, it will be possible to compare these predictions with actual dam performance. The paper provides an integrated description of the dam design, construction and early behaviour. It presents a procedure to interpret available data (laboratory as well as in situ data) on compacted materials from the perspective of modern constitutive models. It also provides an evaluation of the capabilities of advanced numerical tools to reproduce the measured dam behaviour.

KEYWORDS: case history; compaction; dams; field instrumentation; numerical modelling

Le barrage de Lechago (à Teruel, en Espagne) est un structure en terre à zones et enrochements, placée sur des dépôts deltaïques continentaux tendres. Un noyau d'argile central relativement étroit est stabilisé par des épaulements à enrochements larges. Le barrage avait été bien instrumenté, et on dispose de relevés continus de développement de contraintes, pressions d'eau interstitielles et déplacements verticaux effectués au cours de la période de construction. On a suivi les conditions de compactage au moyen de tests de contrôle en laboratoire et « in situ », et examiné le noyau d'argile au moyen d'essais effectués sur des spécimens compactés d'argiles tertiaires. Des échantillons d'enrochement ont été excavés dans des affleurements de schistes quartzites du cambrien, extrêmement fracturés. On a mené un programme d'essais sur des graviers d'enrochement, avec humidité relative contrôlée, dans un oedomètre de grand diamètre et des cellules triaxiales. On a réalisé un modèle accouplé aux éléments finis pour analyser les tests effectués et le comportement du barrage au cours de la construction. On a effectué une comparaison des prédictions de modèle, basées essentiellement sur des essais en laboratoire, avec des mesures effectuées au cours de la construction. En outre, la réaction prévue du barrage soumis à un programme de retenue supposé est également fournie. Dans l'avenir, lorsque l'on procèdera à une retenue, il sera possible de comparer ces prédictions avec les performances effectives du barrage. La communication présente une description intégrée de la conception du barrage, de sa construction, et de son comportement initial, ainsi qu'une méthode d'interprétation des données disponibles (données relevées en laboratoire et « in situ ») sur des matières compactées, sous la perspective de modèles constitutifs évolués. Elle fournit également une évaluation des capacités des outils numériques perfectionnés pour la reproduction du comportement mesuré du barrage.

INTRODUCTION

Lechago dam, a 40 m high earth and rockfill structure (Fig. 1) was built in the period from April 2005 to January 2009. The first impoundment has been delayed to the first months of 2011. The flat upstream and downstream average slopes reveal the soft nature of the foundation soil in the central part of the dam. This situation was of special concern during design because it implied large total and differential settlements caused by the non-symmetrical cross-section of the valley and the stiffness of abutments, located in ancient shales and quarzitic rocks.

The design called for wide stabilising rockfill shells and a central clayey core. Fig. 2 is a photograph of the dam core, filter layer and the rockfill shoulder (shell) materials being compacted in situ. The maximum size of the gravel-like rockfill is about 20 cm but the mean particle diameter is close to 30–50 mm and therefore it may directly be tested in large-diameter laboratory cells, after removing the largest particles. Fig. 3 shows the grain size distributions of the in situ and tested rockfill material. The dam material had maximum sizes close to 9 cm and a somewhat increased content of fines, but otherwise the tested grading is quite similar to real conditions. Lechago rockfill material has been extensively tested during the past decade in the soil mechanics laboratory of Universitat Politècnica de Catalunya (UPC). The most salient feature of this experimental programme is the use of relative humidity (RH) control in the oedometer and triaxial tests performed. Some general results illustrating the effect of suction (or relative humidity) on the rock matrix and rockfill aggregate are collected in Figs 4–6. Brazilian tests on discs of rock equilibrated at different values of humidity were performed. The results (Fig. 4) show the variation of tensile strength with gravimetric water content or, alternatively, with total suction. Tensile strength increases the drier the specimen. Full wetting of an initially

Manuscript received 4 March 2010; revised manuscript accepted 21 December 2010. Published online ahead of print 22 March 2011. Discussion on this paper closes on 1 October 2011, for further details see p. ii.

* Department of Geotechnical Engineering and Geosciences. Universitat Politècnica de Catalunya, Barcelona, Spain
† Universidad Politécnica de Madrid, Madrid, Spain
‡ Confederación Hidrográfica del Ebro, Zaragoza, Spain

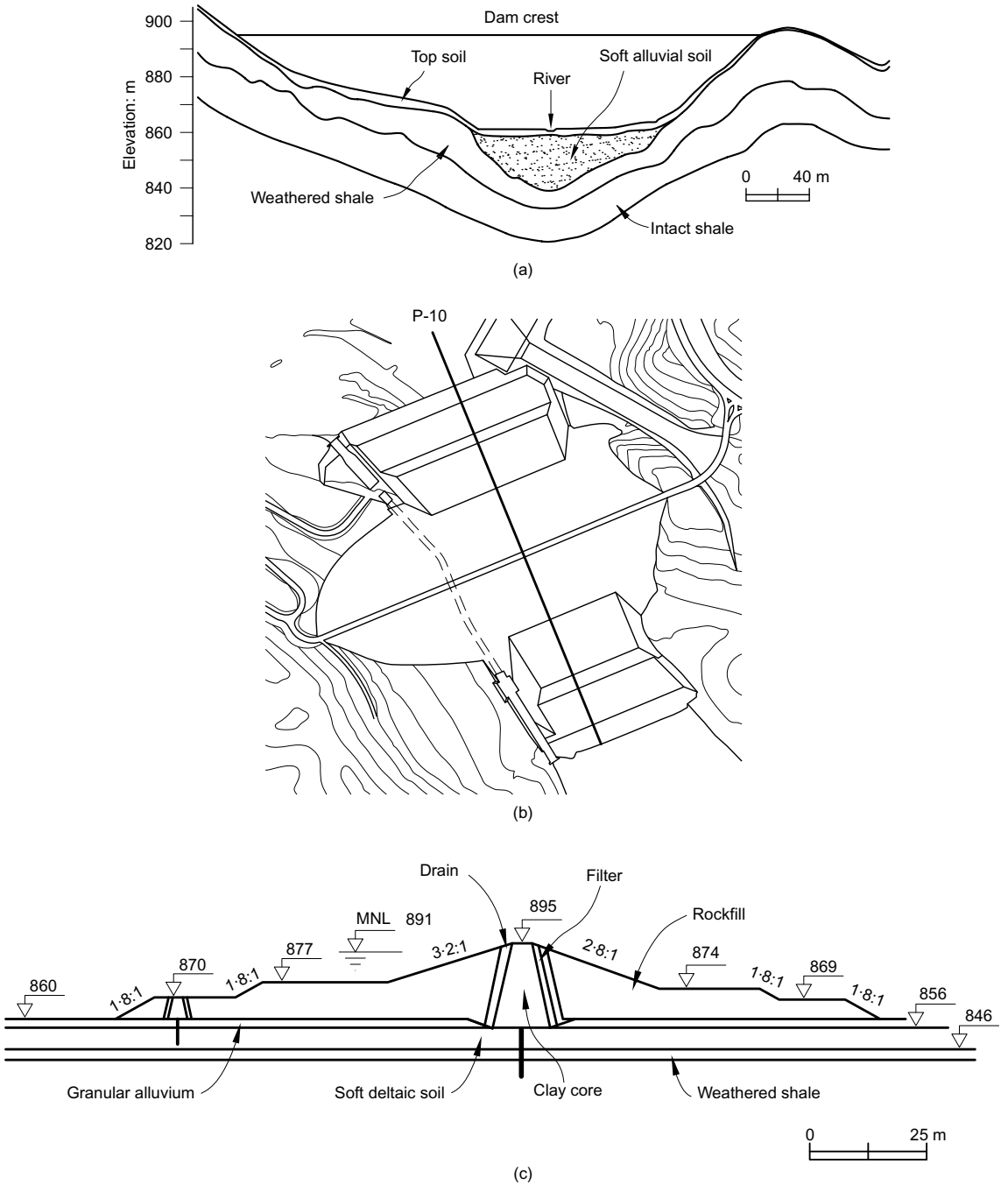

Fig. 1. (a) Valley cross-section; (b) plan view; (c) central cross-section P-10 of Lechago dam

dry rock reduces by half its tensile strength. The figure indicates the procedure to achieve a given humidity: equilibrating the rock specimen with salt solutions (indicated) or drying the specimens at the laboratory relative humidity (50%) (air) or submerging them in water.

Figure 5 provides the change in oedometric stiffness with applied total suction. It was found (Oldecop & Alonso, 2007) that the vertical stress–strain relationship could be approximated by a linear relationship

$$\varepsilon = \lambda \Delta \sigma \tag{1}$$

provided $\varepsilon < 8\%$. Rockfill specimens were compacted to an energy equivalent to standard Proctor energy. Compressibility also reduces substantially when the rockfill evolves from a very dry state (total suction, Ψ, equal to 255 MPa) to a saturated state.

The long-term deformation coefficient

$$\lambda^t = \frac{\mathrm{d}\varepsilon}{\mathrm{d}(\ln t)} \tag{2}$$

was also found to be linearly dependent on the compressibility coefficient λ.

However, the ratio λ^t/λ also depends markedly on current suction and it changes from 0·05 to 0·005 when suction changes from zero (full saturation) to $\Psi = 255$ MPa.

Figure 6 indicates the effect of RH on the strength envelope determined in a large-diameter triaxial cell on rockfill specimens compacted to standard Proctor energy (Chávez, 2004). The figure shows the expected curvature of the envelope. The effect of suction is in this case not so significant (RH = 36% is equivalent to $\Psi = 130$ MPa at 20°C from the psychrometric relationship).

A number of publications describe the relevance of RH in the behaviour of rockfill materials, the testing cells built and

Fig. 2. Clay core, filter and rockfill shoulder of Lechago dam during construction

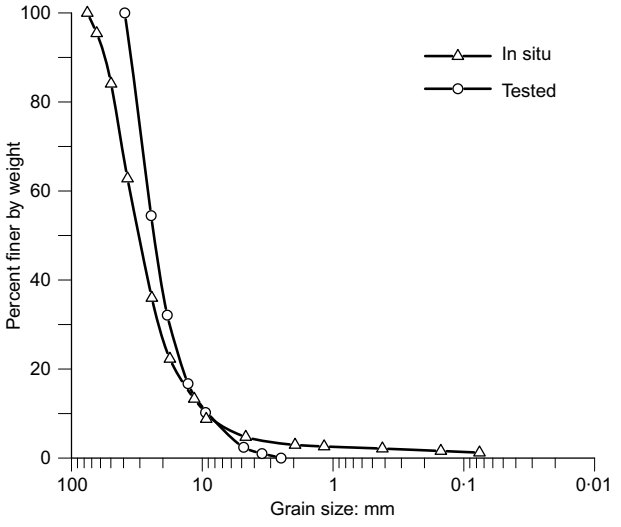

Fig. 3. Grain size distribution of Lechago rockfill material tested in the laboratory

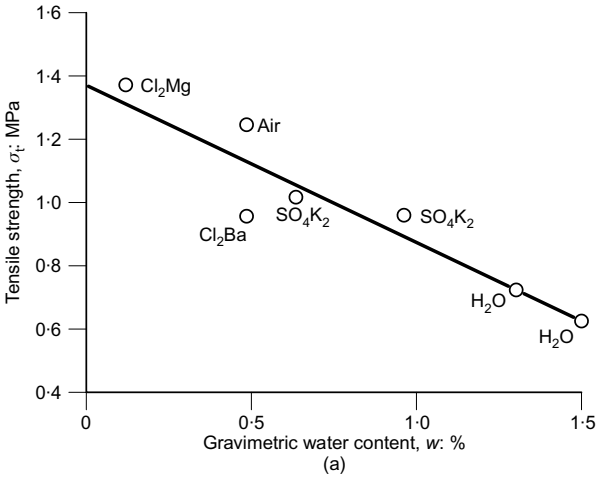

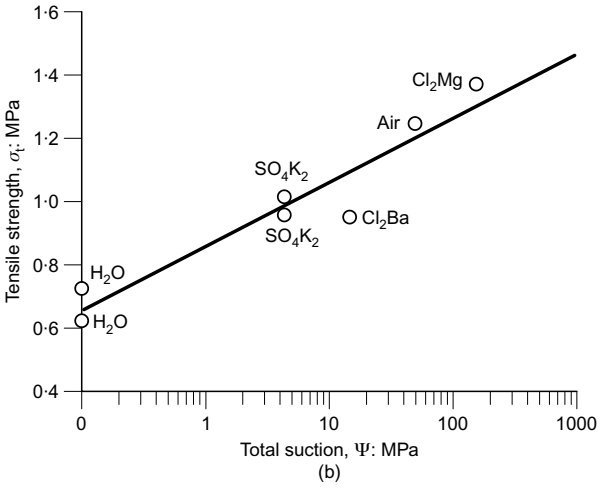

Fig. 4. Results from Brazilian tests on samples (84 mm diameter; 50 mm thick) in terms of (a) gravimetric water content; (b) total suction (Oldecop, 2000)

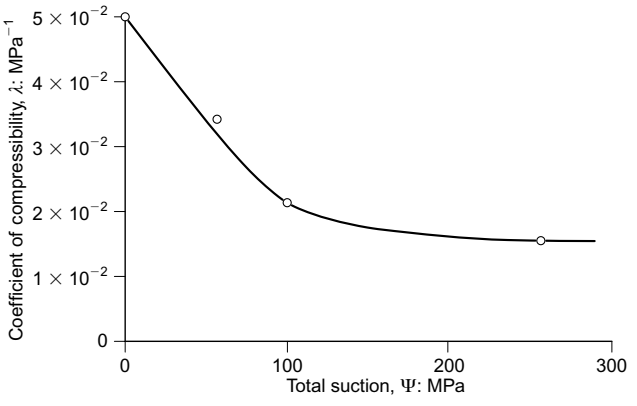

Fig. 5. Oedometric compressibility plotted against suction

the experimental results (Oldecop & Alonso, 2001; 2003; 2007; Chávez, 2004; Chávez & Alonso, 2003; Chávez *et al.*, 2009).

Piezometers (vibrating wire type), hydraulic settlement gauges and total stress cells were located in five cross-sections of the dam. The most detailed instrumentation corresponds to the central cross-section P-10, in the position of the maximum thickness of the soft alluvial deposits under the dam. Fig. 7 shows the instrument layout in section P-10. Surface topographic marks and levelling points were also located on the dam crest and downstream shoulders once the dam was completed.

Data recorded during dam construction will be later compared with the results of the model developed. Model parameters for the clay core and rockfill shoulders were derived from the analysis of tests performed on compacted clay from the core and the RH controlled triaxial tests reported in Chávez (2004). The foundation soil and, in particular, the soft alluvial clay and sand sediments were characterised at the design stage of the dam in the period 1998–1999.

The model has developed benefits from theoretical and applied contributions in the field of unsaturated soil mechanics performed by the authors and their colleagues in the past few years. The finite-element program Code_Bright, whose basic formulation is described by Olivella *et al.* (1994; 1996) and DIT-UPC (2002) has been used in a variety of applications, including dam and embankment analysis (Alonso *et al.*, 2005) and nuclear waste applications (Olivella & Alonso, 2008; Gens *et al.*, 2009), among others. It handles in a unified manner saturated and unsaturated states and transitions between them.

The saturated foundation soils were characterised by a modified Cam-clay model. The central clay core was described by the so-called Barcelona basic model (BBM) for

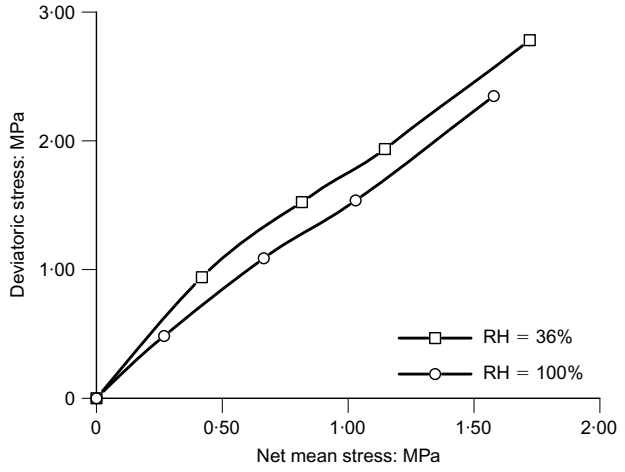

Fig. 6. Effect of RH on the strength envelope of compacted rock specimens in large-diameter triaxial cells

unsaturated soils (Alonso *et al.*, 1990). For rockfill shoulders and filters the isotropic elastoplastic model initially described by Oldecop & Alonso (2001) and later generalised to include deviatoric states in Alonso *et al.* (2005) was used.

The paper describes first a few relevant features of the dam design and construction, the foundation soils and field compaction data. Then, a back-analysis of large-diameter tests on compacted rockfill specimens and conventional tests on the compacted core clay is presented. Identified soil parameters are then used to simulate the dam construction. The model has been extended to simulate the first dam impoundment following a protocol that is often used in practice. The latter part of the paper provides a prediction of future dam performance, which may later be compared with actual dam performance.

DAM DESIGN AND CONSTRUCTION

The design of Lechago dam faced a number of challenging situations, namely the soft continental deltaic sediments filling the bottom of the valley, the marked non-symmetry of the valley, the sharp transition between highly deformable and rigid substrata and the fractured and pervious shale substratum in the entire area.

Earth dam construction on soft soil deposits is not common but several cases have been described in published papers (Daehn, 1985; Ramírez *et al.*, 1991; Rizzoli, 1991; Tellería and Gómez Laa, 1991; Torner and Novosad, 1991; Trkeshdooz *et al.*, 1991). Construction settlements in excess of 1 m have often been reported. In general, upstream and downstream slopes are controlled by global stability considerations and values in the range 4H–5H/1V are often found. This is also the case for Lechago dam.

Lechago has two definite cross-sections. On both sides of the central alluvial deposits a conventional zoned dam having 3·2H/1V and 2·8H/1V slopes (upstream and downstream) was designed. On the valley bottom this design was stabilised by wide rockfill berms to improve stability. In Lechago the project required a further improvement of the undrained strength of the soft alluvial deposits by means of a preloading operation of the downstream shoulders which would be carried out during construction. The actual construction involved a smaller preloading intensity than originally designed, supplemented by a water table lowering. Both operations were included in the model described below.

The actual construction sequence is plotted in Fig. 8 in terms of the evolution in time of the embankment height. In order to minimise differential settlements the design envisaged that the central section of the dam, directly founded on the soft alluvium, would be first built and then extended to occupy the valley slopes. However, in view of the fast consolidation of the alluvial soils, it was decided to build the dam in horizontal layers.

The three intermediate stops of construction activity shown in Fig. 8 were motivated by the difficulties in building the large spillway, excavated on the right abutment. The dissipation basin in the lower part encountered deep soft deposits and the construction involved a larger-than-expected excavation dewatering by means of deep wells and a piling foundation of the base slab. The downstream dam shell was affected and therefore the entire dam construction schedule was delayed. It was also decided to improve the foundation soils by reducing the water table under the downstream shell. The third and more extensive water lowering (third stop in Fig. 8) involved an average water table lowering of 2·5 m. In addition, surcharge preloading was resolved by a fill, 3 m high, emplaced on the downstream berms of the dam, at elevations of 869 and 874 m. Fig. 8 also indicates the measured piezometric level in the bedrock, below the dam downstream toe. Piezometric variations of about 3–4 m are a consequence of dewatering operations. The upstream

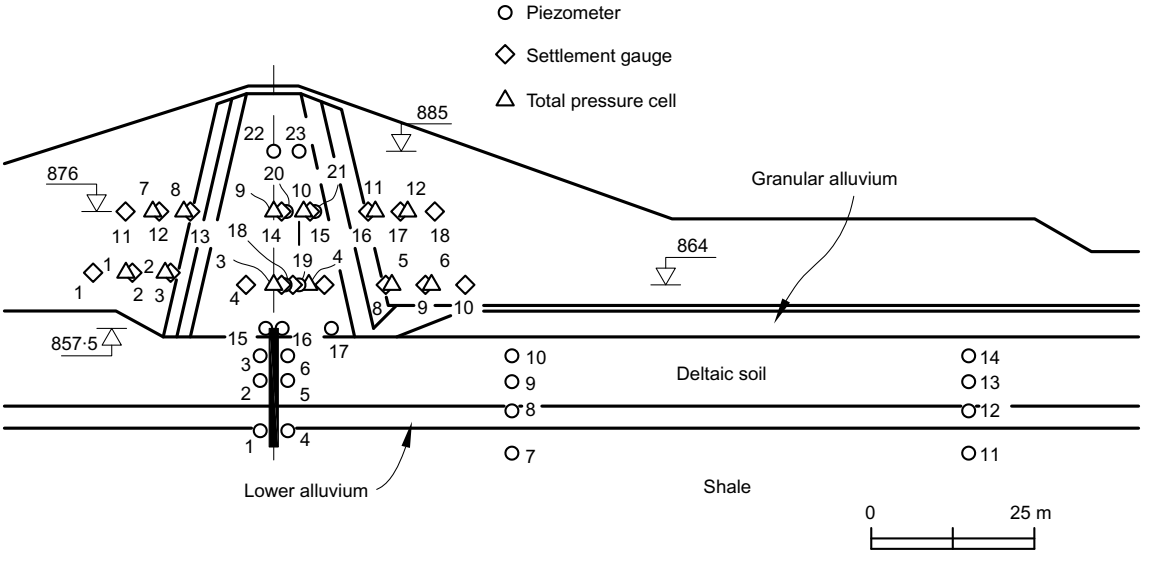

Fig. 7. Instrument layout in cross-section P-10

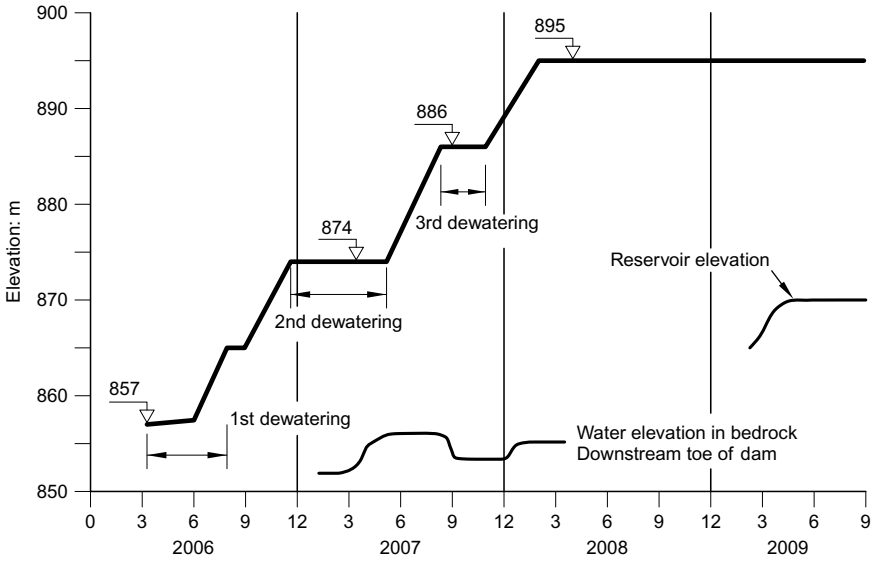

Fig. 8. Construction sequence

cut-off wall allowed a limited impoundment (beginning in March, 2009) as well, which is also shown in the same figure.

The dam reached its maximum elevation in March 2008, 24 months after the placement of the first compacted layer. The first control of dam surface settlements was performed in April 2009.

FOUNDATION SOILS AND CONSTRUCTION MATERIALS

The alluvium of the Pancrudo River was identified as a sequence of three horizontally layered strata: an upper layer of pervious sandy silt and gravels, 5 m thick, an intermediate soft clayey and silty stratum (deltaic deposits), 12 m thick, and a lower level of clayey sands and gravels 4 m thick directly over the shale substratum. In all levels thin sequences of impervious/pervious soils explain the fast consolidation of the entire alluvial stratum.

In the upper alluvium standard penetration test (SPT) values in the range 4–14 were measured. The central soft clayey stratum was often classified as low-plasticity clay (CL) or low-plasticity silt (ML), but clayey sands were also found. Void ratios range between 0·6 and 0·75. Liquid limit and plasticity index take values in the range 25–40% and 5–16% respectively. Critical stability conditions of the dam slopes were found under undrained conditions for this layer, whose virgin compression indices $C_c = 0{\cdot}15–0{\cdot}18$ were measured in standard oedometer tests. Horizontal consolidation coefficients in the range $c_h = 0{\cdot}6–6\ \text{cm}^2/\text{min}$ (0·01–0·1 cm^2/s) were obtained in CPTU dissipation tests. However, the frequent interlayering of sandy levels results in substantially higher representative consolidation coefficients. In fact, settlements of the base of the dam during construction increased in parallel with dam height. The lower thin alluvial sand was quite dense ($N > 30$).

The shale substratum was dissected by several faults which crossed the dam site. The upper decomposed and weathered shale level, 5–10 m thick, in contact with the alluvial or colluvial soils of the valley slopes, was moderately pervious ($k \approx 10^{-6}$ m/s, determined through Lugeon in situ tests).

A low-plasticity clay of Miocene age was selected for the dam impervious core. Dry densities not lower than 102% of the standard Proctor optimum value and water contents inside a ± 2% band around optimum were initially specified

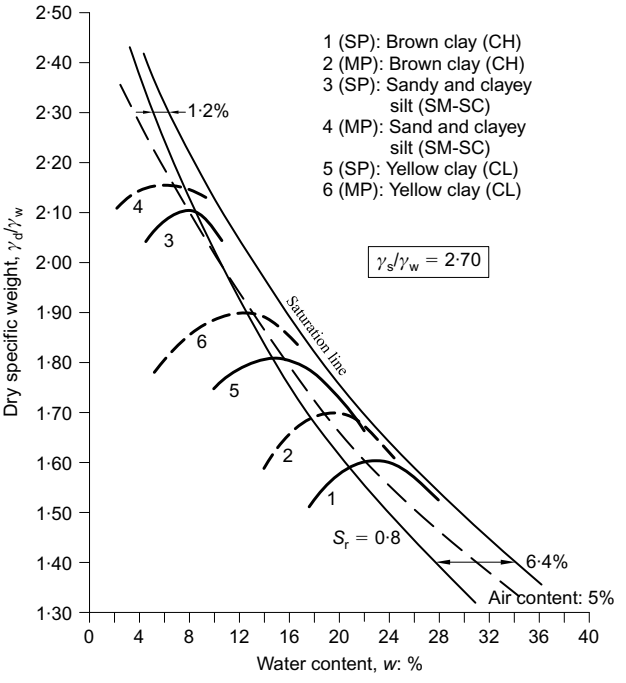

Fig. 9. Compaction tests on materials considered for the core of Lechago dam (SP: standard Proctor compaction; MP: modified Proctor compaction)

for construction. Fig. 9 provides a set of compaction curves, determined during the design stage, on Miocene clayey materials located in the vicinity of the dam. Standard Proctor (SP) and modified Proctor (MP) energies were used. The selected clay for the core was the yellow clay. It reached optimum dry unit weights of 18 kN/m^3 (SP) and 19 kN/m^3 (MP). In all cases optimum conditions correspond reasonably well to a 5% air content. The clay, after a period of exposure to natural weathering, was compacted in 25 cm thick layers by means of six runs of a sheep foot roller and a final run of a smooth roller (when the nuclear probe control measurements were required). In all cases the continuity of layers was ensured by a scarification of the current compacted surface prior to the placement of a new layer. The dry density limit was strictly enforced but water con-

tents were accepted in a wider range (−8% to +2% around optimum). The average compaction water content remained slightly below optimum.

Figure 10 provides the dry unit weight–water content in situ determinations during construction. Most of the dry unit weights remain in the range 18·7–19·7 kN/m^3 ($e_0^c \approx 0{\cdot}38$–$0{\cdot}45$). These values may be compared with the laboratory results in Fig. 9. Field compaction in the core reached densities in the vicinity of the MP optimum. The plot in Fig. 10 shows that the average degree of saturation during construction was around 0·9, a value close to optimum. A small proportion of the core volume seems to have degrees of saturation in the range 0·6–0·8, on the dry side of compaction.

Oedometer tests for specimens compacted to the range of γ_d values reached during construction provided the following compression indices: $C_c = 0{\cdot}07$–$0{\cdot}12$; $C_s = 0{\cdot}03$–$0{\cdot}05$. Measured coefficients of consolidation ranged between $c_v = 1{\cdot}5 \times 10^{-2}$ cm^2/s and $c_v = 3{\cdot}5 \times 10^{-2}$ cm^2/s. Derived permeability was in the range ($k \approx 2 \times 10^{-8}$ to 7×10^{-9} m/s). The measured secondary compression coefficient was a small proportion of C_c ($C_\alpha^c \approx 0{\cdot}013$–$0{\cdot}015 C_c$).

Collapse tests were also performed on several clay samples compacted to several dry specific weights and water contents. Samples were taken to vertical compression stresses of 100 and 400 kPa and were flooded at constant stress. The plot in Fig. 11 shows the measured collapse strains. The boundaries shown in the figure define three regions: very low collapse, medium to low collapse and medium to high collapse. The specimens tested cover a range of Miocene clayey materials having different grain size distributions and plasticity even if most of them are classified as CL or ML. Note that in all cases the collapse increases substantially when the vertical stress increases from 100 kPa to 400 kPa. The plot in Fig. 11 and the field density and water content data given in Fig. 10 indicate that the dam core has a low collapse potential (expected collapse strains smaller than 1% as a rough guide). This information was available at design stage and it was necessarily approximate because the objective at the time was to select the appropriate core material in the vicinity of the dam. More recently, tests were also performed on samples of the core material. The results will be analysed in the next section.

The quartzitic Cambrian shales used in the shells were highly fractured and the combined effect of quarry excavation, transport and placement in layers (40–50 cm thick) resulted in a gravel-like material (maximum sizes of the order of 10 cm). Therefore, compaction control tests could be performed in the laboratory in modified Proctor test moulds, removing the bigger fragments when necessary. The

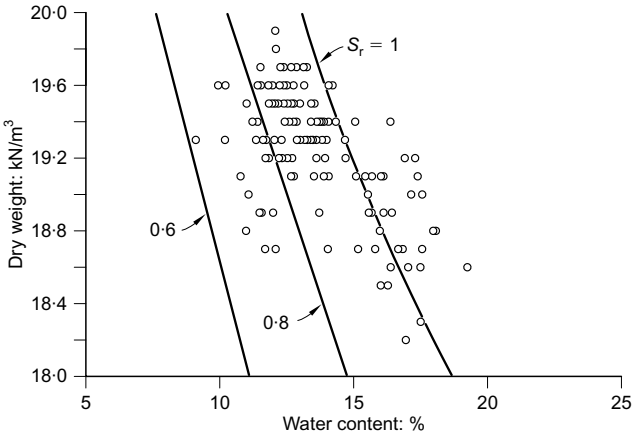

Fig. 10. Compaction data on core clay; in situ determinations

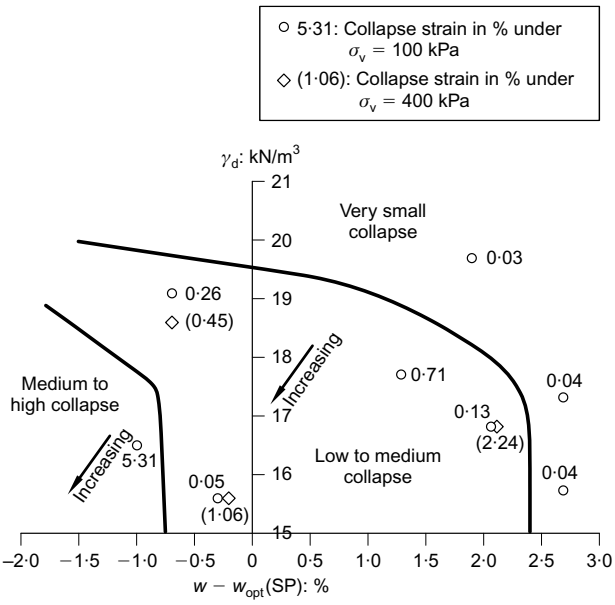

Fig. 11. Oedometer collapse of specimens compacted to the specified dry unit weight and water content (samples recovered in trenches at the design stage of the project)

modified Proctor optimum was taken as a reference for field control, which was carried out by means of nuclear probes that were calibrated by direct density and water content determinations at the beginning of construction works. The rockfill was compacted by a 19 ton vibratory roller (six runs for each layer).

The measured dry unit weights and water contents are collected in Fig. 12 in the conventional compaction plane. Water contents range between 6% and 7% for dry unit

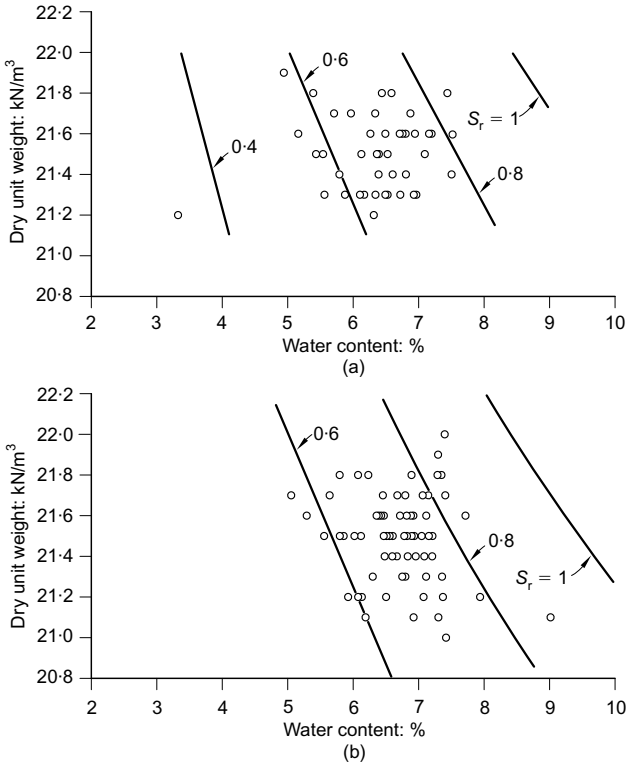

Fig. 12. Field compaction data for (a) upstream shell; (b) downstream shell

weights in the range 21–22 kN/m^3. The resulting degree of saturation varies between 0·6 and 0·8.

Oldecop & Alonso (2001) measured the water retention curve of Lechago shale gravel. They found that the porosity of the rock fragments amounts to 3·5–4%. Since the compacted rockfill has a global water content in the range 6–7%, if the rock fragments are saturated, some additional water partially fills the rockfill pores. This water is probably associated with the fines produced by the heavy compaction and/or by the insufficient drainage of the layer just compacted in situ at the time of the nuclear probe determinations.

The stress–strain behaviour of Lechago rockfill was tested in a RH-controlled large-diameter triaxial chamber, as described by Chávez (2004) and Chávez *et al.* (2009). Some isotropic and triaxial compression tests will be reproduced by the model developed in a next section.

TESTS ON COMPACTED MATERIALS AND THEIR INTERPRETATION

The available laboratory tests performed on the rockfill material and the clay core have been simulated as a boundary value problem with the help of the finite-element code Code_Bright with the purpose of determining material parameters. Table 1 provides a synthetic description of the models (BBM and rockfill model (RM)) used in the representation of the different materials.

Rockfill material

Triaxial samples, 250 mm in diameter and 500 mm high, were prepared by repeated compaction, applying an energy estimated at 600 J/m^3. The maximum size of particles was 40 mm. Samples were subjected to isotropic and triaxial loading at a specified relative humidity, which was controlled by imposing a vapour equilibrium technique (Oldecop & Alonso, 2001).

In order to simulate the tests performed, an axi-symmetric model of the actual triaxial specimens, described by quadrilateral linear elements, was developed. Stress, strain and flow conditions were applied at the specimen's boundaries as required.

Tests are treated as coupled flow and deformation boundary value problems. Both liquid flow and vapour flow were imposed to simulate the wetting of the samples following the test protocol in each case. The list of parameters required in the RM (Oldecop & Alonso, 2001) is indicated in Table 2.

The water retention curve introduced in the calculations, shown in Fig. 13, was based on the curve reported by Oldecop & Alonso (2001) for compacted specimens of the same rockfill. Because of the larger proportion of fines in situ (see Fig. 3) the air entry value was moderately increased, and more water was allowed to be retained at moderate suction values.

The water retention curve was simulated by means of a van Genuchten (1980) equation having a sub-horizontal shape for most of the accessible range of degrees of saturation. The smaller voids inside the rock particles retain water for low degrees of saturation, at high suction. The largest inter-particle voids provide the air entry value. Relative permeability was defined by means of the cubic law according to the following expression

$$k_{\mathrm{rel}} = k_{\mathrm{sat}}(S_{\mathrm{r}})^3 \tag{3}$$

where k_{sat} is the coefficient of permeability for saturated conditions and S_{r} is the degree of saturation.

The calibration of the remaining mechanical parameters indicated in Table 2 was obtained by a back-analysis of the laboratory tests. A comparison of model predictions and measured sample responses is shown in Figs 14–17.

Figure 14 shows the measured and simulated response of an isotropic test at constant suction performed in the triaxial apparatus. The saturated isotropic loading–unloading curve (Fig. 14(a)) shows the linear stress–strain relationship of the rockfill-type material and allows the calibration of the

Table 1. Basic relationships for constitutive models used in the analysis of Lechago dam*

	Barcelona basic model (BBM) (Alonso *et al.*, 1990)	Rockfill model (RM) (Compressibility part described by Oldecop & Alonso, 2001)
Isotropic elastoplastic volumetric deformation†	$\mathrm{d}\varepsilon_{\mathrm{v}} = \dfrac{\lambda(s)}{1+e}\dfrac{\mathrm{d}p}{p}$	For $p \leqslant p_{\mathrm{y}} \Rightarrow \mathrm{d}\varepsilon_{\mathrm{v}} = \mathrm{d}\varepsilon_{\mathrm{v}}^{i} = \lambda^{i}\mathrm{d}p$ For $p > p_{\mathrm{y}} \Rightarrow \mathrm{d}\varepsilon_{\mathrm{v}} = \mathrm{d}\varepsilon_{\mathrm{v}}^{i} + \mathrm{d}\varepsilon_{\mathrm{v}}^{d}$ $= [\lambda^{i} + \lambda^{d}(s)]\,\mathrm{d}p$
Volumetric compressibility index†	$\lambda(s) = \lambda(0)[(1-r)\exp(-\beta s) + r]$	$\lambda^{i} + \lambda^{d}(s)$ $\lambda^{d}(s) = \lambda_0^{d} - \alpha_{\mathrm{s}}\ln\left(\dfrac{s+p_{\mathrm{atm}}}{p_{\mathrm{atm}}}\right)$
Hardening law	$\mathrm{d}p_0^{*} = \dfrac{(1+e)p_0^{*}}{\lambda(0)-\kappa}\mathrm{d}\varepsilon_{\mathrm{v}}^{p}$	$\mathrm{d}p_0^{*} = \dfrac{\mathrm{d}\varepsilon_{\mathrm{v}}^{p}}{\lambda^{i}-\kappa}$
Loading–collapse curve (LC)	$p_0(s) = p^{c}\left(\dfrac{p_0^{*}}{p^{c}}\right)^{[\lambda(0)-\kappa]/[\lambda(s)-\kappa]}$	For $p_0^{*} \leqslant p_{\mathrm{y}} \Rightarrow p_0(s) = p_0^{*}$ For $p_0^{*} > p_{\mathrm{y}} \Rightarrow p_0(s) = p_y + \dfrac{(\lambda^{i}-\kappa)(p_0^{*}-p_{\mathrm{y}})}{(\lambda^{i}+\lambda^{d}(s)-\kappa)}$
Shear strength critical state parameter	$M(s) = M$	$M(s) = M_{\mathrm{dry}} - (M_{\mathrm{dry}} - M_{\mathrm{sat}})\left(\dfrac{M_{\mathrm{sat}}}{M_{\mathrm{dry}}}\right)^{s/(10\,p_{\mathrm{atm}})}$
Tensile strength parameter	$p_{\mathrm{s}}(s) = k_{\mathrm{s}}s$	
Yield surface (triaxial)	$F(p, q, s) = q^2 - M^2[p + p_{\mathrm{s}}(s)][p_0(s) - p] = 0$	
Plastic potential (triaxial)	$G(p, q, s) = q^2 - \alpha M^2[p + p_{\mathrm{s}}(s)][p_0(s) - p] = 0$	

*A common notation was used for equivalent parameters. Material constants are different for the soil and RMs.
†Suction, s, refers to matric suction in the case of BBM, and to total suction in the case of RM.

Table 2. Mechanical parameters for rockfill and drains

Definition of parameter	Symbol	Units	Base case for Lechago dam	
			Shell	Drain
(*a*) *Elastic behaviour*				
Elastic modulus	E	MPa	140	150
Poisson's ratio	ν	—	0·235	0·3
(*b*) *Plastic behaviour*				
Plastic virgin instantaneous compressibility	$(\lambda^i - \kappa)$	—	0·03	0·025
Virgin clastic compressibility for saturated conditions	λ_0^d	—	0·03	0·028
Parameter to describe the rate of change of clastic compressibility with total suction	α_s	—	0·0115	0·0115
Slope of critical state strength envelope for dry conditions	M_{dry}	—	1·8	1·7
Slope of critical state strength envelope for saturated conditions	M_{sat}	—	1·7	1·3
Parameter that controls the increase in cohesion with suction	k_s	—	0	0
Threshold yield mean stress for the onset of clastic phenomena	p_y	MPa	0	0·01
Parameter that defines the non-associativeness of plastic potential	α	—	0·25	0·3
(*c*) *Initial state for dam model*				
Initial suction	s_0	MPa	0·001	0·001
Initial mean yield stress (very dry conditions)	p_0^*	MPa	0·25	0·25

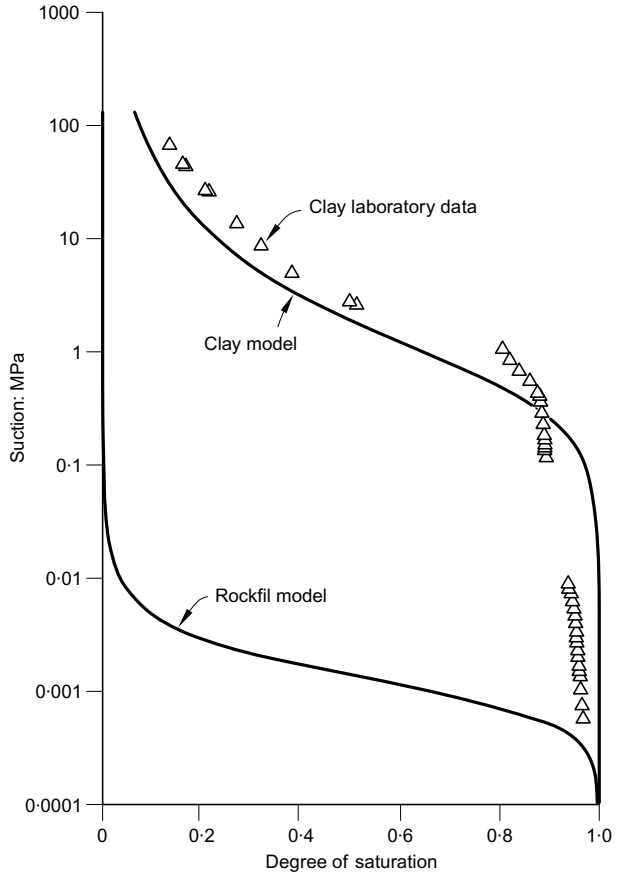

Fig. 13. Retention curves used in calculations for rockfill material and clay core

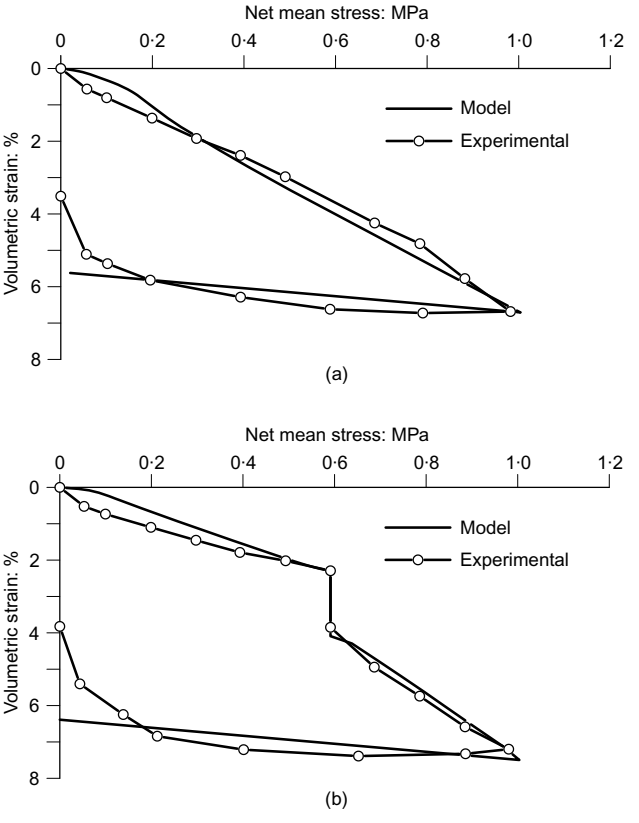

Fig. 14. Isotropic test: (a) saturated; (b) dry loading (RH = 36%) and saturation at a net mean stress of 0·6 MPa (experimental results by Chávez, 2004)

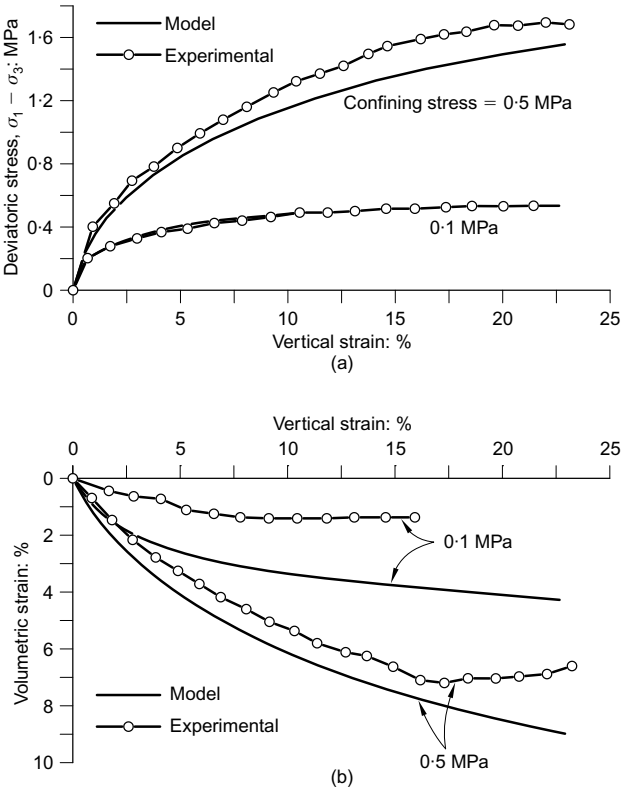

Fig. 15. Saturated triaxial test at two different confining stresses: (a) deviatoric stress–strain curves; (b) volumetric–axial strain curves (experimental results by Chávez, 2004)

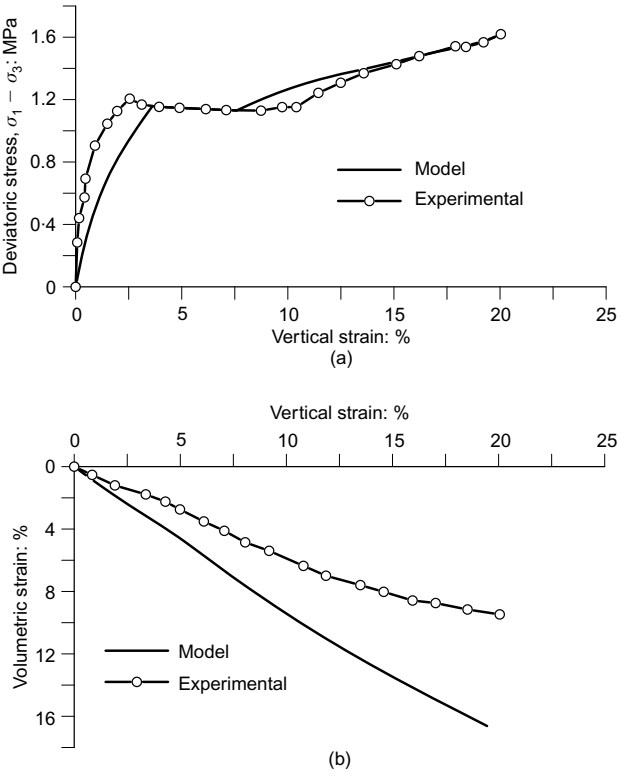

Fig. 17. Triaxial test at 36% RH and saturation at a confining stress of 0·5 MPa and constant deviatoric stress: (a) deviatoric stress–strain curves; (b) volumetric–axial strain curves (experimental results by Chávez, 2004)

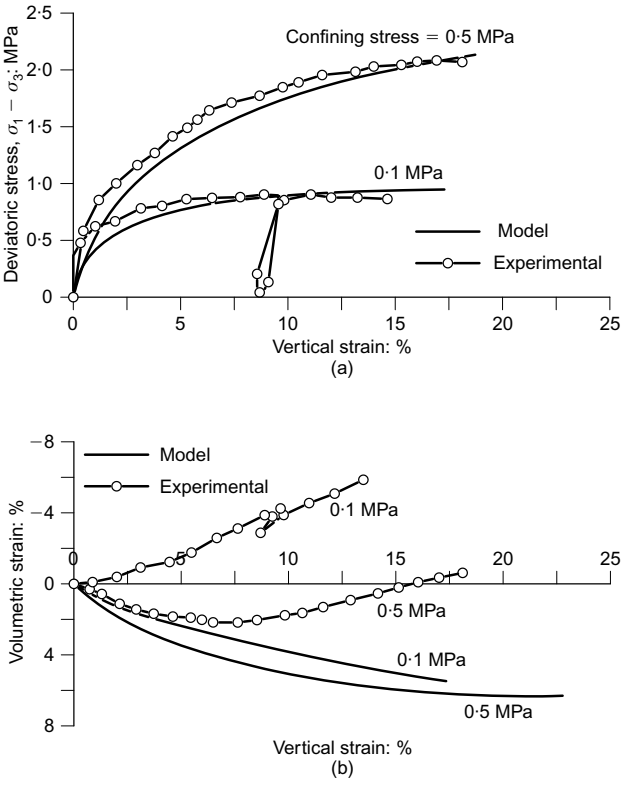

Fig. 16. Triaxial test at 36% RH and at two different confining stresses: (a) deviatoric stress–strain curves; (b) volumetric–axial strain curves (experimental results by Chávez, 2004)

compressibility parameters (λ_i and λ_0^d) and an estimation of the elastic modulus from the unloading curve.

In the second isotropic test (Fig. 14(b)), the sample was initially loaded at a maintained RH = 36%, which approximately corresponds to a value of total suction of 145 MPa according to the psychrometric relationship (Coussy, 1995). Suction was imposed during the first loading and the net mean stress was increased to 0·6 MPa. At this stress level the specimen was saturated. In the simulated test, saturation was reproduced by imposing a suction equal to zero at the top of the sample. The resulting water and vapour flow inside the sample was calculated by the model. Saturation of the sample resulted in a collapse of 2% volumetric strain, which was satisfactorily modelled (Fig. 14(b)). Hydraulic conditions were maintained during the remaining loading and unloading steps, which were performed under full drainage.

The first part of the compression curve at an imposed suction allows the estimation of the $\lambda(s)$ parameter, which describes the variation of compressibility parameter with suction and therefore the magnitude of collapse.

Figures 15 and 16 show the comparison between laboratory data and calculated values for triaxial tests performed at saturated condition and at 36% of RH respectively. The plots show the results for two confining stresses (0·1 and 0·5 MPa). The slope of the critical-state envelope (M) and its change with applied suction, was calibrated by means of the response of the material. A small increment of strength with suction was recorded. This is reflected in the values of M_{dry} and M_{sat} given in Table 2.

The non-associativeness of the plastic potential was estimated through the parameter $\alpha = 0{\cdot}25$. However, the dilatant behaviour was not well reproduced in all the simulated tests. The best approximation is obtained for the case of the

saturated triaxial test at a confining stress of 0·5 MPa (Fig. 15(b)). The behaviour exhibited by the drier specimen at a confining stress of 0·5 MPa (Fig. 16(b)), which initially contracted and then dilated without a marked softening in $p-q$ space cannot be properly reproduced by the implemented RM.

Finally, the triaxial test results given in Fig. 17 were simulated. The specimen was initially loaded in a dry condition (RH = 36%) under $\sigma_3 = 0{\cdot}5$ MPa and then saturated at constant deviatoric stress. The loading stage is resumed under saturated conditions. The parameters calibrated previously with the help of the tests described above were used. The model reproduces this singular test.

Clay core

Some tests were performed on the actual clay ($w_L = 38\%$, plasticity index (PI) = 18·5%) used in the core. Samples were compacted statically to densities of standard Proctor optimum. The optimum corresponds to a dry unit weight of 17·6 kN/m^3 and a water content of 17·8%.

Figure 13 shows the water retention curve obtained in the laboratory and the estimated curve introduced in the calculation using the van Genuchten model. The values of parameters (P_0 and λ) are given in Table 3.

Clay specimens compacted at standard Proctor optimum were tested in an oedometer test with suction control. The test results, plotted in Fig. 18, correspond to oedometric loading–unloading of a sample initially saturated at low level of stress (0·02 MPa). During saturation, the sample expanded. A second sample, compacted approximately at the same conditions, was first loaded at a constant suction equal to 1 MPa and then flooded at constant vertical stress (0·6 MPa) (Fig. 19). Model calculations are compared with experimental data in Figs 18 and 19. The clay behaviour was simulated using BBM (Alonso *et al.*, 1990).

Initial saturation at low stress level allowed an estimation to be made of the parameter κ_s, which controls the elastic volumetric strain for suction changes. Elastic and plastic

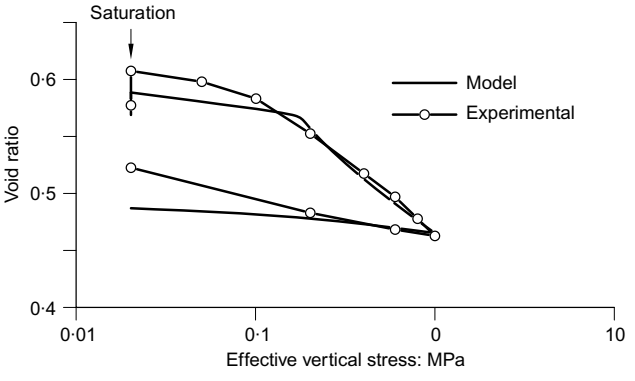

Fig. 18. Saturated oedometric test on a compacted clay sample initially saturated at constant vertical stress (0·02 MPa)

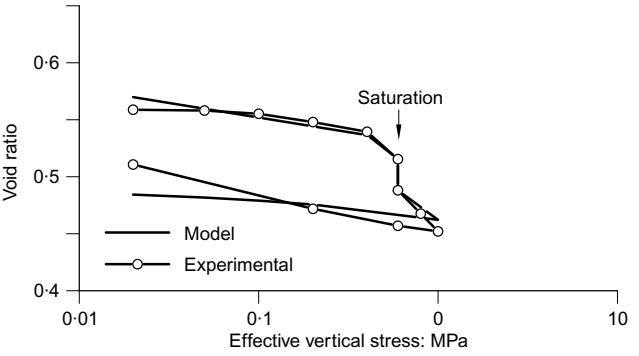

Fig. 19. Oedometric test on a compacted clay sample. Saturation at constant vertical stress (0·6 MPa)

compressibility parameters (κ and $\lambda(0)$) were estimated from the saturated test (Table 4). A comparison between saturated and unsaturated elastic compression curves indicates that the elastic stiffness increases with suction. This dependence has not been considered in the model. The model parameters which define the unsaturated compressibility and the shape of loading collapse (LC) yield surface (in the space net mean stress–suction) are estimated by means the unsaturated loading curve and the collapse intensity. Derived material parameters are collected in Table 4. The table also shows the set of parameters adopted for the natural foundation soil. They are based on field and laboratory data obtained at the design stage of the dam.

THE MODEL

A two-dimensional, plane strain, finite-element model of cross-section P-10 of Lechago dam was developed. The mesh used in calculations is made of linear quadrilateral four-node elements (Fig. 20(a)). Nodes have three degrees of freedom (water pressure, horizontal displacement and vertical displacement). The horizontal layers introduced to simulate construction and the dam materials are shown in Fig. 20(b).

Three materials define the dam: the clay core, the rockfill shells and the filters/drains. Four natural layers are distinguished in the foundation. Starting at the bottom, a stiff shale substratum ($E = 500$ MPa), 12 m thick, having a low permeability (3×10^{-9} m/s) is defined. Above this rock substratum, three soil layers are represented. Two permeable layers (4 and 4·9 m thick) of alluvium soil sandwich a less permeable soft soil (10 m thick). The upper permeable soil layer was excavated to build the clay core while the other two soil layers were cut by an impervious wall, connected with the clay core of the dam. The impervious wall was excavated by means of a slurry-trench technique and later filled with a cement–bentonite mixture, which was simulated by an elastic material (elastic modulus, $E = 100$ MPa; Poisson's ratio, $\nu = 0{\cdot}3$).

Table 3. Initial void ratio and intrinsic permeability adopted in calculations

Material	Initial void ratio, e_0	Intrinsic permeability, k: m^2	Retention curve, P_0: MPa	Retention curve, λ
Rockfill shell	0·43	1×10^{-12}	0·001	0·6
Clay core	0·67	1×10^{-15}	0·5	0·33
Drain	0·43	1×10^{-11}	0·01	0·33
Foundation soil: bed rock	0·43	3×10^{-16}	—	—
Foundation soil: alluvium soil	0·43	1×10^{-12}	—	—
Foundation soil: soft layer	0·54	1×10^{-14}	—	—
Cut-off wall	0·11	1×10^{-18}	—	—

Table 4. Parameters for the mechanical models used for the clay core and the foundation soils

Definition of parameter	Symbol	Units	Base case for Lechago dam			
			Clay core	Alluvium soil	Soft layer	Bed rock
(*a*) *Elastic behaviour*						
Elastic modulus	E	MPa	37	250	—	5000
Poisson's ratio	ν	—	0·3	0·3	0·3	0·3
(*b*) *Plastic behaviour*						
Elastic compressibility	κ	—	—	—	0·014	—
Virgin compressibility for saturated conditions	$\lambda(0) - \kappa$	—	0·046	0·01	0·055	—
Parameter that establishes the minimum value of the compressibility coefficient for high values of suction	r	—	0·7	—	—	—
Parameter that controls the rate of increase in stiffness with suction	β	MPa^{-1}	2	—	—	—
Elastic compressibility for changes in suction	κ_s	—	0·01	—	—	—
Reference stress	p^c	MPa	0·02	—	—	—
Slope of critical state strength line	M	—	0·85	1·2	0·85	—
Parameter that controls the increase in cohesion with suction	k_s	—	0·1	—	—	—
Parameter that defines the non-associativeness of plastic potential	α	—	0·3	0·3	0·3	—
(*c*) *Initial state for dam model*						
Initial suction	s_0	MPa	0·3	Saturated	Saturated	Saturated
Initial yield mean net stress	p_0^*	MPa	0·08	0·25	0·23	—

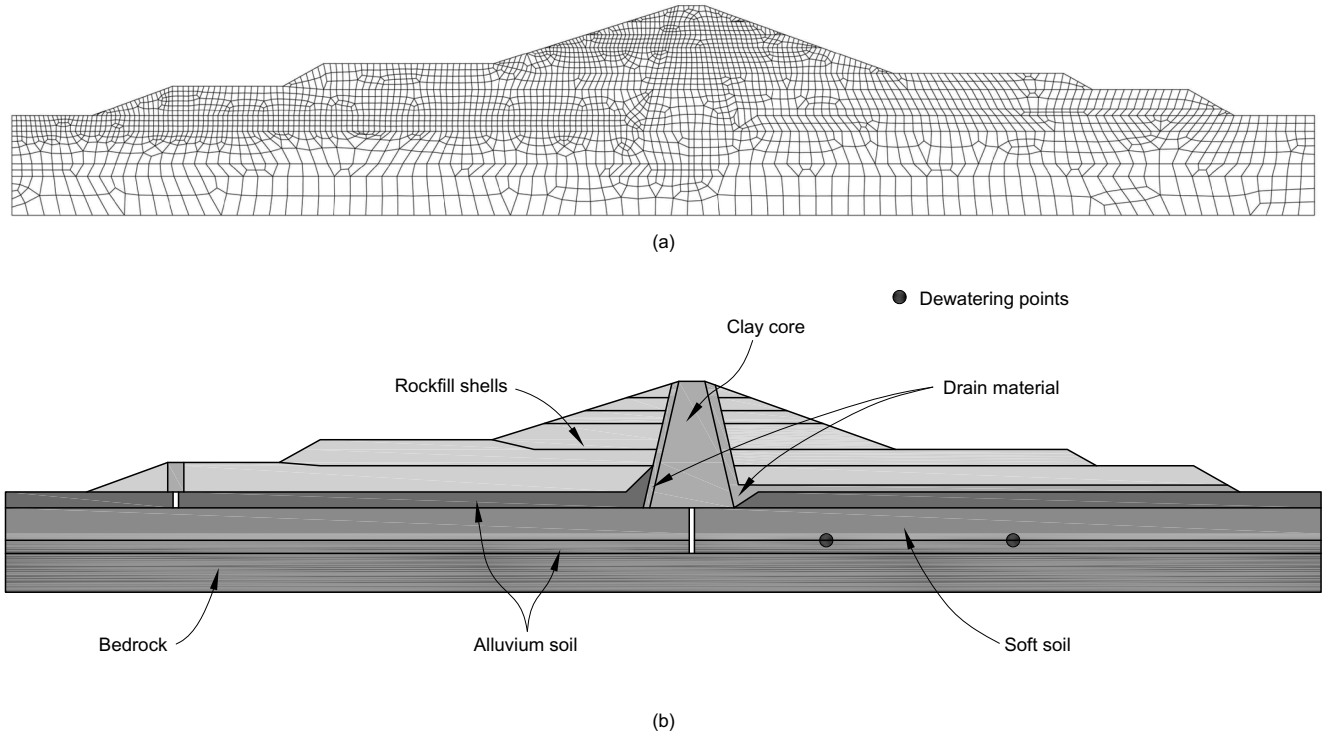

Fig. 20. Discretisation of cross-section P-10 of Lechago dam: (a) finite-element mesh; (b) materials and layers considered in construction simulation

Horizontal and vertical displacements were fixed at the lower plane of the model, which was considered impervious. Horizontal displacements were also fixed to zero and vertical displacements were free along the upstream and downstream vertical boundaries of the foundation.

The phreatic surface is located at the surface of the natural soil at the upstream side of the dam and 5 m below the surface at the downstream side. This jump in water table is created by the impervious wall and it was recorded by the piezometers installed. The water level is simulated by impos-

ing a hydrostatic pressure distribution on the lateral vertical boundaries of the foundation.

An initial geostatic total stress distribution on foundation soils was defined by a K_0 coefficient equal to 0·5. A preconsolidation mean effective stress (p_0^*) equal to 0·25 MPa has been defined for the pervious granular soil of the foundation and a slightly lower value, $p_0^* = 0{\cdot}23$ MPa, for the soft soil.

Construction was simulated by adding layers to the initial geometry of the foundation soils. The weight of each layer is applied in a ramped manner during the specified time period of its construction. The combination of steps and ramp loading gives a sufficiently realistic modelling. Each layer contains clay core elements, rockfill elements and drain elements, which were placed in between the core and shoulders. The dam was built in six steps (Table 5). The initial yield value of mean stress for dam materials should take into account the compaction stresses. For the clay core, the nominal value of the applied stress of the roller compactor, was used to define the initial mean stress, assuming $K_0 = 0{\cdot}5$. The RM requires the specification of the yield stress for very dry conditions. The selected value, $p_0^* = 0{\cdot}25$ MPa (Table 2), was approximated from the back-analysis of triaxial tests. The same parameter values were selected for filter materials.

Concerning initial suction the measured water content in situ (Fig. 10 for the clay core and Fig. 12 for the rockfill) and the water retention curves (Fig. 13) provide an approximate initial mean suction: 0·3 MPa for the clay core and 0·001 MPa for the rockfill.

In order to simulate the water level drawdown that was performed during construction to increase the preconsolidation stress of the soft deltaic deposits, two sink points (Fig. 20(b)) were included in this layer with the purpose of simulating the imposed drawdown by means of a water pressure reduction.

Before the construction of the two uppermost layers of the dam the preloading was simulated on the downstream side. Preloading was modelled through a vertical stress acting on the downstream slope surface. The preload was applied and removed, also using a ramp loading procedure to reproduce the construction and excavation process. During the 4 months of preloading time, dewatering in the lower permeable layer within the natural soil was simulated by means of 2·5 m water level decrease in the two sink points just below the preloading zone.

Granular drains are simulated by means of a RM and the material parameter values are given in Table 2. Compared with the rockfill properties, the sandy filters are assumed to be slightly stiffer and their frictional strength somewhat decreased. The downstream drain is simulated by means of a continuous layer which limits the clay core and continues below the rockfill shoulder to filter possible foundation water leaks and to avoid pressure development in the downstream shell.

BEHAVIOUR DURING CONSTRUCTION

Comparison between model performance and dam behaviour during construction will be based on stress measurements from total stress cells, vertical settlements determined by hydraulic gauges and pore pressure from piezometer readings. Hydraulic settlement gauges require a reference control position which was installed at the downstream edge of the horizontal berms at elevations 866 and 876 m. These points also experience settlements due to water table lowering and dam construction. The settlement gauges record the difference in elevation between a given gauge location and the reference position. The comparison made below refers to this difference in settlements. The reference control positions were levelled also by topographic procedures but the results were considered unreliable.

The total stress evolution recorded in some cells at some points has been compared with calculations. The comparison refers to several cells installed at the elevation 864–867 m. Fig. 21 shows the time records of measured stresses and their comparison with model predictions. The sudden reduction of the stress in the measurements at one of the gauges in the downstream rockfill (Fig. 21(c)) was attributed to an error in the instrument performance. Stress cells seem to provide in this case a fairly accurate indication of the dam construction history. In fact, the periods of rest between periods of construction activity are precisely detected. No significant delayed effects are shown by the readings. Vertical stresses within the clay core at the end of dam construction reach an average value of 0·4 MPa (two determinations). Recorded stresses in neighbouring points within the rockfill shells, close to the granular drains, show higher values, demonstrating the presence of arching effects due to the lower stiffness of the compacted clay core. Note that the dam geometry imposes a rapid change of height of compacted soil away from the core and arching effects develop. The model captures reasonably well the entire set of measurements. Of course, the large recorded stress variations within points close to each other (see, for instance, the records for the two stress cells within the clay core) cannot be reproduced by the model. In other respects the model is remarkably accurate. The model does not predict any significant delayed behaviour of stress development in the rockfill shells, as recorded. However, arching effects induced by the consolidation of the lower part of the clay core result in a calculated decrease of the vertical stresses, a phenomenon not observed in the field. Pore pressures in the core will be discussed below.

Table 5. Construction stages

		Model time	Dates	Modelling interval
Equilibrium of initial conditions		Time 0–100 days		1
Construction until elevation 874 m (see Fig. 1)		Time 100–280 days	1 July 2006–30 December 2006	2 3
Stop construction:		Time 280–460 days	1 January 2007–30 June 2007	4
Construction until elevation 886 m (see Fig. 1)		Time 460–520 days	1 July 2007–30 September 2007	5 6
Phreatic level red. and pre-loading	Pre-loading ramp	Time 520–560 days	1 September 2007–30 December 2007	7
	Pre-loading	Time 560–620 days		8
	Unloading	Time 620–640 days		9
Final construction (until elevation 895 m) (see Fig. 1)		Time 640–680 days	1 January 2008–30 February 2008	10
		Time 680–700 days		11

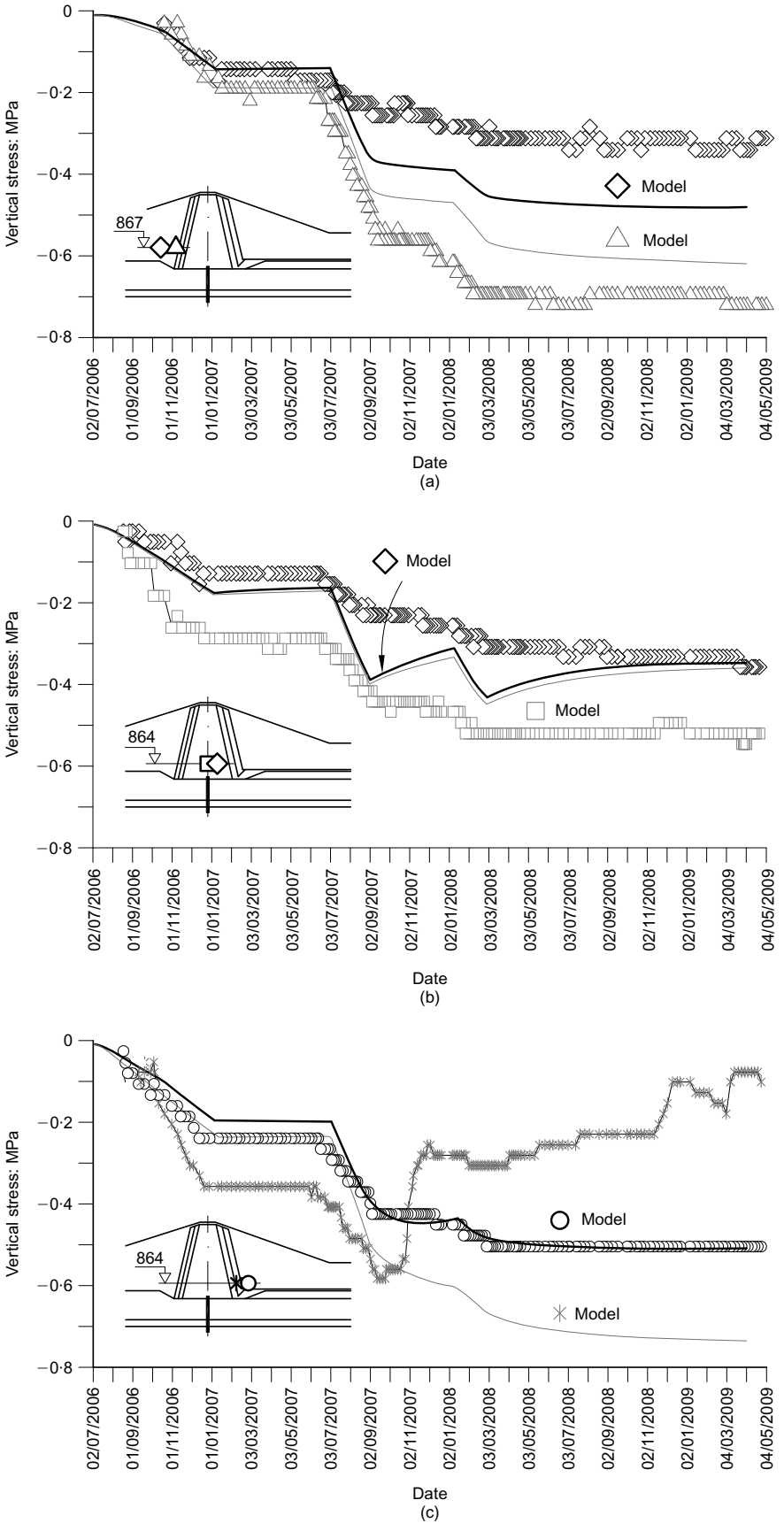

Fig. 21. Comparison of measured and calculated vertical stresses at elevation 867–864 m: (a) upstream rockfill near core; (b) clay core; (c) downstream rockfill near core

Figure 22 shows the calculated distribution of vertical stresses in the dam at the end of construction. Arching effects reduce the reference geostatic distribution of stresses in the core.

Calculated vertical displacements at elevation 876 m are compared with measurements in Fig. 23. In the upstream zone, near the core, measured displacements are somewhat overestimated by the calculated absolute displacements in the corresponding points. The reference for measurements was a fixed point in the slope of the valley. In contrast, in the case of the clay core and the downstream shoulder, the calculated values had to be corrected by substracting the settlement in the location where the reference measurement system was installed, as described above. Obviously this is not the best reference point but it had practical advantages. This situation can lead to measured values which apparently indicate an uplift of the soil, although all points experience settlements at all times. This trend is observed in the measured settlement records and it is more exaggerated in the calculations made. However, the magnitude of the measured values is in general well captured. Settlement records also react to the step-wise history of loading, but in a more progressive manner than the total stresses owing to consolidation effects in the foundation and the compacted structure.

Pore-water pressures are calculated and compared with measurements in Fig. 24. Piezometers could only measure small pressure deficiencies below the atmospheric value. In practice only positive values are measured. Consider first the piezometers located in the saturated foundation soil in vertical borings (Figs 24(a) and 24(c)). The measured time records reflect, in general, a hydrostatic distribution of pore pressures, controlled by the position of the water table. The dewatering period, especially the third one (final months of 2007), is reflected in all measurements. The model also reacts in a similar way.

The piezometer close to the base of the clay core, upstream of the cross-sectional axis (elevation 854·5 m) is interesting because it shows a steady increment of pore pressure due to the pore pressures accumulating slowly in the compacted core. The model calculations follow a sharper rate of pressure accumulation: pressure starts in a negative value (suction) but evolves rapidly to a positive pressure, which increases slowly and also follows the dewatering episodes.

The response of the clay core is plotted in Fig. 24(b). Piezometers located in upper levels (elevations 875·4 and 885 m) cannot record the prevailing suction. The model calculates suction values not shown in the figure because of the pressure scale of the graph. The piezometer located in the vicinity of the foundation (elevation 857 m) soon starts to record positive pore-water pressures. Model calculations start at the compaction suction and they show a progressive decrease in suction and, at some time during construction, the development of positive pore pressures. The model reacts to the rapid increase in total stresses by increasing the pore pressure (or by reducing suction). One period of rapid accumulation of stress was June–September 2007. It can be followed in the calculated response of the model but also on the reaction of the piezometers at lower elevation (857 m). The fast reductions in suction and the transient period towards a new equilibrium predicted by the model do not compare well with measurements. Interestingly, the piezometer at a higher elevation (864 m) begins to record positive pore-water pressures some time after the completion of the dam, in November 2008. This is not well captured by the model, which predicts an earlier development of positive pore pressures. The recorded increase of pore pressures at the end of the time period represented in Fig. 24 reflects the water level elevation upstream (6 m), which took place in March–April 2009.

Figure 25 shows the calculated distribution of pore-water pressures in the core at the end of construction. The model predicts a limited development of positive pore-water pressures in the lower third of the clay core. This result may be compared with the average value of recorded pore pressures in four cross-sections of the dam. The measured pore pressures in all four sections, in February 2008, once the dam was completed, have been plotted together by superimposing, averaging and smoothing the measurements (Fig. 25). The scatter of results in a given section and the limited number of piezometers installed makes this approach a reasonable one to derive an integrated and global picture of the core hydraulic behaviour. Piezometers were located in the downstream half section of the core and therefore no information on the upstream half is available. The calculated response is plotted in Fig. 25 for two dates: February 2008 and April 2009. The model predicts higher pore pressures in the lower part of the core, although it correctly predicts that the upper two-thirds of the dam core remain unsaturated. Once the dam was completed, calculated excess pore pressures dissipate at a relatively fast rate. This dissipation and the associated core settlement was the reason for the transient stress reduction shown in Fig. 21(b). Measured pore pressures were lower and their recorded dissipation was very slow. This discrepancy may be explained by a lower-than-assumed compacted water content in shells and core and also by errors in the assumed water retention and permeability parameters of both materials. However, no attempt to modify them in order to fit the actual measurements was made.

PREDICTION OF DAM BEHAVIOUR DURING IMPOUNDMENT

The protocol for dam impoundment has not yet been defined for Lechago dam. The assumption made here is that impoundment takes place at a maintained rate of 0·1 m/day until the maximum elevation (892 m). Figs 26–28 show the calculated response of the dam in terms of vertical stresses, vertical displacements and pore-water pressures. The plots

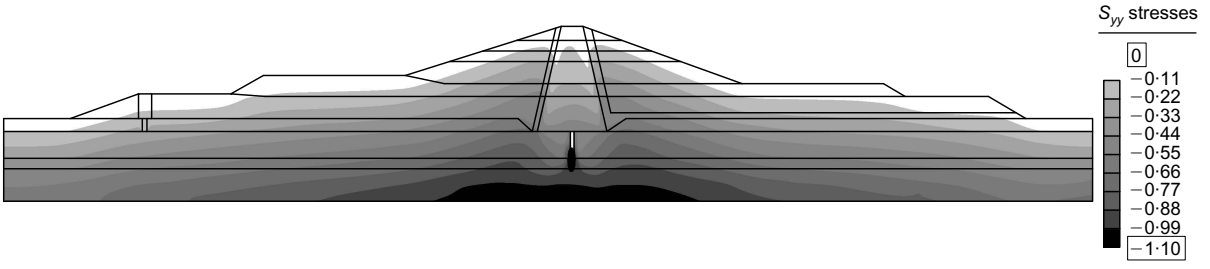

Fig. 22. Calculated contours of vertical stress at the end of dam construction

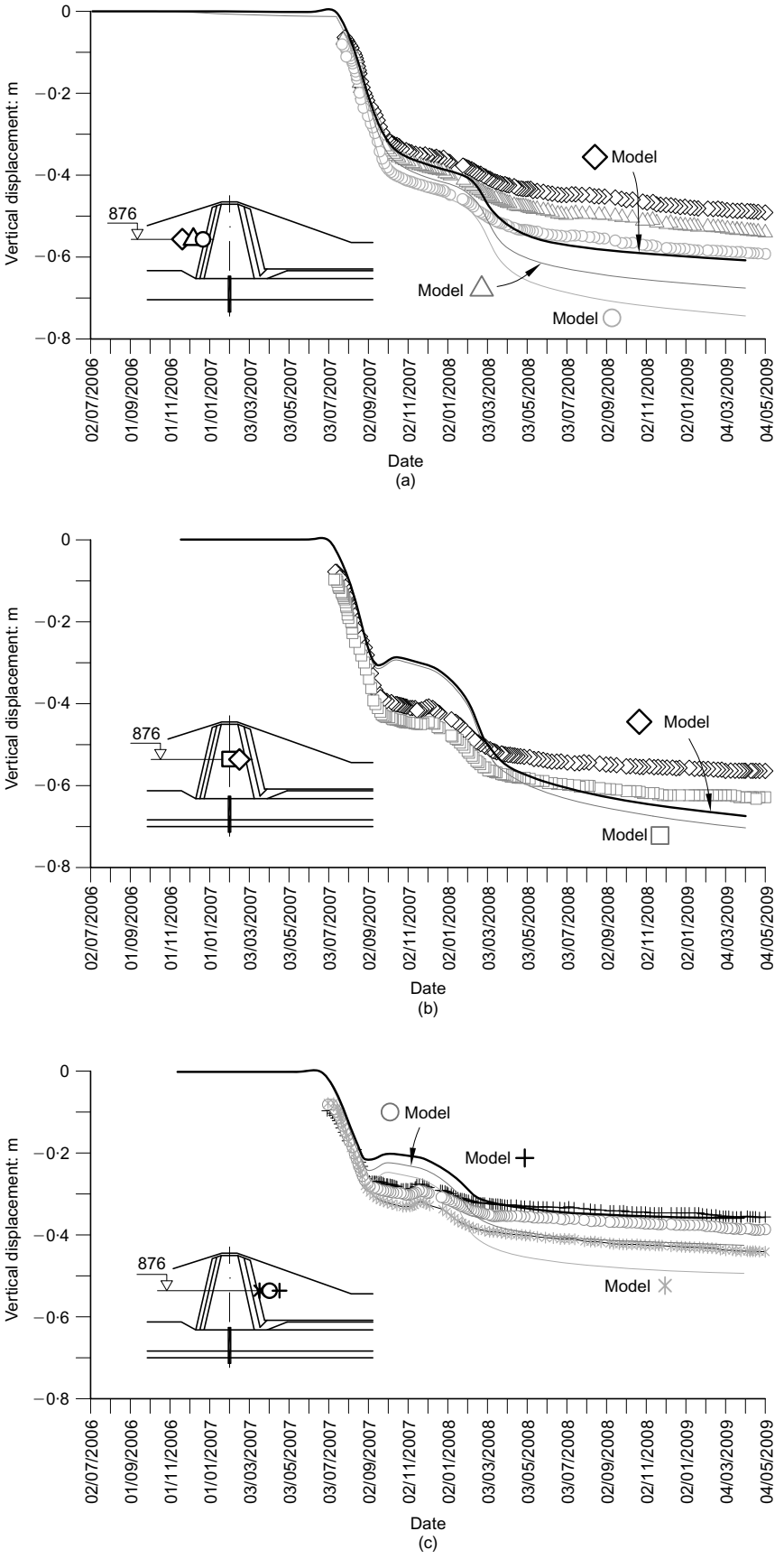

Fig. 23. Comparison of measured and calculated differences of vertical displacements between the measurement gauge and the reference location, elevation 876 m: (a) upstream rockfill near core; (b) clay core; (c) downstream rockfill near core

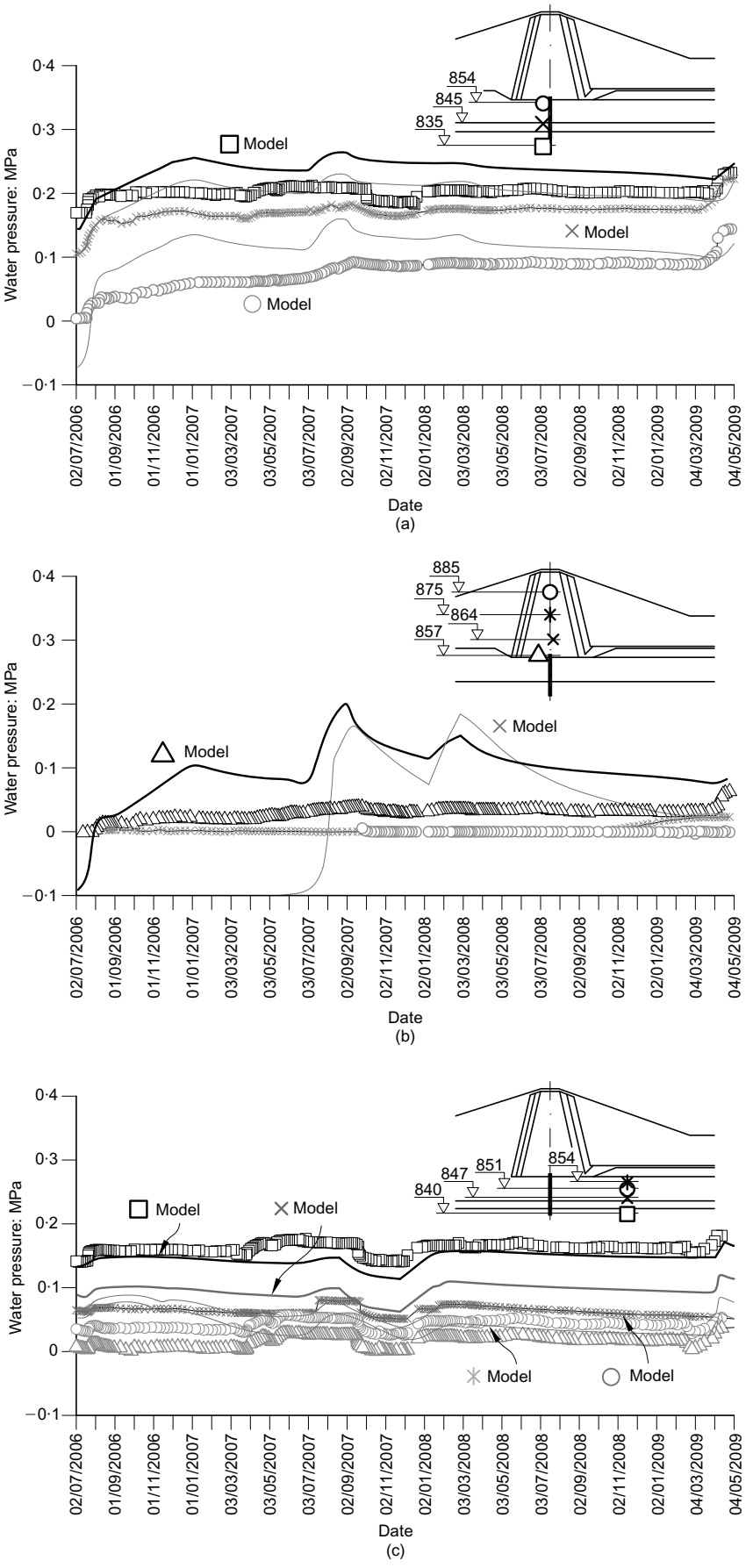

Fig. 24. Comparison of measured and calculated pore-water pressures in the locations indicated: (a) foundation soils, under the core; (b) clay core; (c) foundation soils, downstream

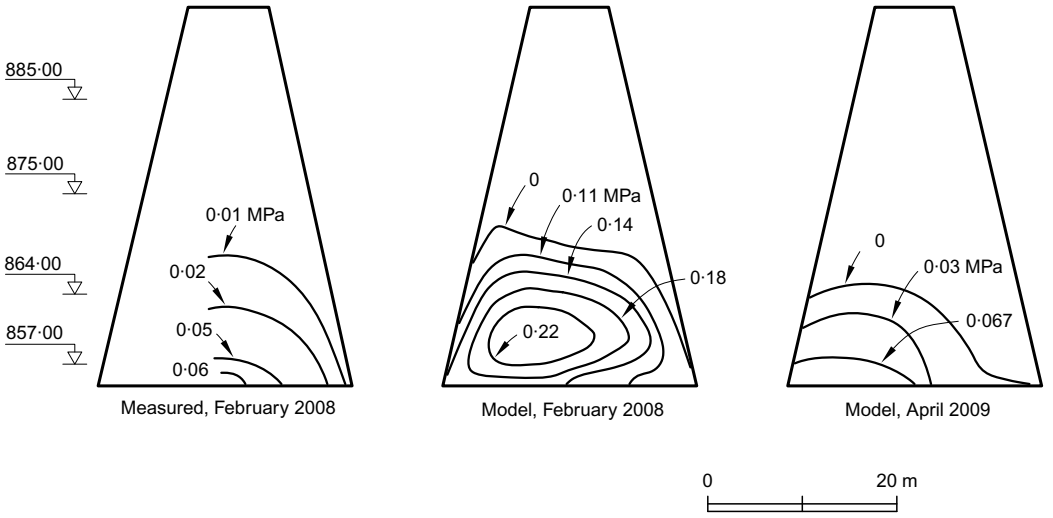

Fig. 25. Average measured pore pressures in cross-sections P-8, P-10 and P-12 in February 2008 and computed results in February 2008 and April 2009

refer to the position of instruments in the central cross-section of the dam, given in Figs 21, 23 and 24. The time origin in Figs 26–28 is the final calculation time for the construction phase. This origin may change when the actual impoundment starts.

Figure 26(a) shows a moderate increase of stresses at elevation 867 m, upstream of the core, due to the increase in total unit weight of the shell during its saturation. Inside the core (close to saturated conditions) and downstream the expected change in stresses is very small. Collapse-induced settlements calculated at elevation 876, are very small and a slight heave is predicted due to reduction of effective stress during impoundment (Fig. 27(a)). Downstream the expected settlement is even smaller. The maximum response concerns expected water pressures. The points within the foundation follow essentially the hydrostatic increase in pressure (Fig. 28(a)). The core is progressively saturated and pore pressures change from negative (suction) to positive values in the manner indicated in Fig. 28.

CONCLUSIONS

Lechago dam integrates widely different materials: a soft saturated clay foundation, wide rockfill shells to ensure stability and a core of compacted, medium-plasticity Miocene clay. Material properties could be derived from different sources. The dam provision process followed standard practice, which provided initial information on the properties of the foundation soils, the clay core and the rockfill.

Rockfill behaviour, however, was investigated in more detail and large-diameter tests on compacted specimens of the quartzitic shale used in the shells became available. These tests were performed under RH control, following recent developments which highlight the relevance of this variable to control the constitutive behaviour of coarse granular aggregates. The highly fractured quartzitic shale led, after quarrying, to a coarse gravel-like granular material whose grain size distribution can be reasonably well reduced to be tested in a 25 cm diameter triaxial cell.

Triaxial tests on rockfill have been simulated by discretising the specimens and following the actual sequence of RH changes and load increments. The RM used reproduces satisfactorily the isotropic stress–volumetric strain as well as the deviatoric stress–strain records. Difficulties are found in capturing the measured dilatancy.

Conventional wetting under load oedometer tests was simulated in a similar way to derive material parameters for the clay core.

The central cross-section of the dam was discretised and the actual construction sequence was applied. Specific features of Lechago construction are the preloading of the downstream shell to improve the undrained strength of the soft foundation deposits and the dewatering of the foundation soils for the same purposes. These operations resulted in a staged construction of the dam, which lasted 2 years.

The comparison between dam performance and model calculation involved three types of measurements in time: vertical total stress in core and rockfill, settlements of the dam at different levels and (positive) pore-water pressures in the clay core. These measurements are available at different elevations and at several vertical profiles in the natural foundation soils.

Measured vertical stresses were remarkably consistent despite the difficulties often encountered with these instruments. They indicated some arching phenomena in the softer core, which was captured by the model. Stress developments also closely matched calculations in most cases.

Settlement includes the response of the soft foundation and the compacted structure. Despite the difficulties in matching actual field conditions with the laboratory experiments available, the model performance is reasonably good. Lechago experienced large total settlements close to 1 m in the central section.

Pore-water pressures in the core cannot be determined unless they reach positive values. This prevents the proper evaluation of model performance in the unsaturated regions. However, the development in time of positive pore pressures (starting at a condition of partial saturation) is an indirect and useful check of the calculations. It has been shown that the lower third of the core develops positive pore pressures in the range 0·01–0·06 MPa (the latter in the base of the dam core). The model also predicts positive pore-water pressure developments in the lower part of the dam. This is a check and a further validation of the model and the set of parameters selected.

However, there are difficulties in practice which cannot be overlooked. At the design stage properties of compacted materials are established on the basis of a few laboratory tests performed in a variety of specimens with the purpose of selecting the most appropriate soil type. Later, field

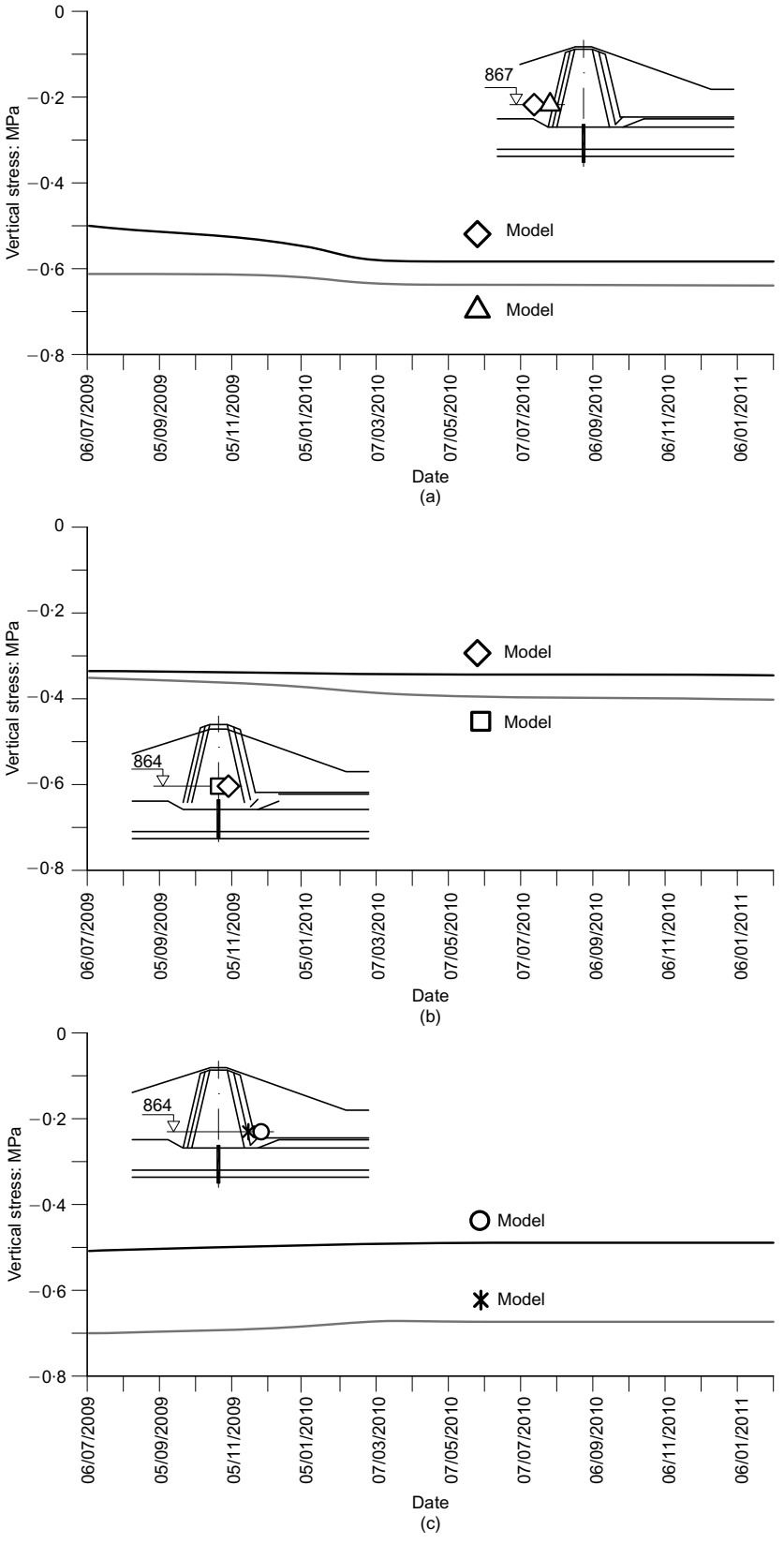

Fig. 26. Calculated vertical stresses at elevation 867–864 m during dam impoundment: (a) upstream rockfill near core; (b) clay core; (c) downstream rockfill near core

compaction techniques and specifications may experience significant changes if compared with the project specifications. Lechago is not an exception.

Attained densities, reference compaction energies and water content limits were modelled to a certain extent. The natural variability of quarries adds further uncertainties. Therefore, the reasonable response of the model and its satisfactory comparison with some measurements may include some fortuitous coincidences.

The model was used to explore the future behaviour of

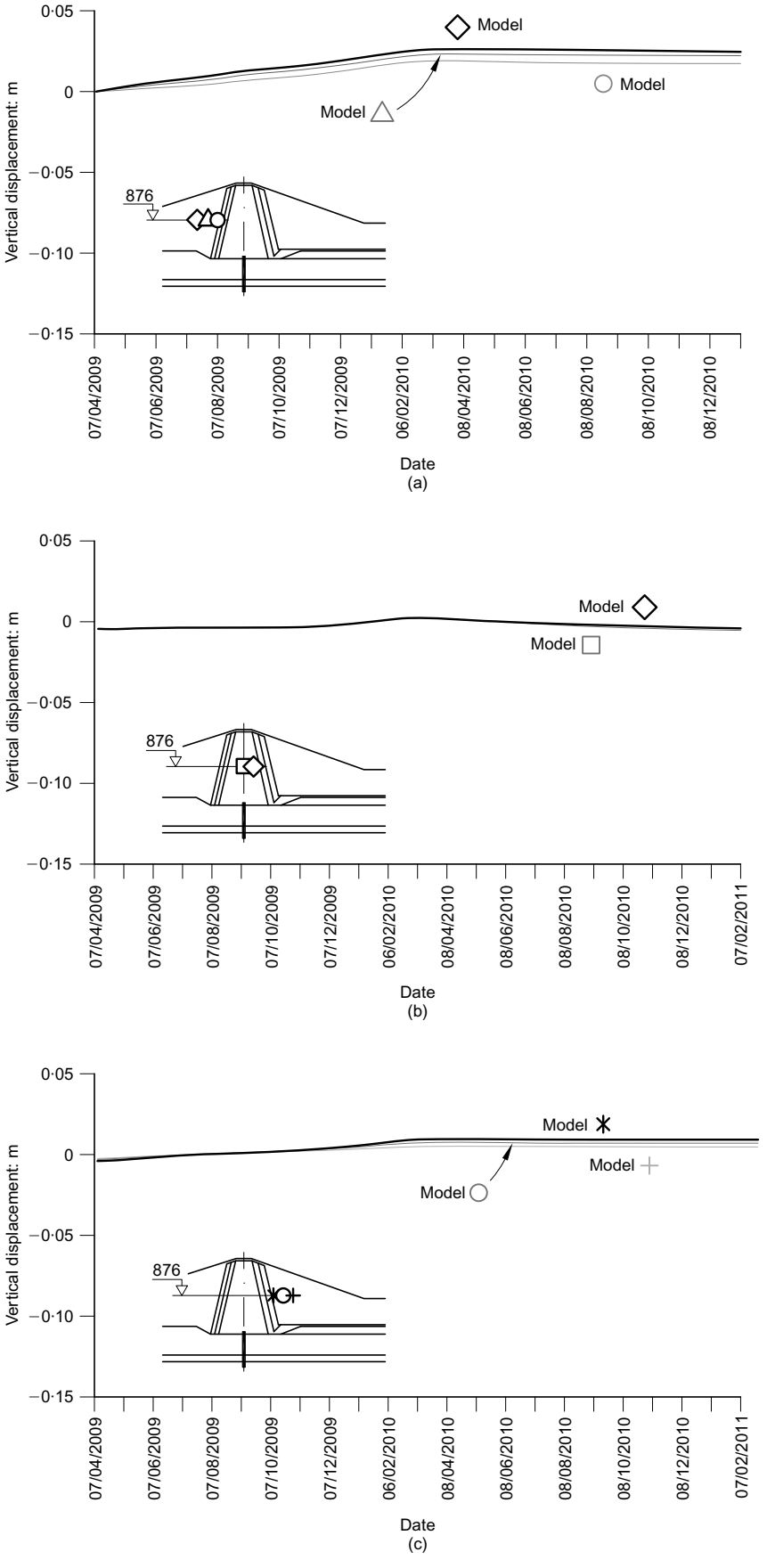

Fig. 27. Calculated differences of vertical displacements between the measurement gauge and the reference location during dam impoundment, elevation 876 m: (a) upstream rockfill near core; (b) clay core; (c) downstream rockfill near core

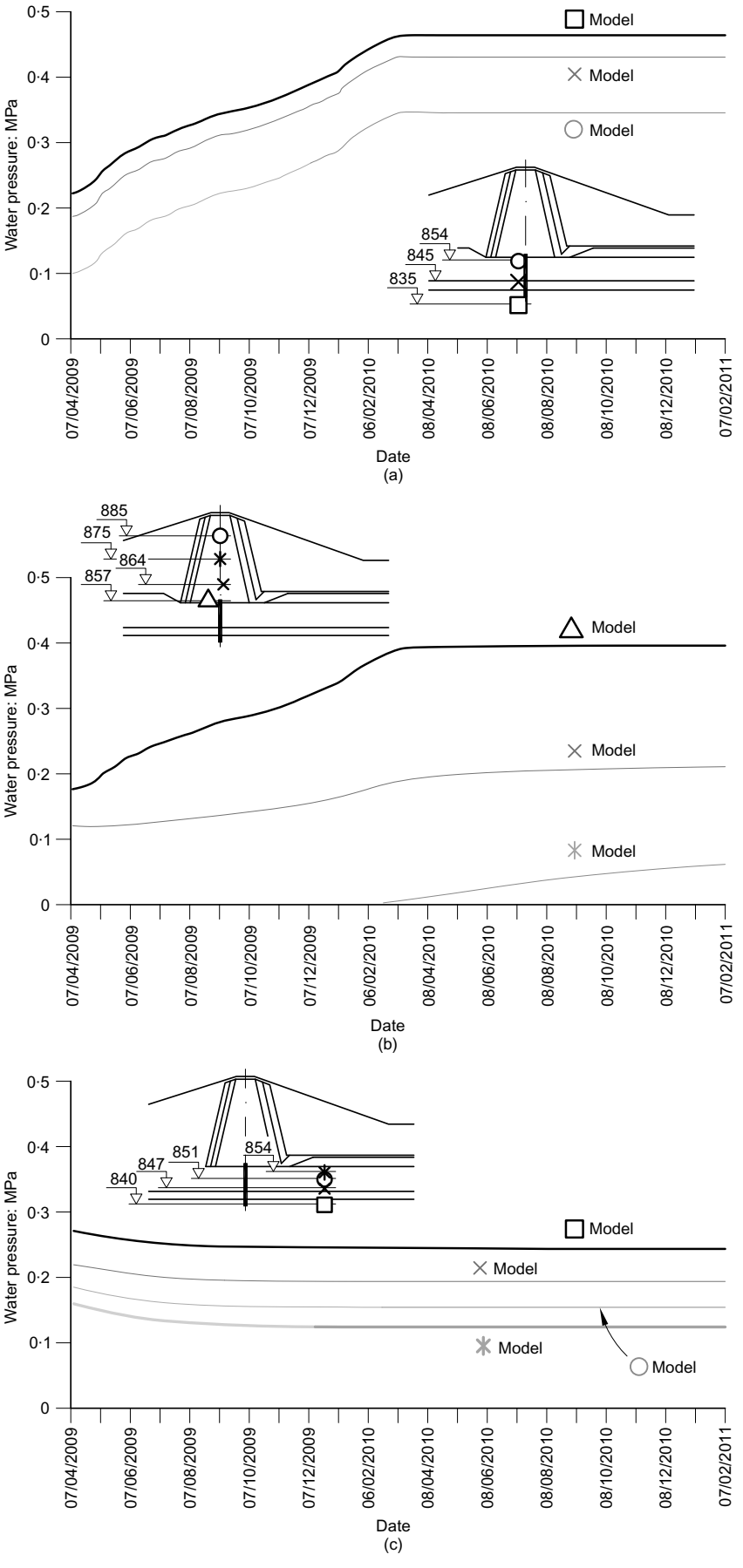

Fig. 28. Calculated pore-water pressures in the locations indicated during dam impoundment: (a) foundation soils, under the core; (b) clay core; (c) foundation soils, downstream

the dam during impounding and some predictions of stress, settlements and pore pressure developments at the position of installed instruments have been given in the paper in order that they could be compared in the future with actual measurements.

REFERENCES

Alonso, E. E., Gens, A. & Josa, A. (1990). A constitutive model for partially saturated soil. *Géotechnique* **40**, No. 3, 405–430, **doi**: 10.1680/geot.1990.40.3.405.

Alonso, E. E., Olivella, S. & Pinyol, N. M. (2005). A review of Beliche Dam. *Géotechnique* **55**, No. 4, 267–285, **doi**: 10.1680/geot.2005.55.4.267.

Chávez, C. (2004). *Estudio del comportamiento triaxial de materiales granulares de tamaño medio con énfasis en la influencia de la succión*. PhD thesis, Universitat Politècnica de Catalunya, Barcelona, Spain.

Chávez, C. & Alonso, E. E. (2003). A constitutive model for crushed granular aggregates which includes suction effects. *Soils Found*. **43**, No. 4, 215–227.

Chávez, C., Romero, E. & Alonso, E. E. (2009). A rockfill triaxial cell with suction control. *Geotech. Testing J.* **32**, No. 3, 219–231.

Coussy, O. (1995). *Mechanics of porous continua*. Chichester, UK: Wiley.

Daehn, W. W. (1985). Behaviour of a rolled earth dam constructed on a compressible foundation. *Proc. 5éme Congrès des Grands Barrages, Paris* **Q18**, R7, 171–191.

DIT-UPC (2002). *Code_Bright. A 3-D program for thermo-hydro-mechanical.analysis in geological media. User's guide*. Barcelona, Spain: Centro Internacional de Métodos Numéricos en Ingeniería (CIMNE).

Gens, A., Sanchez, M., Guimaraes, LdN. *et al.* (2009). A full-scale in situ heating test for high-level nuclear waste disposal: observations, analysis and interpretation. *Géotechnique* **59**, No. 4, 377–399, **doi**: 10.1680/geot.2009.59.4.377.

Oldecop, L. (2000). *Compresibilidad de escolleras. Influencia de la humedad*. PhD thesis, Universitat Politècnica de Catalunya, Barcelona.

Oldecop, L. & Alonso, E. E. (2001). A model for rockfill compressibility. *Géotechnique* **51**, No. 2, 127–139, **doi**: 10.1680/geot.2001.51.2.127.

Oldecop, L. & Alonso, E. E. (2003). Suction effects on rockfill compressibility. *Géotechnique* **53**, No. 2, 289–292, **doi**: 10.1680/geot.2003.53.2.289.

Oldecop, L. & Alonso, E. E. (2007). Theoretical investigation on the time dependent behaviour of rockfill. *Géotechnique* **57**, No. 2, 289–301, **doi**: 10.1680/geot.2007.57.2.289.

Olivella, S. & Alonso, E. E. (2008). Gas flow through clay barriers. *Géotechnique* **58**, No. 3, 157–176, **doi**: 10.1680/geot.2008.58.3.157.

Olivella, S., Carrera, J., Gens, A. & Alonso, E. E. (1994). Non-isothermal multiphase flow of brine and gas through saline media. *Transp. Porous Media* **15**, No. 3, 271–293.

Olivella, S., Gens, A., Carrera, J. & Alonso, E. E. (1996). Numerical formulation for simulator (CODE_BRIGHT) for coupled analysis of saline media. *Engng Comput*. **13**, No. 7, 87–112.

Ramírez, J. L., Soriano, A. & Serrano, C. H. (1991). Design and construction of Barbate dam. *Proc. 17th ICOLD, Vienna, Austria* **Q67**, R8, 129–163.

Rizzoli, J. L. (1991). Observations du comportement de fondations compressibles: barrages des retenues Seine, Aube et dique de Lazer. *Proc. 17th ICOLD, Vienna, Austria* **Q66**, R8, 129–163.

Tellería, J. & Gómez Laa, G. (1991). Arbon dam: A didactic experience about problems of a dam built on a deformable foundation. *Proc. 17th ICOLD, Vienna, Austria* **Q66**, R9, 135–156.

Torner, V. & Novosad, S. (1991). The effect of difficult foundation conditions on the conceptual solution and construction of the Slezská Harte dam. *Proc. 17th ICOLD, Vienna, Austria* **Q66**, R40, 719–730.

Trkeshdooz, R., Nafissiazar, F. & Rastegari, Y. (1991). Effects of foundation conditions on the design of Taleghan embankment dam. *Proc. 17th ICOLD, Vienna, Austria* **Q66**, R75, 1415–1488.

van Genuchten, M. T. (1980). A closed-form equation for predicting the hydraulic conductivity of unsaturated soils. *Soil Sci. Soc. Am. J.* **44**, 892–898.

Thorel, L. *et al.* (2011). *Géotechnique* **61**, No. 5, 409–420 [**doi:** 10.1680/geot.10.P.029]

Physical modelling of wetting-induced collapse in embankment base

L. THOREL*, V. FERBER*†, B. CAICEDO‡ and I. M. KHOKHAR*

The relevance of the oedometer tests used for the prediction of wetting-induced deformations in embankments is examined. Single and double oedometer tests are carried out. A comparison is made between laboratory tests and geotechnical centrifuge modelling at 100*g* conducted to examine an inundated embankment made of a sand–clay mixture. A 20 cm high embankment model is built and instrumented. The material is compacted on the 'dry side' of the optimum Proctor curve at a low compaction rate in order to emphasise settlement phenomena. The inundation simulation is conducted in two successive sequences during centrifuge flight up to a water table of 5 cm. The results prove that the prediction of the dry density after settlement due to inundation is good.

KEYWORDS: centrifuge modelling; collapsed settlement; compaction; embankments; settlement

On examine la pertinence de tests sur oedomètre effectués pour la prédiction de déformations induites par l'imbibition dans les talus. On effectue des essais oedométriques simples et doubles, ainsi qu'une comparaison entre des essais en laboratoire et une modélisation en centrifuge géotechnique à 100 *g*, réalisée pour étudier un talus inondé constitué d'un mélange de sable et d'argile. On réalise une maquette du talus de 20 cm de haut, dûment instrumentée. Le sol est compacté du côté sec de l'optimum Proctor, pour obtenir une faible compacité afin de magnifier le phénomène de tassement. L'inondation est simulée en deux phases successives, au cours de la centrifugation, jusqu'à atteindre un niveau de nappe de 5 cm. Les résultats permettent d'affirmer que la prédiction de la densité sèche après un tassement dû à une inondation est bonne.

INTRODUCTION

The use of dry soil materials for the construction of roadway and railway embankments is limited to small embankments, which, however, must plainly comply with compaction requirements (LCPC, 2003). The compaction of dry soils is energy consuming and does not prevent settlement from happening in the case of soaking. A survey of the literature reveals that the compaction rate is one main parameter affecting long-term deformations of embankment bases (Lawton *et al.*, 1992; Auriol *et al.*, 2000).

This problem is crucial for countries combining naturally dry soils and notable flood hazard, where highways construction programmes involving the construction of high embankments are developed (e.g. in Morocco: ADM, 2006). Therefore, the understanding of dry compacted soil behaviour must be improved in order to optimise embankment compaction for better stability in relation to settlement risks.

Frequently, the wetting-induced behaviour of compacted soils results in 'collapsing'. Settlement mechanisms depend on the following factors.

(*a*) The compaction water content (or the suction) and the dry density after compaction. Collapse occurs mainly in dry and loose soils (Lawton *et al.*, 1992). The compaction of dry soils can induce low dry densities if the compaction energy is not high enough. According to Ferber *et al.* (2008), the dry density after wetting under a given vertical stress is affected by the initial dry density and not by the compaction water content. However, some authors have observed some effects relative to the water content (Basma & Tuncer, 1992).

(*b*) The vertical stress applied during the inundation. Collapse settlement, in fact, increases with increasing vertical stress (Lawton *et al.*, 1992); that is, the collapse potential increases within the embankment deeper layers.

(*c*) The intrinsic properties of the soil, such as critical clay content (Lawton *et al.*, 1992; Rollins *et al.*, 1993) or plasticity index (Lim & Miller, 2004), which depends on the non-clayey fraction of the soil. This critical clay content ranges between 10 and 40% (El Sohby & Rabbaa, 1984), depending on the vertical stress and probably on the grain size distribution of the non-clayey fraction (Basma & Tuncer, 1992).

(*d*) The stress anisotropy during the inundation (Lawton *et al.*, 1989).

(*e*) The water content increase (or the suction decrease). The settlement increases non-linearly with the suction decrease (El-Ehwany & Houston, 1990; Pereira & Fredlund, 2000).

Regarding soil physical properties, the dry density after compaction is the predominant parameter affecting wetting-induced deformations under vertical stress (Lawton *et al.*, 1992; Rao & Revanasiddappa, 2000; Estabragh *et al.*, 2004; Ferber *et al.*, 2008). Moreover, the long-proposed experimental methods for the prediction of wetting-induced deformations, like the single or double oedometer tests (Jennings & Knight, 1957), although remaining pertinent (Basma & Tuncer, 1992), need to be compared with observations like physical models. Physical modelling has already been used to study the collapse of embankments (Miller *et al.*, 2001) without, however, ever focusing on the relationship between initial dry density and settlement.

This paper presents a study conducted on a small-scale embankment made of a dry and loosely compacted sand–clay mixture (SCM) using the Laboratoire Central des Ponts et Chaussées (LCPC) geotechnical centrifuge. The objective of the comparison with oedometer tests is to examine and quantify the effect of a low compaction rate on settlement in

Manuscript received 8 March 2010; revised manuscript accepted 20 December 2010. Published online ahead of print 22 March 2011. Discussion on this paper closes on 1 October 2011, for further details see p. ii.

* L'Université Nantes Angers Le Mans, Laboratoire Central des Ponts et Chaussées, Centre de Nantes (Geotechnical Engineering, Environment and Risks Department, Physical Modelling in Geotechnics Unit), Bouguenais, France.

† Entreprise Charier, Montoir de Bretagne, France.

‡ Civil and Environmental Engineering Department, Universidad de los Andes, Bogotá, Colombia.

case of inundation, and to assess the relevance of laboratory test-based predictions. As the model embankment is compacted in loose conditions, which do not represent actual field conditions, the results are presented at the model scale only. The extrapolation to prototype scale has to be carried out using the classical scaling laws for displacement, time and flow velocity (Garnier *et al.*, 2007).

The laboratory tests carried out to measure soil geotechnical characteristics and hydromechanical performances are first presented. Then, the centrifuge test is described and the results discussed. Finally, a comparison is made between centrifuge and laboratory results.

LABORATORY RESULTS

The SCM components used for the centrifuge tests are presented first. The oedometer test results are discussed in a separate subsection.

Materials

The SCM consists of a mixture of Speswhite kaolin and NE34 Fontainebleau sand. The sand is characterised by a very narrow particle size range (Fig. 1) and a negligible fine content (Table 1). Because of these unusual properties, the compaction of the sand is not very sensitive to water content, which accounts for the 'flat' shape of the Proctor curve (Fig. 2). The absence of fines makes it difficult to densify, as illustrated by the low maximum dry density (MDD = 1·51 t/m^3, Table 1).

The clay is a purified kaolin made of 77% clay particles (Table 1, Fig. 1) and characterised by a plasticity index of almost 23. The optimum moisture content is 29% for MDD = 1·42 t/m^3 (Fig. 2). The clay fraction is mostly composed of kaolin minerals, among which some traces of illite have been detected.

The SCM used for the tests is composed of 40% Speswhite kaolin and 60% Fontainebleau sand. Therefore, the material characteristics are a combination of those of the clay and the sand. The clay content places it within the range of collapsible soils (El Sohby & Rabbaa, 1984). The compaction characteristics and the shape of the standard Proctor curve are similar to those of a clayey sand material and the plasticity index is low (Table 1).

The SCM water retention curve, obtained using the osmotic method, is presented as a function of suction and height of water above the water table (Fig. 3).

Single and double oedometer tests

Collapse is a wetting-induced phenomenon, which must be studied by describing accurately the effects of both inundation and vertical stress. In this section the procedures and the results of the laboratory tests involving both saturation and vertical stress variation are presented.

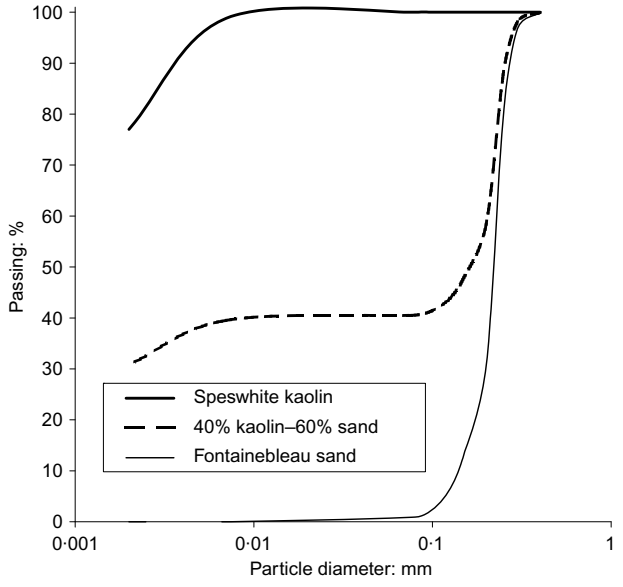

Fig. 1. Grain size distribution of the Fontainebleau sand, the Speswhite kaolin and the SCM

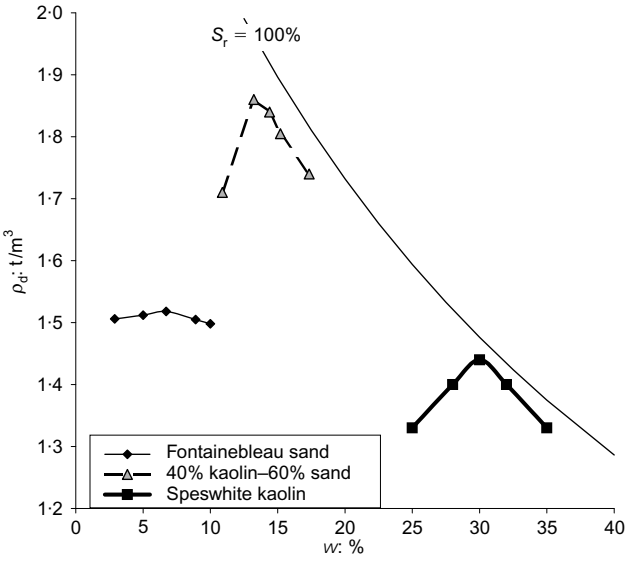

Fig. 2. Standard Proctor curves on the Fontainebleau sand, the Speswhite kaolin and the SCM

Table 1. Geotechnical characteristics of the soils

Characteristic	Fontainebleau sand	Speswhite kaolin	40% kaolin–60% sand
$C_{400\ \mu m}$: %	100	100	100
Fines content: %	0·01	100	40
Clay content: % < 2 μm	0	77	31
Liquid limit, w_L: %	—	55·1	25
Plastic limit, w_P: %	—	32·3	14
Plasticity index, I_P: %	—	22·8	11
Methylene blue absorption value: g/100 g	0·1	1·54	0·6
Density of solid particles, ρ_s : g/cm^3	2·64	2·65	2·65
Std Proctor optimum water content: %	7	29	13·5
Std Proctor optimum dry density MDD: g/cm^3	1·51	1·42	1·87
Std Proctor optimum degree of saturation: %	24·7	88·7	85·8

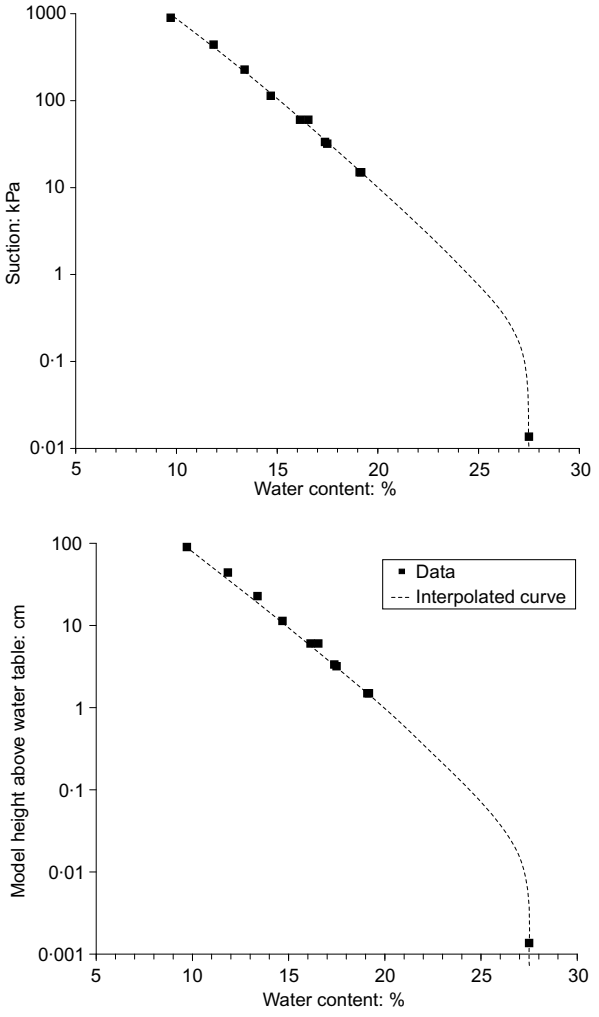

Fig. 3. SCM water retention curve

Procedures. The tests are carried out in oedometer cells 70 mm in diameter and 19 mm thick. After the sand and clay are mixed, tap water is added to reach the required water content. The material is kept in sealed bags for at least 24 h.

After the curing time, the specimens are compacted directly in the oedometer cells using a miniaturised dynamic hammer (Ferber *et al.*, 2008). Thus, the dry density is directly related to the number of blows of the hammer, in other words, to the compaction energy. The method has the advantage of reproducing the compaction phenomena associated with the Proctor test compaction. Two tests, during which the same compaction energy is applied on the material at constant water content, give similar dry densities.

The tests consist of loading and/or soaking the specimens according to three different paths (Fig. 4):

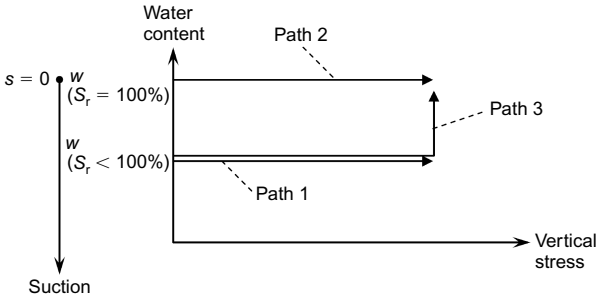

Fig. 4. Hydromechanical paths

(*a*) loading unsaturated specimens at a constant water content (path 1), simulating the construction of an embankment
(*b*) loading saturated specimens (path 2) according to the conventional oedometer test
(*c*) soaking specimens after loading at a given vertical stress (path 3) to simulate the inundation of compacted fills occurring by way of, for instance, flooding.

In the case of path 1, the water content is kept constant during the test by protecting the cells from the ambient air using a plastic membrane (Delage & Fry, 2000). The increase in vertical stress is obtained by loading the frame with increasing masses. The specimen mass is measured before and after the test to determine water content variations, showing a decrease of 0·5 points at the highest water content (e.g. from 11 to 10·5%). The degree of saturation corresponding to a water content of 11% is 39% for an initial void ratio of 0·75 and 43% for $e = 0{\cdot}68$.

Path 2 corresponds to a conventional oedometer test carried out on a soil compacted at a given water content and a given compaction energy, then loaded under a 3 kPa vertical stress, and finally soaked. Very small deformations result from this saturation since the soil is not expansive. The mechanical load is applied when all deformations are completed. Paths 1 and 2 correspond to the elementary tests of the double oedometer test procedure.

Path 3 is performed on specimens compacted at different dry densities but at the same water content. Six different vertical loads are applied on the specimens, between 3 and 800 kPa. These vertical stresses correspond to the stress undergone by a material found at the base of an approximately 40 m high embankment. The initial void ratio range between 0·39 and 0·74 corresponds to initial dry densities between 1907 kg/m^3 and 1526 kg/m^3.

Test results. The unsaturated and saturated oedometer test results are plotted together in Fig. 5. Because of their low dry density (high void ratio), no preconsolidation stress is observed for the specimens compacted for the saturated oedometer tests. The resulting compression index is approximately 0·2. The four saturated test results do not merge, showing a discrepancy, which illustrates an inherent uncertainty. A void ratio amplitude of approximately 0·4 is observed. This uncertainty is highly dependent on the initial void ratio because the tests reveal that the void ratio at all the stresses increases with increasing initial void ratio (3 kPa) (Fig. 5).

The unsaturated tests present a substantial preconsolidation stress (400–800 kPa). It is the limit between the elastic (for low stresses) and plastic (for high stresses) zones, which is typical of the unsaturated behaviour of low-plasticity compacted soils (Alonso *et al.*, 1990). The elastic compression index, which corresponds to the slope of the curve for a vertical stress lower than the preconsolidation stress, is 0·01, whereas the plastic compression index determined from the data obtained at 800 and 1400 kPa, is 0·25. Finally, the void ratio difference for the three tests is only 0·025 on average. As for the saturated tests, this uncertainty is probably controlled by the initial void ratio.

The unsaturated curves are located ‘above’ the saturated curves for vertical stresses higher than 30–60 kPa. It shows that, above this threshold, the specimen is subject to settlement if water is added. On the contrary, below 30 kPa, swelling occurs with the addition of water.

The vertical stress influence on the deformation type and amplitude is confirmed by the results of the single oedometer tests (Fig. 6) according to path 3 (Fig. 4). Swelling

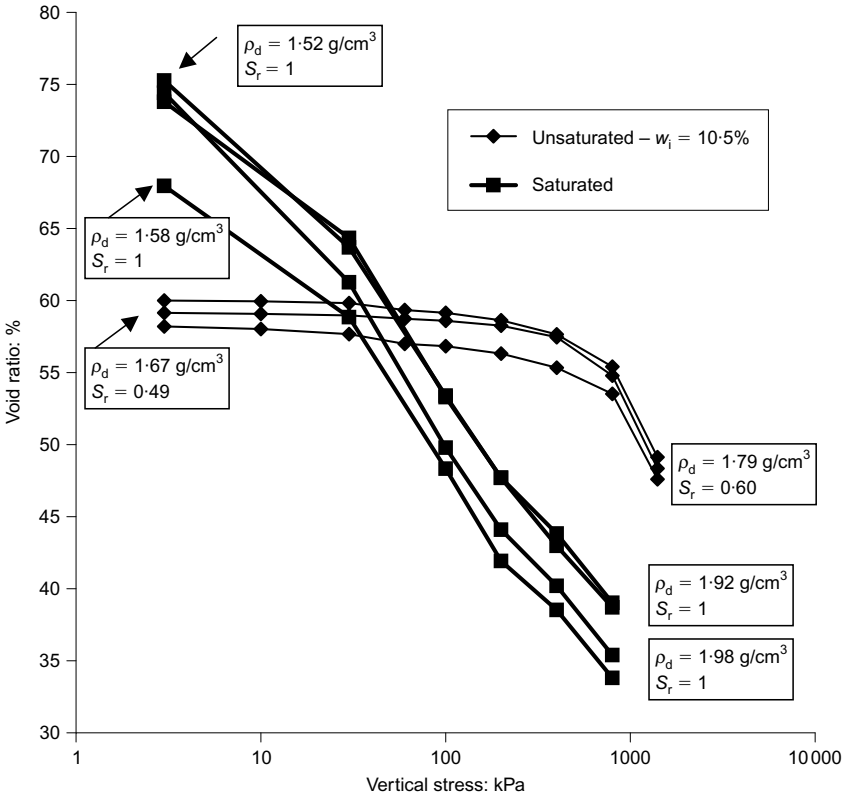

Fig. 5. Double oedometer tests on the compacted SCM

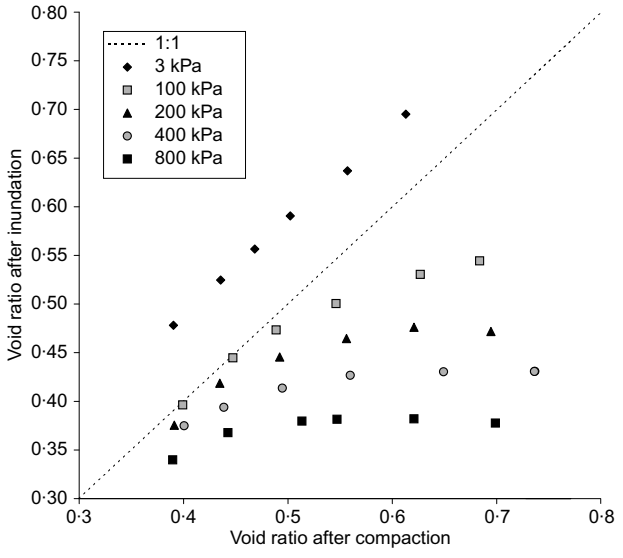

Fig. 6. Void ratio after inundation in single oedometer tests on the compacted SCM ($w_i = 11\%$)

occurs within specimens inundated with a vertical stress of 3 kPa, but, when the vertical stress is higher than 100 kPa, settlements occur all the more extensively since the initial void ratio is high. Therefore, the void ratio after inundation does not depend on the void ratio after compaction. For example, the void ratio after inundation of specimens inundated with an 800 kPa vertical stress is about 0·38 for the four loosely compacted specimens (void ratios within the range 0·5–0·7). Similar characteristics are observed for 200 and 400 kPa. This is consistent with the observations from the literature on low-plasticity compacted soils (Ferber *et al.*, 2008).

When the final void ratio after collapse of loose specimens is plotted against vertical stress (Fig. 7), the data are found on the compression curve of the saturated oedometer test. This means that the conventional compression curve of the saturated oedometer test can be used to predict the void ratio after collapse and, consequently, the collapse deformations.

CENTRIFUGE TEST PREPARATION AND PROCEDURE

A two-dimensional SCM embankment scale model, represented on the 1/100 scale, is inundated during a centrifuge flight at 100***g***. A description of the experiment is first

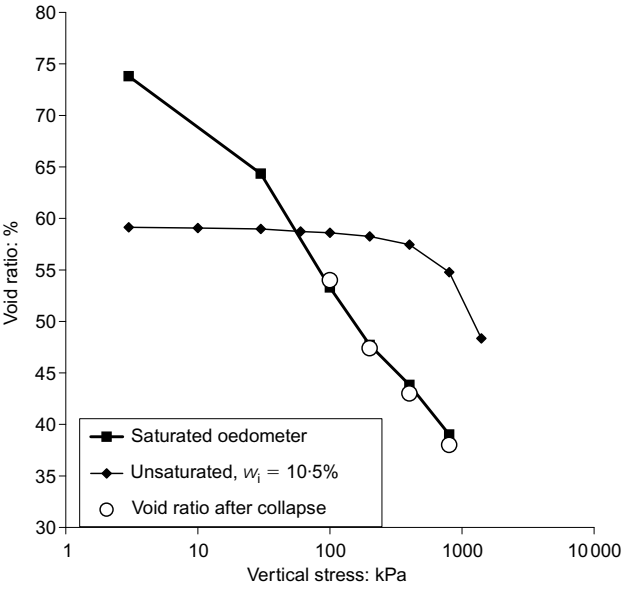

Fig. 7. Comparison between the results of single and double oedometer tests

proposed, then some information on the model post-construction SCM characteristics is given to characterise the initial state.

Experimental set-up and preparation

For the purposes of the experiment, a two-dimensional half cross-section of the embankment, which is assumed symmetrical, is built (Fig. 8) inside a strongbox consisting of (Fig. 9):

(*a*) a main compartment, 20 cm wide and 60 cm long, in which the material is compacted
(*b*) some lateral compartments communicating with the main compartment, in which the height of water can be measured

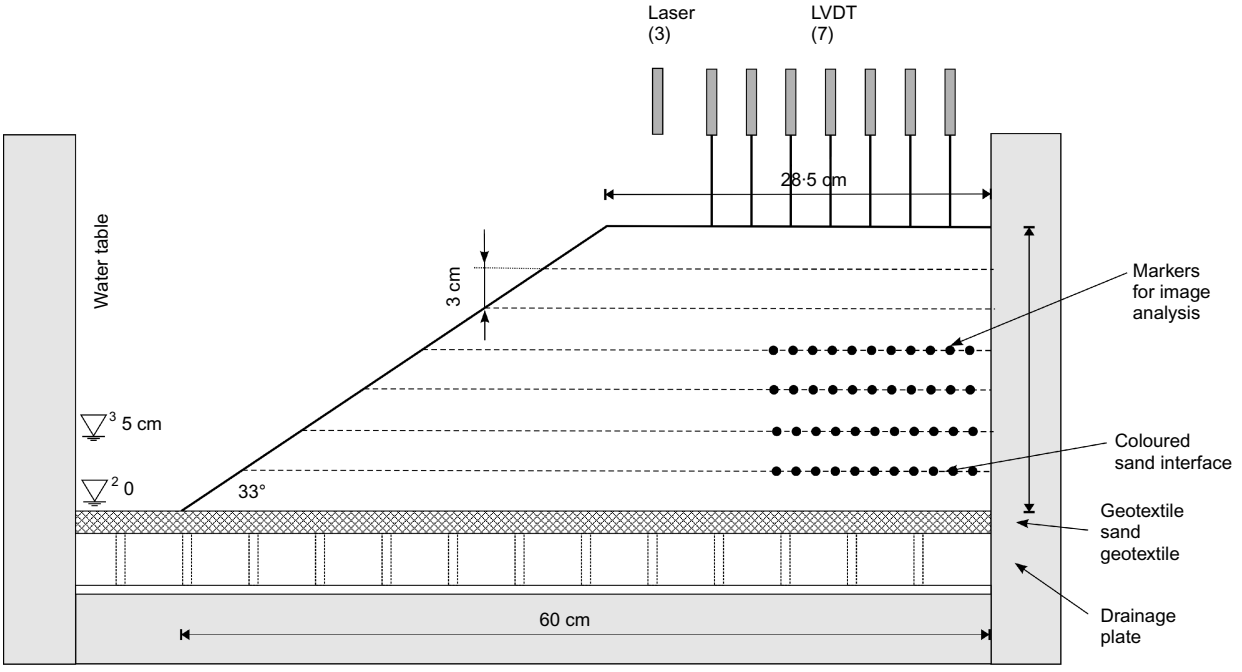

Fig. 8. Cross-section of the embankment model in the strongbox

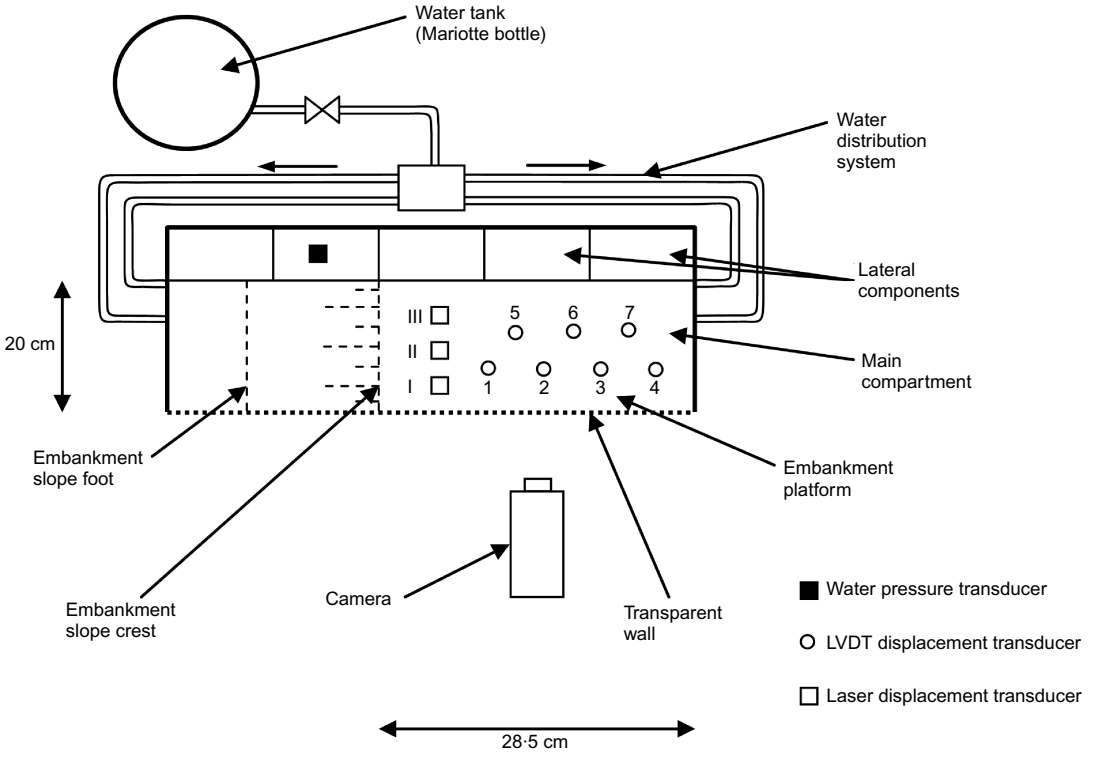

Fig. 9. Experimental set-up and instrumentation

(*c*) a transparent wall in the main compartment, which is used to film the model during the test.

A 2 cm thick sand layer, surrounded by a geotextile, is laid on the bottom of the strongbox. This draining layer is used to simulate the water table rise below the embankment base before the inundation event. The SCM, with a water content of 10·5%, is compacted on the 'dry side' of the Proctor curve in seven successive layers, each approximately 3 cm thick (Fig. 2).

Concerning the friction on the walls, previous research work conducted on the bearing capacity of strip footings built on a dry and dense sand model (Bakir, 1993) shows that failure occurs with an average value 8% higher on a two-dimensional model than on three-dimensional models, whereas settlement is 16% lower. If those results are linked to the model geometry only, they come within the range of the variability due to uncontrolled soil properties, and consequently Bakir (1993) neglected this effect. In the present study, the compaction process is simple, without using the wall effect reduction technique. Side friction may appear on the glass window and reduce settlement. To evaluate such behaviour linear variable differential transducer (LVDT) sensors and laser sensors have been implemented on several rows. As those displacement sensors are located at different distances from the walls (Fig. 9), the consequence of friction of the SCM on the walls should be differential settlements between sensors. This behaviour was not observed (see Fig. 12 later), except at the final stage of phase 3 and near the crest where the settlement is affected by the slope. This low friction is the result of the roughness of the glass. If the maximum roughness corresponds to a micrometre, and the friction developed at the SMC–glass interface follows the behaviour of a sand–glass interface, Uesugi & Kishida (1986) have identified a surface friction angle of about 6°. This would lead to a surface friction equivalent to 5% of the vertical stress. As a consequence, the side friction effect has not been taken into account in the present analysis.

Each layer is compacted with 96 blows of a conventional standard Proctor hammer, evenly distributed on the surface. Loosely compacted material is needed here to emphasise the displacement phenomena caused by wetting.

At the interface between each layer, circular pins are placed close to the transparent wall as geometrical reference points. The image analysis makes it possible to follow the point displacements using a specially dedicated LCPC piece of software (Thorel *et al.*, 2000). The results correspond to the mean value of the vertical displacement of the pins of each row.

After compaction, the structure is carved manually to form a slope of 33°, a classical inclination for actual road embankments filled with the same material. The final lengths of crest and base are 28·5 cm and 60 cm, respectively (Fig. 8). The corresponding prototype embankment would be scaled by a factor 100. Finally, a plastic sheet is placed on top of the model to stop evaporation between the end of the preparation phase and the centrifuge test.

The water level (0 and 5 cm from the base of the embankment) is controlled using a Mariotte bottle (Thorel *et al.*, 2002) connected to the main compartment (Fig. 9). The test is conducted according to three successive sequences:

(*a*) no hydraulic connexion
(*b*) water table at the bottom of the embankment
(*c*) water table up to 50 mm above the base of the embankment.

The total displacement of the embankment crest is calculated using some laser transducers placed above the crest, at a few centimetres from the slope crest and an LVDT, regularly applied above the central part of the crest (Fig. 9).

Geotechnical properties of the embankment model

A 'reference' embankment, which is not subjected to increasing $\boldsymbol{g}$ level, is devoted to the characterisation. It is prepared identically and in the same conditions as the model devoted to centrifugation. Characterisation consisted in measuring:

(*a*) the water content and dry density after compaction
(*b*) the soil resistance using cone penetration tests (CPTs) and a hydraulic penetrometer (Thorel *et al.*, 2008).

In each layer, 28 specimens are sampled: 12 for water content measurements and 16 undisturbed ones for dry density measurements. The water content is measured according to the oven-drying procedure and the dry density by hydrostatic weighing. In total, 196 specimens were sampled in the reference model after compaction.

The results (Fig. 10) show the following.

(*a*) The average water content is 10·4%, with a standard deviation of 0·2%, which demonstrates the good

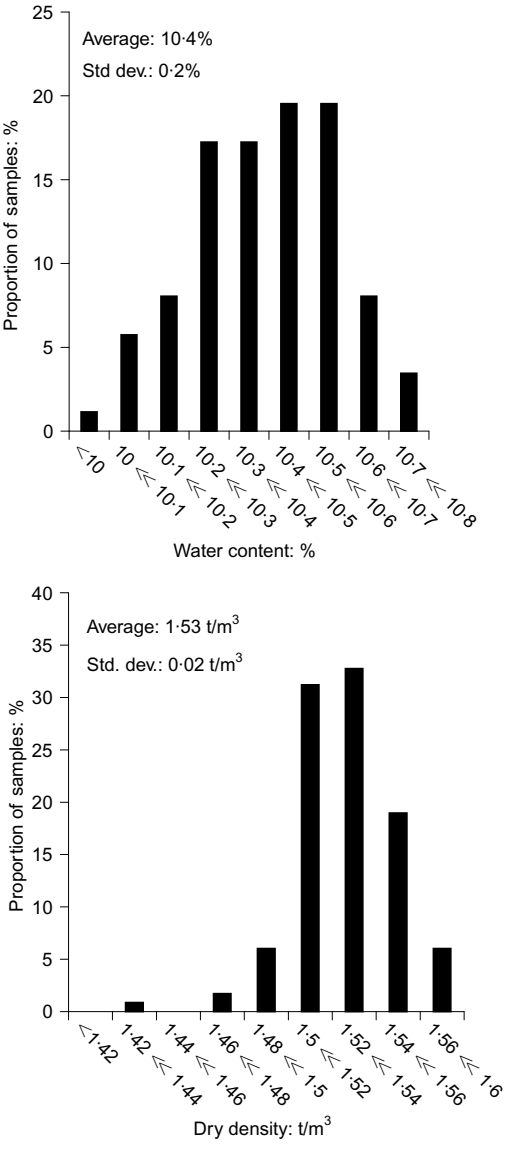

Fig. 10. Water content and dry density histograms of the compacted SCM in the embankment model

homogeneity (0·2% being approximately equivalent to the uncertainty). The soil is very dry in proportion to earthworks as a whole (LCPC, 2003). A water content of 10·4%, indeed, corresponds to 77% of the optimum moisture content (Table 1 and Fig. 2).

(*b*) The average dry density is 1530 kg/m^3 (82% of the MDD), with a standard deviation of 20 kg/m^3, which is also a good index of homogeneity. This very low compaction ratio (generally, a minimum compaction rate of 95% is required in conventional embankments) is the result of both the water content and the compaction energy applied. With such a density, substantial deformations are bound to occur.

Thirteen CPTs are carried out at 1***g*** on the 'reference' embankment on three rows: one row of five along the longitudinal axis (Fig. 11(a)), and two rows of four on either side of the first row, at 5 cm from the compartment walls (Fig. 11(b)). These two rows are intended for assessing the wall effect.

The results show that the resistance is homogeneous both vertically and horizontally, which confirms the water content and dry density results. There is no discernible wall effect during the lateral CPTs, although a larger range of resistance is noted.

Water content, dry density and mechanical property results confirm the good homogeneity of the model soil.

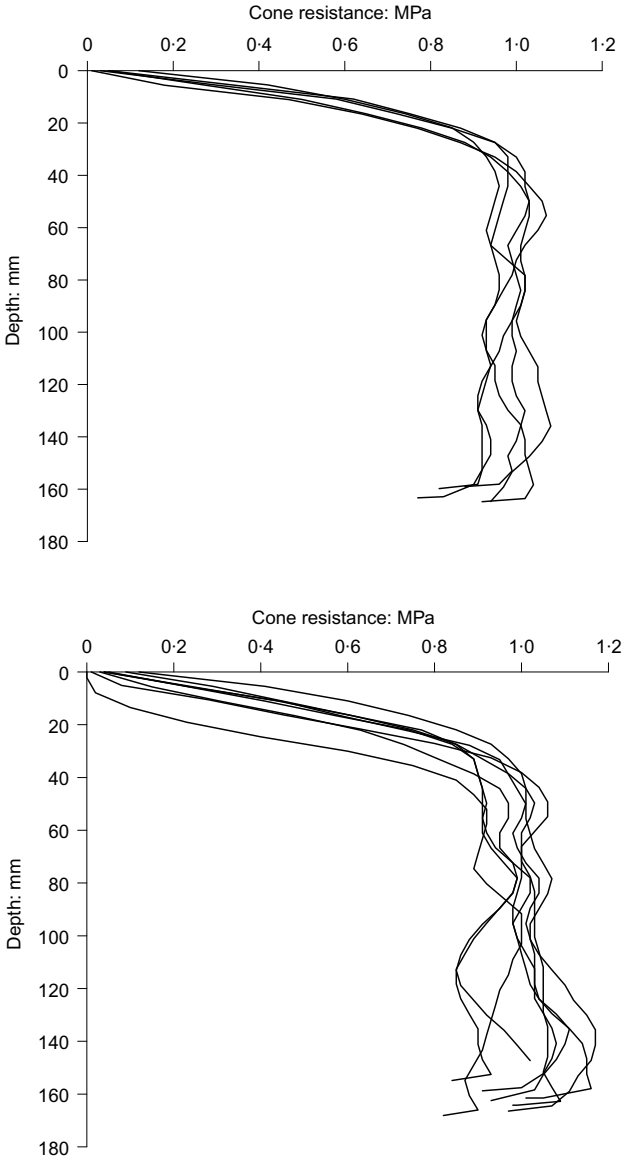

Fig. 11. CPT profiles along the longitudinal axis of the reference embankment (a) and at 5 cm from the strongbox face (b)

Test sequences

Three sequences simulating the different stress states that embankment materials are susceptible to undergo, are described as follows:

(*a*) stress state 1 – embankment construction with increasing vertical stress
(*b*) stress state 2 – a possible water level rise beneath the embankment causing capillary rises
(*c*) stress state 3 – a possible inundation event, leading to water infiltrations from both the slope and the base of the embankment.

These three stress states are simulated by three different sequences during the test:

(*a*) phase 1 – ***g*** level application to the embankment model to increase the vertical stress in the soil
(*b*) phase 2 – saturation of the sand layer under the embankment by maintaining the water table just above the sand–embankment interface level
(*c*) phase 3 – inundation of the strongbox with a water table located 5 cm above the sand–embankment interface.

CENTRIFUGE TEST RESULTS

The objective of the centrifuge tests is to examine the wetting-induced settlements of the embankment model before comparison with laboratory results. The settlements are measured according to two different principles (Fig. 8):

(*a*) for each layer, according to the reference points filmed by a camera placed in front of the transparent wall (Fig. 9); image analysis allows for the monitoring of the lowest four layers throughout a height of 12 cm
(*b*) at the crest level.

The total crest settlements (for which the zero value corresponds to the measurements before centrifugation) and the crest settlement due to inundation (for which the zero value corresponds to the beginning of the first inundation event) are presented as measurements continuous with time (Fig. 12) or as average values at the end of the three main sequences of the test (Fig. 13 and Fig. 14):

(*a*) before inundation (phase 1), that is when the settlements caused by the ***g*** level increase are stabilised
(*b*) after inundation with a water table of zero (phase 2), that is when the settlements due to capillary rises from the sand layer are stabilised
(*c*) after inundation with a water table of 5 cm (phase 3), that is when the settlements due to the saturation of the soil are stabilised.

Two acceleration/deceleration cycles are performed (Fig. 12) at the beginning of the test (first hour) because of unexpected technical problems. These unexpected events have generated a succession of positive and negative displacement readings: the model heave due to deceleration (Fig. 12) caused irreversible loading-induced settlements, preventing any possibility of returning to the initial value.

The settlement due to the centrifuge acceleration ranges from 0·7 to 4 mm (1·8 mm on average). Part of these differences may come from the use of contact (LVDT) and non-contact (laser) sensors. Laser transducers, for instance,

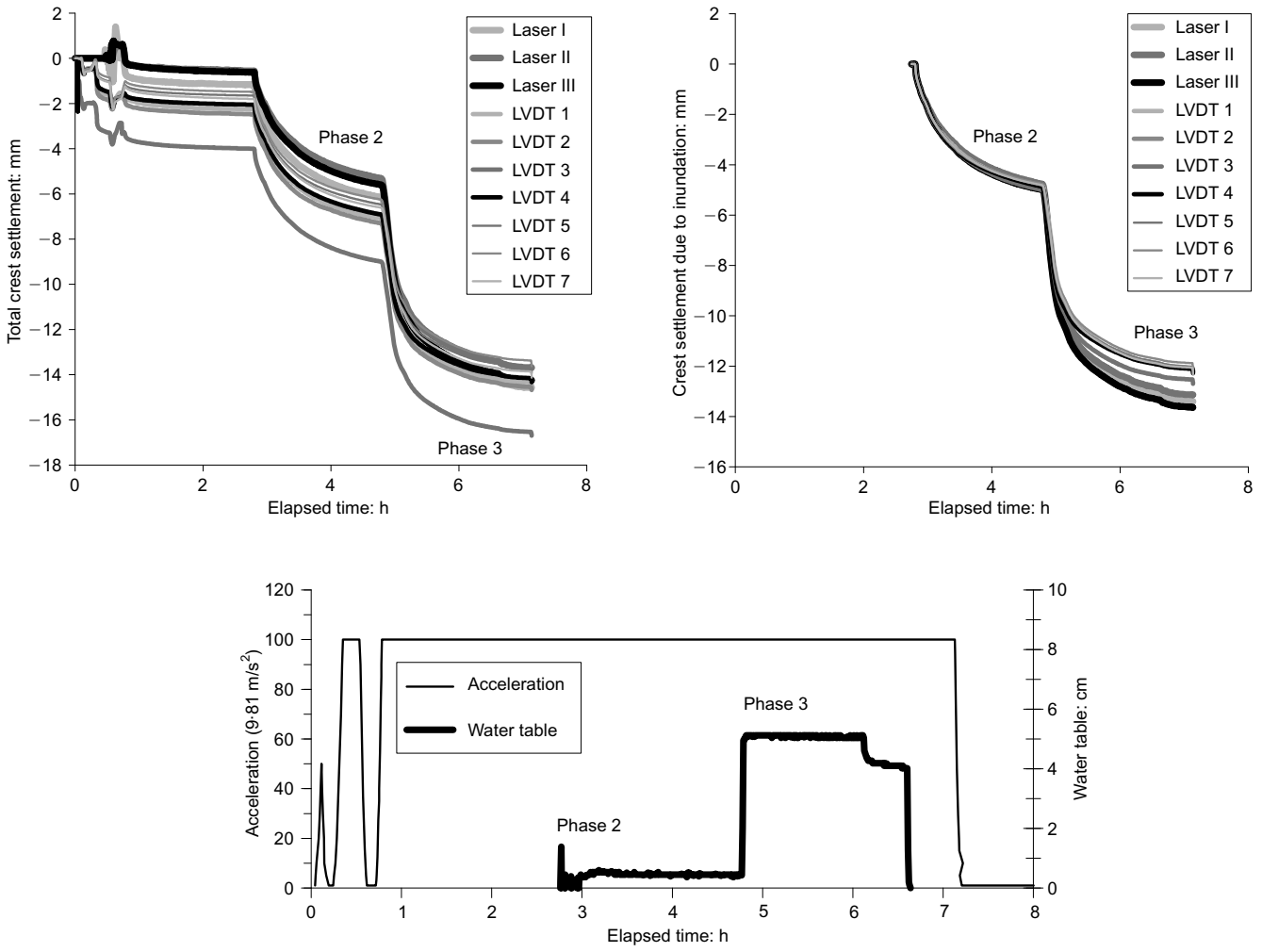

Fig. 12. Cumulative crest settlement, acceleration and water table measurements: focus on the inundation sequences (model time)

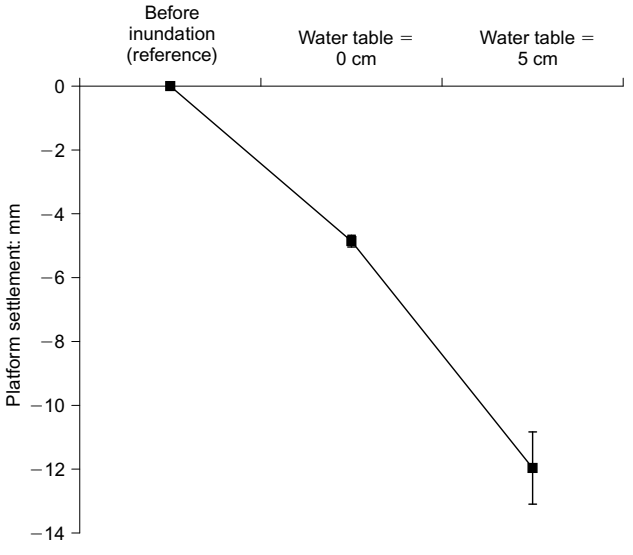

Fig. 13. Cumulative crest settlement (model scale) at the end of the two main inundation sequences (average displacement sensor measurements; the error bar represents the standard deviation)

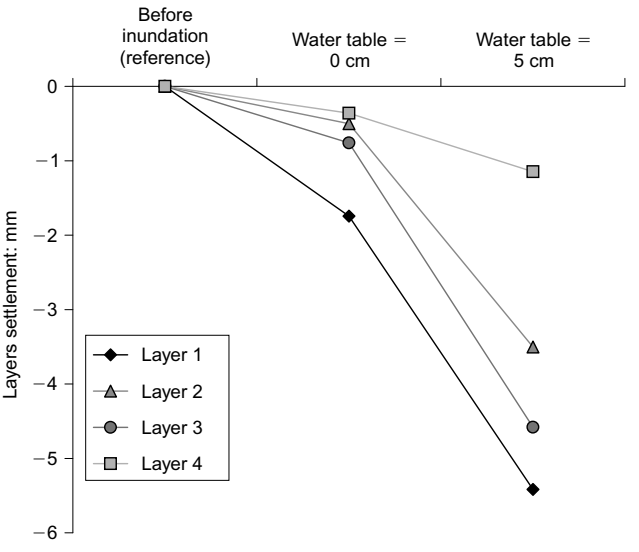

Fig. 14. Layer settlement (variation in height) at the end of the two main inundation sequences measured by image analysis (model scale)

show lower settlement values than LVDTs. This probably can be accounted for by the load applied by the rod of the LVDT sensors, which generates a stress producing a small overestimation of the settlement values.

These settlements due to loading are not observed on field-compacted soils, because they occur progressively during the construction of the embankment. On full-scale embankments, measurements focus on settlements occurring after their construction.

After this self-weight-induced settlement phase, the two inundation sequences taking place 3 h and 5 h after the beginning of the test, respectively (Fig. 12), generate two distinct crest settlement periods. Each phase begins when settlement has reached an asymptotic value. The first inundation event (phase 2) generates homogeneous settlements on the embankment crest. The second event (phase 3) generates more extensive settlements near the slope crest (laser sensors) because of a combination of lateral displacement. This lateral displacement combined with settlement has to be linked with the natural rotation of the stresses in the vicinity of the slope. Apparently, this phenomenon is not observed on the crest, far from the slope. This gives an indication that there is probably no rotation of the stresses in this zone, on which the study is focused.

During the test, the settlements are recorded on two (for LVDTs) or three (for laser transducers) locations on the transversal axis (Fig. 9). The results show, for both types of measurement, no gradient of settlement in the transverse direction. This confirms that the assumption of a translatory symmetry of the vertical plane of the embankment, which is parallel to the glass, is acceptable. In other words, the assumption of low interface friction on the walls of the container is admissible, even if their natures (glass or aluminium) are different.

The average crest settlement shows that (Fig. 13):

(*a*) the saturation of the sand layer generates a 5 mm settlement
(*b*) the inundation with a water table of 5 cm generates an additional settlement of 7 mm, reaching a total of 12 mm.

The image analysis gives more details on the settlement distribution within the different layers (Fig. 14) as follows.

(*a*) The settlement of each layer increases with each inundation phase.
(*b*) The individual settlement of each layer increases with the depth of the layer. For instance, layer 1, located at the very base of the embankment presents a more extensive settlement than the three other layers. Conversely, the extent of the settlement of layer 4 is the less significant. Layer 3 appears to be an exception, since its settlement is more extensive than the settlement of layer 2.
(*c*) The total settlement (Fig. 15) is 3·4 mm and 14·6 mm after the first and the second inundation sequences, respectively. These values are similar to the average values of 4·8 mm and 12 mm measured on the crest (Fig. 13).

The coefficient of variation (standard deviation divided by the mean) ranges between 6% and 17% during phase 2 (water table ~0) and between 1 and 13% during phase 3 (water table ~5 cm). As the measurements are performed at the model boundary, the glass window may affect the results. Nevertheless, all the results appear consistent.

The inundation of the embankment generates extensive settlements due to the wetting-induced collapse behaviour of loosely compacted soils. The maximum crest settlement after the last inundation sequence is higher than 12 mm (model scale), which corresponds to a 1·2 m settlement in a full-scale embankment. This value, probably due to the initial loose soil compaction rate (82% of the MDD), is not acceptable for a transportation embankment.

The settlement values (measured using transducers or image analysis) are consistent and increase with increasing depth and increasing water table height. This result is coherent considering that:

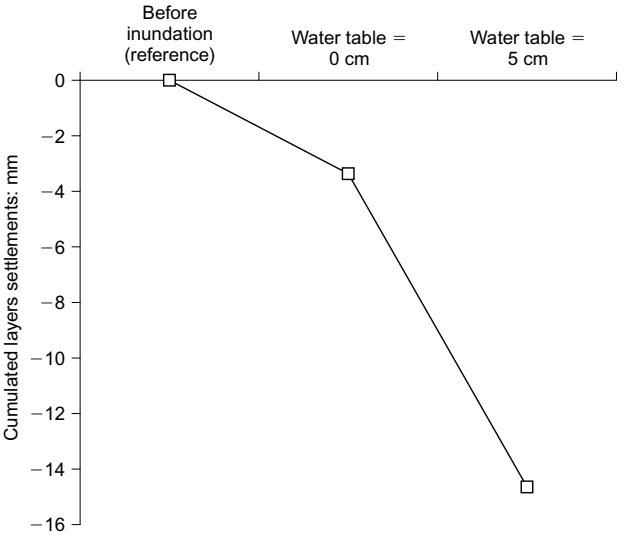

Fig. 15. Total layer settlement measured by image analysis at the end of the two main inundation sequences (model scale)

(*a*) the vertical stress amplifies the deformation due to collapse
(*b*) the rise of the water table causes saturation, and consequently, the collapse of an increasing thickness of compacted material.

DISCUSSION

The void ratio before and after inundation is modelled on the basis of the unsaturated and saturated oedometer tests, characterised by the following parameters.

(*a*) Saturated compression curve: the compression index (Cc) is equal to 0·2 (Fig. 16).
(*b*) Unsaturated compression curve: the elastic compression index is equal to 0·011 and the plastic compression index is equal to 0·25 (Fig. 16). The variation with increasing suction of these compression indices is known to be negligible (Chen *et al.*, 1999). On the other hand, the preconsolidation stress depends on the initial void ratio (Fig. 16). For instance, with an initial

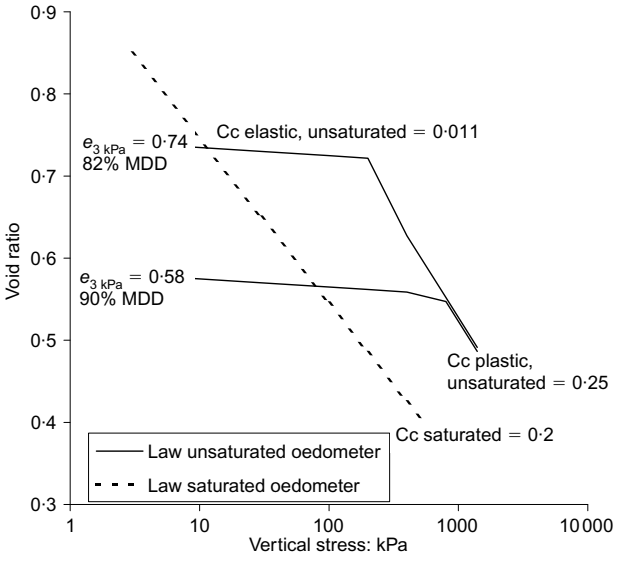

Fig. 16. Oedometer tests and compressibility used for displacements prediction

void ratio of 0·58 or 0·74 (corresponding to the centrifuge embankment model), the preconsolidation stress would be 800 kPa or 200 kPa, respectively.

To compare void ratios obtained with the centrifuge test and with the oedometer tests, respectively (Fig. 17), the following assumptions are made.

(*a*) In the embankment, only the zone far from the slope is taken into account. It has been shown (Fig. 12), that the measured settlements of the crest were very close to each other, and comparable to the settlement deduced from image analysis. In this zone it is assumed that there is no rotation of the stresses, and consequently that the principle of the comparison with oedometer tests is relevant.
(*b*) The dry density after compaction is equal to 1530 kg/m^3 (Fig. 10) in the embankment.
(*c*) The vertical stress, $\sigma(z)$, at a given depth, z, in the embankment, is related to the material height above this point by the initial density of the material. With a dry density after compaction of 1530 kg/m^3 and a water content of 10·4% (Fig. 10), the wet bulk density, ρ, used for calculations is $1530 \times 1{\cdot}104 = 1690$ kg/m^3. The vertical stress is given by equation (1) and the calculations are made using the centrifuge acceleration value measured during the test (Fig. 12), namely $100 \times \boldsymbol{g} = 981$ m s^{-2}, with $\boldsymbol{g}$ being acceleration due to Earth's gravity.
(*d*) The void ratio for each test sequence is determined, in the four layers, as a function of the initial state after compaction and of the variation of the layer height provided by the image analysis (equation (2)).

$$\sigma(z) = \rho \boldsymbol{g} z \tag{1}$$

$$\frac{h_\mathrm{f} - h_\mathrm{i}}{h_\mathrm{i}} = \frac{e_\mathrm{f} - e_\mathrm{i}}{1 + e_\mathrm{i}}, \quad e_\mathrm{f} = \frac{h_\mathrm{f} - h_\mathrm{i}}{h_\mathrm{i}}(1 + e_\mathrm{i}) + e_\mathrm{i} \tag{2}$$

where e_i and e_f are the void ratio after compaction and after the test phase, respectively, and h_i and h_f are the layer height after compaction and after the test phase, respectively.

The consequences of the inundation may be considered in terms of cumulative displacement as a function of the height in the embankment (Fig. 18). This parameter is calculated from the following results.

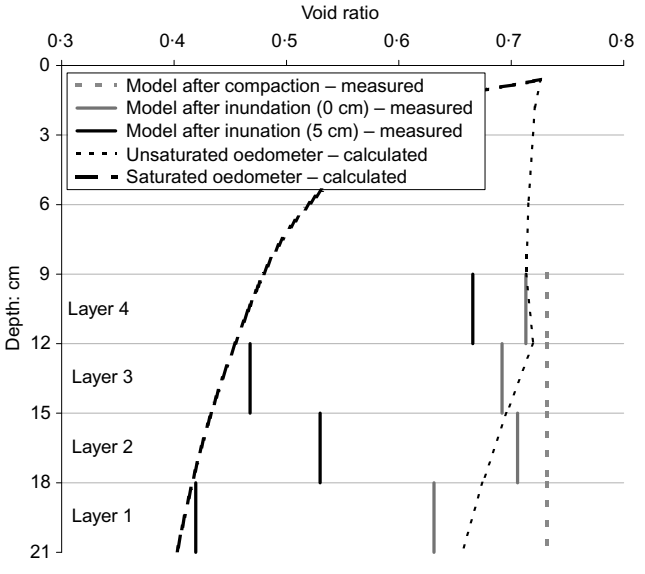

Fig. 17. Comparison of void ratio measurements obtained with the centrifuge and oedometer tests (centrifuge model scale)

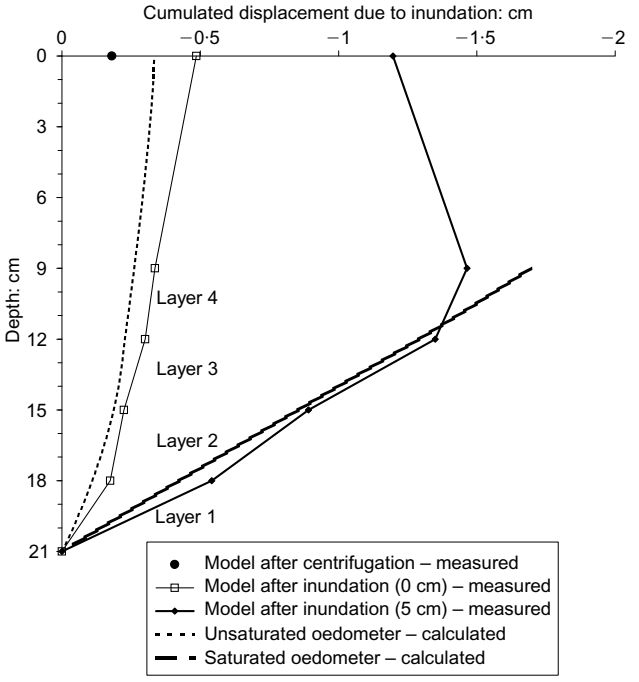

Fig. 18. Comparison of the cumulative vertical displacement due to inundation obtained with the centrifuge test and oedometer tests (model scale)

(*a*) The oedometer tests: the displacement is calculated with the variations of the void ratio in the elementary layers (equation (3)), assuming that their thickness is low enough to neglect the vertical stress variation. The cumulative displacement at a given height is the sum of variations of the lower elementary layer height (equation (4)).
(*b*) The displacement measurements on the embankment: the cumulative displacement is deduced from the image analysis information or from the crest displacement.

$$h_\mathrm{f}^k - h_\mathrm{i}^k = h_\mathrm{i}^k \frac{e_\mathrm{f}^k - e_\mathrm{i}^k}{1 + e_\mathrm{i}^k} \tag{3}$$

where e_i^k and e_f^k are the void ratio of the kth elementary layer after compaction and after the test phase, respectively, and h_i^k and h_f^k are the kth elementary layer height after compaction and after the test phase, respectively.

$$H_\mathrm{f} - H_\mathrm{i} = \sum_{k=1}^{n} h_\mathrm{f}^k - h_\mathrm{i}^k \tag{4}$$

where H_i and H_f are the embankment height after compaction and after the test phase, respectively, and n is the number of elementary layers.

The variations of the void ratio observed during the different sequences (Fig. 17) reveal the following.

(*a*) After the first inundation event (water table = 0 cm), the void ratio decrease is relatively small, and, except for the first layer, the value is very close to that of the void ratio predicted by the unsaturated oedometer test. Considering the high values obtained for crest settlement during this sequence (Fig. 12), layer 1 was probably already partly saturated because of capillary rises, which explains why the void ratio decrease is larger than the unsaturated oedometer test prediction (a difference of 0·2 mm is observed);
(*b*) After the second inundation event (water table = 5 cm), the void ratio decreases in the three lowest layers

because of the increasing water level. In the fourth layer, a limited decrease is observed, which can be explained by the fact that the capillary rise does not reach the full height of the fourth layer. The saturated oedometer test results give a good prediction of the final void ratio in layers 1 and 3 but a discrepancy occurs regarding the second layer.

The cumulative displacements as a function of depth in the model (Fig. 18) show the following.

(*a*) The application of the centrifuge force generates a crest settlement (2 mm) less extensive than the one predicted with the unsaturated oedometer tests (3·5 mm). This relatively low value for the model scale would represent a difference of 15 cm on a full-size embankment, which is quite significant. However, this settlement would occur during the construction of the embankment and, therefore, would not be actually observed.
(*b*) The first inundation sequence presents a cumulative displacement profile similar to the unsaturated oedometer profile. The small shift between both curves might be the consequence of the saturation of the lowest layer, most probably by capillary rise. The difference between both curves on the crest also reaches 1·5 mm at model scale.
(*c*) The second inundation sequence presents a profile which is very close to the saturated oedometer profile in the three first layers. Above, the fourth layer, only, is partly affected by the inundation. Extensive settlements, consistent with the predictions, are observed in the third and in part of the fourth layer. This suggests that the inundation event comes with notable and very fast capillary rise, causing the saturation of the soil at a height of approximately 5 cm in a few hours. Previous research studies have shown that, in sand materials, capillary rises occur very rapidly under the effect of macro-gravity because of an increase of the capillary velocity by N times (Depountis *et al.*, 2001), which can explain the fast capillary rises observed in layers 3 and 4.

A reasonable consistency is observed between oedometer and centrifuge tests. Assuming that the oedometer tests are representative of embankment settlements far from the slope (no horizontal displacements observed or allowed), these tests are satisfactory for prediction. In the shallower zones and under the slopes, the stress ratio may noticeably modify performances (Lawton *et al.*, 1992), and this approach should not be used.

The prediction is associated with uncertainty, since model scale discrepancies of 1 to 2 mm are observed between laboratory and centrifuge tests, corresponding to differences between 10 cm and 20 cm at full scale, that is 10–20% of the settlement. This gives the order of magnitude of the prediction uncertainty obtained with the oedometer tests.

CONCLUSION

An inundation is simulated during a centrifuge test in two-dimensional geometry in order to examine the collapse behaviour of embankments. The test embankment model is built with a loosely compacted (82% MDD) clay–sand mixture to increase the collapse phenomenon. This material is studied by carrying out single and double oedometer tests.

The maximum water height reached during the inundation events is 5 cm, which causes 12 mm crest settlements at model scale (at full scale, a 20 m high field embankment subjected to a 5 m high inundation would settle by approximately 1 m).

It must be emphasised that the quality of the prediction depends mainly on the two following parameters:

(*a*) the height of the capillary rises, that is the saturation final height
(*b*) the dry density profile before inundation.

The analysis of the laboratory results shows that the settlements far from the slope (where there are no rotations of the stresses) can be roughly predicted on the basis of the double oedometer test. The method presented could also be used to define dry density objectives during the placement process depending on the embankment height. These objectives are given by the saturated oedometer test. The inundation simulation study conducted at the same time on a full-scale embankment confirms the transposition potential of this approach (Vinceslas *et al.*, 2009). This method, however, would not be relevant for high-plasticity clays (Ferber *et al.*, 2008), knowing that such soils are generally banned from common compacted fills.

ACKOWLEDGEMENT

The authors would like to thank the LCPC technical staff involved in this study, particularly Jean-Pierre David.

REFERENCES

ADM (Autoroutes du Maroc) (2006). *Autoroutes du Maroc: Rapport d'activités 2006*, 44 pp. See www.adm.co.ma for further details (accessed 21/09/2010).

Alonso, E. E., Gens, A. & Josa, A. (1990). A constitutive model for partially saturated soils. *Géotechnique* **40**, No. 3, 405–430, **doi**: 10.1680/geot.1990.40.3.405.

Auriol, J. C., Havard, H., Mieussens, C. & Queyroi, D. (2000). Résultats d'enquêtes sur la pathologie des remblais en service. *Routes/Roads*, No. 306, 57–74.

Bakir, N. (1993). *Investigation on centrifuged models of bearing capacity of shallow foundations*. PhD thesis, Nantes University, France (in French).

Basma, A. A. & Tuncer, E. R. (1992). Evaluation and control of collapsible soils. *J. Geotech. Engng* **118**, No. 10, 1491–1504.

Chen, Z. H., Fredlund, D. G. & Gan, K. M. (1999). Overall volume change, water volume change, and yield associated with an unsaturated compacted loess. *Can. Geotech. J.* **36**, No. 2, 321–329.

Delage, P. & Fry, J. J. (2000). Comportement des sols compactés: apports de la mécanique des sols non saturés. *Revue Française de Géotechnique* **92**, 17–29.

Depountis, N., Davies, M. C. R., Harris, C. *et al.* (2001). Centrifuge modelling of capillary rise. *Engng Geol*. **60**, No. 1–4, 95–106.

El-Ehwany, M. & Houston, S. L. (1990). Settlement and moisture movement in collapsible soils. *J. Geotech. Engng* **116**, No. 10, 1521–1535.

El Sohby, M. A. & Rabbaa, S. A. (1984). Deformational behaviour of unsaturated soils upon wetting. *Proc. 8th Regional Conf. for Africa Soil Mech. Found. Engng* **1**, 129–137. South African Institution for Civil Engineers.

Estabragh, A. R., Javadi, A. A. & Boot, J. C. (2004). Effect of compaction pressure on consolidation behaviour of unsaturated silty soil. *Can. Geotech. J.* **41**, No. 3, 540–550.

Ferber, V., Auriol, J. C., Cui, Y. J. & Magnan, J. P. (2008). Wetting-induced volume changes in compacted silty clays and high-plasticity clays. *Can. Geotech. J.* **45**, No. 2, 252–265.

Garnier, J., Gaudin, C., Springman, S. M. *et al.* (2007). Catalogue of scaling laws and similitude questions in geotechnical centrifuge modelling. *Int. J. Phys. Modelling in Geotechnics* **7**, No. 3, 1–24.

Jennings, J. E. & Knight, K. (1957). The prediction of total heave from the double-oedometer test. *Transactions of a symposium on expansive clays*, pp. 13–19. Midrand, South Africa: South African Institution of Civil Engineering.

Lawton, E. C., Fragaszy, R. J. & Hardcastle, J. H. (1989). Stress

ratio effects on collapse of compacted clayey sand. *J. Geotech. Engng* **117**, No. 5, 714–730.
Lawton, E. C., Fragaszy, R. J. & Hetherington, M. D. (1992). Review of wetting-induced collapse in compacted soil. *J. Geotech. Engng* **118**, No. 9, 1376–1394.
LCPC (Laboratoire Central des Ponts et Chaussées) (2003). *Practical manual for the use of soils and rocky materials in embankment construction* (Techniques et méthodes des laboratoires des ponts et chaussées), 60 pp. Bouguenais, France: LCPC.
Lim, Y. Y. & Miller, G. A. (2004). Wetting-induced compression of compacted Oklahoma soils. *J. Geotech. Geoenviron. Engng* **130**, No. 10, 1014–1023.
Miller, G. A., Muraleetharan, K. K. & Lim, Y. Y. (2001). Wetting-induced settlements of compacted-fill embankments. *Transpn Res. Rec*. **1755**, 111–118.
Pereira, J. H. F. & Fredlund, D. G. (2000). Volume change behavior of collapsible compacted gneiss soil. *J. Geotech. Geoenviron. Engng* **126**, No. 10, 907–916.
Rao, S. M. & Revanasiddappa, K. (2000). Role of matric suction in collapse of compacted clay soil. *J. Geotech. Geoenviron. Engng* **126**, No. 1, 85–90.
Rollins, K. M., Rollins, R. L., Smith, T. D. & Beckwith, G. H. (1993). Identification and characterization of collapsible gravels. *J. Geotech. Engng* **120**, No. 3, 528–542.
Thorel, L., Noblet, S., Garnier, J. & Bisson, A. (2000). Capillary rise and drainage flow through a centrifuged porous medium. *Proceedings of the international symposium on physical modelling and testing in environmental geotechnics*, La Baule, 15–17 May 2000, pp. 251–258.
Thorel, L., Favraud, C. & Garnier, J. (2002). Mariotte bottle in a centrifuge: a device for constant water table level. Technical Note. *Int. J. Phys. Modelling in Geotechnics* **2**, No. 1, 23–26.
Thorel, L., Rault, G., Garnier, J. *et al.* (2008). Macro-gravity measurements on reduced-scale models of geotechnical structures. *Bull. de Liaison des Ponts et Chaussées* **272–273**, Spécial Métrologie, 93–131.
Uesugi, M. C & Kishida, H. (1986). Frictional resistance at yield between dry sands and steel. *Soils Found*. **26**, No. 4, 139–149.
Vinceslas, G., Khay, M., Sagnard, N. & Ferber, V. (2009). Moisture state variations on embankments located in flood zones: Instrumentation and behavioral monitoring of an experimental embankment. *Bull. des Laboratoires des Ponts et Chaussées* **274**, 5–30.

ice
Institution of Civil Engineers
publishing

Selected Questions and Answers

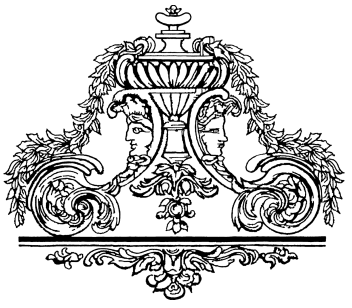

Partial Saturation in Compacted Soils, 197–201 [http://dx.doi.org/10.1680/geot.sip11.qa]

Keynote Speeches

Questions posed by **Professor Eduardo E. Alonso** (Department of Geotechnical Engineering and Geosciences, Universitat Politècnica de Catalunya, Barcelona, Spain) to **Mr Anthony O'Brien** (Mott MacDonald, Croydon, UK) in relation to the keynote speech "The assessment of Old Railway Embankments. Time for a change?" by A.S. O'Brien:

(*a*) *In an embankment poorly compacted collapse phenomena induced by rain infiltration are likely. Since collapse strains are far from being homogeneous, they will result in shearing strains throughout the embankment mass, especially during the early stages of operation (several years?). These shearing strains will degrade the strength of the compacted soil and will contribute, as an additional mechanism, to instabilities.*

(*b*) *Details of the numerical analysis by means of the computer code FLAC are requested. In particular, what is the driving mechanism in FLAC to simulate swelling (or collapse) strains?*

(*c*) *It appears that the main mechanism leading to the eventual failure of a given embankment is a progressive process. This mechanism is especially relevant in plastic clays because of the large drop in strength from the initial as compacted conditions to residual conditions. However, in low plasticity materials (involved in many failures), this process of strength reduction is of secondary importance. What is then the explanation for the delayed failures observed in embankments built with low plasticity soils?*

Response from Anthony O'Brien:

(*a*) There can be several different triggers which may initiate the development of non-uniform strains across an embankment. Shortly after construction of these old railway embankments, collapse settlement usually developed and the resulting drop in crest level was made good by tipping locomotive ash over the clay fill. This phenomenon was quite widespread, and is now reflected in the thickness of ash which is commonly observed when drilling through the crest of these embankments. An ash thickness of about one metre is fairly typical, both across embankments which have remained stable and those which have been prone to delayed failure. Hence, additional factors also need to be considered in order to explain the delayed failures and the differing rate of long term degradation of embankments composed of plastic clay fills. These other factors include, inter alia: failures during construction; vegetation/climate interactions; clay fill permeability; presence of underlying soils which may increase or decrease the risk of progressive failure (due to differing permeability, compressibility or strength characteristics); effectiveness of drainage (especially in vicinity of embankment toe). Some embankments suffered failures during construction, especially larger embankments (in excess of 6m height), as previously discussed by Skempton (1996). Although construction was eventually completed successfully, sometimes by novel techniques such as forming "burnt clay", there is little doubt that in some locations the old shear surfaces from the construction failures were not fully removed. Hence, these remaining zones now act as "hidden defects". As discussed in my paper these old embankments "breathe" seasonally, and the seasonal shrink-swell movements (which have been monitored across many embankments) are not fully reversible. The plastic deformation at the end of each shrink-swell cycle leads to a "ratcheting" mechanism with a net outward movement at the embankment toe. After several decades, these movements will inevitably lead to a substantial loss of strength in the base of the embankment, if the embankment fill is composed of "brittle" plastic clay (with a substantial post-peak drop in strength towards residual). The magnitude of seasonal shrink-swell movement, and the associated risk of instability depends on several factors as outlined in my paper. The permeability of the clay fill is a key factor since this will fundamentally affect the vulnerability of the embankment to seasonal changes in climate. Many of the dumped (or poorly compacted) clay fills have an intermediate range of permeability (between 10^{-7}m/s and 10^{-9} m/s), between what could be considered to be practically impermeable and free draining, (when compared with the rainfall and evaporation rates which are usually experienced in the UK). Within this intermediate permeability range, rainfall can infiltrate but not easily drain, and therefore the clay fill can experience relatively large seasonal changes in pore water pressure. In contrast, well compacted clay fills (typical of modern Civil Engineering construction) would have a far lower permeability and would experience smaller seasonal changes in pore water pressure.

(*b*) The soil model used in the FLAC code is a bespoke model which uses specific "FISH" functions to simulate seasonal shrink-swell behaviour, together with post-peak strain softening towards residual strength. The model has been described in detail by Ellis and O'Brien (2007), where it was used to analyse progressive collapse of cuttings in stiff plastic clays. Referring to Appendix 1 of my paper, the compressibility and swelling behaviour of the clay fill, and underlying natural soils, are described by a linear elastic-perfectly plastic soil model. Prior to yield, the elastic Young's Modulus is dependent on the mean effective stress. Hence, the modulus decreases when swelling towards low effective stress, and increases when consolidating towards high stress. Figure 1 shows comparisons between FLAC simulations, and oedometer tests (with unload-reload cycles) on hand cut block samples. It is appreciated that this type of stress-strain model oversimplifies the soils non-linear small-strain behaviour (which is important for many practical soil-structure interaction problems). However, for delayed failure analyses it is more important to correctly capture the soil's large strain behaviour, and this type of model is satisfactory for this purpose. A similar soil model has also been successfully used by Nyambayo *et al.* (2004), for simulating the progressive failure of embankments. Comparisons between FLAC simulations and observed seasonal embankment deformations showed that this type of soil model could predict shrink-swell movements of a similar order of magnitude as those observed (although given the complex range of factors which influenced seasonal behaviour precise matches could not be

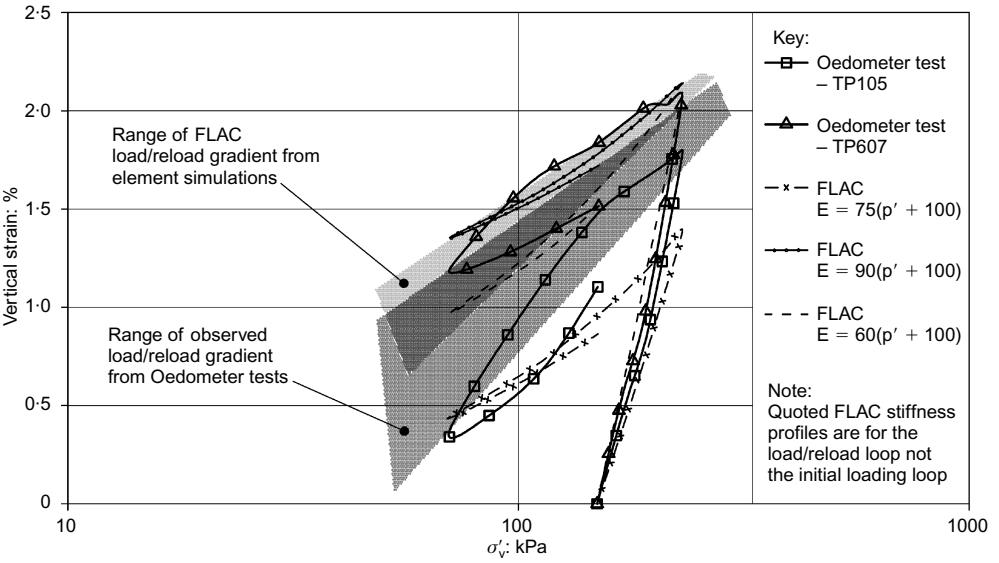

Figure 1. Compressibility and swelling of a dumped clay fill, flac simulation and oedometer data (block samples)

achieved). More rigorous soil models could be implemented, however, this additional complexity would have precluded the comprehensive suite of sensitivity studies (some of which are outlined in the paper) which were carried out. These sensitivity studies were essential in order to assess the relative importance of the different factors which can affect the risk of delayed failure.

(*c*) In the context of UK Railway embankments, the cause of the delayed failures which affect embankments built with low plasticity clays was very clear (based upon the surveys which have been reported across the network, following each failure). The terms used to describe these failures are "wash-out" or "flow" failures. Typically, they are relatively shallow (about one or two metres deep), and are triggered by intense rainfall (Winter, 2006), and are usually associated with faulty drainage, or non-uniform ground surface topography, which leads to concentrated flows of water across the embankment surface. These failure mechanisms are quite different to the deeper failure mechanisms which can be seen in more plastic clay fills. For low plasticity soils, the most important factors are to understand the overall hydrological regime, and to ensure the drainage systems are adequate. For high plasticity clays, the causative factors are more complex, as discussed in the paper.

REFERENCES

Ellis, E.A. & O'Brien, A. S. (2007): Effect of Height on Delayed Collapse of Cuttings in Stiff Clay, *Proc. of the I.C.E., Geotechnical Eng.*, **GE2**, p. 73–84, April 2007

Nyambayo, V.P. Potts, D.M., & Addenbrooke T.I. (2004): The Influence of Permeability on the Stability of Embankments Experiencing Seasonal Cyclic Pore Water Pressure Changes, Proc. The Skempton Conf., London, Thomas Telford, Vol 2, p. 898–910.

Skempton, A.W. (1996): Embankments and cuttings on the early railway, *I.C.E. Proc., Construction History* **11**: p. 33–49

Winter, M. (2006): Unstable Natural Slopes, Climate Change and Impacts on Scottish Infrastructure, Presentation to 2nd CLIFFS workshop at http://cliffs.Iboro.ac.uk/.

Material Characterisation

Question posed by **Professor Domenico Gallipoli** (Laboratoire SIAME, Université de Pau et des Pays de l'Adour, France) to **Dr Anh Minh Tang** (Ecole des Ponts ParisTech, UMR Navier/CERMES, Paris, France) in relation to the paper "Effects of the maximum soil aggregates size and cyclic wetting–drying on the stiffness of a lime-treated clayey soil" by A.M. Tang, M.N. Vu and Y.-J. Cui

The results from this experimental campaign show that the shear stiffness of lime-treated soils is almost insensitive to variations of water content and suction (provided that excessive drying is prevented) suggesting that, within the explored suction range, cementation dominates the behaviour of inter-granular contacts rather than suction. If this was proven to be a general result, the effect of suction on cemented soils could possibly be disregarded at least within a limited range of water contents, thus enabling extension of models developed for saturated cemented soils to the case of unsaturated cemented soils. Of course, this also requires that inter-granular cementation stays relatively undamaged, and hence soil strains remain relatively small, throughout service life of the structure. In spite of these restrictions, the above hypothesis has the potential of introducing significant simplifications in constitutive modelling of unsaturated cemented soils and is probably worth further exploration. I would be interested to know the Authors' opinion on this issue and whether they have performed additional tests to explore the relative importance of water capillarity and inter-granular cementation on other soil properties such as, for example, normal compression behaviour and strength, which might corroborate or refute the above hypothesis.

REFERENCES

Tang, A. M., Vu, M. N. & Cui, Y.-J. (2011). Effects of the maximum soil aggregates size and cyclic wetting–drying on the stiffness of a lime-treated clayey soil. *Géotechnique* **61**, No. 5, 421–429, doi: 10.1680/geot.SIP11.P.005

Response from Anh Minh Tang:

In the authors' opinion, we cannot say that the shear stiffness of lime-treated soils is almost insensitive to variations of water content and suction because the results show clear increase of G_{max} when water content is decreasing and clear decrease of G_{max} when water content is increasing. A more precise statement is: the shear stiffness of lime-treated soils is almost insensitive to suction cycles when excessive drying is prevented. It is actually interesting to investigate the relative importance of water capillarity and inter-granular cementation on soil mechanical properties. Nevertheless, from the experimental point of view, some difficulties remain in performing such a study. Actually, in the work presented by the authors, the values of G_{max} of lime-treated soils are compared to that of untreated soils. The difference includes not only the effect of inter-granular cementation but also others effects of lime treatment. The best option would be performing suction-controlled mechanical test. But the results from this kind of test are difficult to analyse because of the evolution of mechanical properties due to the pouzzolanic reactions during the test.

Experimental Observation and Modelling

Question posed by **Professor Domenico Gallipoli** (Laboratoire SIAME, Université de Pau et des Pays de l'Adour, France) to **Dr Enrique Romero** (Department of Geotechnical Engineering and Geosciences, Universitat Politècnica de Catalunya, Barcelona, Spain) in relation to the paper "An insight into the water retention properties of compacted clayey soils" by E. Romero, G. Della Vecchia and C. Jommi

In equation (2) the suction s_m^* is introduced as a soil parameter corresponding to the suction for which the water ratio e_w becomes equal to e_m^* and micropores are fully saturated while macropores are empty. However, when the water ratio e_w increases above e_m^* and s drops below s_m^* equation (2) is no longer used to calculate the microstructural void ratio e_m (which coincides with the microstructural water ratio, given that micropores are fully saturated) as a function of suction. The model assumes instead that the microstructural void ratio e_m is calculated by equation (3) as a function of total water ratio e_w. This assumption leads to the consequence that the reference suction s_m calculated by equation (5) when $s < s_m^*$ has no physical meaning but it is only a mathematical parameter, which corresponds to the suction value at which the two branches of the water retention curve given by equations (2) and (4) join together. The Authors are invited to comment whether they have explored the possibility of using equation (2) instead of equation (3) to calculate the microstructural void ratio e_m when $s < s_m^*$, in which case equation (5) is not needed and the value of suction s_m^* can be used in equation (4) instead of s_m.

REFERENCES

Romero, E., Della Vecchia, G. & Jommi, C. (2011). An insight into the water retention properties of compacted clayey soils. *Géotechnique* **61**, No. 4, 315–330, doi: 10.1680/geot.2011.61.4.315

Response from Enrique Romero:

The microstructural void ratio under saturated conditions (for $s < s_m^*$, corresponding to $e_w > e_m^*$) cannot be directly estimated using equation (2) (microstructural branch of the water retention curve). There are two main reasons for this. To begin with, the extrapolation into the microstructural saturation range of this equation significantly over-estimates the amount of microstructural void ratio, compared to measured values using mercury intrusion porosimetry and digital image analysis of photomicrographs in which equation (3) is based. Particularly for $s \rightarrow 0$, the extrapolation of equation (2) predicts higher microstructural values than soil void ratio. Conversely, the physically based equation (3) always results in a microstructural void ratio lower than void ratio. Secondly, since equation (2) does not depend on void ratio, its extrapolation into the saturation range will predict the same microstructural void ratio for densely and loosely compacted clayey soils. This is not the case, since low-density samples display greater capacity for microstructural expansion due to the larger amount of water stored at saturation. The proposed water retention model only considers the extrapolation of equation (2) into the microstructural saturated range ($e_w > e_m^*$) to determine the reference suction s_m when e_m is known (equation (5)). This reference suction, which presents a different value on main drying and main wetting to tackle hydraulic hysteresis, is used to smooth the transition between the microstructural and macrostructural water retention domains. The incursion of s_m into microstructural saturation (equation (5)) generally extends over a limited suction range in most clayey soils, which depends on the activity of the clay (parameter β in equation (3)) and the amount of water stored (e_w in equation (3)).

Benchmarking of Techniques and Models

Question raised by **Professor Eduardo E. Alonso** (Universitat Politècnica de Catalunya, Barcelona, Spain) to **Professor Alessandro Tarantino** (University of Strathclyde, Glasgow, UK) in relation to the paper "Benchmark on experimental techniques for measuring and controlling suction" by A. Tarantino, D. Gallipoli, C.E. Augarde, V. De Gennaro, R. Gomez, L. Laloui, C. Mancuso, G. El Mountassir, J.J. Munoz, J.-M. Pereira, H. Peron, G. Pisoni, E. Romero, A. Raveendiraraj, J.C. Rojas, D.G. Toll, S. Tombolato and S. Wheeler

Some of the discrepancies reported may be explained if enough time for equilibrium is allowed during tests. It seems that time is the missing parameter in the explanation given. Simulating the different tests as boundary value problems, including water transfer mechanisms, may help to reduce discrepancies.

REFERENCES

Tarantino, A., Gallipoli, D., Augarde, C., De Gennaro, V., Gomez, R., Laloui, L., Mancuso, C., McCloskey, G., Munoz, J., Pereira, J.M., Peron, H., Pisoni, G., Romero, E., Raveendiraraj, A., Rojas, J.C., Toll, D., Tombolato, S. & Wheeler, S. (2011). Benchmark of experimental techniques for measuring and controlling suction. *Géotechnique* **61**, No. 4, 305–314, doi: 10.1680/geot.2011.61.4.305

Response from Alessandro Tarantino:

We agree that equilibrium time and hydraulic boundary conditions are critical when measuring or applying suction. Nonetheless, we have concluded that this was not the explanation for the discrepancies observed between different techniques.

Tensiometer measurement was carried out with the sample placed in a small closed cell and we assumed that equilibrium between liquid pore-water and vapour water surrounding the sample was reached when the water pressure measured by the tensiometer attained a constant value. Suction and water content measured were therefore associated with a 'static' equilibrium condition.

For the case of the osmotic technique, the specimens were enveloped by a semi-permeable membrane, which was submerged into the osmotic solution. Under these conditions, we assumed that water vapour transfer was negligible and that water was only transferred via liquid phase. Equilibrium was considered to be reached when water content attained a constant value (checked by successive weighing). Suction and water content measured were therefore associated with a 'static' equilibrium condition.

Equilibrium is more complex in the axis translation technique because samples are placed in an open system, with water vapour possibly evaporating into the air supply system. In the axis translation oedometer, liquid water exchanged with the sample could be measured. It was therefore possible to check whether significant evaporation was taking place (water volume exchanged with the water supply system tends to change linearly with time) and, if it was the case, a correction was made to the water content measurement.

For the pressure plate, it was difficult to assess whether water vapour lost by evaporation was significant. It is clearly possible that a dynamic equilibrium was achieved, with the rate of water withdrawn from the porous ceramic disc equating the rate of water evaporating into the air pressure chamber/air supply system. However, if this was the case, water content should have been underestimated whereas the pressure plate seems to overestimate the water content with respect to the tensiometer at given suction. This is the reason why we have been looking for other explanations and found that the contact pressure may in part explain the observed discrepancies. In this respect, it is worth noticing that the weight applied at the top of the samples tested by USTRAT to improve contact had negligible effect on the water flow process. The change in total isotropic stress on the initially saturated samples and, hence, the excess pore-water pressure generated, was very small compared to the initial suction of the sample.